WOODHEAD PUBLISHING IN MATERIALS

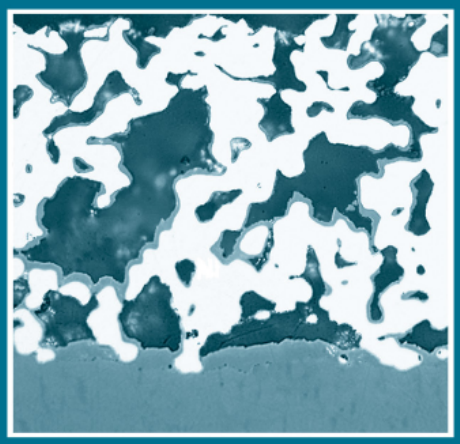

Materials for fuel cells

Edited by Michael Gasik

CRC

WP

Materials for fuel cells

Related titles:

Materials for energy conversion devices
(ISBN 978-1-85573-932-1)
This book discusses a range of materials that can be used to harness and convert solar energy, and explores the properties of oxide materials and their uses in producing hydrogen fuel. It also covers thermoelectric materials and devices for power generation, ionic conductors and new types of fuel cells. Chapters review the use of such materials in the immobilisation of nuclear waste and as electrochemical gas sensors for emission control.

Solid-state hydrogen storage: Materials and chemistry
(ISBN 978-1-84569-270-4)
The next several years will see an emergence of hydrogen fuel cells as an alternative energy option in both transportation and domestic use. A vital area of this technological breakthrough is hydrogen storage, as fuel cells will not be able to operate without a store of hydrogen. The book focuses on solid-state storage of hydrogen. Part I covers storage technologies, hydrogen containment materials, hydrogen futures and storage system design. Part II analyses porous storage materials, while Part III covers metal hydrides. Complex hydrides are examined in Part IV, and Part V covers chemical hydrides. Finally, Part VI is dedicated to analysing hydrogen interactions.

The air engine: Stirling cycle power for a sustainable future
(ISBN 978-1-84569-231-5)
The Stirling air engine is the core component of combined heat and power systems, and is becoming an important sustainable technology in other areas. Increasing demands are being placed on the technology to further increase its thermal efficiency and specific power. This important new book discusses how redesign of the regenerator can maximise the potential of this important technology.

Details of these and other Woodhead Publishing materials books, as well as materials books from Maney Publishing, can be obtained by:

- visiting our web site at www.woodheadpublishing.com
- contacting Customer Services (e-mail: sales@woodhead-publishing.com; fax: +44 (0) 1223 893694; tel.: +44 (0) 1223 891358 ext. 130; address: Woodhead Publishing Limited, Abington Hall, Granta Park, Great Abington, Cambridge CB21 6AH, England)

If you would like to receive information on forthcoming titles, please send your address details to: Francis Dodds (address, tel. and fax as above; e-mail: francisd@woodhead-publishing.com). Please confirm which subject areas you are interested in.

Maney currently publishes 16 peer-reviewed materials science and engineering journals. For further information visit www.maney.co.uk/journals

Materials for fuel cells

Edited by
Michael Gasik

Woodhead Publishing and Maney Publishing
on behalf of
The Institute of Materials, Minerals & Mining

CRC Press
Boca Raton Boston New York Washington, DC

WOODHEAD PUBLISHING LIMITED
Cambridge England

Woodhead Publishing Limited and Maney Publishing Limited on behalf of
The Institute of Materials, Minerals & Mining

Woodhead Publishing Limited, Abington Hall, Granta Park, Great Abington,
Cambridge CB21 6AH, England
www.woodheadpublishing.com

Published in North America by CRC Press LLC, 6000 Broken Sound Parkway, NW,
Suite 300, Boca Raton, FL 33487, USA

First published 2008, Woodhead Publishing Limited and CRC Press LLC

British Library Cataloguing in Publication Data
A catalogue record for this book is available from the British Library.

Library of Congress Cataloging in Publication Data
A catalog record for this book is available from the Library of Congress.

Woodhead Publishing ISBN 978-1-84569-330-5 (book)
Woodhead Publishing ISBN 978-1-84569-483-8 (e-book)
CRC Press ISBN 978-1-4200-7970-8
CRC Press order number: WP7970

The publishers' policy is to use permanent paper from mills that operate a sustainable forestry policy, and which has been manufactured from pulp which is processed using acid-free and elementary chlorine-free practices. Furthermore, the publishers ensure that the text paper and cover board used have met acceptable environmental accreditation standards.

Project managed by Macfarlane Book Production Services, Dunstable, Bedfordshire, England (e-mail: macfarl@aol.com)

Typeset by Replika Press Pvt Ltd, India
Printed by T J International Limited, Padstow, Cornwall, England

Contents

x

Contributor contact details

(* = main contact)

Chapter 1

Michael Gasik
Helsinki University of Technology
Otakaari 1
PO Box 6200
FI-02015 TKK
Finland

E-mail: mgasik@cc.hut.fi

Chapter 2

Karl Föger
Ceramic Fuel Cells Ltd
170 Browns Road
Noble Park, VIC 3174
Australia

E-mail: karl.foger@cfcl.com

Chapter 3

E. Gülzow* and M. Schulze
German Aerospace Center (DLR)
Institute of Technical Thermodynamics
Pfaffen Walding 38–40
70569 Stittgart
Germany

E-mail: erich.guelzow@dlr.de
mathias.schulze@dlr.de

Chapter 4

Christoph Hartnig*, Ludwig Jörissen, and Joachim Scholta
Zentrum für Sonnenenergie- und Wasserstoff-Forschung (ZSW)
Helmholtzstr. 8
89081 Ulm
Germany

E-mail: christoph.hartnig@zsw-bw.de

Jochen Kerres
ICUT
University of Stuttgart
Germany

Werner Lehner
Forschungszentrum Jülich GmbH
IEF-3
S 2425 Jülich
Germany

Chapter 5

Christoph Hartnig*, Ludwig Jorissen, Joachim Scholta
Zentrum für Sonnenenergie- und Wasserstoff-Forschung (ZSW)
Helmholtzstr. 8
89081 Ulm
Germany

E-mail: christoph.hartnig@zsw-bw.de

Werner Lehner
Forschungszentrum Jülich GmbH
IEF-3
S 2425 Jülich
Germany

Chapter 6

Thomas F. Fuller* and Kevin G. Gallagher
School of Chemical and Biomolecular Engineering, and Center for Innovative Fuel Cell and Battery Technologies
Georgia Tech Research Institute
Georgia Institute of Technology
Atlanta, GA 30332
USA

E-mail: tom.fuller@gtri.gatech.edu

Chapter 7

Stephen McPhail*, Elisabetta Simonetti and Angelo Moreno
ENEA – Hydrogen and Fuel Cell Project
C.R. Casaccia
Via Anguillarese 301
00123 S.M Galeria (Roma)
Italy

E-mail:
stephen.mcphail@casaccia.enea.it

Roberto Bove
European Commission
Joint Research Centre
Institute for Energy
Petten
The Netherlands

Chapter 8

Kevin Huang
Stationary Fuel Cells
Siemens Power Generation, Inc.
1310 Beulah Road
Pittsburgh, PA15235
USA

E-mail: kevin.huang@siemens.com

Chapter 9

John Andrews* and Arun Kumar Doddathimmaiah
School of Aerospace,
Mechanical and Manufacturing Engineering
RMIT University
Bundoora East Campus
P O Box 71
Bundoora 3083
Australia

E-mail: john.andrews@rmit.edu.au
arun.doddathimmaiah@of.rmit.edu.au

Chapter 10

A. Smirnova
University of Connecticut
Connecticut Global Fuel Cell Center
44 Weaver Rd
Unit 5233
Storrs, CT 06269
USA

E-mail: alevtina@engr.uconn.edu

Chapter 11

Robert Steinberger-Wilckens*, Jürgen Mergel, Andreas Glüsen, Klaus Wippermann, Ico Vinke, Peter Batfalsky and Martin J. Smith
Institute of Energy Research (IEF) and Central Department of Technology (ZAT)
Forschungszentrum Jülich GmbH
Leo-Brandt-Str.
52425 Jülich
Germany

E-mail: r.steinberger@fz-juelich.de

Chapter 12

Joyce Smith Cooper
University of Washington
Seattle
Washington
USA

E-mail: cooperjs@u.washington.edu

1

Introduction: materials challenges in fuel cells

M G A S I K, Helsinki University of Technology, Finland

1.1 What is a fuel cell?

A fuel cell is an electrochemical device that converts the chemical energy of a reaction (between fuel and oxidant) directly into electrical energy. The basic physical structure, or building block, of a fuel cell consists of an electrolyte layer in contact with a porous anode and cathode on either side [1]. In a typical fuel cell, gaseous fuels are fed continuously to the anode (negative electrode) and an oxidant (i.e. oxygen from air) is fed continuously to the cathode (positive electrode); the electrochemical reactions take place at the electrodes to produce an electric current. A fuel cell should not be confused with secondary batteries (accumulators). The battery (primary) is an energy storage device. The maximum energy available is determined by the amount of chemical reactant stored within the battery itself. The battery will cease to produce electrical energy when the chemical reactants are consumed (i.e. discharged). In a secondary battery, the reactants are regenerated by recharging, which involves putting energy into the battery from an external (electricity) source. The fuel cell, on the other hand, is an energy conversion device that theoretically has the capability of producing electrical energy for as long as fuel and oxidant are supplied to the electrodes [1, 2].

The history of the fuel cell principle dates back to 1839, when Sir William Grove made his famous invention [3, 4]. That fuel cell was in fact the earliest version of a lead-acid accumulator, but it employed platinum electrodes with sulphuric acid electrolyte. Platinum here was seemingly working as both a catalyst and a current collector. However, Grove did consider a fuel cell not as a primary source of power but rather a method "effecting the decomposition of water by means of its composition" [3]. Initially, fuel cells were seen as an attractive means for the generation of power because the efficiencies of other technologies were very poor. For instance, the coal-burning generation station built by T. Edison in Manhattan in 1882 converted only about 2.5% of the available energy into electricity. W. Ostwald has written in his visionary paper about the wastefulness of steam engines already in 1894 and expressed

his hope that the next century would become the ''Age of Electrochemical Combustion" [5]. Still in the 1920s the overall thermodynamic efficiency of reciprocating steam engines was approximately 13–14%, and steam turbines obtained just under 20%. These poor thermal efficiencies provided one of the major motivations for the pioneers of fuel cell development [4]. Because of the role of coal as the major fuel at the beginning of the 20th century, the emphasis was put on coal-derived fuels first. One of the pioneering works was done by L. Mond (founder of INCO) and C. Langer to develop a coal gasification process producing a hydrogen-rich gas [4, 6]. At that time, however, sulphur and other impurities in the gas resulted in fast poisoning of platinum catalysts and thus high costs of the fuel cells' energy. As the efficiency of other technologies rapidly improved, the interest in fuel cells waned. Only when the ''space race'' began in the late 1950s were fuel cells rapidly developed for deployment in space [2, 4].

1.2 Why fuel cells?

Today (and likely still tomorrow) increased energy and power generation demand is being met largely by reserves of fossil fuel that emit both greenhouse gases and other pollutants. Those reserves are diminishing and they will become increasingly expensive [7]. Currently, the level of CO_2 emissions per capita for developing nations is 20% of that for the major industrial nations. As developing nations industrialise, this will increase substantially. By 2030, CO_2 emissions from developing nations could account for more than half the world's CO_2 emissions. These emissions, however, could be substantially reduced, even if hydrogen is derived from fossil fuels, due to the much higher efficiency of fuel cells [2].

The efficiency of a fuel cell (besides absence of moving parts, noise and less emissions) has been the most attractive feature since their invention – unlike a heat engine, the fuel cell does not need to achieve the large temperature differential to achieve the same Carnot cycle efficiency as the heat engine. This is because of the added energy gained from Gibbs free energy as opposed to simply the thermal energy – the theoretical efficiency limit for a fuel cell is thus simply $\Delta G°/\Delta H° = 1 - T \cdot \Delta S°/\Delta H°$. For hydrogen oxidation into water this value is about 80–90% depending on temperature and pressure. The resulting freedom from large temperature differentials in the fuel cell provides a great benefit because it relaxes material temperature problems when trying to achieve comparable efficiency [1].

1.3 Which fuel cell?

A variety of different fuel cell types exist classified by use of diverse categories, depending on the combination of type of fuel and oxidant, whether the fuel

is processed outside (external reforming) or inside (internal reforming) the fuel cell, the type of electrolyte, the temperature of operation, whether the reactants are fed to the cell by internal or external manifolds, etc. [1]. Theoretically, any substance capable of chemical oxidation that can be supplied continuously (as a fluid) can be "burned galvanically" as fuel at the anode of a fuel cell. Similarly, the oxidant can be any fluid that can be reduced at a sufficient rate. Gaseous hydrogen has become the fuel of choice for most applications, because of its high reactivity when suitable catalysts are used, its ability to be produced from hydrocarbons for terrestrial applications, and its high energy density when stored cryogenically for closed environment applications, such as in space. Similarly, the most common oxidant is gaseous oxygen, which is readily and economically available from air for terrestrial applications, and again easily stored in a closed environment [1]. The most common classification of fuel cells is by the type of electrolyte used. It includes:

1. polymer electrolyte fuel cell (PEFC), also known as proton exchange membrane (PEM) fuel cell
2. alkaline fuel cell (AFC)
3. phosphoric acid fuel cell (PAFC)
4. molten carbonate fuel cell (MCFC), and
5. solid oxide fuel cell (SOFC) [1, 2].

PEM fuel cells may also use methanol as a fuel so these fuel cells are often called also "direct methanol fuel cells" (DMFC). "Direct" means that fuel (methanol in this case) is not being externally reformed in any way, but rather oxidised directly. It is clear that the operating temperature, and useful life and power density of a fuel cell dictate the physicochemical, thermomechanical and other properties of materials used in the components (i.e., electrodes, electrolyte, interconnect, current collector, etc.).

1.4 Fuel cells and materials challenges

Fuel cells thus are demonstrating excellent efficiency, high reliability and low emissions. Why are they not yet in our everyday use? Since their invention, fuel cell deployment has been hindered by several major technical factors: high costs of basic elements and materials, uncertain long-term stability of the components, sensitivity to different poisons present in fuels (SO_2, CO, H_2S, NaCl, etc.). Independently of fuel cell types, costs have been the major drawback, raising the fuel cell electricity costs far beyond "conventional" electricity prices despite higher efficiency values. More efficient membranes, electrodes, and catalysts are continually being developed. It is becoming clear that the success of fuel cells will be mainly based on the ability of industry to offer cheaper and better materials: catalysts without noble metals,

new carbon materials, novel electrolytes and membranes, reliable interconnect materials, etc.

Materials challenges for fuel cells are very demanding. In this book only some of the examples will be shown to demonstrate the multifunctionality of the fuel cells environment and the multi-science approach one should use to find proper solutions. Different fuel cell types present different demands for materials combinations and their working conditions. Different applications employ additional constraints. For instance, for fuel cell electrical vehicles (FCEV) current limitations for extreme operating conditions are based on the properties of the materials used in current FCEV prototypes. Increasing the power of a fuel cell stack thus corresponds linearly to increased use of materials like, for example, platinum in the catalyst and weight and volume of the stack. Catalysts are one of the key materials in fuel cells in respect of both performance and costs. It is known that the best catalytic activity in fuel cells reactions is provided by noble metals like platinum, palladium, etc. Unfortunately, extensive use of noble metals is cost-prohibitive – if one considers the US car fleet shifting towards fuel cell vehicles, worldwide platinum and palladium recovery should be increased by at least for 48% at current price levels. It is unlikely that substantial noble metal mining would increase so, and a significant (a few times) price reduction would be expected. Thus, fuel cells must employ alternative catalysts with less noble metals [1, 8–11]. Car manufacturers have noted that strategies have to be developed to increase the specific power density of fuel cells stacks with minimum loss in cell efficiency. New catalysts, oxidant enrichment technologies and catalytic activity increasing are the major directions.

As authors [9] point out, it is of note, that materials presently being used in PEMFC and SOFC are essentially the same as those that were suggested in the 1980s. Despite innovative fabrication processes and materials tailoring, only in the last few years have engineering and commercialisation issues highlighted the inadequacies of originally chosen materials [9].

1.5 Structure of the book

Fuel cells have already been proven to have excellent efficiency versus other means of power generation. The major obstacles seen during the last few years concern cost, long-term durability and service issues. For any material, performance, manufacturing and applications are essential issues. Today, more than ever, the global community can see that the predictions of Jules Verne may finally come to reality. He wrote: “I believe that water will one day be employed as fuel, that hydrogen and oxygen which constitute it, used singly or together, will furnish an inexhaustible source of heat and light, of an intensity of which coal is not capable” (“The Mysterious Island”, 1874). To take a small step towards this vision, the authors of this book have made

a substantial contribution to further research, and critically analysed the most recent developments and trends in fuel cells materials. Readers will be given an insight to general materials issues and challenges, specific fuel cells types and materials thereof, cross-cutting issues like recycling, LCA, novel materials solutions, etc.

As editor of the book, I thank all the contributors for their efforts and hope that this book helps the reader to find new opportunities in development of better materials solutions for fuel cells. On behalf of the contributors, support from numerous international, national and private sources, which have made many of these studies possible, is gratefully acknowledged.

1.6 References

1. M. C. Williams (ed.), *Fuel Cells Handbook*, 6th edn (CD-ROM), NETL/DoE, 2002, 451 pages.
2. M. M. Gasik, *Materia*, 1, 2005, 45–51.
3. W. R. Grove, *The Correlation of Physical Forces*, Longmans-Green, London, 1874, 298.
4. M. L. Perry, T. F. Fuller, *J. Electrochem. Soc*., 149, 7, 2002, S59–S67.
5. W. Ostwald, *Z. Elektrochem*., 1, 1894, 122.
6. L. Mond, C. Langer, *Proc. Royal Soc. London*, 46, 1889, 296.
7. The European Hydrogen and Fuel Cells Technology Platform (http://www.HFPeurope.org/)
8. V. Mehta, J. S. Cooper, *J. Power Sources*, 114, 2003, 32–53.
9. N. P. Brandon, S. Skinner, B. C. H. Steele, *Ann. Rev. Mater. Res*., 33, 2003, 183–213.
10. T. Nissinen, Y. Kiros, M. Gasik, M. Leskelä, *Chem. Mater*., 15, 2003, 4974–4979.
11. T. Nissinen, T. Valo, M. Gasik, J. Rantanen, M. Lampinen, *J. Power Sources*, 106, 2002, 109–115.

2

Materials basics for fuel cells

K FÖGER, Ceramic Fuel Cells Ltd, Australia

2.1 Introduction

This chapter is designed to give an overview of fuel cell technology rather than discuss detailed issues (these will be covered by the individual technology chapters), and is structured into five segments:

1. general introduction
2. fuel cell principles and types of fuel cells
3. overview over stack components and materials issues
4. overview over balance of plant (BOP) components and materials issues
5. summary.

The principle of fuel cells has been known for over 170 years, and despite extensive development efforts during the periods 1955 to early 1970s and from the mid-1980s to now, few commercial products have emerged. Commercial products to date are still primarily focused on space and military applications where other market criteria (costs, life, and durability) prevail compared with civil applications. Reliability is achieved through extensive over-engineering to create redundancy and use of expensive materials in quantities not viable in a civil application. Examples are the United Technologies Corporation (UTC) alkaline fuel cells used in space shuttles and the Siemens proton exchange membrane (PEM) systems for submarines.

Over the past 15 years the substantial effort in making fuel cells a commercial reality funded by some billions of USD in development investment are bearing fruit with (see Figs 2.1 and 2.2):

- > 600 prototype light duty vehicles and >100 buses built and demonstrated with the vehicles clocking up many millions of miles;
- > 800 large stationary fuel cells (>10 kW) built and tested (over 500 installed before 2000), with some phosphoric acid fuel cell (PAFC) and molten carbonate fuel cell (MCFC) systems having shown lifetimes of >30 000 hours;

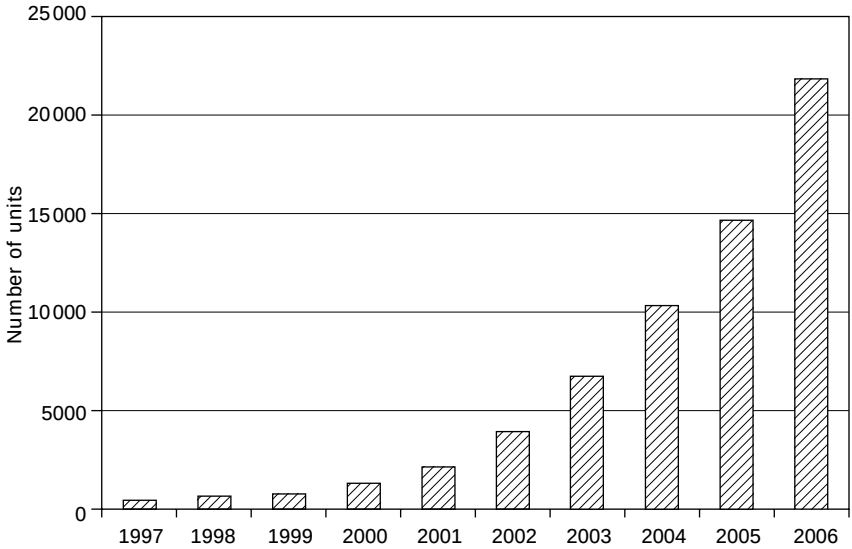

2.1 Cumulative fuel cell units 1997–2006 [1].

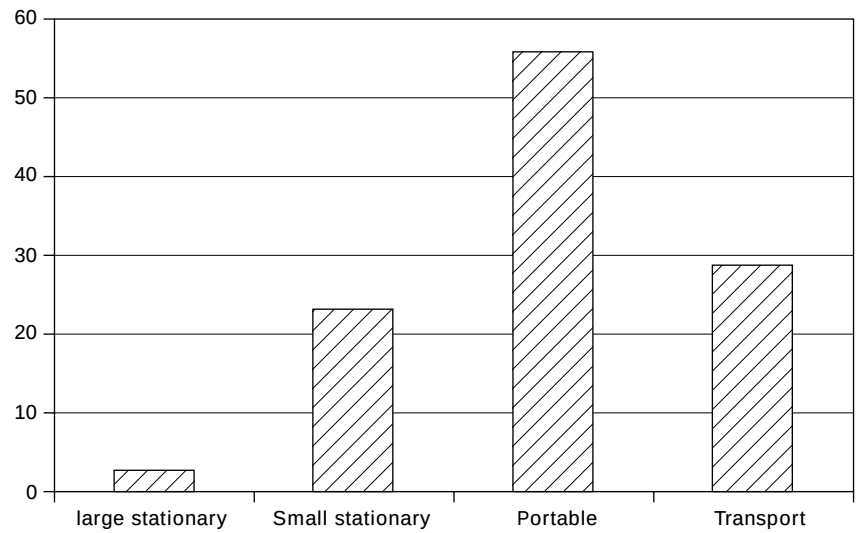

2.2 Fuel cell installations 2006 [1].

- > 5000 small stationary fuel cells (<10 kW) as uninterruptible power supply (UPS) or residential combined heat and power (CHP) installation;
- large numbers of micro-fuel cells and portable systems – 55% of all installations (dominated by number but many of them are very small);
- proton exchange membrane fuel cells (PEMFCs) and direct methanol

fuel cells (DMFCs) are the dominating technologies when only numbers are considered, and of the 2006 installations PEMFC make up over 80%.

The lessons from these demonstrations at real operating conditions (outside laboratories) have been substantial and have shown that fuel cells potentially can fulfil the promises of high efficiency and environmental friendliness. However, the challenges of costs, reliability and volume manufacture are still upon the industry and intensive development and investment is under way to overcome these hurdles. Costs have been decreasing but are still too high by factors of 3–10, and life and reliability is still not commercially viable.

Materials R&D is one critical approach to push fuel cells into commercialisation, as materials hold the key to their commercial success by controlling critical specifications such as performance, lifetime and costs. This applies universally to both low temperature (alkaline, polymer electrolyte, direct methanol and phosphoric acid) and high temperature (molten carbonate and solid oxide) fuel cells; for example the former requiring expensive membranes and catalysts to overcome slow reaction kinetics at low temperatures and the latter requiring materials with long-term stability at temperatures >600 °C. Increased focus is on materials for improved performance, yielding smaller and more compact fuel cell stacks, and replacement of expensive materials with cheaper ones wherever possible. For example, in solid oxide fuel cells (SOFC), improved electrolytes and electrodes allow operation at lower temperature and thus expensive high temperature alloys are replaced with significantly cheaper stainless steel components. The current "rage" in materials science is nanotechnology. Nanomaterials promise to offer higher performance, improved mechanical and electrical properties and better uniformity/homogeneity, but costs and processing difficulties prevent their use to date. Nevertheless the field needs to be closely monitored in order to harness the technology advantages for fuel cells.

In the past, developments often focused primarily on optimising fuel cell stack components (cells, interconnect and flow plates, seals), but neglected other components of a complete fuel cell system including manifolding and insulation. With the increased deployment of field test units, the industry identified that a cost competitive, reliable and durable fuel cell support system (balance of plant – BOP) is equally important, and indeed cost projections assume that in general the fuel cell stack only contributes <30% to the fuel cell system costs. In addition, the assumption that the system can be assembled entirely from commercially available components has proved flawed, as many system components need to be tailored to allow optimised operation of the fuel cell and thus maximise the fuel cell advantages.

Applications largely determine product specifications requiring different

design and operating parameters, life expectations and cost targets and thus have a critical influence on material choices. For example, a mobile application demands fast start-up, many cycles, low volume, low weight and high mechanical robustness whereas in a stationary system high electric and total efficiency, long life, low maintenance and high availability are critical. In addition, cost expectations vary widely from application to application – from one extreme of low cost sensitivity for space and military applications (space shuttle, submarines) with tolerable costs of tens of thousands of USD per kW to the highly cost sensitive automotive sector with price expectations of <50 USD per kW. Stationary systems allow system costs of between 500 and 1500 USD per kW, but require longer life, and in the battery replacement market (e.g. micro fuel-cells and UPS systems) significantly higher costs/kW are acceptable. Technologies (even within a fuel cell type) developed for one application may not be able to fulfil price expectations of a different market segment.

Fuel cells are also not unique in their function – there is a spectrum of well-proven technologies available for the production of electricity. They need to be seen as "replacement/improvement" technology for

- various types of internal combustion (IC) engines in mobile applications
- central power stations, gas turbines and diesel generator sets in the stationary power market, and
- numerous battery types in the secure power (UPS), portable and micro-device markets.

Thus fuel cells need to outperform their competitors, many of them optimised through intensive development over the past 50–100 years such as the IC engine. For example, in a modern car the engine-based drive train (engine + gearbox) costs <$50 per kW. In a fuel cell car this equates to the fuel cell plus electric motors – a very challenging cost target for this application. Operational parameters such as start-up/shut-down time, number of cycles, temperature, fuel types and purity control degradation, corrosion, failure modes through stresses strongly influence materials selection.

Volume manufacturing with high yield, uniform high quality and being within cost targets is key to high market penetration of fuel cells. Materials selected for components of the stack and BOP need to support volume manufacture, and supply chains need to be built to avoid substantial input material shortages and associated cost penalties.

In summary, for fuel cells to become commercially successful, the fuel cell industry needs to solve the issues of reliability, costs, design of "real" products and mass production. R&D needs to focus on:

- material quantity reduction through higher performing materials and/or design optimisations: the development of combinatorial design approaches may prove very useful and time saving

- optimisation of materials selection (design solution versus material solution) – replacing expensive materials for cheaper ones wherever possible
- reducing complexity of the integrated products (part count reduction)
- selection of designs and materials supporting cost effective volume manufacture and streamlined manufacturing processes as well as building of supply chains and use of common components.

2.2 Types of fuel cells

2.2.1 Operating principles and efficiencies

Fuel cells convert hydrogen-containing fuels via an electrochemical process into electricity and thermal energy. The electrochemical fuel conversion leads to a *highly efficient and low polluting process for conversion of fuel energy to electric energy*. Fuel cells can also be viewed as complementary to renewable energy technologies, and have the potential to play a critical role in the transition from a fossil fuel dominated world as well as in a future renewable energy era, but only if they can deliver economic and environmental advantages over current technologies. Fuel cell efficiencies are not determined by the Carnot cycle principles of heat engines and therefore have the potential for very high conversion efficiencies (Fig. 2.3).

The overall efficiency of the fuel cell is defined as the product of fuel efficiency (η_f), electric efficiency (η_e) and fuel utilisation (U_f):

$$\eta = (\eta_f)\ (\eta_e)\ (U_f)$$

The fuel efficiency (φ_f) is defined by the reversible energy of the fuel conversion process. The value varies with temperature depending on the entropy of the reaction:

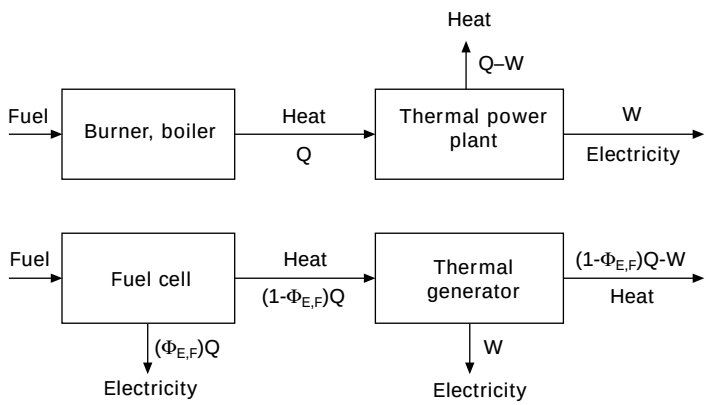

2.3 Fuel conversion Carnot cycle and fuel cell.

$$\eta_f = (\Delta G/\Delta H)100$$

U_f = mass of fuel reacted in cell/mass of input fuel (commonly up to 90%)

$$E_{OC} = -\Delta G/nF$$

where n = number of electrons transferred and F = Faraday constant

The electric efficiency (η_e) includes all resistive (IR) and overpotential (ν) losses:

$$(\eta_e) = E_{OC} - IR - \nu$$

Hydrogen conversion:

$$H_2 + {}^1/_2O_2 \rightarrow H_2O \text{ (2 electrons transferred)}$$

$$E_{OC} = E_o + (RT/2F)\ln(P_{H_2}/P_{H_2O}) + (RT/2F)\ln(P_{O_2})^{\frac{1}{2}}$$

Carbon monoxide conversion:

$$CO + {}^1/_2O_2 \rightarrow CO_2 \text{ (2 electrons transferred)}$$

$$E_{OC} = E_o + (RT/2F)\ln(P_{CO}/P_{CO_2}) + (RT/2F)\ln(P_{O_2})^{\frac{1}{2}}$$

Methane conversion:

$$CH_4 + 2O_2 \rightarrow CO_2 + 2H_2O \text{ (8 electrons transferred)}$$

$$E_{OC} = E_o + (RT/8F)\ln(P_{CH_4}/P_{CO_2}P_{H_2O}^2) + (RT/8F)\ln(P_{O_2}^2)$$

When electric losses are minimised, fuel cells have the potential for very high conversion efficiencies (>60%). For example, the theoretical efficiency for hydrogen conversion at 80 °C (common operating temperature of polymer fuel cell) is 80% (HHV). For hydrogen fuel this value is strongly temperature dependent, 77% at 200 °C, 70% at 600 °C and 62% at 1000 °C. For methane in contrast the theoretical conversion efficiency is close to 100% at all temperatures. The real efficiency of a hydrogen fuel cell at 80 °C would thus be defined as:

$$\eta = 0.8 \times V_{cell}/E_{ideal} \times U_f = 0.8 \times V_{cell}/1.18 = 0.678 \times V_{cell} \times U_f$$

Operation of fuel cells does not involve high temperature thermal combustion processes and in addition the electrolyte membrane separates the oxidant (air) and the fuel. This ensures very low NO_x emissions. Most fuel cells are sensitive to sulphur, thus compounds containing sulphur need to be removed from the fuel before entering the fuel cell. Thus sulphur emissions are also very low.

A fuel cell system can be dissected into four primary sub-systems each with a number of critical components:

1. Cell: anode, electrolyte, cathode and their support structures
2. Stack: cell, interconnect, flow fields, contact layers, manifold, end plates, current collectors, pressure (spring) plates
3. "Life" BOP: manages critical functions for stack operation such as fluid inputs and outputs (fuel, air, water management) and thermal control
4. External BOP: provides connections to the "outside world": fuel, electric power, control system including remote control, water, and heat recovery.

A single cell under load delivers about 0.5 to 0.8V and current densities of 0.15 to several A/cm^2. In order to achieve useful devices, cells need to be stacked in series and parallel to form a fuel-cell stack. A number of these stacks will form the fuel cell module. Thus fuel cells are fully modular technologies. A prime objective of all fuel cell R&D is to increase power density per area of membrane or per volume of stack for cost reduction and operation at the highest possible efficiency point. Volumetric power density in particular scales directly into costs as quantities and thus costs of materials per kW are minimised.

This module needs a life-support system commonly called "critical", "essential" or "life" BOP and an input/output control. On the input side the fuel cell requires the fuel and the air supply system, and often a recycle stream for reactant recycle and cooling. The fuel supply consists of the fuel flow control (pump, compressor), a fuel cleaning system (e.g. sulphur removal), fuel processing (reformer) and, if required, fuel inlet heat exchangers. The air supply system consists of a filter, a blower or compressor and an air inlet heat exchanger. On the output side the fuel cell needs a power conditioning system (fast load response unit, inverter, control system) and a heat management system to recover heat for internal (parasitic) use and for export.

The different types of fuel cell technologies offer special features that may favour specific applications [2], but their full product potential will only be understood after commercial introduction. High conversion efficiencies, low pollution, low noise, modular construction and potential for low costs are critical parameters to open up large market segments.

The common classification of fuel cells is according to their electrolyte material, but in this chapter, the fuel cells will be classified according to their operating temperature into low temperature fuel cells with operating temperatures up to 300 °C, intermediate temperature fuel cells operating between 300 and 600 °C and high temperature fuel cells operating above this temperature. The operating temperature regime determines material choices, fuels used in the fuel cells and fuel processing options (Table 2.1).

2.2.2 Low temperature fuel cells

These are characterised by fast start-stop and use of carbon and polymer construction materials, but require (with the exception of the direct alcohol

Table 2.1 Fuel cell types and characteristics

Fuel cell type	Operating temperature (°C)	Transfer species/ electrolyte	Electrodes/ reactions	Power densities
Alkaline	LT 60–90	OH^--KOH	Anode: Pt, Ni, others $2H_2 + 2OH^- \rightarrow 2\,H_2O + 2e$	<200 mW/cm^2
	HT (pressurized) >100		Cathode: Pt or Ag $^1/_2\,O_2 + H_2O + 2e \rightarrow 2\,OH^-$	>500 mW/cm^2
Polymer	LT	H^+, Nafion type	Anode: Pt $H_2 \rightarrow 2\,H^+ + 2e$	>500 mW/cm^2
	HT	H^+, Phosphoric acid	Cathode: Pt $^1/_2\,O_2 + H^+ + 2e \rightarrow H_2O$	
Direct methanol	50–100	H^+, Nafion type	Anode; Pt, Pt-Ru $CH_3OH + H_2O \rightarrow CO_2 + 6H^+ + 6e$ Cathode: Pt $\frac{3}{2}O_2 + 6H^+ + 6e \rightarrow 3\,H_2O$	<100 mW/cm^2
Phosphoric acid	150–220	H^+, Phosphoric acid	Anode: Pt $H_2 \rightarrow 2H^+ + 2e$ Cathode: Pt $^1/_2\,O_2 + H^+ + 2e \rightarrow H_2O$	150–175 mW/cm^2
Low temperature SOFC	400–600	O^{2-}, GDC/SDC, LGSM H^+, cerates, zirconates	Oxide ion conductor: see SOFC Proton ion conductor: see PEMFC	
Molten carbonate	650	Alkali carbonates in $LiAlO_2$ matrix	Anode: Ni $H_2 + CO_3^{2-} \rightarrow H_2O + CO_2 + 2e$ $CO + CO_3^{2-} \rightarrow 2CO_2 + 2e$ Cathode: Li doped NiO $^1/_2\,O_2 + CO_2 + 2e \rightarrow 2CO_3^{2-}$	100–150 mW/cm^2
Solid oxide	>700	O^{2-}, 3YSZ, 8YSZ, LSGM	Anode: Ni-cermet $H_2 + O^{2-} \rightarrow H_2O + 2e$ $CO + O^{2-} \rightarrow CO_2 + 2e$ Cathode: Perovskites $O_2 + 2e \rightarrow 2\,O^{2-}$	Small cells up to 1 W/cm^2

fuel cells) pure hydrogen as fuel. At these low temperatures only noble metal catalysts are active enough for oxygen activation (except for alkaline fuel cells (AFCs)) and for fuel conversion at the electrode–electrolyte interfaces, and these catalysts are costly and very sensitive to poisons, such as carbon monoxide and sulphur compounds. The lack of a hydrogen infrastructure (production and storage of hydrogen) has proven a significant impediment to commercialisation. Conversion of hydrocarbon fuels (e.g. natural gas) by reforming to syngas and extensive cleaning to remove CO significantly lowers the efficiency of conversion of natural gas to electricity. However, the potential environmental benefits the technologies could bring in transport, portable and stationary power has driven substantial development efforts, and significant progress has been made addressing the above commercialisation hurdles.

Alkaline fuel cell

AFCs have been very successfully used in space applications since the 1960s – US Apollo and Space Shuttle program (supplied by United Technologies Corporation) and the Russian space program. During the past 10 years AFCs have been revived by a small number of companies – Astris Energi (Canada), Intensys, AFC Energy (UK, technology from Elenco), Apollo Energy Systems (US), ZAO Independent Power (Russia), DLR (Germany), Gaskatel (Germany), Ovionic Fuel Cell (US) and Oy Hydrocell (Finland) for terrestrial applications, in particular for the transport and portable power sector [3].
The basic fuel cell reactions are:

$$\text{Cathode: } {}^{1}/_{2}\ O_2 + H_2O + 2e \rightarrow 2\ OH^-$$

$$\text{Anode: } 2\ OH^- + H_2 \rightarrow 2\ H_2O + 2e$$

AFCs operate in the temperature range 60–250 °C (but mostly <100 °C), and can be built both in monopolar and bipolar stack configurations. Space and submarine applications use pressurised AFCs operating with pure hydrogen and oxygen, which ensures high power densities (up to 1 kW/kg). For example, the United Technologies space shuttle fuel cell operates at 4 atmospheres and 90 °C and has a power density of about 300 W/kg [4]. For terrestrial applications the recent focus has been on monopolar stacks operating at 60–100 °C and ambient pressure with hydrogen and air. Power densities under these conditions are in the vicinity of 100–180 mW/cm^2, but developers claim that with more optimisation significantly higher performance is possible.

The prime advantages of AFCs of (i) excellent electrochemical performance over a large temperature and pressure range; (ii) high efficiency (50–60% on ambient air/hydrogen and >70% on pressurised O_2/H_2), (iii) fast start and freeze start, (iv) cheaper electrode materials with some CO tolerance, (v) cheap stack construction materials, and (vi) simple system design drive the

current renewed interest in the technology. In the 1960s Union Carbide built a 125 kW fuel cell system for a small bus, the United Technologies Orbiter fuel cell produces 12 kW at 28 V and recent portable AFC demonstration ambient pressure systems are being offered by Astris Energi (5 W to 2.5 kW), Gaskatel (250 W) and ZAO Independent Power Technologies (6 kW at 30 V). Ovionics Fuel Cells is developing a 5 kW metal hydride AFC portable power system and claims that scaling to 100 kW is possible, while Oy Hydrocell offers "fuel cell battery" systems from 7 Ah to 220 Ah. CO_2 poisoning has been addressed by effective scrubbers (lime and amine) and recirculating electrolyte, but further improvements in performance, life and costs will be necessary for most commercial applications.

Proton exchange membrane fuel cell

PEMFCs have demonstrated the widest spread in applications and size, from micro-fuel cells to large stationary, but the prime focus is in the micro-/portable market, transport and small stationary – over 80% of all fuel cell units built were PEMFCs [5]. The latter application is predominantly pursued in Japan with cumulatively over 1200 units installed by the end of 2006 (780 in 2006 alone) and a further 1000+ are scheduled for installation in 2007 [6]. PEMFCs also dominate the transport market segment in light duty and in the bus market (but the cost targets of <USD50 per kW for this segment are very challenging), and they share the speciality vehicle sector and portable/micro-fuel cell market segment with DMFCs. However, PEMFCs were unsuccessful in the large stationary market segment (only a few units were built and tested) [7]. The main issue in the stationary market is the complex reforming and gas cleaning process required to supply clean hydrogen (CO concentrations of <50 ppm) from fuels such as natural gas, propane and liquid hydrocarbons causing a significant efficiency penalty, and thus such systems are only attractive if fast heat-up is desired. Power back-up (e.g. Plug Power's Gencor and Gensys systems) appears an attractive early market [8] with lower entry hurdles (higher allowable costs and lower lifetime targets).

A large number of companies are developing PEMFC technology, and the sector also has developed a reasonably "mature" supply chain, making it the only fuel cell technology where stack construction is possible without significant infrastructure investment. Some of the leading players are Ballard Power Systems, UTC, Plug Power, General Motors, Honda, Toyota, Nuvera, Sanyo, Matsushita, Toshiba, Nedstack, Voller, Intelligent Energy.
The basic fuel cell reactions are:

$$\text{Cathode: } {}^{1}/_{2}\, O_2 + H^+ + 2e \rightarrow H_2O$$

$$\text{Anode: } H_2 \rightarrow 2\, H^+ + 2e$$

In general, PEMFCs work in the temperature range 70–80 °C and under

pressure. However, for automotive applications operation at temperatures between 120 and 150 °C is desirable for (i) efficient heat removal (similar cooling system required as in internal combustion) and (ii) increased CO tolerance. The main advantages of PEM fuel cells are:

- fast start-up and capability of many thermal cycles
- potential for low cost and
- efficiency of hydrogen conversion.

Challenges for the technology (in particular for the transport segment where large volume potential exists) are still improved performance, durability, freeze start, costs, water and thermal management. According to Ballard's Technology Roadmap, 60% of the value for targets such as performance and life are already achieved whereas for costs and freeze start time, improvements by a factor >3 are necessary. For high temperature PEMFCs information about stability, corrosion and catalyst deactivation is still limited [9].

A prime commercial hurdle for the transport segment is the lack of a hydrogen infrastructure and efficient on-board hydrogen storage to achieve a driving range of above 300 km. In the stationary fuel cell market, efficiency will become a major driver, as the competition is a very efficient condensing burner for heat generation (>95% efficient) and an ever increasing grid efficiency (currently in Europe 35% and expected to get to 40% in the future). Fuel cells will have to significantly outperform this established energy infrastructure. The US Department of Transportation (DOT) published targets for the transport sector of USD30 per kW for vehicle fuel cells (production volume of 500 000 per year in 2010) at a maximum power density of 0.8 W/cm^2 and a platinum metal loading of 0.25 mg/cm^2 [10].

The large number of demonstration PEMFC systems deployed in the various application segments, allows developers to assess the technology against real product specifications, and clearly identify deficiencies in the design and materials properties and so focus the development effort to solve these issues.

Phosphoric acid fuel cell

PAFC technology is the most mature fuel cell technology. About 100 MW of PAFC systems have been installed and operated worldwide over the past 20 years with installations in the size range from 50 kW to 11 MW. Some of the field test systems supplied by UTC and Fuji Electric have demonstrated the "magical" 40 000 h operational lifetime mark [11]. Up to the mid-1990s there were a number of developers in the USA, Europe and Japan, but currently only UTC Power, Fuji Electric and more recently HydroGen LLC (acquired Westinghouse's air cooled technology) are still producing PAFC. The major hurdle to large-scale commercialisation is still the cost of the units of 4000–

5000 USD/kW that needs to be reduced by a factor of three. Interest in PAFCs has been revived as PEMFC have not been able to match the lifetimes demonstrated by PAFC, and UTC, HydroGen and Fuji Electric believe that a target market price of USD 1500 is achievable through further development and through economies of scale.

PAFC is a proton ion fuel cell, governed by the following electrochemical reactions:

$$\text{Anode: } H_2 \rightarrow 2\,H^+ + 2e$$

$$\text{Cathode: } {}^1/_2\,O_2 + H^+ + 2e \rightarrow H_2O$$

PAFCs need clean hydrogen as fuel, but are significantly less sensitive to small amounts of carbon monoxide in the fuel stream (up to 0.5% CO can be tolerated) compared with for example PEMFCs (<50 ppm), making fuel cleaning less complex and costly. Power densities of atmospheric systems are in the range of 120–180 mW at cell voltages of 0.7 V (voltages above 0.8 V result in increased corrosion). For pressurised systems power densities of up to 350 mW/cm^2 have been achieved, but pressurisation can also lead to higher corrosion. Electric conversion efficiencies, depending on design and operational parameters are in the range 36–42%.

The prime advantages of PAFC are (i) proven fuel cell technology (many field systems installed and operating), (ii) life of 40 000 h demonstrated, (iii) higher CO tolerance compared with other low temperature fuel cells and (iv) suitability for CHP application. The main application for PAFCs is seen in large stationary systems, operating on various fuels, predominantly natural gas. UTC's standard product is the 200 kW AC Purecell200 Combined Heat and Power (CHP) unit (the successor to the P25) with more than 275 installations worldwide [12]. UTC/Toshiba built PAFC power stations up to 11 MW in size. Overal, UTC installed 75 MW of PAFCs in 19 countries, achieving >7 million running hours and generating over 1.1 million MWh. Fuji Electric is commercialising a 100 kW unit, and HydroGen a 400 kW system.

Direct methanol fuel cell

Direct alcohol fuel cells (DMFC and DEFC) are a type of proton exchange fuel cell converting alcohols directly on the anode. Originally developed by JPL Laboratories in California [13] and Los Alamos National Laboratories [14] in the early 1990s, they attracted significant interest in the late 1990s for transport applications in order to overcome the hydrogen infrastructure issues. Daimler Chrysler in collaboration with Ballard had a significant programme and in 2000 demonstrated a 3 kW go-cart vehicle [15]. However, due to methanol leakage from the anode to the cathode, lowering cell voltage (referred to as crossover) and thus power density and efficiency, the interest in DMFC

for mass transport has reduced. Interest remains in specialty applications, e.g. FZ Jülich presented a forklift with a 2 kW DMFC [16]. The main market focus for DMFCs is in the areas of portable and micro-fuel cells (battery replacements). With the vast increase in high functionality portable consumer electronic devices (phones, laptops and entertainment devices) the need for increased battery power has driven micro-fuel cell development. Apart from specialty fuel cell companies (Polyfuel, Smart Fuel Cells, MTI, CMR, and others) all major electronic giants have programmes in the field (Matsushita, Toshiba) and power densities of up to 1200 W/L (three times the density of Li-batteries) have been reported [17]. This market segment has the added advantage of allowing costs of >10 000$/kW. In the small portable sector they also show significant potential due to the simple fuelling infrastructure (methanol cartridges).

The basic electrochemical reactions are:

$$\text{Anode: } CH_3OH + H_2O \rightarrow CO_2 + 6H^+ + 6e^-$$

$$\text{Cathode: } 3/2\ O_2 + 6H^+ + 6e^- \rightarrow 3H_2O$$

Recent announcements by leading developers claim significant progress with improved membranes and diffusion layers and clever fluidic designs. The mixed reactant approach with selective cathode and anode catalyst appears an interesting concept in this market segment. Despite the issues outlined above, DMFCs may become the first volume commercial products [18].

2.2.3 Intermediate temperature fuel cells

Low temperature solid oxide fuel cells

These cells operate below 600 °C, using high conductivity oxygen ion conductors such as gadolinia- or samaria-doped ceria (GDC or SDC) electrolytes or ceramic proton conductors (only in R&D phase). Advantages of operation at low temperatures are fast heat-up and easier insulation, but options such as internal reforming of hydrocarbon fuels are no longer available. Apart from hydrogen and syngas, methanol and dimethyl ether (DME) are very suitable fuels for this operation range. Ideal applications are in the portable (military and recreational) and mobile sector (APUs), but Ceres Power [19] is pursuing a micro-CHP application fuelled with natural gas. Ceres Power claims to build stacks in the kW range, but most other development is still in an early R&D phase.

Ceramic proton exchange fuel cell

These are still in the early R&D stages. Protonic conductivity at temperatures in the 400–600 °C range is generally higher than oxygen ion conductivity.

Oxide based proton conductors of high enough stability to be useful in fuel cells such as barium-cerates and zirconates, are doped with yttria or scandia. Molten salts such as LiNaSO4 in an alumina matrix have also been considered [20(d)]. Noble metals, the standard SOFC cathodes and anodes as well as silver based cathodes are under consideration for electrodes. Alcohols and ammonia have been proposed as useful fuels [20].

2.2.4 High temperature fuel cells

Operating at temperatures above 600 °C, high temperature fuel cells have the potential of high conversion efficiency for hydrocarbon fuels (indeed they may become the most efficient electricity generation technology known), as they allow direct internal reforming of the hydrocarbon fuels in the cell stack giving the dual benefits of efficient fuel conversion and effective thermal management (intimate coupling of the endothermic steam reforming reaction with the exothermic electrochemical fuel conversion reaction). However, the high temperatures of operation pose other challenges, such as high temperature corrosion, creep, materials interdiffusion, thermal expansion issues and in general slow heat-up/cool-down. Thus high temperature fuel cells are more suited for stationary generators rather than mobile and portable applications.

Molten carbonate fuel cell

After some spectacular failures of MW installations, the demise of one of the leading players (MC-Power) in the mid-1990s and plagued by corrosion issues caused by the molten alkali carbonate, MCFCs appeared to be destined for failure. However, some of the leading players, Energy Research Corporation (ERC), now Fuel Cell Energy (FCE) and its partner MTU (now CFC Solutions), Ansaldo and Hitachi battled on and overcame many technical problems through materials and design improvements. To date FCE and the other developers have demonstrated life of three years, have proven electric generation efficiencies in a single cycle of > 50% (and further improvements are expected), have increased the availability of the systems to over 95%, have reduced the costs to about USD 3000–4000 per kW [21], have scaled the systems to MW size (and designs for tens and hundreds of MW power stations are being developed) and established production facilities of >50 MW per year. The complexity and bulkiness of MCFCs restricts their use to the large installations, and therefore the players target the industrial CHP and power station market.

MCFCs are powered by the following fuel conversion reactions:

Anode: $H_2 + CO_3^{2-} \rightarrow CO_2 + H_2O + 2e$

$CO + CO_3^{2-} \rightarrow 2CO_2 + 2e$  CO_2

Cathode: $^1/_2\ O_2 + CO_2 + 2e \rightarrow CO_3^{2-}$

The electrolyte transfer species is the carbonate ion (CO_3^{2-}), and the electrolyte is a combination of lithium- and potassium-carbonate in a structural matrix of α-lithium-aluminate. Nickel oxide and nickel metal structures act as cathodes and anodes. Due to the corrosive nature of the electrolyte melt, the matrix substrate suffers from crystal phase stability and particle growth and leading to changes in the pore structure. MCFCs operate at 650 °C. The power densities are low compared to other fuel cells (in the range 100–140 mA/cm^2 at 0.8–0.85 V) and are strongly temperature dependent (performance at 600 °C is 15–20% lower than at 650 °C caused by the temperature dependence of ionic conductivity and electrode kinetics). Operation at 650 °C offers the option of direct internal steam reforming of methane (from NG, biogas or pre-reformed liquid hydrocarbons) in the fuel cell stack but an active reforming catalyst layer is deposited on top of the anode. The need for CO_2 in the oxidant stream requires the recycling of CO_2 from the spent anode gas into the cathode stream. Residual hydrogen in the spent fuel stream is combusted, but for further efficiency gains separation of the hydrogen (for recycling to the anode) may be advantageous, but would require effective membrane technology.

The prime advantages of MCFCs are (i) high efficiencies on hydrocarbon fuels (50–60%), (ii) ideal for anaerobic digester gas as MCFCs work on diluted fuel and CO_2 in the fuel boosts performance, (iii) apart from sulphur, insensitive to many impurities, e.g. efficiently converts ammonia, and (iv) a high temperature exhaust stream for efficient waste heat recovery.

Fuel Cell Energy (FCE) based in Danbury, USA, is the leading developer of MCFC and offers three system platforms producing 300 kW, 1.2 MW and 2.4 MW. The company has operated over 60 installations producing combined >160 million kWh of electricity. Their annual production capacity is 50 MW and FCE has plans to scale-up to 150 MW [22]. Their Korean partner POSCO is planning a production facility with an annual capacity of 50 MW in 2008 and 100 MW in 2010. FCE's German partner CFC Solutions (owned by Tognum, formerly MTU) has installed and is operating its 250 kW systems in 17 locations and combined these systems have clocked up over 300 000 operating hours [23]. Ansaldo Fuel Cell Company (AFCo) in Terni, Italy, has run demonstrations with 100 kW proof of concept prototypes and is now focusing on a 500 kW power block. AFCo has manufacturing capability of 3 MW pa scaleable to 15 MW pa. Ishikawajima Harima Heavy Industries (IHI) in Japan was involved in the 1 MW demonstration in 1999, and is now

developing a 300 kW pressurised (external reforming) system and operated two units at 2005 World Expo. GenCell Corp in Southbury, USA, claims that its system design and low cost production methods allows the development of cost effective MCFC products in the 40–125 kW range [24], but to date the company has only installed one 40 kW unit.

The progress over the past few years has been impressive, but further improvements in life, reliability and costs are required for large-scale commercialisation. Corrosion of stack and BOP components by volatile alkali compounds are challenging technical issues, and cost reduction to the target values of USD 1000–2000/kW is a significant challenge due to the complexity of the power plant.

Solid oxide fuel cell

SOFCs are characterised similar to the other high temperature fuel cell – MCFC – by highly efficient conversion of carbon based fuels to electricity, but as their multi-layer solid state construction (electrolyte, anode, cathode and possible catalyst and contact layers) allows significant design freedom – various tubular and flat plate concepts are under development [25]. Thus SOFC technology appears to be suitable for a wide range of applications in portable/transport (e.g. auxiliary power units), residential combined heat and power (CHP), commercial CHP and power stations covering the size ranges from a few watts to hundreds of MW (most flexible fuel cell technology). Temperatures of operation depend on the cell structure and chosen cell materials in the range 650 °C–1000 °C, allowing internal reforming of methane from hydrocarbon fuels for high conversion efficiency and generation of high quality heat for CHP applications or for combined cycle (with gas turbine) operation in large systems – projected to lead to power stations with the highest possible electric efficiency (70%).

Development of SOFC technology was pursued intensely during the period 1960–1970 and then again from the late 1980s onwards. Westinghouse (now Siemens) has had an ongoing programme for almost 50 years, and their 100 kW field test unit clocked up over 20 000 hours operation between 1998 and 2002, and after installation of a new stack has been operating in Italy for >16 000 hours [26]. Intensive investment in materials and fabrication R&D over the past 15 years has led to significant increases in power density and stability of single cells, reduction in operating temperature to 700 °C, deployment of field test units from 500 W to 250 kW in size and projected cost reduction to <800 USD/kW in mass production (>250 MW pa) – US DoE SECA Program [27].

The following electrochemical reactions occur in an SOFC:

Anode: $H_2 + O^{2-} \rightarrow H_2O + 2e$

$$CO + O^{2-} \rightarrow CO_2 + 2e$$ (significantly slower than H_2 conversion)

Cathode: $^1/_2\ O_2 + 2e \rightarrow O^{2-}$

The number of SOFC developers is substantial due to the design flexibility and wide applicability of the technology (Table 2.2).

Table 2.2 SOFC developers and technologies

Developer	Technology type	Status
Siemens (Westinghouse)	Cathode supported round and flat tubes	To 250 kW (field tests)
Rolls Royce	Inert supported segmented flat tube	To 40 kW
MHI	Anode supported segmented round tube	To 40 kW (field test)
TOTO	Round tube (similar to Siemens)	kW size
Acumentrics	Anode supported (ASC) round tubes	Up to 10 kW (field tests)
Kyocera	Anode supported round tubes	kW size (field tests)
Universities, R&D organisations;	Various configurations	R&D
Nanodynamics	Electrolyte Supported (ESC) microtubes	50 W (listed as product)
Alpps	ESC and ASC microtubes	Aim for 3–20 kW APU
Toho Gas	ESC microtubes	kW size
Adelan	ESC microtubes	–
Various R&D organisations (AIST, ANL, LBNL, NRC/Can, ARC/Can)	ESC and ASC and metal microtubes	R&D
BMW	ASC and metal supported planar (square)	Stack developer
Ceramic Fuel Cells Ltd	ESC and ASC planar (square)	Micro-CHP (field tests)
Ceres Power	Metal supported planar (square)	–
Delphi	ASC planar (square)	3 kW (APU)
Hexis AG	ESC planar (circular)	Micro-CHP (100 field tests)
GE	ASC planar (circular)	3 kW (discontinued)
Mitsubishi HI	ESC planar (square)	30 kW (field test)
Mitsubishi Materials	ESC planar (circular)	10 kW (field test)
Staxera/Webasto	ESC planar (square)	kW size (APU, micro-CHP)
Topsoe Fuel Cells	ASC planar (square), metal supported	2 kW (field test APU)
Versa Power	ASC planar (square)	3 kW (micro-CHP-field tests)
St Gobain, HC Starck, Ceramtec	ESC and ASC planar cells	Cell suppliers
Plansee/DLR/ Sulzer MetCo	Metal supported cells	–

The large number of developers and the experience gained from field testing in particular in the market segments residential micro-CHP, auxiliary power units (APU) and larger systems will progress the technology significantly, but for full-scale commercialisation, further improvements in stack and system reliability, demonstration of volume manufacture and further cost reductions are required.

2.3 Fuel cell stack

2.3.1 Stack concepts

Fuel cells are low voltage (<1 V) high current (10–500 A) devices and need to be connected in series and parallel to derive a useful generator known as the fuel cell stack. A single repeat unit (Fig. 2.4) consists of the cell (also called MEA – membrane/electrode/ assembly), the interconnector, a gas/ liquid flow structure (can be incorporated in an interconnector or cell) and fuel/air sealing. A number of these repeat units (depending on desired output) are stacked. Critical design parameters include: cell active area, number of cells in the stack, gas and fluid (cooling) manifolding, flow configurations, current collection and sealing/clamping/mechanical loading concept.

The cell stack is terminated by the manifold plate (connects stack to operation critical balance of plant), top end plates and stack thermal insulation. All these components fulfil critical functions and materials selection according to functionality is essential for a high performance, robust and cost effective fuel cell technology.

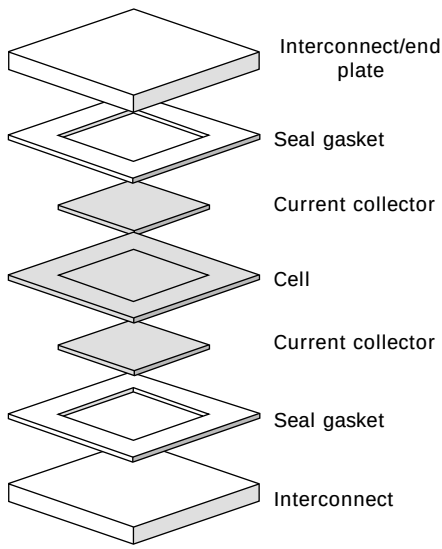

2.4 Schematic of fuel cell repeat unit.

Flat plate or planar stacking concepts are common in most fuel cell technologies, but in the field of solid oxide fuel cells, tubular concepts are of equal importance. The patent portfolio in the field stack/cell materials is extensive and Fig. 2.5 shows the patent distribution according to fuel cell type [28].

2.3.2 Stack components

Cells

Similar to a battery, a fuel cell consists of an electrolyte membrane (ionic conductor for either H^+, OH^- CO_3^{2-}, O^{2-} species) attached to a cathode (positive electrode) and an anode (negative electrode). These functions can be dispersed in support structures that can also act as gas/liquid diffusion layers. Additional catalytic functions can also be added as well as contact layers (Fig. 2.6). Construction materials, geometric shapes and dimensions as well as cell structures vary widely according to the type of fuel cell and the chosen application. Cells need to be produced in volume, thus fabrication methods and materials handling need to be suitable for mass production.

Cell specifications are tightly linked to system and stack specifications, and in general include:

- Geometrical specifications: shape, physical dimensions and tolerances
- Functional specifications: power output and power density, cell efficiency, fuel conversion, air conversion
- Operational specifications: life/degradation; thermal cycle ability, strength/toughness, leak tightness
- Manufacturing specifications: costs, design for volume production, manufacturing process technology.

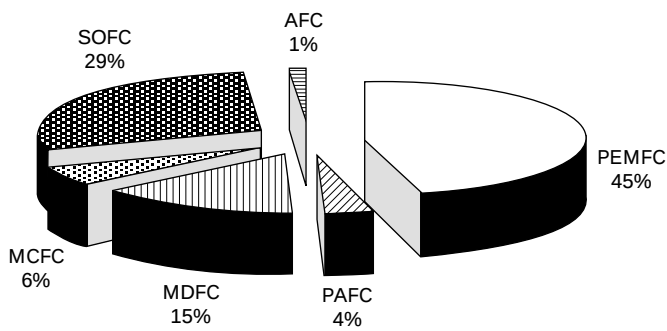

2.5 Materials patents: different fuel cell types.

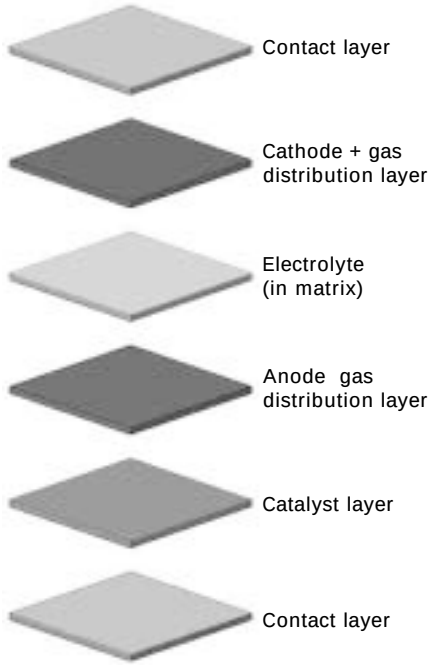

2.6 Schematic of cell structure.

Detailed layer (cell design) specifications:

- Cell materials: support, electrolyte, electrodes, interfacial layers, gas distribution layers, contact layers
- Layer by layer specs and tolerances: thickness and porosity of each layer, conductivity, other properties, e.g. compliance.

Verification of the specifications is critical and requires agreed universal tests able to be conducted at both vendor and developer facilities.

R&D has focused on increasing performance, decreasing degradation and decreasing costs. Materials research is essential, but by itself will not lead to commercially viable fuel cells – similar to other high tech devices this is achieved by an optimised design/materials compromise. Cost reductions are intimately linked to performance (fewer repeat units, less costs), but in addition developers are actively pursuing the options of (i) minimising expensive materials (e.g. noble metals), (ii) substituting expensive materials with cheaper ones, and (iii) simplifying manufacturing processes.

Membrane structures

Critical parameters for membranes in fuel cells include (i) high ionic conductivity (related thickness of membrane layer) – increased cell performance, (ii) phase stability during operation (all states and modes and temperature ranges) and during cell fabrication, (iii) compatibility with other cell (electrodes) and stack components (interconnectors, seals) and (iv) strength and toughness as required by the particular cell/stack design (stresses during operation and assembly).

Alkaline fuel cells

AFCs use a hydroxyl ion conductor as electrolyte, commonly potassium hydroxide solution either circulating with various flow regimes (terrestrial) or immobilised in an asbestos layer (space application) or as a gel layer (micro AFC) [29]. Recently anion exchange membranes have been shown to exhibit good hydroxyl ion conductivity [30]. The lifetime of AFCs can be significantly reduced by CO_2 presence in the gas stream, thus circulating electrolyte is preferred for terrestrial applications.

Polymer electrolyte fuel cells

In PEMFCs the transport species is also a proton, thus the electrolyte is a fast proton exchange membrane. Perfluoro-sulphonic acid membranes (Nafion type) are most commonly used, but due to their expense, low glass transition temperature, stability issues (loss of mechanical properties with time) and high humidification need, a significant effort into developing alternatives has been pursued, such as acidified polymers (sulphonated) and composites containing aromatic or aliphatic polymers. High temperature membranes based on phosphoric acid groups and amide polymers (e.g. polyimidazole) for operation up to 200°C have been developed by companies such as BASF, Asahi, VW, Sartorius and others [9]. These have the added advantage of reduced humidification needs. Thin membranes (20–30 microns) are preferred as they achieve significant improvements in power densities. PEMFC are the first fuel cells in which combinatorial approaches have been used to design new materials [31].

Phosphoric acid fuel cells

In PAFCs the proton conducting electrolyte is phosphoric acid (commonly 100%) held by capilliary forces in a porous structure of PTFE and silicon carbide (SC) (60% porosity). Cell sizes up to about $1\,m^2$ are common. Operation above $160\,^{o}C$ is necessary to expel the water on the cathode side, and good thermal management is essential to keep the concentration constant.

Direct methanol fuel cells

In DMFCs proton exchange membranes similar to PEMFCs are effective (operation temperature 50–100 °C) and similar development efforts to improve the membrane and lower the costs are under way, but the added challenge is prevention of methanol crossover from the anode to the cathode. The required careful design of hydrophilic/hydrophobic properties is often achieved by composite membranes [32].

Molten carbonate fuel cells

In MCFCs the electrolyte transfer species is the carbonate ion (CO_3^{2-}), and the electrolyte is a combination of lithium- and potassium-carbonate held in a structural ceramic matrix (lithium-aluminate). This matrix is produced by tapecasting from the appropriate slurry. For long life the amount of electrolyte in the matrix must be maintained at an appropriate level requiring stable pore structure and surface properties. Issues with the matrix include crystal phase stability and particle growth leading to a changed pore structure (α-lithium aluminate shows increased stability and is the preferred matrix).

Solid oxide fuel cells

SOFCs are solid state devices using a dense ceramic oxygen ion conducting membrane as electrolyte. The membrane can be a structural component (thickness >100 μm) or supported on porous anode or cathode structures (5–50 μm). Common electrolyte materials include the oxygen ion conductors yttria (3 mol% or 8 mol%) stabilised zirconia (YSZ), scandia doped zirconia (SSZ), lanthanum-strontium-magnesium-gallate (LSGM), gadolinia (GDC) or samaria doped ceria (SDC) (for operation <600 °C), and cerates as high temperature proton conductors. The ceramic structures are produced by common ceramic mass production techniques, but the brittle nature of the ceramic material can lead to cracked cells during thermal cycling and operation causing stack failure. Tubular geometries are more robust and for planar cells, developments are under way to support the cell layers on a ductile metallic support structure [33].

Electrodes and support structures

Maximising the three-phase boundary between the reactant gas (removal of diffusion barriers), the catalyst particle and the ionic conductor surface, and providing low resistance paths for the conduction of electrons liberated or used by the electrochemical reactions determine good electrode performance in all fuel cells. At operating temperatures of <200 °C (low temperature fuel

cells), platinum-group metals are the best electrocatalysts and are used extensively in space and military (submarine) applications where high power density per kg is critical but costs are of secondary concern [34].

AFCs, due to the easier oxygen activation in alkaline media allow substitution of these expensive catalysts for cheaper non noble metal catalysts, for example silver on the cathode and finely divided nickel particles on the anode side. Ovionics [35] developed metal hydrides as fuel electrodes providing, in addition, a hydrogen storage capability.

Platinum group metals supported on carbon diffusion media is a major cost item in a PEMFC [10], and platinum loadings in the electrodes have been reduced substantially (to 0.5–0.6 mg Pt/cm^2) by controlled deposition of platinum where it is most effective while maintaining power densities of 0.7 mW/cm^2, but there is a trade-off between costs and life. Platinum alloys are being considered due to better long-term stability [36]. Carbon (fibre cloths, fibre paper), graphitised carbon, carbon composites and polymer materials are most commonly used to fabricate electrodes and gas diffusion layers. They are characterised by large surface area (allowing high metal dispersions), good chemical stability and high electronic conductivity.

Platinum is used as an electrocatalyst on both the anode and cathode side in PAFCs, generally dispersed on carbon black in a porous PTFC structure supported on a porous graphite layer. The combination of materials provides the tailored three-phase interface necessary for efficient gas exchange and phosphoric acid retention. Platinum loadings have been carefully optimised (to reduce costs) and current loadings are about 0.5 mg/cm^2 on the cathode side and 0.1–0.2 mg/cm^2 on the anode side.

Electrocatalysts in DMFCs are Pt on the cathode and Pt-Ru on the anode side. Issues with DMFC include low efficiencies and power densities due to slow kinetics and methanol crossover and complex water management (recycled from cathode to anode).

High temperature fuel cells (MCFCs, SOFCs) do not require noble metals as electrocatalysts, and offer in addition the option to convert a hydrocarbon fuel (such as methane) directly in the fuel cell. Electrode materials in MCFCs are nickel-based – a porous Ni layer (containing chromium or aluminium to increase creep resistance) as anode catalyst and *in-situ* oxidised lithiated nickel oxide as cathode material. Maintaining the pore structure and corrosion of the cathode and cathode current collector have a significant influence on fuel cell life, and a number of coating solutions have been patented to solve these issues.

SOFCs use a nickel-zirconia cermet structure as the anode, and perovskites consisting of strontium (calcium) doped lanthanum-manganite, lanthanum-cobaltite and/or lanthanum-ferrite as the cathode. The anode is often modified to include catalytic functions for internal steam reforming of methane without carbon deposition (or an additional catalytic layer is deposited on the anode).

In metal-ceramic stack structures, cathodes need to be protected from volatile chromium species that evaporate from chromia high temperature protection layers and cause accelerated degradation.

Contact layers

Depending on the type of fuel cell and the cell/stack design, contact layers (current collector layers) can be separate stack components (e.g. meshes) or incorporated in the cell structure (part of electrode structure, layer deposited on electrodes). In low temperature fuel cells these are commonly carbon type materials whereas in high temperature fuel cells these layers are fabricated from modified electrode materials (nickel, perovskites) or metal components (steels, nickel).

Additional catalytic layers

Anodes are optimised for electrochemical reactions, thus if special catalytic functions are required to, for example, process the fuel further to hydrogen for electrochemical conversion such as direct internal reforming, additional "overlayers" may be deposited on the anode or in gas distribution channels specially designed to achieve maximal reactivity for the targeted catalytic reaction (optimised micro-structure and active sites).

2.3.3 Interconnects, flow plates and current collectors

The majority of fuel cells are stacked with bipolar interconnectors as they ensure the lowest contact resistance losses. Exceptions are monopolar alkaline fuel cell stacks and tubular solid oxide fuel cell designs. Interconnector plates commonly act both as flow structures and current collectors, but separate current collectors in forms of meshes, grids and other porous structures (e.g. metal foams) are often used. The flow field design – geometry (parallel, serpentine, biomimetic), channel width to depth – largely impacts the performance of the stack as it governs the delivery of reactant gases across the active area of the cell and removal of reaction products, thermal management and in low temperature fuel cells also water management [37]. Interconnectors are multifunctional and thus pose significant challenges to materials selection. In particular, stability/corrosion resistance in the fuel cell environment (dual atmosphere, current flow), and low costs are issues for most fuel cells, and significantly limit materials choices. Critical requirements include:

- resistance to dual atmosphere exposure (surface and bulk corrosion)
  - fuel environment: hydrogen, methane, carbon monoxide, carbon dioxide, water/steam

  - oxidizing environment: air
- resistance to all corrosive fluids/gases in the fuel cell (phosphoric acid, halides, alkali)
- leak tight for fuel and air
- high electrical conductivity (low resistive losses)
- compatibility with other stack components (seals, contact layers)
- suitability for mass production and low cost.

In low temperature fuel cells (PEMFCs, PAFCs), carbon based interconnectors are commonly used with graphite as the standard, but due to poor mechanical properties and costs, graphite/polymer composites are being considered (at the expense of lower conductivity). Metal interconnectors (titanium, aluminium, stainless steel, other metal alloys) have advantages in particular for transport applications (weight, volume, manufacturability, costs) but surface corrosion is a serious issue, and thus requires surface cladding. For example, metallic bipolar plates are used in MCFCs, but hot corrosion is a serious issue, in particular on the anode side. Austenitic stainless steel of the 300 Series (310, 347, 304) are the materials of choice for the hot components in a MCFC. In order to avoid hot corrosion on the anode side, nickel cladding proved a very effective but expensive solution and alternatives are under development.

In high temperature all-ceramic (tubular) SOFCs (T_{OP}>850 °C), cells are connected via ceramic interconnector strips made of lanthanum-chromite [38] and nickel felt. In SOFCs operating below 850 °C, metallic interconnectors are used. High temperature corrosion resistance (in dual atmospheres) and close thermal expansion matching over the complete temperature range demanded by the brittle nature of the ceramic cells/layers, limits the choice of suitable materials to chromium alloys [39] and high chromium ferritic stainless steels [40]. Volatile chromium species are poisons to the cathode and their evolution needs to be prevented by suitable surface coatings (e.g. cobalt-manganese spinels, cathode materials). On the anode side, nickel contact layers are often used.

2.3.4 Seals

In low temperature fuel cells, silicone elastomers provide good sealing, adequate chemical stability and thermal cycle capability. Seals can be applied by dispensing, printing or provided as gaskets. The molten alkali carbonate is used as wet-seal in molten carbonate fuel cells. In order to prevent corrosion of the steel interconnect the seal areas are protected by alumina coatings. In planar SOFCs sealing is a significant challenge and a substantial development effort is in progress to achieve an optimised solution. Glass based wet-seals and glass-ceramic composites are most common, but corrosion of stack components and matching thermal expansion (thermal cyclability) are still

challenges. Leak rates of compression fibre or mica seals are still too high on the fuel side. Other options under development are brazing – particularly suitable for porous metal supported SOFC cells [41].

2.3.5 Secondary stack components

Manifold to balance of plant

Manifolding between stack and BOP for uniform gas flow (in particular on the fuel side) is critical for stack performance and life. Temperature gradients, materials compatibility issues and complex shapes can lead to plate distortions and contact loss in the end cells (end cell effect) – particularly relevant to a vertical stack supported on a manifold. Materials choices, optimised designs and sealing of the manifolds are particular challenges in high temperature fuel cells due to CTE matching and sealing requirements, and in addition in SOFCs the prevention of formation of volatile chromium species.

Load frame and pressure layers

A critical parameter for stack performance and life is uniform contact (lateral and vertical). This is a substantial design challenge for the load frame and pressure ("spring") layers. Uniform contact is achieved easier in low temperature fuel cells due to the more compliant nature of the polymer stack construction materials and the low operating temperature. However, designers need to carefully consider materials properties (strength, creep, embrittlement) over long periods of time at operating conditions to prevent contact loss and shorten stack life. High operating temperature and associated temperature gradients in high temperature fuel cells limit materials choices for these components severely due to CTE matching requirements and mechanical properties limitations such as hot strength, creep and corrosion resistance. Oxide dispersion (ODS) and super alloys have properties suitable for this application, but they are generally expensive.

External current collectors

Fuel cell stacks are commonly high current–low voltage d.c. devices. This voltage–current characteristic requires excellent electrical conductors to prevent high resistive losses. Materials with the highest electronic conductivity are gold (too expensive), silver, copper and aluminium. Larger cross-sections will be required for metals with lower conductivity such as nickel or stainless steel. Unfortunately excellent electronic conductivity also comes with high thermal conductivity, and the current collector can become a major source for heat loss (particularly in high temperature fuel cells).

Stack insulation

Thermal insulation of stacks is critical to avoid thermal losses and large temperature gradients. Materials used for stack insulation are similar to BOP insulation materials (see Section 2.5.6).

Stack assembly

Most stacks to date are assembled by labour intensive laboratory fabrication processes. Stack assembly lends itself to fully automated (robotic) assembly processes, significantly lowering assembly costs and substantially increasing stack quality. Fuel cell stacks as serial devices are very sensitive to defects (damage due to manual handling – breakage, stresses, finger prints) and assembly faults (misalignment, anode-cathode reversal of cell and interconnect, seal gaskets), and only automated assembly can eliminate these manufacturing defects. Similar experiences are known from other high technology industries, e.g. the electronic industry.

2.4 Balance of plant systems

2.4.1 General system requirements

The balance of plant (BOP) supplies fuel and air, ensures constant stack temperatures and manages required gas/fluid recycles (for example, water in low temperature fuel cells, CO_2 in MCFCs), provides infrastructure for start-up and shut-down as well as ancillary systems for control and power conditioning. Fuel cell BOP varies widely in size (mW to MW) and design depending on type of fuel cell (temperature and pressure of operation), fuel specifications (type of fuel, purity), additional requirements (water management, fluid/gas recycles), and applications such as automotive, portable, battery replacement or stationary. This section deals primarily with essential BOP, the equipment necessary for operation of the fuel cell, not the adaptation of the fuel cell to a special application (heat recovery, combined cycles). Efficient and cost effective thermal and fluids management is a substantial challenge in fuel cell systems. As the emphasis of the book is on materials, this section does not deal with control hardware/software of the fuel cell, readily available and proven equipment, electrical/electronic components and external BOP.

Advanced polymers are used for many BOP components in low temperature fuel cells, whereas stainless steel alloys (predominantly austenitic SS) are the preferred materials for BOP in fuel cells operating above 150 °C. Corrosive liquid streams often containing acids, alkalis or molten salts, fuel streams containing hydrogen, CO, hydrocarbons and poisons such as sulphur compounds, high operation temperatures (for example in SOFCs and MCFCs

and in fuel reformers), temperature gradients and fast temperature changes pose substantial challenges for materials selection to achieve commercially viable fuel cell products (reliability and cost). The fuel cell community has primarily focused on stack issues and costs, but due to the complexity of many fuel cell systems (humidification, thermal and water management, recycles) the BOP may become a formidable challenge in commercialising fuel cells in terms of reliability and costs, and efforts need to be concentrated on simplifying BOP with acceptable trade-offs in performance characteristics. For example, Kenner *et al.* [42] carried out a reliability analysis of a series of field tests using natural gas fuelled PEMFC systems, and Fig. 2.7 shows that the BOP issues caused over 80% of system shut-downs. BOP reliability is controlled by the engineering design, the manufacturing QC and costs ("built-in" reliability). In fuel cell systems for aerospace and military applications reliability has been achieved with multiple redundancy, top quality

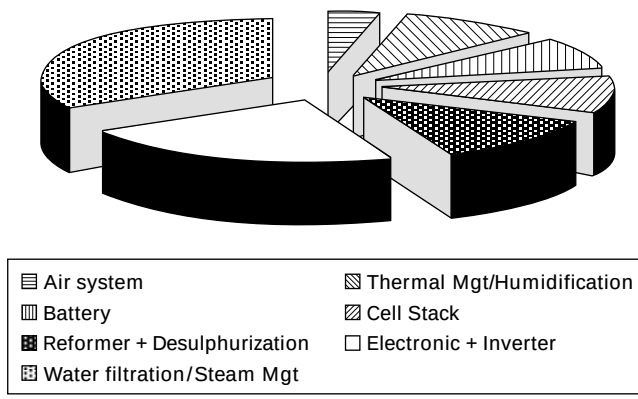

2.7 Reliability of PEM fuel cell system [42].

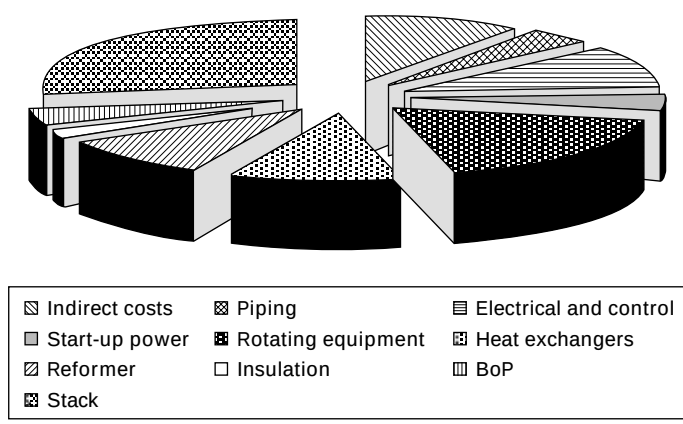

2.8 SOFC costing study [43].

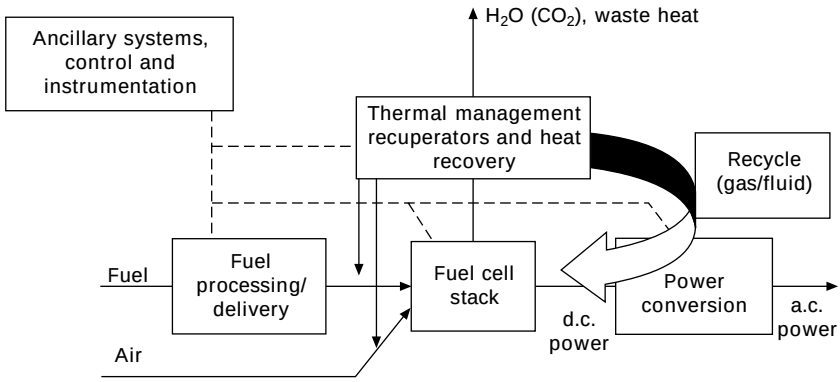

2.9 Schematic of a generic fuel cell power plant.

components and high build quality, but this approach is costly and may never lead to the cost targets necessary for mass market fuel cells. According to a costing study for a 5kW SOFC by TIAX [43] (see Fig. 2.8), the BOP makes up almost three-quarters of the fuel cell system cost, with heat exchangers, rotating equipment, reformer and electrical system contributing over 70% of BOP costs. Design simplification, reduction in parts count, cost optimised packaging and an effective supply chain in combination with high volume manufacturing may prove critical cost down strategies.

2.4.2 System process flow diagrams

Figure 2.9 shows a generic fuel cell system block diagram.

Three primary BOP groups have been defined, each containing a number of sub-systems:

1. *Essential ("life") BOP* supports all system operating modes such as cold start, cool-down to ambient, standby at T_{OP} or $<T_{OP,}$ power-up from stand-by, cool-down to stand-by, load following and emergency shut-down:
   - air delivery system (blower, compressor, metering, pipe work, humidification, pre-heat)
   - fuel delivery system (fuel pump/blower, metering, fuel cleaning, fuel processing, humidification, cooling/pre-heat)
   - thermal management system – air or water cooled (heat exchangers, after/start-up burner, steam generator)
   - recycle streams (water, fuel, CO_2, liquid electrolyte).
2. *Ancillary BOP* ("cold" BOP) supports power management and system control:
   - power conditioning (DC-DC, DC-AC conversion)

- Control system and instrumentation (sensors, hardware, software).

3. *External BOP* is application specific and maximises energy efficiency:
   - housing/pressure vessels
   - waste heat recovery (CHP, CCP, Combined cycle)
   - electricity and thermal storage.

In micro-fuel cells, microfluidic architectures – MEMS type integration – [44] form the essential BOP, whilst MW sized MCFC systems look more like a chemical plant/power station [45] (see Fig. 2.10).

Automotive proton exchange membrane fuel cell propulsion system (hydrogen fuel)

A PEM propulsion system is illustrated in Fig. 2.11.

Challenges:

- air compressor for air delivery
  - within a very tight pressure range ($<<\Delta P$ between air and fuel side to avoid rupturing of membrane)
  - constant flow.
- humidification of air and fuel
  - very clean, de-ionised water
  - requirement for pressure pump.
- efficient cooling
  - small ΔT (heat rejection at 80 °C is difficult)
  - requirement for large radiators.
- operating modes
  - fast thermal cycles
  - fast power cycles
  - sub-ambient start.
- effective on board hydrogen storage
  - low losses over time
  - driving range of >300 km.

Low temperature stationary fuel cell system (phosphoric and fuel cells/ natural gas fuel)

A stationary PAFC system is illustration in Fig. 2.12.

Challenges:

- reformer and fuel cleaning system
  - high temperature (>800 °C)
  - transient operation (temperature, gas throughput)

(a)

(b)

(c)

(e)

(d)

(f)

(g)

(h)

2.10 The wide application field of fuel cells: (a) micro-fuel cell (Fraunhofer IZM); (b) Efoy portable systems (Smart Fuel Cell); (c) 1 kW PEMFC (Ballard Power Systems); (d) residential PEMFC system (Ballard Power Systems); (e) 1 kW SOFC residential CHP system (Ceramic Fuel Cells Ltd); (f) PEMFC stacks (Ballard Power Systems); (g) fuel cell bus (Ballard Power Systems); 1.5 MW MCFC system (Fuel Cell Energy). [The author thanks the companies for providing the images.]

  - requirement of low CO concentrations (high and low temperature shift, staged cooling of reformer exit gas).
- Thermal matching of reformer and fuel cell
  - cooling of reformer gases (ΔT of >600 °C).

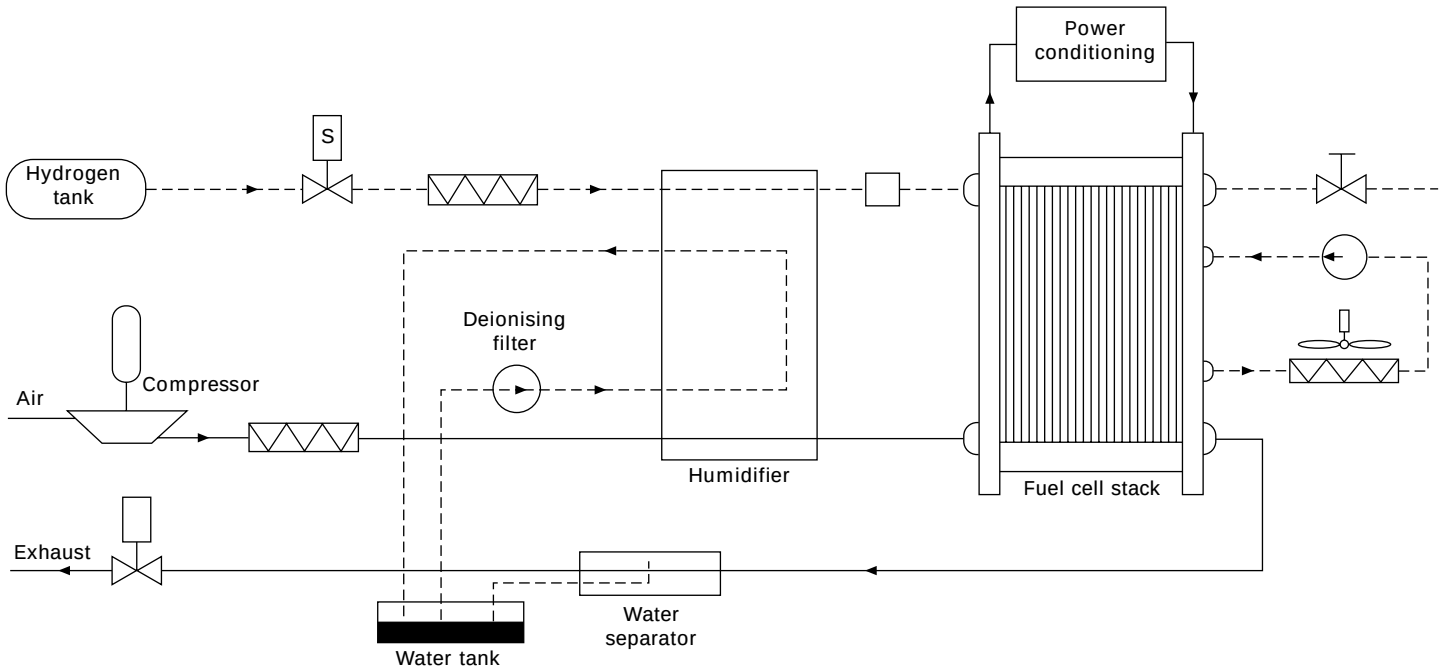

2.11 Schematic of PEM propulsion system.

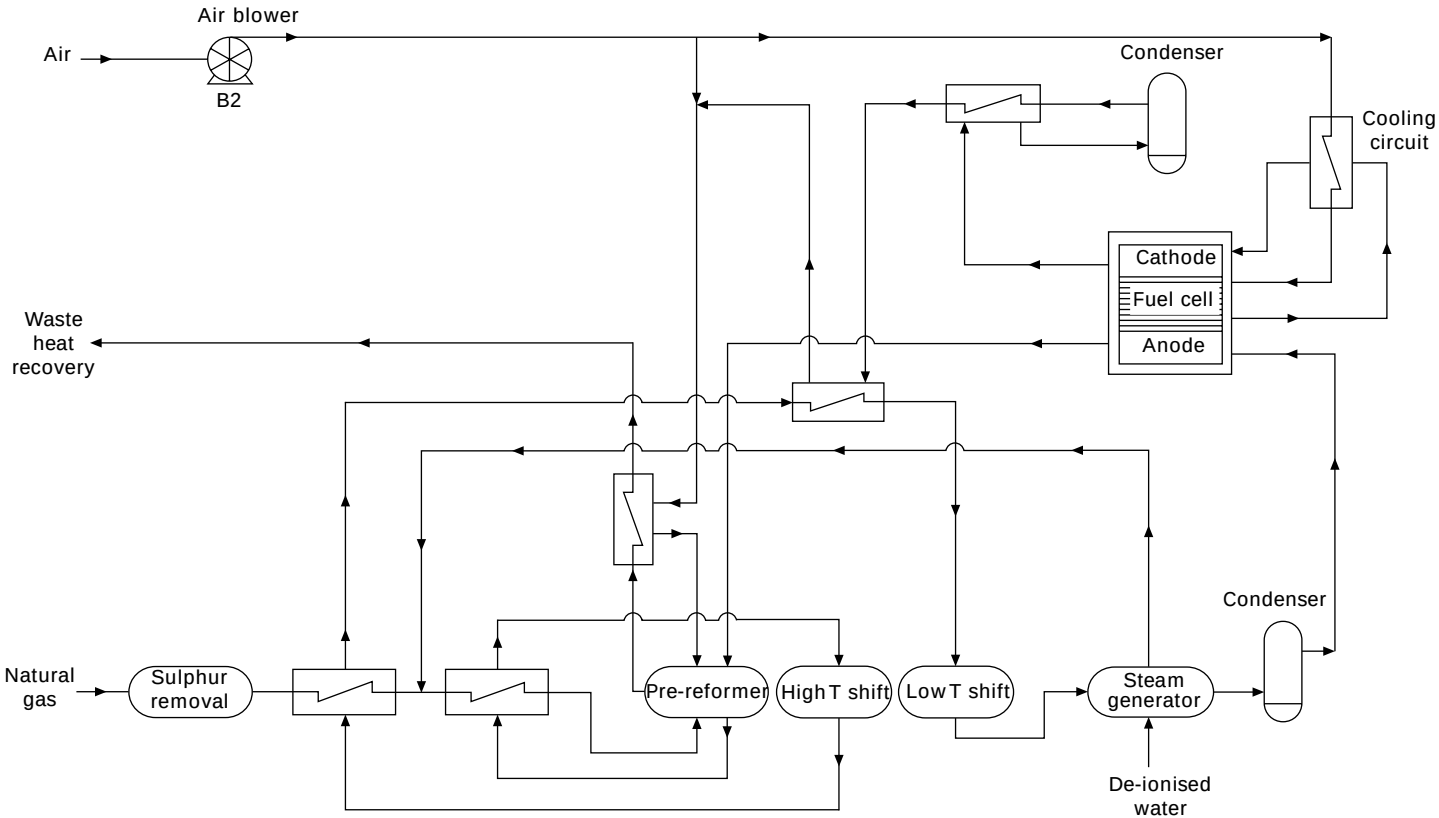

2.12 Schematic of stationary PAFC system.

- water management.
  - water cleaning (de-ionised water)
  - corrosion (acid leaching).

High temperature stationary system (molten carbonate fuel cell-natural gas fuel)

An MCFC system is illustrated in Fig. 2.13.

Challenges:

- heat exchangers and burners
  - high operating temperatures (600–1000 °C)
  - large temperature gradients (<100 °C)
  - thermal expansion matching of materials
  - high temperature corrosion.
- water management for reforming
  - constant steam to carbon ratios
  - water cleaning (de-ionised) to avoid deposits in steam generator and pipes
  - water or steam recycle.
- operational modes
  - start-up and shut-down (heat-up/cool-down times, stress minimisation)
  - emergency shut-down (protection of stack).
- CO_2 separation and recycle (for MCFC).

2.5 Major components and materials requirements for essential balance of plant systems

2.5.1 Fuel delivery sub-system

Fuel pump

Similar to other system components, liquid or gaseous fuel pumps cannot be simply adapted from other industries, for example, components in stationary fuel cell systems require significantly longer life compared to automotive applications. In addition, the specifications are for low parasitic power consumption and special flow and pressure requirements (e.g. no surges). Bearing and sealing failure are the most common failure mechanisms of rotating devices. Careful materials selection, ensuring effective cooling and design features of bearings will be critical criteria in the selection of a fuel pump technology. For example, Capstone Turbine Corp, a manufacturer of micro-turbine generators developed a helical flow pump [46] to achieve required performance parameters and long life. This assembly has the advantages of simple design (only one rotating assembly), surge free operation

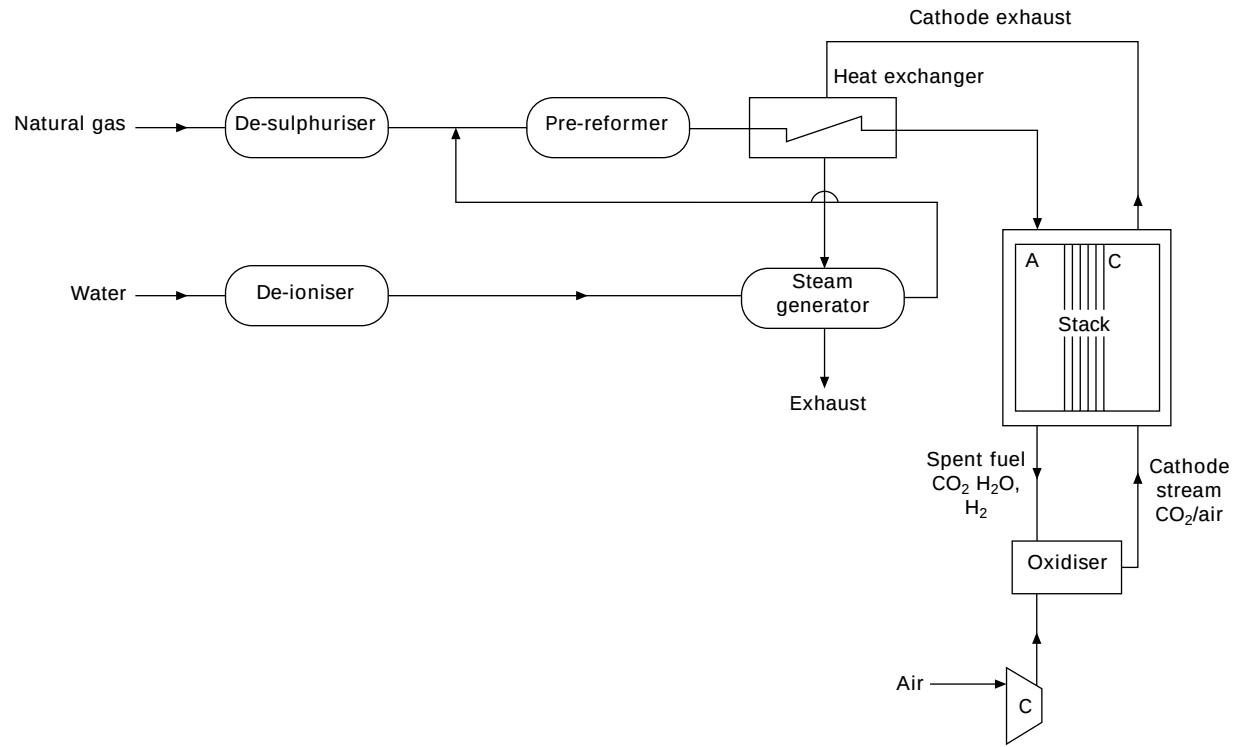

2.13 Schematic of MCFC system.

over a wide operating window, high efficiency, no wear parts and thus long life. Mechanical devices such as ejectors look attractive as they have no rotating parts and do not consume power [47].

Fuel cleaning

The degree of fuel cleaning is determined by the fuel cell type, its operating parameters and whether the fuel is conditioned on-board or clean hydrogen from a central production source (large scale electrolysis, coal/biomass gasification, hydrocarbon steam reforming) is supplied [48]. The challenge with on-board production is ensuring consistent fuel quality (impurity levels) at the transient operation of the catalytic reactors [49].

Hydrogen fuel

The purity levels are strongly influenced by the on-board/on-site production method. Hydrogen produced by electrolysis requires removal of trace oxygen and water, whereas more extensive gas cleaning is essential using reformed gas. Catalytic gas cleaning is shown in Fig. 2.14. The watergas shift reaction converts CO with steam to hydrogen and carbon dioxide. It is a reversible reaction and thus conversions are limited by the equilibrium. Iron-chromium catalyses the high temperature shift reaction (350–500 °C) and copper-zinc catalysts are commonly used for the low temperature shift process (200–250 °C). In fuel cell applications their pyrogenicity makes them difficult to use, and alternatives such as noble metal catalysts on monolithic support structures are available [50]. Membrane reactors (still in development stage) for selective removal of CO_2 would enable single stage reaction and lead to substantially increased removal rates of CO thus avoiding further gas cleaning steps. Removal of trace CO either by selective oxidation or methanation is not required for recirculating AFCs (require CO_2 removal) and PAFCs, and high temperature fuel cells are able to use reformer gas directly.

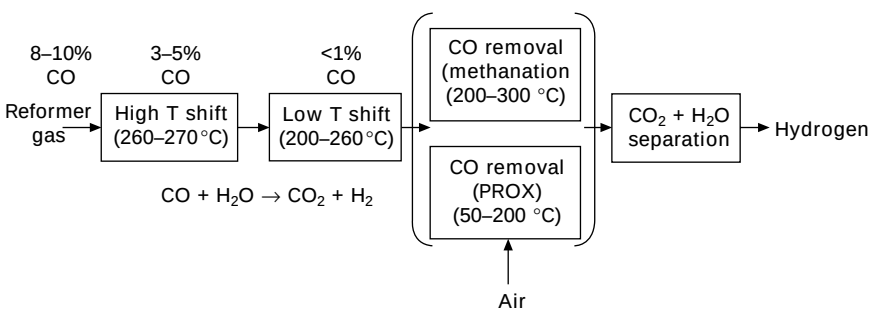

2.14 CO removal scheme.

Alternative cleaning technologies involve pressure swing adsorption systems [51] and membrane technologies [52]. Membranes made of palladium and its alloys have been used for many years for hydrogen purification, but high costs and low throughput limits their use. Significant progress has been made with polymer membranes over the past few years, and these promise effective and low cost hydrogen purification [53].

Hydrocarbon fuels

Most hydrocarbon fuels contain sulphur compounds (from its origin or added as an odorant), for example various mercaptans, dimethylsulfide, tetra-hydro thiophene, COS and H_2S in concentrations 5 to 100 ppm. Higher hydrocarbon fuels such as diesel contain aromatic sulphur compounds such as di-benzothiophene. These sulphur compounds are poisonous to fuel cell electrodes (low and high temperature fuel cells) as well as many fuel processing catalysts and thus need to be removed. Sulphur removal from hydrocarbon gases and liquids is well proven technology in the gas and petroleum industry [54]. Options include:

- *Gas adsorption technology* at ambient and elevated temperatures (activated carbons, metal exchanged zeolites, zinc-oxide formulations) [55, 56]: compared to other systems, the room temperature absorption system offers relatively low sulphur loading at bed breakthrough. Also, the sorbents tend to selectively remove some sulphur species, allowing other species to pass-through.
- *Sulphur compound extraction* from liquid fuels (transition metal-based adsorbents): organic sulphur compounds are selectively adsorbed from the liquid fuel on specially designed sorbents [57], for example transition metals or alloys dispersed in a highly porous inert substrate [58], or Cu^+ and Ag^+ ions anchored in Y zeolites [59]. These sorbents can be regenerated by heating.
- *Hydrodesulphurisation* over cobalt-molybdenum-catalysts plus H_2S adsorption at elevated temperatures on zinc oxide.
- *Oxidation* of sulphur compounds to SO_2 and removal of SO_2 (e.g. calcium-oxide, potassium carbonate).

Humidification, steam delivery

Humidification of the hydrogen fuel is essential in low temperature PEMFC systems. This adds complexity and costs to the system, and significant efforts are in progress to minimise the need for humidification. Membrane humidification systems are commonly used in fuel humidification. Water purity is critical and is cleaned using deionising filters. Water is recovered

from the exit gas to avoid the need for an external water circuit. High temperature PEM systems and PAFC systems have no humidification requirements.

Steam addition to the fuel stream is necessary for the reforming process of hydrocarbon fuels to hydrogen and for prevention of carbon deposition. The steam generator becomes a critical component in the BOP of hydrocarbon fuelled (natural gas, LPG, diesel, alcohol), and high temperature fuel cells. Water purity and constant flow steam generation (no pulsing) are challenging issues. Water can be supplied from external sources (water cleaning system needs to cope with the widely varying water quality at installation sites – identified as a common failure mode) or by condensing the fuel cell exhaust stream. However, even in the latter case a deionising filter may be essential to prevent depositions and clogging in the steam generator. For lowering the load on the steam generator part of the steam could be supplied by direct anode exhaust gas recycle [60].

Fuel reforming

All fuel cells need hydrogen fuel either supplied externally or produced in the fuel cell system. Currently, the most common route for hydrogen production is by reforming of carbon based fuels (natural gas, higher hydrocarbons and alcohols) in a steam reforming [61], partial oxidation or autothermal reforming process. Natural gas is considered the fuel of choice for stationary applications and externally produced hydrogen (hydrocarbon reforming, electrolysis) and methanol for mobile/portable applications. Large scale hydrogen production by hydrocarbon reforming has been practised in the chemical/petrochemical industry for many years, but over the past 15 years a significant development effort has gone into the development of compact reformers for hydrogen production. The tight volume and weight limitations, particularly in the automotive applications but also in distributed generation systems, have forced innovations related to compact fuel processing technologies. Interesting developments are plate type heat-exchange reactors, micro-channel reactors, sorbent enhanced reactors and membrane reactors. All these developments achieve smaller reactors, and the latter two increased conversion at lower temperatures due to the removal of products (CO_2, H_2). These developments have been reviewed in detail by Ogden [49].

Steam reforming of methane is an endothermic reaction and performed at 700–900 °C. It therefore can be efficiently thermally coupled (exothermic fuel oxidation reaction and endothermic steam reforming reaction) with the high temperature fuel cells MCFC and SOFC. In low temperature fuel cells, external heat needs to be supplied to the reformer, the exit stream needs to be cooled and the hydrogen cleaned (see page 41). In industrial reformers, steam to carbon ratios of >3 are used to avoid carbon deposition, but lower

steam ratios are desirable in fuel cell systems.

$$CH_4 + H_2O \rightarrow CO + 3H_2$$

$$CO + H_2O \rightarrow CO_2 + H_2 \text{ (watergas shift)}$$

$$CH_4 + 2H_2O \rightarrow CO_2 + 4H_2$$

Partial oxidation (POX, CPOX) and autothermal reforming (ATR) allow faster start-up.

$$CH_4 + {}^1/_2\, O_2 \text{ (air)} \rightarrow CO + 2H_2 + (N_2) \text{ POX}$$

$$CO + H_2O \rightarrow CO_2 + H_2 \text{ (watergas shift)}$$

$$CH_4 + {}^1/_2\, O_2 \text{ (air)} + H_2O \rightarrow CO_2 + 3H_2 + (N_2) \text{ ATR}$$

However, they lead to lower system electrical efficiency due to

- production of fuels with lower heating value, and in addition if air is used as oxidant, substantial fuel stream dilution by nitrogen
- the exothermic/thermal neutral nature of the reaction prevents efficient coupling with the exothermic fuel cell reaction.

Both catalytic (CPOX) and non-catalytic partial oxidation routes have been developed, and operation temperatures of >800 °C are required for complete conversion of methane. Carbon deposition is controlled by carbon to oxygen ratios in partial oxidation and carbon to oxygen/steam ratios in ATR. The option is favoured for mobile/portable applications where compactness and fast heat-up is critical and where water supply can be a substantial hurdle but where the efficiency penalty is less of an issue.

Three approaches are possible for steam reforming of hydrocarbon fuels:

1. external reforming (the only option for low and intermediate temperature fuel cells)
2. integrated reforming (close thermal integration of reformer and fuel cell stack) and
3. direct internal reforming inside the fuel cell stack.

Efficiencies and operational flexibilities increase when fuel reforming is closely thermally integrated with the fuel cell stack, but integrated and direct internal reforming are the only options with high temperature fuel cells MCFC and SOFC. Integrated reforming is preferred in MCFC to avoid exposure of the reforming catalyst with electrolyte vapours [62]. In SOFC systems using direct internal steam reforming on the anode, the exothermic fuel oxidation reaction is closely coupled to the endothermic steam reforming reaction, and in addition the oxidation product water further drives the reforming equilibrium leading to increased conversions at lower temperatures and lower risk of carbon deposition. Pre-reforming of the higher hydrocarbons (at

temperatures 300–450 °C) to a methane rich fuel is required for both integrated and direct internal reforming to avoid carbon deposition in the fuel feeding pipes and heat-exchanger [63]. The concept leads to electrical system efficiencies of = 50% LHV. Technologies such as plate heat exchange reactors and micro-channel reactors which enable high heat exchange and high reaction rates, are being used in pre-reformers, and planar fuel cell stacks resemble plate heat exchangers, or micro-channel devices.

Materials issues

Careful materials selection for the fuel delivery system is essential to overcome the challenges of:

- stability and life of catalysts for fuel processing (reforming, water gas shift, selective oxidation) due to poisoning, sintering of the active phase at the high temperatures and coke formation: *BOP components need to be designed to allow easy exchange or* in-situ *regeneration of the active catalyst. Recycling of the catalysts will be essential for cost and environmental reasons.*
- corrosion of components due to the high operating temperature and corrosive atmospheres (CO, hydrogen, sulphur compounds): High temperature corrosion resistant alloys are used for reformers. In addition, in carbon containing atmospheres at high temperatures "metal dusting" (a form of high temperature corrosion of steels due to carbon dissolution) is well known from the refining and chemical industries. Repeated temperature cycles accelerate corrosion and dusting, and only alumina protected alloys are able to withstand numerous cycles in these atmospheres with minimal damage [64]. *Careful materials selection will be essential to achieve long life of fuel processing components.*
- metal components made of particular steel compositions, titanium, aluminium become brittle and crack due to a phenomenon known as hydrogen embrittlement. High alloy steels and carbon composites are the preferred materials for high pressure hydrogen vessels/pipes.
- thermal cycling and large temperature gradients of the fuel processing components lead to stresses and thus fatigue failures of, for example, joints.

2.5.2 Air delivery subsystem

Air blower/compressor

The performance characteristic of the air supply blower/compressor is determined by delivery volume, delivery pressure and pressure differential. However, in all applications, reliability and long life and high efficiency

(low power consumption) are critical specifications. Similar to all rotating devices, bearing wear and friction needs to be minimised by applying low-friction and wear-resistant coatings.

Special requirements

Humidification of the air stream, required in low temperature PEMFC systems, is achieved with either a membrane humidifier or an enthalpy wheel [65]. CO_2 needs to be recycled into the air stream in MCFCs [66], and in SOFCs the formation of volatile chromium(6^+) compounds needs to be avoided by appropriate surface protection (for example alumina surface layers) of high temperature components such as heat exchanger, manifold and piping [67].

Air pre-heat

Air needs to be pre-heated to the operating temperature of the fuel cell. In high temperature fuel cells in particular the air stream is used for heat-up of the stack and thermal management and thus is described in more detail in Section 2.5.3.

2.5.3 Thermal management sub-system

Start-up/afterburner

Fuel cells commonly convert between 60 and 85% of the fuel, and the remainder is burnt in an afterburner (anode gas oxidiser). The afterburner can also be used as start-up burner pre-heating the air stream for heating up the fuel cell stack to the operating temperature, but some system designs include both an afterburner plus a start-up burner. In MCFC systems the anode gas oxidiser also directly pre-heats the air cathode stream and supplies the CO_2 for recycle to the cathode – complete fuel conversion and low pressure drop are essential design criteria [68]. Both flame and catalytic burners have been used as after-/start-up burners, each having advantages and drawbacks:

- a flame burner is more reliable and possibly simpler, but the design of a flame burner exhibiting stable operation at all operational modes (start-up, full and partial load, transients) is an engineering challenge.
- catalytic burners (including noble metal catalysts deposited on monolithic structures) operate over a wider fuel composition range, but are sensitive to catalyst poisons, sintering and other thermal damage.

The high temperature operation, the gas atmospheres present in the burners

and the cyclic operation require careful choice of materials characterised by high temperature corrosion resistance.

Stack temperature management

Effective thermal management preventing overheating and high thermal gradients is critical for fuel cell performance and life. Both gas–gas heat exchange and liquid cooling is being used for thermal management (Table 2.3), but the design challenges are simplicity (integrated sub-system designed for manufacturability and assembly) and low weight, volume and cost.

In low temperature fuel cells both liquid cooling using a separate cooling circuit or as in AFCs circulation of electrolyte and air cooled systems have been developed [69]. Liquid cooling is more effective but air cooling may lead to a simpler system. In intermediate and high temperature fuel cells, gas phase cooling is the only option – air cooling or a combination of endothermic reaction cooling (internal reforming) plus air cooling. Radiator technology similar to automotive cooling systems are used for liquid cooling with cooling plates inserted into the fuel cell stack. Gas–gas heat exchangers are used for air cooling. Compactness and heat exchange efficiency (micro-channel devices and foams are being considered) are prime design criteria with often added challenges of low pressure drop, laminar flows and high temperature gradients. Automotive type heat exchangers made of aluminium or graphite due to their low density and outstanding thermal properties are effective for low temperature fuel cells, but corrosion control may prove a challenge. Austenitic stainless steel, superalloys and ceramic heat exchangers are used for fuel cells operating at >500 °C. The materials are chosen for high temperature oxidation resistance and scale spallation prevention (debris from spalled oxidation layers causes blocking of gas channels and possibly short circuiting). In addition, large temperature gradients in both x-y and z dimensions lead to substantial distortions and stresses, and only careful materials selection for both long term and thermal cycling stability will ensure a durable, reliable effective fuel cell system. Fuel cells also have to achieve challenging cost targets requiring clever designs where costly materials are selected only

Table 2.3 Cooling options for fuel cells

PEMFC	AFC	PAFC	MCFC	SOFC
Cathode gas + liquid cooling or cathode gas + water evaporation	Cathode gas + electrolyte circulation	Cathode gas + liquid cooling or steam generation	Cathode gas only or internal reforming + cathode gas	Cathode gas only or internal reforming + cathode gas

where absolutely necessary, and concepts leading to simplified BOP. For example, in high temperature fuel cells (MCFC and particularly SOFC) options have been considered to avoid the need for large air–air heat exchangers and large blowers and thus save significant costs. These include preheating the air by mixing of hot fuel cell exit air with cold incoming air (recycle stream). This recycle can be driven by ejector technology [70] or by entrainment using the Coandă Effect [71].

2.5.4 Recycle streams

Water management

Effective water management avoiding both insufficient humidification of the membrane or flooding of the electrodes is key to the design of robust and efficient PEM fuel cell systems affecting stack performance, system performance (e.g. freeze start), fuel cell life and especially system costs. In traditional PEM fuel cell systems a series of components (humidifiers, several compressors, pumps and de-ionising filters) make up the water management system leading to complexity, reliability issues and increased costs. For commercially viable systems design simplifications will be essential. Examples of such approaches are passive water management within the fuel cell stack combined with latent heat cooling used by UTC, leading to a much simpler system without external humidifiers and compressors including fuel recycle compressor and a smaller cooling circuit [72]. Other approaches suggested are integrated electro-osmotic pumping [73]. As discussed on page 42 effective water management is also a critical issue in high temperature fuel cells to provide steam for steam reforming (integrated and direct internal reforming) – the only option to achieve high electric efficiency.

Gas recycle streams

CO_2 in MCFC

CO_2 is a reactant on the cathode and a reaction product on the anode. It therefore needs to be recycled from the cathode to the anode compartment. The standard configuration is an external recycle, including a flame or catalytic burner to combust left over fuel, high temperature piping and a blower. This sub-system adds complexity and costs and reduces response to load changes thus innovative solutions have been developed to simplify the recycle. For example, direct injection of anode off-gas into air stream [74], or fuel cell energy [75] couples the anode exhaust compartment directly with the cathode compartment and combusts the left over fuel in the cathode compartment, eliminating a separate burner and high temperature piping. An interesting stack internal CO_2 recycle was patented by IHI [76] consisting of an electrolyte

plate with a plurality of fine holes allowing off-gas to pass from the anode to the cathode side.

Steam/anode off-gas recycle

Anode off-gas recycle could assist in boosting fuel utilisations and thus electric efficiencies, and alleviate the very tight manufacturing tolerances needed when high fuel utilisation is carried out in a single pass. Recycle compressors or blowers are available at low operating temperatures. For example, PEM fuel cell systems contain anode recycle loops to assist with humidification of the fuel stream and fuel utilisation [77]. In high temperature fuel cells anode gas recycle could in addition solve the issue of external water supply for steam reforming, avoiding system failures (steam generator blocking) due to water purity, but the design of a reliable hot gas recycle blower is a significant technical challenge. Ejector technology is more suited but difficult to apply in small systems [78].

2.5.5 Manifolding and piping

Extensive piping is expensive and should be replaced by plenum manifolding wherever possible – for example, in low temperature fuel cells moulded pre-formed plastic structures and formed sheet metal or cast structures in high temperature fuel cells. Materials selection is critical due to atmospheres of hydrogen, carbon compounds, high temperatures, and corrosive off-gases. Thermal expansion matching is advisable to avoid fatigue failures during thermal cycling.

2.5.6 Thermal insulation

Thermal losses from the fuel cell stack and essential BOP need to be minimised, thus highly effective insulation is critical. Vacuum insulation is known for its low heat transfer but in general is expensive. Gas filled polymer panels (Ar, Kr) or closed pore foam structures can be used for low temperature fuel cells, but reformers and medium and high temperature fuel cells require insulation exhibiting:

- high thermal transfer resistance (low thermal conductivity, low radiation and convection heat transfer)
- high temperature resistance up to 1000 °C
- thermal shock resistance
- easy to shape (near-net shaping)
- no health hazard
- not combustible
- light weight and low cost.

Microporous insulation (including aerogel) appears ideal and the cost is decreasing with a number of companies now manufacturing the material. Aerogel insulation is made from very small oxide particles forming open cell, nanoporous materials with a free void volume of >95%. The high pore volume, tortuous pore structure and low solids content leads to very low thermal conductivity values. Most aerogels are silica based [79] but high alumina content materials are also available [80]. The insulation is available in panels, can be preformed around components and spray-on versions have also been developed [81].

2.6 Maturing technology

2.6.1 Materials testing and lifetime prediction

Apart from cost issues, reliability and lifetime are still significant hurdles for the commercialisation of fuel cell technology. Different applications demand demonstration of life of 1 to 10 years – automotive 5000 to 7000 hours with many thousand thermal cycles and stationary applications 5–10 years. To demonstrate these targets by "real life testing" is a difficult if not impossible task. Manufacturers need to develop new products in record time and at the same time improve quality and reliability. Products are getting more complex and technologies embedded in high technology products often change faster than the real time testing cycle – the technology is out of date before the test is completed. This is a particular issue during market entry (maturing phase of the technology). Therefore the industry needs to develop accelerated testing regimes and lifetime prediction modelling, just as other high tech industries (e.g. electronics, batteries). Every product deteriorates due to changes caused by intrinsic materials characteristics, operational parameters, build quality and design flaws as well as handling (including abuse) by the customer. High reliability can be designed and built into a product (redundancy, build quality, extensive QA/QC programmes, modularity, high quality robust components), but often achievement of cost targets demand compromises. This requires a clear understanding of the product life cycle: manufacturing, trade-offs, operation, end of life definition and better understanding of reliability issues and constraints (see Fig. 2.15) through:

- development of operational models
- collection of reliability data
- analysis of reliability data and correlation to operational parameters
- real time performance and life testing – understanding of degradation/failure mechanisms
- development of accelerated testing methodology
- development of reliability/lifetime prediction models
- feedback mechanisms into design and manufacture.

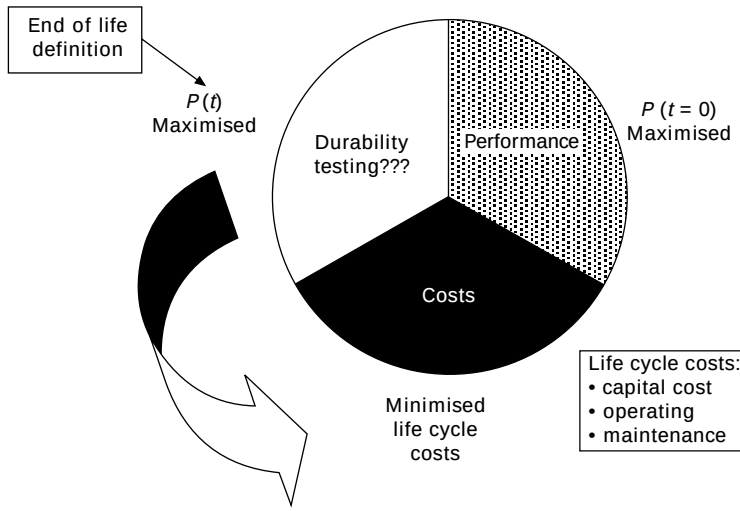

2.15 Commercial product characteristics.

Lifetime prediction modelling requires testing methodologies (industry standardised) for all levels of the product integration – materials, components, sub-system and complete system (including accelerated testing regimes), an extensive reliability database with data on materials stability, component reliability, system reliability and failure modes, as well as development of operational models/simulations to predict stresses imposed on components and materials. During the past two years a number of symposia have been devoted to durability and life of fuel cell systems, most of them on PEM fuel cell technology [82].

Accelerated testing

Accelerated testing is testing of components, sub-systems and complete products under conditions that accelerate their failures, and is commonly classified as qualitative life testing (HALT, HASS, STRIVE) for identification of failure modes and quantitative testing (QALT) for obtaining life prediction data [83]. Accelerated testing is applicable more to the lower integration levels, such as materials and components, and needs careful experimental design to

- obtain a sound understanding of the stress levels the product is exposed during operation including specifications, design limits and destruct limits
- find accelerating variables and understanding their effect on various degradation modes, and
- avoid new failure modes dominating at high stresses.

Use of statistical methods for analysis and correlation of the data, and sound physical/engineering judgment to assess their validity are critical.

Lifetime prediction

The aim of a life data analysis is to define mean times to failure distribution of a component, an assembly, a sub-system or a full system. Common correlation models for reliability data used are Weibull, exponential and lognormal distributions. Assemblies or systems life distributions are constructed from the distributions of its components. Reliability analysis of a system is only possible if not only the individual component reliability distributions are known but also their interdependencies. The reliability relationship between components in the systems is commonly expressed using correlation diagrams such as reliability block diagrams (RBD) and fault trees which are a graphical representation to demonstrate the effect of failure of a component on the failure of the system. The topic has been extensively researched (Fig. 2.16) and commercial software for modelling system reliability is available.

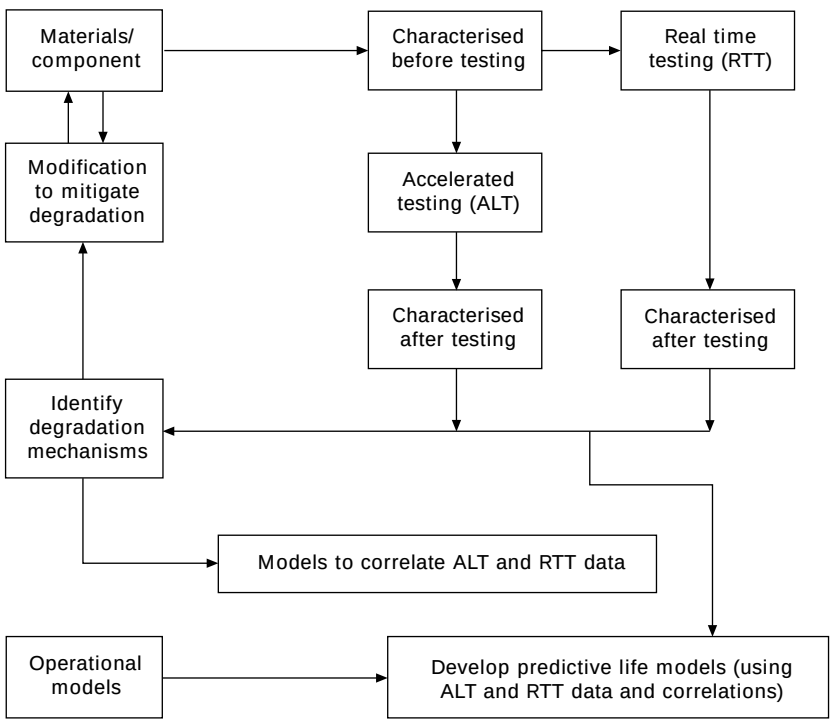

2.16 Flow diagram of development of predictive life models.

2.6.2 Supply chain development

A supply chain is a network of companies to bring a product to market. Effective supply chain management (SCM) is the hallmark of an efficient and mature(ing) industry. Fuel cell systems are complex integrated products and therefore the industry has to develop extensive supply chains, spanning from raw materials processing (metals, ceramic powders, plastics, carbons) to components (MEAs, interconnectors, catalysts, heat exchangers, pumps, blowers/compressors, thermal insulation, seal gaskets), sub-assemblies (fuel cell stack, hot BOP, cold BOP, power conditioning) to full systems (APU, fuel cell drive train, stationary generator, portable generator, micro-fuel cell) as well as associated distribution networks, manufacturing equipment and testing infrastructure. ESCOVALE assembled a fuel cell source book that is a useful resource to identify supplier companies [84]. Each developer has built a supply chain for materials, components and sub-assemblies for their prototype systems, but they are generally focused on a customised design produced in small/pilot-scale volume. For the industry to achieve successful commercialisation, building a supply chain capable of supplying fuel cell tailored materials/components in volume and at target costs will be critical. In 2004 ABI Research produced an analysis of the transportation fuel cell supply chain [85] and discussed some of the issues and challenges. The importance and challenges of supply chain building and management in emerging industries and new product development has been the topic of numerous publications, in particular in an era of fast product development cycles [86].

The concept of integrated value systems attempts to align objectives of the processes of product development and supply chain management. This requires involvement of suppliers early in the product development cycle having the benefit of increasing expertise base (supplier technology and knowledge in specialty area), spreading risk (supplier takes some development risks for future benefits – supply contract) and reducing time to market. However, there are risks such as:

- being locked into a material or technology or component that may not be optimal
- supplier time lines and business strategies that are not aligned with the developer
- conflicting interests.

It is therefore vital to make the right partner choice. However, it can be difficult in the early days of an emerging industry to attract the attention of volume suppliers as developers cannot enter into volume supply contracts. Governments have also recognised the importance of supply chain building for commercialisation of fuel cells, and are offering subsidies to establish “commercialisation” clusters [87]. In PEMFC, Japan has initiated a programme

to encourage component suppliers to develop common components for a number of fuel cell system developers in order to achieve cost targets.

2.7 Summary

Fuel cell technology has been known for over 150 years, but significant investments into their development and upscale during the past 20 years and particular the past 10 years has brought the technology to the commercialisation phase. The challenges are no longer "does the fuel cell work", but does "the fuel cell meet performance, cost and life targets required in *commercial products not just demonstration prototypes*."

Costs and reliability remain the prime hurdles to commercialisation, and the industry is focusing on these issues. The targets for both criteria vary significantly according to application, and some fuel cell technologies are closer to the targets than others (e.g. PAFC systems have demonstrated 40 000 h life, and both PAFC and MCFC with cost of 2500–4000 USD/kW are about a factor 2–3 away from cost targets). Cost targets are most challenging in the automotive sector where fuel cells compete with IC engine based drive trains of 50 USD per kW power, and least challenging in the battery replacement market. In contrast reliability targets are most challenging in stationary power applications with life targets of >40 000 hours (5–10 years).

2.7.1 Materials selection and optimisation

Many materials used in fuel cell stacks and systems have been known for some time, but improved understanding of critical materials parameters (intrinsic properties, microstructure and stability) affecting fuel cell performance through extensive R&D programmes during the past decade has lead to substantial improvements in performance (power density per litre volume) and life of fuel cell stacks. Materials selection is also critical for achieving cost targets, and the objective has to be to *minimise expensive materials* wherever possible. This requires a thorough functional analysis of materials/components used in fuel cell systems to arrive at clear detailed specifications for each component.

Combinatorial methods combined with fast materials screening techniques are increasingly used in the difficult task to find new materials and improve existing ones. Materials used in fuel cells commonly have to fulfil multiple functionalities and the mathematical methods are ideally suited for defining the path to performance improvements [31].

2.7.2 Design for manufacture and maintenance

Volume manufacturing holds the key for achieving cost targets for fuel cell stacks and systems. However, fuel cells are currently produced largely by

labour intensive laboratory fabrication and assembly methods. This approach also poses the challenge whether the design is suited to mass manufacturing, or whether the fuel cell stack/system requires extensive redesign to make it mass manufacturable-an expensive and time consuming exercise. Maintenance costs closely link into the value-preposition for fuel cell systems. System complexity and difficult accessible components substantially increase maintenance costs. As fuel cell technology is entering the commercialisation phase, stack and system designs need to satisfy the well established engineering principles of design for manufacturability and maintenance. Design for manufacturability is built on a detailed understanding of the influences of manufacturing processes and their variabilities on fuel cell performance. This knowledge leads to definition of meaningful tolerances and specifications for materials, components and sub-assemblies. Similar to other commercial products, volume manufacture with high yield significantly influences product costs, and production of consistently high quality components determines reliability and life – *the keys to successful commercialisation of the technology*.

2.7.3 Materials supply chain and recycling

Only through building of competitive supply chains (see Section 2.6.2) spanning from raw materials to sub-assemblies will successful commercialization of fuel cell products be possible. A full product/materials life cycle analysis – encompassing all direct and auxiliary materials used in manufacturing, operation and disposal – not just emissions and energy consumption/savings [88] will help identifying critical issues in the supply chain [89]. The industry also has to consider in detail how to dispose of fuel cell stacks and systems at the end of their useful life. Many contain valuable but also often toxic materials, and a recent article by D. Cohen published in *New Scientist* predicts shortages of materials used in fuel cells [90]. Guidance and technology can be obtained from the electronics industry – EU recycling directive [91] – and the catalyst industry [92].

2.8 Conclusions

Although continuous improvement of the technology will be essential to achieve improved performance, lower cost and higher reliability, it is critical that the industry focuses on getting products into the market place in order to create the income necessary to support further development and improvement of the technology rather than use investor funds. However, for fuel cells to become commercially successful, the fuel cell industry needs to solve the issues of reliability, costs, design of “real” products and mass production. The major technical challenge is the improvement of durability and performance

of the fuel cell stack and a cheaper and simpler balance of plant (BOP). Thus R&D needs to focus on:

- material quantity reduction through higher performing materials and/or design optimisations: in the pharmaceutical industry and in catalysis where complex interaction and multi-functionality of compounds/materials is critical, combinatorial design approaches have proven successful and cost and time saving [93]
- optimisation of materials selection (design solution versus material solution) - replacing expensive materials with cheaper ones wherever possible
- reducing complexity of the integrated products (part count reduction)
- selection of designs and materials supporting cost effective volume manufacture and streamlined manufacturing processes (requires supply chain analysis). Different developers need to look at common components as economies of scale will be necessary to achieve the cost targets in particular in the automotive sector
- building of supply chains considering a full life cycle analysis
- work with the certification authorities to achieve uniform codes and standards.

2.9 References

1. K.-A. Adamson and G. Crawley, Fuel Cell Today Worldwide Survey 2006, Jan 2007, *Fuel Cells Today* (www.fuelcelltoday.com)
2. (a) R. O'Hayre, S.-W. Cha, W. Colella and F. B. Prinz, *Fuel Cell Fundamentals*, John Wiley & Sons, 2006.
   (b) S. Srinivasan, *Fuel Cells from Fundamentals to Applications*, Springer, 2006.
   (c) J. Larminie and A. Dicks, *Fuel Cell Systems Explained*, 2nd edition, Wiley, 2003.
   (d) N. Brandon and D. Thompsett, *Fuel Cell Compendium*, Elsevier Science, 2005.
   (e) K.-D. Kreuer, T. Van Nguyen, T. Zhao (eds), *Advances in Fuel Cells*, Vol. 1, Elsevier Science, 2007.
   (f) S. Basu (ed.), *Fuel Cell Science and Technology*, Springer, 2007.
   (g) W. Vielstich, A. Lamm and H. Gasteiger (eds), *Fuel Cell Handbook – Fundamentals, Technology and Applications*, Wiley, 2003.
   (h) Fuel Cell Handbook, 7th edition, US Department of Energy, 2004.
3. E. Guelzow, Jiri K. Nor, P. Nor and Mathias Schulze, "A renaissance for alkaline fuel cells", *Fuel Cell Review*, Vol. 3, Issue 1, 2006.
4. K. A. Burke, "Fuel Cells for Space Applications", NASA/TM-2003-212730, 2003.
5. Frano Barbir, *PEM Fuel Cells: Theory and Practice* (Sustainable World Series), Academic Press, 2005.
6. Shinji Nishikawa, "Current Status of the Large-Scale Stationary Fuel Cell Demonstration Project in Japan", Presentation 2006 Fuel Cell Seminar, Honolulu, Hawaii, November 2006.
7. (a) K. Washington, "Development of a 250 kW Class PEM Fuel Cell Stack", Abstracts 2000 Fuel Cell Seminar, Portland, Oregon, November 2000, pp. 468.

(b) B. Kohlstruck and R. Keitel, "Applications with PEM Fuel Cells for a Deregulated Market Place", Proceedings Fuel Cell 2000, Lucerne, Switzerland, July 2000, pp. 127.

8. S. Feitelberg, C. Smith, Lam F. Wong, D. B. Parry and R. J. Graham, "Ongoing Development of Plug Power's Next Generation Stationary PEM Fuel Cell System", Presentation 2006 Fuel Cell Seminar, Honolulu, Hawaii, November 2006.
9. (a) Gordon Calundann, "High Temperature PEM Fuel Cells – The New Generation", Presentation 2006 Fuel Cell Seminar, Honolulu, Hawaii, November 2006.
   (b) Eiji Endoh, Satoru Honmura and Hisao Kawazoe, "Highly Durable MEA for PEMFC Under High Temperature and Low Humidity Conditions", Presentation 2006 Fuel Cell Seminar, Honolulu, Hawaii, November 2006.
   (c) A. Reiche, K. Foli, O. Gronwald, S. Haufe, S. Kiel, U. Maehr, D. Melzner, F. Walter and S. Weisshaar, "Sartorious HT-PEM Fuel Cell Technology", Abstracts 2006 Fuel Cell Seminar, Honolulu, Hawaii, November 2006, pp. 300.
10. (a) E. J. Carlson, P. Kopf, J. Sinha, S. Sriramulu and Y. Yang, "Cost Analysis of PEM Fuel Cell Systems for Transportation", TIAX LLC, NREL/SR-560-39104, December 2005.
    (b) E. J. Carlson, P. Kopf, J. Sinha, S. Sriramulu and Y. Yang, "PEM Fuel Cell Cost Status – 2005", Abstracts 2005 Fuel Cell Seminar, Palm Springs, November 2005, pp. 330.
    (c) I. Bar-On, R. Kirchain and R. Roth, "Technical cost analysis for PEM fuel cells", *Journal of Power Sources*, Vol. 109, N. 1, 2002 , pp. 71.
11. (a) P. David, "The PureCell™ Fuel Cell Powerplant", Presentation 2006 Fuel Cell Seminar, Honolulu, Hawaii, November 2006.
    (b) O. Yoshihira, "Current Status and Future Prospect of PAFC Power System", Presentation 2006 Fuel Cell Seminar, Honolulu, Hawaii, November 2006.
12. (a) N. M. Josefik, M. J. Binder, W. R. Taylor and F. H. Holcomb, "The Department of Defense Fuel Cell Demonstration Program", Abstracts 2002 Fuel Cell Seminar, Palm Springs, November 2002, pp. 932.
    (b) M. J. Binder, W. R. Taylor and F. H. Holcomb, "Experience with the fleet of 30 Fuel Cell Generators", Proceedings Fuel Cell 2000, Lucerne, Switzerland, July 2000, pp. 109.
13. (a) S. Surampudi, S. R. Narayanan, E. Vamos, H. Frank, G. Halpert, A. Laconti, J. Kosek, G. K. Surya Prakash and G. A. Olah, *J. Power Sources*, Vol. 47, 1994, pp. 377.
    (b) George Apanel and Eric Johnson, "Direct methanol fuel cells – ready to go commercial?", *Fuel Cells Bulletin*, 2004, Issue 11, pp 12.
14. P. Zelenay, X. Ren, F. Guyon, H. Dinh, J. Davey and S. Gottesfeld, "Direct Methanol Fuel Cells", Annual OTT Fuel Cells Program Review, Pacific Northwest National Laboratory, June 2000.
15. Daimler Chrysler, "Concept Vehicles – The Fuel Cell before your very Eyes", EIHP Meeting, Nabern, June 2002.
16. Forschungszentrum Jülich, Hannover Fair, April 2007.
17. (a) "Matsushita battery develops micro DMFC", *Fuel Cells Bulletin*, Vol. 2006, Issue 3, pp. 4.
    (b) G. Allen, P. Bishop, C. Carlstrom, M. Fannon, D. Leach, J. Prueitt, J. Reichard and G. Dolan, "DMFC Prototype Demonstration for Consumer Electronic Applications", 2007 DOE Hydrogen Program, Annual Review, May 2007.
18. Smart Fuel Cells: http://www.smartfuelcell.de/

19. Ceres Power, "Metal Supported SOFC Cells – Development of Innovative Metal-Supported IT-SOFC Technology", DTI Report: F/01/00277/Rep, 2005.
20. (a) T. Shimada, C. Wen, N. Taniguchi, J. Otomo and H. Takahashi, The high temperature proton conductor $BaZr_{0.4}Ce_{0.4}In_{0.2}O_{3-\alpha}$", *Journal of Power Sources*, Vol. 131, Issues 1–2, 2004, pp. 289.
(b) US Patent Application US20060188760A1: "Proton conducting solid oxide fuel cell".
(c) F. Iguchi, T. Tokikawa, T. Miyoshi, T. Tsurui, Y.Nagao, N. Sata and H. Yugami, "Performance of $BaZrO_3$ based Proton Conductors as an Electrolyte for Intermediate Temperature Operating SOFC", Proceedings SOFC X, Nara, Japan, June 2007, ECS Transactions, Vol 7, 2007, pp. 2331.
(d) S. W. Tao, Q. Y. Wu, D. K. Peng and G. Y. Meng, "Electrode materials for intermediate temperature proton-conducting fuel cells", *Journal of Applied Electrochemistry*, Vol. 30, 2000, pp. 157.
21. D. Brdar, C. Bentley, M. Farooque, P. Oei and T. Rauseo, "Stationary Fuel Cell Power Plants Status", Presentation 2006 Fuel Cell Seminar, Honolulu, Hawaii, November 2006.
22. Fuel Cell Energy: http://www.fuelcellenergy.com/
23. CFC Solutions: http://www.mtu-cfc.com/en/down/down/referenzliste.pdf
24. D. Connors, R. Bernard and J. Allen, "Application of Continuous Manufacturing Methods to Reduce Bipolar Plate Costs", Presentation 2006 Fuel Cell Seminar, Honolulu, Hawaii, November 2006.
25. (a) Nguyen Q. Minh, *Science and Technology of Ceramic Fuel Cells*, 2nd edition, Elsevier Science, 2005.
(b) S. C. Singhal and K. Kendall (eds) *High-temperature Solid Oxide Fuel Cells: Fundamentals, Design and Applications*, Elsevier Science, 2004.
(c) A. Wereszczak, E. Lara-Curzio and N.P. Bansal, "Advances in Solid Oxide Fuel Cells II", Ceramic Engineering and Science Proceedings, Cocoa Beach (Ceramic Engineering and Science Proceedings), Wiley-American Ceramic Society, 2006.
(d) S. P. S.Badwal and K. Foger, "Materials for solid oxide fuel cells", *Materials Forum*, Vol. 21, 1997, pp. 187.
26. Klaus Hassmann, "SOFC power plants, the Siemens–Westinghouse approach", *Fuel Cells*, Vol. 1, Issue 1, 2001, pp. 78.
27. US DOE SECA Program: http://www.netl.doe.gov/technologies/ coalpower/fuelcells/seca/
28. Patent Search using Delphion: "Fuel Cell Materials".
29. US Patent Application 20070128500A1: "Alkali fuel cell unaffected by carbonation".
30. (a) J. R. Varcoe and R. C. T. Slade, "Review: prospects for alkaline anion-exchange membranes in low temperature fuel cells", *Fuel Cells*, Vol. 5, Issue 2, 2005, pp. 187.
(b) Jin-Soo Park, Gu-Gon Park, Seok-Hee Park, Young-Gi Yoon, Chang Soo Kim and Won Yong Lee, "Development of solid-state alkaline electrolytes for solid alkaline fuel cells", *Special Issue: Advanced Polymers for Emerging Technologies*, Vol. 249–250, Issue 1, 2007, pp. 174.
31. (a) M. A. R. Meier and U. S. Schubert, 'Combinational polymers research and high-throughput experimentation: powerful tools for the discovery and evaluation of new materials', *J. Mater. Chem.*, 2004, 14, pp. 3289–3299.
(b) K. D. Kepler, "Novel Combinatorial Method for developing Cathode Catalysts for Fuel Cells", Presentation DoE Hydrogen Program Review, May 16019, 2006.

(c) J. C. Meredith, “Chemical screening to assess fuel cell materials”, *Fuel Cells Bulletin*, Vol. 2006, Issue 11, pp. 6.

32. (a) A. Ainla and D. Brandell, “Nafion®– polybenzimidazole (PBI) composite membranes for DMFC applications”, *Solid State Ionics*, 178, Issues 7–10, 2007, pp. 581–585.
(b) V. S. Silva, S. Weisshaar, R. Reissner, B. Ruffmann, S. Vetter, A. Mendes, L. M. Madeira and S. Nunes, “Performance and efficiency of a DMFC using non-fluorinated composite membranes operating at low/medium temperatures”, *Journal of Power Source*s, Vol. 145, 2005, pp. 485.
33. (a) Ceres Power, “Metal Supported SOFC Cells – Development of Innovative metal-supported IT-SOFC Technology”, DTI Report: F/01/00277/Rep, 2005.
(b) A. Refke, H.-M. Hoehle and M. Gindrat, “New high efficient thermal spray solutions for perovskite coatings and dense thin electrolytes using TriplexPro-200 APS and LPPS-thin film technology”, Proceedings SOFC X, Nara, Japan, June 2007, *ECS Transactions*, Vol. 7, 2007, pp. 339.
(c) I. Villarreal, C. Jacobson, A. Leming, Y. Matus, S. Visco and L. De Jonghe, “Metal-supported solid oxide fuel cells”, *Electrochem. Solid-State Lett.*, Vol. 6, Issue 9, 2003, pp. A178.
(d) G. Schiller, R. Henne, M. Lang and M. Müller, “Development of solid oxide fuel cells by applying DC and RF plasma deposition”, *Fuel Cells*, Vol. 4, Issue 1–2 , 2004, pp. 56.
34. (a) A. E. Hammerschmidt, “Fuel Cell Propulsion of Submarines”, Proceedings Advanced Naval Propulsion Symposium 2006, October 2006, Arlington, VA, USA.
(b) K. A. Burkl, “Fuel Cells for Space Applications”, NASA/TM-2003-212730, 2003.
(c) E. J. Carlson, P. Kopf, J. Sinha, S. Sriramulu and Y. Yang, “Cost Analysis of PEM Fuel Cell Systems for Transportation”, TIAXLLC, NREL/SR-560-39/04, December 2005.
(d) E. J. Carlson, P. Kopf, J. Sinha, S. Sriramulu and Y. Yang, “PEM Fuel Cell Cost Status – 2005”, Abstracts 2005 Fuel Cell Seminar Palm Springs, November 2005, pp. 330.
(e) I. Bar-On, R. Kirchain and R. Roth, “Technical cost analysis for PEM fuel cells,”, *Journal of Power Sources*, Vol. 109, No. 1, 2002, pp. 71.
35. Ovionics: http://www.ovonic.com/eb_fc_fuel_cell_solutions.cfm
36. (a) S. Mukerjee and S. Srinivasan, *J. Electroanal. Chem*. 357, 1993, pp. 201.
(b) R. Hector R. Col´on-Mercado and B. N. Popov, “Stability of platinum based alloy cathode catalysts in PEM fuel cells”, *Journal of Power Sources*, Vol. 155, 2006, pp. 253.
37. (a) US Patent Application 20040265675A1: “Fuel Cell Flow Field Design”.
(b) US Patent Application 20050221152, “Flow Field Plate Geometries”.
(c) A. R. Chapman and I. M. Mellor, “Development of Biomimetic Flow Field Plates for PEM Fuel Cells”, Proceedings 8th Grove Symposium, London, September 2003.
38. (a) S. D. Vora, “SECA Program at Siemens”, Presentation SECA Annual Workshop and Peer Review Meeting, Boston, May 11–13, 2004.
(b) Rolls-Royce plc, DTI Report F/01/00197/REP, URN 04/556, 2004.
39. Plansee: http://www.plansee.com/hlw/fuel_cell_components_ENG_ HTML.htm
40. (a) ThyssenKrupp Crofer APU: http://thyssenkruppvdm.de/_pdf/ Crofer22APU_e.pdf
(b) T. Horita, H. Kishimoto, K. Yamaji, Y. Xiong, N. Sakai, M. E. Brito and H. Yokokawa, “Oxide scale formation and stability of Fe–Cr alloy interconnects under

dual atmospheres and current flow conditions for SOFCs", *J. Electrochem. Soc.*, Vol. 153, Issue 11, 2006, pp. A2007.
(c) A. Venskutonis, G. Kunschert, E. Mueller and H.-M. Höhle, "P/M Processing and Coating Technologies for Fabrication of Interconnect for Stationary and Mobile SOFC Applications", Proceedings SOFC X, Nara, Japan, June 2007, *ECS Transactions*, Vol. 7, 2007, pp. 2109.

41. (a) Ceres Power, "Metal Supported SOFC Cells-Development of Innovative Metal-Supported IT-SOFC Technology", DTI Report: F/01/00277/Rep, 2005.
(b) G. Schiller, T. Franco, M. Lang, P. Metzger and A.O. Störmer, "Recent Results of the SOFC APU Development at DLR", Proceedings SOFC 9, Quebec City, May 2005, pp. 66.
(c) Michael C. Tucker, Craig P. Jacobson, Lutgard C. De Jonghe and Steven J. Visco, "A braze system for sealing metal-supported solid oxide fuel cells", *Journal of Power Sources*, Vol. 160, Issue 2, 2006, pp. 1049.
42. S. A. Kenner, "Component Failure Analysis from the US Army ERDC/CERL Residential Proton Exchange Membrane Fuel Cell Demonstrations", Presentation 2006 Fuel Cell Seminar, Honolulu, Hawaii, November 2006.
43. TIAX LLC, "Solid Oxide Fuel Cell Manufacturing Cost Model: Simulating Relationships between Performance, Manufacturing, and Cost of Production", Final Report to NETL, DE-FC26-02NT41568, 2004.
44. S. K. Kamarudin, W. R. W. Daud, S. L. Ho and U. A. Hasran, "Review: overview on the challenges and developments of micro-DMFC", *Journal of Power Sources*, Vol. 163, Issue 2, 2007, pp. 743.
45. Fuel Cell Energy, Direct Fuel Cell, DFC 3000 Product Brochure from www.fce.com.
46. US Patent 5,873,235: Liquid fuel pressurization and control method, Robert W. Bosley, Edward C. Edelman, Steven W. Lampe, Ronald F. Miller, Capstone Turbine Corp.
47. (a) US Patent US4002805 "Method and apparatus for controlling fuel flow to a steam reformer in a fuel cell".
(b) Patent application WO 2006/010212 "A fuel cell system".
48. R. Kothari, D. Buddhi and R. L. Sawhney, "Sources and technology for hydrogen production: a review", *International Journal of Global Energy Issues* (IJGEI), Vol. 21, No. 1/2, 2004.
49. J. M. Ogden, "Review Of Small Stationary Reformers For Hydrogen Production" IEA/H2/TR-02/002, 2002.
50. (a) J. R. Ladebeck and J. P. Wagner, "Catalyst development for watergas shift", in *Handbook of Fuel Cells – Fundamentals, Technology and Applications* Vol. 3, W. Vielstich, A. Lamm and H. A. Gasteiger (eds), John Wiley & Sons Ltd, 2003, pp. 190.
(b) W. Ruettinger, O. Ilinich and R. J. Farrauto, "A new generation of water gas shift catalysts for fuel cell applications", *Journal of Power Sources*, Vol. 118, 2003 , pp. 61.
51. Questair, Product Specification: http://www.questairinc.com/pdf/H-3200.pdf.
52. Sushil Adhikari and Sandun Fernando, "Hydrogen membrane separation techniques", *Ind. Eng. Chem. Res.*, 2006, Vol. 45, pp. 875.
53. R. Switzer, "Next generation polymer membranes for hydrogen production", *Membrane Technology*, Vol. 2006, No. 8, pp. 7.
54. "Sulfur removal to produce clean fuels", *Catalysis Today*, Vol. 116, Issue 4, 2006, pp. 445.

55. P. J. de Wild, R. G. Nyqvist, F. A. de Bruijn and E. R. Stobbe, "Removal of sulphur-containing odorants from fuel gases for fuel cell-based combined heat and power applications", *Journal of Power Sources*, Vol. 159, Issue 2, 2006, pp. 995.
56. G. Israelson "Results of testing various natural gas desulfurization adsorbents", *Journal of Materials Engineering and Performance*, Vol. 13, Number 3, 2004, pp. 282.
57. G. O. Alptekin, S. DeVoss, M. Dubovik and J. Monroe, Proceedings 2004 Fuel Cell Seminar, 2004, pp. 864.
58. (a) X. Ma, L. Sun, C. Song, "A new approach to deep desulfurization of gasoline, diesel and jet fuel by selective adsorption for ultra-clean fuels and for fuel cell applications", *Catal. Today*, 2002, Vol. 77, pp. 107.
(b) X. Ma, U. Turaga, S. Watanabe, S. Velu and C. Song, "Deep Desulfurization of Diesel Fuels by a Novel Integrated Approach" Final Technical Report, Award Number: DE-FG26-00NT40821, May 2004.
59. (a) A. J. Hernández-Maldonado and R. T. Yang, "Desulfurization of liquid fuels by adsorption via π-complexation with Cu(I)-Y and Ag-Y zeolites", *Ind. Eng. Chem. Res.*, Vol. 42, No. 1, 2003, pp. 123.
(b) A. J. Hernández-Maldonado and R. T. Yang, "Desulfurization of transportation fuels with zeolites under ambient conditions", *Science*, Vol. 301, No. 5629, 2003, pp. 79.
60. D. A. Berry, "Effects of Recycle on Catalytic Fuel Reforming" Office of Fossil Energy Fuel Cell Program, FY 2006 Annual Report, pp. 186.
61. (a) J. R. Rostrup Nielson, "Catalytic steam reforming", in *Catalysis – Science and Technology*, Vol.5, J. R. Anderson and M. Boudart (eds) Springer Verlag, Berlin, 1984, pp. 1.
(b) V. Twigg, *Catalyst Handbook*, 2nd edition, Manson Publishing Ltd, 1996.
62. H. C. Maru and M. Farooque, "Molten Carbonate Fuel Cell Product Design Improvement", Semi-Annual Technical Progress Report, December 2001 to June 2002, Contract No. De - Fc21-95mc31184.
63. K. Ahmed, J. Gammon and K. Föger, "Demonstration of LPG fuelled SOFC systems", *Solid State Ionics*, Vol. 152, 2002, pp. 485.
64. (a) H. J. Grabke, *Materials and Corrosion*, 49, 303, 1998.
(b) C. H. Toh, "Metal Dusting on Heat Resistant Alloys under Thermal Cyclic Conditions, PhD Thesis, University of New South Wales, December 2002.
(c) D. J. Young, "Metal dusting reaction mechanisms", *Materials Science Forum*, Vols 522–523, 2006, pp. 15.
65. G. Pont, "Development of a Thermal and Water Management System for PEM Fuel Cells", DOE Hydrogen Program FY 2005 Progress Report, pp. 1000.
66. K. Sundmacher, A. Kienle, H. J. Pesch, J. F. Berndt and G. Huppmann (eds) *Molten Carbonate Fuel Cells: Modeling, Analysis, Simulation, and Control*, Wiley-VCH, 2007.
67. (a) K. Hilpert, D. Das, M. Miller, D. H. Peck, and R. Weib, "Chromium vapor species over solid oxide fuel cell interconnect materials and their potential for degradation processes", *J. Electrochem. Soc.*, 143, 1996, pp. 40.
(b) C. Paulson and V. I. Birss, "Chromium poisoning of LSM-YSZ SOFC cathodes", *Journal of The Electrochemical Society*, Vol. 151, No. 11, 2004, pp. A1961.
(c) S. P. S. Badwal, R. Deller, K. Foger, Y. Ramprakash and J. P. Zhang "Interaction between chromia forming alloy interconnects and air electrode of solid oxide fuel cells", *Solid State Ionics*, Vol. 99, 1997, pp. 297.

68. (a) G. Pont, “Development of a Thermal and Water Management System for PEM Fuel Cell”, DOE Hydrogen Program PY 2005 Progress Report, pp. 1000.
(b) M. Farooque and H.C. Maru, “Carbonate fuel cells: milliwatts to megawatts”, *Journal of Power Sources*, Vol. 160, Issue 2, 2006, pp. 827.
(c) E. Gülzow, M. Schulze and U. Gerke, “Bipolar concept for alkaline fuel cells”, *Journal of Power Sources*, Vol. 156, Issue 1, 2006, pp. 1.
(d) X. Yu, B. Zhou and A. Sobiesiak, “Water and thermal management for Ballard PEM fuel cell stack”, *Journal of Power Sources*, Vol. 147, Issues 1–2, 2005, pp. 184.
69. (a) E. Gülzow, M. Schulze and U. Gerke, “Bipolar concept for alkaline fuel cells”, *Journal of Power Sources*, Vol. 156, Issue 1, 2006, pp. 1.
(b) X. Yu, B. Zhou and A. Sobiesiak, “Water and thermal management for Ballard PEM fuel cell stack”, *Journal of Power Sources*, Vol. 147, Issues 1–2, 2005, pp. 184.
(c) G. Pont, “Development of a Thermal and Water Management (TWM) System for PEM Fuel Cells, 2005 DOE Hydrogen Program Review, May 2005.
70. D. Bernardi, M. Bozzolo, F. Marsano, O. Tarnowski and G. Agnew, “Ejectors design in the Rolls-Royce 1MW hybrid system”, ASME Paper GT2005-68085, 2005.
71. (a) US Patent 6444345: “Fuel cell system”.
(b) Patrick Louka, “Advanced Thermal Management of High Temperature Fuel Cells via Active Flow Control”, PhD Thesis, Georgia Institute of Technology, 2007.
72. Mike L. Perry and Eric Strayer, “Fuel-Cell Based Back-Up Power for Telecommunication Applications: Developing a Reliable and Cost-Effective Solution”, Proceedings INTELEC 2006, Rhode Island, USA, September 2006.
73. Cullen R. Buie, Jonathan D. Posner, Tibor Fabian, Suk-Won Cha, Daejoong Kim, Fritz B. Prinz, John K. Eaton and Juan G. Santiago, “Water management in proton exchange membrane fuel cells using integrated electro-osmotic pumping”, *Journal of Power Sources*, Vol. 161, Issue 1, 2006, pp. 191.
74. R. B Bernard, J. Allen, F. Chimbole and J. Pesotini, “Prototype Development of an Industrial Fuel Cell Micro-Generator”, Abstracts 2002 Fuel Cell Seminar, Palm Springs, November 2002, pp. 498.
75. US Patent 5,422,195: “Carbonate fuel cell with direct recycle of anode exhaust to cathode”.
76. US Patent 5,897,972: “Molten Carbonate Fuel Cell”.
77. US Patent Application 20050260480A1: “Cathode humidification of a PEM fuel cell through exhaust gas recirculation”.
78. (a) G. D. Agnew, D. Bernardi, R. D. Collins and R. H. Cunningham, “An internal reformer for a pressurised SOFC system”, *Journal of Power Sources*, Vol. 157, Issue 2, 2006, pp. 832.
(b) US Patent 6,764,784: “Standard Package Design for both Atmospheric and Pressurized SOFC Power Generator”.
(c) Patent Application: WO 2002AU0001184, “Fuel Cell System and Method for Recycling Exhaust”.
79. Product properties for aerogel insulation:
(a) http://www.aerogel.com/features/termal.html
(b) http://www.microtherm.uk.com/site/download-category.asp
(c) http://www.promat-hti.be/promalight_320.htm.
(d) http://www.unifrax.com/index.html.
(e) http://www.thermalceramics.com.
80. B. Nair, A. Akash, J. Nachlas, K. Cameron, S. Elangovan, M. Timper and J. Hartvigsen,

"CERCANAM® Insulation for Solid Oxide Fuel Cells", The SECA Core Technology Program Workshop, Albany, NY, September 30, 2003.
81. Akash Akash, "Advanced Net-Shape Insulation for Solid Oxide Fuel Cells", Office of Fossil Energy Fuel Cell Program, FY 2006 Annual Report, pp. 246.
82. (a) The Knowledge Foundation, "Symposia on Fuel Cells Durability and Performance", 2005, 2006 and 2007.
(b) International Workshop on Degradation Issues in Fuel Cells, Crete, Greece, September 19–21, 2007.
83. (a) W. Nelson, *Accelerated Testing-Statistical Models, Test Plans and Data Analysis*, John Wiley and Sons, 1990.
(b) W. Q. Meeker and L. A. Escobar, *Statistical Methods for Reliability Data*, John Wiley and Sons, 1998.
(c) K. Reifsneider and Xinyu Huang, "Durability and Accelerated Characterization of Fuel Cells," in *Fuel Cell Technology – Reaching Towords Commercialization*, N. Sammes (ed.), Springer, 2007, pp. 53.
84. EscoVale Consulting Services, "Fuel Cells: The Source Book", Report #3407, July 2007.
85. ABI Research: Report "The Transportation Fuel Cell Supply Chain", 2002.
86. (a) Margherita Pero and Andrea Sianesi, "Aligning supply chain management and new product development: a general framework", PLM-SP3 – 2007 Proceedings, pp. 489.
(b) Robert B. Handfield and Ernest L. Nichols Jr., *Supply Chain Redesign: Transforming Supply Chains into Integrated Value Systems*, FT Press, August 22, 2002.
(c) Chong Leng Tan and Michael Tracey, "Collaborative new product development environments: implications for supply chain management", *The Journal of Supply Chain Management*, Vol. 43, No. 3, 2007, pp. 2.
87. (a) Freesen, "Hydrogen and Fuel Cell Technology from North-Rhine Westfalia", Germany, *NHA News*, Autumn 2006.
(b) Ohio Fuel Cell Coalition: http://www.fuelcellsohio.org/fuelcellcorridor.html
88. (a) K. Jeong and B. Oh, "Fuel economy and life-cycle cost analysis of a fuel cell hybrid vehicle", *J. Power Sources*, Vol. 105, No. 202, pp. 58–65.
(b) J. Brouwer, M. Nogu Nogués, G. S. Samuelsen, C. C. Lee and G. L. Huffman, "Life Cycle Analysis of Air Quality and Greenhouse Gas Emissions Impacts", National Fuel Cell Research Center and U.S. Environmental Protection Agency, 2006.
(c) M. Pehnt, "Life Cycle Assessment of Fuel Cell Systems", *Fuel Cell Handbook*, Vol. 3, John Wiley, 2003, Chapter 94.
89. (a) P. Lunghi and R. Bove, "Life cycle assessment of a molten carbonate fuel cell stack", *Fuel Cells*, Vol. 3, Issue 4, 2003, pp. 224.
(b) B. Sorensen, *Hydrogen and Fuel Cells*, Academic Press, 2005.
90. D. Cohen, "Earth Audit", *New Scientist*, May 26, 2007, pp. 34.
91. "Waste electrical and electronic equipment (WEEE), Directive 2002/96/EC of The European Parliament and of The Council, 27 January 2003.
92. "Catalyst recycling essential for the environment", *Focus on Catalysts*, Vol. 2006, Issue 4, April 2006, pp. 1.
93. (a) James N. Cawsey (ed.) *Experimental Design for Combinatorial High Throughput Materials Development*, John Wiley and Sons, 2002, pp. 336.
(b) X. Xiang and I. Takeuchi (eds), *Combinatorial Materials Synthesis*, Marcel Dekker, 2003.

3

Alkaline fuel cells

E GÜLZOW and M SCHULZE, DLR, Germany

3.1 Introduction

"*The alkaline fuel cell (AFC), also known as the Bacon fuel cell after its British inventor, is one of the most developed fuel cell technologies and is the cell that flew Man to the Moon. NASA has used alkaline fuel cells since the mid-1960s, in Apollo-series missions and on the Space Shuttle.*" [1] While the history of fuel cell technology is impressive and tremendous progress has been made, full commercialization remains elusive.

The English lawyer, judge and physical scientist William R. Grove (1811–1896) [2] described the principle of the fuel cell in 1839, but his invention is closely coupled with the work of German chemist Christian Friedrich Schönbein (1799–1868) [3] who co-discovered the principle. These pioneers investigated the fuel cell reaction in acid electrolytes, and the first real alkaline fuel cell was described by J. H. Reid in 1902 [4] and Noel [5] in 1904.

The performance of the early fuel cells was poor, and traditional materials had to be improved or alternative materials found in order to obtain technically relevant values. The materials, catalysts and electrode structures were developed intensively and eventually acceptable performance levels were reached. A. Schmid [6, 7] improved the electrodes in 1923, P. Scharf [8] developed the hydrogen diffusion electrode and M. Raney (1926) [9] developed the well-known catalyst structure 'Raney nickel', which provided far greater surface areas of active catalyst. Over subsequent decades, F.T. Bacon [10] at Cambridge made major contributions towards developing fuel cells for integration into early demonstration projects, such as the Allis Chalmers Tractor (1959/ USA), which had a 15 kW fuel cell system.

In Germany, E. W. Justi and A. Winsel advanced AFC technology during the 1950s and 1960s [11]. They invented double skeleton electrodes, an important milestone for terrestrial development in Europe and subsequently developed further by Siemens. At around the same time, Austrian K. Kordesch [12] developed alkaline fuel cells and used them to power demonstration vehicles, including a bicycle and a car.

In the 1960s and 1970s, space programmes in Russia and the US promoted further development. In 1994, Belgian company Elenco demonstrated a Citybus powered by a 78 kW fuel cell. Also in the 1990s, Siemens demonstrated a military submarine with a fuel cell power system of about 100 kW (they later abandoned AFC development in favour of proton exchange fuel cell (PEFC) systems). The most recent AFC developments are described later in this chapter, as well as a look at trends and a review of some institutions and companies currently active in this field.

AFCs take different forms. The materials used in an AFC depend strongly on the type of fuel cell, hence the materials for a classic AFC are significantly different from those in an anion-exchange membrane (AEM) or direct methanol AFC. Because of the function of the components, defined structural and chemical properties have to be realized, e.g. the electrodes have to be highly electro-catalytically active and must exhibit specific transport properties required by the structure. Different materials are needed to ensure that each component meets the necessary functional requirements.

Over time, many solutions to problems and technical issues have been described in the literature. In general, AFCs are easy to handle, have very high electrical efficiency and are very suitable for dynamic operating modes. They can be built into small compact systems as well as in large power plants. However, many groups in Europe have stopped working on this technology. As well as the advantages, this chapter describes the problems and disadvantages of AFCs, and some misconceptions that have appeared in the literature will be critically discussed.

3.2 Principles

The AFC has the highest electrical efficiency of all fuel cells, but it typically uses very pure gases. This is often considered a major constraint for most applications, however, the restrictions are probably not that important (as discussed below). The oxygen reduction kinetics are much faster in the alkaline KOH electrolytes used in AFCs (usually in concentrations of 30–45 wt.%) than in acid fuel cells, making the AFC a very attractive system for specific applications. The AFC was one of the first fuel cells used in space. AFCs were used in the Apollo missions and the space shuttle programme, and were included in the European Hermes space project, which was cancelled in the early 1990s.

In alkaline media, the relevant reactions involve OH^- ions. The OH^- species formed by the reduction of oxygen at the cathode move through the electrolyte to the anode, where recombination with hydrogen produces water (Fig. 3.1). The reactions taking place at the electrodes are:

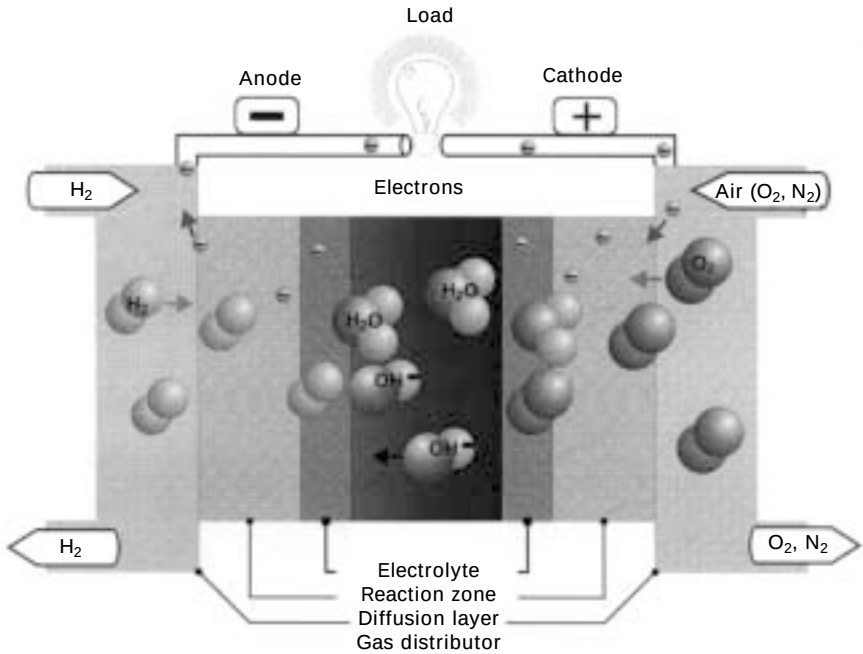

3.1 Scheme of an alkaline fuel cell.

CCathode: $\frac{1}{2}\ O_2 + H_2O + 2e \rightarrow 2\ OH^-$

Anode: $H_2 + 2OH^- \rightarrow 2\ H_2O + 2e^-$

3.3 Alkaline fuel cell designs

The stack design of AFCs is different from the most common designs of polymer-electrolyte or solid oxide fuel cells. Alkaline fuel cells contain a liquid electrolyte in most cases, so in principle the cell has three chambers which are divided by electrodes or separators. There are two chambers for the reactants and one for the electrolyte. An AFC can be operated at up to 230 °C depending on the fuel cell model used.

New developments foresee the integration of stable anion exchange membranes, which can be used like the proton exchange membrane in a proton exchange fuel cell (PEFC) and hence the design will be similar to the PEFC stack. Various designs are described briefly below.

3.3.1 Traditional stacks

The traditional fuel cell stack has a fuel chamber, which contains the energy carrier. The fuel might be either a gas, such as hydrogen or an admixture

with a high volume of hydrogen obtained from reformers, or a liquid, such as ammonia or hydrazine. The fuel chamber is separated from the electrolyte by the diffusion electrode. Normally there is an additional electrolyte loop.

The cooling system is combined with the electrolyte loop. There is no need to separate the cooling system as in a PEFC, but a reconcentration unit is needed to compensate for the dilution effects due to the production of water. It is important to maintain a constant KOH concentration because conductivity is decreased if the flow of water to the electrolyte increases.

3.3.2 EloFlux

The main difference between EloFlux and other systems is the reduced number of plates between cells. EloFlux was described in 1965 by Wendtland and Winsel [13–16].

The EloFlux principle is based on flexible electrodes and a liquid electrolyte. The electrodes are extremely porous, with a thin separator between them. In contrast with other cell designs, the electrolyte is transported through the separator and the electrodes in a direction perpendicular to the electrode plane. To permit this, the electrodes and diaphragms contain an interconnecting system of narrow and large, hydrophilic and hydrophobic pores. The electrolyte passes through the narrow pores, while the bigger pores and the hydrophobic character of the polytetrafluoroethylene (PTFE) on the electrodes allow the passage of pressurized hydrogen or oxygen. The gases do not enter the narrow pores, so gas transport is independent of electrolyte and ion transport. Water is removed from the circulated electrolyte using an external water vaporizer or dialytic reconcentrator.

3.3.3 Falling film cell

A new type of fuel cell stack is the falling film fuel cell developed by Hoechst. The first falling film process was used in 1981 in chlor-alkali electrolysis in order to save electrical power [17].

In the falling film fuel cell, the electrolyte flows from the top to the bottom through the cells. The hydrostatic pressure is compensated by an equally large, but opposing hydrodynamic pressure drop [18]. The pressure difference between the electrolyte on one side of the electrode and the gas on the other side remains constant over the whole area of the vertical electrode. This is important if the cell is to work without a diaphragm. The gap between the electrodes is 0.5 mm and the cell operates at very high current densities, of more than 25 kA/m^2. The cost of this new type of stack is relatively low and the power densities very high [19].

The largest cell using this new technology is 0.25 m wide and 1 m high and has been tested as an electrolyser. From 1990, gas-diffusion electrodes have been used successfully in falling film cells. This example shows that, as with other types of low-temperature fuel cells, innovations can lead to higher current densities.

3.3.4 German Aerospace Centre bipolar stack

Alkaline fuel cell stacks are frequently monopolar, with single cells being connected externally. A bipolar configuration is commonly used for PEFCs, with the monopolar configuration only used for some specific low-power applications.

Bipolar AFCs have also been developed. Bipolar AFC systems for space applications all work using an immobilized electrolyte. In the Apollo missions, a bipolar AFC operated at 200–230 °C with 85 wt% KOH electrolyte, the electrolyte requiring heating to over 100 °C to melt it and achieve sufficient ion conductivity. In the Apollo cells, the electrolyte was immobilized in a matrix material. Bipolar AFC stacks have been used for other space missions, including the American Space Shuttle and in the Russian Foton and Buran programmes. A bipolar configuration for liquid electrolyte was developed at the German Aerospace Centre (DLR) [20, 21]

Figure 3.2 shows a bipolar AFC stack, which consists of two end plates, the bipolar plates, the electrodes, the diaphragms and the sealing. The connections for the gas supply, electrolyte circulation and electrical cables are integrated into the end plates. The end plates also serve to distribute the contact pressure over the total area of the cell. The first and last cells have monopolar plates. The bipolar plates distribute the gases in each cell using the flow fields and an internal manifold within the individual cells. Due to the greater thickness of typical AFC electrodes and the resulting higher gas diffusion in the electrodes, optimizing the flow fields in AFC is significantly less complex than for PEFCs. The diaphragms prevent direct contact between electrodes, which would lead to a short circuit.

3.3.5 Hydrocell

The Finnish company Hydrocell [22] develops portable fuel cells. This type of fuel cell has the electrode outside the stack for air intake, so the stacks are single cell with a large active area. Hydrocell's fuel cells are based on a cylindrical electrode. The electrolyte is a gel, developed by the company, so there are no problems with leakage. The advantage of the gel electrolyte compared with a liquid electrolyte is that the fuel cell can be operated independent of its orientation. The fuel cell contains a hydride storage system with capacity for 40 litres of hydrogen [23]. For larger power needs, several mono cells can be connected.

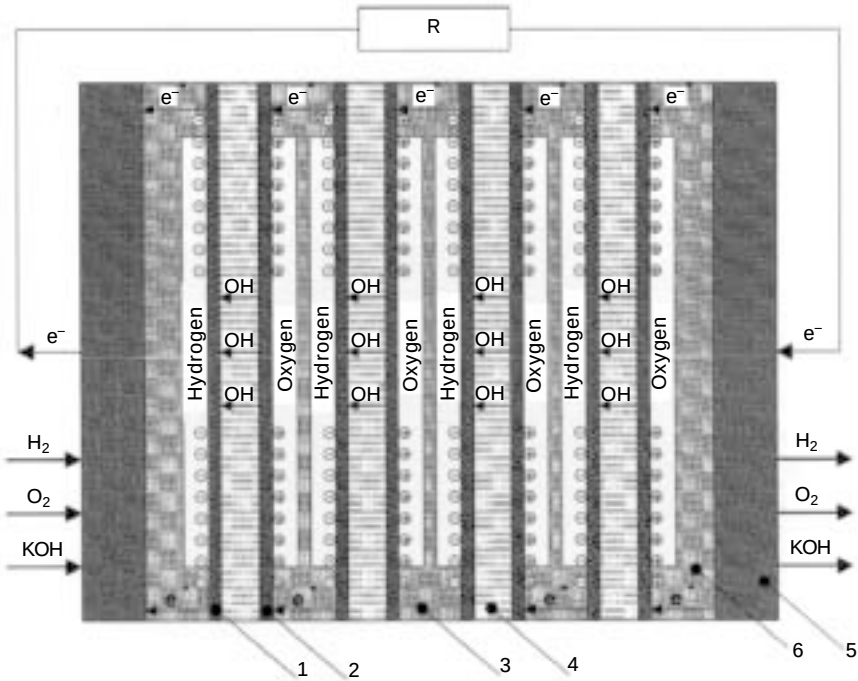

3.2 Scheme of an AFC in bipolar configuration: 1 anode, 2 cathode, 3 bipolar plate, 4 electrolyte with spacer (diaphragm), 5 end plate, 6 monopolar plate [20].

3.3.6 Ovonics

Ovonics developed an AFC with hydride catalysts on the anode and a non-noble metal oxide on the cathode [24–26]. These cells store electrical energy by loading the anode catalysts with hydrogen produced by electrolysis [27]. The hydrogen stored in the anode catalyst means that this fuel cell can also be operated like a nickel hydride accumulator, which allows ultra fast start-up as well as start-up at temperatures below –20 °C [27]. These AFCs are expected to be used for different applications in stationary, portable and transportable power supply. The application field includes military, telecom, automotive and auxiliary power supplies as well as uninterruptible power supplies [27, 28].

3.3.7 Stack design with anion exchange membranes

The stack design incorporating anion exchange membranes (AEM) is similar to the design of a PEFC stack. The electrolyte loop is eliminated in this case, which makes the system simpler but also means that it requires cooling, like

PEFCs. However, this disadvantage is outweighed by the reduced need for expensive noble metal catalysts.

At present, only a few AEM materials are available as stability requirements have not been met yet, so this type of stack is still under development. Various companies and groups that are active in the field are listed in the appropriate section below. One recent demonstration that stands out is a new stack concept from the University of Applied Science in Offenburg, Germany, which uses novel catalysts developed by the Italian company ACTA and the Japanese membrane producer Tokuyama [29]. This consortium created a successful demonstration of an ethanol-fuelled alkaline fuel cell with an AEM, using a stack that was installed in an electric vehicle. The stack did not function for a long time, because the system was built without an ethanol loop and without a water reconcentrator, but it was an impressive demonstration of the new technology.

3.4 Types of electrode

For a high performance electrode, the electrochemical reaction must be catalyzed and the transport of the reactants as well as the products must be efficient. Pore systems suitable for gas transport are needed to transport the reactants to the active layer, along with ion conduction to or from the catalytic active centres. In alkaline fuel cells, different types of electrode are used. The main types are PTFE-bonded gas diffusion electrodes (GDE) and double skeleton electrodes (DSK).

3.4.1 Polytetrafluoroethylene bonded gas diffusion electrodes

PTFE-bonded gas diffusion electrodes are prepared in different ways. One method takes place under wet conditions, the alternative is a dry preparation process which avoids the need for solvents. The dry preparation process for gas diffusion electrodes is described below. In the wet process, the electrode is prepared as a paste and then this paste is spread over a structure, such as a net. The wet process requires a drying step, and the electrodes prepared by this method are thicker than those prepared by the dry method [30].

3.4.2 Double skeleton electrodes

Double skin or skeleton (DSK) electrodes [31] contain three different types of pores. Within the Raney nickel granules there are pores with diameters in the range of 20–80 Å, which produce a large inner surface with high catalytic activity. This pore system is, even at very high gas pressure, filled with electrolyte. Between the grains of the supporting skeleton there are pores

with diameters up to a few μm which, under operating conditions, are also filled with electrolyte. Only the coarse pores, preferably formed in the neighbourhood of the Raney nickel granules, are filled with gas.

It is important that the electrolyte-containing pores as well as the gas-containing pores are interconnected. Thus both phases may flow through the pores nearly independently from each other, if they are exposed to pressure gradients.

In hydrogen fuel cells, DSK-electrodes are used in the form of Janus electrodes [32], which consist of three layers. The middle one, the working layer, contains the catalyst as well as the coarse, gas-filled pores. The outer ones are covering layers, the fine pores of which are filled with electrolyte, preventing the gas from escaping from the electrode.

3.5 Materials used for electrodes and their preparation

Today the most commonly used electrodes are PTFE-bonded gas diffusion electrodes. These electrodes are a composite of a metal catalyst and PTFE supported by a metal grid on the back of the electrode. The PTFE is used as an organic binder to hold the catalyst particles together. The metal grid is responsible for high electrical conductivity and for mechanical support and stability.

In gas diffusion electrodes, hydrophobic and hydrophilic pore systems are required. The hydrophilic system allows the penetration of electrolyte into the electrode and the transport of the ions to or from the reaction zone; the hydrophobic pore system allows the transport of gases to the reaction zone. The hydrophobic pore system is created by the PTFE, and it also provides mechanical stability. Electrolyte cannot enter the hydrophobic pores, so the electrode can be supplied with the fuel gas from the back. The structure can be compared to a spider web of PTFE fibres on and in the electrodes.

3.5.1 Anode catalysts

Different catalysts are used in AFCs. For the hydrogen oxidation reaction, noble metal catalysts include carbon-supported platinum and platinum–palladium. But one of the advantages of the AFC compared with acid electrolyte fuel cells is that non-noble metals are also stable in alkaline environments, and as a consequence the catalyst material costs can be reduced.

The most commonly used catalyst for hydrogen oxidation in AFCs is porous nickel prepared from Raney nickel. The initial material is a nickel–aluminium alloy containing 50% by weight of each metal. The catalyst is activated by dissolving the aluminium in KOH at 80 °C. After this procedure, the catalyst contains less than 5 wt.% aluminium. During the activation

process, the nickel is loaded with 0.5–1.2 hydrogen atoms per nickel atom [33] forming a pyrophoric nickel hydride. After this, the powder is washed and dried. Since hydrogen is present in the metal and due to the high reactivity of a metallic nickel surface, contact with oxygen must be avoided during the drying process. In this state, the Raney nickel has pyrophoric characteristics and consequently cannot be handled in air, neither as catalytic powder nor processed in electrodes. Therefore after drying, the catalyst powder is passivated by controlled oxygen exposure under temperature control in order to make it easier to handle by eliminating its pyrophoric nature. During this step, the absorbed hydrogen is removed and the catalyst surface is oxidized. Before using the electrode in fuel cells, the oxide must be reduced. To increase electrical conductivity in the electrode, metallic copper powder is added to the mixture of nickel catalyst and PTFE.

3.5.2 Cathode catalysts

Different materials have been used for cathode catalysts. Noble metal catalysts, platinum and gold, were mainly used in fuel cells for space applications. For terrestrial use, cost is a more important factor, and non-noble metal catalysts are mainly used. Bacon used lithium-doped nickel oxide as the cathode catalyst in his high temperature AFC. Lithium-doped nickel oxide has sufficient electrical conductivity at temperatures above 150 °C. Today, silver-based and pure silver catalysts are favoured. Silver catalysts are prepared from silver oxides, Raney-silver and supported silver catalysts. Typically the catalysts on the cathode are supported by PTFE because it has high stability in basic and acid environments. If carbon were used as support, it would be oxidized in the cathodes.

In the past, silver catalysts frequently also contained mercury, which was intended to increase the stability and active life of the cathodes. Mercury is partially dissolved due to the activation procedure (see below) and also during fuel cell operation, which contaminates the electrolyte with the mercury. Because of the environmental hazards of mercury, it is no longer used in silver catalysts.

Oxides are used as cathode catalysts, for instance spinel ($MnCo_2O_4$) [34] or perovskite (e.g. $La_{0.1}Ca_{0.9}MnO_3$) catalysts [34] are used in the hydrocell AFC [34]. Other perovskite catalysts, such as $La_{1-x}Sr_xMnO_3$ [35], which has well-known SOFC applications [36], and MnO catalysts [37, 38] have also been tested for AFC cathodes, as has W_2C [39].

3.5.3 Additives

Gas diffusion electrodes need a hydrophobic pore system in order to transport the reactant gases to the three-phase reaction zone formed from the electrolyte,

the catalyst and the reactant, where the electro-catalytic reactions take place. Therefore, the electrodes need hydrophobic pore systems that prevent the electrolyte from completely flooding the pore system and crossing the electrodes. PTFE is a highly hydrophobic material which is also extremely resistant in all corrosive environments, including under electrochemical conditions. Therefore, PTFE is frequently used to make the electrodes hydrophobic. PTFE also functions as an organic binder in the electrodes because its form becomes inelastic under mechanical stress, so the electrode is covered in PTFE fibres using a rolling process to create the necessary mechanical stress. PTFE powder is typically used in dry preparation methods. For wet preparation, a PTFE suspension is used, for instance in the production of PEFC-electrodes or GDLs.

In order to adjust the pore system during the preparation process, pore former materials are sometimes used. These pore formers have to be completely eliminated after electrode preparation – either by dissolution in water or gas decomposition into compounds such as sodium or ammonium bicarbonate.

Other components may also be added to improve particular electrode properties. Electrical conductivity at the anode can be improved by adding other metallic components, mainly as powders, to the initial powder mixtures.

Another component of PTFE-bonded gas diffusion electrodes is a metal net on the back of the electrode, which gives the electrode its mechanical stability and also acts as a current collector. The metal grid has to be resistant to corrosion. Nickel or nickel-coated metal grids are frequently used at the anode. Silver-coated grids are generally used on the cathode, because a nickel grid here would be oxidized, leading to higher contact resistances.

3.6 Dry preparation of polytetrafluoroethylene bonded gas diffusion electrodes

3.6.1 Preparation of anodes with Raney nickel catalysts

The preparation methods for gas diffusion electrodes based on Sauer [40] and Winsel [41] have been adapted for electrodes used in alkaline fuel cells [42–47]. The anode consists mainly of a mixture of Raney nickel catalyst with copper powder and PTFE powder, on a copper grid. The Raney nickel catalyst has a highly porous structure which is formed by dissolving the aluminium from an aluminium–nickel alloy. After reactive mixing of the different components, the PTFE, copper powder and oxidized nickel catalyst, the powder is rolled in a knife mill into a self-carrying strip, which is rolled in a second step onto a metal grid to form the electrode. The rolled electrode has a thickness of approximately 350 µm. A schematic of the preparation technique is given in Fig. 3.3. This preparation technique can be fully automated

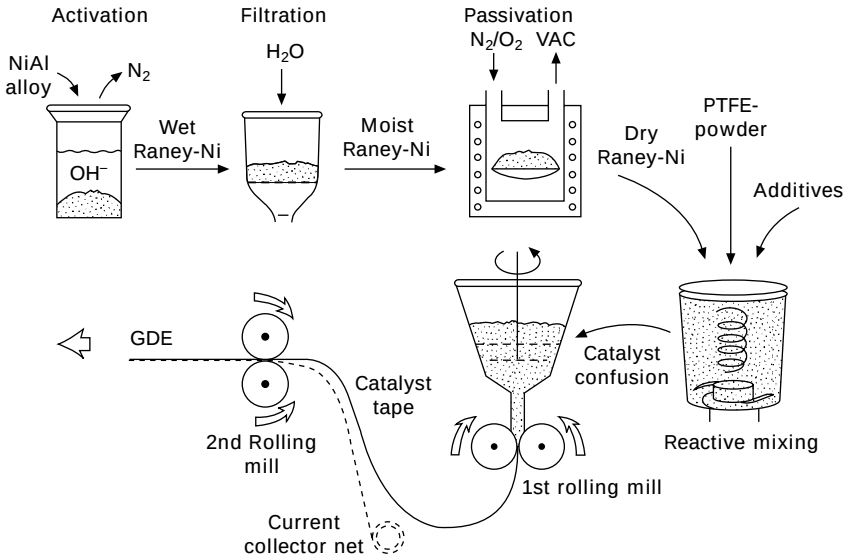

3.3 Schematic of the preparation of gas diffusion electrodes (GDE) with Raney nickel catalyst (VAC = Vacum).

and avoids environmentally harmful steps or waste emission, thus allowing continuous, environmentally friendly manufacturing of low-cost gas diffusion electrodes.

During the process, the PTFE is flattened and forms ultra-thin PTFE fibres and a PTFE film. The film covers the oxidized catalyst (Fig. 3.4) and so no porosity can be measured for the rolled electrode, thus the active surface is very small [47]. The pore system and the specific surface activity of the anode are determined by the surface of the metallic catalyst that is uncovered by activation. A pore system with a pore radius of 2 nm has been measured for the nickel catalyst. The PTFE does not exhibit a measurable surface in nitrogen adsorption measurements [47]. Because of the rolling process, the specific surface of the electrode before activation is only approximately 7 m^2/g, which is significantly smaller than that of the nickel catalyst (Fig. 3.5).

3.6.2 Reactivation of anode gas-diffusion electrodes

Due to the PTFE film and the oxidized state of the Raney nickel catalyst following passivation, the electrode must be reactivated before it can be used in a fuel cell. The standard activation procedure is to reduce the nickel oxide in 30 wt.% KOH electrochemically, using the electrode as a hydrogen generating electrode in an electrolyzer at a current density of 5 mA/cm^2 for 18 h [48].

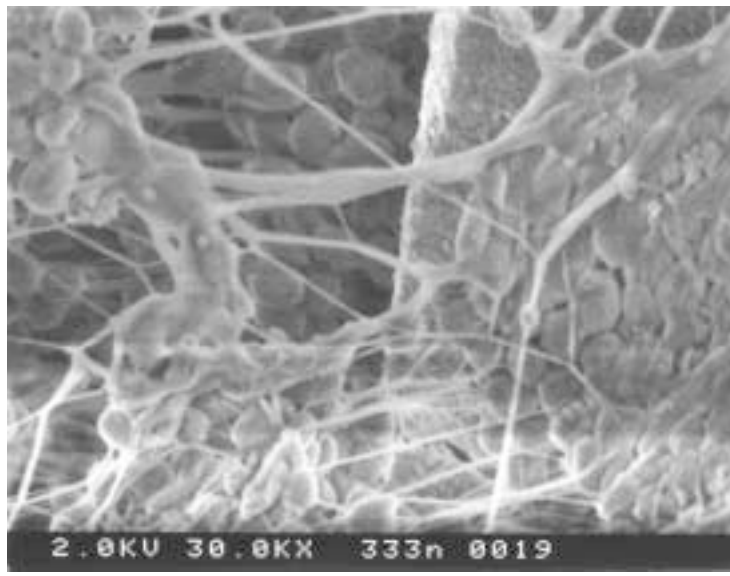

3.4 SEM image of a non-activated electrode recorded with an electron beam voltage of 2 kV.

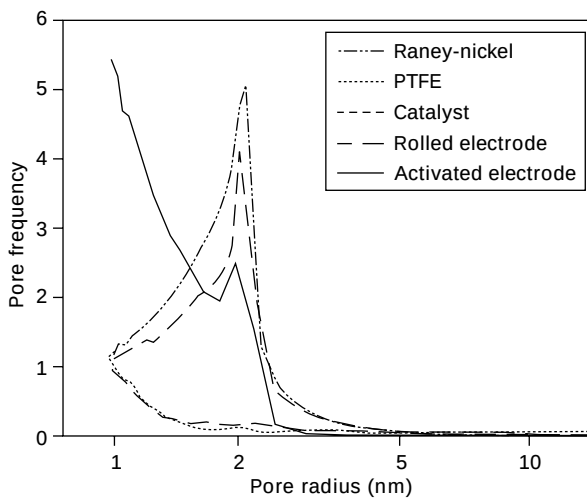

3.5 Pore frequency of the electrode components and after different steps of electrode preparation.

In addition to the electrochemical reduction conditions, the rear surface of the electrode is exposed to hydrogen.

During the reactivation process, several alterations in the composition and structure of the electrode take place: the polymer changes, the nickel

oxide is reduced to metallic nickel, and residual aluminium from the Raney nickel is dissolved.

3.6.3 Effect of activation on the polymer in the alkaline fuel cell electrode

During the activation process, the specific surface measured by nitrogen adsorption increases with time, and an increase in pore frequency at 2 nm (shown in Fig. 3.5) is observed, thus the activation process re-exposes the pore system of the nickel catalyst. Only a 2 nm pore radius system is observed, and the specific surface does not increase linearly with time. Between activation times of 4.5 and 8.5 h at 5 mA/cm^2, a significant increase in pore frequency and specific surface, from 21 to 53 m^2/g, is observed (Fig. 3.6). During further activation, the specific surface increases slowly from a low value to 64 m^2/g after 18 h and only up to 72 m^2/g after 115 h. The increase in specific surface clearly indicates that the PTFE film covering the catalyst is removed during the activation process. The change in PTFE at the anodes is the time determining step in the activation procedure [49].

3.6.4 Reduction of the NiO

The electrode activation process was investigated by X-ray photoelectron spectroscopy (XPS). Transfer from solution to the UHV chamber was controlled. Depth profiling by sputtering was performed to obtain information about the surface composition. Nickel oxide is observed on the surface of the catalyst in the XPS spectra when starting the depth profiling. This surface nickel oxide layer may be formed during the process of transferring the electrode from the KOH electrolyte into the vacuum system. The interaction of nickel surfaces with water vapour is described in more detail in [50, 51]. The oxidation state of the electrodes can be determined from the contributions of the metallic nickel and the nickel oxide to the XP spectra recorded in the depth profile.

The nickel surface is reduced after 4.5 h at a current density of 5 mA/cm^2. It is very surprising that the electrodes are reduced after such a short activation time because the catalysts are still significantly covered by the PTFE film, as observed in the XP spectra and in the specific surface area measurements. The perforations in the PTFE film are sufficient to allow contact between the electrolyte and the nickel catalyst, and therefore for the nickel oxide to be reduced. During the activation process, the number of perforations in the PTFE film may increase or the electrolyte might find an alternative access to the metal catalyst. This access may be created by the hydrogen generated, which forms on the nickel surface and separates the PTFE film from the catalyst surface. This explains the initial nickel signal observed in the XP

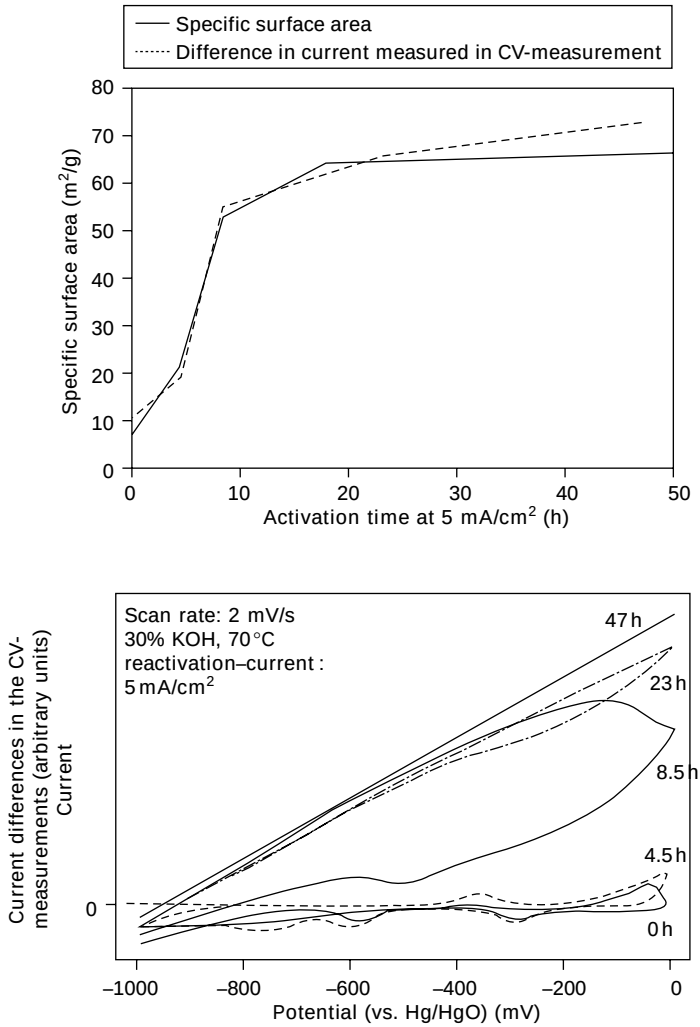

3.6 Specific surface area (top) measured by nitrogen adsorption (solid line) and current differences in the cyclic voltametry measurements bottom after different activation times at 5 mA/cm^2 (dashed line).

spectra of the activated electrode. In addition, the specific surface increases without total removal of the PTFE film.

From the XP spectra of electrodes that were activated for different periods of time, the nickel oxide appears to be totally reduced. This result seems to contradict the results of the specific surface measurements. From the XPS measurements, it cannot be concluded that the nickel is also reduced in the bulk volume of the electrode, which is relevant for its electrochemical

behaviour. In the specific surface measurements, the surface of the catalyst particles in the volume of the porous electrode determines the value measured.

In cyclic voltametry measurements, hydrogen loading can be observed after longer activation times [49]. Electrochemical measurements support the results from the specific surface area measurements, which increase due to the activation procedure. Surface area determinations by gas adsorption experiments and by cyclic voltametry are well correlated. Both measurements are shown in Fig. 3.6, the correlation of cyclic voltametry and specific surface area can be seen.

From the specific surface measurements it can be deduced that, at short activation times, most of the catalyst remains covered by the PTFE film. This film prevents both gas and electrolyte from reaching the catalyst. Therefore it can be concluded that the activation process starts on the surface of the electrode and the activation zone grows in depth with increasing activation time. Two effects lead to this behaviour. The penetration of the electrolyte into the electrode is hindered by the hydrophobic character of the PTFE, but with increasing PTFE damage over time, the electrolyte and activation zone shift deeper into the electrode. In addition, perforations in the PTFE film can increase electrolyte penetration.

The electrochemical reduction is coupled to a charge transfer and ion transport, where an electrical field is necessary. Due to good electrical conductivity in the electrode and the low penetration depth at the beginning of the activation process, the gradient is maximal on the electrode surface and so the nickel at the surface is reduced first. After nickel reduction has begun and the electrolyte is in contact with a metallic nickel surface, the over-voltage due to hydrogen generation decreases. Further reduction of the nickel oxide in the bulk of the electrode continues at a slower pace, since the active part is already able to maintain current density.

Our EDX analysis does not allow for any conclusions regarding the oxidation state of the nickel because the oxygen signal is overlapped by other signals. The SEM images of the activated electrodes show a slight formation of cracks in the nickel catalyst. At a constant current density, the formation of the cracks in the nickel increases over time. The crack densities in the nickel are similar for all electrodes if they are activated with constant charge. The cracks in the nickel may be the result of loading the nickel with hydrogen during activation and electrochemical operation, and their formation is known as hydrogen embrittlement [52, 53].

3.6.5 Dissolution of aluminium

Most of the aluminium is dissolved during preparation of the nickel aluminium alloy. Some of the residual aluminium is dissolved during the activation process. A loss of one-third of the residual aluminium content after activation

was determined by EDX measurements. The amount of aluminium dissolved increases with increasing activation times at constant current density. For a constant charge, approximately the same aluminium loss was determined by EDX.

3.6.6 Production of cathode gas diffusion electrodes

Silver is commonly used as a cathode catalyst for oxygen reduction in alkaline solution. A large surface area is required, and, in porous gas diffusion electrodes (GDE), silver particles are dispersed in a porous matrix. A common preparation technique involves mixing reactive powder and polymer followed by rolling (RMR), similar to that used for anodes [54]. The porous PTFE-bonded gas diffusion electrodes consist of the electro-catalytic powder, e.g. silver as silver oxide, the organic binding agent (PTFE), and metal wire gauze to mechanically stabilize the electrode and to collect the current. In order to increase the activity of the cathode, the silver oxide has to be reduced to its metallic form. This can be performed galvanostatically, prior to use or *in situ* in the fuel cell, where it occurs simultaneously with the oxygen reduction reaction (ORR), as shown in Fig. 3.7.

The following equations can be assumed for the reactions taking place:

$$Ag_2O + H_2O + 2e^- \rightarrow 2Ag + 2OH^-$$

$$E_0 = 247 \text{ mV vs. Hg/HgO} \qquad 3.1$$

$$O_2 + 2\ H_2O + 4e^- \rightarrow 4\ OH^-$$

$$E_0 = 303 \text{ mV vs. Hg/HgO} \qquad 3.2$$

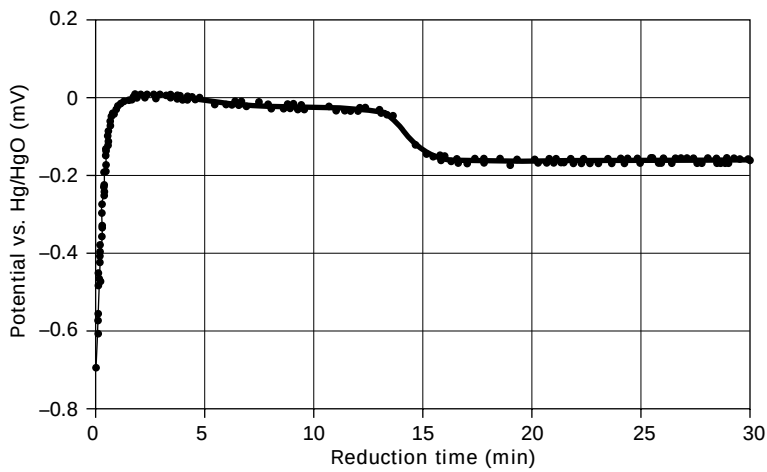

3.7 Simultanous reduction of silver oxide and oxygen at 100 mA/cm^2 and 80 °C in 30 wt% KOH [54].

The chronopotential curve shows an initial increase. This is correlated with the oxidation of impurities adsorbed from air onto the electrode surface, e.g. CO. The oxide states of silver produce the subsequent plateau in potential. The plateau is determined by the combined potential given by the oxygen reduction reaction and the silver oxide reduction reaction, whereby the slow decrease of potential shows the increasing influence of the oxygen reduction reaction. Silver loading in the electrodes can be calculated from the integration of the charging (reduction) current. After the silver oxide is completely reduced, the potential decreases to approximately ± 150 mV vs. Hg/HgO and remains constant while the experiment continues, because now only the oxygen reduction reaction takes place and there is no further change in the electrode. The silver oxide is completely reduced after approximately 15 minutes at a current density of 100 mA/cm^{-2}. During the reduction process, the dark-coloured silver oxide electrodes turn bright silver. The electrochemical performance of the silver GDE can be improved by varying electrode composition, production parameters and silver oxide reduction conditions. The activation process leads to an enlargement of the surface area, which can be attributed in the first place to oxide reduction and secondly to the change in the hydrophobic character of the PTFE-covered surface.

3.7 Electrolytes and separators

There are three electrolyte types, liquid electrolytes, e.g. potassium hydroxide, sodium hydroxide or mixtures of both, immobilized electrolytes where the liquid electrolyte is fixed in a matrix or gel, and anion exchange polymer electrolytes such as the solid polymer electrolytes in PEFC.

With liquid electrolytes, a diaphragm or separator material is needed to separate the electrodes. Asbestos was commonly used as a diaphragm material before the 1980s because it has very good stability in alkaline environments. But restrictions on the use of asbestos in many countries led to its abandonment, and alternatives had to be found [20]. Sintered, porous polyethylene (PE) plates, polypropylene as non-woven material and a polypropylene plate with micropores (Celgard) can be used as diaphragms. The characteristics of these materials are listed in Table 3.1 for a 30 wt.% KOH electrolyte solution.

The internal resistance of the cell depends on the thickness of the electrolyte film between the electrodes. Other factors affecting the conductivity are the diaphragms, which determine the distance between the electrodes, the concentration of the electrolyte, and the average length of the electrolyte paths. The electrolyte resistance for the various diaphragm materials are listed in Table 3.2. The resistance of the electrolyte decreases with increasing temperature.

The resistance measurements show that non-woven polyproplyene has the best conductivity. The specific resistance is nearly the same as for the

Table 3.1 Diaphragm materials

Name	Material	Thickness	Pore size (μm)
PE plates	Polyethylene, sintered	1–3 mm	125–175
PP non-woven material	Polypropylene	2–3 mm	–
Celgard 3401	Polypropylene plate	25 μm	0.117

Table 3.2 Resistance of the electrolyte filled diaphragms, active area 50 cm^2, T = 70 °C

Material	Measured resistance (mΩ)	Specific resistance (Ω cm^2)	Specific resistance of diaphragm[1] (Ω cm^2)	Specific resistance of diaphragm thickness[2] (Ω cm)
Polyethylene plates, 3 mm	20.47	1.02	0.78	2.6
Celgard 3401 (on anode surface as well as on cathode surface), the distance between the electrodes was 1.5 mm	7.00	0.35	0.23	11.5
Non-woven polypropylene, 3 mm distance between the electrodes	5.15	0.26	0.09	0.3

[1]Additional resistance induced by the diaphragm which increases the electrolyte resistance.
[2]Specific resistance of the diaphragm material.

free electrolyte. In contrast, the resistance of the polyethylene plates is approximately four times higher. The microporous polypropylene material Celgard exhibits the highest specific resistance, but it is thin, at only 25 μm, and so the total resistance is relatively low. The advantage of the Celgard diaphragm is that it improves the stability of the electrodes under pressure.

3.8 Degradation of fuel cell components

3.8.1 Gas diffusion electrodes with Raney nickel catalysts

The life of fuel cells is a decisive factor in their commercialization, and so the degradation of fuel cell components is under intensive investigation, currently focused mainly on PEFC [55–66]. Several studies of the degradation of electrodes in alkaline fuel cells have been carried out [46, 47, 53, 67–74]. The most commonly used electrodes are PTFE bonded electrodes.

Three different types of electrode have been investigated at DLR [68]: type 1 consists of a mixture of pure Raney nickel and PTFE powder on a

nickel grid; type 2 consists of a mixture of a Raney nickel catalyst with added copper and PTFE on a copper grid; and in type 3 the nickel catalysts were size-selected before electrode preparation. The basic alloy used for the catalyst and the PTFE powder is the same in all electrodes.

The degradation of type 2 electrodes is described in detail in [53]. As well as the decrease in electrochemical performance [47, 75], different properties of the electrodes and their components changed during fuel cell operation. The physical characterization of the electrodes after operation showed that the pore size distribution had changed [75] (Fig. 3.8), while the specific surface was almost the same. The nickel catalyst particles disintegrated during

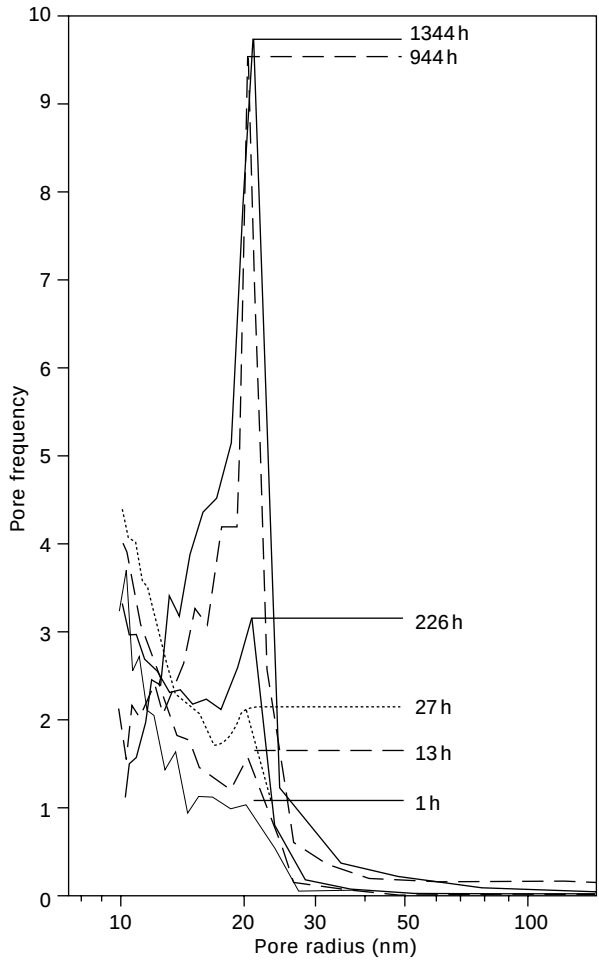

3.8 Pore size distribution measured by nitrogen adsorption measurements of electrodes after various operation times at 100 mA/cm^2 [53].

electrochemical operation (Fig. 3.9). Hydrogen embrittlement, caused by hydrogen loading and discharging of the nickel catalyst, was influenced by the electrochemical conditions. Finally, the disintegration of the nickel catalyst also depended on operating conditions, such as current density. The pore system measured by nitrogen adsorption is determined by the open pores in

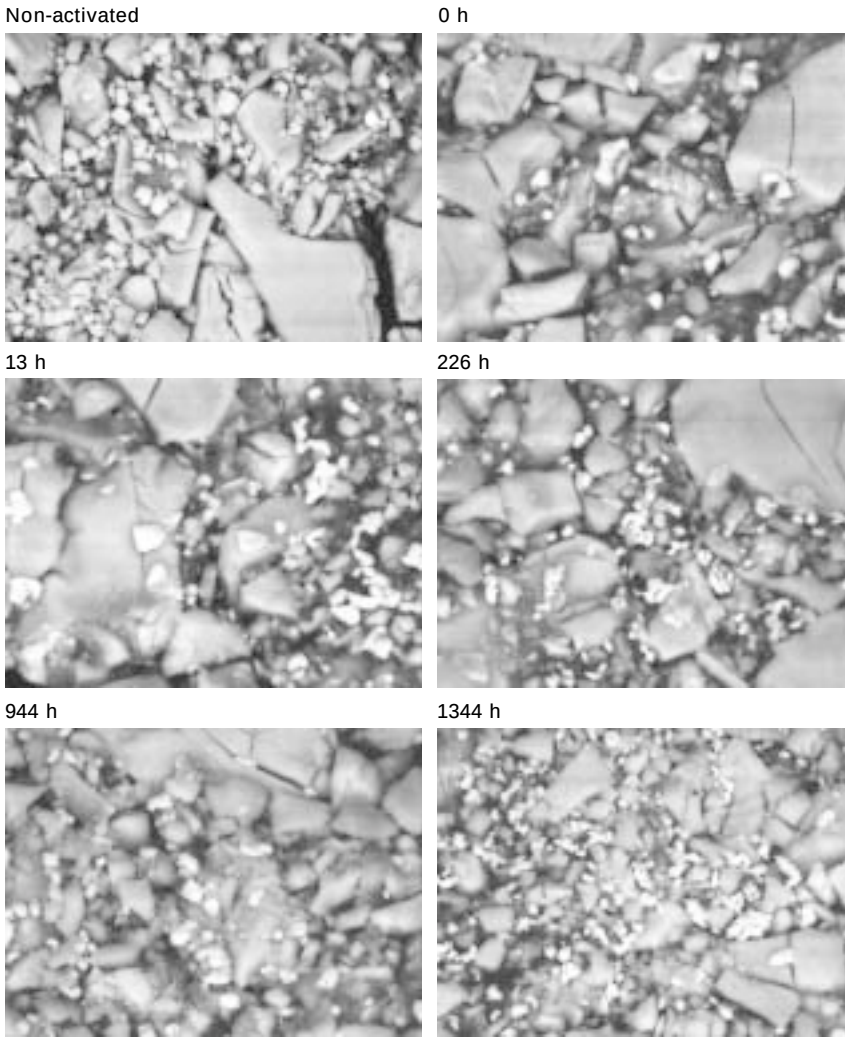

3.9 SEM images of anodes unstressed and electrochemical stressed various periods at a current density of 100 mA/cm^2. Top: a non-activated (left) and an activated and operated electrode (right). Below: electrodes after 13 h, 226 h, 944 h and 1344 h operation time [53].

the nickel catalyst, therefore the disintegration of the nickel particles influences pore size distribution.

If the overpotential at the anode is high, the nickel will be oxidized [47]. The copper is partially dissolved in the electrolyte. Residual aluminium in the electrode is further dissolved during fuel cell operation [47], and the PTFE decomposes [71]. This result is very surprising because PTFE should be stable in all electrochemical environments.

The same changes are also observed during the electrode activation process [53]. In addition, the copper dissolves, being transported through the surface to the electrolyte. In XPS measurements, a change in copper concentration that depended on time and current density was observed at the electrode surface [53].

Type 1 and type 2 electrodes have nearly the same initial electrochemical performance after activation. The initial performance of type 3 electrodes is slightly better. Type 1 and 2 electrodes have the same initial electrochemical performance due to the identical nickel catalyst in both electrodes. The improvement in electrical conductivity due to the copper does not result in a better electrochemical performance. In contrast, the size-selected nickel catalyst in type 3 electrodes leads to improved electrochemical performance. In long-term electrochemical experiments, all three types show a non-linear decrease in performance (which can be conductance, current density or voltage) (Perf) which can be approximated with a function of the following type:

$$\mathrm{Perf}_1(t) = a \exp\{-t/t_0\} + c \qquad 3.3$$

If polarization, induced by decreasing electrochemical performance during electrochemical loading, increases significantly over 100 mV, the electrochemical performance of the electrode rapidly deteriorates, as shown in the curve for a type 1 electrode over an operating time of 1200 h.

Type 2 electrodes were loaded with a current density from 25 mA/cm^2 up to 300 mA/cm^2. Type 3 electrodes were loaded at 100 and 150 mA/cm^2 in long-term experiments. Figure 3.10 shows the decrease in electrochemical performance for type 2 electrodes operating at different current densities. In Fig. 3.10c, the time curves for electrochemical performance have been normalized against the different initial electrochemical performances in order to compare the different samples.

The decrease in electrochemical performance for type 2 electrodes cannot be described with a single exponential function of the type in equation 3.3. The time-dependent electrochemical performance can be described by a combination of two exponential functions in the following form:

$$\mathrm{Perf}_2(t) = a \exp\{-t/t_0\} + b \exp\{-t/t_1(\mathrm{i})\} + c \qquad 3.4$$

The first exponential function depends only on time, the second exponential function depends on both current density (i) and time.

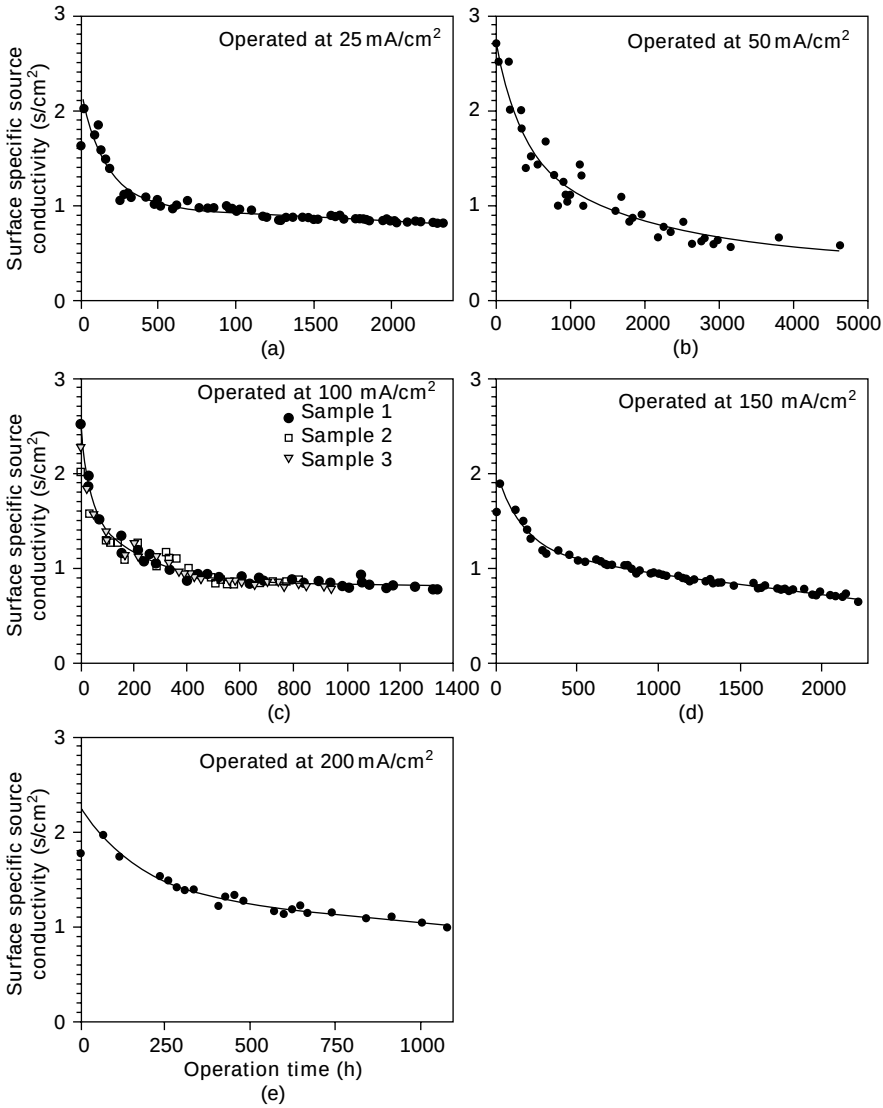

3.10 Time-dependent surface specific source conductivity of a nickel anode of type 2 recorded at different current densities: (a) 25 mA/cm^2, (b) 50 mA/cm^2, (c) 100 mA/cm^2, (d) 150 mA/cm^2, (e) 200 mA/cm^2 [68].

In contrast, for type 3 electrodes, the time-dependent electrochemical performance can be described with a single exponential function, whereby the e-function depends on the charging density.

$$\text{Perf}_3(t) = a \exp\{-t/t_0(i)\} + c \qquad 3.5$$

The decrease in electrochemical performance is similar for all three types of electrode. For type 1 and 3 electrodes under the described operating conditions and a current density of 100 mA/cm^2, a time constant t_0 of approximately 250 h was determined from the long-term behaviour of the surface specific source conductivity using equations 3.3 and 3.5. For type 2 electrodes at 100 mA/cm^2, one of the two time constants (t_0) in equation (3.4) was also determined to be approximately 250 h. The time constants for all three types of electrode are nearly the same.

The disintegration of nickel particles is expected to be comparable for type 1 and type 2 electrodes because the same catalyst is used in both electrodes. Due to the size of the nickel particles selected for type 3 electrodes, the disintegration differs from that of the other electrodes. For all electrode types, the concentration of small nickel particles increases, but because of the disintegration of large nickel particles in type 1 and 2 electrodes, different particle sizes are formed. The change in size distribution is not as significant for type 1 and 2 electrodes because large particles are simply being removed. For type 3 electrodes, the initial particle size distribution is shifted to lower particle sizes.

A decrease in electrochemical performance induced by electrochemical stressing was observed for all the gas diffusion electrodes with nickel catalyst anodes investigated in alkaline fuel cells. For all electrodes, a time constant of approximately 250 h was observed at a current density of 100 mA/cm^2. This time constant depended on the current density, and dependence on current density is stronger for type 3 electrodes than for type 2. The second time constant for describing the degradation of the electrochemical performance of type 2 electrodes depends strongly on the current density.

It is surprising that electrodes containing nickel catalysts with defined particle size have nearly the same time constants as electrodes with the standard nickel catalyst, because the disintegration of the nickel particles, which affects electrochemical activity, is different. The different time dependencies of pore frequency at 2 nm radius for type 2 and 3 electrodes reflect the different nickel particle disintegrations (Fig. 3.11). In contrast to the strong correlation between electrochemical performance (surface specific conductivity) and pore frequency observed for type 2 electrodes [53], a strong correlation between these two characteristics was not observed for type 3 electrodes.

During high loads, the electrode potential becomes so positive that the nickel reaches oxidation potential, which passivates the electrode. This loss of electrochemical performance is not correlated with an alteration in pore size distribution or pore frequency. However, the importance of nickel oxidation as a degradation effect depends strongly on the activation routine and the morphology of the electrodes. Nickel oxidation is not generally a dominant degradation process, thus it must be expected that the life-time of the electrodes

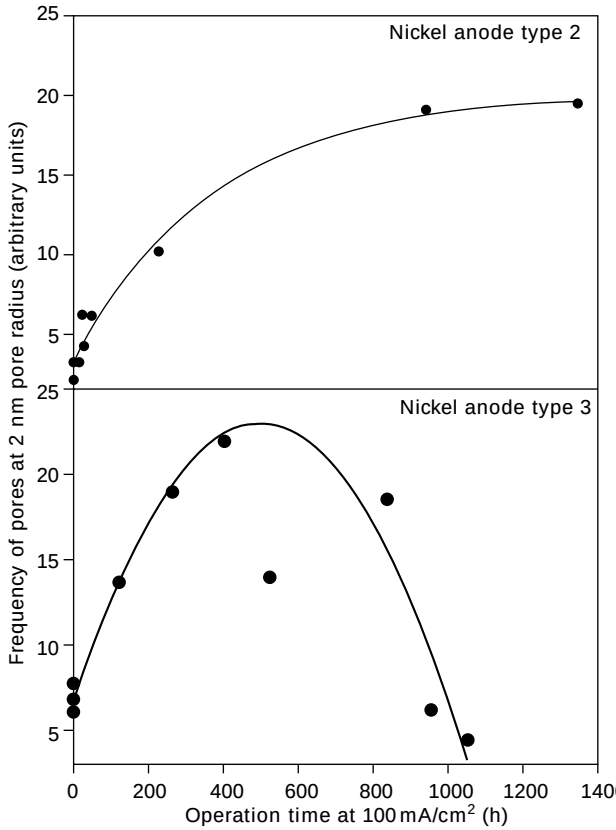

3.11 Pore frequency at 2 nm as function of time recorded with nitrogen adsorption measurements of electrodes of type 2 (top) and type 3 (bottom). [68].

depends on the current density caused by higher anodic polarization at higher current density.

In type 2 and 3 electrodes, the copper distribution changes because the copper is partially dissolved and transported across the surface during operation, and some of the copper is re-deposited. A significant effect due to long-term behaviour of the copper cannot be concluded from the measurements shown.

The disintegration of the nickel particles leads to the formation of more grain boundaries, and therefore poor electrical contacts between the particles should yield an increasing electrical resistance, resulting in higher losses. But the most significant effect is that the potential differences in the electrodes increase, and so the three-phase zone may be less extensive and hence electrochemical performance decreased.

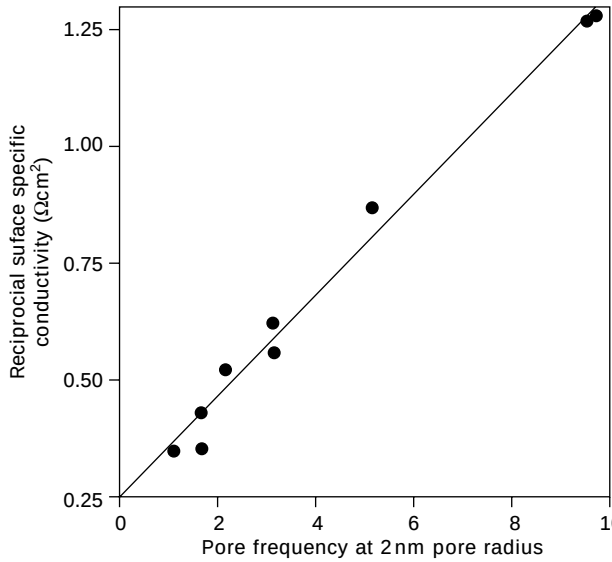

3.12 Correlation between the final reciprocal surface specific conductivity and pore frequency at 2 nm of the electrodes after various operation times at 100 mA/cm^2 [53].

In Fig. 3.12, the correlation between the final reciprocal surface specific conductivity, which means the reciprocal value of the last determined surface specific conductivity towards the end of the electrochemical experiment, and the pore frequency is displayed for electrodes stressed at 100 mA/cm^2. It can be clearly seen that the parameters are strongly correlated.

3.8.2 Gas diffusion electrodes with silver catalysts

Silver was investigated as a GDE cathode catalyst. For a silver GDE in a complete alkaline fuel cell, under certain circumstances the solubility of the silver can lead to a transfer of silver to the anode, and the resulting plating may damage the catalysts (usually Raney nickel) at the anode. During open circuit operation (idle periods), the silver may be oxidized. Carbon-containing cathodes in particular suffer from oxidation at higher temperatures. Shut down and restarting procedures can lead to damage as well.

Silver GDEs show a decrease in electrochemical performance during oxygen reduction at 70 °C in 30 wt% KOH. The decrease is linear, with a gradient of approximately 20 µV/h. Over an operating period of 5000 h, the total voltage loss will be approximately 100 mV. Taking into account the high cell voltages in AFCs, the loss in electrochemical performance related to the cathode is approximately 12–15 % of the cell voltage over 5000 h.

This means that the stability of silver cathodes is sufficient for mobile applications, but not for stationary applications. Stationary applications require improved long-term behaviour, and so the degradation processes must be understood.

To understand the results of physical and electrochemical characterization, two different pore systems must be distinguished: first, the pore system in the electrode formed by the spaces between the catalyst particles, which determines the gas transport, and second, the pores in the silver catalyst. In the first pore system, the hydrophobic character is dominant.

Physical characterization of the electrodes has shown that as the roughness of the catalyst decreases, the surface area of the catalyst also decreases [76]. Surface roughness is correlated to the second type of pore system. For platinum

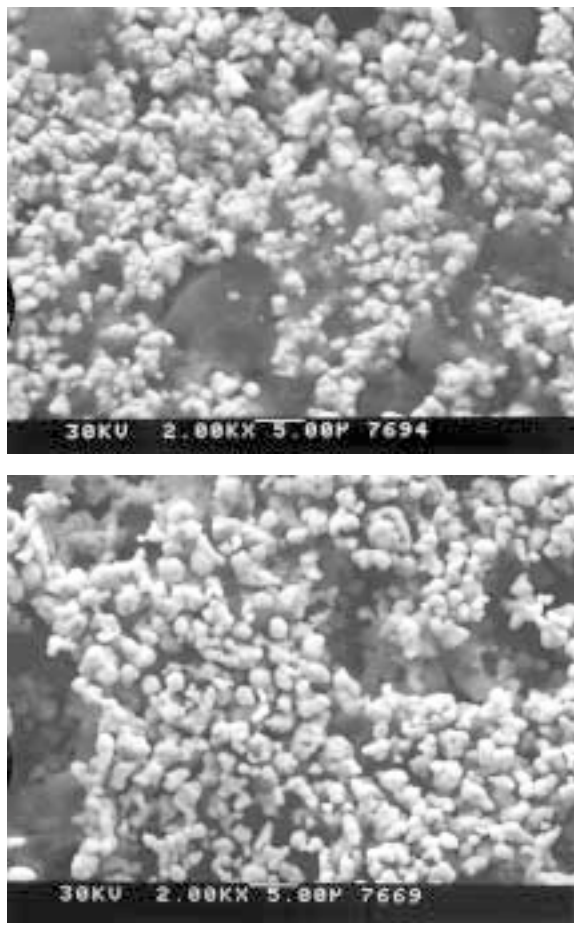

3.13 SEM micrograph of an unused (top) and a used (bottom) silver cathode for AFC [76].

catalysts in PEFC fuel cells, the electric field gradient was found to be the driving force behind the mobility of the platinum [75]. For the silver GDE, transport is hindered and the electric field gradients are expected to be enhanced in the pores. The decrease in surface roughness for the silver catalyst can be explained if the electric field gradient represents the driving force. Electrochemical characterization shows that the active surface area becomes smaller in relation to the double layer capacity, which is expected from the decrease in roughness (Fig. 3.13).

Due to the decrease in surface roughness, the pores become flatter and surface area decreases, and transport becomes easier. The decrease in specific surface area concerns mainly the surfaces where transport was most obstructed. Therefore, the effect of the decrease in surface roughness on electrochemical performance is not very strong. This can also be seen in the results of electrochemical impedance spectroscopy, where charge transfer resistance is almost constant (Fig. 3.14).

The second degradation effect at the electrodes observed by physical characterization is changes in the PTFE. The partial decomposition of PTFE can be related to a loss in hydrophobicity. Spectroscopic investigation of electrochemical impedance showed an increase in the Warburg impedance, which is related to an increase in transport resistance. The hydrophobic properties are important for gas transport in the electrode. A decrease in hydrophobicity means that more pores can be flooded by electrolyte, which hinders gas transport.

Both degradation effects are observed via both electrochemical and physical methods. The physical methods allow an easy description of the alteration, and the electrochemical methods enable the influence on electrochemical performance to be quantified. Consequently, a combination of electrochemical and physical methods is very helpful for studying degradation processes.

3.9 The impact of carbon dioxide on fuel cell performance

An important problem often mentioned in the literature is the formation of carbonates at the electrodes when using air instead of oxygen. This has been studied at DLR. Electrodes (both anode and cathode) were operated in pure and CO_2-contaminated fuel gases and investigated afterwards. The tests continued without problems for 3500 h.

The electrodes were electrochemically stressed and characterized in an electrochemical half-cell configuration consisting of the electrode in a holder manufactured from acrylic glass, a nickel counter electrode and an Hg/HgO reference electrode. In the experimental setup, the electrodes were supplied with gases without overpressure from the underside (the side with the metallic

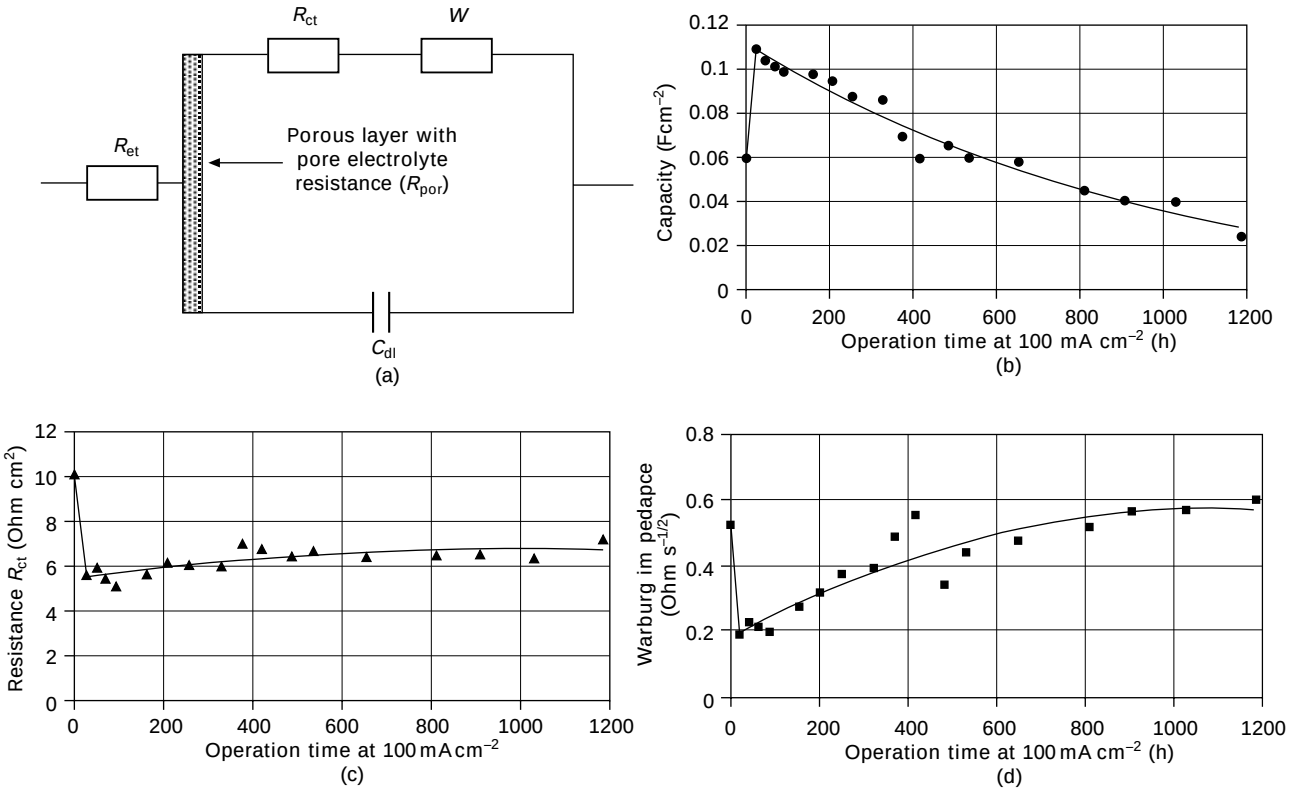

3.14 Equivalent circuit (porous electrode model) for the evaluation of the impedance spectra of the silver gas diffusion electrodes (a) and time dependency of double layer capacity (b), of charge transfer resistance (c) and of Warburg impedance (d) obtained with a least square fit of the measured impedance spectra at open circuit potential on the silver GDE after different periods of operation [76].

web). The electrode holder was inserted into a temperature controlled vessel (80 °C) containing 30 wt.% KOH. The vessel contained approximately 1.5 litres of electrolyte. The electrode had an active area of 6 cm^2. The gas diffusion electrodes (GDEs) were operated for up to several thousand hours with a constant loading of 100 or 150 mA/cm^2. The advantage of the half-cell tests compared with long-term experiments using a full cell configuration is that the electrodes and their degradation can be investigated individually.

To investigate the mechanism of carbon dioxide poisoning, the electrodes were operated with gases containing 5% CO_2 and with pure gases as reference. Before operation with contaminated gases, all electrodes were operated with pure gas for 100 h. The CO_2 content in the gases was 150 times higher than that of air, the high concentration being used to enhance the potential effects of the carbon dioxide.

For electrochemical characterization, V-i curves were recorded and corrected by I-R drop measurements to compensate for the ohmic losses in potential. The V-i curves were recorded every 24 h. A characteristic parameter for the electrochemical performance of the anodes is the slope of the V-i curve (surface specific conductivity) as described in [68]. The electrochemical performance of the cathodes can be described in the same way. In parallel to electrochemical characterization, the CO_2 content of the gases was investigated by gas chromatography and the concentration of carbonate in the electrolytes was determined after various operating times.

All cathodes investigated show very similar initial electrochemical performance. The electrochemical performance of the anodes was also very similar, but differed from that of the cathodes. The electrochemical performance of the electrodes decreased during the electrochemical experiments.

Figure 3.15 shows electrochemical performance during long-term experiments conducted with silver cathodes. The decrease in electrochemical performance for all cathodes is independent of whether the experiments were performed with pure or with CO_2-contaminated oxygen. This indicates that carbon dioxide neither influences electrochemical performance nor accelerates the degradation process. The slope of the time-dependent electrochemical performance shows a decrease of 17 μV/h for the cathode [77]. Electrochemical impedance spectroscopy measurements recorded during a long-term experiment with silver cathodes in pure oxygen [74] have shown that the decrease in electrochemical performance is induced by a decrease in active surface along with reduced transport [76]. The decrease in electrochemical performance could be explained by alteration or decomposition of the PTFE. PTFE is necessary for gas transport and influences the extension of the three-phase zone [76].

Silver anodes were operated for more than 2600 h and XPS measurements were taken. The element distributions in the depth profile measurements of the electrodes operated with pure oxygen and oxygen containing carbon

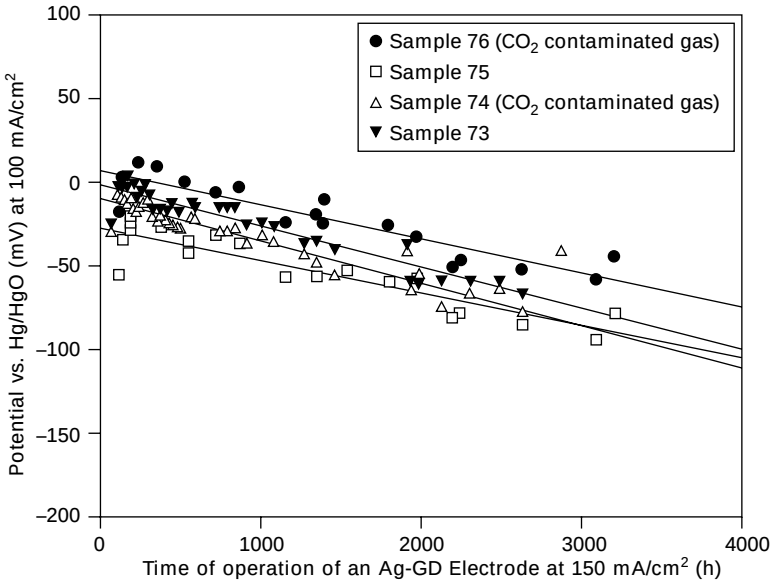

3.15 Change of the electrochemical performance of the silver cathode during operation with pure oxygen and oxygen containing 5% CO_2 [77].

dioxide were equal. The carbon signal on the XP spectra is of particular interest, because the carbon dioxide can form carbonates which may be deposited on or in the electrodes. The XP spectra of electrodes operated with pure and CO_2-containing gases do not differ significantly, which is an indicator that no carbonate is deposited onto the electrode surfaces or in the pore systems of the electrodes.

Electrochemical performance decreases as described in [68] under both operating conditions. The decrease is very similar, and therefore does not indicate any influence of carbon dioxide.

The pore system and the specific surface area of the nickel anodes were investigated by nitrogen adsorption measurements. The specific surface area of anodes operated with pure hydrogen and with CO_2-containing hydrogen for various periods was nearly constant and no change induced by the carbon dioxide was observed.

In addition, the anodes were investigated by XPS after operating for over 2600 h in pure hydrogen and hydrogen containing CO_2. As in the XPS analysis of silver cathodes, the depth profiles of both anodes were very similar and no deposited carbonate was observed. In addition, SEM measurements were also carried out on the electrodes, and again no effects due to the carbon dioxide were observed (Fig. 3.16). The electrochemical performance and the physical characterization of both anodes and cathodes showed no significant influence due to carbon dioxide.

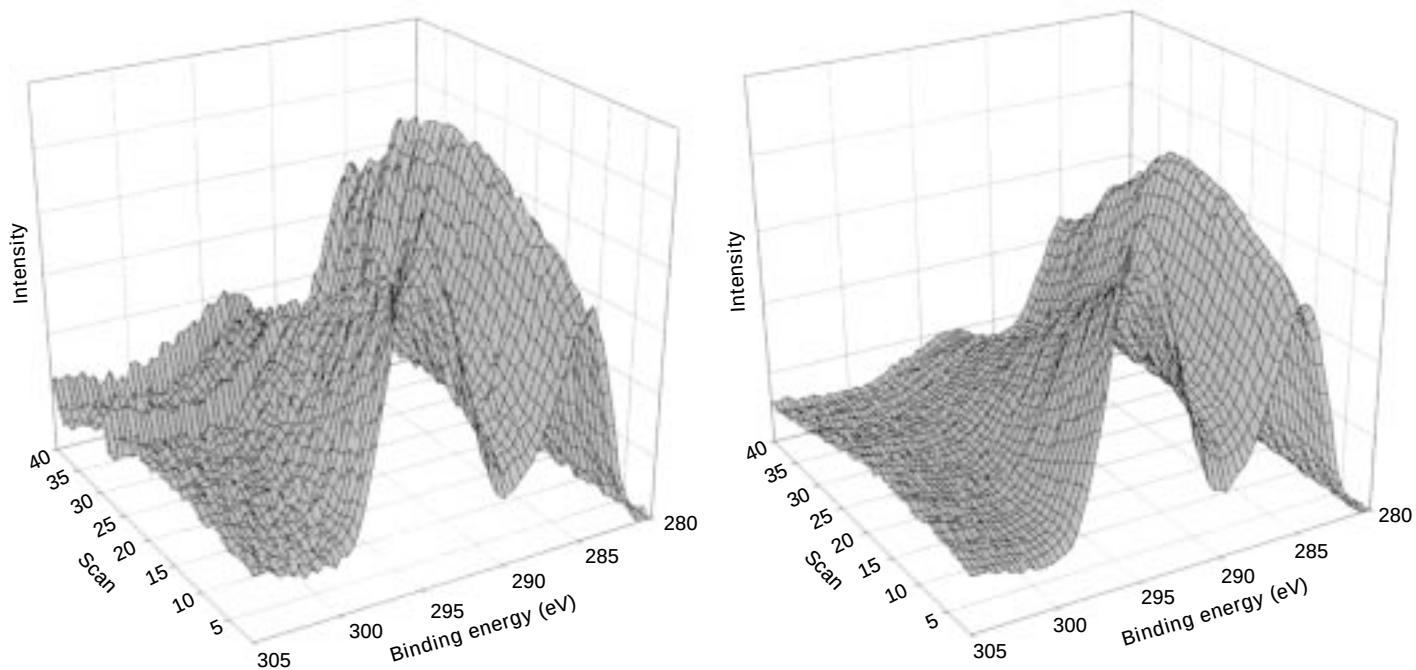

3.16 XP spectra of the carbon C1s signal recorded during depth profile measurements of a cathode operating 2633 h with pure oxygen (left) and of a cathode operating 2682 h with oxygen containing 5% CO_2 (right) [77].

The third electrochemical component in an AFC besides the two electrodes is the liquid electrolyte. Gas chromatography measurements of the CO_2 content in the residual gas behind the electrodes showed that the residual gas at the anode contains approximately 10 % of the amount of CO_2 recorded in the feed gas, and that the residual gas at the cathode contains approximately 20 % of the CO_2 in the feed gas. This indicates that most of the CO_2 is dissolved in the alkaline solution through the formation of K_2CO_3. Therefore, the carbonate concentration in the alkaline electrolyte increases, as shown in Fig. 3.17. As expected, the carbonate concentration increases linearly during operating time if gases containing CO_2 are used, while no difference between anode and cathode operation is observed. In long-term experiments with higher K_2CO_3 concentration, up to 450 g/l, the conductivity of the electrolyte was reduced but the electrodes were not affected. The solution limit for K_2CO_3 is between 50 and 60 wt% in the temperature range investigated [78], and therefore was not reached in the experiments described.

The long-term experiments were terminated after 3500 h. An overall charge transfer of 525 A h/cm^2 was achieved at CO_2 concentrations 150 times higher than that of air. The electrodes were fully operable when the long-term experiment was terminated. This duration corresponds to an operating time of about 3000 h for internal combustion engines. Since exchanging the electrolyte in an AFC is very simple, it can easily be carried out after a few hundred hours to maintain performance.

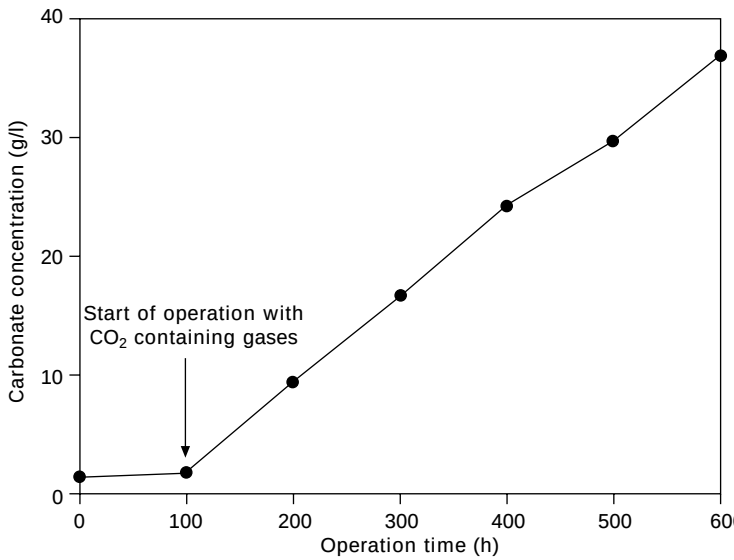

3.17 Carbonate content in the electrolyte after various operation times with CO_2-containing gases [77].

Taking all the results into account, it must be concluded that CO_2 in air is not really a problem for AFCs, therefore AFCs can be used for mobile applications.

3.10 Future trends

The two main problems for AFCs are CO_2 behaviour and the liquid electrolyte. The first problem can be solved using a cleaning step or by optimizing structures. The problem of the liquid electrolyte leaking, which necessitates expensive sealing technologies, can be solved by using anion exchange membranes. Many companies are working on this kind of membrane, and not only for fuel cell applications – electrochemical reactors would benefit from anion exchange membranes as well. But to date no membrane has been developed with long-term stability and the ability to work without a liquid electrolyte phase, and it is not yet clear if there is an additional problem with carbonate formation inside the membrane when operating with air.

3.11 Sources of further information and advice

3.11.1 Astris

Founded in Canada in 1983, Astris Energi has steadily developed the AFC. The Astris line of AFC power products comes in a variety of configurations. For the industrial market, the POWERSTACK™ MC250 is offered in sizes from 300 W to 2.4 kW per stack. Designed for the educational and scientific market, the LABCELL™ LC50 comes in stacks rated from 4–60 W, and the slightly larger LABCELL™ LC200 comes in sizes ranging from 15–240 W [79]. Astris Energi has signed a binding letter of intent with Cyprus-based Green Shelters Innovations Ltd (GSI) to sell substantially all of its assets for US$5.8 million [80].

3.11.2 DLR

The German Aerospace Centre (DLR) in Stuttgart started developing AFCs in 1986. The main area of research was electrode technology with CO_2 tolerance. In the 1990s, the focus shifted to degradation investigations and new cell concepts.

3.11.3 Gaskatel

Gaskatel GmbH, founded in the 1990s, has worked on the development, production and distribution of electrochemical electrodes and electrochemical converters, in particular the Eloflux cell of Professor Winsel [16].

3.11.4 Ovonics

The Ovonic Fuel Cell Company develops rugged, kW-scale metal hydride fuel cells targeted at backup and mission-critical power for military and commercial applications. The metal hydride fuel cell is a fundamentally new approach to fuel cells that avoids the traditional noble catalysts and incorporates charge storage materials in the electrodes [81]. Meanwhile, US-based Energy Conversion Devices (ECD Ovonics) is restructuring its business activities, and substantially reducing its R&D efforts in fuel cell technology [80].

3.11.5 Hydrocell

Hydrocell's fuel cells are based on a cylindrical electrode which provides a strong and lightweight unit. The electrolyte employed is a gel developed by Hydrocell. The advantages of gel-type electrolytes are that they can store, release and transport the water released during operation [22].

3.11.6 More Energy

More Energy Ltd – a subsidiary of US-based Medis Technologies – has signed a joint business cooperation and distribution agreement with fuel cell developer Oy Hydrocell Ltd in Finland. Hydrocell possesses advanced technology and know-how to manufacture and use gel electrolytes in fuel cell products, and is developing fuel cells with capacity of 20 W and above [82].

3.11.7 Intensys

Intensys develops systems with fuel cells. The parent company, E-Vision, incorporated the knowledge of Elenco and Zetek, so this company has a strong knowledge of AFC and fuel cell systems. The company presented a 6 kW residential system at the Fuel Cell Seminar 2007 in San Antonio [83].

3.12 References

1. http://en.wikipedia.org/wiki/Alkaline_fuel_cell
2. http://en.wikipedia.org/wiki/William_Robert_Grove
3. http://en.wikipedia.org/wiki/Christian_Sch%C3%B6nbein
4. J. H. Reid, US Patent No. 736 016 017 (1902): US Patent No. 757 637 (1904)
5. P. C. L. Noel, French Patent No. 350 111 (1904)
6. A. Schmid, *Die Gasdiffusionselektrode*, Verlag F. Enke, Stuttgart 1923
7. A. Schmid, *Helv. Chim Acta* 7 (1933) 7
8. DRP 48 466 (1888)
9. http://en.wikipedia.org/wiki/Murray_Raney

10. http://en.wikipedia.org/wiki/Francis_Thomas_Bacon
11. Justi, Winsel, *Kalte Verbrennung*, Franz Steiner Verlag GmbH, Wiesbaden 1962
12. K. Kordesch, *Fuel Cells and Their Applications*, Wiley-VCH 1999
13. O. Führer, S. Rieke, C. Schmitz, B. Willer and M. Wollny, Alkaline Eloflux fuel cells and electrolysis cells using a new kind of gas diffusion electrodes *International Journal of Hydrogen Energy*, 19 (4), April 1994, p. 343–348.
14. A. Winsel, *The Eloflux Fuel Cell System*, Dechema-Monogr. aphien Bd 92 (1983) 1885–1913.
15. A. Winsel, R. Wendtland, US Patent No. 3, 597, 275 (1971)
16. http://www.gaskatel.de
17. R. Staab, *Chem.-hzg.-Tech.*, 59 (1987) 316–319
18. K-H. Tetzlaff, W. Wendel DECHEMA-Monographien Bd 112 (1988) 325–337
19. K.-H. Tetzlaff, R. Walz and C. A. Gossen, *J. Power Sources* 50 (1994) 311–319
20. E. Gülzow, M. Schulze, U. Gerke, *J. Power Sources* 156 (2006) 1
21. E. Gülzow, M. Schulze, U. Gerke, *Development of an alkaline fuel cell stack with bipolar configuration*, Fuel Cell Seminar 2004, San Antonio
22. http://www.hydrocell.fi/en/fuel_cells/
23. http://www.hydrocell.fi/en/fuel_cells/hc-100.html
24. S. R. Ovshinsky, Z. Menjak, S. Venkatesan, L. Gradinarova, A. Menjak, H. Wang, alkaline fuel cell pack with gravity fed electrolyte circulation and water management system, US Patent Application 2004–0161652, August 19, 2004
25. B. Reichman, M. A. Fetcenko, S. R. Ovshinsky, K. Young, W. Mays, J. Strebe, Low temperature alkaline fuel cell, US Patent Application 2005–0064274, March 24, 2005
26. http://www.ovonics.com/PDFs/fuel_cell/ovonic-fuel-cell-patents.pdf
27. http://www.ovonics.com/PDFs/fuel_cell/ovonic-fuel-cell-overview_mar07.pdf
28. http://www.ovonics.com/PDFs/fuel_cell/ovonic-fuel-cell-patent-applications.pdf
29. F-Cell Vortrag Offenburg
30. Y. Kiros, S. Schwartz, *J. Power Sources* 87 (2000) 101
31. A. Winsel, *Electrochim Acta* 14 (1969) 961
32. H. Sauer, D. Spahrbier, US Patent 1976, No. 3 977 902
33. Justi, Winsel, *Kalte Verbrennung*, Franz Steiner Verlag GmbH, Wiesbaden 1962, p. 117
34. http://www.hydrocell.fi/en/materials/
35. K. Miyazaki, N. Sugimura, K. Matsuoka, Y. Iriyma, T. Abe, M. Matsuoka, Z. Ogumi, $La_{1-x}Ca_xMnO_3$ als AFC cathoden *J. Power Sources* 178 (2008), 683
36. S. C. Singhal, K. Kendall, *High Temperature Solid Oxide Fuel Cells: Fundamentals, Design and Applications*, Elsevier 2003
37. Y. Wang, Y. Xia, *Electrochemistry Communication* 8 (2006) 1775
38. A. Verma, A.K. Jha, S. Basu, *J. Power Sources* 141 (2005) 30
39. H. Meng, M. Wu, X.X. Hu, M. Nie, Z.D. Wie, P.K. Shen, W_2C *Fuel Cells* 6 (2006) 447
40. H Sauer, German Patent No. DE 2 941 774 (CI H01M4/88)
41. A. Winsel, German Patent No. DE 3 342 969 (CI C25B11/06)
42. E. Gülzow, W. Schnurnberger, Dechema-Monographien Bd 124 (1991) 675
43. E. Gülzow, B. Holzwarth, M. Schulze, N. Wagner, W. Schnurnberger, Dechema-Monographien Bd 125 (1992) 561
44. E. Gülzow, K. Bolwin, W. Schnurnberger, Dechema-Monographien Bd 121 (1990) 483

45. E. Gülzow, K. Bolwin, W. Schnurnberger, Dechema-Monographien Bd 117 (1989) 365
46. Sleem-Ur Rahman, M. A. Al-Saleh, A. S. Al-Zakri, S. Gultekin, *J. Appl. Electrochem.* 27 (1997) 215
47. E. Gülzow, B. Holzwarth, W. Schnurnberger, M. Schulze, G. Steinhilber, N. Wagner, *PTFE bonded gas diffusion electrodes for alkaline fuel cells*, 9th World Hydrogen Energy Conference 92, Paris, S 1507
48. K. Rühling, *Untersuchungen an neuartigen PTFE-gebundenen Raney nickel- und Silberelektroden*, Diploma work, University of Kassel, 1986
49. M. Schulze, E. Gülzow, in preparation
50. M. Lorenz, M. Schulze, *Fresenius J. Anal. Chem.*, 365 (1999) 154
51. M. Schulze, R. Reißner, M. Lorenz, W. Schnurnberger, Photoelectron-analysis of water adsorption on defined nio surface layers *Electrochim. Acta*, 44(1999) 3969
52. S. Kitagawa, Proceedings JIMIS-2, *Hydrogen in metals*, Minikami, Japan 1979, p. 497
53. M. Schulze, E. Gülzow, *J. Power Sources* 127 (2004) 252
54. E. Gülzow, N. Wagner, M. Schulze, *Fuel Cells* 3 (2003) 67
55. D.P. Davies, P. L. Adcock, M. Turpin, S. J. Rowen, *J. Appl. Electrochem.* 30 (2000) 101
56. D. P. Davies, P. L. Adcock, M. Turpin, S. J. Rowen, *J. Power Sources* 86 (2000) 237
57. B. Mattsson, H. Ericson, L. M. Torell, F. Sundfolm, *Electrochim. Acta* 45 (2000) 1405
58. G. Hübner, E. Roduner, *J. Material Chemistry* 9 (1999) 409
59. M. Schulze, M. Lorenz, N. Wagner, E. Gülzow, *Fresenius J. Anal. Chem.* 365 (1999) 106
60. F. N. Büchi, B. Gupta, O. Haas, G. G. Scherer, *Electrochim. Acta* 40 (1995) 345
61. E. Gülzow, A. Helmbold, T. Kaz, R. Reißner, M. Schulze, N. Wagner, G. Steinhilber, *J. Power Sources* 86 (2000) 352
62. S. Gupta, D. Tryk, S. K. Zecevic, W. Aldred, D. Guo, R. F. Savinell, *J. Appl. Electrochem.* 28 (1998) 673
63. E. Gülzow, M. Fischer, A. Helmbold, R. Reißner, M. Schulze, N. Wagner, M. Lorenz, B. Müller, T. Kaz, *Innovative production technique for PEFC and DMFC electrodes and degradation of MEA-components*, Fuel Cell Seminar 1998, Palm Springs, 16–19. November, p. 469
64. E. Gülzow, T. Kaz, M. Lorenz, A. Schneider, M. Schulze, *Degradation of PEFC components*, Fuel Cell Seminar 2000, Portland, October 30–November 2 p. 156
65. M. S. Wilson, J. A. Valerio, S. Gottesfeld, *Electrochim. Acta* 40 (1995) 355
66. P. G. Dirven, W. J. Engelen, C. J. M. Van Der Poorten, *J. Appl. Electrochemistry* 25 (1995) 122
67. E. Gülzow, M. Schulze, G. Steinhilber, K. Bolwin, *Carbon dioxide tolerance of gas diffusion electrodes for alkaline fuel cells*, Fuel Cell Seminar, 1994, San Diego, p. 319
68. E. Gülzow, M. Schulze, G. Steinhilber, *J. Power Sources* 106 (2002) 126
69. S. Gultekin, M. A. Al-Saheh, A. S. Al-Zakri, K. A. A. Abbas, *Int. J. Hydrogen Energy* 21 (1996) 485
70. Y. Kiros, S. Schwartz, *J. Power Sources* 87 (2000) 101
71. M. Schulze, K. Bolwin, E. Gülzow, W. Schnurnberger, *Fresenius J. Anal. Chem.* 353 (1995) 778

72. A. Khalidi, B. Lafage, P. Taxil, G. Gave, M. J. Clifton, P. Cezac, *Int. J. Hydrogen Energy* 21 (1996) 25
73. M. Schulze, E. Gülzow, G. Steinhilber, *Appl. Surf. Sci*. 179 (2001) 252
74. N. Wagner, E. Gülzow, M. Schulze, W. Schnurnberger, Gas diffusion electrodes for alkaline fuel cells in Solar Hydrogen Energy, German–Saudi Joint Program on Solar Hydrogen Production and Utilization Phase II 1992–1995, H Steeb, H. Aba (Eds) Oud, Stuttgart 1996
75. M. Schulze, A. Schneider, E. Gülzow, *J. Power Sources* 127 (2004) 213
76. N. Wagner, E. Gülzow, M. Schulze, *J. Power Sources* 127 (2004) 264
77. E. Gülzow, M. Schulze, *J. Power Sources* 127 (2004) 243
78. D. R. Lide (ed.), *Handbook of Chemistry and Physics*, 77th edition, CRC Press, Boca Raton 1996
79. https://www.astris.ca
80. Astris Energi sells assets, ECD Ovonics restructures *Fuel Cells Bulletin*, 2007 (6), June 2007, p. 8
81. http://www.ovonic.com/eb_fc_fuel_cell_solutions.cfm
82. Medis cooperation with Finnish on gel materials; *Fuel Cells Bulletin*, 2006, (7), July 2006, p. 8–9
83. http://www.intensys.com

4

Polymer electrolyte membrane fuel cells

C HARTNIG, L JÖRISSEN, J KERRES, W LEHNERT and J SCHOLTA, Centre for Solar Energy and Hydrogen Research (ZSW), Germany

4.1 Introduction

The basic set-up of a polymer electrolyte membrane fuel cell (PEMFC) is in line with the previously mentioned types: the two electrodes are separated by means of an electrically insulating but ionically conductive membrane (polymer electrolytes). In a PEM fuel cell, the anodic reactant is hydrogen which is oxidized to form protons; at the cathode, oxygen is reduced and forms water with protons that are transported through the proton conductive membrane. The overall reaction is

$$H_2 + {}^1/_2\, O_2 \rightarrow H_2O \qquad 4.1$$

Maximum power densities range up to 1 W/cm^2 which are achieved at pressurized gas supply; this mode leads, owing to the necessary compressor at an operating pressure of 5 bar, to a parasitic power loss of around 12% of the performance[1]. In a low-pressure operation the power densities are below the above given value and lie around 0.5 W/cm^2.

In Fig. 4.1 the characteristic curve of a PEM fuel cell is displayed. By means of the curve, different contributions forming the potential of the cell can be explained. U_0, the thermodynamic reversible potential, is the potential which can be measured in a currentless set-up, also called rest potential. For PEMFCs, the rest potential amounts to 1.23 V. The initial exponential decay of the voltage with increasing current density in the first region of the curve denoted by (1) is caused by the poor electrode kinetics. This part can be improved by the characteristics of the electrocatalytic layer. The middle part, (2), is the so-called ohmic-loss region: here a linear relationship due to the ohmic resistance of the cell components can be observed which is underlined by the solid line A. Deviations from the rest potential U_0 are therefore caused by ohmic contributions (R) and contributions caused by the overpotential η (denoted by the sum $R + \eta$). Finally, in (3) mass transport limitations lead to a sharp decrease of the potential with increasing current densities. These transport limitations are caused by several factors, the diffusion of reactant

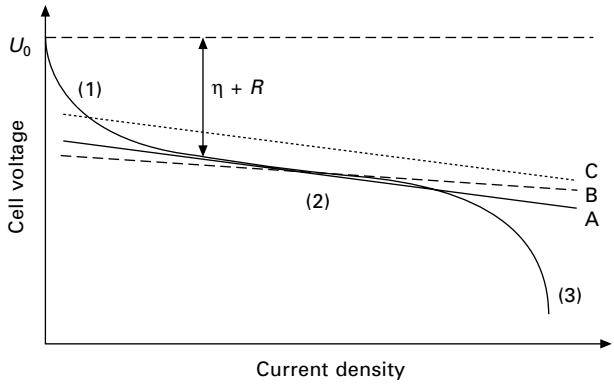

4.1 Characteristic curve (*U-i* curve) of a fuel cell.

gases (as in PEMFC) is limited, liquid reaction products lead furthermore to blocked channels enhancing the performance decrease.

Optimization of the cell performance is guided by mainly two strategies: an improved conductivity would lead to a shallower slope of the ohmic resistance curve, exemplified by the dashed line B. Thereby, an enhanced conductivity has only a minor effect on the overall performance. To underline the importance of the ohmic loss and the overpotential, one should compare the different contributions: at a current density $i_0 = 1500\,\text{mA/cm}^2$, the ohmic loss is approximately 80 mV; however, the overpotential loss at this current density amounts to 400 mV[2,3], which underlines the importance for improved electrocatalysts.

Another more effective strategy would therefore aim at region (1): here, a decrease of the activation overpotential and an improvement of the electrode kinetics would lead to an overall shift of the curve to higher voltages, as described by the dotted line C. Optimization strategies usually include both ways, the latter will be discussed in more detail in the catalyst section.

The chapter outline follows the path of the protons: from the membrane via the catalysts and the gas diffusion media to the flow field; finally, system related aspects are discussed.

4.2 Membrane development for polymer electrolyte fuel cells

Fuel cell membrane materials have to be capable of conducting protons. The choice of materials depends on the temperature range at which the fuel cells are operating. For fuel cells operating at temperatures below 100 °C, here called 'low-temperature fuel cells' (LTFC), cation-exchange materials such as sulfonated polymers are used. They require liquid water for dissociation of the proton from the sulfonic acid group bound to the polymer backbone.

For the temperature range between 100 and 200 °C where the H_2O partial pressure decreases progressively with temperature, amphoteric proton self-conductive materials such as phosphoric acid/phosphonic acid, acidic phosphates or heterocycles which are capable of donating and accepting protons without requiring the 'vehicle molecule' water have to be used as proton-conducting electrolyte between the electrodes of the fuel cell. Fuel cells operated in this temperature region are here called 'intermediate-temperature fuel cells' (ITFC). In Section 4.3, an overview will be given of the state of the art of the different types of fuel cell electrolytes for H_2 polymer electrolyte fuel cells (PEFC) and direct methanol fuel cells (DMFC).

4.3 Sulfonated ionomer membranes: perfluorinated ionomer membranes

4.3.1 Homogeneous perfluorinated ionomers

The perfluorinated polyether ionomers are composed of a perfluoroalkyl backbone and perfluoroether side chains carrying a sulfonic acid group at their end. This ionomer type was invented by Grot *et al*. at DuPont[4–6]. The ionomers are copolymers, where tetrafluoroethylene and the unsaturated sulfonyl fluoride ether compound $CF_2{=}CF(OCF_2CF_2)_nOCF_2CF_2SO_2F$, where n is 1 to 3, are copolymerized by free-radical polymerization. The preparation of the sulfonyl fluoride monomer is disclosed by Harper and Norman[7]. Up to now, the perfluorinated aliphatic polyethers from the Nafion® type are the most economically important due to their excellent proton conductivities, chemical stabilities and therefore long operation durability of several thousand hours[8]. Apart from the pioneering development of the Nafion® membranes by DuPont, other companies such as Dow Chemical[9] (no longer in production), Asahi Chemical (Aciplex), Asahi Glass (Flemion)[10] and 3M[11] have developed alternative perfluoro ionomers which are distinguished from Nafion by different type and length of the ionomeric side chain. Over the past decades, these materials have been strongly varied and optimized in terms of type and length of their side chain, in terms of molecular weight and polymeric chain end groups, wherein a reduction of end groups led to a marked increase of membrane durability[12]. The joint characteristic of this material group is the strong micro-phase separation between strongly hydrophilic micro-phase which contains the sulfonic acid groups and therefore form the proton-conducting polymeric phase, and the strongly hydrophobic polymeric phase which is composed of the perfluoroalkyl backbone which serves for the high mechanical strength of the perfluoro ionomers[13–15]. Disadvantages of the perfluorinated ionomers are:

- the complicated and environmentally unfriendly production process which involves toxic intermediates and waste products

- the high price
- the strong decrease of proton conductivity when the water content of the membrane is reduced[16,17]
- the high methanol permeability when they are operated in direct methanol fuel cells[18,19].

These disadvantages have led to the development of a huge number of alternative ionomer membrane types which will be presented and described in the following sections.

4.3.2 Perfluorinated composite ionomers

The principle of reinforcing the perfluorinated ionomers by embedding into thin porous polytetrafluoroethene (PTFE) foils was introduced by Gore and Associates who earlier developed the porous PTFE foil with the trade name Gore-Tex® for use in weather proof functional clothings. These porous foils were filled with a perfluorinated ionomer of the Nafion® type[20–23]. The advantage of these membranes is that, because they are very thin (10–30 μm), they show very high proton conductivities and therefore excellent fuel cell performance. Moreover, this PTFE reinforcement provides excellent mechanical stabilities despite their low thickness. The membranes were tested for several thousand hours in fuel cells, without membrane failure[1].

4.4 Partially fluorinated membranes

Several types of partially fluorinated sulfonated ionomer membranes have been developed by different research groups. A selection of these membrane types is given below.

4.4.1 Sulfonated poly(α,β,β–trifluorostyrene) and its copolymers

Ionomers of this type have been developed by Ballard. The production procedure involves first the (co)polymerization of α,β,β–trifluorostyrene and similar unsaturated compounds, followed by sulfonation of the polymers[25–30]. The advantages of this ionomer-type are its excellent chemical stability and fuel cell performance, which is comparable with that of the perfluorinated ionomers[31]. The disadvantage are the difficult polymerization process of the monomers (the monomers tend to dimerization which deactivates them for the radical polymerization process), and the difficult sulfonation of the polymer. Because of the strong electron deficiency of the aromatic groups, strong sulfonation agents such as oleum, which can lead to cross-linking of the polymer during the sulfonation procedure, are required to

achieve sufficient degrees of sulfonation and therefore sufficient proton conductivities of the resultant ionomer membrane. To our knowledge, this polymer has not been produced in significant amounts up to now due to these disadvantages.

4.4.2 Radiation-grafted ionomers

Radiation-grafted ionomers are produced in a three-step process. The first step is the irradiation of a partially fluorinated or perfluorinated polymer foil with γ- or β-irradiation (literature for radiation grafting: FEP-g-PS (γ irradiation)[32,33], PVDF-g-PS (electron irratiation)[34–36]) which produces radical sites within the foil. In the second step, the irradiated foils are immersed and swollen in an unsaturated monomer-containing liquid. At this stage, at the radical sites polymeric side-chains are growing within the polymeric foils by reaction of the radical site with the monomer which in most cases is styrene, divinylbenzene or other unsaturated aromatics. In such systems, divinylbenzene serves as a cross-linker. In the third step, the grafted polymer foils are sulfonated by immersing them in a sulfonation agent containing mixtures such as tetrachloroalkane/chlorosulfonic acid. The advantage of this ionomer membrane type is that the educt materials (perfluorinated or partially fluorinated fluoropolymer foils and styrene/divinylbenzene) are inexpensive, the membrane preparation procedure can easily be upscaled, the sulfonation degree and therefore the proton conductivity can be adjusted easily by suitable choice of sulfonation agent, concentration, sulfonation time and sulfonation temperature. The possibility of varying many ionomer membrane parameters of this membrane type makes it an excellent model system for studying the dependence of ionomer membrane properties on membrane structure[37]. The disadvantage of this membrane type is that the grafted and sulfonated side chains of these ionomers are chemically and thermally as unstable as sulfonated polystyrene, which disqualifies this ionomer membrane type for fuel cell operation at temperatures higher than 60 °C.

4.5 Nonfluorinated membranes

Nonfluorinated ionomers such as sulfonated and cross-linked polystyrene[38] were among the first materials to be tested as proton conductor and separator in membrane fuel cells. It was shown, however, very early that these materials cannot withstand the severe chemical conditions present in a working fuel cell: namely the α-C–H bond is very prone to being attacked by radicals which are always present in fuel cells[39,40]. Apart from sulfonated polystyrene, similar sulfonated polymer materials such as Dais Analytic's PEMs (and related materials) which are based on well-known commercial block copolymers of the styrene-ethylene/butylenes styrene family[41], for which Kraton G1650

is an example, have been investigated in fuel cell application. However, as with sulfonated polystyrene, they show insufficient radical stability which limits the fuel cell operation temperature to a maximum 60 °C[29].

Further interesting materials for fuel cell membranes are poly(phosphazene)-based ionomer membranes. The poly(phosphazene) backbone is, as an inorganic polymer backbone, chemically quite stable. Poly(phosphazene) ionomers can be readily obtained by the reaction of poly(dichlorophosphazene) with phenolates, followed by sulfonation of the phenoxy side chain[42–44]. The poly(phosphazene) ionomers showed, when being applied to DMFC, much lower meOH permeabilities, compared with Nafion or similar ionomers[43].

4.6 (Het)arylene main chain ionomer membranes

Because arylene main-chain polymers show the best chemical stabilities apart from perfluorinated ionomer membranes, a huge number of different polymers of this polymer type have been developed in recent decades. The most common method for the preparation of arylene main-chain polymers is the nucleophilic displacement polycondensation of either dihalogeno aryl monomers (e.g. 4,4′-difluorodiphenylsulfone, 4,4′-difluorobenzophenone, 4,4′-difluorodiphenyl-phenylphosphinoxide) with dihydroxy aryl monomers (e.g. bisphenol A, bisphenol AF or bisphenol S) or the nucleophilic displacement polycondensation of halo-hydroxy aryl monomers (e.g. 4-fluoro-4′-hydroxydiphenylsulfone or other AB-monomers[45–48]). Owing to the facts that arylenic compounds show much better stabilities against radicals than polymers of the styrene type and that many arylene monomers are available commercially, numerous types of arylene main-chain polymer types have been prepared up to now. Among the arylene main-chain polymers are the polymer families of poly(phenylene)[49,50], poly(ethersulfone)[51–53], poly(etherketone)[54–57], poly(phenylene oxide)[58,59], partially fluorinated poly(phenylene ether)s[60,61], poly(phenylene sulfide)[62], poly(phenylene phosphine oxide ether)s[63], poly(thioether sulfone)s[64], poly(arylene thioether ketone ketone sulfone)s[65], poly(sulfone)s by oxidation of the poly(thioethersulfone)s[66] and poly(thioetherketone)s[67]. Moreover, arylene main-chain polymers containing different types of the abovementioned structural units in the same polymer have been prepared over the past years. Heterocyclic and heteroaromatic ionomers such as sulfonated polybenzimidazoles[68], polyimides[69], polytriazoles and polyoxadiazoles[70], poly(phthalazinone)s[71] and poly(quinoxaline)s[72] have also been and are currently prepared in macromolecular synthesis labs around the world. Some of these arylene main-chain polymers have been tested in PEFCs and/or DMFCs and yielded good results, partially having better fuel cell performance than the perfluorinated ionomer membrane types. The partially superior performance of sulfonated arylene main-chain ionomers in DMFCs is mainly

due to the markedly lower methanol permeability of the arylene main-chain ionomers, compared with the perfluorinated ionomers[73,74].

In the following, some examples of the synthesis and fuel cell application of polyarylene ionomers will be briefly reviewed.

Meta-sulfone-sulfonated poly(ethersulfone)s have been prepared by McGrath *et al*. by statistical copolycondensation of bis-4-chlorophenyl sulfone and disulfonated bis-4-chlorophenyl sulfone and 4,4′-biphenol in different molar ratios[75]. These polymers have been tested in PEFCs as well as in DMFCs and yielded operation times of 800 hours in PEFCs at 80 °C, and 2000 hours in DMFCs at 60 °C without membrane failure[76].

In[54] sulfonated poly(etheretherketone) (sPEEK), membranes are described which were prepared by sulfonation of PEEK and show a good performance in PEFCs at temperatures up to 80 °C. At a 60 °C operation temperature, stable PEFC operation of these membranes over several thousand hours was reported. An interesting modification of the sPEEK membrane type are bilayer sPEEK membranes with layers having different ion-exchange capacities. In the bilayer membranes an optimization of the water management could be obtained by placing the membrane layer with the higher IEC towards the anode, leading to a marked increase of sPEEK membrane durability in PEFCs – the fuel cell could be operated up to 800 hours at temperatures from 90–110 °C[77].

Disulfonated poly(arylene ether benzonitrile) copolymers containing hexafluoroisopropylidene diphenol (6FCN-35) were prepared by direct aromatic nucleophilic displacement copolycondensation of 4,4´-hexafluoroisopropylidene diphenol, 2,6-dichlorobenzonitrile, and 3,3´-disulfonate-4,4´-dichlorodiphenylsulfone in N-methyl-2-pyrrolidone (NMP) at 200 °C[78,79]. The membranes were tested in a DMFC and compared with Nafion®. Tests showed that the benzonitrile copolymer membrane electrode assemblies (MEAs) outperformed Nafion® MEAs – at a DMFC temperature of 80 °C, 200 mA/cm^2 were obtained with these MEAs at a voltage of 0.5 V. Under the same DMFC conditions, Nafion®-based MEAs reached only a current density of 150 mA/cm^2 (at 0.5 V). It was concluded from these results that the two-fold lower meOH crossover of the benzonitrile copolymer membrane was responsible for this finding[78].

Guiver *et al*. prepared sulfonated poly(phthalazinone ether ketone) (SPPEK) membranes and tested them in a DMFC[80]. In a single cell DMFC test at 70 °C with the MEA containing SPPEK, the maximum power density was 55 mW/cm^2 as the current density was 276 mA/cm^2 and the ultimate (limiting) current density was 360 mA/cm^2. The lower meOH permeability of SPPEK, compared with Nafion, led to lower methanol crossover. Therefore, the optimal concentration of aqueous feed methanol (3 M) for the SPPEK MEA was higher than that of Nafion® (2 M) under the same operation conditions.

Schuster *et al*. prepared sulfonated poly(sulfone)s from polymeric

thioethers[66] which were synthesized by polycondensation of disodium 3,3′-disulfonate-4,4′-difluorodiphenylsulfone with 4,4′-thiobisbenzenethiol, followed by oxidation of the polythioethersulfone with H_2O_2. The polymers had excellent thermal, hydrolytical and oxidative stabilities and high proton conductivities, making them interesting candidates for fuel cell application.

The disadvantage of the (het)arylene main-chain ionomers is that in many cases they swell too much or even dissolve at high degrees of sulfonation which are required for good proton conductivity. The reason for the higher water uptake/swelling of the (het)arylene main-chain ionomers at conductivities similar to that of Nafion® lies in the less pronounced separation between the hydrophilic proton-conductive ionomer phase, and the hydrophobic ionomer phase which is due to the lower hydrophobicity and mobility of the arylene main-chain polymer backbone, compared with the backbone of the perfluorinated ionomers[15,18]. To avoid an excessive swelling of ionomers, the following approaches have been suggested in the literature:

- *Synthesis of phase-separated block copolymers* consisting of a hydrophilic, sulfonated polymer microphase which overtakes the proton conduction, and a hydrophobic polymer microphase which mechanically stabilizes the membrane by suppressing swelling of the sulfonated microphase. Up to now only a few arylene main-chain ionomers for application in fuel cells have been reported in the literature. Among them is a contribution of Scherer *et al*. who synthesized and characterized a series of nonfluorinated sulfonated multiblock-*co*-poly(arylene ether ketone)s[82]. It could be observed that the physical cross-linking of the block homopolymer membranes by phase-separation into hydrophilic and hydrophobic domains led to a reduction in the degree of swelling and therefore to an increase in mechanical stability, compared with the hydrophilic copolymer. Moreover, these membranes showed good performance both in DMFC (0.5 M meOH/air, 90 °C, 100 mW/cm^2 at 270 mV) and PEMFC (H_2/O_2, 80 °C, 275 mW/cm^2 at 270 mV).

  Meier-Haack *et al.* dealt with the synthesis of nonfluorinated sulfonated multiblock-*co*-poly(ether sulfone)s[83]. The block copolymer membranes were tested in DMFC and showed similar performance to Nafion® although they showed a lower meOH permeability than Nafion®. The reason for this finding was probably a non-optimized electrode structure.

  Recently, Miyatake *et al.* have shown that sulfonated multiblock-*co*-polyimides have superior proton conductivity, particularly at low humidity, compared with the corresponding sulfonated statistical *co*-polyimides[84]. McGrath's group reported the synthesis and characterization of a multiblock-*co*-poly(arylene ether sulfone) consisting of highly hydrophobic partially fluorinated segments and sulfonic acid groups in the hydrophilic segment being located *meta* to a sulfone bridge[85–87]. The electron-

withdrawing effects (-M and -I effects) of the sulfone bridge led to high acid strength of the ionogenic groups[88–90] while the highly fluorinated hydrophobic segments in the multiblock architecture counteract the inherent tendency of the sulfonic acid group to attract water molecules which should be favorable for high proton conductivity and mechanical stability. Moreover, under partially hydrated conditions, the block copolymers showed improved proton conductivity over random copolymers having comparable ion exchange capacity (IEC). The proton conductivity for the block copolymer series increased with increasing block lengths under partially hydrated conditions.

- *Reinforcement of the ionomer* by embedding it into nonwovens, textiles or porous support materials such as ultrafiltration (UF) or microfiltration (MF) membranes or porous PTFE foils of the Gore® type. Recently, Zhang *et al.* have reported the preparation, characterization and fuel cell application of a composite membrane from a porous PTFE matrix filled with a sulfonated polysolfone (PSU) ionomer[91,92]. This membrane, having a thickness of 20 μm, showed excellent performance in an LTFC at 80 °C: a peak power density of more than 2.4 W/cm^2 (at 0.45 V) could be obtained. An interesting reinforced composite membrane concept was presented by the same group, which consisted in a reinforced self-humidifying membrane. The membrane constitutes a porous PTFE foil which was filled with sulfonated PEEK containing 0.05% of Pt/C catalyst[93]. The configuration of the MEAs was as follows: (1) anode; (2) Pt-C/SPEEK self-humidifying layer (d = 0.010–0.020 mm); (3) sPEEK layer (d = 0.010–0.030 mm); (4) sPEEK/PTFE (d ~ 0.015 mm) composite membrane layer; (5) cathode. During fuel cell operation, water was formed in the membrane from permeating O_2 (from the cathode) and H_2 (from the anode) catalyzed by the Pt particles in layer (2), leading to an improved fuel cell performance, compared with a membrane without the self-humidifying layer.
- *Physical or covalent cross-linking of the arylene main-chain ionomers* (see Section 4.7).
- *Blending of the ionomers with inert polymers.*
- *Organic/inorganic composites* (see Section 4.8).

4.7 Cross-linked membrane systems

Cross-linked membrane systems can be subdivided into covalently cross-linked membrane systems and physically cross-linked membrane systems. By cross-linking, the swelling/water uptake of fuel cell membranes can be reduced markedly, or water-soluble ionomers can even be transformed into water-insoluble membranes. The research group of the author of this chapter have been active in the development of cross-linked ionomer membranes for

fuel cells and other electromembrane applications such as electrodialysis for more than 10 years. This work was recently reviewed by the author of this contribution[94], therefore only some highlights will be mentioned here. The covalent cross-linking procedure which was developed by the group consisted of the sulfinate *S*-alkylation reaction with α,ω-dihalogenoalkanes such as 1,4-diiodobutane or with fluoroaromatics such as decafluorobiphenyl, decafluorobenzophenone or 4,4′-difluorodiphenylphenyl-phosphinoxide[95]. Two types of covalently cross-linked ionomer membranes have been developed: The first are blends of sulfinated PSU Udel® with sulfonated PSU Udel®[96] or blends of sulfinated PSU with sulfonated poly(etherketone)s[97], and the second are ionomer membranes which were obtained by cross-linking of the sulfinate groups of PSU-sulfinatesulfonate[98] or by cross-linking of the sulfinate groups of PEEK-sulfinatesulfonate[99]. Membranes were obtained which showed reduced water uptake along with high proton conductivity and therefore good performance in DMFCs up to temperatures of 130 °C[91,99]. They also developed ionically cross-linked blend membranes by mixing sulfonated ionomers which were in some cases even water-soluble (up to exchange capacity (EC)s of 4.2 meq/g) with basic polymers, using both self-developed basic polymers from lithiated PSU Udel® or lithiated Radel R®[100–104] and/or highly stable basic polymers such as polybenzimidazole (PBI) Celazole®[61,105–109]. Many of these membranes have been tested in PEMFCs[110] and DMFCs[111,112] and yielded excellent performance in PEMFCs at temperatures up to 100 °C (maximum power densities of up to 1.2 W/cm^2 were reached at 80 °C[90,107,113]) and at DMFC temperatures up to 130 °C (maximum power densities of up to 0.25 W/cm^2 were reached at 110 °C[114], and of up to 0.28 W/cm^2 were reached at 130 °C[94,115]). The thermal stability[61,90,108,116] and the radical stability[61,90] of the arylene main-chain ionomers could also be markedly improved by blending with basic polymers. To explain this finding it can be speculated that the basic polymer blend component in acid–base blend membranes has radical-scavenging properties – it is known from radical chemistry that, for example, imidazole-containing compounds have radical-scavenging properties[117,118]. The concept of blending sulfonated ionomers with basic polymers was also picked up by other research groups. For example, Wicisk *et al.*[119] and Ainla and Brandell[120] prepared Nafion®/PBI blend membranes and obtained a marked increase in DMFC performance, compared with Nafion®. Wycisk *et al.* prepared acid–base blend membranes from sulfonated poly(phosphazene) and PBI which showed a meOH permeability reduction of a factor of 2.6, compared with Nafion, and a DMFC which was slightly worse than that of Nafion® (maximum power density 89 mW/cm^2, vs. 96 mW/cm^2 with Nafion®117)[121]. Manea and Mulder prepared sulfonated poly(ethersulfone)/PBI blend membranes[122]. The characterization of these membranes yielded the result that their meOH permeability was significantly lower than that of Nafion. Schauer *et al.*

prepared acid–base blend membranes from sulfonated poly(phenylene oxide) (sPPO) and PBI. They found that the blend membranes were markedly more stable than sPPO alone using Fenton´s test procedure[123]. Recently, Fu *et al*. prepared two different types of acid–base blends, the first being blends of polysulfone-2-amide-benzimidazole and sPEEK[124], the second being blends of polysulfone- bearing benzimidazole side groups (PSf-BIm) and sPEEK[2,3]. These membranes have been applied to PEMFCs[125], where better performance at 90 and 100 °C was obtained than with pure sPEEK and Nafion® 115 membranes, and in DMFCs[124,126], where a remarkably superior long-term performance, compared with Nafion 112®, was reached, which is thought to be due to significantly reduced methanol crossover.

Apart from ionically cross-linked blend ionomer membranes, ionomers which are physically cross-linked via hydrogen bridge interactions, have also been prepared. Systems of this type include blends of polyvinylalcohol (PVA) with different polyanions, such as Nafion®/PVA[127], or sulfonated polystyrene/PVA[128]. A marked reduction in meOH permeability could be obtained using these membranes; however, there are concerns about the electro-chemical stability of PVA in the fuel cell environment. Other hydrogen-bridge cross-linked ionomer systems which have been taken into account for fuel cell application are blends between sPEEK and the polyamide Trogamid® and PEI Ultem®[101]. However, the hydrolytical stability of the polyamide or the PEI blend component is questionable.

4.8 Composite systems

Numerous composite membrane systems have been taken into account for fuel cell membranes. Owing to limited space in this contribution, only a small selection of these systems can be presented here. The two most important material classes are composite systems of an organopolymer with inorganic particles and composite membranes from organopolymer (blends) with heteropolyacids. In the organopolymer/inorganic particle composite membranes the inorganic particles are better for the retention of water when the membranes are operating in fuel cells at temperatures about the water boiling point, 100 °C. As already mentioned, the proton conductivity of sulfonated polymer membranes decreases drastically when they are impoverished in water due to water evaporation[16,17]. Some of the inorganic particle material classes, such as acidic phosphate or phosphonate salts also contribute to proton transport. In the heteropolyacid composite systems the heteropolyacid blend component strongly contributes to proton conductivity, since the heteropolyacids are superacids containing protons which are delocalized within the heteropolyacid molecules.

4.8.1 Organopolymer–inorganic particle systems

As already mentioned, the organopolymer/inorganic particle composite membranes can be subdivided into systems, where the inorganic nanoparticle phase of the composite membrane retains water at temperatures >100 °C, and into systems where the inorganic nanophase contributes to proton transport. One example of the first type are Nafion®/silicalite composite membranes which can be either prepared by simply mixing Nafion® suspension with silicalite nanoparticles in an ultrasonic bath, followed by membrane casting[129,130], or by formation of the SiO_2 nanoparticles inside an Nafion membrane via sol–gel processes by swelling the Nafion® membranes in alkoxysilanes, whereas the sol–gel process inside the membranes is catalyzed by the superacidic Nafion® SO_3H groups[131–133]. Another approach for the formation of organopolymer/inorganic nanoparticle composite systems is to perform the sol–gel process in the polymer solution by addition of silanes to the polymer solution and by subsequent hydrolysis of the silanes to sols, and by casting of the membrane. The formation of the nanoparticles starts during membrane formation and solvent evaporation and is completed by acidic membrane post-treatment[134]. Nafion®/SiO_2 membranes have been tested in DMFCs at temperatures of 145 °C and yielded a good performance at this temperature, approaching a peak power density of 240 mW/cm^2 at 0.6 A/cm^2 and 0.4 V. As mentioned above, also proton-conductive compounds such as layered acidic (hydrogen)phosphates and (hydrogen)phosphonates have been precipitated in organopolymer membranes. In this field, Alberti[135], Jones and Roziere[136–140] and Yang *et al*.[141] have performed pioneering work. Yang *et al*. prepured Nafion®/layered zirconium hydrogen phosphate (Nafion®/ZrP) membranes and investigated them in DMFC at temperatures up to 140–150 °C, wherein maximum power densities of 380 and 260 mW/cm^2 were achieved under oxygen and air feed, respectively. The precipitation of the layered hydrogen phosphates and phosphonates inside organopolymer membranes can be performed by the following procedure: first the H^+ ions of sulfonated organopolymer membranes are exchanged against ZrO^{2+} ions by immersion of the membrane in aqueous $ZrOCl_2$ solution, followed by immersion of the membrane in diluted phosphoric acid. Using this method we have prepared ionically as well as covalently cross-linked blend ionomer membranes having a ZrP content of up to 50 wt% which showed improved PEFC performance at T >100 °C, compared with the pure organomembrane (for example, an ionically cross-linked ZrP composite membrane showed a peak power density of 0.6 W/cm^2 at a PEFC operation temperature of 115 °C, while the corresponding undoped organomembrane showed a peak power density of only 0.35 W/cm^2 at an operation temperature of 80 °C)[94]. Other methods for producing Zr hydrogen phosphate/phosphonate salt-containing hybrid membranes have been reviewed by Alberti *et al*.[135].

4.8.2 Low molecular acid/high organopolymer blend systems

As mentioned above, heteropolyacids (HPA) such as tungstophosphoric acid (TPA) $H_3PW_{12}O_{40}{\cdot}xH_2O$ are solid inorganic acids. They are strong Bronstedt acids because of proton delocalization within their structure[142,143], resulting in a high proton conductivity. Consequently, they are interesting candidates for the application as proton-conducting material in fuel cells. Phosphotungstic acid was investigated as an electrolyte in a PEFC. An output electrical power of 700 mW/cm^2 was obtained at 25 °C and 1 atm, which was stable for more than 300 hours[144]. A problem with heteropolyacids is their excellent water solubility which generates the need for immobilization of the heteropolyacid molecules in the solid materials such as organopolymers. Therefore, a lot of work has been performed in preparation of composite membranes from sulfonated polymer membranes which were doped with different heteropolyacids. Some examples for such systems will be presented below. Nafion® was impregnated with TPA and investigated in PEFCs at temperatures up to 120 °C. It was observed that the PEFC performance at 120 °C was markedly improved by the added TPA, compared with undoped Nafion®[145]. McGrath *et al.* prepared composite membranes from sulfonated PSU and TPA[146]. By using Fourier transform infrared (FTIR) spectroscopy, interactions between the sPSU macromolecules and TPA could be observed, and are thought to be responsible for the good stability of the TPA in the ionomer matrix. Conductivity measurements showed an increased proton conductivity at 130 °C, compared with the pure organomembrane. Therefore, these membranes were regarded as promising candidates for PEFCs. As already mentioned, the excellent water solubility of HPAs gives rise to concerns that they are washed out from the organomembrane during fuel cell operation. Therefore much effort has been made to reduce or even exclude the bleeding-out of the HPAs from the membrane matrix. For example, Nunes *et al*. have prepared composite membranes of sulfonated poly-ether-keton (sPEK) containing ZrO_2 or SiO_2 nanoparticles which have been doped with different HPAs such as TPA and molybdophosphoric acid (MoPA)[147]. It was found that the bleeding-out of the HPAs could be markedly reduced by adsorption of the HPA particles to the inorganic nanoparticles. In addition, the water and meOH permeability of the membranes could be significantly reduced, compared to the pure sPEK membrane. In order to overcome the problem of bleeding-out of HPAs, the same group prepared composite membranes from sPEEK, a NH_2-modified SiO_2 phase and divacant $[\gamma\text{-}SiW_{10}O_{36}]^{8-}$, containing epoxy groups which reacted with the amino-groups in the oxide phase, leading to covalent tethering of the HPA molecules to the inorganic membrane phase[148]. Herring *et al*. prepared composite membranes using lacunary $H_8SiW_{11}O_{39}$ in polymer matrices based on polyethylene glycol by a sol–gel method[149]. Nuclear

magnetic resonance (NMR) and IR investigations of the membranes indicated that the HPA molecules were covalently bound to the polymer backbone. However, this membrane showed poor performance in a PEFC, compared with Nafion®. Another approach to reduce HPA bleeding-out from the membrane matrix was introduced by Kerres *et al*. who immobilized TPA and MoPA in acid–base blend membranes from sulfonated poly(etherketoneetherketoneketone) (sPEKEKK) and PBI[150]. Membranes with superior proton conductivities to Nafion® were obtained. It was found that the bleeding-out of MoPA from the acid–base blend membranes was much higher than the bleeding-out of TPA by aqueous membrane post-treatment. For example, a blend membrane which initially contained 40 wt% TPA, still contained 34 wt% TPA after the aqueous post-treatment, while the MoPA was nearly completely washed out from the membrane under the same conditions. Tan *et al*. performed a similar approach: composite polymer membranes based on sulfonated poly(arylene ether sulfone) (SPSU) containing benzimidazole derivatives (BlzD) and TPA were prepared and characterized[151]. It was reported that washing out of the TPA could be markedly reduced by addition of the BIzD compounds.

4.9 Intermediate-temperature membrane systems

The operation temperature of the fuel cell should be as high as possible to allow for fast electrode kinetics and therefore high fuel cell efficiency. However, as already pointed out before, the SO_3H proton conductors dry out at T >100 °C because of evaporation of the SO_3H group hydration shell water, leading to a severe H^+ conductivity drop and therefore strong decrease in the fuel cell efficiency. Therefore, for the ITFCs other types of proton conductors have to be used. Several types of ITFC membranes have been developed within the past decades which can be roughly classified into the following material classes:

- Basic polymers or basic polymer-rich polymer blends which are doped with (poly)phosphoric acid. This polymer class will be reviewed in Section 4.9.1.
- Heterocyclic amphoteric proton conductors. This material class will be discussed in Section 4.9.2.
- Phosphonic acid proton conductors. This ionomer type will be presented in Section 4.9.3.

4.9.1 Basic polymer polybenzimidazole phosphoric acid

Savinell and coworkers[153–157] have introduced a proton conductor which is able to work in the 100–200 °C operation temperature range. This H^+ conductor

consists of the highly stable basic polymer PBI[105] which is doped with phosphoric acid, at which the H_3PO_4 molecules act as proton-conducting species, being bound to the PBI imidazole moieties via acid–base (ionical) and hydrogen bridge interactions. H_3PO_4 has the advantage that it is an H^+ conductor without need for H_2O molecules acting as proton 'vehicle', making this H^+–conductor suitable for operation temperatures above 100 °C – the H_3PO_4 molecule itself is amphoteric[81]. PBI–H_3PO_4 blends can be prepared via two different routes, the first being the immersion of PBI films in highly concentrated H_3PO_4 at elevated temperatures, the second being polymerization of PBI in polyphosphoric acid, followed by the hydrolysis (depolymerization) of polyphosphoric acid present within the PBI chains[158–160]. The PBI/H_3PO_4 membranes also show high thermal stability in a fuel cell environment[155], and a H_2O electroosmotic drag coefficient of nearly 0[154]. Application of these membranes both to PEFC (at 150 °C)[153] and to DMFC (at 190 °C)[156] showed encouraging results. Long-term stability tests of PBI/H_3PO_4 MEAs, which have been commercialized by the former PEMEAS company (now part of BASF Fuel Cell Corp.) under the trade name 'Celtec®', showed an excellent performance stability[161] for 14 000 hours at 160 °C operation temperature (initial cell voltage at 0.2 A/cm^2: 0.67 V, cell voltage at 0.2 A/cm^2 after 14 000 hours: 0.6 V; operation conditions: H_2/air, ambient pressure, cathode $\lambda = 2.0$, anode $\lambda = 1.2$, active area 45 cm^2, no humidification).

One disadvantage of PBI–H_3PO_4 blend membranes is the deterioration of their mechanical stability, particularly at high H_3PO_4 concentrations and high doping temperature, leading even to dissolution. Therefore, apart from pure PBI, also other basic polymers or polymer blends have been doped with H_3PO_4, among them blends of PBI with a copolymer from 2,5-bis(4-hydroxypheny1)pyridine, bisphenol A and bis(4-fluorophenyl)-sulfone[162]. The oxidative stability of the blend membranes was tested via Fenton's reaction and found to be stable against oxidative attack. In particular, the membrane retained its excellent mechanical stability after the Fenton reaction. Doping of the basic blend membranes led to proton conductivities in the 10^{-2} range, which is a prerequisite for the application in fuel cells above 100 °C. Kallitsis and co-workes also took up the concept of acid–base blend membranes composed of sulfonated arylene main-chain polymers and basic polymers (see Section 4.7) and extended it to ternary blend membrane sulfonated polymer–PBI–H_3PO_4 where the basic blend component was in molar excess over the sulfonated blend component, allowing the H_3PO_4 molecules to bind via acid–base interactions and hydrogen bridges to the PBI blend component[163,164]. They found that the ternary blend membranes showed better H^+ conductivities and better mechanical stability than binary blends of PBI–H_3PO_4. The membranes were investigated in a PEFC up to T = 190 °C and showed good performance. Recently, blend membranes composed of 70 wt% PBI and 30 wt% of a sulfonated polymer from

decafluorobiphenyl and bisphenol AF (M_n = 82 442 g/mol, polymer dispersity index (PDI) = 1.65, IEC = 2.1 meq/g)[61] were doped with H_3PO_4 and tested in a PEFC at temperatures up to 200 °C, yielding good performance (450 mA/cm^2 at 500 mV). Moreover, the membranes showed better mechanical stability than PBI–H_3PO_4 membranes having comparable proton conductivity[165].

4.9.2 Heterocyclic amphoteric proton-conducting systems

It is known that in liquid imidazole (melting point 89–91 °C, boiling point 256 °C), correlated proton transfers take place, leading to proton diffusion[81]. Self-diffusion coefficients of imidazole-type proton conductors are much higher than that of water. Therefore the idea arose that imidazole could possibly be used as proton solvent or even proton conductor in ITFCs. The research groups of K.D. Kreuer and W.H. Meyer performed pioneering work in the investigation of imidazole as potential proton solvent/conductor for ITFCs. When the use of imidazole as proton conductor in fuel cells is intended, it must be immobilized, because it would otherwise bleed out during fuel cell operation. As a strategy for immobilization, the connection of imidazole molecules via a flexible spacer or the tethering of imidazole-containing flexible side chains to different polymer backbones was chosen[15,166–168]. However, one of the problems of these systems was that the intrinsic concentration of protonic charge carriers can be increased only moderately through acid doping. This is particularly the case in fully polymeric systems, which is probably due to a reduced dielectric constant. The combination of such immobilized imidazole systems with low-molecular sulfonic acids such as triflic acid leads to conductivities being insufficient for the application to membrane fuel cells ($\sigma < 3 \times 10^{-3}$ S/cm)[81,166]. Another disadvantage of imidazole-containing oligomeric and polymeric systems is their limited thermo-oxidative stability and the very high overpotential for oxygen reduction on platinum[169].

4.9.3 Phosphonic acid systems

As pointed out in Section 4.9.1, the use of H_3PO_4, which is bound ionically or via hydrogen bridges to a host polymer, as proton conductor in ITFCs has the disadvantage that the H_3PO_4 molecules can bleed out of the membrane when the fuel cell operation temperature is decreased below 100 °C. Therefore, the use of phosphonic acid-containing ionomers has been taken into account for use in ITFCs since the phosphonic acid group is, analogous to H_3PO_4, capable of conducting protons at $T > 100$ °C without the need for water to be present inside the membrane, as could be shown with phosphonic acid-containing oligomeric model compounds (conductivity range between 10^{-1} and 10^{-2} S/cm)[81,169]. Novel perfluorinated polyethers have been developed

by Yamabe *et al.*[170]. The phosphonated membranes, having an IEC of 2.05 meq/g, had proton conductivities $\sigma = 7 \times 10^{-2}$ S/cm (measured at 25 °C under full humidification). Conductivity data at T >100 °C and under reduced humidification have not been provided by the authors of this study. Allcock and co-workers have developed phenyl phosphonic acid functionalized poly(aryloxyphosphazenes) and tested their suitability for DMFC[171,172]. The membranes had IECs of 1.17 and 1.43 meq/g, proton conductivities between 10^{-2} and 10^{-1} S/cm^{-4}, equilibrium water swelling values between 11 and 32%, and methanol diffusion coefficients for both radiation cross-linked and non-cross-linked membranes were found to be at least 12 times lower than for Nafion 117. Phosphonated poly(4-phenoxybenzoyl-1,4- phenylene) (P-PPBP) has been prepared by Rikukawa and co-workers by a three-step reaction[173]. The polymer possesses high thermal and mechanical stability, but P-PPBP films containing 40 mol % phosphonic acid groups showed a proton conductivity of only about 10^{-4} S/cm at 90 % relative humidity (RH), which is not sufficient for the fuel cell application. Recently, Steiniger *et al.* have prepared and characterized novel phosphonated poly(siloxanes)[174]. The phosphonated compounds show conductivities of up to 2×10^{-3} S cm at $T \approx$ 130 °C and RH ≈ 37%, a value not being sufficient for use in fuel cells. Liu *et al.* prepared a fluorinated poly(aryl ether) containing a 4-bromophenyl pendant group and its phosphonated derivative[175]. This polymer was characterized and revealed very good thermal stabilities and very low MeOH permeabilities. However, the proton conductivities of a phosphonated ionomer with one pendent PO_3H_2 group per polymer repeat unit are 2.9×10^{-6} S/cm at 45% RH, and 2.0×10^{-6} S/cm at 25% RH at 120 °C, respectively. The authors of the article conclude that it is necessary to improve the proton conductivities of the phosphonated polymers by increasing the degree of phosphonation. Lafitte and Jannasch prepared new polysulfone ionomers functionalized with benzoyl(difluoromethylenephosphonic acid) side chains[176]. Membranes made from ionomers having 0.90 mmol of phosphonic acid units/g of dry polymer takes up 6 wt% water when immersed at room temperature, and conductivities up to 5 mS/cm at 100 °C were recorded. It could be ascertained by thermogravimetry that the aryl CF_2–PO_3H_2 arrangement decomposed at approximately 230 °C via cleavage of the C–P bond.

Summarizing the reported effort in preparation of phosphonated ionomer systems, one must state that up to now their proton conductivities at T >100 °C and under reduced humidification are too low to be regarded as polymer electrolytes for ITFC. Particularly, this material class has to be improved in the following terms:

- increase in the number of PO_3H_2 groups per polymer repeat unit;
- increase in the acidity of the PO_3H_2 groups, since most phosphonated polymers prepared so far have too low acid strength;

- avoidance of PO_3H_2 group condensation which normally takes place in the temperature region 100–150 °C if insufficient H_2O partial pressure is present.

4.10 Catalyst development

Ths section is structured in the following way: it starts with a short description of state-of-the-art catalysts, all of them based on platinum, followed by an explanation of the carbon monoxide issue when designing a catalyst for fuel cell applications. As the oxygen reduction reaction is the main source of kinetic performance losses of the cell, the reaction is discussed in more detail to set the guidelines towards new catalyst concepts. New approaches cover different platinum alloys and platinum-containing core shell catalysts (both classes aim for a reduction of the platinum content) as well as platinum-free alternatives which are discussed in more detail. Finally, the influence of carbon supports on the performance is pointed out. Alternative catalyst supports are presented in Section 4.11.

4.10.1 State-of-the-art catalysts

In low-temperature applications, platinum is used as a catalyst which is the most active species of the noble metals. In comparison, high-temperature fuel cells such as, for example, solid oxide fuel cells (SOFC) do not bear the requirement of noble metal catalysts. The metal loadings usually depend on the kind of application; the lowest ones are usually required for automotive applications. At present, total loadings of 0.6–0.8 mg_{Pt}/cm^2 (both anodic and cathodic catalysts) are employed; the resulting power density is in the range of 0.7 W/cm^2 at a cell voltage of 0.7 V, which amounts to an efficiency of 58%.

On the cathode, the current loading is around 0.4 mg_{Pt}/cm^2 (which is required owing to low kinetics of the oxygen reduction reaction (ORR)[2]) and 0.2 mg_{Pt}/cm^2 on the anode. For automotive applications, the target is a total loading of 0.2 g_{Pt}/kW at $U \geq 0.65$ V comprising a total noble metal content of 0.20 mg_{Pt}/cm^2 (anode + cathode) with 0.05 mg_{Pt}/cm^2 at the anode (due to the good performance of the anodic catalysts) and 0.15 mg_{Pt}/cm^2 at the cathode. These values are estimated for CO-free hydrogen[2,177].

The cost target is set to $125/kW by the US Department of Energy (DOE) calculated on basis of the complete system. Of this, 20% are considered to be stack-related costs, most of which are related to the catalyst materials.

Other materials considered for the anode include platinum alloyed with molybdenum, iron and nickel (see also in page 121). The corrosion of the alloys in the acidic medium (H^+-concentration is at 0.5 $\mu mol/cm^2$) is still an unresolved issue leading to a leaching of the non-noble metal, which in turn

influences the long-term stability. The problems caused by the metal ion pollution are manifold: in the membrane, metal ions lead to blocked transport paths resulting in a hindered conductance. The formation of hydrogen peroxide on the cathode (and enhanced on the anode due to permeated oxygen) is catalyzed by metal ions (where iron ions play the most active part for this reaction). Hydrogen peroxide represents an aggressively oxidizing reactant; its radical character stimulates a fast degradation of the membrane material and reduces the long-term stability of the employed materials. The formation of hydrogen peroxide also leads to an enhanced leaching of the less noble component of the alloy. These stability problems are increased by elevated temperatures.

4.10.2 CO/CO_2 tolerance

Catalyst layers based on pure platinum require comparatively clean reactants; pure platinum works with CO contaminations below 1 ppm and a CO_2 less than 10%. Appropriate fuels are therefore either pure hydrogen or purified reformate. Higher concentrations of CO or CO_2 lead to a steady decrease of the performance due to catalyst poisoning. For reformate use without a purification step, platinum–ruthenium alloys are used leading to a typical loading of $0.3\,g_{PtRu}/kW_{el}$ on the anode and $0.3\,g_{Pt}/kW_{el}$ cathode.

4.10.3 Oxygen reduction reaction

As stated in the introductory section, the main source of performance losses is the cathodic overpotential caused by the ORR, which has therefore been subject of several studies. As stated in the beginning of this section, the largest contribution to the performance loss is caused by the slow kinetics of the ORR. In order to reconsider the given example, at a current density $i_0 = 1500\,mA/cm^2$ the ohmic loss amounts just to 80 mV whereas the performance loss due to the ORR is 400 mV. The reduction reaction by itself depends on factors such as the catalyst composition, particle sizes, pH value and potential. The mechanism of the ORR is either a two- or four-electron transfer step. The four-electron transfer step leads directly to H_2O, whereas the two-electron transfer step leads to the unwanted H_2O_2. The degrading effect of this compound has been pointed out in the previous section[178].

Four different pathways are considered to describe the complete reaction[179]. In acidic media, a direct four-electron transfer step leads to the formation of water on the catalyst surface:

$$O_2 + 4\,H^+ + 4e^- \rightarrow 2H_2O \qquad 4.2$$

For most active catalyst such as Pt, this one-step reaction is considered to be the most common.

A second pathway is a two electron-transfer leading to an intermediate product, hydrogen peroxide. This pathway has been reported to be more common for less active catalyst metals such as Au and Hg and has also been observed on highly dispersed supported Pt[177].

$$O_2 + 2\ H^+ + 2e^- \rightarrow H_2O_2 \qquad 4.3$$

A third pathway might be a series of the two aforementioned pathways (which is usually called a 'series pathway'). And finally there is a 'parallel pathway' which is a combination of the three previous ones.

The reaction by itself is a series of separate steps: generally, the first electron transfer step is considered the rate-determining step (rds) which is a simultaneous proton and electron transfer reaction[180–182]:

$$O_{2,ads} + H_3O^+ + e^- \rightarrow O_2H_{ads} + H_2O \qquad 4.4$$

The general reaction scheme has been investigated by means of different experimental and theoretical approaches, leading to the assumption that the reaction continues after the first combined electron/proton transfer step via the intermediate formation of H_2O_2 respectively HO_2 (adsorbed on the surface); the O–O bond is split immediately, leading to adsorbed OH groups which react further to form water:

$$Pt–O_2H + H^+ + e^- + Pt \rightarrow 2\ Pt–OH \qquad 4.5$$

$$Pt–OH + H^+ + e^- \rightarrow Pt + H_2O \qquad 4.6$$

In a recent theoretical study, solvation effects which influence the energetic of the reaction have been taken into account by a water cluster[183]. A similar approach can be used to theoretically design bimetallic catalysts for the ORR[184]: two metallic components are coupled and based on their thermodynamics, their efficiency for rds (4.4) and therefore their activity in the ORR is estimated. In general, as stated by Adzic[179], the main problem is in this field that 'there is no simple adequate spectroscopic method for identifying adsorbed intermediates', increasing the importance of theoretical approaches.

The suitability of different metals as ORR catalysts has been calculated taking binding energy and the measured activity into account. The correlation leads to so-called 'volcano plots' where the best materials resemble the 'top' of the distribution[185]. The maximum in this correlation curve is achieved for platinum which is in line with experimental findings. The inactivity of elementary metals such as iron or molybdenum (alloys have not been considered) is due to the high stability of the adsorbed oxygen species which makes proton and electron transfer reactions improbable. On the other hand, a too low binding energy inactivates the metals towards the ORR owing to the missing interaction with oxygen. The experimentally observed overpotential

was explained by the formation and adsorption of oxygen-containing species. In general, observing such a reaction does not only include the adsorption of a species, but also (as in the case of ORR) the formation of reaction products by dissociation. Therefore, when talking about catalytic activity, dissociation as well as the binding stability have to be taken into account.

4.10.4 New approaches

Besides pure platinum-based catalysts a variety of replacements for the traditional catalyst metal, platinum, has been investigated targeting for mass application which requires a much lower price of the final system (compared with the above-given estimations of the DoE). The research is mainly focused on two aspects, either a reduction of the platinum content or platinum-free compounds based either on substitute noble metals (which might unfortunately not necessarily reduce the price framework) or alloyed transitional metals. The main criterion, next to the price, is the long-term stability of the new materials and the synthesis of these compounds. The synthesis should include a fast, efficient reaction scheme avoiding multi-step reaction as well as polluting solvents which in the end increase the processing costs.

Here, examples for both approaches will be discussed: first the so-called core shell catalysts which most of the time consist of non-noble metal cores which are covered by a noble metal such as platinum. Platinum-free materials, especially when based on non-noble components, have to fulfil the criterion of stability in acidic media. Recently, electrocatalysts including cobalt or iron proved their suitability in fuel cell application where the metal ion is incorporated in a nitrogen macrocycle comparable to the natural porphyrin-ring system.

Platinum alloys

As stated above, pure platinum electrocatalysts are poisoned by carbon monoxide, which leads to a steady decrease of the fuel cell performance when operated with hydrogen containing trace amounts of CO[186]. In order to circumvent this problem and allow for an operation with CO-containing hydrogen such as reformate gas, platinum is alloyed with ruthenium (the issue of CO poisoning will be revisited in Chapter 5). Recently, bimetallic alloys containing platinum and molybdenum or tin with up to 25% of the non-platinum metal have been reported aiming for an improved tolerance towards CO[187–189]. Currently, this class of catalysts suffers from the missing stability in electrochemical applications, resulting in a gradual loss of the non-noble compound owing to dissolution in the electrolyte, which renders them useless for fuel cell applications[190].

Core shell catalysts

As mentioned previously, a reduction of the platinum content of the electrocatalysts in fuel cells is a key target in order to reduce the overall costs of this technology. The platinum content is reduced either by alloying with less expensive metals or the application of nanoscopic catalysts which bear a layered structure including a non-noble (or at least a less expensive) core covered by a platinum shell. These bimetallic catalysts are produced that way to achieve an optimum dispersion, leading to advantageous properties such as a maximized interface; at the same time, agglomerations and the formation of larger particles are avoided.

Cu-cores supported on Vulcan XC72 can be modified in a so-called colloid reaction: Cu-acetylacetonate is reduced, leading to finely dispersed metal cores on the carbon support. In a subsequent reduction step, platinum shells are deposited on these particles; the resulting electrocatalyst shows a higher activity in the hydrogen oxidation reaction (HOR) compared with pure platinum-based commercial catalysts, whereas a slightly lower ORR performance has been observed[191]. A finely dispersed catalyst with constant size distribution and uniform distribution of platinum on rhenium has been prepared by means of electroless deposition of $PtCl_6^{2-}$ on Rh-seeded carbon supports using dimethylamine borane (DMAB) as a colloid-forming reactant[192]. Shell-structured alloys containing platinum, iron and vanadium were reported to have a high activity for the ORR in *ex situ* experiments. The applied synthesis route allows for a controlled deposition of the different compounds leading to finely tunable loading, composition and size distribution[193]. Mixed non-noble/noble metal cores with platinum monolayers show a mass activity which is one order of magnitude higher than commercial platinum catalysts[194]. The high activity of Pt on Au/Ni or Pd/Co is explained by geometric effects of the pseudomorphic monolayer, which also leads to a shift of the formation of platinum oxides to higher potentials.

These examples have not been tested for long-term durability. Further research will focus on this criterion.

Pt-free catalysts: Fe/Co/Ni

Platinum-free catalysts usually feature two general problems, the stability in acidic environments and that none of the alternatives has reached the activity level of platinum so far[195]. The first criterion excludes almost all pure non-noble metals as well as their alloys, unless an extraordinary stability combined with a change of the non-noble properties can be observed. The leaching of metal ions from the catalyst catalyses the formation of hydrogen peroxide, which leads to a self-destroying oxidation of the catalyst and to a membrane degradation[196].

A new approach aims at a strong adhesion of the active centers on a carbon-based matrix. The model is taken from natural components, the physiological equivalent of a catalyst, the porphyrin ring system. These N_4-macrocycles lead to an activation of the O–O bond in natural environments, but do not have a direct application in fuel cells in this form[197]. For fuel cell purposes, derivates are employed including Fe and Co as central ion. The final compounds, iron or cobalt–tetramethoxyphenyl porphyrin (Fe/Co-TMPP), are thermolytically activated and the same time stabilized as they are connected to the underlying carbon support.

In order to enhance the activity, two different pathways have been considered, one for iron-based materials and the other for cobalt-based ones. The preparation might differ but the products are the same in principle, with the metal ion forming the active centre in a chelate structure. Several aspects have to be considered in order to explain the activity of such catalysts. By thermal treatment of these precursor structures, $M\text{-}N_{2/4}$ centers are formed which resemble the structure within the TMPP complex with a chelate-like bonding situation of the metal ions. The most important aspect is that the connection to the substrate as well as the interconnection of several active centers as one isolated complex does not contribute to the conductivity. Therefore, the connection with the carbon support, which serves as a kind of electron reservoir, as well as the electronic coupling influence the activity and, directed by the number of transferred electrons, also the distribution of the reaction products (which is in this case the percentage of formed hydrogen peroxide). The formation of side products will be taken into account below in the discussion of different active centers.

As stated previously, two different macrocycles will be considered, iron- and cobalt-based structures. The pyrolysis of unmodified Co-TMPP (tetramethoxyphenyl porphyrin) leads to compact, non-porous materials if the precursor is heat-treated without any additives. In Fig. 4.2(a), the morphology of the resulting electrocatalyst is displayed; the pyrolized structure forms a dense layer bearing an accessible surface of around 100 m^2/g. Additionally, the structures of the pyrolized graphene layer and carbon support do not match perfectly resulting in a poor performance in *in situ* tests. A first step towards an increased surface area has been achieved by thermolysis of a mixture of the Co-TMPP precursor and iron oxalate acting as a foaming agent. The formed iron oxide is leached out by means of an acidic solvent[198]. The resulting sponge-like structure is displayed in Fig. 4.2 (b); two positive effects can be observed from the addition of the foaming agent: the accessible area of the catalyst is much higher (800 m^2/g compared with the aforementioned 100 m^2/g for the unmodified component) and the added iron ions modify the resulting carbon phase in such a way that a perfect match to the support is achieved. This is monitored by an increased performance in terms of higher current densities in fuel cell applications compared with the additive-free

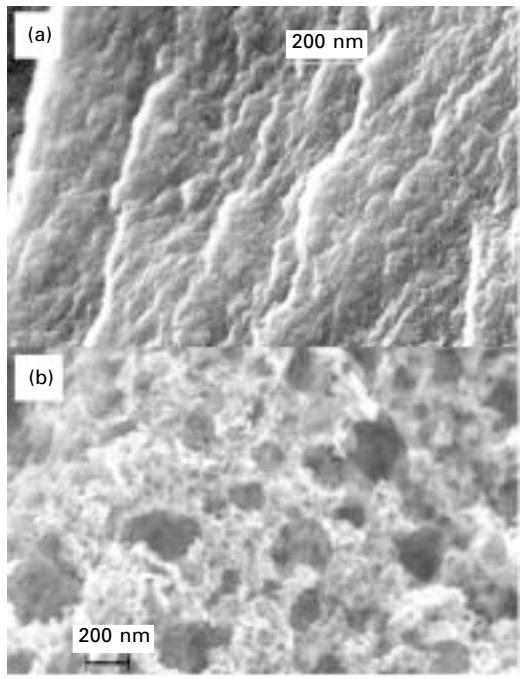

4.2 Pyrolized Co-TMPP-based electrocatalyst support on Black Pearls. (a) Heat treatment without any additives. (b) Metal oxalates added as foaming agents. The additive leads here to a sponge-like structure with an increased surface area.[199]

catalyst caused by the high surface area. The improved electronic coupling can be derived directly from the lowered hydrogen peroxide production rates underlining an improved electron transfer mechanism. Therefore, the catalytically active center is not just the carbon support or the metal-containing N_4-center, but the combination of these two interacting components.

The pyrolysis of the Co-TMPP precursor leads, owing to the thermal effects, to a destruction of the N_4 centers and a melting of the metallic centers. Thereby, the particles become rather large, which prevents the preparation of catalyst layers by means of spraying techniques. Improvements have been achieved by means of low-temperature plasma treatment of the precursor structures. The carbonization of the porphyrin structure is achieved by electric energy instead of pyrolysis[200]. The particle size distribution is shifted towards smaller particles compared with the one obtained by pyrolysis of the TMPP precursor (see Fig. 4.3)[201–203].

The enhanced properties of the plasma-treated electrocatalysts can also be monitored as a function of the hydrogen peroxide production rate where the different influencing contributions are reflected. The unpyrolized Co-TMPP compound with isolated active centers leads to H_2O_2 production rate

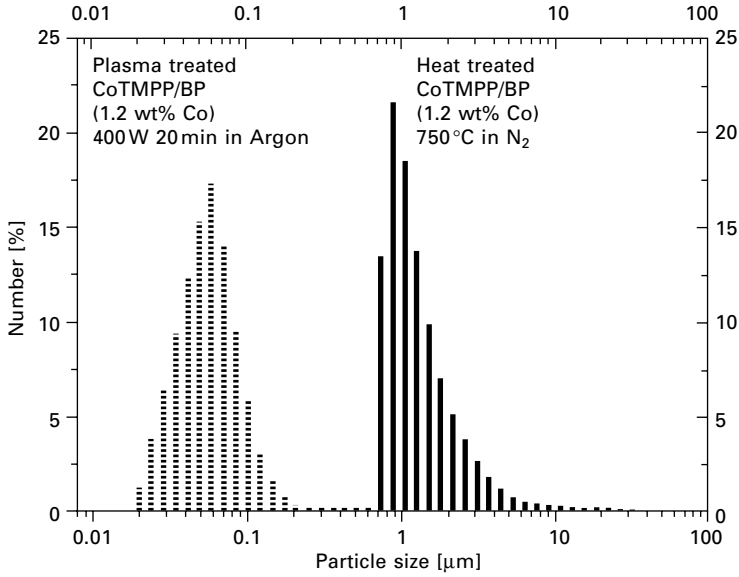

4.3 Particle size distribution of pyrolyzed and plasma-treated cobalt TMPP-based electrocatalysts supported on Black Pearls.[204]

of almost 50%. Products resulting from a traditional heating (pyrolysis) decrease the rate to around 10%. Finally, the low-temperature plasma products lead to hydrogen peroxide productions of less than 5%. Although this amount is too much for fuel cell applications, this method shows the right way to produce new, noble metal-free catalysts where the underlying functionality has been proven. For further improvements, an optimization of the carbon matrix will be necessary.

One attempt to control the H_2O_2 production and enhance the activity was done via a co-deposition of titanium oxide nanotubes with Co-TMPP on Black-Pearls; the resulting electrocatalysts show a higher catalytic activity and an improved stability compared with pure Co-TMPP on the same support[205].

A similar class of alternative electrocatalysts for fuel cell applications is based on iron as core atom of the chelate centers. The pyrolysis of ClFeTMPP in an $NH_3/H_2/Ar$ atmosphere leads to the formation of catalytically active FeN_4/C and FeN_2/C centers[206]. They exhibit the same structure of interconnected molecules, incorporated in the carbon support, as well as in the case of Co-based materials. The selectivity towards a four-electron transfer step can be adjusted by varying the amount of nitrogen. High nitrogen contents (the nitrogen percentage has a higher influence on the activity rate than the catalytically active surface) result in a majority of FeN_2 centers. The FeN_2 centers appeared to be more active and selective towards the complete reduction

of oxygen than the FeN_4 centers, thus producing less H_2O_2[207]. In a further step towards a cost-efficient mass production of fuel cell catalysts, a synthesis route via iron acetate as precursor leads to a similar composition with slightly reduced activities[207]. Since the H_2O_2 formation has not yet been completely avoided in fuel cell conditions, pyrolized Fe–TMPP-based catalysts are still unusable for fuel cell applications since H_2O_2 will cause a decomposition of the catalytic sites by releasing the iron compound of the active centers. Formation of oxygen containing iron compounds results in higher H_2O_2 percentages especially when using iron acetate as precursor[208]. Optimum loadings of these catalysts is ~1%-wt metal; higher loading will result in a blockage of micropores, causing a performance decrease again. Typical turnover rates on the Fe sites are in the range of $0.36 \pm 0.03\ e^{-1}\ \text{site}^{-1}\text{s}^{-1}$ at an operating temperature of 80 °C.

As mentioned earlier, platinum-free alloys with non-noble metal compounds are rather unstable in acidic environments. However, recently a catalyst based on a palladium–iron alloy on Vulcan XC-72 was presented, which combined an extraordinary performance with a suitable stability[209]. The catalytic activity of Pd (which is less active for the ORR in its pure form) is thereby promoted by alloying with the non-noble compound.

4.11 Catalyst supports

For an optimum performance of the fuel cell, the ionic as well as the electronic conductivity of the electrochemically active layer has to be guaranteed. Therefore, the three-phase interface between the involved components catalyst, reactant gas (hydrogen or oxygen) and polymer has to be maximized. The catalyst has to be accessible by the reactant gas, and at the same time the electronic coupling of the particle as well as the contact with the polymer phase to ensure proton transport have to be fulfilled. At the cathode, water is formed by the reduced oxygen species and the protons. These result from the anodic hydrogen oxidation and the following transport through the membrane. An electronically isolated catalyst particle is inactive and does not contribute to the performance of the cell. The electronic contact is achieved with the carbon support; the use of supporting materials allows for finely dispersed catalyst particles in combination with high surface areas. A sufficient protonic conductivity at the reactive spots is usually achieved using a suitable catalyst ink. The ink is a mixture made of an ionomer compound, the supported catalyst and a solvent. The catalyst ink can be either sprayed on the membrane, resulting in a so-called catalyst-coated membrane (CCM), or the mixture can be applied to the gas diffusion medium which is termed afterwards the gas diffusion electrode (GDE). In the next sections the different catalyst supports as well as criteria for the catalyst handling will be further discussed.

4.11.1 Support structure

State-of-the-art platinum-based catalysts are usually supported on carbon materials with loadings of between 20% and 40% metal content. This percentage enables the highest activity since transport limitations are minimized. Higher or lower loadings would result in increased transport pathways. The various support materials differ from each other by the active surface, surface properties (see Fig. 4.4) and pore structure. Examples of support trade names are HS300, Printex XE-2, Norit SX-Ultra, Ketjenblack 300J/600JD, Acetylene Black, Vulcan XC-72R or Black Pearls. A high surface area does not necessarily lead to high activity; this area has to be divided into an accessible part and contribution due to micropores. The micropores raise the absolute area detected by Brunauer–Emmett–Teller (BET) measurements but turn into inaccessible spots when processed and employed in fuel cell catalyst layers[210–212]. A short overview of the different contributions to the overall BET surface is given in Table 4.1.

Besides the electronic coupling to the catalyst particles, the surface structure is also considered to influence the Ostwald ripening. Carbon supports, bearing a fractal surface which includes 'traps' to fix the catalyst particles, are supposed

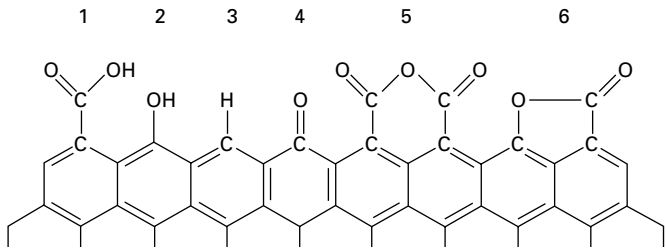

4.4 Oxygen-containing groups on the surface of carbon supports ranging from acidic to basic: 1 carboxyl, 2 phenol, 3 hydrogen (inactive), 4 carbonyl, 5 carboxyl anhydride, 6 lactone.

Table 4.1 Pore size characteristics of different carbon supports employed for catalytical applications

	BET surface/ (m^2/g)	Microporous surface/(m^2/g)	Mesoporous surface/(m^2/g)
Vulcan XC-72R	230	125	105
Black Pearls 2000	1443	1000	443
Printex XE2	1080	279	801
Norit SX Ultra	901	618	283
Ketjenblack 300J	860	515	345
Ketjenblack 600JD	783	84	699
Timrex HSAG	279	111	168

to slow down the particle migration and therefore reduce the effects of catalyst ripening which would otherwise lead to a steady performance decrease.

For commercial catalysts based on platinum, the carbon support Vulcan XC-72R is generally considered to be the most active. A new Sibunit-type support illustrates how an increased accessibility of the catalyst particles improves the activity. The individual supports differ by surface and pore structure; the BET surface is in the range of 20–420 m^2/g (see Table 4.2). In order to compare the different supports in cell tests, the metal loading per unit area is kept constant. In Fig. 4.5, the *in situ* performances of the catalysts on different supports are given. The best performing species are the ones with large BET surfaces (292 and 415 m^2/g); the performance exceeds the one of platinum on Vulcan XC-72 by almost a factor of 4 which cannot only be explained by the increased BET surface (Vulcan XC-72R: 210–235 m^2/g)

Table 4.2 Characteristic data of cathode catalysts supported on various kinds of Sibunit-type carbons and on Vulcan XC-72

Catalyst	BET surface (m^2/g)	Pt specific surface area (m^2/g)	Mean particle diameter (nm)
10%Pt@Sibunit 2677	21.1	52.5	3.0
10%Pt@Sibunit 19P	72.3	83.7	2.0
30%Pt@Sibunit 20P	292	69.5	2.7
40%Pt@Sibunit 619P	415	49.6	2.7
20%Pt@Vulcan XC-72	215	76.6	2.7

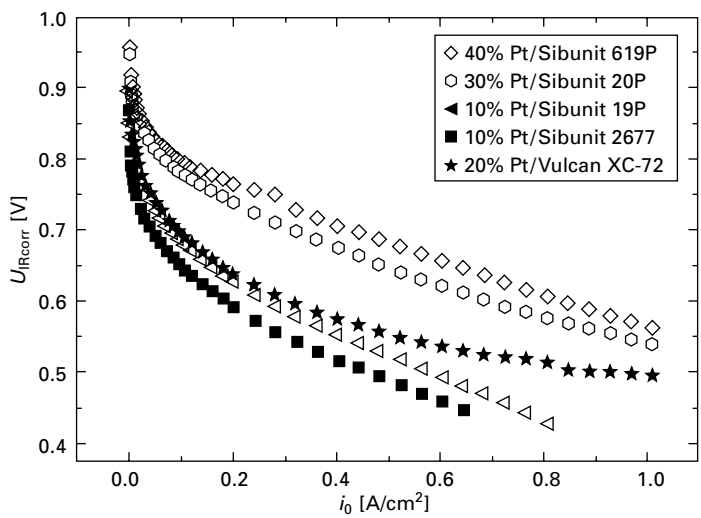

4.5 Characteristic curve (*U-i* curve) of platinum catalysts supported on different carbon supports. Operating conditions: cell temperature 60 °C, anode 0.4 g_{Pt}/cm^2, cathode: 0.6 mg_C/cm^2.

but is also induced by the improved mass transport of the reactants and products[213].

As mentioned earlier the electronic coupling of the catalyst influences the performance as well which has been observed by changes in the microporous layer (see Section 4.12)[214]. During the past years, nanotubes have been discussed as replacements for traditional catalyst supports[215]. In an attempt to improve the electrical contact, nanotubes have been grown directly on the gas diffusion medium, resulting in a decreased ohmic resistance and an improved conductivity.

4.11.2 Surface modifications

Two main phenomena have been identified to influence the long-term stability of electrocatalysts: catalyst dissolution and Ostwald ripening. Catalyst dissolution is an erosion of electrochemically active material. The escaping metal ions might cause further damage by depositing to other particles or, which is even worse, migrate through the membrane and block the pathways for proton transport by strong adsorption to the charge carriers. In case of platinum–ruthenium alloys, permeation of ruthenium ions from the anode through the membrane to the cathode side has been observed.

The second contribution, the Ostwald ripening, is caused by the agglomeration of small particles. Two ways are considered, a dissolution and subsequent deposition as mentioned previously on a neighboring catalyst particle or a migration of the particle to combine with an adjacent one to form a larger particle. In either case, a decreased surface and therefore a reduction of the electrochemically active area is observed.

Surface modifications of platinum-based catalysts are an approach to reduce particle agglomerations and, at the same time, increase the activity of electrocatalysts in the ORR. Modifications with Keggin-type heteropolyacids, such as heteropolytungstate ($H_3PW_{12}O_{40}$), result in an increased *ex situ* performance; the measured higher kinetic parameter are speculated to be due to the role of the polytungstates as carrier of mobile interface protons which cause the higher observed activity[216–218]. Owing to the hydrophilic character of these electrocatalysts, adapted catalyst inks have to be prepared to avoid flooding effects and transfer the *ex situ* performance to *in situ* applications.

4.11.3 Electrode preparation: catalyst layer preparation/morphology

In order to reduce the transport limitations caused by the thickness of the catalyst layers, a new approach has been reported. CCMs are manufactured with reduced loadings and improved transport properties[219–220]. The catalyst support is formed by a dense layer of perylene red (*N*,*N*-di(3,5-xylyl)perylen-

3,4,9,10-bis(dicarboximid), an organic pigment stable in acids and resistant in the potential region of PEM fuel cells. This so-called 'whisker' is coated by platinum (or any other electrocatalyst) and then attached to the polymer membrane. Adjusted by the preparation method this CCM exhibits a nanostructured interface with an overall thickness of less than 1 μm. Owing to the enhanced transport properties and a high active surface the reported surface-related activity of the catalyst is significantly higher compared with carbon supported commercial catalysts.

4.11.4 Carbon replacements (WC support, Magneli phases)

In order to replace carbon-based catalyst supports and reduce the decrease in performance caused by carbon corrosion, inorganic replacements are considered to represent an alternative route not only to improve the stability but also to enhance the activity. Non-stoichiometric titanium oxides and Magneli phases bear strong interactions with the deposited platinum particles, leading to the desired activity. In addition, the increased interactions, in comparison with carbon supports, force the ORR towards the four-electron step, thus avoiding a production of hydrogen peroxide[221,222].

Tungsten carbide (WC) has been employed as catalyst support; platinum-based electrocatalysts on WC have been tested for the HOR and ORR and show a remarkable performance[223]. Initially observed stability problems have been reduced by the addition of Ta[224].

4.12 Gas diffusion media

A gas diffusion layer (GDL) is the mediator between the nanostructured electrode and the flow field which has structures in the millimeter range. Most commonly the GDL consists of carbon fiber paper or carbon cloth

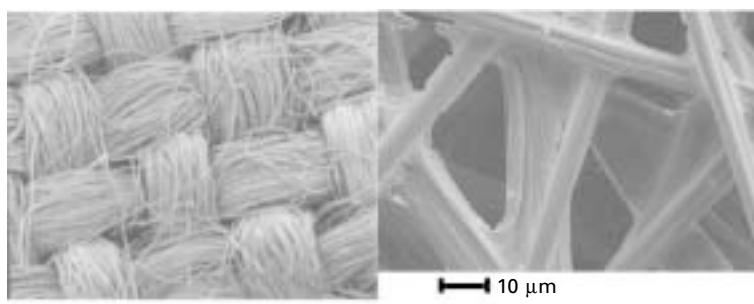

4.6 SEM pictures of GDL substrates. Left: carbon cloth, right: carbon fiber paper.

(Fig. 4.6). Several companies, such as SGL[225], Freudenberg[226], Spectracorp[227] or Toray[228], are GDL producers.

A GDL has to fulfill several tasks in a PEM fuel cell (compare Fig. 4.7):

- The GDL must have high electronic conductivity.
- Heat must be transported through the material. Therefore a high heat conductivity is desirable.
- The GDL should mechanically support the MEA.
- The GDL should provide gas access from the flow-field channels to the catalyst layer and allow removal of gaseous products.
- Finally the GDL should provide a passage for water removal from the electrode to the flow field.

Several of the features mentioned above are in contradiction to each other. For example a high electronic conductivity of the material would require a dense material, whereas an unhindered gas transport requires a high porosity of the material. Therefore a compromise has to be found for which the material fulfills the required properties for a given cell design and for the projected operating conditions. Typical characteristics for some materials are shown in Table 4.3 for Toray material.

The influence of different GDL materials on the characteristic curve of a PEMFC is presented in Fig. 4.8. All cells had the same geometry, were equipped with the same MEA and were operated at the same operating conditions, but the GDL substrate material used in the experiment had a different structure. In order to improve the water transport in the GDL, the samples in Fig. 4.8 were all hydrophobized with PTFE, applying the same procedure. The PTFE content and the thickness of the material were the

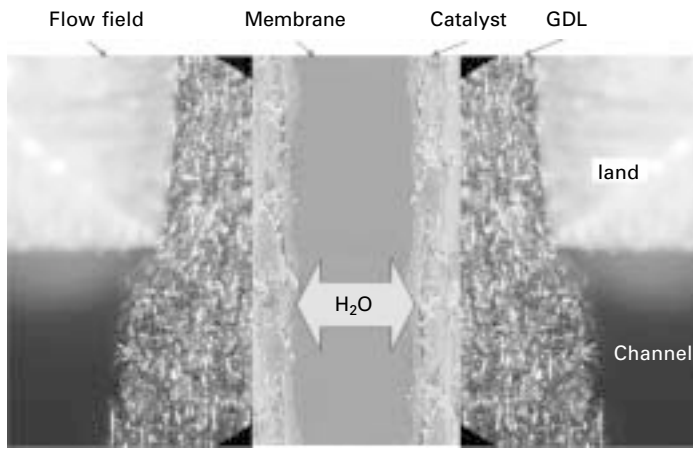

4.7 Cross-section through a PEMFC, GDL compressed under the land, uncompressed under the channel.

Table 4.3 Physical properties for Toray GDLs

Material	Thickness (mm)	Gas permeability (ml mm/(cm^2 h mmAq))	Porosity (%)	Bulk density (g/cm^3)
TGP-H-030	0.11	2500	80	0.40
TGP-H-060	0.19	1900	78	0.44
TGP-H-090	0.28	1700	78	0.44

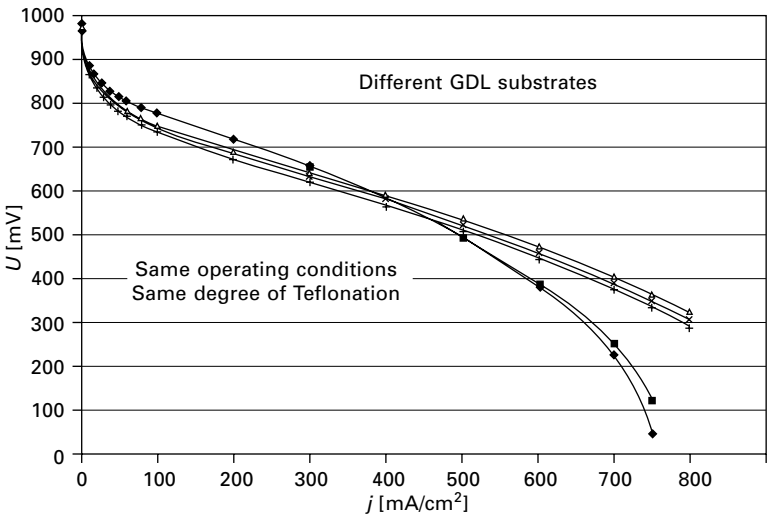

4.8 Characteristic curves of a single cell with different GDL substrate materials.

same. A simultaneous measurement of the electrical resistance proved that the differences can be attributed to water transport and water storage behaviour of the material.

The use of materials with the same structure but with different PTFE content has a similar influence on the fuel cell behavior, as shown in the literature[229]. From these findings it becomes obvious that the GDL has a strong impact on fuel cell behavior and that intense research and development effort is required in order to understand the relation between structure and functionality of GDL material.

4.13 Gas diffusion layer treatment

GDLs are produced from different companies with different processes. A detailed description of the production processes can be found in Mathias *et al.*[230]. Usually the base material is hydrophilic and all pores would be flooded by water if the cell was operated at conditions where a large amount

of water will be produced. As a result all pores necessary for gas transport would be closed by water and the cell would stop working. To prevent these flooding phenomena the GDL has to be treated to gain hydrophobic pores and to prevent flooding. Typically a PTFE suspension is used in a dip coating process. After drying and sintering the PTFE is located on the surface of the fibers preferably in the wedges as can be seen in Fig. 4.9. The through plane distribution of PTFE in a GDL is shown in Fig. 4.10.

The amount of PTFE ranges typically from 5 wt% to 30 wt% depending on cell design, cell material and operating conditions but there is no general rule for the optimum amount of PTFE in a GDL. The production process and the final treatment lead to materials with random fiber structures and a random distribution of the PTFE located primarily in the wedges.

4.13.1 Characterization methods: structure

The random nature of the GDL makes it difficult to characterize the structure and to find simple relations between this structure and the functionality of the material. In the following we will focus on the structure and the media transport in the material.

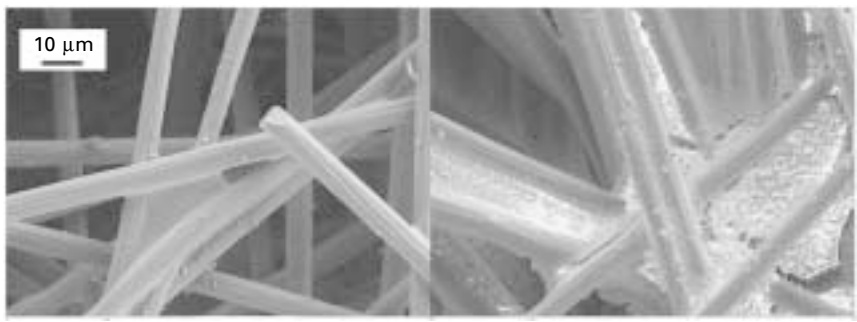

4.9 Carbon fiber paper GDL without (left) and with (right) PTFE.

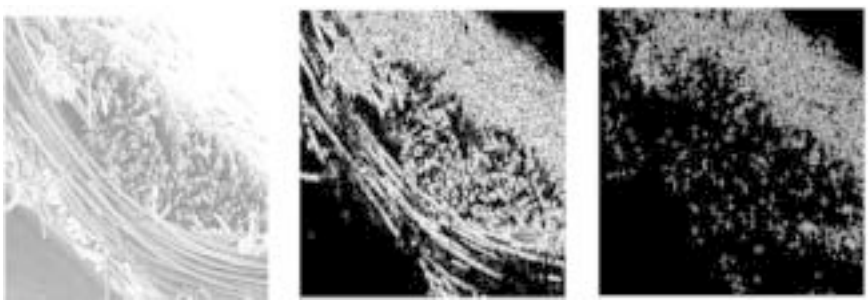

4.10 Cross-section through a GDL. Left: SEM picture, middle: carbon distribution, right: fluorine distribution (from EDX measurements).

A well-known method for characterization of porous materials is mercury porosimetry. Mercury has a high surface tension and has to be forced into the pores of the material in order to fill the pores. From the uptake of mercury as a function of pressure one can calculate the pore size distribution based on volume in terms of equivalent cylindrical capillaries. The total uptake of mercury at the maximum applied pressure gives the porosity.

Another method, which uses a completely wetting liquid in contrast to mercury porosimetry, is capillary flow porometry[213]. If the material of interest is brought into contact with the wetting liquid, all pores will be flooded. In order to remove the liquid a pressure across the sample has to be applied. When slowly increasing the pressure difference at a certain pressure the gas flow steps, which means that the pore with the largest diameter was emptied according to

$$D = 4\gamma_{l/g} \cos \Theta / p$$

where D = diameter of pore
γ = surface tension
l/g = liquid gas
Θ = contact angle ($\Theta = 0$ for completely wetting liquid)
p = pressure difference

This point is called the bubble point (Fig. 4.11, Table 4.4). A further increase of the pressure will open smaller pores. This method allows a flow-based pore size distribution to be determined. One advantage of this method over mercury porosimetry is that one can distinguish between in-plane and through-plane pores which is important because of the anisotropy of the material. Furthermore, experiments can be performed with uncompressed and compressed samples to simulate the compression under the lands and the channels of the flow field in a fuel cell.

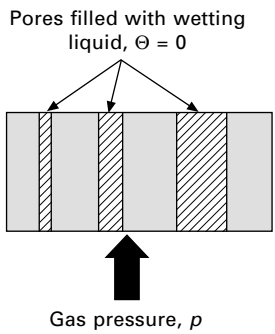

4.11 The gas pressure from one side of the sample is gradually increased; at a critical pressure the gas empties the largest pore in the sample and starts to flow through the sample. This pressure is called the bubble point pressure.

Table 4.4 Results of bubble point measurements through plane for TGP-H-060 with different Teflon contents

Toray TGP-H-060	Bubble point (μm)
0% PTFE	47
16% PTFE	42
35% PTFE	40

Table 4.5 Mean pore radii measured with different methods

Toray TGP-H-060	Mean pore radius (μm)	
	Flow based	Volume based
0% PTFE	23	39
16% PTFE	19	35
35% PTFE	17	34

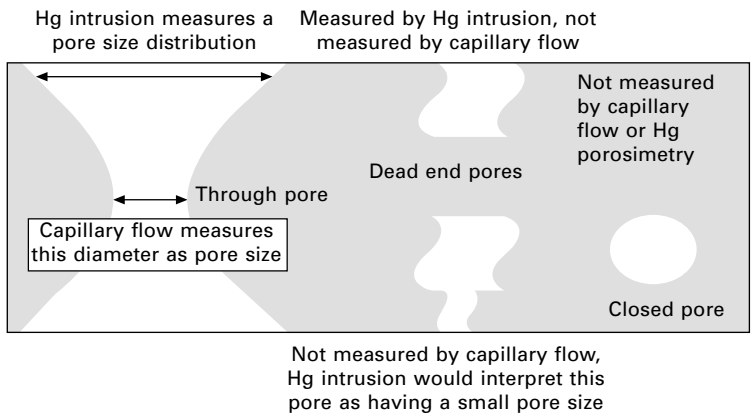

4.12 Different types and interpretations of pores.

Comparing the results one will find that the average pore size distribution measured with mercury porosimetry and capillary flow porometry are not identical (Table 4.5). A flow-based average pore size distribution is smaller than the volume based average pore size. This can be explained by means of a schematic drawing of a porous material (see Fig. 4.12). Capillary flow identifies the narrowest part of the pore whereas mercury porosimetry will detect the pore shown on the left side of Fig. 4.12 as having a pore size distribution. Some other differences are also shown schematically.

Owing to the random nature of the material under observation it is not yet possible to find a simple correlation between the results obtained by different methods. In order to do so it would be necessary to model and simulate fine

structures of the material in detail. From Fig. 4.12 it will also be obvious that one has to be careful when comparing porosities measured with different methods. At least three different porosities can be distinguished:

- all pores including closed pores: ε_a
- to gas or liquid-accessible pores, e.g. dead end pores with a connection to the outside, ε_d
- pores with a connection from one side to the other side (through pores), ε_{th}

with

$$\varepsilon_a > \varepsilon_d > \varepsilon_{th}$$

For very open GDL materials bearing high porosities and high permeabilities, the three porosities are similar. Typical porosities for untreated GDL material are in the range of 70–90% (compare Table 4.3).

Another method which should be mentioned here is the 'standard porosimetry' developed by Volfkovich and co-workers[232–234] Based on a well-characterized reference material the pore size distribution of a sample can be determined making use of a capillary equilibrium between the sample and, the reference. This variant of porosimetry is a very sensitive and, like capillary flow, a non-destructive method.

The measurements above are often used to determine the structure of the materials and the influence of coating effects (PTFE) on the structure. One drawback of all the methods is that only the mean values of the characteristics of the materials are estimated. No detailed information about the structure on pore level will be obtained when using standard analysis of the results. More advanced analysis methods can be found elsewhere[235] (from a theoretical point of view two samples with different structures might give the same results when applying the above-mentioned methods, although this is fairly unlikely).

Another very helpful but cost-intensive method which has received significant attention over the past few years is the examination of the material by synchrotron tomography[236]. The 3*D* pictures (Fig. 4.13) can be analysed by image processing and the characteristic properties, such as coordination number, porosity or isotropy of the material, can be extracted. The knowledge of these parameters in combination with calculated stochastic characteristic can be used to model the structure[237–240] (see Section 4.13.4).

4.13.2 Gas transport

One of the main goals of the GDL is the transport of gaseous species. From an experimental point of view the determination of the gas permeability (pressure-driven flow) is easier than the determination of the diffusion (driving

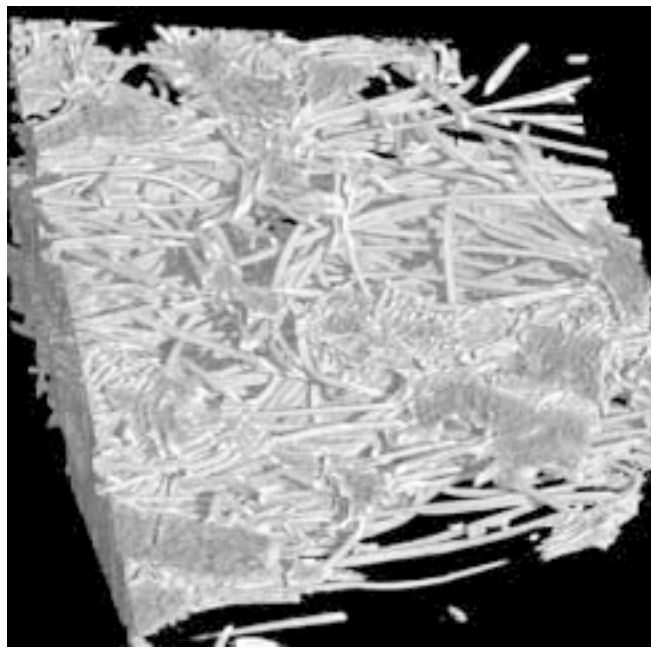

4.13 Tomogram of a non-woven type GDL.

force: concentration difference) of gases. This might be the reason that literature values for the permeability for GDL material can be found much more often than diffusion coefficients or structural parameters of the materials which are necessary for the determination of the effective diffusion coefficient[241]. In particular, when looking in the specification for GDLs provided by manufacturers, one will find values for gas permeation but no data relevant for gas diffusion.

From a physical point of view diffusion and permeation are coupled processes inside the GDL, with diffusion usually being the dominating process. Owing to the large average pore sizes, Knudsen diffusion does not play a role; volume diffusion is the predominant process which will be described by the Stefan–Maxwell equation. Knudsen diffusion will dominate the transport process only when the pore diameters are in the same order of magnitude as the mean free path of the gas molecules.

In order to determine the diffusion coefficient, the gas–gas diffusion coefficient has to be multiplied by a factor which takes into account the structure of the porous material. The diffusion coefficient inside the porous material can be written in the following form:

$$D_{\mathrm{ef}} = \psi D_{\mathrm{AB}}, \quad \psi = \frac{\varepsilon}{\tau}$$

where D_{ef} = effective diffusion coefficient inside the GDL
D_{AB} = gas–gas diffusion coefficient
ε = porosity
τ = tortuosity
ψ = prefactor

ψ is the factor which decreases the diffusion coefficient inside the GDL due to the internal structure of the material. An estimation of this factor can be calculated according to the Bruggemann correction[242]:

$$\tau = \frac{1}{\varepsilon^{1/2}}$$

Alternatively, tortuosity can be calculated according to the Tomadakis–Sotirchos model which takes the anisotropy of the material[241] into account.

A direct measurement of ψ can be performed with a modified Wicke Kallenbach cell[243–246]. Measured values of ψ are in the order of 0.2 which is much smaller than would be expected from the Bruggemann correction or the Tomadakis–Sotirchos model.

Permeability data seem to be more reliable to model gas transport phenomena. Measured data for compressed and uncompressed GDLs were successfully fitted to the Carman–Kozeny model[241].

4.13.3 Water transport and storage

Understanding and improvement of water management in fuel cells is one of the main challenges in fuel cell research and development. The first measurements of water permeability were published by Mathias *et al.*[230]. Even though the water flux was several orders of magnitude higher than in a working fuel cell, it became clear that even at these high flow rates hydrophobic pores remained open for gas transport as long as no condensation took place inside the pores; at the same time, all pores were involved in the transport processes when a wetting liquid was used. Another observation was that a certain amount of water remains inside the GDL after a liquid permeability experiment. Repeated experiments without drying the sample between runs led to an increasing amount of water remaining in the porous structure. This was observed indirectly by the measurements of the hydrohead pressure (the minimum pressure necessary to force water through the pores). The experiments were perfomed with a PMI instrument[247]. The hydrohead pressure is highest for dry samples and decreases for wet samples as shown in Table 4.6.

Similar results were recently obtained by Benziger *et al.*[248]. The authors also determined the amount of water remaining in the material and the overall water permeability. Recently some papers have been published which observed the liquid water transport in great detail in *ex situ* measurements. The most

Table 4.6 Hydrohead pressure for dry and wet samples with different degrees of Teflonation

Material	Hydrohead pressure dry sample (pa)	Hydrohead pressure wet sample (pa)
Toray 0%PTFE	6200	2070
Toray 13% PTFE	6900	2760

important finding was that the liquid water will be transported through distinct pores and that the water will not be transported via a converging capillary tree, as suggested in earlier works[249,250].

In situ observation of water transport and water evolution supports these results. Several approaches employing cells with transparent parts were described in order to visualize the water transport[251,252]. However, these modifications led to unpredictable influences on the water distribution. Owing to the high sensitivity towards hydrogen, neutron radiographic visualization became important to detect liquid water in operating fuel cells[253–257]. Most of these works focused on the transport of rather large trunks and accumulation of water in the flow-field channels and the GDL, taking only the perpendicular viewing direction (through plane) into account. Furthermore the resolution of around hundred micrometers is not suitable to gain a detailed cross-sectional view of the active area. These limitations were overcome by means of synchrotron X-ray radiography: the initial formation of small water clusters, the transport processes in the GDL and the transition from the GDL to the gas channel were visualized engaging a resolution down to 3 μm[258].

Figure 4.14 shows the evolution of water clusters (top view). Most of these clusters can be found under the lands of the flow field. The water transport took place in preferred pathways from the GDL into the gas channel. The water droplets started to grow at the interface between GDL and flow field. After reaching a certain size the droplets were removed from the channel. The flow field used was machined into graphite composite material and an SGL GDL was used.

The results raised further questions: Is it possible to distinguish between hydrophilic and hydrophobic pores and what is their pore size distribution? Up to now it seemed difficult to distinguish between hydrophilic and hydrophobic pores on a pore scale. From a macroscopic point of view an estimation of pore size distributions for the different pores can be measured. Using water and mercury porosimetry Lee *et al.*[259] showed the mixed wetting characteristics of GDLs for the first time. With mercury porosimetry all pores were detected whereas water porosimetry was used for the detection of hydrophilic pores. For an (unspecified) GDL material under observation they found that about 50% of all pores were hydrophobic. The volume-based

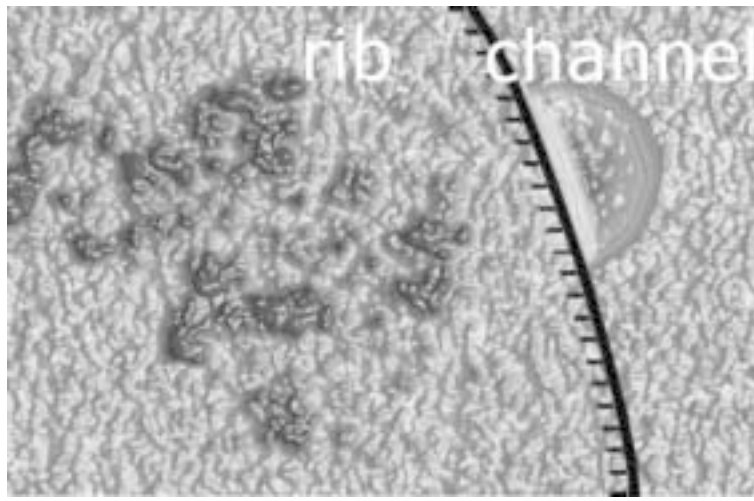

4.14 Eruptive transport mechanism of liquid water from the gas diffusion layer to the flow field channel: left, area under the rib; right, gas diffusion media in the channel area. Dark areas under the rib represent reduced amounts of water in the GDL pores while bright-grey spots in the channel indicate an increased water level. Emptied pores are filled within a period of around 100 seconds and a cyclic behavior of the ejection mode is observed.

mean pore diameter of the hydrophobic pores was determined to be 17 μm. The mean pore diameter of all pores was determined as being 16 μm. The measured pore size distributions are displayed in Fig. 4.15.

Using the method of standard porosimetry Gostick *et al*. investigated several different GDL samples. Their results support the common assumption that the hydrophilic and hydrophobic pore size distributions have similar shapes[260]. They furthermore measured the saturation/capillary pressure curve for several GDLs with and without microporous layer and showed that the measured curves can be well described with the van Genuchten model, which also allows relative permeabilities to be estimeted as a function of saturation. The results are important for all kinds of macroscopic two-phase flow modeling in PEM fuel cells.

In this respect the wetting behavior between water and the surface is most important. The contact angle of a water droplet formed on a flat surface is a measure of the wetting behavior. The porous GDL has a rough surface and, due to coating with PTFE (at least at some points), a random mixture of surface material (PTFE, carbon) can be expected. The observed contact angle of a sessile drop on a GDL will thus be a mixture of surface properties and surface roughness and it is well known that the surface structure has a strong impact on the observed contact angle. Owing to the surface roughness there are two possible wetting states: the Cassie and the Wenzel states[261–264].

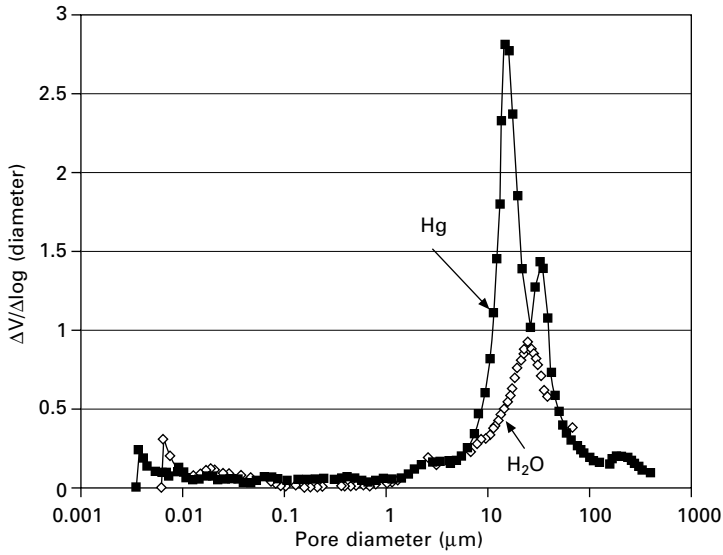

4.15 Pore size distribution of a GDL determined with mercury and water porosimetry.

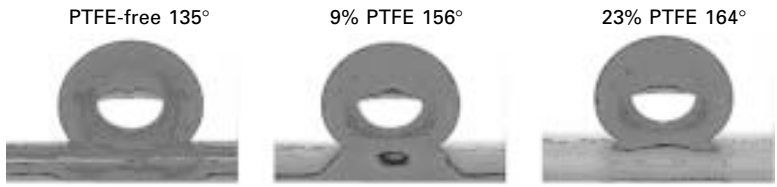

4.16 Water droplets on a GDL with different PTFE content.

The Cassie state seems to be metastable because a transition between the Cassie and Wenzel state can simply be induced by vibrations of the surface. On Teflonized Toray material a Wenzel state has yet to be observed; the Cassie state seems to be energetically favorable.

Measurements of the contact angle on a GDL with different amounts of PTFE are shown in Fig. 4.16. Increasing PTFE content results in an increasing contact angle but the situation is not as clear as it appears. Depending on the base material and the coating method the contact angle does not necessarily increase with PTFE content as expected. Results are presented in Table 4.7. With the amount of Teflonation the change in surface structure seems to be significant and dominates the wetting behavior.

In order to understand the two-phase flow behavior it is necessary to gain information on the wetting behavior of water inside the material. A sessile drop analysis as is usually done, does not seem to be appropriate to gain information about the average contact angle inside the pores, and the result

Table 4.7 Contact angle on a GDL with different degree of Teflonation

Material Toray TGP-H-120	Contact angle (°)
9% PTFE	156
14% PTFE	151
23% PTFE	155
37% PTFE	152

is not a quantitative measure of the degree of Teflonation. The observed contact angles would have to be corrected for surface roughness. For untreated Toray TGP-H-090 Gostick *et al*.[260] used the Cassie–Baxter equation to estimate the contact angle of water on the GDL material. The observed value was 146° whereas the effective contact angle was estimated to be 112°. An alternative method to gain the necessary information is the usage of the Washburn absorption method[265], which allows measuring the average contact angle inside the porous material. The contact angle for Toray TGP–H120 was determined to be 123°, which is in good agreement with the data presented by Gostick *et al*.[260].

In conclusion, one has to be careful in the interpretation of the results. Research activities are necessary to understand the influence of different GDLs in a working cell. Modeling and simulation techniques provide better understanding of the structure of a GDL, the transport processes taking place inside the GDL and the interaction between the GDL and the flow field and the electrode.

4.14 Modeling and simulation

Modeling and simulation of two-phase flow processes inside GDLs are the focus of several research groups. Different approaches can be distinguished. Over the past years the focus has mainly been on macroscopic models[266,267]. These models are based on the theory of volume averaging and do not take into account the morphology of the material but make use of macroscopic measurable quantities such as porosities, permeabilities and capillary pressure/saturation curves. A typical water saturation profile inside the GDL based on the 1D macroscopic model of Pasaogullari *et al*.[268] is shown in Fig. 14.17.

As mentioned above the interaction between the GDL and the flow field has a strong impact on the behavior of water transport in the cell. Therefore this interaction has been examined in detail by several authors[266–270]. A simulated water distribution for a single channel is shown in Fig. 4.18. As expected the water saturation increases with increasing current density. The water saturation is higher under the ribs (also called lands) of the flow field

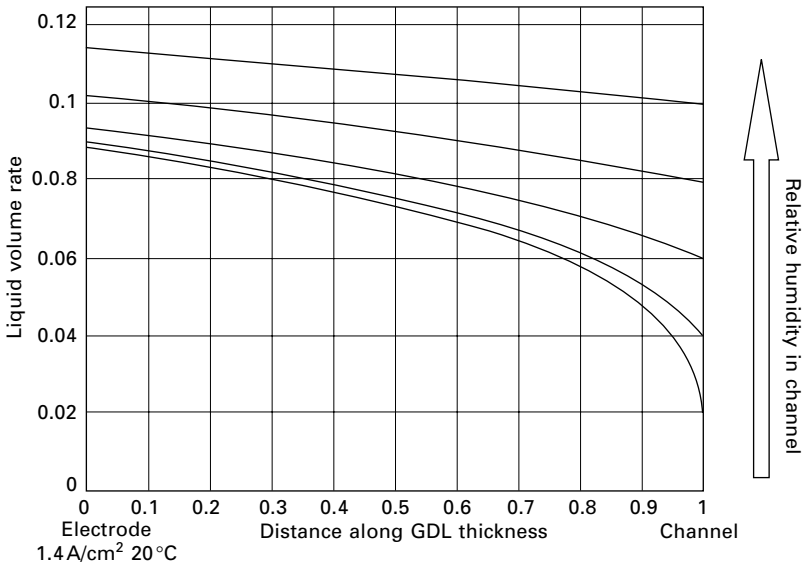

4.17 Water saturation inside a cathode side GDL (cross-section). Water will be transported from the left side (electrode) to the right side (channel). The saturation inside the GDL depends on the relative humidity in the cathode gas channel.

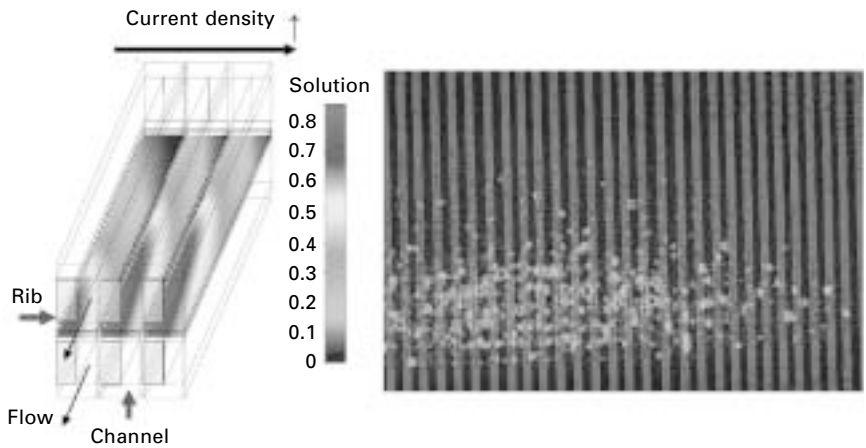

4.18 Left: simulated water saturation in the cathode side gas diffusion layer for three different current densities. Right: liquid water in a running cell with straight channels visualized with neutron radiography (grey shaded areas refer to rib positions).

and increases along the channel. Comparing this result with neutron radiography experiments (Fig. 4.18) shows that the simulation at least shows the correct trend.

Assuming a simple straight channel (ladder) flow field (Fig. 4.19(top)) it

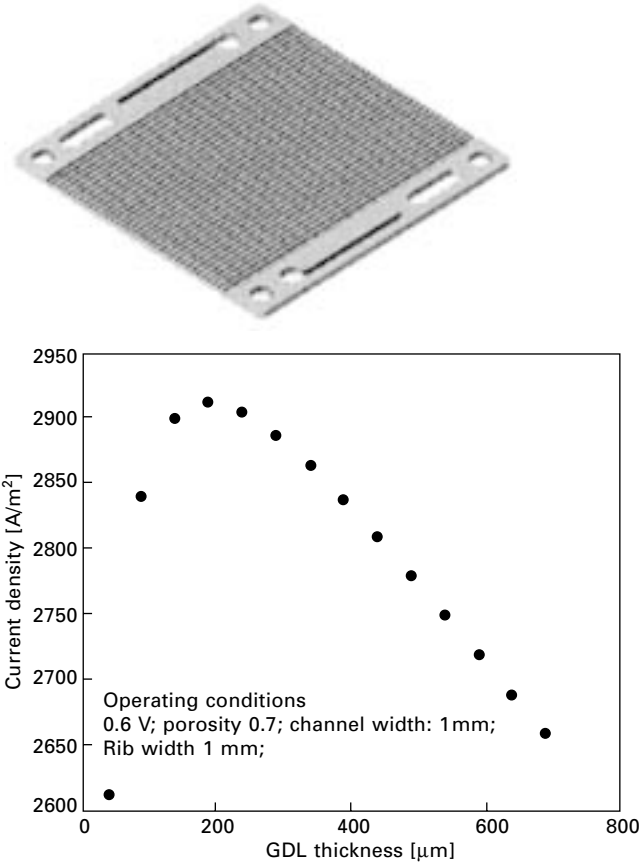

4.19 Top simple ZSW ladder flow field. Bottom Influence of GDL thickness on current density for a ladder flow field.

is obvious that the thickness of the GDL has to be optimized in order to reach the maximum output. Using a very thin GDL, the mass transport limitations under the channel will be small whereas under the rib of the channel the mass transport limitation will be large. In the borderline case of vanishing GDL thickness only half the active area will be used for current production. In the opposite case of a very thick GDL the gas transport from the gas channel to the electrochemical active area will be very long, resulting in a high mass transport limitation. Both cases will result in a strong mass transport limitation, resulting in current densities at a given cell voltage (Fig. 4.19(bottom)). Therefore, there should be an ideal GDL thickness, leading to the optimum performance. Simple simulations which take only the gas transport inside the GDL into account show that for the flow field specified above the optimum thickness is around 200 μm, which was verified experimentally. It

is noteworthy, that the cell reacts more sensitively on thin GDLs than on thick ones.

Simulation including two-phase flow inside the GDL, the contact resistance between the neighboring components and a detailed model of the membrane led to comparable results. Figure 4.20 shows a simulated case where the GDL was kept constant and the land to channel ratio was varied. As can be seen a certain rib to channel ratio results in optimum performance of the cell (see also Section 4.15).

These simple simulations for simple flow fields show that there are mutual interactions between the GDL and the flow field (compare also Fig. 4.8). The situation becomes more complex when serpentine-type flow fields are used. Owing to the pressure loss and the change in gas composition in the channels, diffusive and convective flow under the ribs can occur which might have strong impact on the fuel cell behavior. Figure 4.21 shows a simulation result of a worst case scenario where the oxygen does not follow the channel but flows preferentially under the ribs from one part of the channel to a neighboring part. A decrease of the GDL thickness or a decrease of the in-plane permeability would improve the oxygen distribution for the flow field used.

When looking at the neutron radiography data in more detail and at the synchrotron radiography data it is obvious that the water distribution does not show a smooth distribution, as shown in the simulation results. The water

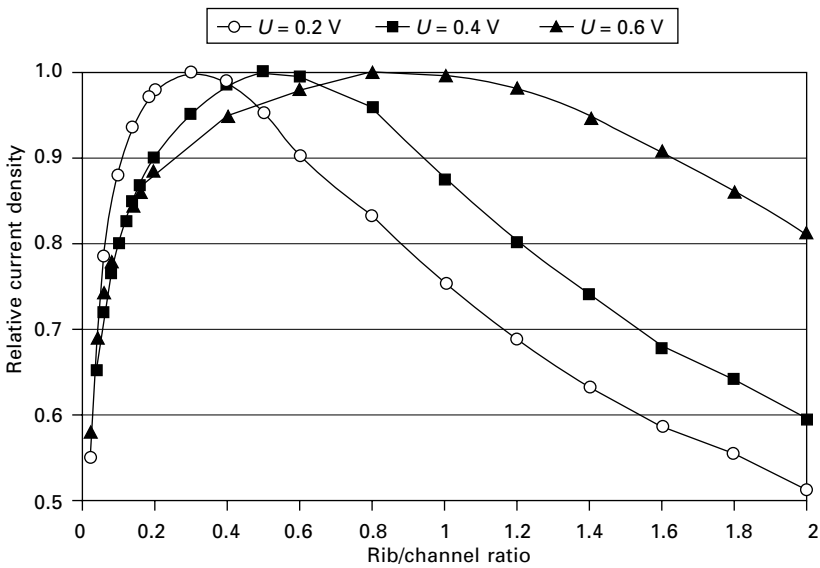

4.20 Relative current density as a function of land to channel ratio for different cell voltages.

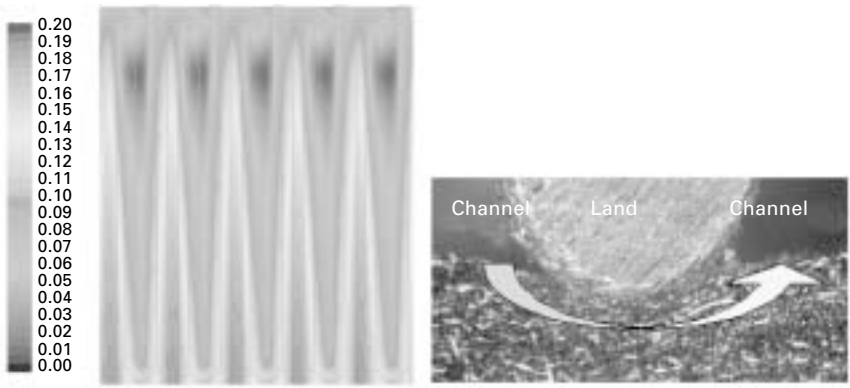

4.21 Contours of O_2 mole fraction on the cathode side GDL in a meander flow field.

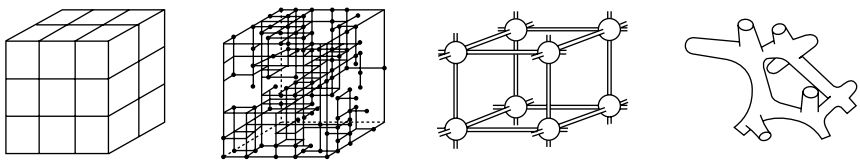

4.22 Different network structures.

exists in a more cluster-like state which cannot be described with macroscopic models.

In order to understand the water transport in the random hydrophobic GDL structures in more detail the morphology and the wetting characteristic of the single pores have to be taken into account. One approach is the use of pore network models. In these models the structure is represented by a network of pores which are connected by throats. The relevant physics is applied to simulate the flow inside the network.

In the 1950s the first pore network models were developed by Fatt[271]. With the help of these 2D network models, insight into the complex behavior of transport processes could be generated. Later it was shown that with 2D models, 3D structures could not be described sufficiently which can easily be understood when looking at the percolation thresholds of 2D and 3D systems[272]. Different network models are shown schematically in Fig. 4.22. The network models were originally developed in soil physics as all the other models for describing two-phase flow. The network models recently received attention in the fuel cell community[273–276]. These 2D and 3D models provide a deep insight into the water transport mechanisms. Capillary fingering and water clustering as observed with *in situ* synchrotron radiography cannot be explained with macroscopic models but will easily be detected in pore

network models. Furthermore a capillary pressure/saturation curve will be gained from these calculations which can be used in macroscopic models.

One drawback of network models is that an equivalent network has to be constructed from the real structure. In order to overcome this problem, a full morphological approach can be applied. The microstructure of the GDL will be reconstructed using stochastic techniques (Fig. 4.23)[237,238,278].

The lattice-Boltzmann method[280] appears to be appropriate to simulate flow phenomena due to its ability to handle boundary conditions in any geometric structure with little numeric effort. A different approach is the simulation of water transport in the frame of Monte Carlo simulations[281]. As can be seen in Fig. 4.24 water clusters and preferred water pathways can be observed. Furthermore wetting films in the wedges can be observed where

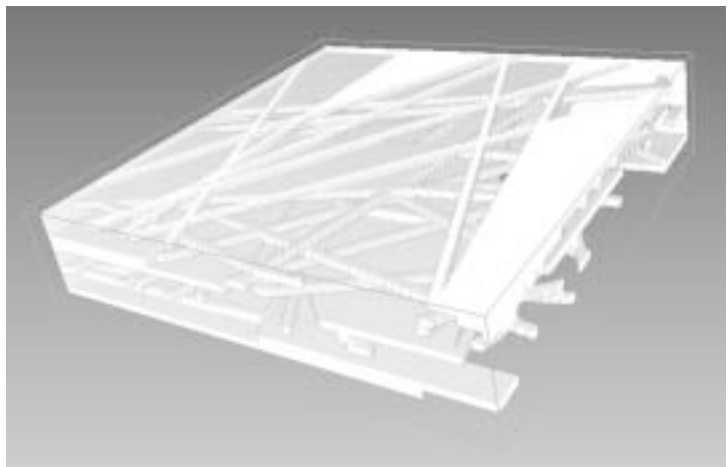

4.23 Random line tessellation-based reconstruction of Toray paper with Bernoulli filling to simulate the glue as illustrated in SEM pictures[237,279].

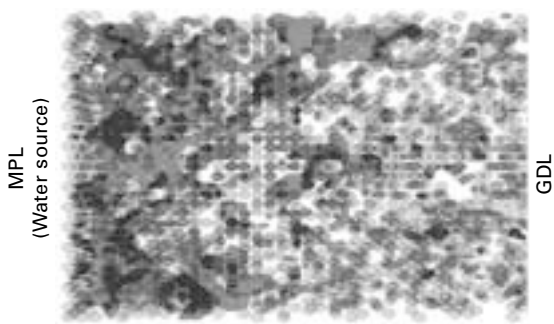

4.24 3D Monte Carlo simulation of liquid water transport in a GDL.

the Concus Finn condition[282] is fulfilled. The Monte Carlo simulation results agree well with the results obtained with lattice-Boltzmann simulations.

None of the models presented in the available literature describes the oscillating behavior of a water droplet at the interface between GDL and gas channel as was observed in synchrotron radiation and *ex situ* experiments. A first approach in order to simulate this behavior was made by Zhu *et al.*[283], who used the method of VOF (volume of fluid) to show the influence of air flow in the channels on the deformation and removal of drops from the GDL surface with a two-dimensional model, which will be a first step to a better understanding of the dynamic water behavior at the interface between GDL and flow field.

4.15 Flow-field design

Between the separator plates and the gas diffusion layers an additional functional unit is necessary, which is responsible for the gas distribution as well as the electrical contacting of the gas diffusion layer. This functional unit is called gas distributor or flow field. The flow field consists of a series of channels and ribs, which lead from the gas inlet to the gas outlet, passing over all regions of the cell's active area. In most cases, the flow field is mechanically integrated into the bipolar plate, although also other solutions exists, e.g. (a) a separate layer (mesh flow field) or (b) a flow-field structure which is integrated into the GDL. The active area should be covered fully by the channel/rib area of the flow field. The GDL should be somewhat larger (e.g. 1 mm on each side) to avoid a media flow bypass at the borderlines of the GDL and sinking of the GDL into the border channel of the flow field.

4.15.1 Flow-field parameter survey

A flow field is characterized by a set of mechanical parameters which describe the construction of a single repeating unit consisting of one channel and one rib. These are:

- channel depth;
- channel width;
- rib width.

If the flow field is not machined other additional characteristics are necessary to describe the channel/rib structure of a flow field:

- rib-wall radius (upper radius);
- channel-bottom-wall radius (lower radius);
- wall angle.

The meaning of those characteristics is explained by a cross-sectional view of the flow field (Fig. 4.25). Other non-rectangular forms (such as V-shape) are possible.

The repeating unit of a serpentine flow field including channels flowing in parallel is given by the geometric structure within 'rib width' and 'channel width' (upper side).

4.15.2 Flow-field types

Flow fields should allow media transport and removal from and to all sections of the active area. There are many possible configurations to achieve that goal. It is not necessary that the channel/rib dimensions remain the same all over the flow field[284,285]. Figure 4.26 shows some examples of possible flow field configurations.

A detailed survey on flow-field design types is given for example, in Li and Sabir[286]. Interdigitated flow fields are described in, for example, Vielstich *et al*.[287]. From all configurations shown, the serpentine flow field has the highest technical meaning. Therefore, this flow-field type is described in more detail in the following sections.

4.16 Serpentine flow fields

4.16.1 Design considerations

As a result of the dimension of the repeating unit, and the number of channels which are conducted hydraulically in parallel with each other, a certain

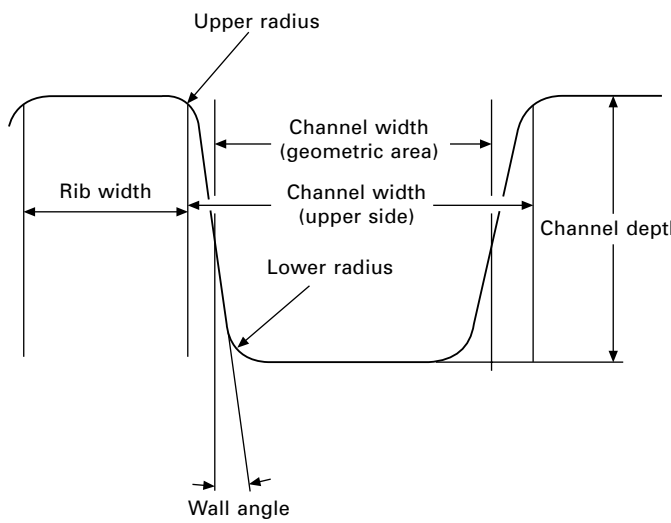

4.25 Cross-section view of a channel/rib unit.

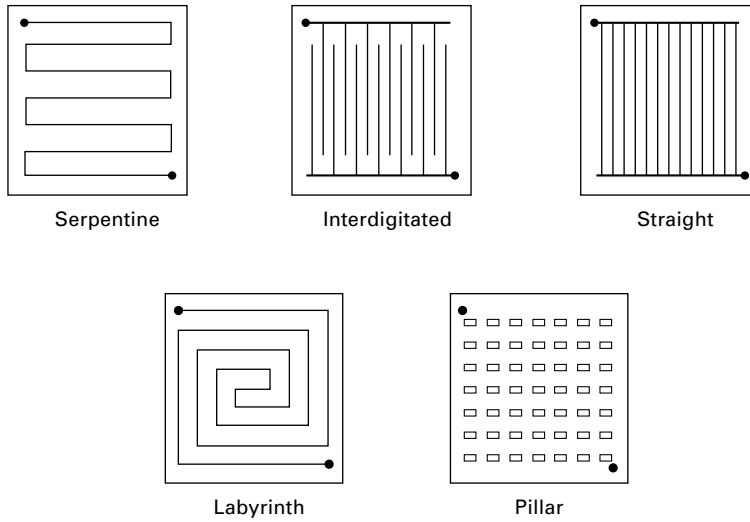

4.26 Flow-field configurations.

channel length is necessary to cover the whole active area. These parameters are not independent of each other; a high degree of parallelization leads to short channel lengths, whereas a low degree (especially one single channel) leads to quite high overall channel lengths, normally resulting in a high pressure drop across the flow field.

The resulting pressure drop is one of the key parameters for the resulting flow field. The pressure drop depends on channel geometry and, degree of parallelization, as well as on the specified design parameters for the stack (current density, gas utilization, gas composition (including water content) and operating temperature). In general, a low-pressure difference across the flow field is desired because of lower auxiliary energy demand e.g. for air compression. On the other hand, a certain pressure drop is necessary to remove condensate from the flow-field channels. Therefore, flow-field design should be a compromise between those targets.

4.16.2 Influence of rib and channel width and depth on performance

Fuel cell performance is highly dependent on rib and channel dimension. There are many pathways for the dimensioning effects on cell performance:

- pressure level and differential pressure;
- condensate removal;
- electrical conductivity;
- media transport properties.

The differential pressure influences both the condensate removal properties and the pressure level mainly in the cell inlet section, thus influencing kinetics as well as cell water household by changes in RH. Moreover, the influence of differential pressure on auxiliary energy demand has to be considered. Information on this topic can be found in, for example, Scholta *et al*.[288].

Influence of rib to channel ratio on performance

The non-pressure-related effects of rib-channel geometry can be divided into two fields, one being the influence on GDL electrical contact, which can be described to a good approximation by the ratio of rib and total area, r/t. Figure 4.27 shows experimentally determined data of cell resistance on rib to channel ratio. It is clearly shown that an r/c ratio of less than 0.45 (equivalent to a rib to channel ratio of 0.8) leads to a significant increase of ohmic losses. On the other hand, an r/c ratio of greater than 0.57 (rib/channel ratio of 1.3) does not lead to a significant further decrease of cell resistance. Therefore, an r/c ratio $0.45 < r/c \leq 0.57$ is recommended for flow-field design.

Influence of rib width on performance

Although the influence of rib width cannot be discussed without considering the channel width used (see above), there is also a strong impact of the

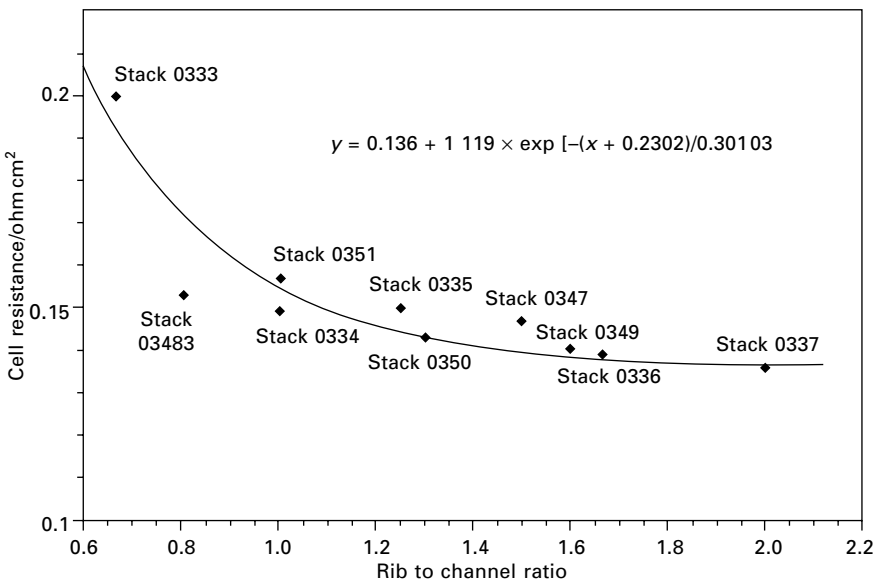

4.27 Cell resistance of a 100 cm^2 cell dependent on rib to channel ratio.

absolute rib width on the cell performance driven by mass transport effects. The reason for that dependence is the limited mass transport (media supply, water removal) under the rib. Moreover, there is a significant interaction between well-performing rib widths and the thickness and transport properties of the gas diffusion layer. The transport effects are visualized in a FLUENT^{TM} calculation (Fig. 4.28) of the oxygen concentration in a single channel at a current density of 0.4 A/cm^2. The following operating parameters were assumed: parallel flow field, length of single channel 103 mm, 60 °C, dew point temperature (cell inlet) 40 °C, oxygen utilization degree 50%, GDL thickness of 0.27 mm, air permeability in air of 1.76×10^{-11} m^2.

It is obvious that the mass transport under the ribs becomes more sensitive for very small GDLs, especially below 0.2 mm thickness. However, for high GDL thicknesses (> 0.4 mm) mass transport also becomes an issue because of longer total media pathways. The relevance of this calculation to channel depth will be discussed below.

At a GDL thickness of 0.27 mm, as used in the model calculation, it becomes clear that at a rib width of 2 mm, significant oxygen starvation occurs in the middle section of the rib. This oxygen starvation corresponds with a localized peak in water concentration in the same region, corresponding with the risk of additional water condensation in the rib area. Therefore, it can be concluded that at current densities of 0.4 A/cm^2 or above, the rib width should be less than 1.5 mm. Experimental data[286] let us conclude that the optimal rib width for a mid-size GDL (0.27 mm) is around 1 mm (see Fig. 4.29).

4.16.3 Influence of channel depth on performance

The channel depth influences several operation parameters and therefore influences the cell performance in several ways. In this subsection, the influence on pressure drop and water removal is neglected, and the main focus is set on media concentration and GDL effects. The influence of oxygen distribution

4.28 Oxygen concentration profile (50% utilization) at a single channel/rib system at a current density of 0.4 A/cm^2 (1 and 2 mm rib width, 1 mm channel depth).

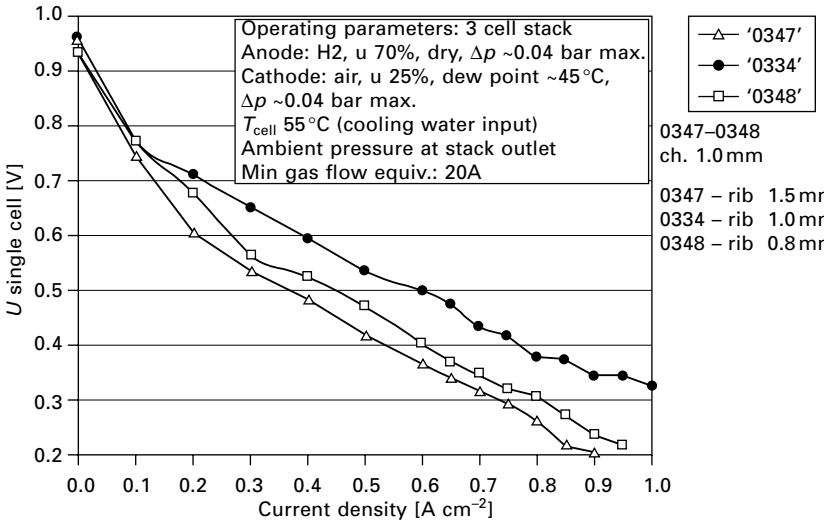

4.29 C.V. characteristic curves for different channel/rib geometries.

in a single channel/rib/GDL structure (representative of a parallel flow field) is shown in Fig. 4.30.

It can be observed that there is a slight influence of an increased channel depth from 1 to 1.5 mm on the lowered oxygen concentration at the GDL/electrode interface (up to –0.4%). By increasing the channel depth to 2.0 mm, the oxygen concentration is further reduced by another 0.4%. So, channel depths of greater than 1 mm or more lead to a stronger gradient in oxygen concentration profile in the *z* direction of the channel. In consequence, some of the oxygen fed to the cell is wasted by purging it over the channel bottom from inlet to outlet never reaching the electrode active area. A comparative assessment of the model calculations show that even channel depths of more than 1.5 mm should be avoided for the same reason. However, deep channels lead to a very low pressure drop which is advantageous especially for low-pressure applications. Other model calculations (not shown here) lead us to the conclusion that in a serpentine geometry the *z*-axis concentration profile is almost equilibrated by the serpentine U-turns. In consequence, in a serpentine flow field only few restrictions exist for the depth of the channel, such that other issues become important for the selection of channel depth. These are manufacturability, condensate removal capabilities and also the thickness of the repeating unit ('cell thickness') which is strongly influenced by channel depths. The minimum useful channel depth should also be discussed. The effects relevant for this topic are pressure difference, condensate removal, effects of dimensioning tolerances, and the risk of GDL-sinking into the channel, leading to irreproducible gas flow distribution, excessive pressure differences, and in consequence a performance deviation between single

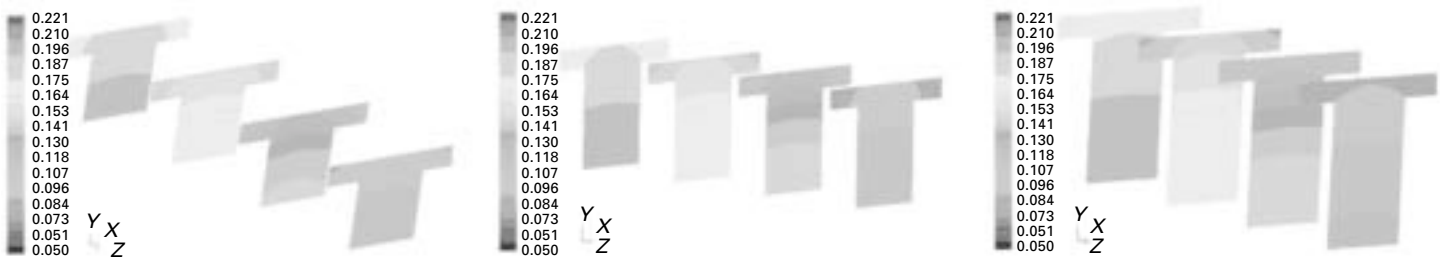

4.30 Oxygen concentration profile (50% utilization) at a single channel/rib system at a current density of 0.4 A/cm^2 (1 mm rib width, 1, 1.5 and 2 mm channel depth).

cells and strong overall performance losses. As a rule of thumb, the channel depth should not be less than 0.4 mm or less than two-thirds of the channel width.

4.16.4 Influence of channel width and depth on condensate removal behavior

Investigations on condensate removal are known for bigger channel dimensions usually used for fuel cell applications[290]. Moreover, there are studies on condensate removal using neutron spectroscopy[291,292].

Experimental data[293] from single channel experiments with channel cross-section areas from 0.25 to 1 mm^2 show that the removal of channel filling droplets (which can be considered as a minimum criterion for a proper condensate removal of a flow field) can be described by a minimum pressure difference per channel length, if the plate material is considered to be fixed. According to those measurements, the pressure drop should exceed 23 mbar/m channel length for all desired operating points. The exact value depends on the bipolar plate material selected and the flow field manufacturing process applied. A flow field which fulfills or exceeds this individual pressure difference criterion should be able to remove condensate independent from the individual channel geometry.

4.16.5 Summary of design criteria

Summarizing the design criteria developed in this section the rib width should be in the range of 0.5 to 1 mm. Significantly higher values should be used only for low current density applications. The appropriate channel width should be in the range of 0.4–0.6 mm (0.5 mm rib width) resp. 0.7 to 1.2 mm (1 mm rib width). The channel depth as well as the parallelization degree should be selected such that the pressure difference criterion of 20–30 mbar/m channel length (dependent on bipolar plate material) could be fulfilled.

4.17 System layout

Operation of fuel cells requires the timely supply of reactants, e.g. hydrogen and oxygen, as well as the removal of the product water as well as the heat generated. Furthermore, the fuel cell itself is generating unregulated DC. The electric energy thus needs to be converted into a form which is compatible with the application intended. In the case of PEMFC, water management imposes an additional task to system engineering. Figure 4.31 shows the general components of a fuel cell system. The integration of fuel cells into an application thus constitutes a system challenge. Since issues related to the

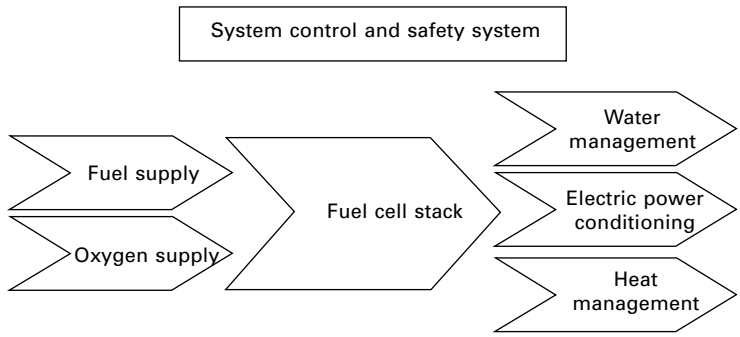

4.31 General components of a fuel cell system.

fuel cell stack have been discussed in detail above, the following section is concentrated on the so-called 'balance of plant'.

4.18 Reactant supply

The generation of electric current in a fuel cell is governed by Faraday's law, demanding that the electric current is proportional to the reactant flow:

$$I = zF\frac{\dot{m}}{M}$$

where I = electric current
z = number of exchanged electrons
F = Faraday constant (96 485.3 C/mole^{-1})
$\dot{m}$ = mass flow of reactant
M = molecular weight

In a fuel cell operating on hydrogen and oxygen, Faraday's law is demanding a mass flow of 622 μg/min H_2 (310.9 μmole/min) and 4.973 mg/min O_2 (155.4 μmole/min), when running an electric current of 1 A. For all practical purposes, it can be implied that the fuel cell is operated in a current driven mode. If the reactant supply system fails to supply a sufficient flow of hydrogen to the anode and oxygen to the cathode, side reactions involving water or functional and structural materials of the fuel cell electrodes are likely to occur.

In the case of cathode starvation, it is likely that instead of oxygen reduction, hydrogen evolution from water present at the cathode will take place. Since the hydrogen redox reactions are taking place with high exchange current density, the potential of the cathode will drop slightly below the potential of the reversible hydrogen electrode:

Normal reaction: $^1/_2\ O_2 + H_2O + 2e^- \rightarrow 2OH^-$

Side reaction: $2H_2O + 2e^- \rightarrow H_2 + 2OH^-$

In the case of anode starvation, an anodic side reaction is required. Owing to the low exchange current density of the oxygen redox reactions even in the presence of a noble metal catalyst, other side reactions (e.g. Pt dissolution or carbon corrosion) will take place in parallel to oxygen evolution. The potential of the anode will therefore rise significantly.

Normal reaction: $H_2 \rightarrow 2H^+ + 2e^-$

Side reactions: $H_2O \rightarrow {}^1/_2O_2 + 2H^+ + 2e^-$

$Pt \rightarrow Pt^{2+} + 2e^-$

$C + H_2O \rightarrow CO + 2H^+ + 2e^-$

Although cathode starvation will lead to the evolution of hydrogen, and the low potential of the oxygen-consuming electrode to increased peroxide formation, it is to be expected that the side reactions occurring upon fuel starvation will lead to more severe damage to the electrode in a short time. The consequences of fuel and oxygen starvation must be considered when designing flow fields, system layout and the system control strategy.

4.18.1 Anode reactant supply (hydrogen)

Systems using pure hydrogen

The most simple way of supplying hydrogen to a fuel cell system is from a hydrogen storage device such as a pipeline, a pressurized gas cylinder, a metal hydride vessel or, in the case of larger systems, a liquid hydrogen storage tank. Figure 4.32 shows a fairly simple hydrogen supply configuration for a PEMFC system for operation in dead end mode. Hydrogen is taken from a compressed gas storage cylinder having a pressure reducer to set the fuel cell anode operating pressure. The anode exhaust is closed by a purge valve which is opened during fuel cell start-up. The valve remains closed during fuel cell operation. If inert gas originating from the fuel supply or crossing from the cathode side is accumulating inside the anode compartment,

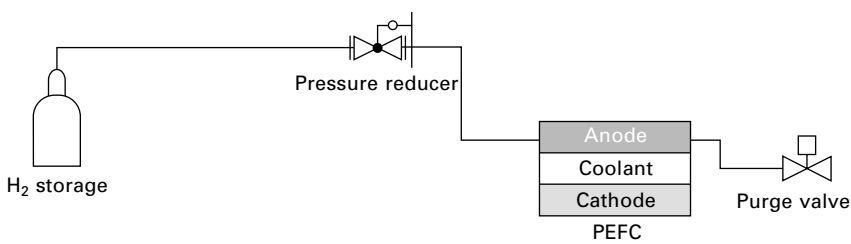

4.32 Hydrogen supply subsystem of a PEFC system operated in dead end mode.

the purge valve is opened for a short time in order to release these impurities. The purge valve normally is operated as a controlled valve. Regular purging not only removes inert gases from the anode compartment, but also prevents water droplets getting stuck in the anode compartment, eventually causing local fuel starvation.

Although the simple hydrogen supply system layout as shown in Fig. 4.32 is operational in a laboratory environment, normally additional valves are used in order to enhance the safety of system operation. This is normally achieved by inclusion of a shut-off valve upstream of the pressure reducer and a pressure relief valve (safety valve) which will prevent hazardous pressure build-up in case of failure of the pressure reducer (Fig. 4.33). The shut-off valve can be operated manually or as a controlled valve. Additional safety features may include a thermally activated fuse between the storage cylinder and shut-off valve, filters, flow restrictors as well as a flame arrestor.

The performance of fuel cell stacks operated under dead end conditions is likely to cause local fuel starvation. Therefore, frequent purging or the operation of the fuel cell system at less than 100% gas utilization is required. Figure 4.34 shows the dependence of the average cell voltage of a 5-cell short stack as a function of gas utilization. It is evident that the cathode is more sensitive to variations in gas utilization than the anode. When looking at the sensitivity of the anode with respect to variations in gas utilization one easily recognizes a significant drop of the average cell voltage at a hydrogen gas utilization above 70% at a current density of $0.1\,A/cm^2$. Additionally, the error bars associated with each point are increasing, thus indicating unstable operating conditions. At $0.5\,A/cm^2$ the range of stable stack operation is extended to 90% hydrogen gas utilization. After that one observes a significant drop in average cell voltage as well. Similar effects can be seen when regarding the cathode utilization curves. This behavior can be explained by local fuel/oxygen starvation effects caused by the formation of water droplets in the gas distribution channels at high utilization.

In order to avoid anode starvation effects at high overall hydrogen gas utilization, fuel leaving the anode compartment at a utilization of 70% is

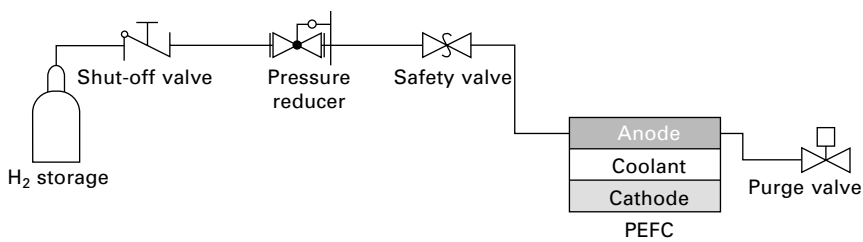

4.33 Hydrogen supply subsystem including a shut-off valve and a pressure relief valve.

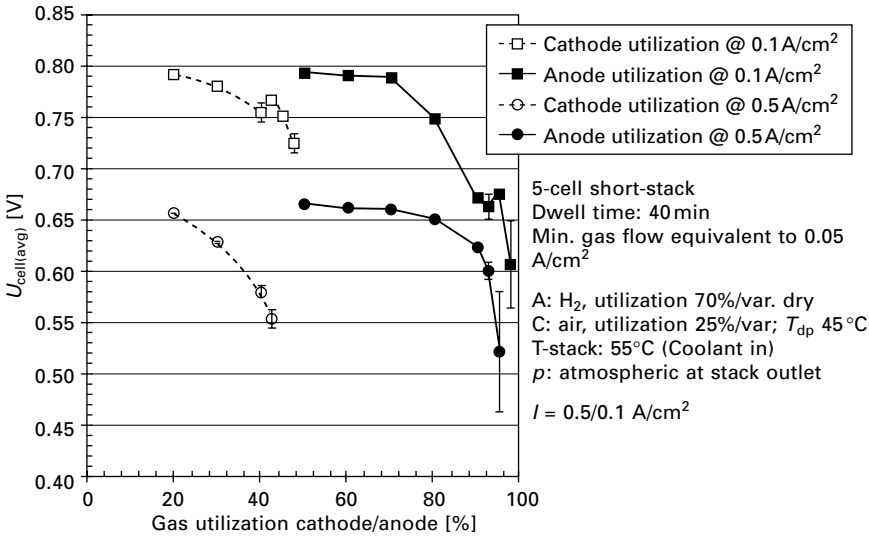

4.34 Dependence of average cell voltage on gas utilization at anode and cathode side.

recirculated to the anode inlet. Recirculation can be done either by a mechanical pump or by the use of ejectors (jet pump). In order to remove liquid water droplets which may be formed in the anode compartment, the implementation of a water knock-out vessel might be required before feeding recirculated hydrogen back to the fuel cell. Furthermore, for some applications, it might even be advisable to humidify the hydrogen slightly before feeding it to the anode. Figure 4.35 shows the hydrogen supply part for a PEFC system, including fuel recirculation.

Despite the fact that hydrogen is used in large quantities for industrial processes such as petroleum refining, ammonia synthesis as well as a process gas in, for example powder metallurgy, or in the semiconductor industry, currently there is no retail infrastructure for hydrogen available. It is expected that a hydrogen fuelling infrastructure will be established in parallel to the market introduction of fuel cell powered vehicles.

System using a fuel processor for on-site hydrogen generation

In order to establish fuel cell technology in applications such as combined heat and power (CHP) generation, hydrogen needs to be produced on site starting from hydrocarbon fuels such as natural gas, liquid petroleum gas, or liquid petroleum fractions. Alcohols such as methanol or ethanol can also be used for on-site production of hydrogen.

Fuel processing may be defined as the conversion of a raw fuel to a hydrogen-containing gas being compatible with the requirements of a PEMFC.

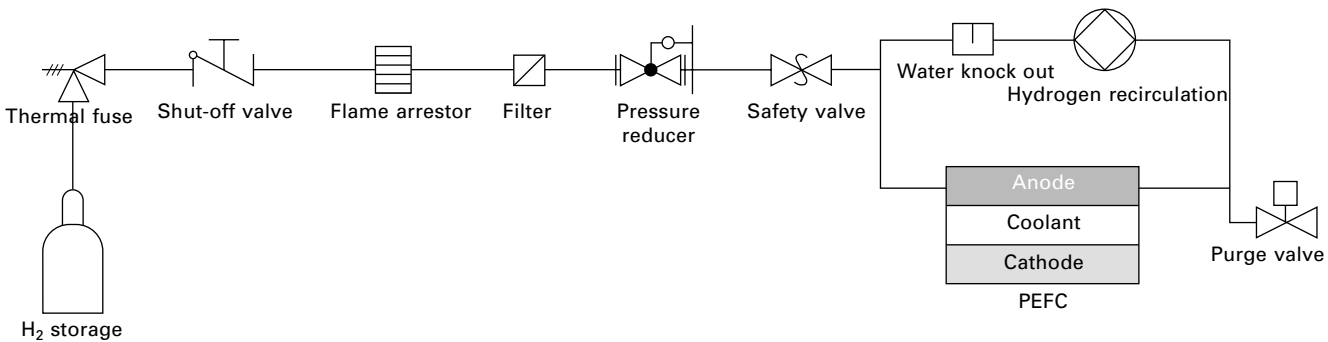

4.35 Hydrogen supply subsystem including a hydrogen recirculation pump.

Since it is well known that PEMFC stacks are sensitive to fuel contaminants such as CO, sulfur-containing compounds, ammonia, unsaturated hydrocarbons, etc., a fuel processor typically is built up of different reaction stages.

The fuel initially is converted to a hydrogen-containing synthesis gas by a reforming stage. For reasons of simplicity, the following discussion is limited to methane processing. Processing of higher hydrocarbons or alcohols can be treated in an analogous way. The basic reactions of methane reforming are the following:

$$\text{Reforming: } CH_4 + H_2O \rightarrow CO + 3H_2 \quad \Delta H = +206\,\text{kJ/mole}$$

$$\text{Water gas shift: } CO + H_2O \rightarrow CO_2 + H_2 \quad \Delta H = -41\,\text{kJ/mole}$$

The yield of both reactions is dependent on the temperature and the so-called steam to carbon ratio (S/C). Temperatures above 700 °C are necessary to completely decompose methane in the reforming step, as seen in Fig. 4.36. Processing of higher hydrocarbons as well as higher alcohols will result in the formation of methane as an intermediate. Furthermore, the formation of soot has to be taken into account as a side reaction, particularly at low S/C or when processing higher hydrocarbons or ethanol. The following reactions are involved:

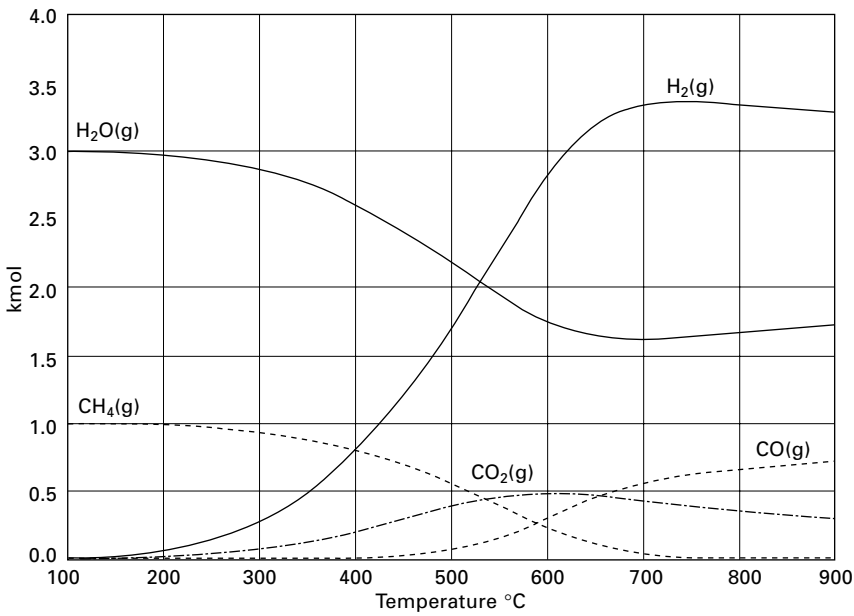

4.36 Equilibrium composition of methane steam reforming reaction at a steam to carbon ratio of 3.

Boudouard reaction: $2CO \rightarrow C + CO_2$ $\Delta H = -172\,kJ/mole$

Methane cracking: $CH_4 \rightarrow C + 2H_2$ $\Delta H = +75\,kJ/mole$

Figure 4.37 shows the equilibrium composition of the CO shift reaction at S/C = 2. It is evident that low temperatures are preferred to achieve a high yield of H_2. Considering the kinetic aspects of the water gas shift reaction, temperatures above 200 °C are common to achieve a sufficiently high reaction velocity. Frequently, the water gas shift reaction is carried out in a two-stage reactor operating at approximately 450 and 230 °C respectively.

Looking at the gas composition at the exit of the shift reactor, CO concentrations of 0.3% to 0.6% are common. In order to feed the gas to a PEMFC, the CO content must be reduced below 20 ppm. In larger fuel processors, gas cleaning is done by pressure swing adsorption simultaneously removing CO_2 and CO. In small gas processors as they are common in residential combined heat and power generators (CHP), CO fine-cleaning is achieved by either selective oxidation, by selective methanization or by diffusion of hydrogen through a thin palladium membrane.

Methane reforming is catalyzed by catalysts containing nickel or noble metals. The water gas shift reaction at temperatures above 400 °C is catalyzed by an iron and chromium-containing catalyst. Water gas shift at temperatures below 270 °C is catalyzed by a catalyst containing copper and zinc oxide.

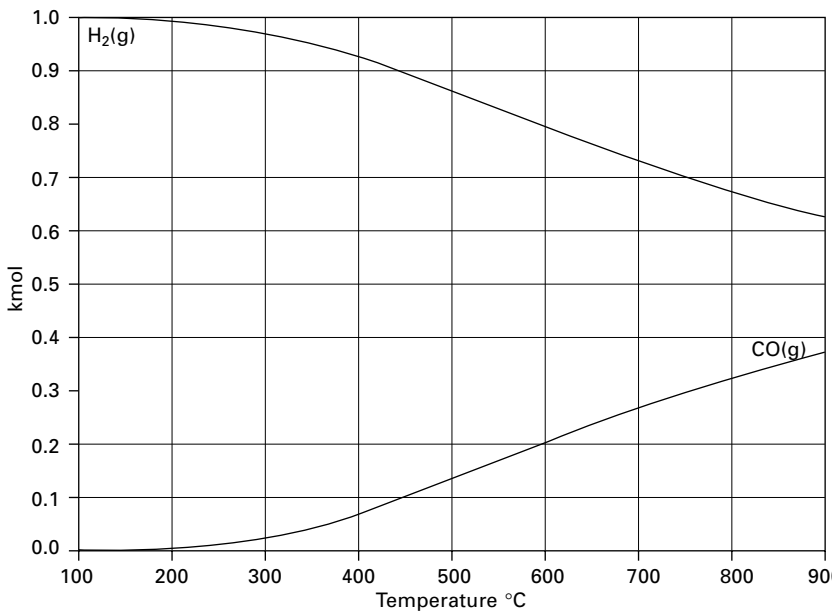

4.37 Equilibrium composition of the CO-shift reaction at a steam to carbon ratio of 2.

Both shift catalysts are sensitive to poisoning by sulfur-containing species. Therefore, hydrocarbon fuels must be desulfurized before gas processing.

Reforming, the key step of fuel processing, is a strongly endothermal reaction. The heat needed for decomposition of methane can be fed from outside the reactor. This process is called 'allothermal reforming' or 'steam reforming'. Steam reforming of methane is a mature and quite well-established technology in the chemical industry where large-scale reformers are operating under continuous load operation. The steam reforming process leads to reformate containing a rather high concentration of hydrogen. However, it requires the transfer of large amounts of high temperature heat into the reformer.

A way to avoid the transfer of heat from a burner into the reactor is provided by the so-called autothermal reforming process, where fuel, steam and a limited amount of air are fed simultaneously into the reformer. The highly exothermal reaction of fuel combustion in this case provides the heat for reforming. Autothermal reformers thus can react to load changes faster than allothermal steam reformers. In case hydrogen is not separated by either membrane diffusion or pressure swing adsorption, the nitrogen content of air leads to a rather low hydrogen concentration in the autothermal reformate fed to the fuel cell.

As already mentioned in the case of fuel cell systems operating on neat hydrogen, the hydrogen generated in the fuel processor is not completely used inside the fuel cell stack. Therefore, the anode exhaust normally is burned. The heat can be used for fuel processing. Figure 4.38 shows a simplified system layout for a fuel cell system including a fuel processor.

It is evident that such a fuel processor as shown in Fig. 4.39 is complicated and expensive. A variety of different reforming reactor concepts and process diagrams have been presented in the literature in order to improve efficiency, enhance the safety and reduce the cost of fuel processing. Figure 4.39 shows an improved gas processor design. In this case, the steam reformer is operated at reduced temperature thus yielding a lower CO content. The temperature of the shift converter is set slightly above the LT shift shown in Fig. 4.39. Subsequently CO fine purification is carried out by selective methanization at approximately the same temperature. This fuel processor design avoids two heat exchangers and one reactor. Furthermore, no air feed to the selective oxidation is required which is improving the overall system safety.

The lower reforming temperature automatically generates an increased methane slip through the reformer. Since methane can be considered as inert at the operating temperature of the PEMFC, it will increase the heating value of the anode off gas. If the anode off gas is fed to the reformer burner, an increased hydrogen utilization in the PEMFC is required compared with the process shown in Fig. 4.39 in order to prevent overheating of the reformer.

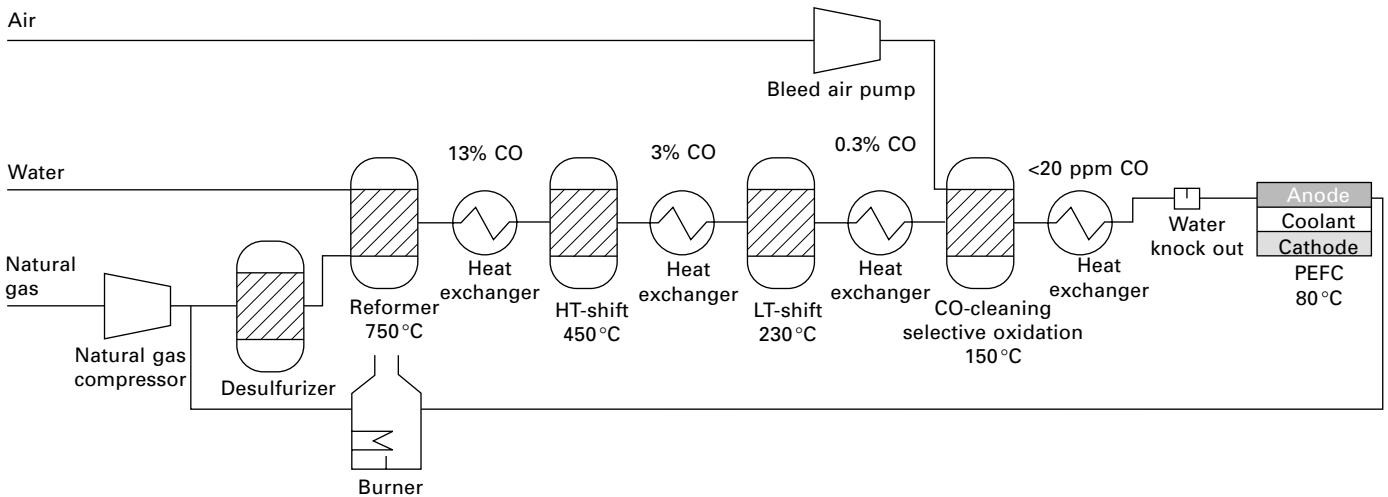

4.38 Simplified system layout for a fuel cell system including a natural gas processor using the steam reforming process.

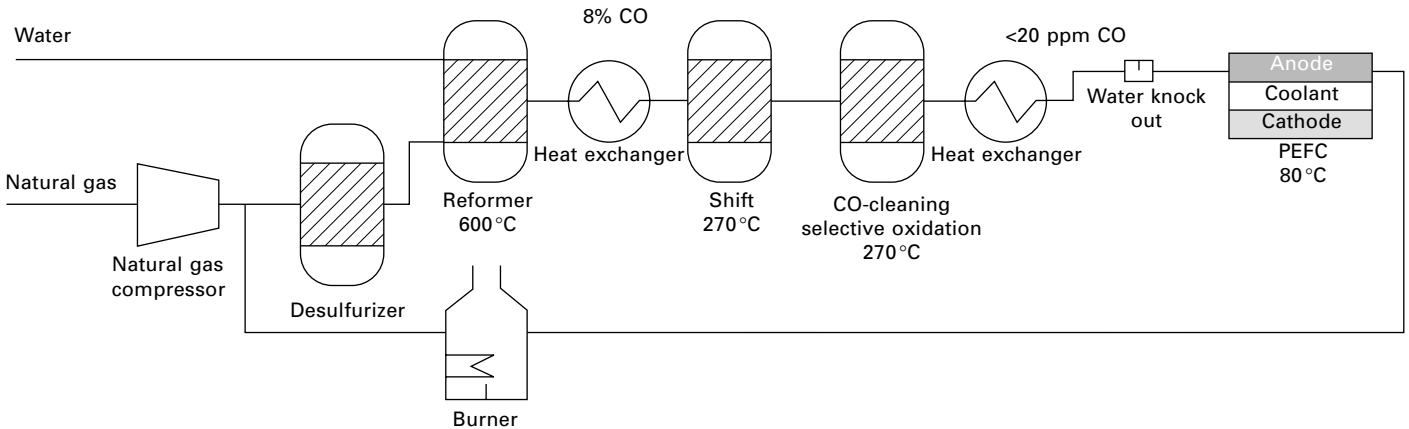

4.39 Simplified system layout for a fuel cell system including an improved gas processor.

4.18.2 Cathode reactant supply (oxygen)

The following discussion is dealing with the requirements of fuel cell systems having an active air supply by a blower or a compressor since only very low-power fuel cell systems are capable of being operated in the so-called self-breezing mode. The cathode operation conditions have significant influence on the water and thermal management thus determining the overall system efficiency. In the most simple case as shown in Fig. 4.40, an active air supply subsystem consists of an air intake filter to remove particles and possibly impurities poisoning the cathode catalysts, a compressor or blower and an air humidifier, which can also include the function of an air cooler.

Air humidification plays an important role in stack efficiency and durability. In order to minimize electrolyte resistance in the fuel cell, operation under conditions close to 100% relative humidity at the MEA inside the cathode compartment are desired. Therefore, incoming air normally must be conditioned with respect to temperature and humidity before entering the fuel cell stack. However, when 100% relative humidity is exceeded in the gas distribution channels and the GDL, formation of liquid water and possibly clogging of gas transport paths are likely to occur.

Similar to the situation on the anode side, the fuel cell will not be operated at full gas utilization. In fact, owing to the comparatively slow kinetics of oxygen reduction, the oxygen utilization at the cathode in most cases will be less than 60%. Although small PEMFC systems are typically operated close to atmospheric pressure, larger systems are sometimes operated at elevated pressure. Variation of the system operating pressure influences the stack voltage via a 'Nernstian voltage boost' proportional to the logarithm of the pressure ratio:

$$\Delta E \sim \ln\left[\frac{p}{p_0}\right]$$

This voltage boost directly can be translated into a power gain. A voltage increase of approximately 14 mV per cell can be expected when doubling the operating pressure at the anode and the cathode side. However, air compression also leads to losses due to limited compressor efficiency and thermodynamic work to be expended when compressing air.

Pressure variation also influences the water management significantly. The following considerations assume that dry air is fed to the fuel cell. Water saturation at the cathode outlet is achieved only by water produced inside the fuel cell. Figure 4.41 shows the amount of water contained per kg of air at saturation (100% relative humidity). It is evident that the amount of water contained in saturated air decreases with increasing pressure. Therefore, less water is transported out of the fuel cell cathode at the same air mass flow.

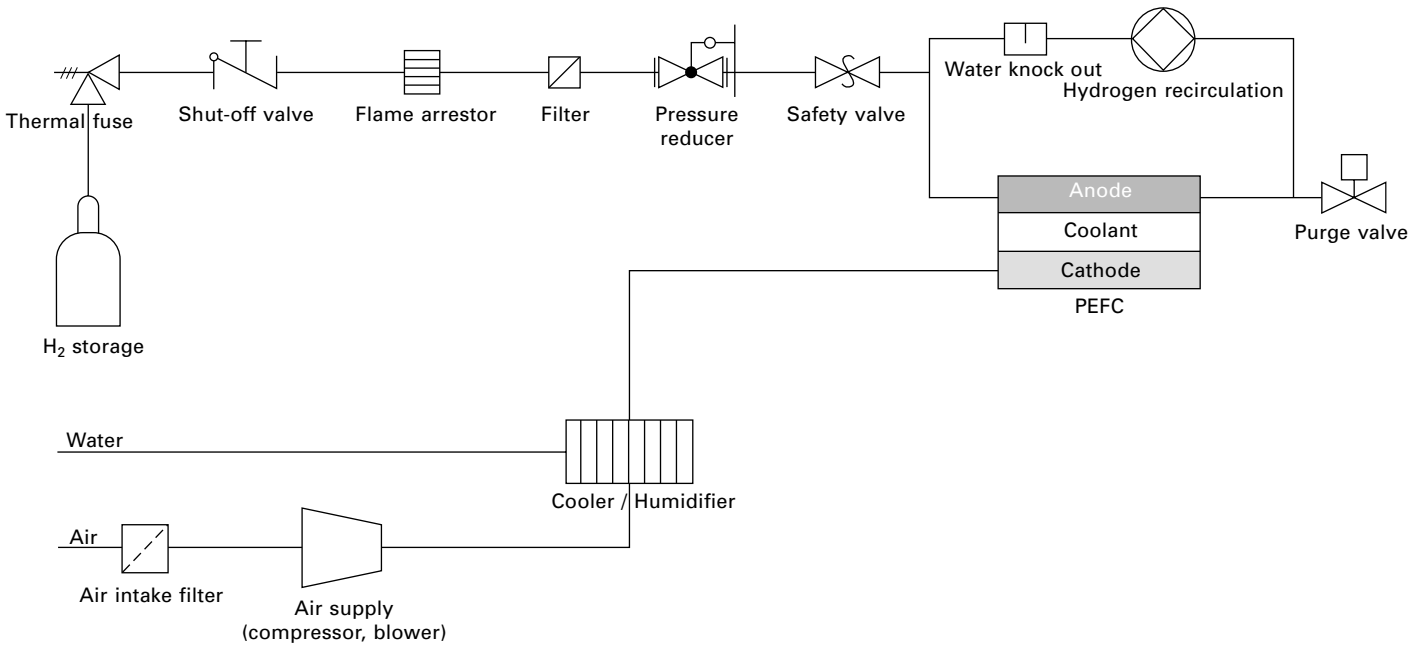

4.40 System layout of a hydrogen powered PEMFC system as shown in Fig. 4.36 completed by a simple air supply subsystem.

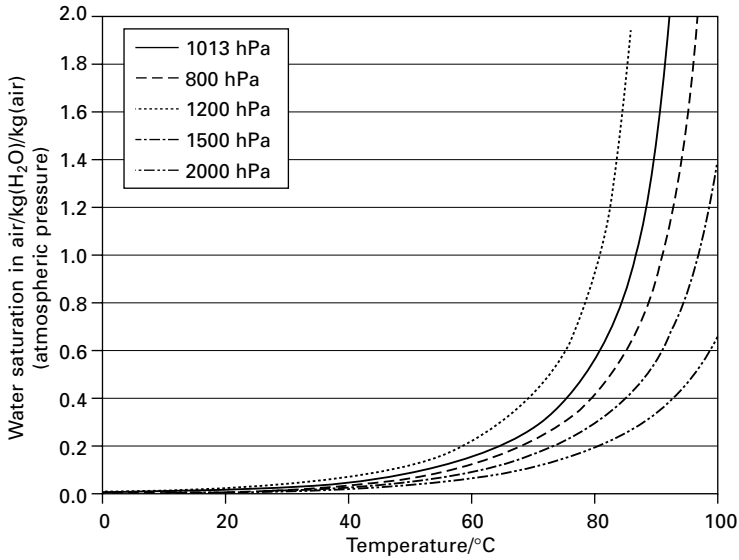

4.41 Water saturation of air as a function of temperature and pressure.

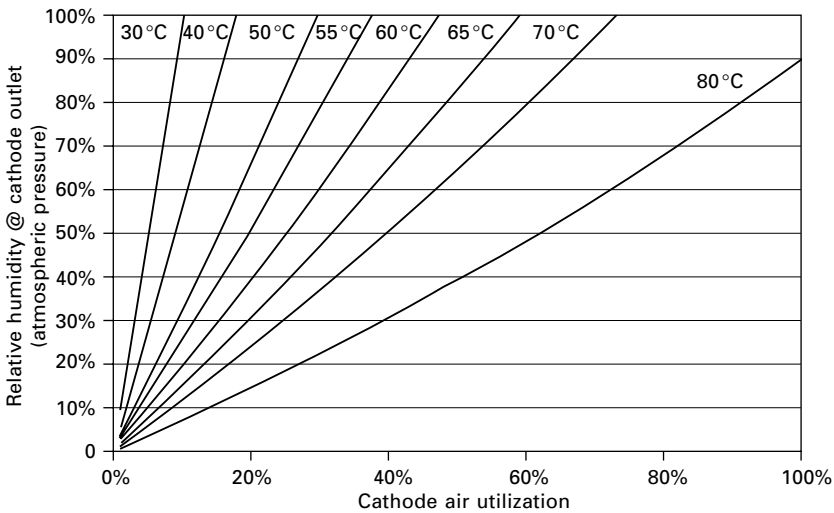

4.42 Relative humidity at the cathode outlet as a function of cathode air utilization and temperature.

Figure 4.42 shows the relative humidity at the cathode outlet as a function of temperature and air utilization at atmospheric pressure. As soon as the relative humidity reaches 100%, condensation of water inside the gas distribution channels and the gas diffusion layer will occur as a consequence,

clogging of the air distribution channels and unstable fuel cell operation might happen depending on the pressure drop across the cathode. It is evident that at temperatures above 65 °C 100% water saturation of the exhaust air is reached above 50% cathode utilization. Eventually, the electrolyte membrane will dry out if the capacity for water removal of the cathode air exceeds the amount of water generated inside the fuel cell.

Figure 4.43 shows the cathode utilization required to achieve 100% water saturation of the cathode exhaust air from the product as a function of temperature and pressure. It is evident that for operation at elevated pressure it is essential to retain water in the membrane electrolyte when operating the fuel cell at reasonable gas utilization at elevated temperature. In order to avoid large gradients in membrane humidity and conductivity, air is humidified before entering the cathode compartment (Fig. 4.44). Normally, the water used for humidifying the incoming air is recovered from the cathode exhaust, e.g. via a membrane humidifier.

For small systems, partial recirculation of the moist cathode exhaust air to the cathode inlet can be used for humidification. In such a configuration air is circulated at high flow rate through the cathode compartment (Fig. 4.45). Sufficient oxygen supply and water removal is achieved by opening the cathode exhaust valve depending on the relative humidity in the cathode loop.

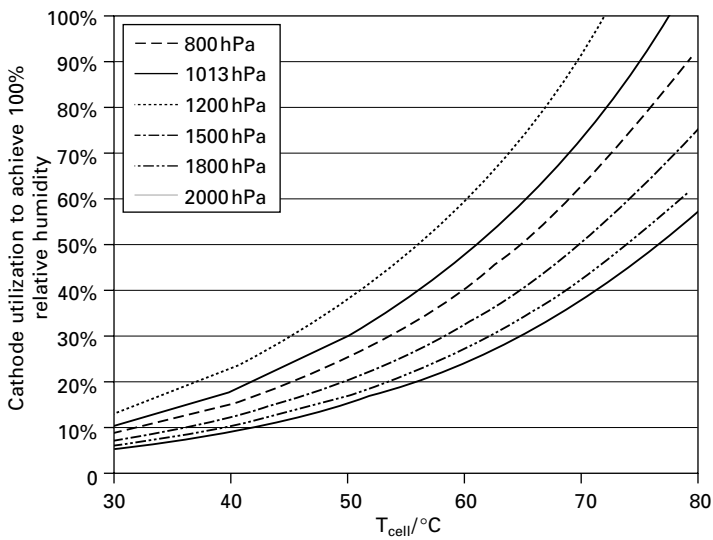

4.43 Cathode utilization to achieve 100% relative humidity as a function of temperature and pressure.

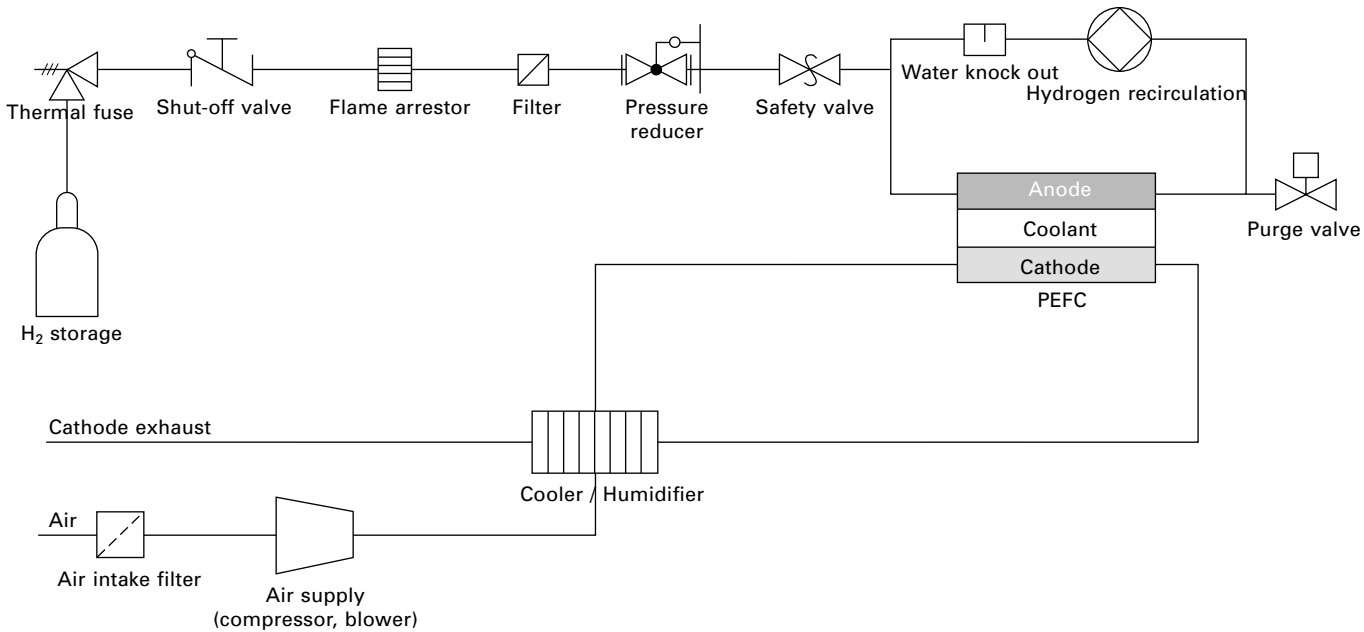

4.44 System layout of a hydrogen-powered PEMFC system including cathode humidification from the cathode exhaust.

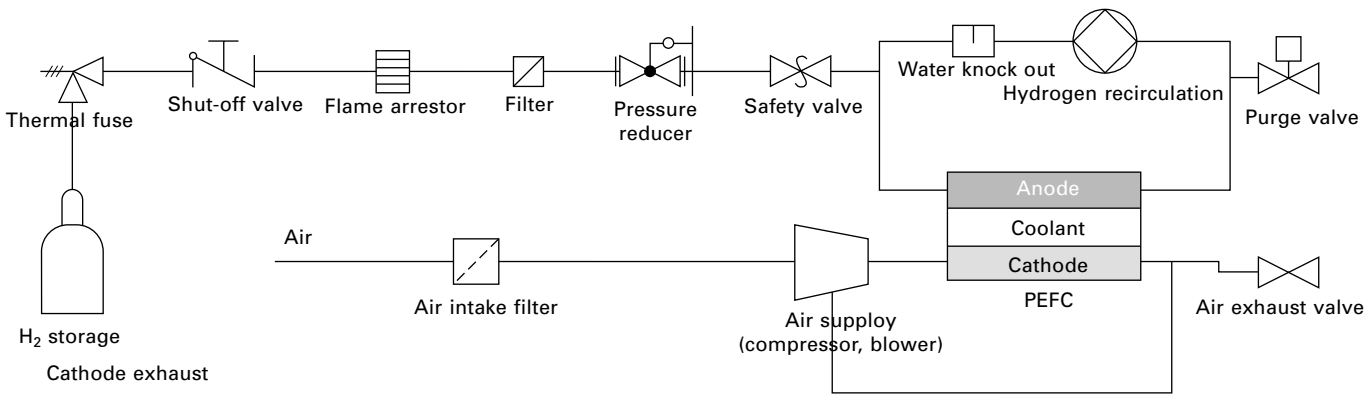

4.45 System layout using cathode air recirculation for humidity control.

4.19 Thermal management

The efficiency of a fuel cell primarily is determined by the thermodynamics of electrochemical hydrogen combustion. Only Gibbs free enthalpy can be converted into electricity. As shown in Fig. 4.46, additional losses in the fuel cell stack are encountered mainly by limitations in the electrochemical kinetics of oxygen reduction, ohmic resistances in the electrolyte membrane and the current collectors as well as mass transport losses in the electrodes. All these losses cause the operating voltage of the fuel cell to deviate from the theoretical cell voltage. In case of a PEMFC operated on hydrogen-containing fuel, losses caused by crossover of hydrogen and oxygen through the membrane can be neglected. Eventually, all losses in the fuel cell are released as heat. Figure 4.46 shows the amount of heat released per kW h of electricity generated as a function of cell voltage.

When operating the fuel cell at high power, active cooling of the fuel cell stack is inevitable. Low-power PEMFC systems are frequently air cooled in order to minimize the amount of auxiliary equipment. However, high-power systems normally are liquid cooled. Figure 4.47 shows a simplified system layout including a liquid cooling system. Since the liquid coolant is in direct contact with the electrically active parts inside the fuel cell stack, it must be highly isolating in order to avoid shunt currents and corrosion effects. If water-based coolants are used, an ion exchange cartridge is normally integrated in the coolant loop to minimize coolant conductivity.

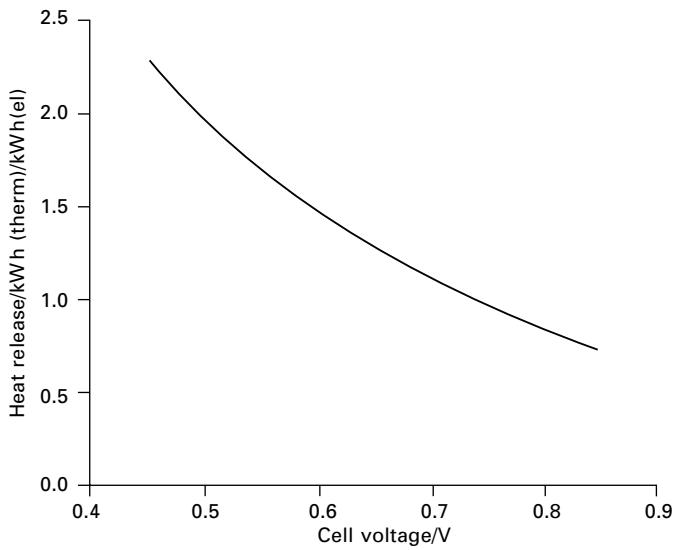

4.46 Heat release from a fuel cell as a function of operating voltage.

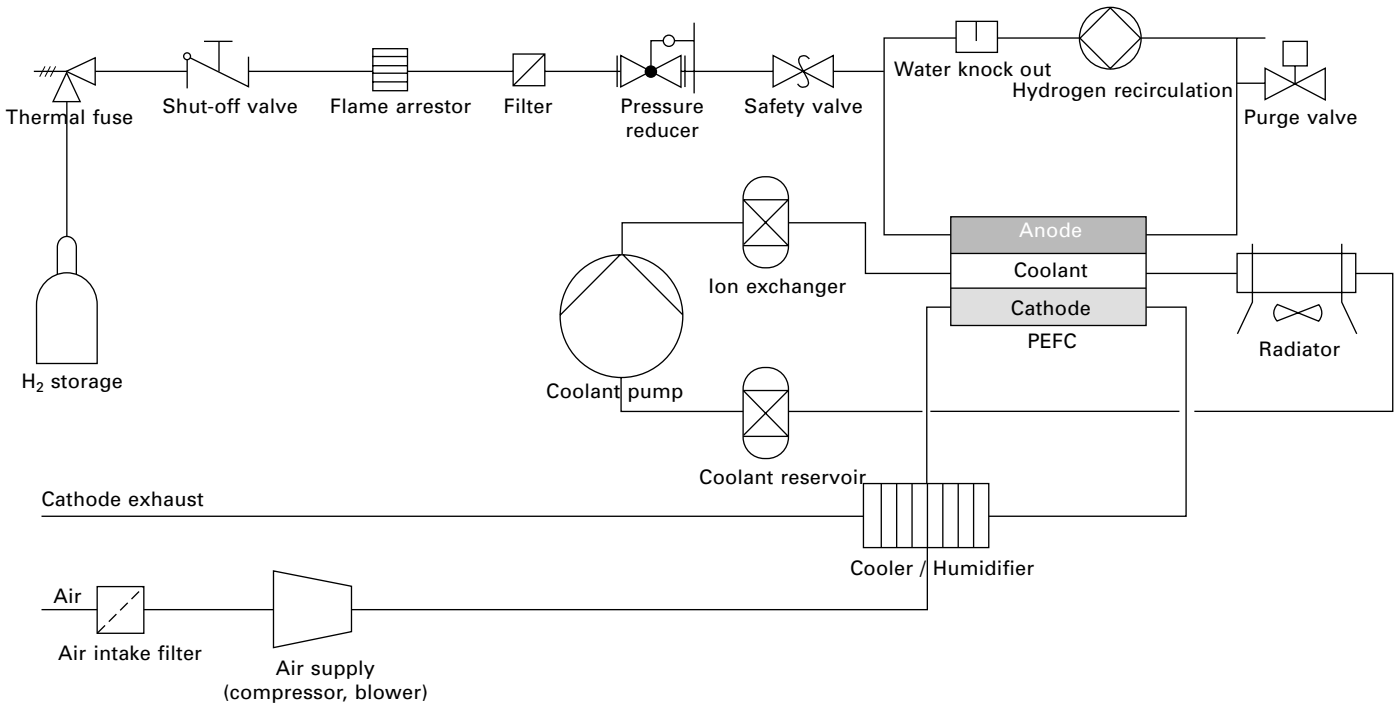

4.47 Simplified PEMFC system layout including liquid coolant loop.

4.20 Electric power conditioning

Since PEMFC stacks have a rather large difference between open circuit and operating voltage, a power conditioning unit is frequently used. This can be a DC/AC converter to feed the electric power generated in the fuel cell to the AC grid. For stand-alone systems, batteries or super capacitors are frequently used as a buffer for power surges as well as to provide power during the system start-up and shut-down phases.

4.21 System control

As shown in the previous sections, PEMFC systems require a significant amount of auxiliary equipment for operation. It can be seen from the discussions above that careful control of reactant flow as well as heat removal are required for stable system operation. Furthermore, monitoring of temperature, humidity and single cell voltage are beneficial to avoid unfavorable operating conditions causing fast degradation of system performance. Frequently programmable logic controllers or dedicated microcontrollers are used in PEMFC systems.

Since hydrogen is considered as a hazardous substance, system monitoring is also required in order to ensure safe operation of the system under regular conditions. Fast system shut-down is necessary in case of irregular operation conditions or possible safety concerns. An independent safety interlock system is frequently set up.

4.22 Conclusions

Successful operation of PEMFC is a system challenge. The components and operating conditions of the system must be adapted to the requirements of the application. Integration of a PEMFC system involves a plenitude of auxiliary equipment. A system controller must take care to maintain the optimum operating conditions with respect to power and endurance. An example of a PEMFC system in a brass board set-up is shown in Fig. 4.48. This system uses cathode recirculation for humidity control including thermal management, electric power conditioning. The system can supply unregulated and regulated DC as well as AC. Careful selection of the system components and the operating conditions ensure high electric efficiency by minimization of the auxiliary power demand.

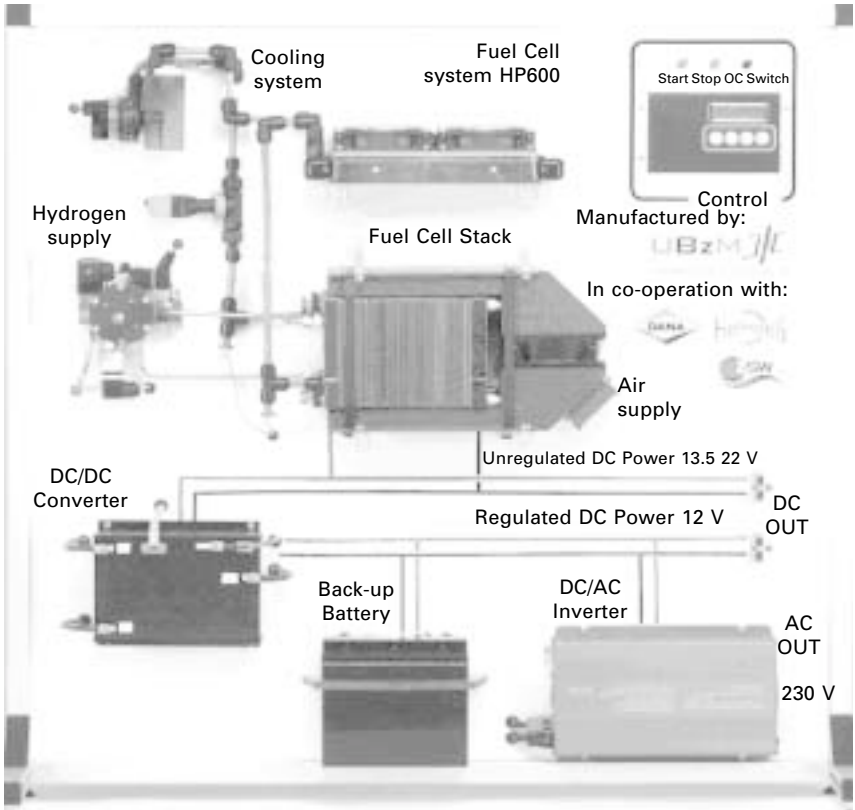

4.48 Hydrogen fuelled 600 W PEMFC system for education purposes.

4.23 References

1. A. Hammett in: W. Vielstich, A. Lamm, H. Gasteiger (Eds.), *Handbok of Fuel Cells–Fundamentals, Technology and Applications*, Chapter 6, Vol. 1, Wiley, Chichester, 2003.
2. H.A. Gasteiger, S.S. Kocha, B. Sompalli, F.T. Wagner, *Appl. Cat. B: Environmental* **56** (2005) 9.
3. T.R. Ralph, M.P. Hogarth, *Plat. Met. Rev*. **46** (2002) 3.
4. W.F. Grot, DuPont de Nemours, US Patent No. 3,718,627, 1973.
5. W.F. Grot, S.A. Grot, Ion Power, US Patent No. 6,733,914, 2004.
6. W.F. Grot, G. Rajendran, DuPont de Nemours, US Patent No. 5,919,583, 1999.
7. G.H. Harper, G.R. Norman, US Patent No. 3,041,317, 1962.
8. W.G. Grot, *Macromol. Symposia* **82** (1994) 161–172.
9. M.R. Tant, K.P. Darst, K.D. Lee, C.W. Martin, *ACS Symp. Ser.* **395** (1989) 370.
10. M. Rikukawa, K. Sanui, *Prog. Polym. Sci*. **25** (2000)1463.
11. S.J. Hamrock, N. Jing, H. Shane, L.C. Hardy, 3M Innovative Properties Company, US Patent 6,833,412, 2004.
12. K.H. Lochhaas, K. Hintzer, S.J. Hamrock, M.A. Yandrasits, 3M Innovative Properties Company, US Patent 7,214,740, 2007.

13. J.A. Elliott, S. Hanna, A. M. S. Elliott, G. E. Cooley, *Macromolecules* **33** *(*2000) 4161-4171.
14. T.D. Gierke, G.E. Munn, F.C. Wilson, *ACS Symp. Ser*. **180** (1982) 195–216.
15. K.D. Kreuer, *J. Memb. Sci*. **185** (2001) 29–39.
16. S.C. Yeo, A. Eisenberg, *J. Appl. Polym. Sci.* **21** (1977) 875.
17. K.T. Adjemian, S. Srinivasan, J. Benziger and A.B. Bocarsly, *J. Power Sources* (2002) 356–364.
18. X. Ren, T.E. Springer, S. Gottesfeld, *J. Electrochem. Soc*. **147** (2000) 92.
19. V.M. Barragán , C. Ruiz-Bauzá , J.P.G. Villaluenga, B. Seoane, *J. Power Sources* **130** (2004) 22–29.
20. B. Bahar, A.R. Hobson, J.A. Kolde, D. Zuckerbrod, Gore&Associates, US Patent No. 5,547,551, 1996.
21. B. Bahar, A.R. Hobson, J.A. Kolde, Gore & Associates, US Patent 5,599,614, 1997.
22. A.R. Hobson, S.J. Mackenzie, Gore Enterprise Holdings Inc. (US), US Patent 6,613, 2003.
23. B. Bahar, C. Cavalca, S. Cleghorn, J. Kolde, D. Lane, M. Murthy, G.J. Rusch, *New Mater. Electrochem. Syst*. **2** (1999) 179.
24. http://www.gore.com/MungoBlobs/primea_56_mea_datasheet.pdf
25. C. Stone, A.E. Steck, W. Jinzhu, *Ballard* Power Systems, US Patent 5,773,480, 1998.
26. M. Prober, *J. Am. Chem. Soc*. **75** (1952) 968.
27. M. Prober, General Electric, US Patent 2,651,627, 1953.
28. R.B. Jr. Hodgdon, J.F. Enos, E. Aiken, General Electric, US Patent 3,442,825, General Electric, 1969.
29. R.B. Hodgdon, *J. Polymer Sci*. **6**, 171 (1968).
30. R.B. Jr. Hodgdon, J.F. Enos, E. Aiken, General Electric, US Patent 3,423,278, 1969.
31. (a) A.E. Steck, *Proceedings of the First International Symposium of New Materials for Fuel Cell Systems*; Ecole Polytechnique de Montreal: Montreal, 1995; p. 74. (b) A.E. Steck, C. Stone, *Chem. Rev*. **104** (2004) 4609, *Proceedings of the second International Symposium on New Materials for Fuel Cell and Modern Battery Systems*; l'Ecole Polytechnique de Montreal: Montreal, 1997; p. 792.
32. K. Gupta *et al*., *Solid State Ionics* **61** (1993) 213.
33. F. Büchi *et al*., *Electrochimica Acta* **40** (1995) 345.
34. S.D. Flint, C.T. Slade, *Solid State Ionics* **97** (1997) 299.
35. D.I. Ostrovskii, L.M. Torell, M. Paronen, S. Hietala, F. Sundholm, *Solid State Ionics* **97** (1997) 315.
36. N. Walsby, Diss., University of Helsinki, Helsinki, Finland, 2001.
37. S. Holmberg, P. Holmlund, R. Nicolas, C.-E. Wilén, T. Kallio, G. Sundholm, F. Sundholm, *Macromolecules* **37** (2004) 9909–9915.
38. G. D'Alelio, General Electric, US Patent 2,366,007,1944.
39. R.A. Assink, C. Arnold Jr., R.P. Hollandsworth, *J. Membr. Sci*. **56** (1991) 143–151.
40. G. Hübner, E. Roduner, *J. Mater. Chem*. **9** (1999) 409–418.
41. J.M. Serpico, S.G. Ehrenberg, J.J. Fontanella, X. Jiao, D. Perahia, K.A. McGrady, E.H. Sanders, G.E. Kellogg, G.E. Wnek, *Macromolecules* **35** (2002) 5916.
42. H. Tang, P.N. Pintauro, Q. Guo, S. O'Connor, *J Appl. Polym. Sci*. **71** (1999) 387.
43. Q. Guo, P.N. Pintauro, H. Tang, S.J. O'Connor, *Memb. Sci*. **154** (1999) 175.
44. R. Wycisk, P.N. Pintauro, W. Wang, S. O'Connor, *J. Appl. Polym. Sci*. **59** (1996) 1607.
45. J.-B. Baek, F.W. Harris, *J. Polym. Sci. Part A: Polym. Chem*. **43** (2005) 6465–6479.

46. T.J. Matray, R.J. Twieg, J.L. Hedrick, *ACS Symp. Ser*. **624** (1996) 266–275.
47. R. Twieg, T. Matray, J.L. Hedrick, *Macromolecules* **29** (1996) 7335–7341
48. V.M. Svetlichnyi, V.V. Kudryavtsev, *Polym. Sci. – Ser. B* **45** (2003) 140–185.
49. N. Ogato, M. Rikukawa, WO 94/24717, 27 October 1994.
50. Morton Litt, Lecture, Symposium 'Advances in Materials for Proton Exchange Membrane Fuel Cell Systems', Asilomar, California, 20–23 February 2005**.**
51. A. Noshay, L.M. Robeson, *J. Appl. Polym. Sci*. **20** (1976) 1885–1903.
52. F. Wang, T. Chen, J. Xu, *Macromolecular Rapid Commun*. **19** (1998) 135.
53. J. Kerres, W. Cui, P. Reichle, *J. Polym. Sci.: Part A: Polym. Chem*. **34** (1996) 2421–2438.
54. F. Helmer-Metzmann, K. Ledjeff, R. Nolte, *et al*., Hoechst AG, EP 0 574 791 A2 Offen, 1993.
55. J. Rozière, D.J. Jones, *Annu. Rev. Mater. Res*. **33** (2003) 503–555.
56. H.H. Ulrich, G. Rafler, Angew. *Makromol. Chem*. **263** (1998) 71.
57. P. Xing, G.P. Robertson, M.D. Guiver, S.D. Mikhailenko, K. Wang, S. Kaliaguine, *J. Memb. Sci.* **229** (2004) 95.
58. J. Schauer, P. Lopour, J. Vacik, *J. Memb. Sci.* **29** (1992) 169.
59. S. Percec, G. Li, *Polymer Preprints (Am. Chem. Soc., Div. Polym. Chem.*) **27**(2) (1986) 19–20.
60. H.C. Lee, H.S. Hong, Y.-M. Kim, S.H. Choi, M.Z. Hong, H.S. Lee, K. Kim, *Electrochim. Acta* **49** (2004) 2315–2323.
61. J.A. Kerres, D. Xing, F. Schönberger, *J. Polym. Sci. Part B: Polym*. Phys. **44** (2006) 2311–2326.
62. K. Miyatake, H. Iyotani, K. Yamamoto, E. Tsuchida, *Macromolecules* **29** (1996) 6969.
63. K.B. Wiles, Diss., Virginia Polytechnic Institute and State University, Blacksburg, 2005.
64. Z. Bai, M.F. Durstock, T.D. Dang, *J. Memb. Sci*. **281** (2006), 508–516.
65. L. Shen, G. Xiao, D. Yan, G. Sun, *e-Polymers* **31** (2005).
66. M. Schuster, K.-D. Kreuer, H.T. Andersen, J. Maier, *Macromolecules* **40** (2007) 598–607.
67. S. Matsumura, N. Kihara, T. Takata, *Macromolecules* **34** (2001) 2848–2853.
68. S. Rikukawa, K. Sanui, *Prog. Polym. Sci*. **25** (2000), 1463.
69. S. Faure, M. Pineri, P. Aldebert, R. Mercier, B. Sillion, EP 897407 A1, 1999.
70. D. Gomes, J. Roeder, M.L. Ponce, S.P. Nunes, *J. Memb. Sci*. **295** (2007) 121–129.
71. Y.L. Chen, Y.Z. Meng, A.S. Hay, *Macromolecules* **38** (2005) 3564.
72. N.M. Belomoina, A.L. Rusanov, N.A. Yanul, Yu.E. Kirsh, *Vysokomol. Soedin., Ser. A Ser. B* **38** (2) (1996) 355–358.
73. M. Walker, K.-M. Baumgärtner, M. Kaiser, J. Kerres, A. Ullrich, E. Räuchle, *J. Appl. Polym. Sci*. **74** (1999) 67–73.
74. M. Hickner, Diss., Virginia Polytechnic Institute and State University, Blacksburg, 2003.
75. (a) F. Wang, M. Hickner, Y.S. Kim, T.A. Zawodzinski, J.E. McGrath, Membr. J. Sci. **197** (2002) 231. (b) F. Wang, M. Hickner, Q. Ji, W. Harrison, J. Mecham, T.A. Zawodzinski, J.E. McGrath, *Macromol. Symp*. **175** (2001) 387.
76. J.E. McGrath, Lecture, Symposium 'Advances in Materials for Proton Exchange Membrane Fuel Cell Systems', Asilomar, California, 20–23, February 2005.
77. M. Marrony, J. Rozière, D.J. Jones, A. Lindheimer, *Fuel Cells* **5** (2005) 412–428.

78. Y.S. Kim, M.J. Sumner, W.L. Harrison, J.S. Riffle, J.E. McGrath, B.S. Pivovar, *J. Electrochem. Soc*. **151** (2004) A2150–A2156.
79. M.J. Sumner, W.L. Harrison, R.M. Weyers, Y.S. Kim, J.E. McGrath, J.S. Riffle, A. Brink, M.H. Brink, *J. Membr. Sci*., **239** (2004) 199.
80. Y.-M. Sun, T.-C. Wu, H.-C. Lee, G.-B. Jung, M.D. Guiver, Y. Gao, Y.-L. Liu, J.-Y. Lai, *J. Memb. Sci.* **265** (2005) 108-114.
81. K.D. Kreuer, S.J. Paddison, E. Spohr, M. Schuster, *Chem. Rev*. **104** (2004) 4637–4678.
82. C.K. Shin, G. Maier, B. Andreaus, G.G. Scherer, *J Membr. Sci*. **245** (2004) 147.
83. A. Taeger, C. Volen, D. Lehmann, W. Lenk, K. Schlendstedt, J. Meier-Haack, *Macromol. Symp*. **210** (2004) 175.
84. N. Asano, K. Miyatake, M. Watanabe, *J. Polym. Sci. Part A: Polym. Chem*. **44** (2006) 2744.
85. H. Ghassemi, W. Harrison, T.A. Zawodzinski, J.E. McGrath, *Polym. Prepr*. **45** (2004) 68.
86. A. Roy, M.A. Hickner, X. Yu, Y. Li, T.E. Glass, J.E. McGrath, *J. Polym. Sci. Part B: Polym. Phys*. **44** (2006) 2226.
87. H. Ghassemi, J.E. McGrath, T.A. Jr. Zawodzinski, *Polymer* **47** (2006) 4132.
88. F. Schönberger, M. Hein, J. Kerres, *Solid State Ionics* **178** (2007) 547.
89. Y.S. Kim, B. Einsla, M. Sankir, W. Harrison, B.S. Pivovar, *Polymer* **47** (2006) 4026.
90. D. Xing, J. Kerres *Polym. Adv. Techn*. **17** (2006) 591.
91. S. Mitov, B. Vogel, E. Roduner, H. Zhang, X. Zhu, V. Gogel, L. Jörissen, M. Hein, D. Xing, F. Schönberger, J. Kerres, *Fuel Cells* **6** (2006) 413–424.
92. X. Zhu, H. Zhang, Y. Liang, Y. Zhang, Q. Luo, C. Bi, B. Yi, *J. Mater. Chem*. **17** (2007) 386–397.
93. D. Xing, B. Yi, Y. Fu, F. Liu, H. Zhang, *Electrochem. Solid St. Lett*. **7** (2004) A315–A317.
94. J.A. Kerres, *Fuel Cells* **5** (2005) 230–247.
95. J. Kerres, W. Cui, W. Schnurnberger, German Patent 196 22 337.7, 1997; French Patent F 97 06706, 1997; US Patent 6,221,923, 2001; US Patent 6,552,135, 2003.
96. J. Kerres, W. Cui, M. Junginger, *J. Memb. Sci*. **139** (1998) 227–241.
97. J. Kerres, W. Zhang, T. Häring, *J. New Mat. Electrochem. Syst*. **7** (2004) 299–309.
98. J. Kerres, W. Zhang, W. Cui, J. *Polym. Sci.: Part A: Polym. Chem*. **36** (1998) 1441–1448.
99. W. Zhang, V. Gogel, K. A. Friedrich, J. Kerres, *J. Power Sources* **155** (2006) 3–12.
100. J. Kerres, W. Cui, US Patent 6,194,474, 2001; US Patent 6,300,381, 2001; European Patent EP 1 073 690, 2004.
101. W. Cui, J. Kerres, G. Eigenberger, *Sep. Purif. Techn*. **14** (1998) 145–154.
102. J. Kerres, A. Ullrich, *Sep. Purif. Techn*. **22** (2001) 1–15.
103. J. Kerres, A. Ullrich, M. Hein, *J. Polym. Sci.: Part A: Polym. Chem*. **39** (2001) 2874–2888.
104. J. Kerres, A. Ullrich, T. Häring, US Patent 6,590,067, 2003; European Patent EP1 105 433 B1, 2004.
105. D.R. Coffin, G.A. Serad, H.L. Hicks, R.T. Montgomery, *Textile Res. J*. **52** (1982) 466–472.
106. J. Kerres, A. Ullrich, T. Häring, European Patent EP 1 076 676, 2004, US Patent 6,723,757, 2004.

107. J. Kerres, A. Ullrich, Th. Häring, M. Baldauf, U. Gebhardt, W. Preidel, *J. New Mat. Electrochem. Syst*. **3** (2000) 229–239.
108. J. Lee, J. Kerres, *J. Memb. Sci.* **294** (2007), 75–83.
109. J. Kerres, A. Ullrich, F. Meier, Th. Häring, *Solid State Ionics* **125** (1999) 243–249.
110. J. Kerres, M. Hein, W. Zhang, N. Nicoloso, S. Graf, *J. New Mat. Electrochem. Syst*. **6** (2003) 223–229.
111. J. Kerres, W. Zhang, L. Jörissen, V.Gogel, *J. New Mat. Electrochem. Syst*. **5** (2002) 97–107.
112. F. Meier, J. Kerres, G. Eigenberger, *J. New Mat. Electrochem. Syst*. **5** (2002) 91–96.
113. D. Xing, J. Kerres, *J. New Mat. Electrochem. Syst*. **9** (2006).
114. L. Jörissen, V. Gogel, J. Kerres, J. Garche, *J. Power Sources* **105** (2002) 267–273.
115. J. Kerres, A. Ullrich, M. Hein, V. Gogel, K. A. Friedrich, L. Jörissen, *Fuel Cells* **4** (2004) 105–112.
116. J. Kerres, *Fuel Cells* **6** (2006) 251–260.
117. V.V. Agon, W.A. Bubb, A. Wright, C.L. Hawkins, M.J. Davies, *Free Rad. Biol. Med.* **40** (2006) 698–710.
118. K. Reybier, J. Boyer, V. Farines, F. Camus, J.-P. Souchard, M.-C. Monje, V. Bernardes-Genisson, S. Goldstein, F. Nepveu, *Free Rad. Res*. **40** (2006) 11–20.
119. R. Wycisk, J. Chisholm, J. Lee, J. Lin, P.N. Pintauro, *J. Power Sources* **163** (2006) 9–17.
120. A. Ainla, D. Brandell, *Solid State Ionics* **178** (2007) 581–585.
121. R. Wycisk, J.K. Lee, P.N. Pintauro, *J. Electrochem. Soc*. **152** (2005) A892–A898.
122. C. Manea, M. Mulder, *Desalination* **147** (2002) 179–182.
123. B. Kosmala, J. Schauer, *J. Appl. Polym. Sci*. **85** (2002) 1118–1127.
124. Y. Fu, A. Manthiram, M.D. Guiver, *Electrochem. Comm*. **9** (2007) 905–910.
125. Y. Fu, A. Manthiram, M.D. Guiver, *Electrochem. Comm*. **8** (2006) 1386–1390.
126. Y.-Z. Fu, A. Manthiram, M.D. Guiver, *Electrochem. Solid-State Lett*. **10** (2007) B70–B73.
127. N.W. DeLuca, Y.A. Elabd, *J. Memb. Sci*. **282** (2006) 217–224.
128. Z.-G. Shao, X. Wang, I.-M. Hsing, *J. Memb. Sci.* **210** (2002) 147–153.
129. P.L. Antonucci, A.S. Aricò, P. Cretì, E. Ramunni, V. Antonucci, *Solid State Ionics* **125** (1999) 431–437.
130. A.S. Aricò, P. Cretì, P.L. Antonucci, V. Antonucci, *Electrochem. Solid-State Lett*. **1** (1998) 66–68.
131. D.A. Siuzdak, K.A. Mauritz, *Polym. Prepr*. **38** (1997) 245–246
132. J.T. Payne, D.A. Reuschle, K.A. Mauritz, *Polym. Prepr*. **38** (1997) 247–248.
133. Q. Deng, R.B. Moore, K.A. Mauritz, *J. Appl. Polym. Sci*. **68** (1998) 747–763.
134. S.P. Nunes, B. Ruffmann, E. Rikowski, S. Vetter, K. Richau, *J. Memb. Sci.* **203** (2002) 215–225.
135. G. Alberti, M. Casciola, *Ann. Rev. Mat. Res*. **33** (2003) 129–154.
136. D.J. Jones, M. El Haddad, B. Mula, J. Rozière, Environmental Research Forum 'Chemistry and Energy', C. A. C. Sequeira, Ed. Transtec (1996) 1–2, 115–126.
137. J. Rozière, D.J. Jones, *Handbook of Fuel Cell Technology*, Ed. W. Vielstich, A. Lamm, H. Gasteiger, John Wiley and Sons, Chichester (2003), Vol. 3, pp. 447–455.
138. B. Bauer, D.J. Jones, J. Rozière, L. Tchicaya, G. Alberti, L. Massinelli, M. Casciola, A. Peraio, E. Ramunni, *J. New Mater. Electrochem. Syst*. **3** (2000) 87–92.
139. D.J. Jones, J. Roziere, *J. Memb. Sci*. **185** (2001) 41–58.
140. L. Tchicaya-Bouckary, D.J. Jones, J. Rozière, *Fuel Cells* **2** (2002) 40–45.

141. C. Yang, S. Srinivasan, A.S. Aricò, P. Cretì, V. Baglio, V. Antonucci, *Electrochem. Solid-State Lett*. **4** (2001) A31–A34.
142. A.F. Hollemann, E. Wiberg, *Textbook of Inorganic Chemistry*, 101st ed. W. de Gruyter: Berlin, New York, 1995.
143. K.D. Kreuer, *Chem. Mater*. **8** (1996) 610.
144. N. Giordano, P. Staiti, S. Hocevar, A.S. Aricò, *Electrochim. Acta* **41** (1996) 397–403.
145. S. Malhotra, R. Datta, *J. Electrochem. Soc*. **144** (1997) L23–L26.
146. Y.S. Kim, F. Wang, M. Hickner, T.A. Zawodzinski, J.E. McGrath, *J. Memb. Sci*. **212** (2003) 263–282.
147. M.L. Ponce, L. Prado, B. Ruffmann, K. Richau, R. Mohr, S.P. Nunes, *J. Memb. Sci.* **217** (2003) 5–15.
148. M.L. Ponce, L.A.S.de A. Prado, V. Silva, S.P. Nunes, *Desalination* **162** (2004) 383–391.
149. D.R. Vernon, F. Meng, S.F. Dec, D.L. Williamson, J.A. Turner, A.M. Herring, *J. Power Sources* **139** (2005) 141–151**.**
150. J. Kerres, C.-M. Tang, C. Graf, *Ind. & Eng. Chem. Res*. **43** (2004) 4571–4579.
151. A.R. Tan, L.M. de Carvalho, A. de Souza Gomes, *Macromol. Symp*. **229** (2005) 168–178.
152. J.S. Wainright, J–T. Wang, D. Weng, R.F. Savinell, M. Litt, *J. Electrochem. Soc.* **142** (1995) L121–L123.
153. J.-T. Wang, R.F. Savinell, J. Wainright, M. Litt, H. Yu, *Electrochim. Acta* **41** (1996) 193–197.
154. D. Weng, J.S. Wainright, U. Landau, R.F. Savinell, *J Electrochem. Soc*. **143** (1996) 1260–1263.
155. S. R. Samms, S. Wasmus, R.F. Savinell, *J. Electrochem. Soc*. **143** (1996) 1225–1232.
156. J.-T. Wang, J.S. Wainright, R.F. Savinell, M. Litt, *J. Appl. Electrochem*. **26** (1996) 751–756.
157. R. Ameri, PhD Dissertation, CWRU, 1997.
158. L. Xiao, H. Zhang, E.-W. Choe, E. Scanlon, L.S. Ramanathan, B.C. Benicewicz, *2004 AIChE Spring National Meeting, Conference Proceedings* pp. 97–101.
159. L. Xiao, H. Zhang, E. Scanlon, L.S. Ramanathan, E.-W. Choe, D. Rogers, T. Apple, B.C. Benicewicz, *Chem Mater*. **17** (2005) 5328–5333.
160. J.R.P. Jayakody, S.H. Chung, L. Durantino, H. Zhang, L. Xiao, B.C. Benicewicz, S.G. Greenbaum, *J. Electrochem. Soc*. **154** (2007) B242–B246.
161. http://www2.basf.de/en/futurebusiness/service/aktuelles/pm.htm?pmid= 2646&id=a-IZtAgJJbw24Hf
162. M.K. Daletou, N. Gourdoupi, J.K. Kallitsis, *J. Memb. Sci.* **252** (2005) 115–122.
163. C. Hasiotis, Q. Li, V. Deimede, J.K. Kallitsis, C.G. Kontoyannis, N.J. Bjerrum, *J. Electrochem. Soc*. **148** (2001) A513–A519.
164. V. Deimede, G.A. Voyiatzis, J.K. Kallitsis, L. Qingfeng, N.J. Bjerrum, *Macromolecules* **33** (2000) 7609–7617.
165. J. Kerres, F. Schönberger, Q. Li, J. O. Olsen, N, Bjerrum, personal communication, to be published.
166. M.F. Schuster, W.H. Meyer, G. Wegner, H.G. Herz, M. Ise, K.D. Kreuer, J. Maier, *Solid State Ionics* **145** (2001) 85.
167. M.F.H. Schuster, W.H. Meyer, *Annu. Rev. Mater. Res*. **33** (2003) 233.
168. M.F.H. Schuster, W.H. Meyer, M. Schuster, K.D. Kreuer, *Chem. Mater*. **16** (2004) 329.

169. M. Schuster, T. Rager, A. Noda, K.D. Kreuer, J. Maier, *Fuel Cells* **5** (2005) 355–365.
170. M. Yamabe, K. Akiyama, Y. Akatsuka, M. Kato, *Eur. Polym. J.* **36** (2000) 1035–1041.
171. X. Zhou, J. Weston, E. Chalkova, M.A. Hofmann, C.M. Ambler, H.R. Allcock, S.N. Lvov, *Electrochim. Acta* **48** (2003) 2173–2180.
172. H.R. Allcock, M.A. Hofmann, C.M. Ambler, S.N. Lvov, X.Y. Zhou, E. Chalkova, J. Weston, *J. Memb. Sci.* **201** (2002) 47–54.
173. S. Yanagimachi, K. Kaneko, Y. Takeoka, M. Rikukawa, *Synth. Met.* **135–136** (2003) 69–70.
174. H. Steininger, M. Schuster, K.D. Kreuer, J. Maier, *Solid State Ionics* **177** (2006) 2457–2462.
175. B. Liu, G.P. Robertson, M.D. Guiver, Z. Shi, T. Navessin, S. Holdcroft, *Macromol. Rapid Comm.* **27** (2006) 1411–1417.
176. B. Lafitte, P. Jannasch, *J. Polym. Sci. Part A: Polym. Chem.* **45** (2007) 269–283.
177. S. Ball, *Plat. Met. Rev.* **49** (2005) 27.
178. B. Wang, *J. Power Sources* **152** (2005) 1.
179. R. Adzic, in: J. Lipkowski, P.N. Ross (Eds.), *Electrocatalysis*, Chapter 5, Wiley/VCH, New York, 1998.
180. A. Damjanovic, V. Brusic, *Electrochim. Acta* **12** (1967) 615.
181. D.B. Sepa, M.V. Vojnovic, A. Damjanovic, *Electrochim. Acta* **26** (1981) 781.
182. D.B. Sepa, M.V. Vojnovic, L.M. Vracar, *Electrochim. Acta* **29** (1984) 1169.
183. T. Li, P.B. Balbuena, *Chem. Phys. Lett.* **367** (2003) 439.
184. Y. Wang, P.B. Balbuena, *J. Phys. Chem.* **109** (2005) 18902.
185. J. Nørskov, J. Rossmeisl, A. Logadottir, L. Lindqvist, J.R. Kitchin, T. Bligaard, H. Jónsson, *J. Phys. Chem. B* **108** (2004) 17886.
186. N. Wagner, E. Gülzow, *J. Power Sources* **127** (2004) 341.
187. T. Matsui, K. Fujiwara, T. Okanishi, R. Kikuchi, T. Takeguchi, K. Eguchi, *J. Power Sources* **155** (2006) 152.
188. T. E. Shubina, M. T. M. Koper, *Electrochim. Acta* **47** (2002) 3621.
189. T. Ioroi, T. Akita, S.-I. Yamazaki, Z. Siroma, N. Fujiwara, K. Yasuda, *Electrochim. Acta* **52** (2006) 491.
190. N.P. Lebedeva, G.J.M. Janssen, *Electrochim. Acta* **51** (2005) 29.
191. K.S. Nagabushana, C. Weidenthaler, S. Hočevar, D. Strmčnik, M. Gaberšček, A.L. Antozzi, G.N. Martelli, *J. New Mat. Electrochem. Systems* **9** (2006) 73.
192. K.D. Beard, M.T. Schaal, J.W. Van Zee, J.R. Monnier, *Appl. Cat. B: Environmental* **72** (2007) 262.
193. J. Luo, N. Kariuki, L. Han, L. Wang, C.-J. Zhong, T. He, *Electrochim. Acta* **51** (2006) 4821.
194. J. Zhang, F.H.B. Lima, M.H. Shao, K. Sasaki, J.X. Wang, J. Hanson, R.R. Adzic, *J. Phys. Chem. B* **109** (2005) 22701.
195. L. Zhang, J. Zhang, D.P. Wilkinson, H. Wang, *J. Power Sources* **156** (2006) 171.
196. A.B. LaConti, M. Hamdan, R.C. McDonald in: W. Vielstich, A. Lamm, H. Gasteiger (Eds.), *Handbook of Fuel Cells – Fundamentals, Technology and Applications*, Chapter 49, Vol. 3, Wiley, Chichester, 2003.
197. S. Yoshimoto, J. Inukai, A. Tada, T. Abe, T. Morimoto, A. Osuka, H. Furuta, K. Itaya, *J. Phys. Chem. B* **108** (2004) 1948.
198. P. Bogdanoff, I. Herrmann, M. Hilgendorff, I. Dorbandt, S. Fiechter, H. Tributsch, *J. New Mat. Electrochem. Systems* **7** (2004) 85.

199. Image courtesy of Iris Dorbandt, Hahn-Meitner-Institute Berlin, Germany.
200. I. Herrmann, Thesis: 'Development and optimization of new synthesis routes for transition metal based electrocatalysts for the oxygen reduction reaction', FU Berlin, Germany (2006).
201. I. Herrmann, V. Brüser, S. Fiechter, H. Kersten, P. Bogdanoff, *J. Electrochem. Soc*. **152** (2005) A2179.
202. I. Herrmann, V. Brüser, S. Fiechter, H. Kersten, P. Bogdanoff, *J. Electrochem. Soc*. **152** (2005) A2179.
203. I. Herrmann, P. Bogdanoff, S. Fiechter, patent PCT/DE2006/000326 and 10 2006 008 328.8.
204. Image courtesy of Iris Herrmann, Hahn-Meitner-Institute Berlin, Germany.
205. X.-Y. Xie, Z.-F. Ma, X. Wu, Q.-Z. Ren, X. Yuan, Q.-Z. Jiang, L. Hu, *Electrochim. Acta* **52** (2007) 2091.
206. M. Lèfevre, J.P. Dodelet, P. Bertrand, *J. Phys. Chem. B* **106** (2002) 8705.
207. M. Lèfevre, J.P. Dodelet, *Electrochim. Acta* **48** (2003) 2749.
208. C. Médard, M. Lèfevre, J.P. Dodelet, F. Jaouen, G. Lindbergh, *Electrochim. Acta* **51** (2006) 3202.
209. M.-H. Shao, K. Sasaki, R.R. Adzic, *J. Am. Chem. Soc*. **128** (2006) 3526
210. G. Zehl *et al*. *J. New Mat. Electrochem. Systems, accepted.*
211. V. Rao, P. Simonov, E.R. Savinova, G.V. Plaksin, S.V. Cherepanova, G.N. Kryukova, U. Stimming, *J. Power Sources* **145** (2005) 178.
212. F. Goettmann, C. Sanchez, *J. Mater. Chem*. **17** (2007) 24.
213. J. Kaiser, P.A. Simonov, V.I. Zaikovskii, Ch. Hartnig, L. Jörissen, E.R. Savinova, *J. Appl. Electrochem*. **37** (2007) 1429.
214. J. Yu, N. Islam, T. Matsuura, M. Tamano, Y. Hayashi, M. Hori, *Electrochem. Solid-State Lett*. **8** (2005) A320.
215. X. Sun, R. Li, D. Villers, J.P. Dodelet, S. Désilets, *Chem. Phys. Lett*. **379** (2003) 99.
216. R. Wlodarczyk, M. Chojak, K. Miecznikowski, A. Kolary, P.J. Kulesza, R. Marassi, *J. Power Sources* **159** (2006) 802.
217. R. Wlodarczyk, A. Kolary-Zurowska, R. Marassi, M. Chojak, P.J. Kulesza, *Electrochim. Acta* **52** (2007) 3958.
218. M. Chojak, A. Kolary-Zurowska, R. Wlodarczyk, K. Miecznikowski, K. Karnicka, B. Palys, R. Marassi, P.J. Kulesza, *Electrochim. Acta* **52** (2007) 5574.
219. K. Debe in: W. Vielstich, A. Lamm, H. Gasteiger (Eds.), *Handbook of Fuel Cells – Fundamentals, Technology and Applications*, Chapter 45, Vol. 3, Wiley, Chichester, 2003.
220. F. Raimondi, G.G. Scherer, R. Kötz, A. Wokaun, *Angew. Chem. Int. Ed.* **44** (2005) 2190.
221. Lj.M. Vračar, N.V. Krstajć, V.R. Radmilović, M.M. Jakšić, *J. Electroanal. Chem.* **587** (2006) 99.
222. N.V. Krstajić, Lj.M. Vračar, V.R. Radmilović, S.G. Neophytides, M. Labou, J.M. Jakšić, R. Tunold, P. Falaras, M.M. Jakšić, *Surf. Sci*. **601** (2007) 1949.
223. M. Noe, P.K. Shen, M. Wu, Z. Wei, H. Meng, *J. Power Sources* **162** (2006) 173.
224. K. Lee, A. Ishira, S. Mitsushima, N. Kamiya, K. Ota, *Electrochim*. Acta **49** (2004) 3479.
225. http://www.sglcarbon.com/
226. http://www.freudenberg.com/
227. http://www.spectracorp.org/
228. http://www.toray.com/

229. Gu-Gon Park, Y.-J. Sohn, T.-H. Yang, Y.-G. Yoon, W.-Y. Lee, Ch.-S. Kim, *J. Power Sources* **131** (2004) 182.
230. M.F. Mathias, J. Roth, J. Flemming, W. Lehnert, Handbook of fuel cell Technology (as ref 137) Vol 3, Ed. W. Vielstich, H. Gasteiger, A. Lamm, John Wiley & Sons, Chichester 2003, pp. 517–537.
231. A. Jena, K. Gupta, *J. Power Sources* **96** (2001) 214.
232. Y.M. Volfkovich, V.S. Bagotzky, *J. Power Sources* **48** (1994) 327.
233. Y.M. Volfkovich, V.S. Bagotzky, *J. Power Sources* **48** (1994) 339.
234. Y.M. Volfkovich, V.S. Bagotzky, V.E. Sosenkin, I.A. Blinov, *Colloids Surf. A* **187** (2001) 11.
235. http://www.pore-cor.com.
236. A. Rack, Dissertation, Technische Universität Berlin, 2006.
237. R. Thiedmann, F. Fleischer, Ch. Hartnig, W. Lehnert, V. Schmidt, international communication, *J. Electrochem Soc*., 155 (2008) B391–B399.
238. M. Spiess, E. Spodarev, personal communication
239. C. Schroeder, W.C. Regli, A. Shokoufandeh, W. Sun, *Computer-Aided Design* **37** (2005) 339.
240. K. Mecke, C.H. Arns, *J. Phys.: Condens. Matter* **17** (2005) 503.
241. J.T. Gostick, M.W. Fowler, M.D. Pritzker, M.A. Ioannidis, L.M. Behra, *J. Power Sources* **162** (2006) 228.
242. Q. Wang, D. Song, T. Navessin, S. Holdcroft, Z. Liu, *Electrochim. Acta* **50** (2004) 725–730.
243. D. Arnost, P. Schneider, *Chem. Eng. J.* **57** (91) 1995.
244. J. Valus, P. Schneider, *Appl. Catalysis* **1** (1981) 355.
245. P. Fott, G. Petrini, *Appl. Catalysis* **2** (1982) 367.
246. I. Drescher, W. Lehnert, J. Meusinger, *Electrochim. Acta* **43** (1998) 3059.
247. http://www.pmiapp.com.
248. J. Benziger, J. Nehlsen, D. Blackwell, T. Brennan, J. Itescu, *J. Membrane Sci*. **261** (2005) 98.
249. S. Lister, D. Sinton, N. Djilali, *J. Power Sources* **154** (2006) 95.
250. A. Bazylak, D. Sinton, Z.-S. Liu, N. Djilali, *J. Power Sources* **163** (2007) 784.
251. K. Tüber , D. Pócza, C. Hebling, *J. Power Sources* **124** (2003) 403–414.
252. P. Argyropoulos, K. Scott, W.M. Taama, *Electrochim. Acta* **44** (1999) 3575–3584.
253. I. Manke, Ch. Hartnig, M. Grünerbel, J. Kaczerowski, W. Lehnert, N. Kardjilov, A. Hilger, J. Banhart, W. Treimer, M. Strobel, *Appl. Phys. Lett*. **90** (2007) 184101.
254. Ch. Hartnig, I. Manke , N. Kardjilov, A. Hilger, M. Grünerbel, J. Kaczerowski, J. Banhart, W. Lehnert, *J. Power Sources*, 176 (2008) 452–459.
255. R. Satija, D.L. Jacobson, M. Arif, S.A. Werner, *J. Power Sources* **129**, 238–245 (2004).
256. A. Turhan, K. Heller, J.S. Benizger, M.M. Mench, *J. Power Sources* **160**, 1195–1203 (2006).
257. A.B. Geiger, G.G. Scherer *et al*., *Fuel Cells* **2** (2002) 92–98.
258. I. Manke, Ch. Hartnig, M. Grünerbel, W. Lehnert, N. Kardjilov, A. Haibel, A. Hilger, J. Banhart, H. Riesemeier, *Appl. Phys. Lett*. **90** (2007) 174105.
259. W.K. Lee, J.W. Van Zee, A. Jena, K. Gupta, *Proceedings, Fuel cell seminar*, San Antonlo, Texas, 2-5–11. 2004.
260. J.T. Gostick, M.W. Fowler, M.A. Ioannidis, M.D. Pritzker, Y.M. Volfkovich, A. Sakars, *J. Power Sources* **156** (2006) 375.
261. N. A. Patankar, *Langmuir* **20** (2004) 7097.

262. T.S. Meiron, A. Marmur, I.S. Saguy, *J. Colloid Interface Sci*., **274** (2004) 637.
263. G. McHale, *Langmuir* **23** (2007) 8200.
264. E. Bormashenko, R. Pogreb, G. Whyman, M. Erlich, *Langmuir* **23** (2007), 6501.
265. http://www.kruss.de.
266. T. Berning, N. Djilali, *J. Electrochem. Soc*. **150** (2003) A1589.
267. U. Pasaogullari, C.Y. Wang, *J. Electrochem. Soc*. **152** (2005) A380.
268. U. Pasaogullari, C.Y. Wang, *J. Electrochem. Soc*. **151** (2004) A399.
269. D. Natarajan, T.V. Nguyen, *J. Electrochem. Soc.* **148** (2001) A1324.
270. W.M. Yan, C.Y. Soong, F. Chen, H.S. Chu, *J. Power Sorces* **125** (2004) 27.
271. I. Fatt, 'The network model of porous media, I. Capillary pressure characteristics', *PetroleumTransactions AIME* **207** (1956) 144–159; 'The network model of porous media, II. Dynamic properties of a single size tube network', *Petroleum Transactions AIME* **207** (1956) 160–163; 'The network model of porous media, III. Dynamic properties of networks with tube radius distribution', *Petroleum Transactions AIME* **207** (1956) 164–177.
272. B. Berkowitz, R.P. Ewing, *Surveys in Geophysics* **19** 1998 23–72.
273. J.H. Nam, M. Kaviany, *Int. J. Heat Mass Trans*. **46** (2003) 4595.
274. B. Markicevic, A. Bazylak, N. Djilali, *J. Power Sources* (2007), doi:10.1016/j.jpowsour.2007.06.053.
275. J.T. Gostick, M.A. Ioannidis, M.W. Fowler, M.D. Pritzker, *J. Power Sources* (2007), doi:10.1016/j.jpowsour.2007.04.059.
276. P.K. Sinha, P.P. Mukherjee, C-Y. Wang, *J. Mater. Chem*. **17** (2007), 3089.
277. F. Keil, *Diffusion und Chemische Reaktion in der Gas/Feststoff-Katalyse*, Springer-Verlag Berlin, Heidelberg, 1999.
278. V.P. Schulz, J. Becker, A. Wiegmann, P.P. Mukherjee, C-Y. Wang, *J. Electrochem. Soc*., **154** (2007) B419.
279. Image courtesy of Ralf Thiedmann, University of Ulm.
280. M.C. Sukop, D.T. Thorne Jr., *Lattice Boltzmann Modeling*, Springer-Verlag Berlin Heidelberg, 2006.
281. Ch. Hartnig, W. Lehnert, international communication, manuscript in preparation.
282. P. Concus, R. Finn, *Appl. Math. Sci*. **63** (1969) 292.
283. X. Zhu, P.C. Sui, N. Djilali, *J. PowerSources* (2007) doi:10.1016/j.jpowsour.2007.07.024.
284. Patent Application GB 2372626 A.
285. Patent Application DE 10 2004 026 134 B4.
286. X. Li, I. Sabir, *Int. J. Hydrogen Energy* **30** (2005) 359–371.
287. W. Vielstich, A. Lamm, H. Gasteiger, *Handbook of Fuel Cells*, Vol.3, Wiley & Sons, Chichester 2003, pp. 325–336.
288. J. Scholta, V. Gogel *et al*., *Bunsen-Conference Schwerin*, Germany, June 2005.
289. J. Scholta, G. Escher, W. Zhang, L. Küppers, L. Jörissen, W. Lehnert, *J. Power Sources* **155** (2006) 66.
290. A.M. Ribeiro *et al*., *Int. J. Multiphase Flow*, **32** (2006) 1029–1036.
291. J. Park, X. Li, presentation at *2006 Fuel Cell Seminar*, 13–17, Nov. Honolulu, Hawaii, Abstr. No. 716.
292. J.J. Kowal, A. Turhan, K. Heller, J. Brenizer, M.M. Mench, *J. Electrochem. Soc*. **153** (2006) A1971.
293. N. Akhtar *et al.*, International communication, submitted to *Int. Journal of Hydrogen Energy*.

5

Direct methanol fuel cells

C HARTNIG, L JÖRISSEN, W LEHNERT and J SCHOLTA, Centre for Solar Energy and Hydrogen Research (ZSW), Germany

5.1 Introduction

Direct methanol fuel cells (DMFC) represent the only class of fuel cells in which one of the reactants is provided in liquid phase unlike the other, gas-fed, cell types. Owing to the comparatively easy handling of methanol, DMFCs are mostly considered for portable and mobile applications. Their reduced power density compared with hydrogen-driven polymer electrolyte membrane fuel cells (PEMFC) (the current density is around one-tenth of that of PEMFCs) usually leads to larger stack sizes at similar power characteristics. Methanol cartridges are much easier to handle than hydrogen storage media, giving them an advantage in fuel transport. A cartridge system was recently evaluated and licensed by Smart Fuel Cell[1] for use in everyday applications and was approved in 2007 for use in aircraft.

As the material requirements are comparable to hydrogen-driven PEMFCs, the components employed are in general very similar or even identical to this fuel cell type. In this chapter, only extensions towards components used in PEMFC are denoted, so it is advisable to consult the respective chapter.

The structure of this chapter is as follows. After an introduction to the fundamental steps of the electrochemical methanol oxidation reaction, requirements for catalysts employed in DMFCs will be described, followed by the gas (or in this case, aqueous methanol solution) diffusion media, flow-field considerations and finally system requirements and performance aspects. The chapter is concluded by environmental aspects in terms of carbon dioxide separation; carbon dioxide results from the complete oxidation of methanol, which will be discussed in more detail in the first section, has recently been a strong issue in terms of 'green energy conversion'. Requirements for membrane materials are almost identical to the materials employed in hydrogen-driven fuel cells; therefore an in-depth description is skipped in this chapter and the details concerning polymer electrolytes for DMFC applications are covered in Chapter 4.

5.2 Catalysts

Besides the standard requirements for a catalyst such as long-term stability, low price and high activity, especially in DMFCs, a reasonable performance in terms of power density (expressed in W/cm^2) and maximum current density (in mA/cm^2) at low loadings is desirable. As will be explained in more detail below, the slow kinetics of the anodic methanol oxidation reaction is a key issue in catalyst development. Unlike the hydrogen-fed PEMFC, both the cathodic and the anodic reactions lose a great deal of performance due to overpotentials. Usually, a lack of activity can be compensated for by an increased catalyst loading; however, thick layers lead to transport losses, which are therefore not desirable. The second issue, sufficient long-term stability, is currently achieved to a broad extent by means of operating conditions at which corrosive potentials are avoided. In terms of stability, the catalyst support plays a non-negligible role: on the one hand, reduced support degradation decreases aging effects such as loss of active material and on the other hand ensures almost constant wetting characteristics.

5.2.1 Mechanism of methanol oxidation reaction

As stated in the introduction, in a DMFC the two reactants are oxygen and methanol. On the anode of a DMFC, methanol is oxidized (methanol oxidation reaction, MOR) to form carbon dioxide, CO_2, releasing six electrons:

$$CH_3OH + 7H_2O \rightarrow CO_2 + 6e^- + 6\ H_3O^+ \qquad 5.1$$

Methanol is provided as an aqueous solution with a methanol concentration of 1–2 mol/l; this concentration proved to perform best in terms of current density and crossover rate[2,3]. Since DMFCs are almost exclusively operated at temperatures below 80 °C, methanol is in the liquid phase which has to be transported through the diffusion media (see below).

The cathodic reaction is identical to that in PEMFCs, the oxygen reduction reaction (ORR):

$$O_2 + 4H_3O^+ + 4\ e^- \rightarrow 6H_2O \qquad 5.2$$

resulting in an overall reaction as:

$$CH_3OH + 3/2O_2 \rightarrow CO_2 + 2H_2O \qquad 5.3$$

The reaction has been the subject of numerous experimental and theoretical studies; mechanistic aspects based on theoretical considerations will be described and summarized below. The detailed explanation of the reaction mechanism serves as basis for the forthcoming discussion of the appropriate choice of catalysts and requirements due to the different intermediates. Experiments were performed either in the gas phase or in an electrochemical environment, whereas only the electrochemical experiments can be considered

a realistic resemblance of the fuel cell environment. Unlike PEMFCs, where the oxygen reduction reaction features the rate-determing step (rds), in DMFCs the slow kinetics of the MOR represent the limiting factor.

In gas phase conditions, the splitting of the OH bond is considered the rds; once this bond is broken, a series of intermediate products can be identified. In contrast, in aqueous solutions the reaction starts via splitting of the CH bond which represents the rds in electrochemical environments[4,5]. The reaction can proceed via a direct or an indirect pathway as displayed in Fig. 5.1: the direct pathway represents in principle a dehydrogenation of methanol, leading to adsorbed carbon monoxide:

$$CH_3OH \rightarrow CO_{ads} (+ 2H_2) \qquad 5.4$$

In a subsequent step, the carbon monoxide is oxidized to form carbon dioxide which desorbs from the surface. Once the oxygen-providing species is missing or cannot be provided in the required concentration, a decrease in the performance in the fuel application is observed. The commonly described poisoning of pure platinum employed as anodic catalyst is caused by the strong binding energies of both carbon monoxide as well as oxygen-containing species such as surface oxides or adsorbed OH groups.

In the indirect pathway, a reaction cascade is started, which leads to different reaction products such as formaldehyde and formic acid, and reactive intermediates such as adsorbed HCO and COH, which have been detected spectroscopically[6]. Depending on the potential, the catalyst loading and the catalyst composition, varying amounts of the respective species are formed. Desorption and readsorption of the intermediates lead to a dependence of the production rate on the catalyst loading: with increasing catalyst loading (making a desorption without reactive readsorption improbable) the production rate of intermediates is lowered[7,8].

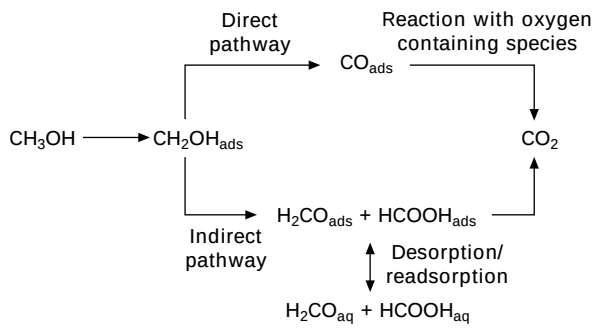

5.1 Direct and indirect pathway of methanol oxidation in electrochemical environments. Following the indirect pathway, products such as formaldehyde and formic acid, as well as reactive intermediates (which are omitted here), are formed.

The reaction by itself is best studied by means of model investigations on platinum single crystal surfaces; steps and terraces on the surface are thereby the most active spots, leading to a preferred reaction on these places[9].

Theoretical aspects of methanol reaction

Numerous theoretical studies have focused on the reaction scheme of methanol on catalytically active surfaces; most have concentrated on platinum as substrate to study the whole reaction scheme[10–17]. In both the electrochemical and gas phase oxidation of methanol, the initial step represents the rds.

In vacuum, the reaction starts with the cleavage of the OH bond; the successive intermediate is an adsorbed methoxy group[15]. Carbon monoxide results as a product which has to be oxidized to carbon dioxide so as not to serve as a catalyst poison. A different route in the gas phase starts with the scission of a CH bond and a successive hydrogenation via hydroxymethyl, hydroxymethylene and hydroxymethylidene[15].

In electrochemical conditions, the initial step, as well as the reaction cascade, is changed and the initial cleavage of one of the CH bonds is considered to be rate limiting. This observation led to the assumption that water plays a crucial role in the reaction scheme and the stabilization of intermediates.

In Fig. 5.2 the initial steps of the oxidation reaction of methanol in the presence of water are displayed. The initial step is the cleavage of a CH bond pointing towards the surface. Unlike the conditions in the gas phase, the second proton can be split off and migrate directly to the aqueous phase without reaching the surface of the catalyst. Formaldehyde results as an intermediate which desorbs and has to readsorb for a further reaction. In experimental studies the dependence of the rate of formaldehyde production has been monitored as a function of the catalyst loading; with increasing catalyst loading (which increases the probability for the intermediate to readsorb on an active site) the percentage of formaldehyde is strongly reduced[7]. The aqueous solution does not only influence the reaction pathway but also leads to a significant stabilization of the intermediates by around 0.7 eV[18].

5.2.2 PtRu catalysts

For the electrochemical ORR, platinum is the most widely used catalyst for fuel cell applications. However, in DMFCs, pure platinum cannot be employed for the following reason: depending on several factors, carbon monoxide is formed as a product which acts, due to its high binding energy of 1.54 eV[17], as a poisoning agent on platinum. In order to avoid a power decrease, platinum is used as a binary alloy in combination with ruthenium. This catalyst composition is the most widely used one which can be considered the state-

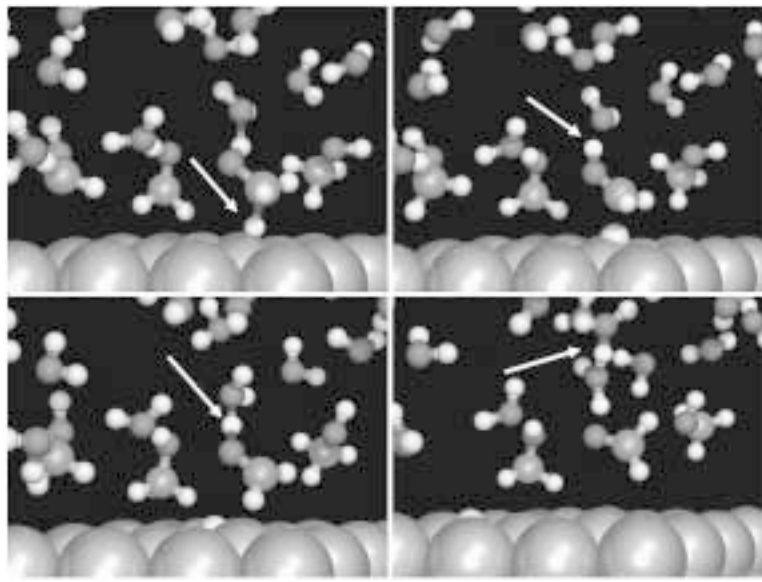

5.2 Chemical reaction dynamics of methanol oxidation to formaldehyde[11].

of-the-art for catalysts; the alloy is supported on Vulcan XC72 carbon which delivered the best performance[19,20]. Until recently, not only the performance but also the price difference between the two metals favored the use of ruthenium, but price increases over the past months (as at August 2007) mean this is no longer the case. The role of ruthenium as the oxygen-providing component has been explained in Chapter 4; in PEMFCs, PtRu alloys are employed to counteract trace amounts of CO in reformate hydrogen.

The alloy composition is usually in the range of 15–50% Ru. The ratio is limited by two factors: a too-high percentage of ruthenium leads to a reduced adsorption of methanol on the catalysts, as this species does not react on ruthenium. On the other side, too little ruthenium leads to negligible effects and a non-optimal removal of dehydrogenation fragments[21]. The surface composition in annealed samples does not therefore represent the bulk composition of the alloys; owing to surface segregation, the surface is enriched with platinum[21]. Depending on the potential, an optimum activity has been observed at a bulk concentration of 15–20% ruthenium[21,22]. This composition was underlined by theoretical considerations[23,24] and the activity has also been proven in model experiments[25]. Approaches to enhance the activity had been undertaken by spontaneous deposition of ruthenium on platinum to form small islands[26]; as these islands bear a high surface energy, the long-term stability has not been proven for a sufficient period. PtRu-based catalysts show the drawback of so-called fading behavior: the performance of the cell

decreases after a period of several hours; at the same time, ruthenium (which is employed only on the anode) can be detected on the cathode where it contributes apparently to an enhanced degradation of the fuel cell membrane[27]. The same problem applies to doped model systems such as ternary alloys PtRuP which show a high activity combined with a rapid decay rendering them unusable for fuel cell applications[28].

In a screening approach including a series of ternary catalysts Pt–Ru–X with X = Au, Co, Cu, Fe, Mo, Ni, Sn and W have been investigated with respect to their activity towards methanol oxidation[29]. The most efficient combination is the molybdenum alloy with a molybdenum amount in the range of 5% which leads to higher power densities compared with the unmodified Pt–Ru alloy. Enhanced activity has also been demonstrated for quaternary alloys made of platinum, ruthenium, rhenium and nickel in half-cell and single-cell measurements[30]; the increase is thereby thought to be due to the chemical states of Rh and Ni. Common to these recent approaches is the difficulty of identifying and reproducing the structure of multinary alloys.

5.2.3 Methanol-tolerant catalysts/new approaches

The permeation of methanol through the membrane from the anode to the cathode (crossover) represents a severe source of performance loss. The combined reaction of methanol and oxygen on the cathodic platinum catalysts (or platinum-based alloys) leads to a mixed potential formation which reduces the maximum achievable potential considerably by up to 200 mV[31]. Two strategies are followed to circumvent this phenomenon. First, there is a general avoidance of methanol permeation through the membrane (compare with the description of novel types of membranes and the influence of the membrane thickness in Chapter 4) which allows the use of standard catalysts. Second is the use of methanol-tolerant catalysts for the cathode of DMFCs; these materials are characterized by a complete inactivity towards methanol which does not react on these catalyst surfaces. At the development of methanol-tolerant catalysts, several prerequisites have to be fulfilled to obtain competitive products: the new material not only has to be as active as a comparable catalyst (platinum-based) but the stability and cost aspects also have to be considered. Recently, selenium-modified ruthenium particles ($RuSe_x$) were found to be a suitable alternative to platinum-based alloys where the addition of selenium increases the activity of pure ruthenium particles to shift these catalysts into a competitive regime[32].

$RuSe_x$ – preparation routes

Since the thermolytic decomposition of ruthenium carbonyl precursors in an Se saturated solution bears a poor controllability of the extent of the selenium

deposition (and therefore the selenium content), a more suitable preparation route has been proposed, starting from ruthenium nanoparticles which are deposited on the respective support (e.g. carbon black, Black Pearls, Vulcan XC72). The selenium modification is introduced in a succeeding step where the supported Ru particles are transferred in an $SeCl_4$-containing solution; this route allows for a precise adjustment of the $RuSe_x$ composition. Excess selenium can be removed by reductive annealing in a hydrogen atmosphere to gain the most active loading.

The general formula $RuSe_x$ describes ruthenium particles which are modified by a small amount of selenium; the optimum activity is achieved for $x \sim 0.1$. As obtained from anomalous small angle X-ray scattering (ASAXS) measurements, ruthenium forms almost spherical nanoparticles on which the selenium content is deposited on the surface[33]. The typical size of the ruthenium particles is around 2.5 nm; selenium forms small clusters on the surface with a diameter of less than 0.6 nm. A mixing of the two components has not been observed. From extended X-ray absorption fine structure (EXAFS) analysis an oxygen-free selenium structure and oxygen containing species on the uncovered ruthenium surface became obvious, underlining the aforementioned role of surface oxide in fuel cell reactions. A transmission electron microscopy (TEM) image of this class of catalyst is displayed in Fig. 5.3: the required uniform dispersion of the catalyst particles on the surface of the catalyst support can be easily estimated. From an in-depth analysis of the particle distribution and sizes, a very narrow size distribution could also be gained.

A special role for new catalysts refers to the catalyst support; as stated in Chapter 4, adapted supports are necessary to gain the optimum performance of new materials. As an example, the state-of-the-art platinum support in

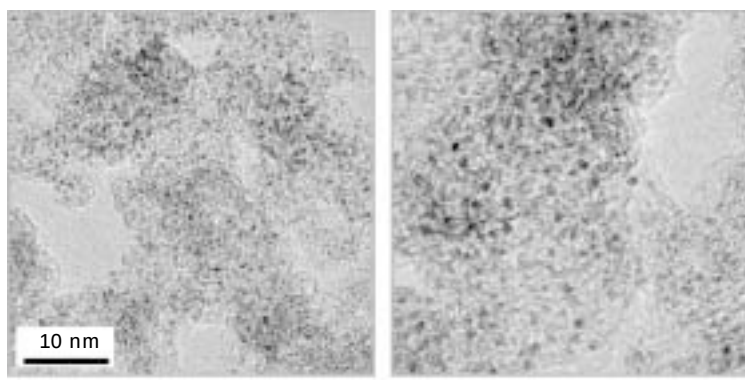

5.3 TEM image of the $RuSe_x$ catalyst supported on Black Pearls. The uniform distribution of particle sizes and dispersion of the catalyst on the carbon support can be estimated from the images.

PEMFC applications is Vulcan XC72, whereas for platinum–ruthenium alloys KetjenBlack proved a better performance[34].

Hydrogen peroxide production

Depending on the amount and the distribution of selenium, up to 5% hydrogen peroxide formation has been observed in the oxygen reduction reaction. As hydrogen peroxide leads to a rapid degradation of the membrane and the gas diffusion media and enhances the corrosion of the carbon catalyst support and finally to a loss of performance due to this side reaction, the formation of hydrogen peroxide has to be minimized. Further details on the effect of particle size, particle distribution and the effect of the carbon support on the hydrogen peroxide production can be found in the respective sections of Chapter 4.

In general, any new catalyst has to compare with the performance of platinum to serve as a reasonable substitute. Lower activity can be partially equalized by a higher loading, which in turn might lead to thicker catalyst layers and therefore increased transport losses.

Methanol-resistant platinum alloys

Alloying of platinum with cobalt leads to a different class of methanol-tolerant catalysts: the high methanol tolerance of Pt–Co/C electrocatalysts during the ORR is ascribed to the low activity of the binary electrocatalysts for methanol oxidation, arising from a composition effect[35]. Thereby, a cobalt atomic fraction of 0.15 appears to be enough to improve the methanol tolerance of these binary electrocatalysts.

Mixed reactant fuel cell

The methanol tolerance of $RuSe_x$-based catalysts (or similar compositions based on rhodium sulfides RhS_x) has been used in a new approach towards a novel class of direct methanol fuel cells, so-called compact mixed reactant DMFCs[36,37]. The architecture of these fuel cells eliminates the need for conventional flow field or separator plates between each cell: a bipolar, series-connected stack is constructed by placing the perforated, conventional MEAs coated with the selective catalyst in direct contact with each other; a porous carbon backing layer is brought in between each MEA acting as the electrical interconnection of the different cells. An oxygen-enriched aqueous methanol solution flows through the different layers; the oxygen respectively the methanol reacts on respective electrochemically active layers formed where the selective catalysts are employed. Even if the activity of the new class of catalysts is slightly lower than platinum (80–150 mV more negative

potentials), elimination of the flow-field plates in this way and the ability to use much thinner PEM layers reduces the cell pitch very substantially and enables an order of magnitude increase in volumetric power density, compared to conventional stack architectures. The required tolerance of the catalysts is almost achieved whereas the selectivity of methanol-selective catalysts which do not interact or react with oxygen still bears potential for optimization.

5.2.4 Electrode composition

Similar to electrodes engaged in PEMFCs, the catalyst layer has to be prepared in that way to optimize the formation of the three-phase boundary between catalyst particles, the ionomer and the liquid phase represented by the methanol solution. Maximization of the three-phase boundary, where the electrochemical reaction takes place, ensures the required electronic as well as protonic conductivity, leading to an optimum performance of the DMFC. For the preparation, a catalyst ink is prepared made of the ionomer (usually dissolved Nafion), a solvent and the supported catalyst. Optimizations can be gained by several modifications: variations of the ionomer content directly influence the performance; depending on the catalyst an optimum concentration has been monitored, which is in the range of 25% for platinum ruthenium catalysts[38].

For fuel cell purposes, the catalyst layer can be included in two ways, either distributed to the membrane (catalyst-coated membrane, CCM) or deposited on the gas diffusion media (catalyst diffusion media, CDM). Recent experiments proved higher open circuit voltages (OCV) and higher limiting current densities for CCMs applied as cathodes in DMFCs; CDMs display advantages in the moderate current density region[39]. The morphology of the catalyst layer of CCMs directly influences the performance[40]. A smooth surface without cracks is highly desirable as here the resistance is minimized and a good interfacial contact can be gained. This surface condition can be achieved either by spraying or rolling the catalyst ink on the membrane or post-treatment of the CCM.

An enhancement of the catalytical activity can be reached *in situ* by an electrochemical activation of the catalyst layer[40]. By applying an external current with current densities in the range of 200 mA/cm^2 on an oxygen-free cathode, hydrogen develops at the cathode by reduction of the migrating protons, leading to an overall reaction scheme:

anode: $CH_3OH + H_2O \rightarrow 6H^+ + CO_2 + 6e^-$

cathode: $2H^+ + 2e^- \rightarrow H_2$

sum: $CH_3OH_{anode} + H_2O \rightarrow \text{membrane} \rightarrow 3H_{2,cathode} + CO_2$

The observed increase of activity is explained by a changed microstructure around the catalyst: provoked by the emerging hydrogen bubbles, the polymer

matrix enclosing the catalyst particles features micro-breaks which increase the accessible surface and as a direct consequence the utilization of the catalyst. An increase of the electrochemical surface area of the catalyst has not been observed; the activation is supposed to increase the number of sites where the three-phase boundary between electrolyte, polymer and catalyst is optimized and the reaction can take place. Depending on the kind of catalyst an increase in the range of up to 60 mV can be monitored. The same behaviour has been observed in hydrogen-driven PEM fuel cells; here an oxygen-free cathode is reached by purging the electrode with nitrogen.

5.3 Gas diffusion media

As stated in Chapter 4 the gas diffusion layer (GDL) is the mediator between the nanostructured electrode and the flow field which has structures in the mm range. On the cathode side, the requirements of the GDLs as employed in DMFCs and PEMFCs are very similar. The prevention of flooding is more critical than in a PEMFC since the water permeates at a much higher rate from the anode side to the cathode side, caused by an increased concentration gradient of liquid water; the excess liquid water has to be removed in order to provide free pathways for the oxygen to the electrochemical active region inside the electrode. An in-detail explanation of cathodic GDL materials will be skipped and the reader is referred to Chapter 4. When considering diffusion media for the anode, we will focus on liquid fueled DMFCs which require a different spectrum of properties from PEMFCs. For higher temperatures, when the reactant methanol is supplied in gas phase, there is not too much difference between the GDLs employed in PEMFCs and DMFCs.

In addition to the tasks of a GDL in a PEMFC the GDL in a DMFC has to provide pathways for the water/methanol mixture on the anode side. Furthermore the GDL is responsible for the removal of the CO_2. The CO_2 evolution in the liquid-fueled DMFC on the anode side leads to complicated two-phase flow phenomena, resulting in a more complex fuel supply and product removal than in a PEMFC.

Summarizing this initial overview, the task of the GDLs in a DMFC is even more complex than that in a PEMFC especially when considering the water management inside the GDL; in addition, the interface GDL/flow-field channel requires special attention as this is one of the key factors as well for the transport of CO_2 bubbles and the synchronous intrusion of methanol.

5.3.1 Transport properties inside a gas diffusion layer

The mass transport inside a DMFC is very complex, especially on the anode side. Methanol has to be transported through the GDL to the electrodes, where it will react and be consumed. Carbon dioxide is produced according

to Faradays law at the catalyst layer. In order to avoid blockage of the reaction area and blocking of the pores by accumulation of the product gases inside the GDL, carbon dioxide has to be removed continuously. Figure 5.4 shows a schematic drawing of the two-phase transport at the anode side in a very simplified manner.

As shown by different groups one can in general distinguish between different two-phase flow characteristics inside a micro-channel[42–44]; in this case, the microchannels are anodic flow channels. One can imagine that the flow characteristics have a strong impact on the transport properties inside the GDL because the interface between GDL and flow field cannot be neglected. Three different two-phase flow regimes are presented in Fig. 5.5.

Looking specifically at a DMFC, several authors used cells with a transparent

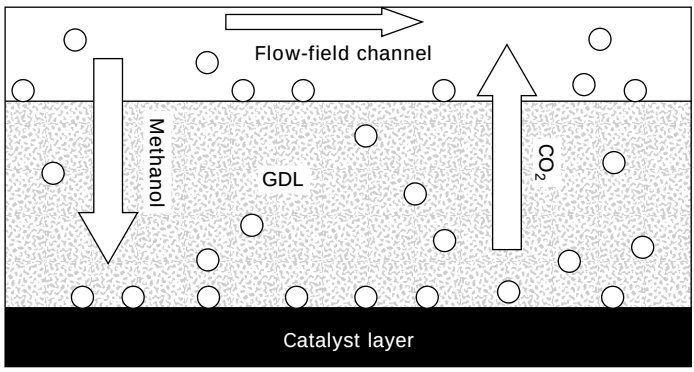

5.4 Schematic drawing of two-phase flow on the anode side of a DMFC. Methanol diffuses from the flow-field channel to the catalyst layer where it will be converted electrochemically. The product CO_2 has to be transported to the channel in order to be removed from the cell.

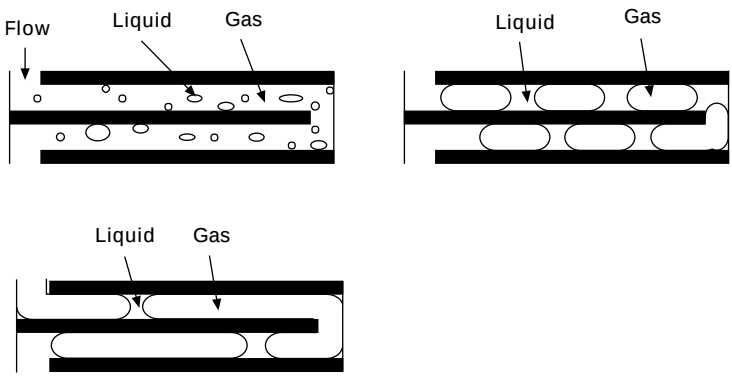

5.5 Different two-phase flow characteristics in a channel, top left: bubbly flow, top right: wedging flow, bottom: slug flow.

cover in order to observe the carbon dioxide evolution and the two-phase flow behavior visually[45–48]. Bubbly flow, wedging flow or slug flow could be observed on the anode side. Furthermore some preferred points could be identified on top of the GDL where the gas evolved. This transition process can be compared with the liquid water evolution in PEMFCs and the eruption of water droplets where preferred pathways for water inside the GDL have been observed (see Chapter 4).

One drawback of the method is that there is a strong impact on the cell; the performance will be disturbed owing to the transparent and mostly non-conductive material which in most cases exhibits also different surface properties than the underlying channel material. Nevertheless the results give a deep insight in the flow and gas-evolving characteristics. More advanced techniques such as neutron radiography allow for an examination of the liquid transport in an undisturbed cell. Results of such an *in situ* observation of slug flow inside a running DMFC are presented in Fig. 5.6. The channels of a serpentine flow field are filled with the aqueous methanol solution which, owing to the high absorption coefficient, imposes a strong hindrance for neutrons resulting in a weak transmission and therefore dark shadows. Once CO_2 bubbles evolve, the aqueous solution is replaced by the gas phase; thereby, the thickness of the highly absorbing liquid is reduced. Normalization of the images with respect to an image with completely filled channels (liquid flow through the flow field without an external load and therefore no net gas production) results in a representation of the carbon dioxide bubbles

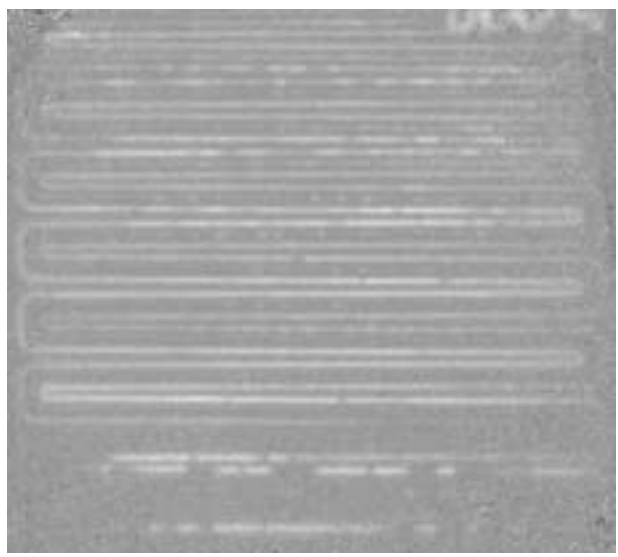

5.6 In situ observation of slug flow in a DMFC by means of neutron radiography. White spots denote gas-filled channels of the flow field.

as bright spots. Examination of the available results show that the two-phase flow characteristic depends on the current density of the cell. Furthermore the surface properties of the channel material, the channel geometry and the GDL surface play a crucial role because of the different wetting properties of water/methanol especially in the wedges of the channel, which will, however, not be considered here in more detail; most of the mentioned effects are also described in the literature[49–51].

A description of the two-phase flow inside the GDL of the anode side appears to be very complicated as well. The methanol of the methanol/water mixture diffuses along the gradient caused by the methanol 'source' in the channel and the 'sink' on the electrochemically active layer through the pores of the gas diffusion media. As shown in the respective section on GDLs in Chapter 4, the 'through plane' porosity and the tortuosity of the material have to be taken into account in order to calculate the diffusion flux. The porosity is in general a material property, whereas the tortuosity is a parameter which can depend on the flow conditions and can be shown by computer simulations[52–54]. In the case of a DMFC most of the carbon dioxide will evolve in the form of gas bubbles and only a small fraction will dissolve in the liquid. The gas bubbles will occupy pores or parts of the pores and therefore reduce the methanol diffusion as the effective porosity will be reduced (the term effective porosity refers to the percentage of pores in which methanol transport can take place in the liquid phase). This would only be a volume-reducing effect which is a function of the gas amount inside the GDL. On the other side the gas bubbles will also block some pathways for the methanol which means that the methanol might diffuse longer pathways. This effect results in a change of the tortuosity. These two effects reduce the methanol transport inside the GDL. The most influential effect on the transport properties has not been determined and studied in more detail and requires intensive research.

5.3.2 Treatment of gas diffusion layer materials

One of the key problems in a liquid DMFC which lead to efficiency losses is the methanol crossover from the anode side to the cathode side. In order to decrease this crossover effect, GDL materials are treated with PTFE. Figure 5.7 shows the effect of the PTFE treatment of the GDL on the methanol crossover which is monitored by means of the cell performance.

In this example the DMFC with the untreated GDL shows the highest performance. When the anodic GDL is treated with PTFE (25% PTFE, which represents almost the upper limit of impregnation of the GDL), the cell shows a slightly lower performance[55–57]. When regarding the methanol crossover, the situation changes almost completely and the following situation is observed: as usual the methanol crossover decreases with increasing current

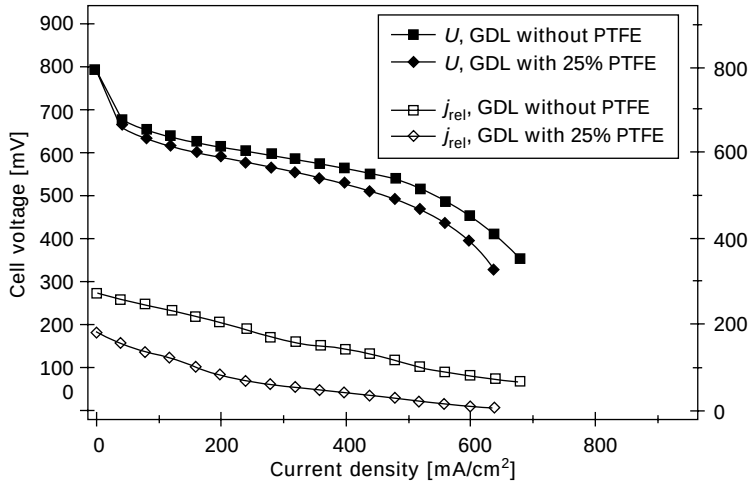

5.7 Performance curves for a DMFC with different polytetrafluoroethyene (PTFE) content in the GDL and methanol crossover measured in terms of equivalent current density.

density; however, in the whole current density region the methanol crossover is higher for the cell with untreated PTFE which in turn leads to performance losses due to the formation of mixed potentials.

The power density of the cell itself is highest when operated with the untreated GDL. On the other hand, considering the complete system, the system efficiency is low because of the tremendous methanol loss owing to the formation of mixed potentials induced by crossover of methanol. A reduction of the methanol loss even at the cost of cell voltage can therefore increase the overall system efficiency.

A thorough understanding of this effect has not yet been reached because of the complicated interaction between the flow properties, the surface and the structural properties inside the complex GDL. In order to understand these complex behavior two-phase flow processes inside the cell further research and development is necessary. Besides experimental work, modeling and simulation proved to be very helpful in understanding the complex phenomena as demonstrated by several authors (see, for example, Wang[58] and references therein).

5.4 Flow-field design

5.4.1 Direct methanol fuel cells with gaseous fuel supply

DMFCs are working with comparable materials to PEMFC. If a gaseous fuel supply is used, all considerations from PEMFC can be directly applied to DMFC (anode and cathode, please compare with Chapter 4).

5.4.2 Direct methanol fuel cells with liquid fuel supply

Most DMFCs are working with a liquid fuel supply at the anode. A general survey on this DMFC type is given in, for example, Mergl *et al.*[59] The requirements of this operation mode on flow-field design are discussed in the following subsections.

Anode flow field

At the anode side of liquid-supplied DMFCs, the requirements are different from those discussed for PEMFC. The DMFC anode flow field should

- allow CH_3OH supply in the liquid phase;
- allow CO_2 removal (gaseous and liquid phase);
- produce a well-distributed flow rate along the cell if a water/CH_3OH mixture is pumped through the cell.

Also, more coarse structures are preferred for this case which allow a simple removal of CO_2 bubbles. It is expected that structures with proven quality in the electrolyzer field show also good results for DMFC anodes. For low current densities (less than 0.1 A/cm^2) and low pumping rates (equivalent to high methanol utilization degrees) and also including so-called self-breathing cells it is expected that a simple parallel flow field with 1.5 mm channel dimension, vertical channel direction and fuel upstream leads to a well-performing cell. In this case, bubble removal is supported by gravity even if fuel velocity does not allow forced bubble removal. Also a pattern flow field (compare with Chapter 4, Fig. 27) may be used for this application. If higher fuel velocities are available, a serpentine flow field with a low degree of parallelization may be used, obtaining a forced bubble removal by convection. Wong *et al.*[60] discuss in detail the influence of channel width with respect to the effect of CO_2 bubbles on mass transport and cell performance. Experiments were performed using a 1 M methanol solution at 30 and 60 °C. In this investigation, the channel depth was fixed at 0.5 mm. The rib width was changed with channel width such that 49% open area was kept for all flow fields. A flow speed in the channels of 0.6 cm/s or more should be kept for forced bubble removal (calculated from Wong *et al.*[60]) For higher current densities, a channel width of 0.58 mm (see above for boundary conditions) was found to lead to best performance. Both smaller and broader channels lead to lower performance, if current densities above 0.1 A/cm^2 are used. From model calculations of liquid fed DMFC anode[61], mass transport was found to be less limited for the 0.7 mm channel width than for the 2 mm channel width. On the other hand, for low current densities (below approx. 100 mA/cm^2), flow-field dimensioning may be more coarse. For that case,

negligible performance changes were observed by Wong *et al.*[60] for dimensions of up to 1 mm channel width. Jörissen *et al.*[62] used a serpentine flow field with 1 mm channel depth and width and 1 mm distance between channels and obtained current densities of up to 0.5 A/cm^2 (@ 0.5 V, 2.5 bar). Litterst *et al.*[63] described a concept with T-shaped anode channels, where the increasing T-depth (from inlet to outlet) should improve CO_2 bubble movement. The effect of CO_2 bubbles on DMFC performance is discussed by Kulikovsky[64].

Proper flow-field dimensioning is a result of many parameters (operating temperature, methanol concentration, pumping rate, electrode and GDL selection), such that the flow-field design should be fine tuned with respect to the materials and operating parameters used. Scott *et al.*[65] reported the dependence of CO_2 bubble formation for different GDLs. It was found that the use of a carbon cloth GDL led to significantly less bubble coalescence than carbon paper GDL. A low tendency of bubble coalescence leads to a more stable cell performance.

Cathode flow field

For DMFCs supplied with methanol in a liquid stage, all topics discussed for PEMFC are also valid for DMFC cathode flow fields. There is one big difference between PEMFC and DMFC cathode which is caused by the supply of an aqueous fuel: PEMFCs are usually operated with moderate to high oxygen utilization degrees to (a) save auxiliary energy and (b) prevent the cell from drying out. For DMFC, the water household requirements are completely different from PEMFC as in almost all cases, huge amounts of water permeating from the anode (electro-osmotic drag effect plus diffusion) have to be removed from the cathode side to prevent electrode flooding. Special attention has to be paid in this regard also to the microporous layer which has been elucidated in more detail in the previous section on GDLs. Therefore, DMFC cathodes are usually operated with lower oxygen utilization degrees (less than 10 to 40 % instead of 30 to 60 %) and without additional humidification. Therefore, the cathode flow field should be able to (a) remove condensate and (b) allow high flow rates with low pressure difference. The influence of operating pressures on DMFC system performance is discussed by Gogel *et al.*[66]. Usually, the operating pressure should be near ambient or up to 1 bar with respect to optimal power and system efficiency. All design guidelines given in Chapter 4 in the flow-field section stay valid but should be reconsidered under the lower current density requirements for DMFC. This leads often to a simple parallel or serpentine flow field at the cathode side having a somewhat coarser flow-field structure than a standard PEMFC. Rib and channel dimensions are usually in the range of 1–1.5 mm instead of 0.5–1 mm as often used for PEMFC. This is even favored in a so-called self-breathing cell. A self-breathing cell does not include any blower or vent for

the air supply and is working by diffusion and/or convection from air to and from the electrode. Figure 5.8 shows one example of such a cell.

5.5 DMFC system architecture

DMFCs anodically oxidize methanol (CH_3OH) in the presence of water in a multi-step reaction to CO_2 and protons. Mechanistic details have been discussed earlier in this chapter.

$$CH_3OH + H_2O \rightarrow CO_2 + 6\ H^+ + 6\ e^-$$

As stated already in Section 5.2.1 it is evident that the complete oxidation of methanol requires the presence of water at the anode.

Most present day DMFC designs are based on polymer membrane fuel cell technology using acid electrolyte membranes, with perfluorinated polymer sulfonic acid membranes being the most common electrolytes. It is well known that these membranes achieve their optimum conductivity at high degrees of water uptake. Due to their similarity, methanol can substitute water in the membrane. Therefore, methanol is also involved as a solvating agent in the transport of protons. As a consequence, methanol is mobile inside the electrolyte membrane and can be transported through the membrane by diffusion and by electro-osmotic drag. Methanol and water transport to the cathode through the electrolyte membrane is one of the key challenges to be solved by the DMFC system design. Methanol will form a mixed potential at the cathode thus reducing the overall cell voltage.

DMFC cells and stacks can be designed and operated according to two different fuel supply concepts:

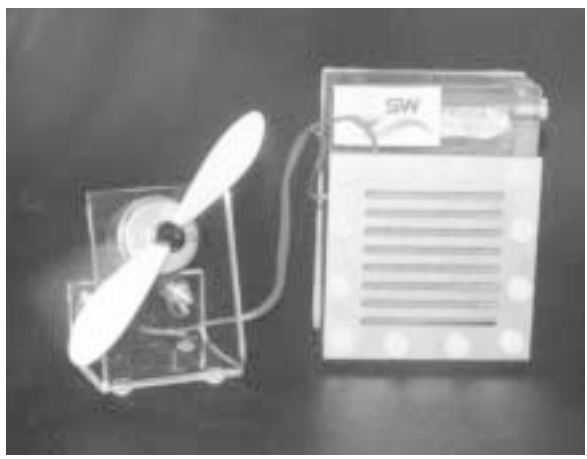

5.8 Self-breathing DMFC unit (ZSW) with more than 20000 h total operation time.

1. DMFC with fuel supply from the vapor phase
2. DMFC with fuel supply from the liquid phase

5.5.1 Vapor-fed DMFCs

Methanol and steam supply from the vapor phase leads to a similar system design as in the case of hydrogen operated PEFCs. In addition the DMFC system needs a fuel mixing unit, an evaporator for the aqueous methanol mixture, as well as recovery units for product water at the cathode side and methanol at the anode side. The methanol recovery unit also fulfils the function of CO_2 separation. Figure 5.9 shows a simplified layout for a vapor-fed DMFC system. Although vapor-fed DMFC stack operation is similar to the operation of a gas-fed PEFC, it is evident that the fuel handling subsystem is more complicated. It is composed of several liquid handling components allowing for precise control of the methanol concentration fed to the evaporator. For efficiency reasons, the energy required for fuel evaporation must be recovered from the overall system heat flow.

The potential of vapor-fed DMFCs has been investigated for automotive applications. However, high noble metal demand, limited power density and complicated balance of plant led to the conclusion that DMFCs are not a near term solution for full size vehicle propulsion.

5.5.2 Liquid-fed DMFCs

DMFCs are an interesting option, e.g. in portable power generation, light traction, etc. For these applications, most system designs rely on feeding fuel from the liquid phase.

Passive DMFCs

The simplest approach to a liquid-fed DMFC is to supply an aqueous solution of methanol directly to the fuel cell anode and use it in combination with an air breezing cathode without any auxiliary equipment in a so called passive design.

Due to the similarity of methanol to water giving rise to a high permeability of methanol through the electrolyte membrane, it is well known that the voltage of a liquid-fed DMFC decreases with increasing methanol concentration despite the expected lowering of the anode potential by Nernst's Law. Figure 5.10 shows the effects observed when changing the methanol concentration in a DMFC from 0.5 moles/l to 0.8 moles/l.

Initially, the cell voltage increases significantly for a short time. During this time, the increase in methanol concentration decreases the anode potential thus increasing the cell voltage. After a short time, the cell voltage starts to

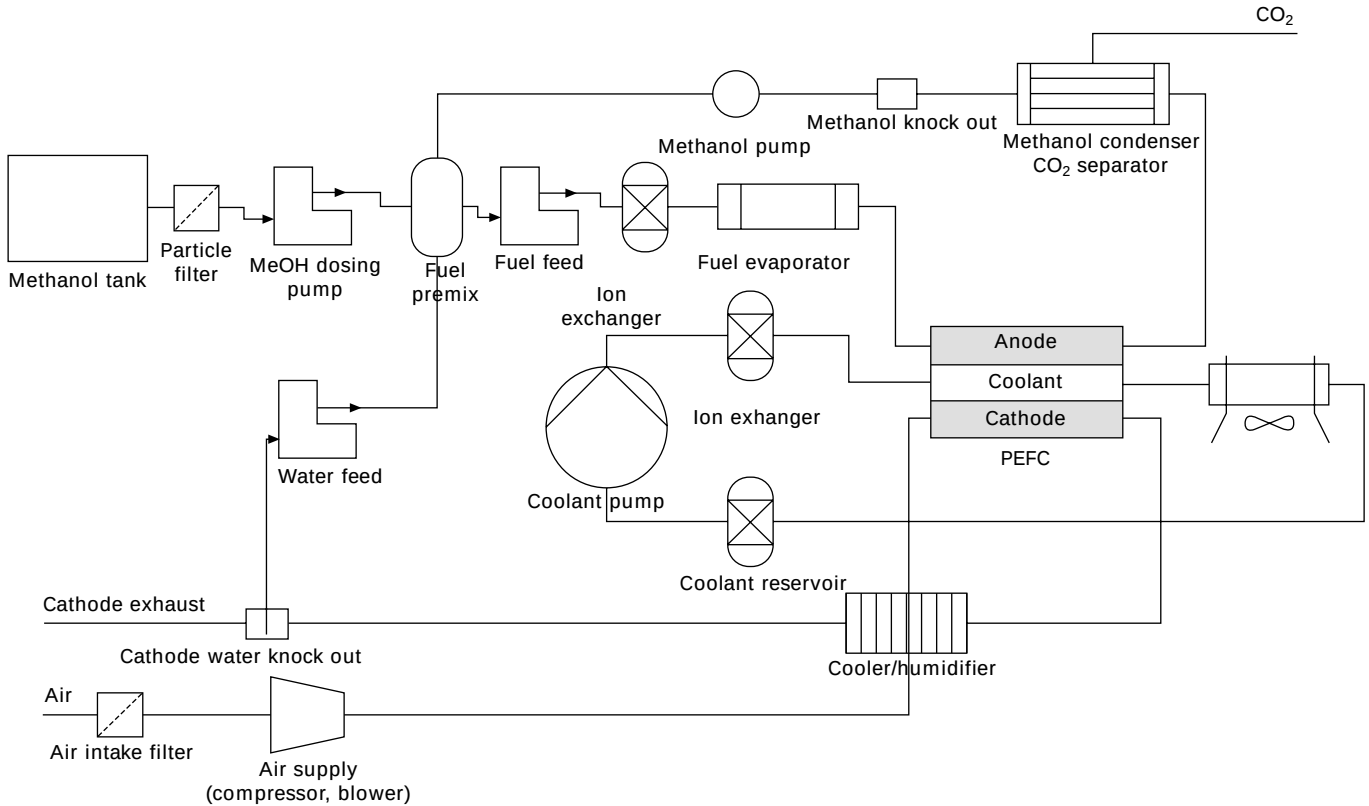

5.9 Simplified vapor-fed DMFC system layout. No sensors are shown.

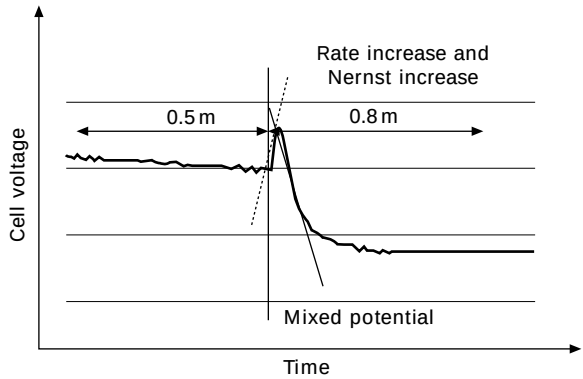

5.10 Change of a DMFC single cell voltage under current flow when increasing the methanol concentration from 0.5 moles/l to 0.8 moles/l.

drop again. This effect begins to be dominant after the increased methanol concentration leads to an increase of methanol transport through the electrolyte membrane caused by diffusion and electro-osmotic drag. Eventually, the cell voltage settles to a new steady state voltage lower than at the beginning. The absolute values of cell voltage and time for voltage change upon change of the fuel concentration are dependent on the selection of the electrolyte membrane as well as the transport properties of the anode backing. It is evident that lowering the water and methanol transport through the anode backing will also lower the methanol crossover through the membrane at the expense of the maximum current that can be achieved. Proper design of the transport properties of the electrode backing including barrier layers and the electrolyte membrane even allow the operation of a passive DMFC on pure methanol. Passive DMFCs also face the challenge of cathode water management. In general, passive DMFCs will typically be operated in low power devices.

Actively operated DMFCs

In order to achieve power above 10 W from a DMFC, actively operated DMFC systems are typically used. The system can be broken down in modules (Fig. 5.11).

The function of the system modules are similar to the ones found in PEFCs. However, there are distinct differences in PEFC and DMFC systems concerning heat and water management:

- Since methanol is fed to the fuel cell in the liquid phase, no separate cooling circuit is required to remove heat from the system.
- When feeding a methanol water mixture to the anode, reaction water,

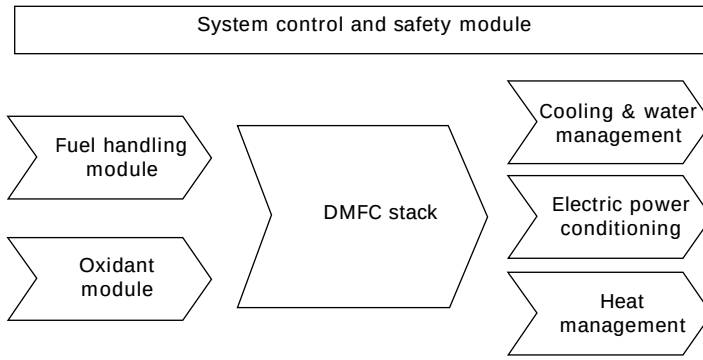

5.11 System modules typically found in actively operated DMFC.

and almost all water moved by electro-osmotic drag and by diffusion will be released at the cathode making it vulnerable to flooding.

- If all water transported to the cathode is evaporated the waste heat from the cell in some cases would not be sufficient to maintain the temperature.

Figure 5.12 shows a simplified system layout for a liquid-fed DMFC system. In order to benefit from the high energy density of methanol, it is necessary to operate the DMFC system from a supply of pure methanol. However, since water is required in the electrochemical reaction and in order to suppress the formation of mixed potentials at the cathode, the anode should be fed with aqueous methanol. Therefore, a mixing unit for water and methanol needs to be present in the system.

Fortunately, DMFC systems are rather tolerant to small deviations in fuel concentration. In case an excess methanol is supplied to the mixing tank, it will eventually be removed by transport through the electrolyte membrane. Since a significant amount of water is transported to the cathode, it has to be recovered by passing the cathode exhaust through a heat exchanger and a water knock out device. Depending on the intended application for the fuel cell system, water condensation and knock out must be independent of the system orientation. When operated in a hot environment, with loss of water from the fuel loop, the use of methanol water premix is recommended in order to keep the methanol concentration in an acceptable range.

CO_2-separation from the anode loop is another challenge in liquid-fed DMFC operation. Fuel and water losses are to be expected from the CO_2 separator and have to be dealt with by the system.

In general, liquid-fed DMFCs are operated at lower power density than vapor-fed DMFCs and PEFCs operated on hydrogen. Due to their simpler system design, liquid-fed DMFC systems are advantageous particularly for applications having only a low power demand.

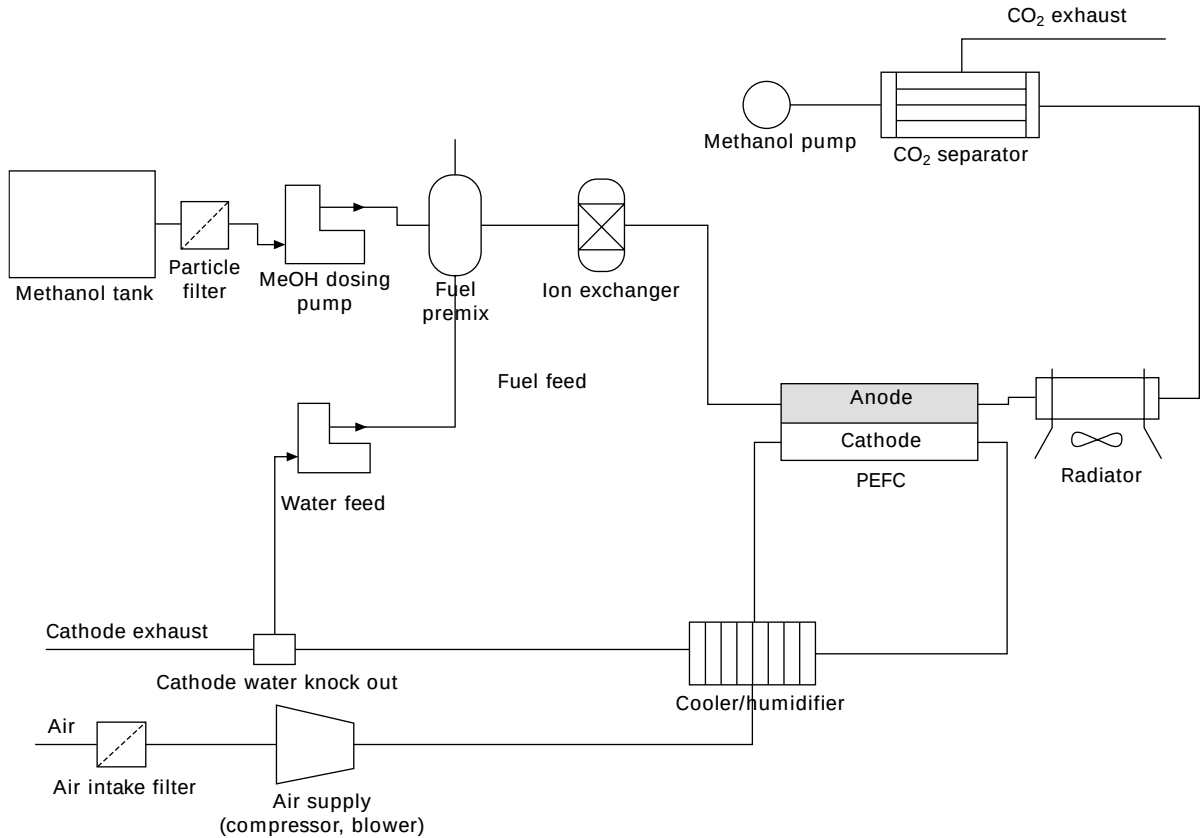

5.12 Simplified system layout of a liquid-fed DMFC.

5.6 Conclusions

In general, DMFC flow-field design is comparable with PEMFC using a somewhat coarser dimensioning. Special considerations have to be made for the liquid anode side and the low air utilization cathode side of the DMFC.

5.7 References

1. www.sfc.com
2. Q. Liao, X. Zhu, Z. Zheng, Y. Ding, *J. Power Sources* **171** (2007) 644–651
3. Y.D. Ding, Q. Laio, X. Zhu, L.J. Bao, *J. Power Eng.* **26** (2006) 599
4. H. Wang, C. Wingender, H. Baltruschat, M. Lopez, M.T. Reetz, *J. Electroanal. Chem.* **509** (2001) 163.
5. D.C. Azevedo, W.H. Lizcano-Valbuena, E.R. Gonzalez, *J. New Mat. Elect. Syst.* **7** (2004) 191
6. Z. Jusys, R.J. Behm, *J. Phys. Chem. B* **105** (2001) 10874
7. Z. Jusys, J. Kaiser, R.J. Behm, *Langmuir* **19** (2003) 6759
8. C. Korzeniewski, C.L. Childers, *J. Phys. Chem. B* **102** (1998), 489
9. T. Housmans, M.T.M. Koper, *J. Phys. Chem. B* **107** (2003) 8557
10. J.-M. Léger, *J. Appl. Electrochem.* **31** (2001) 767
11. Ch. Hartnig, E. Spohr, *Chem. Phys*. **319** (2005) 185
12. J. Kua, W.A. Goddard III, *J. Am. Chem. Soc*. **121** (1999) 10928
13. S.K. Desai, M. Neurock, K. Kourtakis, *J. Phys. Chem. B* **106** (2002) 2559
14. Y. Ishikawa, M.-S. Liao, C.R. Cabrera, *Surf. Sci*. **463** (2000) 66
15. J. Greeley, M. Mavrikakis, *J. Am. Chem. Soc*. **124** (2002) 7193; **126** (2004) 3910
16. M. Neurock, S.A. Wasileski, D. Mei, *Chem. Eng. Sci*. **59** (2004) 4703
17. Q. Ge, S. Desai, M. Neurock, K. Kourtakis, *J. Phys. Chem. B* **105** (2001) 9533
18. Y. Okamoto, O. Sugino, Y. Mochizuki, T. Ikeshoji, Y. Morikawa, *Chem. Phys. Lett*. **377** (2003) 236
19. F. Raimondi, G.G. Scherer, R. Kötz, A. Wokaun, *Angew. Chem. Int. Ed.* **44** (2005) 2190
20. L.P.R. Profeti, F.C. Imoes, P. Olivi, K.B. Kokoh, C. Coutanceau, J.-M. Léger, C. Lamy, *J. Power Sources* **158** (2006) 1195
21. H. Gasteiger, N. Markovic, P.N. Ross, E.J. Cairns, *J. Phys. Chem*. **97** (1993) 12020
22. Z. Jusys, J. Kaiser, R.J. Behm, *Electrochim. Acta* **47** (2002) 3693
23. M.-S. Liao, C.R. Cabrera, Y. Ishikawa, *Surf. Sci*. **445** (2000) 267
24. Y. Okamoto, *Chem. Phys. Lett.* **395** (2004) 279
25. M. Christov, K. Sundmacher, *Surf. Sci.* **547** (2003) 1
26. P. Waszczuk, J. Solla-Gullón, H.-S. Kim, Y.Y. Tong, V. Montiel, A. Aldaz, A. Wieckowski, *J. Catalysis* **203** (2001) 1
27. L.S. Sarma, C.-H. Chen, G.-R. Wang, K.-L. Hsueh, C.-P. Huang, H-S. Sheu, D.-G. Liu, J.-F. Lee, B.-J. Hwang, *J. Power Sources* **167** (2007) 358–365
28. W.D. King, J.D. Corn, O.J. Murphy, D.L. Boxall, E.A. Kenik, K.C. Kwiatkowski, S.R. Stock, C.M. Lukehart, *J. Phys. Chem. B* **107** (2003) 5467
29. A. Lima, C. Coutanceau, J.-M. Léger, C. Lamy, *J. Appl. Electrochem*. 31 (2001) 379
30. K.-W. Park, J.-H. Choi, S.-A. Lee, C. Pak, H. Chang, Y.-E. Sung, *J. Catalysis* **224** (2004) 236
31. T. Schultz, S. Zhou, K. Sundmacher, *Chem. Eng. Techn.* **12** (2001) 1223

32. N. Alonso-Vante, P. Bogdanoff, H. Tributsch, *J. Catalysis* **190** (2000) 240
33. G. Zehl, G. Schmithals, A. Hoell, S. Haas, Ch. Hartnig, I. Dorbandt, P. Bogdanoff, S. Fiechter, *Angew. Chem. Int. Ed*. **46** (2007) 7311
34. K. Han, J. Lee, H. Kim, *Electrochim. Acta* **52** (2006) 1697
35. J.R.C. Salgado, E. Antolini, E.R. Gonzalez, *Appl. Catal. B*: **57** (2005) 283; E. Antolini, J.R.C. Salgado, E.R. Gonzalez, *Appl. Catal. B* **63** (2005) 137
36. CMR Fuel Cells plc, CB2 5GG Cambridge, UK
37. D.C. Papageorgopoulos, F. Liu, O. Conrad, *Electrochim. Acta* **52** (2007) 4982
38. O.A. Khazova, A.A. Mikhailova, A.M. Skundin, E.K. Tuseeva, A. Havranek, K. Wippermann, *Fuel Cells* **2** (2002) 99
39. F. Liu, C.-Y. Wang, *Electrochim. Acta* **52** (2006) 1417
40. Z. Wang, Y. Liu, V.M. Linkow, *J. Power Sources* **160** (2006) 326
41. C. He, Z. Qi, M. Hollett, A. Kaufman, *Electrochem. Solid-State Lett*., **5** (2002) A181
42. J.L. Xu, P. Cheng, T.S. Zhao, *Int. J. Multiphase Flow* **25** (1999) 411
43. T. Cubaud, U. Ulmanella, C-M. Ho, *5th International Conference on Multiphase Flow*, Yokohama, Japan May 30 to June 4, 2004
44. A. Kawahara, P.M.-Y. Chung, M. Kawaji, *Int. J. Multiphase Flow* **28** (2002) 1411
45. C.W. Wong, T.S. Zhao, Q. Ye, J.G. Liu, *J. Electrochem. Soc*. **152** (2005) A1600
46. P. Argyropoulos, K. Scott, W.M. Taama, *Electrochimica Acta* **44** (1999) 3575
47. H. Yang, T.S. Zhao, Q. Ye, *J. Power Sources* **139** (2005) 79
48. Q. Liao, X. Zhu, X. Zheng, Y. Ding, *J. Power Sources* **171** (2007) 644
49. P. Concus, R. Finn, *Proc. Natl. Acad. Sci.* **63** (1969) 292
50. R. Finn, *Notices of the AMS* **46** (1999) 770
51. K. Rejmer, S. Dietrich, M. Napiorkowskii, *Phys. Rev. E* **60** (1999) 4027
52. J.S. Andrade Jr., M.P. Almeira, J. Mendes Filho, S. Havlin, B. Suki, H.E. Stanley, *Phys. Rev. Lett*., **79** (1997) 3901
53. A. Klemm, Transport in percolation clusters: analysis by means of NMR and numerical simulations, dissertation, University of Ulm, Germany (2002)
54. Z. H. Wang, C. Y. Wang, *J. Electrochem. Soc*., **150** (2003) A508
55. V. Gogel, T. Frey, Z. Yongsheng, K.A. Friedrich, L. Jörissen, J. Garche, *J. Power Sources* **127** (2004) 172
56. M. Neergat, K.A. Friedrich, U. Stimming, in: *Handbook of Fuel Cells – Fundamentals, Technology and Application*, Eds. W. Vielstich, A. Lamm, H.A. Gasteiger, Vol. 4, Chapter 63, 2003, John Wiley & Sons
57. A. Oedegaard, C. Hebling, A. Schmitz, S. Møller-Holst, R. Tunold, *J. Power Sources* **127** (2004) 187
58. C.-Y. Wang, *Chem. Rev*. **104** (2004) 4727
59. J. Mergel, P. Bogdanoff, E. Gülzow, *Niedertemperatur-Brennstoffzellen – Stand und Perspektiven der DMFC*, FVS Themen 2004
60. C.W. Wong, T.S. Zhao, Q. Ye, J.G. Liu, *J. Electrochem. Soc*. **152** (2005) A1600
61. Z.H. Wang, C.Y. Wang, *Proc. of Direct Methanol Fuel Cell Symposium*, 199th Electrochem. l Soc. Meeting, Washington DC, March 2001
62. L. Jörissen, V. Gogel, J. Kerres, J. Garche, *J. Power Sources* **105** (2002), 267
63. C. Litterst *et al*., *J. Micromech. Microeng*. **16** (2006) 248
64. A.A. Kulikovsky, *Electrochim. Acta* **51** (2006) 2003
65. K. Scott, W.M. Taama, P. Argyropoulos, *J. Power Sources*, **79**(1999) 43
66. V. Gogel, Th. Frey, J. Scholta, L. Jörissen, 93. *Bunsen-Conference*, Schwerin, Germany, 16–17 June 2005

6

Phosphoric acid fuel cells

T F FULLER and K G GALLAGHER,
Georgia Institute of Technology, USA

6.1 Introduction

Advances in materials have largely driven the development of fuel cells, and phosphoric acid fuel cells (PAFCs) are no exception. Details of the early history have been presented elsewhere,[1,2] and only a few of the significant advances will be considered here. Sir William Grove, who invented the fuel cell in 1839, recognized from the outset the need for intimate contact between the gas, the electrolyte, and the solid electrode. Grove called this the 'notable surface of action.' The liquid nature of the phosphoric acid electrolyte makes establishing a stable three-phase interface critical to achieving good power density and to the long-term operation of PAFCs, particularly at high current densities. Materials, structures, and processing methods to improve and stabilize this contact have been critical in the development of PAFCs.

6.1.1 Historical perspective

About one hundred years after Grove's discovery, Francis Bacon took up the hydrogen/oxygen fuel cell. Bacon, the father of the modern fuel cell, chronicled its early development,[3] and his contributions to improving the electrode structure were seminal. Previously, the electrochemical reactions had been limited to a small interfacial area, resulting in low limiting currents because of the poor access of gases to the catalysts. Bacon developed alkaline-cell electrodes with controlled porosity and almost immediately obtained current densities in excess of 1 A/cm^2 at 0.6 V at temperatures around 230 °C. This concept was subsequently extended to PAFCs. The theme of controlled porosity has proved to be critical for the development of all fuel cells with liquid electrolytes.

Bacon believed that successful commercialization could only be accomplished with non-noble metal catalysts. Many still share this opinion. However, a nonprecious metal catalyst that is stable in aqueous acid and able to reduce oxygen efficiently has yet to be found. It is worth noting that in

contrast to proton exchange membrane fuel cells (PEMFCs) for automotive applications, the cost of the platinum catalyst is not a primary barrier to commercialization of PAFCs for stationary applications. The more important challenge with PAFCs has been corrosion of materials of construction and the high cost of producing these materials.

6.1.2 Accomplishments

Despite early and continuing success in space for the AFC, the intensity of development for military power and commercial applications has been less consistent. The first development focused on commercial applications was associated with the Team to Advance Research on Gas Energy Transformation (TARGET) program in the late 1960s and early 1970s. This effort was sponsored by both gas and electric utilities. Although many PAFCs were demonstrated, further commercial developments were hampered by natural gas supply problems in the early 1970s. Through the 1970s an electric utility-sponsored effort to develop a dispersed generator power plant resulted in a 1 MW pilot plant that operated between 1976 and 1977. In the mid-1970s formation of the Department of Energy (DOE), the Electric Power Research Institute (EPRI), and the Gas Research Institute (GRI) intensified development of all types of fuel-cell power plants, leading to testing of a 4.8 MW unit in the early 1980s and a fleet of 40 kW power plants in the mid-1980s.

In 1992, the first commercial power plant, the 200 kW PC25™, began operation. This was a PAFC that operated at about 200 °C and was fueled by natural gas. Some of the early power plants have operated in excess of four years without overhaul, and a number of units operated continuously for more than one year. Figure 6.1, adapted from Fuller *et al*.[4] shows the operating experience for the 200 kW commercial PAFC from UTC Fuel Cells. This design was introduced about a decade ago. More than 200 units have been delivered and now more than 7 million hours of field experience have been accumulated. The majority of these units are still running. More than 20 systems have gone more than 40 000 hours or 5 years.

In this PAFC stack design more than 200 cells are connected in series in a bipolar stack arrangement. Thus a single cell failure causes the stack to fail. Because of this, many have questioned whether one can achieve the required reliability of individual cells so that adequate system reliability is obtained. The experience of PAFC proved that this is not an insurmountable challenge. It is clear that the design is relatively robust, but compared with alternative power generating technologies, such as gas turbines, PAFCs are expensive. Just as initial materials developments have allowed the development of reliable fuel-cell stacks and systems, new materials will be instrumental in extending the life and lowering the cost of future systems.

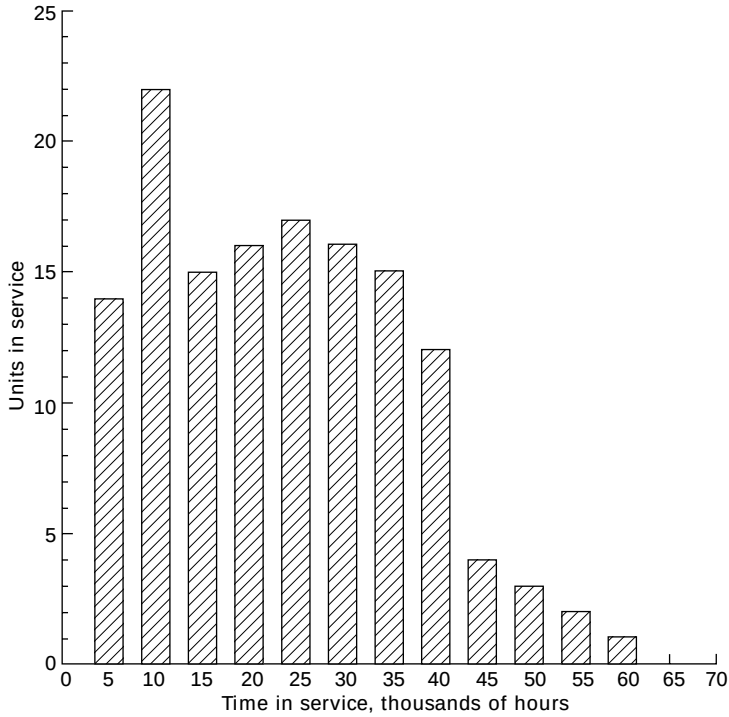

6.1 Field data for the commercial PAFC unit and operating experience of the fleet of PC25 C™ systems. Data adapted from Fuller *et al.*[4] and reproduced by permission of The Electrochemical Society.

6.2 General fuel-cell design issues

6.2.1 Nature of the electrolyte and importance to cell and stack design

Fuel cells are distinguished by their temperature of operation and the type of electrolyte – for good reason. More than anything else, the nature of the electrolyte defines the design of the individual cell, the cell-stack assembly, and even the fuel-cell system. Appleby[5] summarizes electrolytes used in fuel cells and reminds us that the properties of the electrolyte determine the temperature of operation, the electrocatalysts, the approach to water and thermal management, and the system design. Ultimately, these electrolyte properties also drive the materials challenges. Therefore, understanding the physical and chemical properties of the electrolyte is the natural place to begin.

6.2.2 Concentration and structure

In the phosphoric acid fuel cell, concentrated phosphoric acid serves as the electrolyte, and the temperature of operation is 150–220 °C. At room

temperature, orthophosphoric acid, H_3PO_4, is not usually thought of as a strong acid. As the temperature increases though, the acid becomes successively dehydrated,

$$x\mathrm{H_2O}y\mathrm{P_2O_5} \rightarrow (x\text{–}1)\mathrm{H_2O}y\mathrm{P_2O_5} + \mathrm{H_2O} \qquad 6.1$$

and is corrosive at 200 °C. Within the fuel cell community, the concentration of acid is expressed in percent equivalent of H_3PO_4. A value of $x/y = 3$ corresponds to orthophosphoric acid at 100%. Typical concentrations of acids in operating fuel cells are close to 100%; however, as the acid continues to dehydrate, forming pyrophosphate polymer chains, the concentration as defined here may go above 100%. Jameson offers a good overview of the species present in polyphosphoric acid.[6] As the water is removed, pyrophosphoric acid, $H_4P_2O_7$, is formed, then triphosphoric acid, etc., as shown in Fig. 6.2. Rather than thinking of phosphoric acid as an aqueous electrolyte, under typical phosphoric acid fuel-cell conditions, it is better described as a 'molten acid salt.'[5]

In fuel-cell applications the electrolyte performs three main functions. First it conducts ionic current between the electrodes, second it separates fuel and oxidant, and finally it is integral to the heterogeneous electron

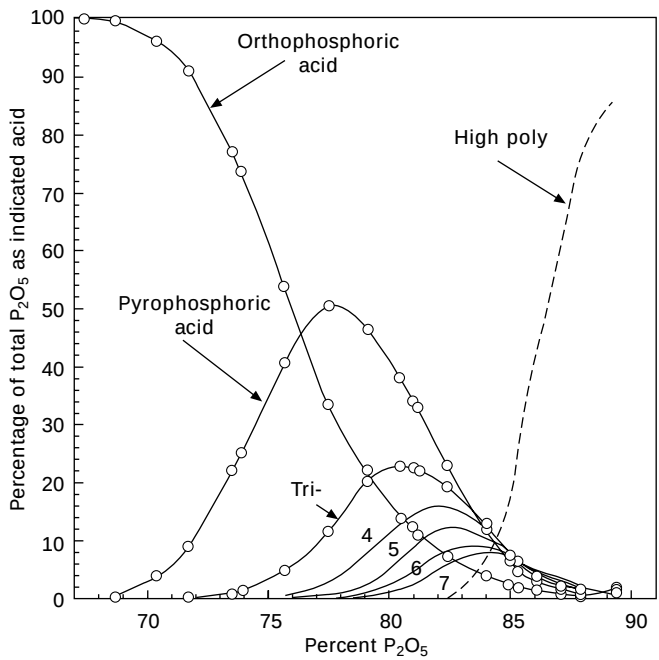

6.2 The composition of strong, phosphoric acid, *J. Chem. Soc.*, 752–759 (1959). Reproduced by permission of The Royal Society of Chemistry.

transfer reactions. Critical design objectives for a fuel-cell system are efficiency, power density, cost, and life. Consequently, the key properties of the electrolyte include electrical conductivity, permeability of oxygen, transference number of protons, mobility of electrolyte, and vapor pressure. In addition the electrolyte should be invariant when exposed to carbon dioxide, stable at both oxidation and reduction potentials, and it should support reasonable oxygen reduction kinetics. Other less important properties include the surface tension, density, and viscosity. As we will see, balancing the system design objectives under the constraints of these physicochemical characteristics drives the component and system design.

6.2.3 Transport properties

Strong phosphoric acid is a mixture of condensed acids[7] as illustrated in Fig. 6.2.

$$n\mathrm{H_3PO_4} \rightarrow \mathrm{H_{n+2}P_nO_{3n+1}} + (n-1)\mathrm{H_2O} \qquad 6.2$$

If we treat the acid as simply a binary electrolyte, albeit a very simplified picture of the actual chemistry,[8,9] we can use well-developed concentrated solution transport equations[10] for three species to elucidate some of the transport phenomena. Using the nomenclature from Newman,[10] the fluxes of these species are given by

$$N_o = c_0 v_0 \qquad 6.3a$$

$$N_+ = \frac{-\nu_+ D c_T}{\nu R T c_o} c \nabla \mu_e + \frac{i t_+^o}{z_+ F} + c_+ v_o \qquad 6.3b$$

$$N_- = \frac{-\nu_- D c_T}{\nu R T c_o} c \nabla \mu_e + \frac{i t_-^o}{z_- F} + c_- v_o \qquad 6.3c$$

In this rudimentary representation, three transport properties of the electrolyte are required: the electrical conductivity, κ, the transference number of the cation, t_+^o, and the diffusion coefficient of the salt, D.

The conductivity of phosphoric acid has been reported.[11,12] Based on the correlations of Chin and Cheng,† the conductivity is plotted as a function of water partial pressure at either fixed temperature or fixed acid concentration and shown in Fig. 6.3. A few features are noteworthy. First the conductivity is high, particularly when compared with any aqueous electrolytes at similar temperatures and water partial pressures. More important, the conductivity is relatively insensitive to the water partial pressure – this is in sharp contrast to aqueous electrolytes, such as sulfuric acid and PEM, and allows operation

† It appears that the reference has a typo in the value for the 3rd constant for B.

of fuel cells at higher temperatures without pressurization. This good ionic conductivity is the result of autoprotolysis,

$$2H_3PO_4 \rightarrow H_4PO_4^+ + H_2PO_4^- \qquad 6.4$$

At very low water content, the conductivity does decrease, but as we will see below this is a region of little interest for fuel cells. Finally, we note that at a fixed temperature the conductivity increases with decreasing acid concentration. On the other hand, lower acid concentrations, which correspond to higher water activity, significantly increase carbon corrosion.

In the absence of concentration gradients, the transference number is the fraction of charge carried by an ion. Ideally, for an acid fuel cell a proton transference number of unity is desired. Transference numbers for dilute acid are reported to be about 0.9.[13,14] Only one report has been made for concentrated solutions. From radiotracer measurements, the transport number of the anion was reported to be less than 0.1 over a large range of concentration.[15]

Since the anions do not participate in the electrode reactions, at steady state the flux of anions will be zero. Therefore, as seen from equation 6.3c, an electrolyte concentration gradient develops to offset the migration due to the electric field. The magnitude of the concentration gradient depends on current density, transference number, diffusion coefficient, and the thickness of the electrolyte. These concentration changes cause a concentration polarization that can limit cell performance. One of the earliest reports of this polarization for PAFCs was made by Lundquist and Vogel.[16] Their work estimated a transference number of about 0.7. This non-unity transference number can result in a small but significant concentration polarization for high current densities and thick electrolytes.

Ruiz-Bevia *et al.*[17] measured the diffusivity of phosphoric acid at high concentrations and compare their data with those found in earlier works of Edwards and Huffman for example.[18] No data are readily available at temperatures of interest in the fuel cell, but in general the diffusivity decreases as the concentration of the acid increases.

6.2.4 Thermodynamic data

Similar to proton exchange membrane (PEM) electrolytes, there is an equilibrium relationship between the water vapor pressure and the concentration of acid at given temperature.[19,20] These data are essential to the system design and water management. MacDonald and Boyack[12] provide a correlation for vapor pressure of water as a function of temperature and concentration over the range of 80–101% acid and up to 170 °C. These data were used to create Fig. 6.3, and the modified correlation (units changed from mmHg to Pa) is given below.

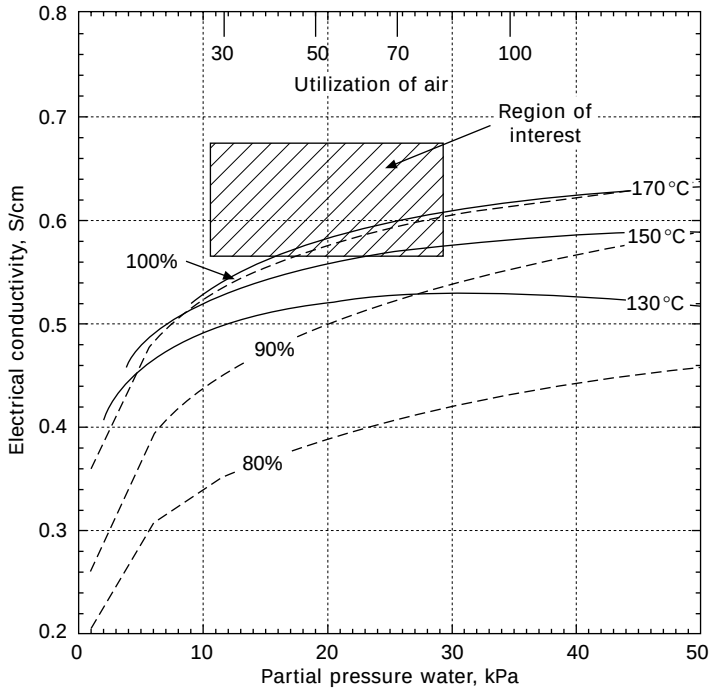

6.3 Electrical conductivity of phosphoric acid. Utilization of air shown at top abscissa assumes the cell is in water balance and the exiting water vapor is in equilibrium with the acid.

Table 6.1 Parameters for equation 6.5

A_0	12.85421	A_4	2838.25
A_1	7.40558	A_5	1812.47
A_2	5.46493	A_6	1256.48
A_3	0.0103388	A_7	816.949

$$\log p_{H_2O} = (A_0 - A_1 X + A_2 X^2 + A_3 X^3) - (A_4 - A_5 X + A_6 X^2 + A_7 X^3) T^{-1} \quad 6.5$$

where p is the vapor pressure of water in Pa, X is the mole fraction of H_3PO_4 and T is the temperature in kelvin. Constants for equation 6.5 are given in Table 6.1.

At the temperatures of interest for PAFCs the vapor in equilibrium with the electrolyte is composed almost entirely of water. The remaining component of the vapor is phosphoric acid. The partial pressure of the acid in the vapor phase is small by most measures and frequently neglected; nonetheless, for long-term operation of the phosphoric acid fuel cell, even a small vapor

pressure can present challenges. Brown and Whitt[19] is one of the few articles available in the literature that discuss the composition of the vapor. In their article they are concerned with design and operation of phosphoric acid plants, and therefore much of the data that show significant acid content in the vapor is at temperatures well above those practical for fuel cells. They report that in addition to water, the acid species in the vapor phase is principally P_4O_{10}. They describe the composition of the vapor phase at 221–228 °C for boiling phosphoric acid to be 0.009 weight percent P_4O_{10}. These data at low temperatures are plotted in Fig. 6.4 along with a linear fit through these four points. Also shown by the hashed area is the region of interest for PAFCs, namely 150–220 °C. Data for temperatures below or near 200 °C are the most relevant for PAFCs but have not been published.

MacDonald and Boyack[12] report the density of phosphoric acid at relevant conditions for PAFCs. Sarangapani *et al.*[21] compiled a detailed summary of many additional properties. This is the most complete source of pertinent data, but this report is not easily accessible. Chang *et al.* have also reported on the physical properties such as density and viscosity.[22]

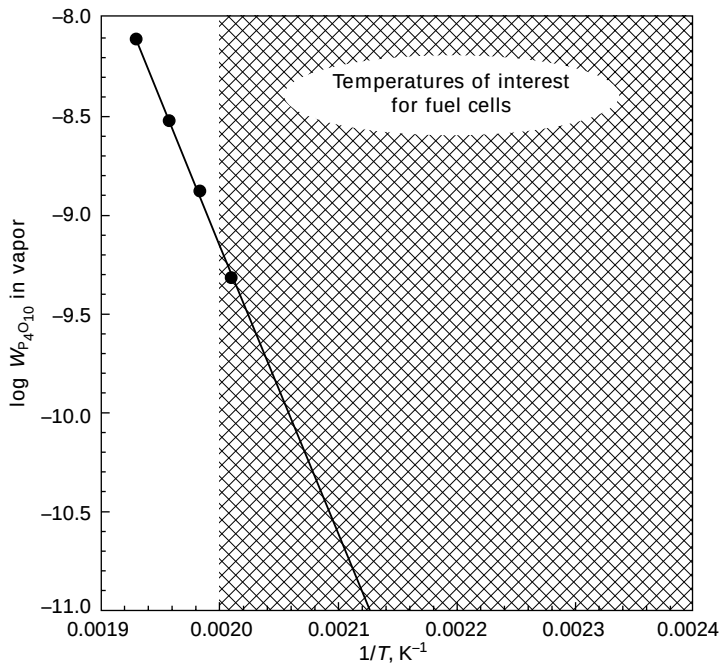

6.4 Vapor pressure of phosphoric acid expressed as weight percent in vapor as a function of temperature.

6.2.5 Kinetics

The kinetics of the oxygen reduction reaction (ORR) has been well studied.[23] Kunz and Gruver[24] reached some important conclusions: the effect of crystallite size is small, the reaction is first order in oxygen concentration, the Tafel slope is RT/F, and the specific activity is the same as that found on flat sheet. Many subsequent researchers have examined these kinetics on platinum.[25–29] Phosphate ions are strongly adsorbed onto platinum. Zelenay *et al.*[30] highlighted this impact by comparing the adsorption of phosphoric acid with that of trifluoromethane sulfonic acid over a wide range of temperatures and potentials. Fourier transform infrared (FTIR) spectroscopy has shown the adsorption of H_3PO_4 follows a Temkin isotherm.[31] The relatively poor oxygen reduction activity is attributed to this strong anion adsorption on platinum at potentials relevant to the fuel cell cathode.[32] In addition to low adsorption of acid on the catalyst, high solubility and diffusivity of oxygen are desirable properties of the electrolyte. Scharifker *et al.*[7] provide critical data on oxygen solubility and diffusivity in concentrated phosphoric acid. Potassium perfluorohexanesulfonate has been examined for its ability to enhance oxygen reduction.[33] Compared with aqueous electrolytes and PEM electrolytes, the kinetics are relatively poor. Nonetheless, the other attributes of phosphoric acid have resulted in it being a better overall choice for low-temperature fuel cells operating on hydrocarbon fuels.

De Sena *et al.*[34] reported that the performance of dispersed catalysts was similar to that of smooth surfaces. Early work showed the importance of platinum migration and dissolution,[35] a topic that is being investigated broadly for PEMFCs today. *In situ* measurement of electrochemical area were reported to be about 25 m^2/g, much lower than other reports.[36] Aragane *et al.*[27] also studied degradation of the electrode and found evidence of fluorine attack. The improved kinetics of alloy catalysts has been well demonstrated.[37–39] PtCr has been studied extensively,[40] and PtCoCr alloy is used in commercial PAFCs.[36] Pt-Fe,[41–43] alloys, and tungsten have also been considered.[44]

CO tolerance has been well studied.[45] Gang *et al.* examined air injection.[46] Chin and Howard[47] studied the effects of hydrogen sulfide on anode performance. Sugishima *et al.*[48] examined impurities in the electrolyte and identified a small oxidation peak that has been ascribed to oxidation of phosphorous acid on platinum in the presence of hydrogen. Szymanski *et al.*[49] showed the effect of ammonia on phosphoric acid fuel cells. Whereas continuous exposure to these poisons cannot be tolerated, to a large extent their effects can be reversed similar to PEMFCs.

6.3 Individual cell design

Because of the elevated temperature of operation (200 °C), the product water is formed as a vapor. Although the adsorption of phosphate ions increases

the polarization at the cathode, without liquid water present PAFCs can be operated at ambient pressure on air at high utilization of oxygen (fraction of entering oxygen consumed electrochemically) without recycling or other special efforts for water management that are required for PEMFCs. Equation 6.5 correlates the vapor pressure of water with temperature and acid concentration. Thus, if the cell is in water balance, the utilization of air at a given temperature and pressure fixes the acid concentration in the cell. The utilization corresponding to removal of all the product water with the cathode exhaust is shown on the top abscissa of Fig. 6.3. The range of utilization shown, 30–100%, is large; and as can be seen, the associated variations in concentration and conductivity are quite small. For a practical device, the utilization of air has an upper limit of about 70%. Above this value the polarization at the cathode is high due to mass transport limitations. Low values of utilization are also undesirable as this both requires greater parasitic power and exacerbates the acid management issues; see below. As a result of the relative insensitivity of electrolyte conductivity to reactant flow, water management is relatively straightforward in PAFCs. A second key advantage of higher temperatures is tolerance to CO found in reformed fuels. At 200 °C, PAFCs are able to operate efficiently with up to 1% CO in the anode gas stream. The major cell components are shown in Fig. 6.5, and each is discussed below.

6.3.1 Matrix

The matrix is composed of micron and submicron particles of SiC powder and a small amount of Teflon, polyethersulfone, or similar binder.[50,51] During operation, the interstitial pores in the matrix are filled with concentrated phosphoric acid. The electrolyte is held in place by capillary forces. This electrolyte provides for ionic conduction and a barrier between reactants, and clearly the matrix material must be an electronic insulator to prevent cell shorting. The cell will be under axial load to minimize contact resistance, and the matrix must resist deformation to prevent the liquid electrolyte from being squeezed out. The total thickness in state-of-the-art matrices is about 50 μm.[52] The matrix is deposited onto one of the electrodes with a wet process, such as screen printing or rolling.[53] Caires *et al.*[54] describe the preparation by screen printing and characterization of the matrix as well as addition of carbides and silicates. Yoon and co-workers [55,56] explain tape casting of the matrix onto electrodes and the impact on performance. Boron nitride has also been proposed for fabrication of the matrix.[57]

6.3.2 Electrodes

In present designs, the electrodes are ‘gas diffusion electrodes’ and typically bonded with Teflon. The catalysts are platinum or platinum alloys supported

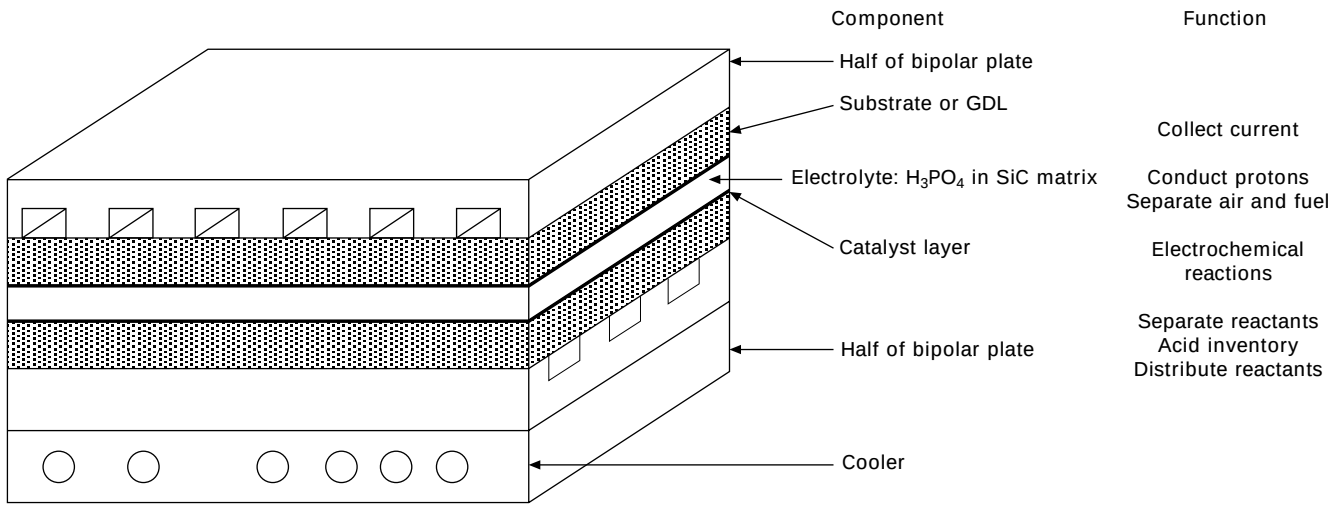

6.5 Major components of a single phosphoric acid fuel cell.

on high surface area carbon black, Vulcan XC-72 for example. These supports may also be heat treated to improve their corrosion resistance. Typical total platinum loadings in commercial units are about 1 mg Pt/cm^2.

The two major enabling events in the development of the PAFCs were (1) the development of carbon blacks and graphite for construction of cell components and (2) the invention of Teflon, which became widely available commercially in the 1950s. Establishing a stable three-phase interface was accomplished by controlling the porosity of components and their wettability. Teflon was critical to the development of PAFCs and the AFCs that followed the Bacon cell. Teflon is extremely inert and its hydrophobicity allows a stable three-phase electrode to be fabricated. The use of graphitized materials in AFCs also played a key role in the PAFC. The supported catalysts are required to achieve high surface areas and minimize the amount of precious metals required. These will be discussed in detail in Section 6.6.

The porous electrode consists of a mixture of the electrocatalyst supported on carbon black and a polymeric binder, usually polytetrafluoroethylene (PTFE). The Teflon binds the carbon black particles together to form an integral (but porous) structure, supported on a porous carbon-paper substrate. Ghouse *et al.*[58] provide an overview of typical electrode fabrication methods. Kinoshita and Stonehart[59,60] also review the dispersion of catalyst on carbon supports. Platinum can be deposited on the carbon through a number of methods such as salt reduction, electrochemical deposition and chemical vapor deposition. Salt reduction using H_2PtCl_6 is commonly found in literature, producing platinum particles in the 2–6 nm range.[61–63]

As noted in the introduction the gas diffusion electrode must simultaneously conduct protons and electrons, and allow for gas access. Thus the electrodes must be wetted partially by the phosphoric acid. Teflon plays a key role in establishing this three-phase boundary, but it is not just the composition that is varied; it is also the processing conditions. Sintering of the Teflon at temperatures of about 340 °C is essential. Much attention has gone into the composition and fabrication parameters of electrodes, but perhaps only a small fraction of the work has been published. Giordano *et al.*[64] demonstrated the importance of acid absorption and how this is influenced by Teflon content and sintering temperature. Since these structures are inherently unstable, there is a trade between initial performance and durability of the electrode. Shim and Lee[65] examined how composition and fabrication methods influenced performance. Hara *et al.*[66] proposed alternative electrode structures where they attempted to separately control the gas diffusion function and the electrolyte wetting. There appear to be opportunities to improve simultaneously life and performance.

Pebler[67] used transmission electron microscopy (TEM) to characterize used and new electrodes. He identified two types of carbon agglomerates, differentiated by the carbon particle size, in the electrodes. Both agglomerates

were smaller than 1 μm. Teflon formed a thin film over the agglomerates, and the size of platinum particles grew much faster in the cathode, suggesting a potential dependent process. Maorka[68] is one of the many contributions to electrodes that build on the work of Kunz and Gruver.[24] In a further example, Breault *et al.*[69] detail fabrication of an electrode employing cryogenic grinding of the catalyst to produce a more uniform coating.

6.3.3 Gas diffusion layers

As in other low-temperature fuel cells the gas diffusion layers (GDLs) collect current and distribute reactants under the ribs of the bipolar plates to ensure more equal access to the electrodes. In the case of PAFCs, GDLs also support the electrodes. Conversely, in many PEMFC designs the catalysts are supported on the solid membrane. As a consequence, the GDLs for PAFCs are sometimes referred to as substrates. The GDL or substrate is made from carbon paper that is highly graphitized for corrosion resistance and, other than surface treatment, is quite similar to those used in many PEMFCs.[70] Key properties include electrical and thermal conductivity in and through the plane, porosity, corrosion resistance, and flexural strength. Heat treatment or graphitization near 2500 °C is used to achieve the desired properties. The substrates have a porosity of about 50% and are 0.02–0.04 cm thick. The pore size is about 30 μm. The cost of these heat-treated papers is high, and very limited information is available in the open literature. Suppliers such as Toray carbon of Japan are few.

6.3.4 Bipolar plates

The major functions of these plates are (1) to isolate reactants, that is to form bipolar barrier, (2) to collect current, (3) to distribute reactants, and, depending on the stack design, (4) to store a reservoir of acid. The typical separator plate is porous with a solid graphite core and is fabricated by molding a blend of graphite powder and resin followed by heat treatment.[71] The design from United Technologies Corp. is called an electrolyte reservoir plate (ERP), highlighting its function to manage the volume of liquid electrolyte.[72] Whereas the core is solid to prevent acid movement between cells, the flow fields are formed in porous carbon. The pore size is about 10–20 μm, much larger than the pore size of the matrix or catalyst layers, but smaller than in the GDL. These plates need to contain a reservoir to make up for acid lost from the cell. Also, since phosphoric acid is a solid above a concentration of 80% at room temperature,[5] the acid must be diluted during storage, shipment, etc. Consequently, there must be sufficient void volume available to account for the changes in density.

In addition to holding an inventory of electrolyte, a key feature of the

bipolar plate is that it must be impermeable to the electrolyte; hence the solid core. This function is accomplished by using a laminated assembly. Information on the construction can be found in the patent literature.[73–75] Based on the transport properties, any electrolyte if not truly immobile will move (see Section 6.4.1 below).

6.3.5 Cooler plates

Heat must be removed from the cells. PAFCs can be either air cooled or water cooled. As shown in Fig. 6.3, the phosphoric acid cell stack assembly may be operated over a broad range of utilization. Nonetheless, it is not generally practical to remove heat using the reactant air for the heat sink, as is done for solid oxide fuel cells (SOFCs) for instance. The lower temperature compared with SOFCs limits the heat removal capability of the air. Moreover, as the rate of air flow is increased, the electrolyte becomes progressively more concentrated, and the ohmic and kinetic polarizations increase. For water-cooled systems, a cooler is not required between every single cell, again a result of the relatively weak dependence of conductivity on temperature and water content. Thus there will be variations across the plane of the cell as well as from cell to cell between coolers. Breault *et al.*[76] provide some of the details required of cooler plate assemblies. Examples of variations in temperature for an operating stack have been provided by Ghouse *et al.*[77]

PAFCs are low or intermediate temperature fuel cells, operating between 150 and 220 °C. At low temperatures, phosphoric acid is a poor ionic conductor, and at higher temperatures the material stability of carbon and platinum is limiting. If one assumes that the water vapor generated within the fuel cell is in equilibrium with the electrolyte, then the current density, operating temperature, and acid concentration are coupled together as shown in Fig. 6.3. This effect is also illustrated by Alderucci *et al.*;[53] and understanding this relationship is essential for controlling water and thermal balance within the stack.

6.4 Stack design challenges and components

The durability challenges for PAFCs and PEMFCs are remarkably similar.[4] Today the focus for PEMFC is on (1) platinum sintering and stability, (2) corrosion of catalyst supports, (3) chemical attack of ionomer membranes, (4) contaminants, and (5) increased mass-transport losses due to loss of triple-phase boundary. With the exception of membrane degradation, PAFCs have faced virtually the same challenges during their development over the past couple of decades. As the developers move toward higher temperatures for PEM fuel cells, the lessons learned from PAFCs become more and more relevant.

6.4.1 Electrolyte management

As we have seen, the GDL, matrix, electrode, and the electrolyte reservoir plates, if used, are all porous components. At equilibrium, acid fills these components so that each is at the same capillary pressure. The capillary pressure[78] is the difference between the wetting (electrolyte) and non-wetting (reactant gases) phases, here it is approximated with the Young–Laplace equation assuming a cylindrical pore,

$$p_c = p_{nw} - p_w = \frac{2\gamma \cos\theta}{r^*} \qquad 6.6$$

γ is the surface tension, J/m^2, r^* is the hydraulic radius of the capillary, and θ is the contact angle. The components with smaller pore sizes have greater capillary pressure. Thus for wetting fluids, i.e. those with a contact angle less than $\pi/2$, the pressure of the non-wetting phase must be larger than the pressure of the wetting phase in order to maintain a stable interface. Most of these components are only partially filled, which brings us to a second key concept, the relationship between fill level, S, and capillary pressure. Typically this would be an empirical relationship, such as the well-known Leverett function.[78] Accordingly the relative fill level of components can be controlled by changing either the hydraulic radius of the capillary (pore size) or the surface energy.

As shown in Fig. 6.5, the cell components are sandwiched together, and the electrolyte is free to move among them. Clearly, the desire is to have the matrix completely filled and the GDL nearly empty. Figure 6.6 shows the relationship between fill level and capillary pressure for three arbitrary cell components with different pore sizes (A < B < C). At equilibrium, the capillary pressure is identical in each component. But, as shown by the center dotted vertical line, the fill levels are different. One can imagine the matrix being completely filled, $S \approx 1$; the GDL nearly empty, $S \approx 0$; and the catalyst layer somewhere in between. Saito *et al.*[79] summarize the filling of components with acid and the consequences of too much or too little. As they note, the density of the acid can change significantly with temperature and water content, related through equation 6.5, and these variations affect cell performance. With too little acid, the resistance of the cell increases; with too much acid volume, the GDL and catalyst layers can flood, also reducing performance. This is illustrated graphically with the additional two vertical dotted lines in Fig. 6.6 representing higher and lower fill levels. Achieving a proper balance during cell operation, start up, and shut down, as well as managing acid fill over the life of the stack, recall that there is a finite and important acid component in the vapor phases, Fig. 6.4, and the acid inventory changes over the life of the stack. These effects are also described by Mori *et al.*[80,81]

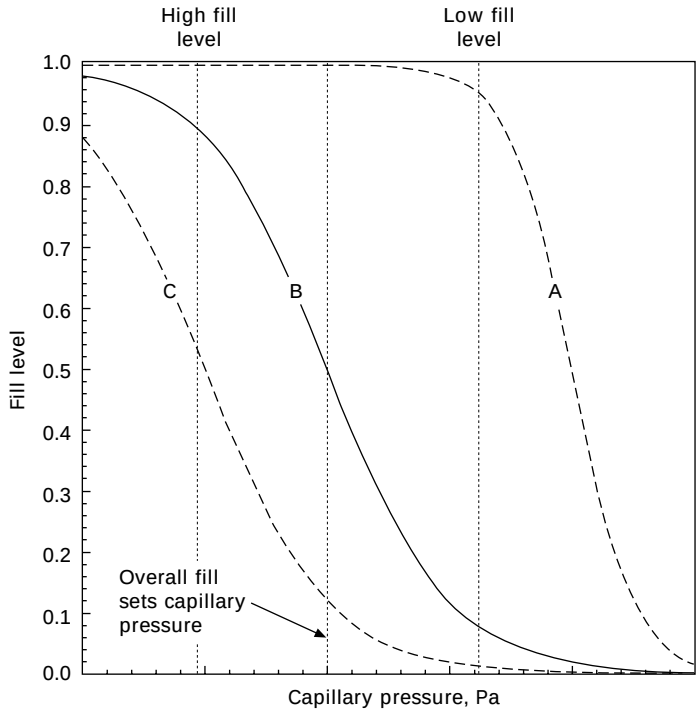

6.6 Fill level of porous components as a function of capillary pressure. The pore radii are such that A < B < C.

A typical fuel-cell stack has a staggering length of seals. Similar to the matrix construction, SiC can be used, on the edges of the substrate for instance, to form a 'wet seal.'[82] With a mobile electrolyte, i.e. PAFCs, molten carbonate fuel cells (MCFCs), and AFCs, the seals are particularly important for electrolyte management. The wet seal is used extensively, but information on seals is mostly limited to the patent literature. Martin *et al.*[83] describe a 'caulk' made from a mixture of carbon and Teflon or fluorinated ethylene propylene (FEP) with a key property of limited absorption of acid. Breault *et al.*[84] developed a seal formed from SiC and binder that combines hydrophilic and hydrophobic elements to provide a good seal and limit loss of acid. Seals fabricated from fluoropolymer have also been proposed.[85]

The above discussion is for equilibrium distribution of electrolyte, and because of the relatively low rates of transport, this assumption is adequate most of the time. Electrolyte transport is a design challenge for any cell with a mobile electrolyte. Kunz[86] discusses the phenomena for molten carbonate fuel cells; the effects are similar for other classes of fuel cells. The mass average velocity, $\boldsymbol{v}$, is appropriate for describing fluid flow. From equation 6.3, the mass average velocity can be written as the sum of the molar fluxes times the molecular weight of species,

$$\boldsymbol{v} = \frac{1}{\rho} \sum M_i N_i \qquad 6.7$$

This definition and equation 6.3 may be rearranged to express the fluid velocity in terms of the current, i, and the mass fraction of acid, ω

$$\boldsymbol{v} = \frac{1}{\rho} \frac{i}{F} \left\{ M_+ + \frac{1-\omega}{\omega} t_-^0 M_E \right\} \qquad 6.8$$

The same velocity is related to pressure gradients and gravitational forces, for example Darcy's law in porous media,

$$\boldsymbol{v} = -\frac{k(S)}{\mu}(\nabla p + \rho g \nabla z) \qquad 6.9$$

k is the permeability of the porous medium. In most cases we can ignore gravity. The notable implication is that concomitant with fluid flow is a pressure difference, which as we have seen above affects fill levels of components. As described by Kunz,[86] long-term operation of a fuel cell stack with imperfect gasketing led to migration of electrolyte from one end of the stack to the other. This highlights the importance of good seals and impervious bipolar barriers.

Acid is lost from a cell stack through evaporation, reaction with cell components, and absorption into bipolar plates.[53,81] The acid loss depends on the cell stack temperature, the reactant flow rates, and the structure of the cell components. Loss of acid affects the life of the stack, but also affects the design of downstream system components. Several patents are available detailing methods to mitigate or control acid loss from fuel cells.[87] The strategies include cooling reactant gases to ensure condensation of acid within the cell and replenishing acid loss to extend life.[88–90] Managing the cell temperature and providing a condensation zone in the planform of the cell is also used to achieve longer life.[91]

6.4.2 Shunt currents

Corrosion of components will be discussed below, but one mechanism that is prevalent in cell stacks with mobile electrolytes is shunt currents. The typical bipolar design used for cell stacks results in a high potential difference between the positive and negative ends of the stack. Certainly if a circulating electrolyte is used, shunt or intercell currents will be present. In addition to reducing efficiency, a more difficult challenge is corrosion of the end cells.[92] Here small currents can cause severe local corrosion. This phenomenon has generally forced developers to abandon circulating electrolytes, and moreover puts demanding constraints on seal and cell designs.

6.5 System design

Figure 6.7 shows a schematic of the commercial phosphoric acid system developed by United Technologies Corporation.[52] This is a system that provides regulated AC power from natural gas. A few things are worth mentioning. First, the cell stack assembly is only a small part of the entire system. Second, a significant number of components are required to reform the fuel and to process the reactants before and after the cell stack. The system is completely self-sufficient in water. The water system is also a large part of the power plant. Finally, the system is highly coupled in order to improve overall system efficiency. Heat removed from the cell stack is used to generate steam, which is provided to the reformer reducing the amount of fuel that must be used to drive the reformation reaction.

Even at relatively high efficiencies, i.e. 40–50%, the fuel cell generates a lot of heat. This puts additional requirements on the fuel-cell system, but also offers the opportunity to recover and put this energy to use either internally for fuel processing – the reforming reaction is endothermic – or externally to provide heat or absorption cooling to the customer. The higher the temperatures the more valuable is the energy liberated as heat. On the other hand, the higher the temperature of operation, the more severe the materials requirements become. The temperature of operation also has a major impact on the potential applications. Low-temperature operation is better for rapid and frequent start-ups and shut-downs. High temperature is better suited to steady-state operation on reformed fuels and for cogeneration. As an example, Ishizawa *et al*.[93] describe uses of the waste heat in a telecommunication application.

6.6 Materials challenges

Broadly speaking, the temperature of operation of any fuel cell is a balance between selecting a temperature high enough so that the kinetic and transport processes are facile and low enough so that materials of construction are stable. For PAFCs, at temperatures above 150 °C carbon monoxide adds only a small polarization for Pt catalysts, the effects of anion adsorption on Pt is mitigated, transport processes are rapid, and the value of the cell waste heat is improved. These contribute to a good system efficiency. Conversely, higher temperatures accelerate nearly all of the degradation processes, most notably corrosion of materials. Chemical attack and corrosion are significant challenges for all fuel cells, particularly as the temperature of operation increases. In fact, the evolution of PAFCs followed a trajectory of ever-increasing temperatures until corrosion and stability were unacceptable. The net result is that PAFCs operate between 150 and 220 °C.

An analogous trend is now unfolding in the development of two other fuel cell types. SOFCs are headed for lower temperatures; and PEMFCs are

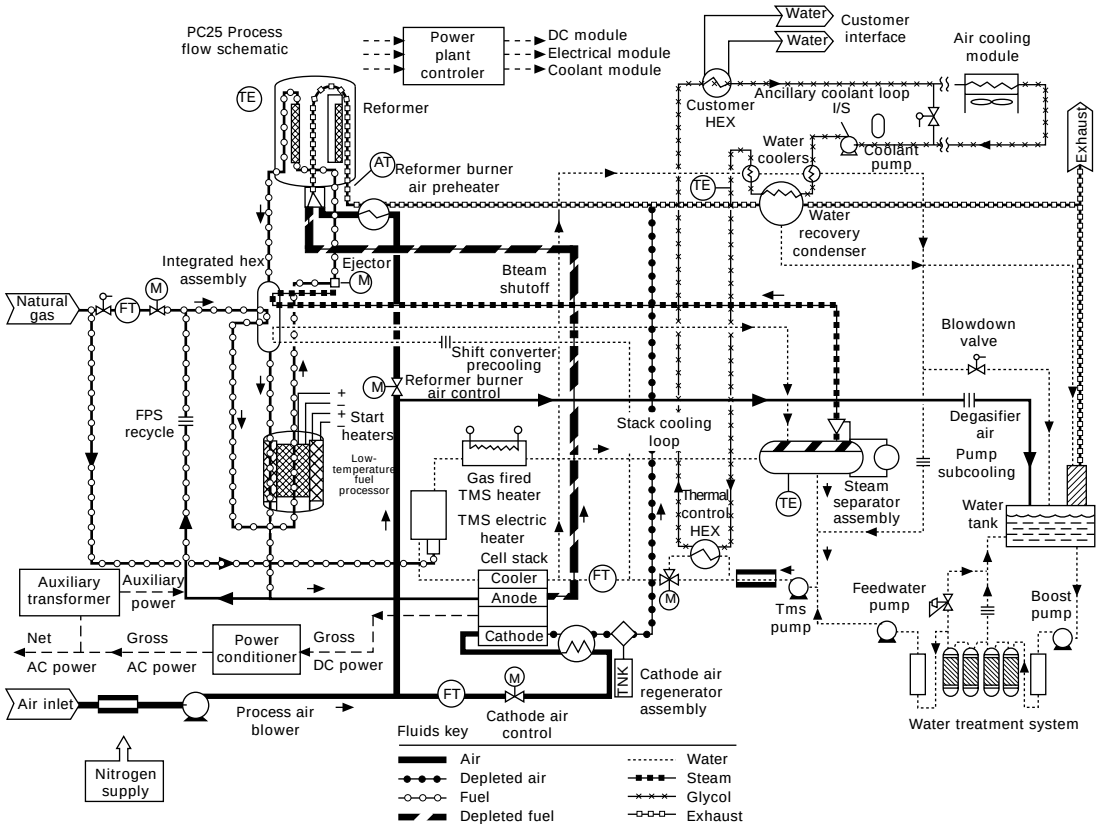

6.7 Schematic of the 200 kW phosphoric acid fuel cell power plant developed by United Technologies. The figure is adapted from Srinivasan[52] and is reproduced by permission of The Electrochemical Society.

trending toward higher temperatures. Selection of an operating pressure is also affected by the stability of the materials as well as efficiency and cost. Generally, the performance increases with pressure, but materials stability is reduced. Today most PAFCs operate at ambient pressure. Thus to a large extent, the development of materials falls into one of two objectives: (1) identifying chemistries and structures with better low-temperature performance, or (2) improving the corrosion resistance and mechanical properties and consequently, allowing the system to be durable at a higher temperature.

6.6.1 General materials compatibility in phosphoric acid

Most of the corrosion literature focuses on lower temperatures associated with the handling and distribution of phosphoric acid rather than under fuel-cell conditions. Pelitti provides a general overview of corrosion in phosphoric acid.[94] It is important to note that most materials, carbon for instance, are not thermodynamically stable under fuel-cell conditions. Durability and long life require that the kinetics are reasonably slow.

6.6.2 Platinum group metals

Platinum metals are relatively stable in phosphoric acid. Corrosion is still a concern because of the long times of operation expected (5–10 years) for these and the desire to minimize the amount of precious metals used and consequently system cost. The stability of platinum is presently being investigated for PEMFCs, which is discussed in Section 6.7.

6.6.3 Fe, Cu, and valve metals (Ta, Nb, Hf, Zr, Ti, V, W, Be, Al)

Hot concentrated phosphoric acid is highly corrosive. Fe and stainless steels are not stable.[95,96] Cu has greater stability than steel, but the rate of corrosion is too high for use in fuel cells. Furthermore, Cu is a poison for electrocatalysts. Gold is relatively stable. Ag and Ta were found to have corrosion rates less than 1 mm/yr at 250 °C.[97] Of the valve metals, which form corrosion-resistant oxide films, tantalum and alloys show the best resistance to corrosion, but stainless steels and other metals are not resistant to corrosion at elevated temperatures.[98,99] Nickel tantalum alloys have been proposed for bipolar plates.[100] The rates of corrosion are still far too high to allow for use in PAFCs. The corrosion resistance of titanium has also been reported.[101] Molybdenum also shows corrosion rates less than 1 mm/yr at 250 °C.[97] The lack of corrosion resistance of these metals has led to extensive use of carbon in PAFCs, which is discussed at length in Section 6.8. Where metals

other than precious metals or carbon are used they need to be coated with Teflon or electroplated with gold. It should be noted that because phosphoric acid has a small vapor pressure, some acid is entrained or carried from the cell stack with the reactants. Corrosion of other system components, such as the water recovery condenser, is also an important design consideration.

6.6.4 Glasses and siliceous materials

Whereas phosphoric acid does not attack glass at room temperature, glass is attacked by hot phosphoric acid[102,103] Although not suitable for a material of construction, glass is used routinely for laboratory testing of phosphoric acid fuel cell electrodes.[24] At temperatures above 150 °C the stability of glass is a significant but manageable problem.

6.6.5 Polymers

The only polymeric material that is used in PAFCs is PTFE and associated fluoropolymers (FEP and perfluoroalkoxy co-polymer resin (PFA)) that fall under the trade name of Teflon.™ These polymers are used extensively in PAFCs, in the electrodes, matrix, and gasketing for instance. It is not useful as structural material, but its high stability under fuel-cell conditions has been instrumental in advancing fuel-cell technology.[104] In addition to its excellent stability, a key feature of Teflon™ is its high hydrophobicity, which allows establishment and control of the three-phase boundary in the electrode. The importance of establishing and controlling the gas-liquid interface was discussed in Section 6.3.2.

Recently, other polymeric materials such as polybenzimidazole (PBI) and polyimides have been explored as alternatives for electrolytes for fuel cells either by doping with phosphoric acid or by sulfonation.[105] However, PBI for instance is soluble in hot concentrated phosphoric acid. Although many polymeric materials are used in the manufacture of components and processing of materials, such as resins to make bipolar plates, these will not be discussed here.

6.7 Electrocatalyst stability

Since both PAFC and PEMFCs use platinum supported on carbon and an acid electrolyte they face similar challenges of platinum stability. From the Pourbaix diagram for platinum, it is clear that there is a region of significant solubility of platinum at low pH and at high potential seen in typical operating fuel cells at low power. For PEMFCs where the principal application is transportation, the stability challenge is exacerbated by frequent potential cycles, which may be more harmful than the temperature of PAFCs. Several

researchers have investigated the stability of platinum for PEMFCs recently. Fuller *et al.*[4] reported the change in platinum surface area for PAFCs under mostly steady-state conditions for both platinum and an alloy of platinum. Because the platinum is highly dispersed on the carbon, it tends to sinter and particle size grows by a factor of 2 to 3. The change in surface area is most rapid during the first few thousand hours and then decreases gradually over the 40 000 hour life. The rate of particle growth is potential dependent, that is the sintering on the cathode occurs more quickly. It has been demonstrated that alloy catalysts show better stability. A key takeaway is that for most of the useful life of the PAFC, the surface area is about 25% of the initial surface area. Therefore focusing too much on initial performance may not be sensible. Ferreira *et al.*[106] measured solubility of platinum in sulfuric acid and compared this with the phosphoric acid data of Bindra *et al.*[107] Although there is some uncertainty about the exact values it is clear that solubility increases with temperature and with increasing potential. Ghouse[108] found evidence of platinum dissolution and migration in PAFC after just 1000 hours of operation.

In order for the hydrogen oxidation reaction (HOR) and the oxygen reduction reaction (ORR) to occur at reasonable rates, a catalyst is required. This catalyst is precious metal in nature and thus represents a significant cost to the fuel-cell system. In order to reduce the catalyst loadings while still maintaining the required level of activity, these precious metals are dispersed on a catalyst support. The general requirements for a catalyst support in low temperature fuel cells include: (1) electrically and thermally conductive, (2) large surface area, (3) inexpensive and abundant, and (4) stable under acidic and oxidizing conditions. The most common support is carbon, a material used in much of the cell components. The high surface area, the presence of a catalyst, and the elevated potentials at the cathode results in a focus on the corrosion of supports, which is discussed below.

6.8 Carbon chemistry and corrosion

Carbon black has successfully met the first three requirements since it was first used in PAFCs in the 1970s. When the cathode potential is near open circuit conditions, 0.9–1.0V_{RHE}, the high operating temperature of PAFCs, ~200 °C, quickly corrodes the carbon supports. This problem was overcome by heat treating the supports and the careful control of temperature and potential. The PAFC system is consequently almost never at open circuit conditions near 200 °C.

Under the majority of fuel-cell operating conditions, carbon is thermodynamically unfavored. The overall reaction for the electrochemical oxidation, equation [6.10], has a formal potential U^{θ} = 0.207 V. Since the potential at the cathode is higher than the formal potential, carbon is

electrochemically oxidized to carbon dioxide. The relative stability of carbon is due to the slow corrosion kinetics:

$$C + 2H_2O \rightarrow CO_2 + 4H^+ + 4e^- \qquad 6.10$$

Although materials exist that exhibit greater stability than carbon under low-temperature fuel cell conditions, no other material has been shown to meet all four criteria as well as carbon black. Furthermore, only a moderate level of research has been conducted on improving the stability of carbon as a support material. The majority of published research on carbon black in fuel cells is reported in the context of the phosphoric acid work in the 1970s at United Technologies Corporation then known as International Fuel Cells. In the 1980s and 1990s a large amount of work involving carbon fibers provided further information about analytical tools and relevant experimental techniques. Only in the past two years has the fuel-cell researcher become re-interested in the challenges of carbon corrosion for PEMFCs.

6.8.1 Structure of carbon black

Carbon is widely available and utilized in a diverse array of applications. The different allotropes of carbon can have disparate characteristics in electrical, optical, and mechanical properties simply by changing the crystal structure. The form of carbon used in low-temperature fuel cells is graphitic in nature and commonly called carbon black. The largest use for this material is in rubber products and dyes, not electrochemical devices such as fuel cells and batteries.

A carbon black particle is 20–30 nm in diameter and joins with other particles to form an aggregate. Each particle is composed of both graphitic and amorphous content. Graphite is a hexagonal structure composed of sheets of aromatic rings known as graphene sheets stacked in an ABABAB layered structure as in Fig. 6.8a. The graphene sheets are held together by π-bonding while the layers interact only through van der Waals forces. The structure of carbon black lacks long-range order with nanocrystalline graphitic clusters near the surface, surrounding a somewhat amorphous center. The structure depicted in Fig. 6.8b displays the turbostratic nature with the graphitic planes ordered parallel to the surface instead of forming long continuous sheets.

Carbon blacks have specific surface areas of 10–1000 m^2/g with Mathias *et al.* suggesting a minimum of 100 m^2/g to obtain adequate dispersion of catalyst in low-temperature fuel cell applications.[109] These materials can have micro- and mesoporosity with lower surface areas occurring for carbons with a larger graphitic nature.

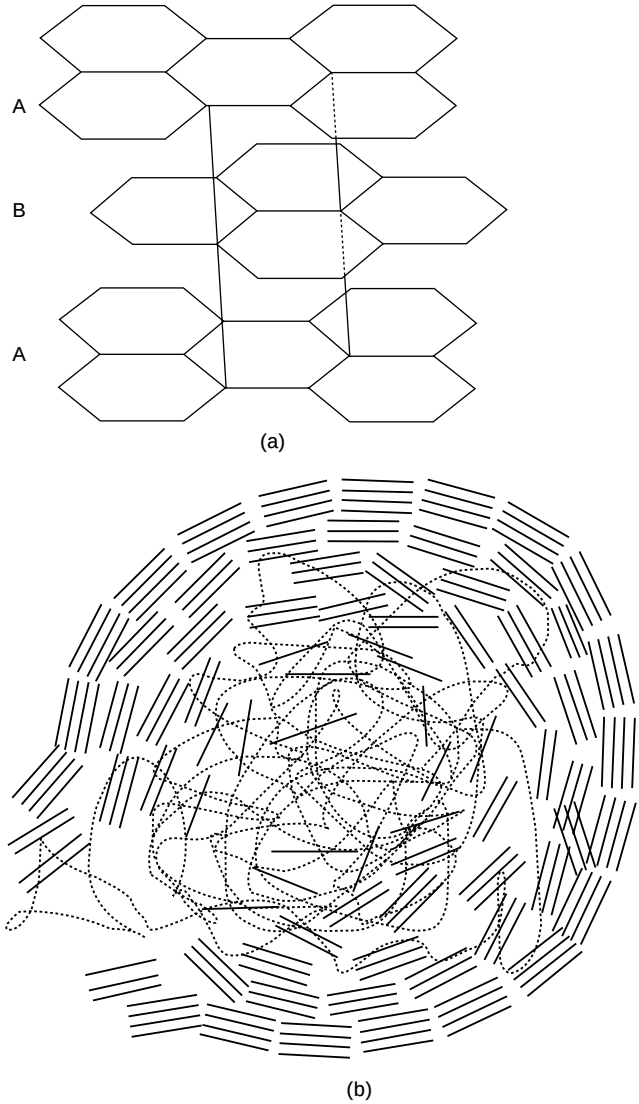

6.8 (a) Layered hexagonal structure of graphite and (b) a carbon particle with amorphous core becoming more graphitic towards the surface outer.

6.8.2 Corrosion of carbon black

The majority of carbon corrosion research has occurred in the context of phosphoric acid fuel cells, which saw a great deal of interest in the 1970s and 1980s. Although many of the published works are elegant and contribute much information to the body of knowledge, the experimental techniques

are limited to those common to that era. The two indispensable works detailing carbon's role in electrochemistry are the work by Kinoshita[110] and the Proceedings of the Workshop on the Electrochemistry of Carbon which took place at Case Western Reserve University.[111] Both works contain a review of microstructure, surface chemistry, and electrochemical oxidation that is still accurate and the basis for our understanding 20 years later.

Kinoshita and Bett first published the logarithmic decay of current with time under a constant potential exposure of the carbon support.[112] Figure 6.9 presents results from our lab showing corrosion in acid. The constant potential current may be modeled with equation 6.11 below in which k depends on the potential. Kinoshita also showed the total current is composed of both surface oxide formation and carbon dioxide evolution.

$$i = kt^{-n} \qquad 6.11$$

Kinoshita suggested the oxidation current resembled the diffusion of a reactant through a passivating film as seen in metal corrosion. Other researchers have suggested growth of both passive and active layers that occur independently in parallel.[113] Few authors have analyzed the ratio of carbon dioxide production

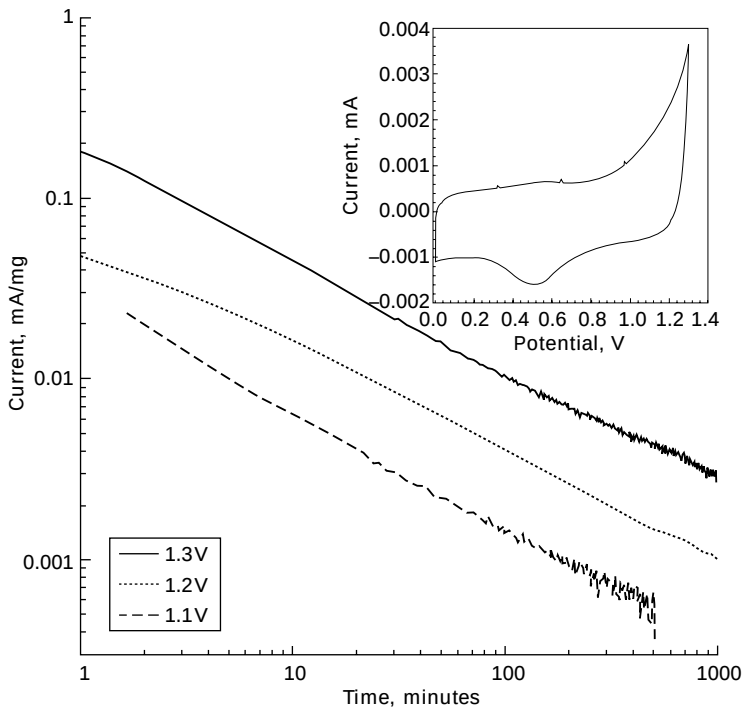

6.9 Corrosion vs. time behavior of carbon in acid solution. The inset is a typical cyclic voltammagram of carbon in acid.

to surface oxide growth, due to Kinoshita's first paper on the subject.[112] In this paper, using a higher surface area carbon in 135 °C phosphoric acid, the carbon dioxide evolution was the dominant current process after a relatively short period of time. The current attributed to carbon dioxide evolution is based on a four-electron transfer and related with Faraday's law. Later, Kinoshita showed this was not necessarily the case for heat-treated supports.[114] However, the vast majority of papers went on to treat the measured oxidation current to be dominated by CO_2 production.

More recent work has shown the CO_2 production current, assuming a four-electron process, to follow the typical Tafel kinetic expression for 50 wt% Pt/C catalyst system.[109] The corrosion of carbon black has been hypothesized to occur mainly in the center of the particle where the structure is largely amorphous. First seen in gas phase oxidation of carbon black particles[115] and later in TEM images of carbon corroded in phosphoric acid,[116] the solid particle appears to become a shell after aggressive corrosion conditions. More recently, Yu *et al.*[117] have correlated CO_2 production with carbon weight loss substituted for the variable *t*, time, in the same logarithmic form as equation 6.8. This relation to weight loss applies only to CO_2 formation and not necessarily to surface oxide growth. Interestingly, when extrapolated to longer times this current intersects the current for a graphitized support at a point that would correspond to a weight loss about equal to the amount of amorphous material at the center of the carbon black particle.

The growth of surface oxides and their resulting effect on mass transport have become of interest as of late for PEMFCs.[118,119] A range of oxide chemistries are possible.[120] The growth of surface oxides increases the hydrophilicity of the material, further complicating water transport or electrolyte management under various operating conditions. Furthermore, the role of these oxides in the gasification of the carbon is unclear and most likely significant.

Characterization of the surface chemistries has been attempted with cyclic voltammetry,[118,121] (Fig. 6.9) titration,[122,123] thermogravimetric analysis coupled with mass spectroscopy (TGA-MS),[118] X-ray photoelectron spectroscopy (XPS),[118,123] as well as other more macroscopic methods. Determination of total oxygen content is robust; however, many challenges exist in understanding the predominant forms of the surface oxide chemistries. The complex nature of the oxides confounds experimental data, leaving the researcher with only hand-waving argument as to their true nature. Only the quinine/hydroquinone (Q/HQ) redox couple is active in the potential window used for cyclic voltammetry; see inset of Fig. 6.9. Comparing the redox peaks to integrated surface oxidation current during a constant potential test shows that the Q/HQ group is only a small percentage of the total oxides produced.[118,123] TGA-MS is hindered by assumptions of leaving groups breaking down into CO and/or CO_2 at a relatively small window of elevated temperature. XPS

is hindered by a complicated C1s spectrum that requires curve fitting to deconvolute the peaks. Also, the O1s spectrum is too broad to have confidence in the peak fit. Most important, XPS is a surface technique penetrating only the top quarter of the carbon particle. Some confidence is possible with the use of all of these techniques to support a conclusion, but an exact understanding of the surface oxides is still elusive.

The platinum catalyst, which dictates the use of carbon supports, also serves to catalyze the electrochemical oxidation of the support. Willsau and Heitbaum presented the first conclusive analysis of platinum-accelerating carbon corrosion.[124] More recently, Roen *et al*. demonstrated this effect in PEMFCs in which they suggested Pt catalyzed the oxidation of CO to CO_2 which may have otherwise been stable.[125] A complete understanding of the platinum carbon couple is lacking, likely due to the stability issues relating to platinum as discussed earlier. Kinoshita's early work in this area was indeed confounded by the dissolution of platinum over the course of the experiment.

During the development of PAFCs, graphitization of carbon black was shown to improve the resistance to oxidation. This microstructural change was commonly achieved with heat treatment after production of the material. The heat treatment results in an ordering of the carbon into larger graphene sheets, reducing the amorphous content and increasing the crystallite size. Interestingly, Kinoshita and Bett measured the current efficiency for the production of CO_2 for three carbon black materials of different graphitic character.[114] The more amorphous material had a higher fraction of the current going to CO_2 production assuming a four-electron transfer. The gain in corrosion resistance generally results in some tradeoff in performance. This is most likely due to the decrease in surface area. The characteristic size of nanoparticles dispersed on the carbon support has been correlated with the support surface area.

X-ray diffraction can be used to determine *d*-spacing of the carbon sample. The *d*-spacing is derived from Bragg's law.[126] As the temperature of heat treatment is raised to 2700 °C the *d*-spacing approaches the theoretical value of pure graphite ($d = 0.3354$ nm). Typical values of carbon black range from 0.33 to 0.37 nm. As the size of the graphitic crystallites grows and the planes become closer together, the specific surface area as measured by Brunauer, Emmett and Teller's model (BET) decreases. This decrease is attributed to the reduction in edges of the graphene sheets. Similarly, a reduction in corrosion current is also seen.

Some research exists in the field of dopants (boron, silicon)[127] and also on carbides (WC). Boron was originally considered as a method to create trap sites for the platinum particles to reduce coarsening. However, the prominent effect was to stabilize the carbon support. The stability of tungsten carbide, WC, is strongly dependent on the method of synthesis.[128] A recent study has

shown advances in the material but has yet to overcome oxidation of tungsten and inadequate dispersion of platinum.[129]

Many advances in carbon corrosion were made during the early days of PAFCs. However, a critical understanding has yet to be realized. Today we do not have all the analytical tools necessary, but science has certainly made dramatic advances in some areas. As an example, the dynamics of carbon corrosion are poorly understood even though this transient environment is closer to fuel-cell operation. This is particularly true for transportation applications. The materials used in PAFCs are summarized in Table 6.2.

6.9 Modeling and analysis

Models can be divided into three broad categories: electrode models, stack models, and system models. A number of electrode models have been presented. These are generally based on the flooded agglomerate concept[130] and the model of Iczkowski and Cutlip. Fuller *et al.*[36] compared alloy catalyst electrode performance with modeling results. Maggio examined the effects of electrode structure on performance.[132] Yamashita and Taniguchi examined the AC response of an electrode.[133] Yang *et al.*[134,135] have presented a series of

Table 6.2 Summary of materials used in phosphoric acid fuel cells

Component	Material	Advantages	Drawbacks
Matrix	SiC	Low cost	
Catalysts	Platinum and its alloys	Relatively stable, good oxygen reduction kinetics	High costs
Catalyst supports	Heat treated carbon (cathode) High surface area carbon (anode)	Low cost, good conductivity and electrode performance	Corrosion, reduced surface area with heat treatment
Binders	PTFE, FEP	Stable, hydrophobic	
Gas diffusion layers	Heat-treated carbon paper	Good conductivity and corrosion resistance	High cost
Flow fields	Porous graphitic carbon	Good conductivity and corrosion resistance	High cost, Difficult to net-shape mold
Bipolar barriers	Solid graphitic carbon	Good conductivity and corrosion resistance	High cost, challenge to make impermeable
Manifolds	Steel coated with polymers	Low cost, high strength	Must be electrically isolated from stack
Electrolyte	Orthophosphoric acid	Good conductivity at low water activity	Absorption of anions, small vapor pressure

extensions to the basic flooded agglomerate model. These models are effective in describing performance, but do not address degradation and stability.

Compared with PEMFC and SOFC, comparatively few models of cells and stacks are available. Choudhury *et al.*[136] present a two-dimensional model of a cell and examined single and two-pass reactant flows. The same group also developed a transient model.[137] The models available in the literature are far less complete and sophisticated than those used by commercial developers. Fluid flows in the stack and flow fields have been modeled.[138,139] The system integration for the PAFC bus has been examined. Betts *et al.*[140] highlight the importance of system integration when using hydrocarbon fuels. Scholta *et al.*[141] report on operation of PAFC on pure hydrogen. Patel *et al.*[142] present approaches to diagnose performance.

6.10 Future trends

Appleby[143] provides an extensive prospectus for fuel cells from about a decade ago. A number of large industrial companies and utilities have made significant investments in phosphoric acid technologies since the 1970s. Hojo *et al.*,[144] Shibata and Watanabe,[145] and Kasahara *et al.*[146] describe progress in Japan through the late 1990s. The participation of gas companies has been extensive and critical. From these field tests valuable data on performance, durability, and maintenance techniques were collected. Field and demonstration results have also been reported for European installations.[147,148] Excellent advancements have been made; nonetheless, reducing cost and improving the life of phosphoric acid fuel-cell systems are identified as the principal challenges for greater market acceptance. As a result, efforts to commercialize PAFCs for on-site power generation have largely been dropped in favor of other fuel-cell technologies. Today United Technologies Corporation is the only large company pursuing PAFCs.

Using technology similar to that found in stationary power plants, a 100 kW PAFC powered by methanol was installed in a transit bus for Georgetown University as part of the US Federal Transit Agencies Bus program. The bus shown in Fig. 6.10 was delivered in 1998. The space constraints and the need for high-power density in transportation applications pushed the technology forward. This fuel-cell bus program has been well documented, and the bus is still operational nearly a decade later.[149] In recent years, the use of reformed fuels for transportation has received much less attention in favor of PEMFCs fueled by compressed hydrogen. This shift has been in part due to a decision in 2004 by the US Department of Energy to abandon on-board fuel processing for transportation programs.

Stationary applications of PAFCs have been and are expected to continue to dominate for the foreseeable future. PAFCs are best suited for installations where the waste heat can be used or in applications where premium power

6.10 The 'Georgetown Bus.' A 100 kW PAFC powered bus that is fueled by methanol.

is needed. Although the majority of installations operate off natural gas, PAFCs operating on hydrogen, propane, and digester gas have been demonstrated. Sammes *et al.*[150] recently summarized many applications, including some of the more unusual installations and their specific challenges, with gas clean-up for instance. Vanhanen *et al.*[151] describe application with solar power. For many years, PAFCs have been installed in treatment plants, such as the one shown in Fig. 6.11. Spiegel and Preston describe operation on anaerobic digester gas and results from a two-year demonstration,[152] which has been followed by several commercial installations.

The economic challenges of PAFCs are highlighted by Kwak *et al.*,[153] who compare the cost of electricity generation by a PAFC with that of electricity generated from a gas-turbine cogeneration plant. The installed cost of PAFCs, in $/kW, needs to be reduced by about a factor of two, and the useful life of the system needs to be doubled. Thus the key ongoing thrust for traditional PAFCs targeted at on-site power generation is to reduce life-cycle cost. This reduction is anticipated through a combination of reducing the capital cost of the system, including installation and any special gas processing, and increasing the useful life of components, particularly of the cell stack. These two design objectives are often at odds. Without question, materials such as heat-treated carbon to improve corrosion resistance and

6.11 Anaerobic digester gas (ADG) fuels this PureCell™ fuel cell powerplant at a wastewater treatment plant in Yonkers, New York. Image Courtesy of: UTC Power Corporation.

platinum electrocatalysts, for instance, contribute to the high cost. Nevertheless, the underlying costs of even these materials is only part of the story. Much of the cost is in processing and manufacturing. As an example, flow fields that are built into bipolar plates are typically machined into these heat-treated carbon plates. This results in high tool wear and also wastes significant material. Thus one essential area of development is establishing the capability to mold net-shape or near net-shape bipolar plates and thereby eliminate the bulk of the machining processes and the associated waste of material. Similar developments and increasing production volumes suggest that life-cycle cost can be reduced substantially.

A second active research thrust has been on developing polybenzimidazole (PBI).[154] Although promoted as a 'high-temperature "PEM" fuel cell,' PBI requires doping with phosphoric acid and closely resembles PAFC, both in the good attributes and in the deficiencies. This has been aggressively pursued both by industry and academia but will not be reviewed in detail here. A few other investigations related to electrolytes that incorporate phosphoric acid have been active avenues of research.[155–157]

6.11 References

1. A. J. Appleby, From Sir William Grove to today: fuel cells and the future, *J. Power Sources*, **29**, 3–11 (1990).
2. H. A. Liebhafsky and E. J. Cairns, *Fuel Cells and Fuel Batteries*, John Wiley & Sons, Inc., New York (1968).
3. F. T. Bacon, Fuel cells, past, present and future, *Electrochim. Acta*, **14**, 569–585 (1969).

4. T. F. Fuller, M. Perry, and C. Reiser, Applying the lessons from PAFC to PEM, *ECS Trans.*, **1** (8), 337–344 (2006).
5. A. J. Appleby, Fuel cell electrolytes: evolution, properties and future prospects, *J. Power Sources*, **49**, 15–34 (1994).
6. R. F. Jameson, Chapter 13 Polyphosphoric acid, in *Phosphoric Acid*, edited by A. V. Slack, Marcel Dekker, New York (1968).
7. B. R. Scharifker, P. Zelenay, and J. O'M. Bockris, The kinetics of oxygen reduction in molten phosphoric acid at high temperatures, *J. Electrochem. Soc.*, **134**, 2714 (1987).
8. R. F. Jameson, The Composition of the 'strong' phosphoric acids, *J. Chem. Soc.*, 752–759 (1959).
9. M. A. Habib, and J. O'M Bockris, Adsorption at the solid/solution interface, *J. Electrochem. Soc.*, **132**, 108 (1985).
10. J. Newman, *Electrochemical Systems*, Prentice Hall, Englewood Cliffs, NJ (1991).
11. D. T. Chin, and H. H. Cheng, On the conductivity of phosphoric acid electrolyte, *J. Appl. Electrochem.*, **19**, 95–99 (1989).
12. D. I. MacDonald, and J. R. Boyack, Density, electrical conductivity, and vapor pressure of concentrated phosphoric acid, *J. Chem. & Eng. Data*, **14**, 380–384 (1969).
13. M. Selvaratnam, and M. Spriros, Transference numbers of orthophosphoric acid and the limiting equivalent conductance of the $H_2PO_4^-$ ion in water at 25 °C, *Trans. Faraday Soc.*, **61**, 360 (1964).
14. M. Kerker, H. E. Bowman, and E. Matijević, The transference number of phosphoric acid by the moving boundary method, *Trans. Faraday Soc.*, **56**, 1039 (1960).
15. O. K. Kudra, Y. Fialkov, and A. N. Zhitomirksii, *Russ. J. Inorg. Chem.*, **9**, 1324 (1964).
16. J. T. Lundquist, and V. M. Vogel, Concentration changes in operating fuel cells, *J. Electrochem. Soc.*, **116**, 1066–1069 (1969).
17. F. Ruiz-Bevia, J. Fernandez-Sempere, and N. Boluda-Botella, Variation of phosphoric acid diffusion coefficient with concentration, *AIChE J.*, **41**, 185–189 (1995).
18. O. W. Edwards, and E. O. Huffman, Diffusion of aqueous solutions of phosphoric acid at 25C, *J. Phys. Chem.*, **63**, 1830 (1959).
19. E. H. Brown, and C. D. Whitt, Vapor pressure of phosphoric acids, *Ind. Eng. Chem.*, **44** 615 (1952).
20. B. J. Fontana, The vapor pressure of water over phosphoric acids, *J. Am. Chem. Soc.*, **73**, 3348 (1951).
21. S. Sarangapani, P. Bindra, and E. Yeager, Physical and chemical properties of phosphoric acid, final report for the department of energy; Case Western Reserve University: Cleveland.
22. H. H. Chang, K-L. Hsueh, D. T. Chin, and S. Srinivasan, Transport properties of phosphoric acid fuel cell electrolytes, *Electrochemical Society Extended Abstracts*, **83–1**, 808–809 (1983).
23. A. J. Appleby, Oxygen reduction on oxide-free platinum in 85% orthophosphoric acid: temperature and impurity dependence, *J. Electrochem. Soc.*, **117**, 328–335 (1970).
24. H. R. Kunz, and G. A. Gruver, The catalytic activity of platinum supported on carbon for electrochemical oxygen reduction in phosphoric acid, *J. Electrochem. Soc.*, **122**, 1279 (1975).
25. L. D. Burke, and J. A. Marrissey, Hydrous Oxide Formation on Platinum in Phosphoric Acid Solution, *J. Electrochem. Soc.*, **141**, 2361–2368 (1994).

26. J. Aragane, H. Urushibata, and T. Murahashi, Proton deficiency in a phosphoric acid fuel cell, *J. Electrochem. Soc.*, **142**, 145–149 (1995).
27. J. Aragane, H. Urushibata, and T. Murahashi, Evaluation of an effective platinum metal surface area in a phosphoric acid fuel cell, *J. Electrochem. Soc.*, **141**, 1804–1808 (1994).
28. T. Torre, A. S. Arico, V. Alderucci, V. Antonucci, and N. Giordano, Analysis of the surface acid–base characteristics Pt/C catalysts for phosphoric acid fuel cells, *Appl. Catalysis A: General*, **114**, 257–272 (1994).
29. J. T. Glass, G. I. Cahen, Jr., and G. E. Stoner, The effect of phosphoric acid concentration on electrocatalysis, *J. Electrochem. Soc.*, **136**, 656–660 (1989).
30. P. Zelenay, B. R. Scharifker, J. O'M. Bockris, and D. Gervasio, A comparison of the properties of CF_3SO_3H and H_3PO_4 in relation to fuel cells, *J. Electrochem. Soc.*, **133**, 2262 (1986).
31. M. A. Habib, and J. O'M. Bockris, Adsorption at the solid/solution interface, *J. Electrochem. Soc.*, **132**, 108–114 (1985).
32. A. J. Appleby, and B. S. Baker, *J. Electrochem. Soc.*, **125**, 404 (1978).
33. L. Qingfeng, X. Gang, H. A. Hjuler, R. W. Berg, and N. J. Bjerrum, Oxygen reduction on gas-diffusion electrodes for phosphoric acid fuel cells by a potential decay method, *J. Electrochem. Soc.*, **142**, 3250–3256 (1995).
34. D. R. de Sena, E. R. Gonzalez, and E. A. Ticianelli, Effect of phosphoric acid concentration on the oxygen reduction and hydrogen oxidation reactions at a gas diffusion electrode, *Electrochim. Acta*, **37**, 1855–1858 (1992).
35. J. Aragane, T. Murahashi, and T. Odaka, Change of Pt distribution in the active components of phosphoric acid fuel cell, *J. Electrochem. Soc.*, **135**, 844–850 (1988).
36. T. F. Fuller, F. J. Luczak, and D. J. Wheeler, Electrocatalyst utilization in phosphoric acid fuel cells, *J. Electrochem. Soc.*, **142**, 1752–1757 (1995).
37. M. T. Paffett, J. G. Beery, and S. Gottesfeld, Oxygen reduction at $Pt_{0.65}Cr_{0.35}$, $Pt_{0.2}Cr_{0.8}$ and roughened platinum, *J. Electrochem. Soc.*, **135**, 1431–1436 (1988).
38. M. T. Paffett, K. A. Daube, S. Gottesfeld, and C. T. Campbell, Electrochemical and surface science investigations of PtCr alloy electrodes, *J. Electroanal. Chem*, **220**, 269–285 (1987).
39. M. Watanabe, K. Tsurumi, T. Mizukami, T. Nakamura, and P. Stonehart, Activity and stability of ordered and disordered Co-Pt alloys for phosphoric acid fuel cells, *J. Electrochem. Soc.*,**141**, 2659–2668 (1994).
40. J. T. Glass, G. L. Cahen, Jr., and G. E. Stoner, The effect of metallurgical variables on the electrocatalytic properties of PtCr alloys, *J. Electrochem. Soc.*, **134**, 58–65 (1987).
41. J. T. Hwang, and J. S. Chung, The morphological and surface properties and their relationship with oxygen reduction activity for platinum–iron electrocatalysts, *Electrochem. Acta*, **38**, 2715–2723 (1993).
42. K. T. Kim, J. T. Hwang, Y. G. Kim, and J. S. Chung, Surface and catalytic properties of iron–platinum/carbon electrocatalysts for cathodic oxygen reduction in PAFC, *J. Electrochem. Soc.*, **140**, 31–36 (1993).
43. S. J. Seo, H. Joh, H. T. Kim, and S. H. Moon, Properties of Pt/C catalyst modified by chemical vapor deposition of Cr as a cathode of phosphoric acid fuel cell, *Electrochim. Acta*, **52** 1676–1682 (2006).
44. O. Savadogo, and A. Essalik, 2% Platinum–H_2WO_4 based electrocatalysts for phosphoric acid fuel-cell cathode, *J. Electrochem. Soc.*, **141**, L92–L94 (1994).
45. Rak-Hyun Song, and Dong Ryul Shin, Influence of CO concentration and reactant

gas pressure on cell performance in PAFC, *Int. J. Hydrogen Energy*, **26**, 1259–1262 (2001).
46. X. Gang, L. Qingfeng, H. A. Hjuler, and N. J. Bjerrum, Hydrogen oxidation on gas diffusion electrodes for phosphoric acid fuel cells in the presence of carbon monoxide and oxygen, *J. Electrochem. Soc.*, **142**, 2890–2893 (1995).
47. D. T. Chin, and P. D. Howard, Hydrogen sulfide poisoning of platinum anode in phosphoric acid fuel cell electrolyte, *J. Electrochem. Soc.*, **133**, 2447–2450 (1986).
48. N. Sugishima, J. T. Hinatsu, and F. R. Foulkes, Phosphorous acid impurities in phosphoric acid fuel cell electrolytes, Parts I and II, *J. Electrochem. Soc.*, **141**, 3325–3335 (1994).
49. S. T. Szymanksi, G. A. Gruver, M. Katz, and H. R. Kunz, The effect of ammonia on hydrogen-air-phosphoric acid fuel cell performance, *J. Electrochem. Soc.*, **127**, 1440–1444 (1980).
50. J. Trocciola, J. Powers, and R. Martin, Silicon carbide matrix for fuel cells, U.S. Patent 516,152 (1983).
51. S. Dheenadayalan, R. H. Song, and D.R. Shin, Characterization and performance analysis of silicon carbide electrolyte matrix of phosphoric acid fuel cell prepared by ball-milling method, *J. Power Sources*, **107**, 98–102 (2002).
52. S. Srinivasan, Fuel cells for extraterrestrial and terrestrial applications, *J. Electrochem. Soc.*, **136**, 41C–48C (1989).
53. V. Alderucci, V. Recupero, E. Passalacqua, R. di Leonardo, M. Laganá, and N. Giodano, Influence of the operating conditions and of the ageing upon the electrochemical performance of phosphoric acid fuel cells, *J. Power Sources*, **42**, 365–376 (1993).
54. M. I. Caires, M. L. Buzzo, E. A. Ticianelli, and E. R. Gonzalez, Preparation and characterization of matrices for phosphoric acid fuel cells, *J. Appl. Electrochem.*, **27**, 19–24 (1997).
55. K. H. Yoon, and B. D. Yang, Preparation and characterization of matrix retaining electrolyte for a phosphoric acid fuel cell by non-volatile solvent, NMP, *J. Power Sources*, **124**, 47–51 (2003).
56. K. H. Yoon, J. Y. Choi, J. H. Jang, Y. S. Cho, and K. H. Jo, Electrode/matrix interfacial characterization in a phosphoric acid fuel cell, *J. Appl. Electrochem.*, **30**, 121–124 (2000).
57. A. Makoto, Phosphoric acid fuel cell, matrix thereof and method for making the matrix, US Patent 5,270,126, December 14, 1993.
58. M. Ghouse, A. al Boeiz, H. Abaqud, and M. al Garni, Preparation and evaluation of PTFE-bonded porous gas diffusion carbon electrodes used in phosphoric acid fuel cell applications, *Int. J. Hydrogen Energy*, **20**, 727–736 (1995).
59. K. Kinoshita, and P. Stonehart, Preparation and characterization of highly dispersed electrocatalytic material, p. 557, *Modern Aspects of Electrochemistry*, Vol. **12**, edited by J. O.'M. Bockris and B. E. Conway, Plenum Press, New York (1977).
60. K. Kinoshita, Small particle effects and structural considerations for electrocatalysis, p. 557, *Modern Aspects of Electrochemistry*, Vol. **14**, edited by J. O.'M. Bockris, B. E. Conway, and R. E. White, Plenum Press, New York (1982).
61. A. Rodriguez-Reinoso, The role of carbon materials in heterogeneous catalysis. *Carbon*, **36** (3), 159–175 (1998).
62. F. Coloma, A. Sepulveda-escribano, and F. Rodriguez-Reinoso, Heat-treated carbon blacks as supports for platinum catalysts, *J. Catalysis*, **154**, 299–305 (1994).
63. D. Thompsett, Pt alloys as oxygen reduction catalysts. In *Handbook of Fuel Cells*,

Vol. 3 edited by A. L. Wolf Vielstich, and H. A. Gasteiger, John Wiley & Sons Ltd, Chichester (2003).
64. N. Giordano, E. Passalacqua, V. Recupero, M. Vivaldi, E. J. Taylor, and G. Wilemski, An investigation of the effects of electrode preparation parameters on the performance of phosphoric acid fuel cell cathodes, *Electrochim. Acta*, **35**, 1411–1421 (1990).
65. J. C. Shim, and J. S. Lee, Development of electrode structure and analysis of electrode pore distribution in phosphoric acid fuel cells, *Materials Chem. Phys.*, **63**, 133–138 (2000).
66. N. Hara, K. Tsurumi, and M. Watanabe, An advanced gas diffusion electrode for high performance phosphoric acid fuel cells, *J. Electroanal. Chem*., **413**, 81–88 (1996).
67. A. Pebler, Transmission electron microscopic examination of phosphoric acid fuel cell components, *J. Electrochem. Soc.*, **133**, 9–17 (1986).
68. T. Maorka, Electrochemical reduction of oxygen on small platinum particles supported on carbon in concentrated phosphoric acid, *Electrochim. Acta*, **33**, 371–377 (1988).
69. R. D. Breault, J. Donahue, and R. L. Haven, Method of preparing a fuel cell electrode, U.S. Patent 5,732,463, March 31, 1998.
70. R. B. Mathur, P. H. Maheshwari, T. L. Dhami, R. K. Sharma, and C. P. Sharma, Processing of carbon composite paper as electrode for fuel cell, *J. Power Sources*, **161**, 790–798 (2006).
71. P. W. T. Lu, and L. L. France, Improved bipolar plate materials for phosphoric acid fuel cells, *Extended Abstracts, The Electrochemical Society*, **2**, 837–838 (1984).
72. R. D. Breault, and J. Donahue, Porous plate for an electrochemical cell and method for making the porous plate, US Patent 4,652,502 May 24, 1987.
73. R. D. Breault, and M. E. Gorman, Method for forming a laminated electrolyte reservoir plate, US Patent 5,300,124, April 8, 1994.
74. R. D. Breault, and M. E. Gorman, Laminated electrolyte reservoir plate, US Patent 5,366,825, November 22, 1994.
75. R. D. Breault, R. G. Martin, R. P. Roche, and R. Kline, Cathode reactant flow field component for a fuel cell stack, US Patent 5,558,955, September 24, 1996.
76. R. D. Breault, R. G. Martin, R. P. Roche, G. W. Scheffler, and J. J. O'Brien, Coolant plate assembly for a fuel cell stack, US Patent 6,050,331, April 18, 2000.
77. M. Ghouse, H. Abaoud, and A. Al-Boeiz, Operational experience of a 1 kW PAFC Stack, *Appl. Energy*, **65** 303–314 (2000).
78. J. Bear, *Dynamics of Fluids in Porous Media*, Dover Publications, New York (1972).
79. T. Saito, M. Nishioka, Y. Itoh, Y. Miyake, S. Murakami, and N. Furukawa, Study of electrolyte management in phosphoric acid fuel cells, *J. Power Sources*, **37**, 345–354 (1992).
80. T. Mori, J. Imahashi, T. Kamo, K. Tamura, and Y. Hishinuma, Phosphoric acid absorption and performance of gas diffusion electrode, *J. Electrochem. Soc.*, **133**, 896 (1986).
81. T. Mori, A. Honji, T. Kahara, and Y. Hishinuma, Acid absorbancy of an electrode and history, *J. Electrochem. Soc.*, **136**, 1104 (1988).
82. R. Breault, M. Rajpolt, and J. Trocciola, Seal structure for an electrochemical cell, US Patent 4,756,981, July 12, 1988.
83. R. Martin, J. Powers, and J. C. Trocciola, Thermally conductive caulks, US Patent 4,157,327 January 5, 1979.
84. R. D. Breault, M. J. Rajpolt, and J. C. Trocciola, Seal structure for an electrochemical cell, US Patent 4,756,981 July 12, 1988.

85. M. Ohsuga, Gasket for fuel cell, US Patent 5,407,759 April 18, 1995.
86. H. R. Kunz, Transport of electrolyte in molten carbonate fuel cells, *J. Electrochem. Soc.*, **134**, 105–113 (1987).
87. H. Suzuki, K. Ohtsuka, T. Kahara, and T. Yoshida, Fuel cell and supplementary electrolyte container and method for supplementing fuel cell with electrolyte, US Patent 5,563,003 October 8, 1996.
88. P. F. Foley, F. J. Luczak, C. R. Teeling, R. D. Breault, R. R. Fredley, and G. W. Scheffler, System for treatment of acid fuel cell fuel gas stream, US Patent 5,792,572, August 11, 1998.
89. R. Sederquist, D. F. Szydlowski, and R. D. Sawyer, Electrolyte vapor condenser, US Patent 4,372,759 February 8, 1983.
90. M. K. Wright, Corrosion free phosphoric acid fuel cell, US Patent 4,978,591 December 18, 1990.
91. R. R. Fredley, and B. V. Nitta, Fuel cell coolers with inverse flow and condensation zone, US Patent 7,150,929 B2, December 19, 2006.
92. M. Katz, Analysis of electrolyte shunt currents in fuel cell power plants, *J. Electrochem. Soc.*, **125**, 515 (1978).
93. M. Ishizawa, S. Okada, and T. Yamashita, Highly efficient heat recovery system for phosphoric acid fuel cells used for cooling telecommunication equipment, *J. Power Sources*, **86**, 294–297 (2000).
94. E. Pelitti, Chapter 10 corrosion and materials of construction, in *Phosphoric Acid*, edited by A. V. Slack, Marcel Dekker, New York (1968).
95. R. K. Swandby, Corrosion charts: guide to materials selection, *Chem. Eng.*, **69**, 193 (1962).
96. F. N. Smith, The corrosion behaviour of metals and alloys in hot phosphoric acid, *Anti Corrosion Methods and Materials*, **38**, 4–6 (1991).
97. R. F. Miller, R. S. Treseder, and A. Watcher, Corrosion by aerds at high temperatures *Corrosion*, **10**, 7 (1954).
98. A. Mitsuhashi, K. Asami, A. Kawashima, and K. Hashimoto, The corrosion behavior of amorphous nickel base alloys in a hot concentrated phosphoric acid, *Corrosion Sci.*, **27**, 957–970 (1987).
99. K. Shimizu, G. M. Brown, H. Habazaki, K. Kobayashi, P. Skeldon, G. E. Thomson, and G. C. Wood, Direct observation of anodic films formed on tantalum in concentrated phosphoric and sulfuric acid solutions, *Corrosion Sci.*, **40**, 963–973 (1998).
100. K. Hashimoto, A. Mituhashi, A. Kawashima, and Y. Takizawa, Amorphous nickel alloys having high corrosion resistance, US Patent 5,634,989, June 3, 1997.
101. V. B. Singh, and S. M. A. Hosseini, The electrochemical and corrosion behaviour of titanium and its alloy (VT–9) in phosphoric acid, *Corrosion Sci.*, **34**, 1723–1732 (1993).
102. M. A. Matveev, E. E. Mazo, and F. T. Kachur, Chemical resistance of glasses to orthophosphoric acid, *Glass and Ceramics*, **20**, 523–525 (1963).
103. M. A. Matveev, E. E. Mazo, and F. T. Kachur, Mechanism of the reaction of glasses with orthophosphoric acid, *Glass and Ceramics*, **20**, 577–580 (1963).
104. M. L. Perry, and T. F. Fuller, A historical perspective of fuel cell technology in the 20th century, *J. Electrochem. Soc.*, **149**, S59–S67 (2002).
105. H. Pu, L. Qiao, Q. Liu, and Z. Yang, A new anhydrous proton conducting material based on phosphoric acid doped polyimide, *European Polymer J.*, **41**, 2505–2510 (2005).

106. P. J. Ferreira *et al*., Instsbility of Pt/C electrocatalysts in proton exchange membrane fuel cells *J. Electrochem. Soc.*, **152**, A2256 (2005).
107. P. Bindra *et al*., Platinum dissolution in concentrated phosphoric acid, *J. Electrochem. Soc.*, **126**, 1631 (1979).
108. M. Ghouse, Characterization of PTFE-bonded porous carbon electrodes tested in a 100 W phosphoric acid fuel cell (PAFC) stack using XPS and ICP±AES techniques, *J. Appl. Electrochem*., **28**, 955–962 (1998).
109 M. F. Mathias, R. Makharia, H. A. Gasteiger, J. J. Conley, T. J. Fuller, C. J. Gittleman, S. S. Kocha, D. P. Miller, C. K. Mittelsteadt, T. Xie, S. G. Yan, and P. T. Yu, Two fuel cell cars in every garage? *The Electrochemical Society Interface*, **Fall**, 24–35 (2005).
110. K. Kinoshita, *Carbon, Electrochemical and Physicochemical Properties*, John Wiley & Sons, Inc. New York (1988).
111. S. Sarangapani, J. R. Akridge, and B. Schumm, Eds. *The Electrochemistry of Carbon*, Cleveland, OH, August 17–19 1983, The Electrochemical Society, Inc., Cleveland, OH, 158–178 (1983).
112. K. Kinoshita, and J. Bett, Electrochemical oxidation of carbon black in concentrated phosphoric acid at 135C. *Carbon*, **11**, 237–247 (1973).
113. P. L. Antonucci, N. Giordano, *et al*., Electrochemical corrosion behavior of carbon black in phosphoric acid. *Carbon*, **26** (2), 197–203 (1988).
114. K. Kinoshita, and J. Bett, In *Effects of Graphitization on the Corrosion of Carbon Blacks*, Proceedings of the Symposium on Corrosion Problems in Energy Conversion and Generation, held in New York, The Electrochemical Society, Inc., Princeton, NJ, 43–55 (1974).
115. F. A. Heckman, and D. F. Harling, Progressive oxidation of selected particles of carbon black-further evidence for new microstructural model, *Rubber Chemical Technol*, **39**, 1 (1966).
116. G. A. Gruver, The corrosion of carbon black in phosphoric acid. *J. Electrochem. Soc.* **125**, 1719 (1978).
117. P. T. Yu, W. Gu, R. Makharia, F. T. Wagner, and H. A. Gasteiger, The impact of carbon stability on PEM fuel cell startup and shutdown voltage degradation, *Electrochemical Society Trans*, **3**, 797–809 (2006).
118. K. H. Kangasniemi, D. A. Condit, and T. D. Jarvi, Characterization of vulcan electrochemically oxidized under simulated PEM fuel cell conditions. *J. Electrochem. Soc*., **151** (4), E125–E132 (2004).
119. C. H. Paik, G. S. Saloka, and G. W. Graham, Influence of cyclic operation on PEM fuel cell catalyst stability. *Electrochem. Solid-State Lett.*, **10** (2), B39–B42 (2007).
120. L. A. Langley, D. E. Villanueva, and D. H. Fairbrother, Quantification of surface oxides on carbonaceous materials, *Chem. Mater.*, **18**, 169–178 (2006).
121. K. Kinoshita, and J. Bett, Potentiodynamic analysis of surface oxides on carbon blacks, *Carbon*, **11**, 403–311 (1973).
122. Z. R. Yue, W. Jiang, L Wang, S. D. Gardner, Jr., C. U. Pittman, Surface characterization of electrochemically oxidized carbon fibers, *Carbon*, **37**, 1785–1796 (1999).
123. B W Chun, C. Randall Davis, Q. He, and R R Gustafson, Development of surface acidity during electrochemical treatment of pan-carbon fibers, *Carbon*, **30** (2), 177–187 (1992).
124. J. Willsau, and J. Heitbaum, The influence of Pt-activation on the corrosion of carbon in gas diffusion electrodes – a DEMS study, *J. Electroanalytical Chem*., **161**, 93–101 (1984).

125. L. M. Roen, C. H. Paik, and T. D. Jarvi, Electrocatalytic corrosion of carbon support in PEMFC cathodes, *Electrochem Solid-State Lett*., **7** (1), A19–A22 (2004).
126. B. D. Cullity, *Elements of X-Ray Diffraction*, second ed.; Addison-Wesley Publishing Company, Inc., Reading, MA (1978).
127. P. Stonehart, and J. MacDonald, In *Corrosion of Carbons in Acid Electrolytes*, The Electrochemistry of Carbon, Cleveland, OH, August 17–19 1983, edited by S. Sarangapani, J. R. Akridge, and B. Schumm, The Electrochemical Society, Inc., Cleveland, OH, 292–312 (1983).
128. I. Nikolov, and T. Vitanov, The effect of method of preparation on the corrosion resistance and catalytic activity during corrosion of tungsten carbide i. corrosion resistance of tungsten carbide in sulfuric acid. *J. Power Sources*, **5**, 273–281 (1980).
129. H. Chhina, S. Campbell, and O. Kesler, Thermal and electrochemical stability of tungsten carbide catalyst supports, *J. Power Sources*, **164**, 431–440 (2007).
130. J. Giner, and C. Hunter, The mechanism of operation of the Teflon-bonded gas diffusion electrode: A mathematical model, *J. Electrochem. Soc.*, **116**, 1124 (1969).
131. R. P. Iczkowski and M. B. Cutlip, Voltage losses in fuel cell cathodes, *J. Electrochem. Soc.*, **127**, 1433 (1980).
132. G. Maggio, Modelling of phosphoric acid fuel cell cathode, *J. Appl. Electrochem.*, **29**, 171–176 (1999).
133. K. Yamashita, and T. Taniguchi, Agglomerate model for DC and AC response of phosphoric acid fuel cell cathode, *J. Electrochem. Soc.*, **145**, 45–49 (1998).
134. S. C. Yang, Modeling and simulation of steady-state polarization and impedance response of phosphoric acid fuel-cell cathodes with catalyst-layer microstructure considerations, *J. Electrochem. Soc*., **147**, 71–77 (2000).
135. S. C. Yang, M. B. Cutlip, and P. Stonehart, Simulation and optimization of porous gas-diffusion electrodes used in hydrogen/oxygen phosphoric acid fuel cells, *Electrochim. Acta*, **35**, 869–878 (1990).
136. S. R. Choudhury, M. B. Desmukh, and R. Rengaswamy, A two-dimensional steady-state model for phosphoric acid fuel cells (PAFC), *J. Power Sources*, **112**, 137–152 (2002).
137 S. R. Choudhury, S. R. Choudhury, J. Rangarajan, and R. Rengaswamy, Step response analysis of phosphoric acid fuel cell (PAFC) cathode through a transient model, *J. Power Sources*, **140**, 274–279 (2005).
138. P. L. Zervas, M. K. Koukou, N. G. Orfanoudakis, and N-C. Markatos, Evaluating low-temperature fuel cell performance for power generation: fluid dynamics study of phosphoric acid fuel cell systems at the cell level, Proc. IMechE Vol. 220 Part A: *J. Power and Energy*, 525–533.
139. P. L. Zervas, M. K. Koukou, and N. C. Markatos, Predicting the effects of process parameters on the performance of phosphoric acid fuel cells using a 3-D numerical approach, *Energy Conversion Manage*., **47**, 2883–2899 (2006).
140. D. A. Betts, V. A. Roan, and J. H. Fletcher, Discussion and analysis of flue gas utilization in a phosphoric acid fuel cell engine during idle operation, *Trans ASME*, **3**, 26–32 (2006).
141. J. Scholta, B. Rohland, and H. Wendt, Hydrogen Fired PAFCs: an experimental investigation into the optimal utilization of impure, recycled hydrogen, *J. Appl. Electrochem*., **30**, 323–331 (2000).
142. D. N. Patel, H. C. Maru, M. Farooque, and C. H. Ware, Methodology for predictive testing of fuel cells, *J. Electrochem. Soc*., **131**, 2750 (1984).

143. A. J. Appleby, Fuel cell technology: status and future prospects, *Energy*, **21**, 521–653 (1996).
144. N. Hojo, M. Okuda, and M. Nakamura, Phosphoric acid fuel cells in Japan, *J. Power Sources*, **61**, 73–77 (1996).
145. K. Shibata and K. Watanabe, Philosophies and experiences of PAFC field trials, *J. Power Sources*, **49**, 77–102 (1994).
146. K. Kasahara, M. Morioka, H. Yoshida, and H. Singai, PAFC operating performance verified by Japanese gas utilities, *J. Power Sources*, **86**, 298–301 (2000).
147. R. Vellone, F. DiMario, V. Cincotti, and M. Brocco, Status of fuel cell r&d programme and perspectives for commercialization in Italy, *J. Power Sources*, **37**, 111–116 (1992).
148. H. Nymoen, PAFC demonstration plants in Europe: first results, *J. Power Sources*, **49**, 63–76 (1994).
149. S. Romano, and J. T. Larkins, Georgetown University Fuel Cell Transit Bus Program, *Fuel Cells*, **3**, 128–132 (2003).
150. N. Sammes, R. Bove, and K. Stahl, Phosphoric acid fuel cells: fundamentals and applications, *Current Opin. Solid State Mater. Sci.*, **8**, 372–378 (2004).
151. J. P. Vanhanen, P. S. Kauranen, and P. D. Lund, Operation experiences of a phosphoric acid fuel cell in a solar hydrogen energy system, *Int. J. Hydrogen Energy*, **22**, 707–713 (1997).
152. R. J. Spiegel, and J. L. Preston, Technical assessment of fuel cell operation on anaerobic digester gas at the Yonkers, NY, Wastewater Treatment Plant, *Waste Management*, **23**, 709–717 (2003).
153. H. Y. Kwak, H. S. Lee, J. Y. Jung, J. S. Jeon, and D. R. Park, Exergetic and thermoeconomic analysis of a 200 kW phosphoric acid fuel cell plant, *Fuel*, **83**, 2087–2094 (2004).
154. J. S. Wainright, J–T. Wang, D. Weng, R. F. Savinell, and M. Litt, Acid-doped polybenzimidazoles: a new polymer electrolyte, *J. Electrochem. Soc.*, **142**, L121 (1995).
155. Y. Abe, D. Yoshikawa, M. Ito, and H. Taguchi, Superprotonic conductors of gypsums containing H_3PO_4 for fuel cells below 200 °C, *Electrochem. Solid-State Lett.*, **10**, B111–B113 (2007).
156. Y. Aihara and A. Sonai, A proton conducting electrolyte based on novel polyparbanic acid doped by H_3PO_4 for medium temperature PEMFC, *ECS Transactions*, **3** (1) 123–135 (2006).
157. A. Bozkurt, M. Ise, K. D. Kreuer, W. H. Meyer, and G. Wegner, Proton conducting polymer electrolytes based on phosphoric acid, *Solid State Ionics*, **97**, 347–358 (1997).

7

Molten carbonate fuel cells

S McPHAIL, E SIMONETTI and A MORENO,
ENEA – Hydrogen and Fuel Cell Project, Italy and
R BOVE, Institute for Energy, The Netherlands

7.1 Introduction

What distinguishes the molten carbonate fuel cell (MCFC) from other hydrogen-oxygen fuel cells is the employment of a molten salt electrolyte. The high temperature at which the fuel cell operates (650 °C, to keep the salt in liquid state) offers distinct advantages: (electro)chemical reactions are more rapid, resulting in faster reduction and oxidation kinetics, thereby eliminating the need for noble metal catalysts. In addition to cost reduction, this implies that carbon monoxide does not exhibit any poisoning effect on the fuel cell, and on the contrary can be used as an additional fuel. The high temperature is also eminently suitable for hydrocarbon reforming, which can take place directly inside the cell.

The MCFC offers considerable opportunities especially for medium to large-scale power generation, thanks to their highly efficient conversion efficiency (>45%), potential for cogeneration and added bottoming cycle, quiet operation and essentially clean products with low environmental impact. Compared with other fuel cell technologies, the MCFC has the steepest polarization curve (*V–I* characteristic). This means it is advantageous at low current density operation, resulting, however, in relatively low power densities (see Fig. 7.1).

After a brief explanation of the basic operating principles of the molten carbonate type fuel cell (Section 7.2), and an overview of the raw materials utilized (7.3), in the sections that follow, various requirements and difficulties will be dealt with – of chemical, physical and mechanical nature – of each key component for satisfactory operation of the system (7.4 and 7.5). References to the current research for alternative materials and solutions that could improve this operation are provided.

7.2 Operating principles

The typical structure of a MCFC is schematically illustrated in Fig. 7.2. The overall reaction that takes place in a molten carbonate fuel cell is:

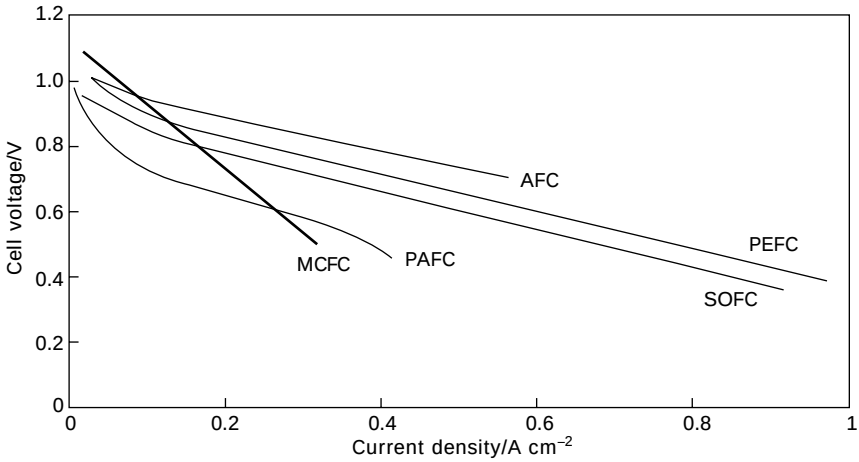

7.1 Polarization curves for various fuel cell types – AFC alkaline fuel cell, MCFC molten carbonate fuel cell, PAFC phosphoric acid fuel cell, PEFC polymer electrolyte fuel cell, SOFC solid oxide fuel cell (Tomczyck, 2006).

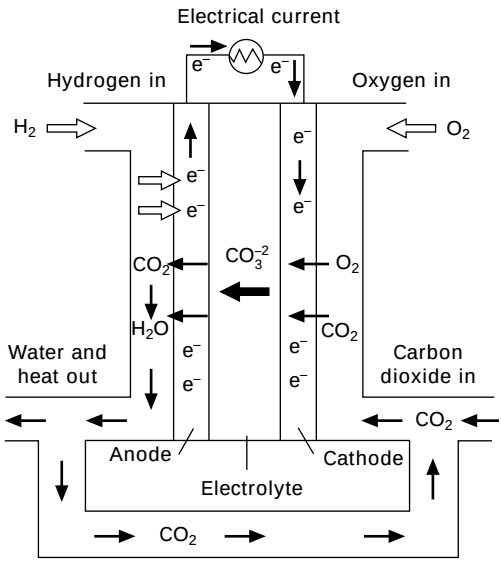

7.2 Schematic representation of MCFC operation.

$$H_2 + CO_3^{2-} \rightarrow H_2O + CO_2 + 2e^- \qquad 7.1$$

which corresponds to the reduction mechanism on the anode side. Ionic transfer inside the electrolyte is conducted via CO_3^{2-} ions that migrate to the anode from the cathode, where they are created through the oxidation reaction:

$$CO_2 + {}^1/_2 O_2 + 2e^- \rightarrow CO_3^{2-} \qquad 7.2$$

Since the CO_2 required for reaction (7.2) is the same that is formed as a consequence of reaction (7.1), anodic gas is generally recycled from the anode to the cathode, though any CO_2 transfer device may be employed.

7.3 Materials utilized

To give a wider context to the following discussion on material issues of the key components, it is interesting to take a look at the impact of the raw materials that make up a state-of-the-art molten carbonate fuel cell. After more than 20 years of field implementation, it can be stated that there is a general standard of MCFC that serves as a baseline model, which is efficiently operational, but leaves ample room for improvement, as will be discussed in depth in Sections 7.4 and 7.5.

The main materials that constitute such a cell are nickel (for the electrodes), lithium aluminate (electrolyte-containing support), lithium–sodium or lithium–potassium carbonate (electrolyte), stainless steel (for secondary equipment such as the bipolar plate and gas manifolds) and chromium and/or aluminium for reinforcement and corrosion protection. The proportions at which these materials make up an entire stack are depicted in Fig. 7.3 (Biedenkopf *et al.*, 2000).

Investigation through life-cycle analysis (LCA) of the contribution of each of these components to cell cost, environmental impact and cradle-to-grave efficiency merits a chapter in itself, but it is enlightening to give some results of such a study to comprehend the overall 'weight' of the raw materials utilized in the realization of a MCFC stack. In Table 7.1 the contribution of

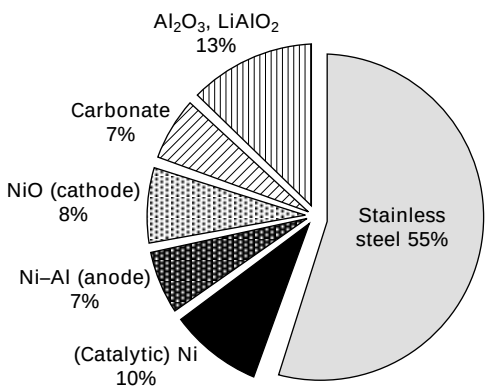

7.3 Materials composition of a MCFC stack (adapted from Biedenkopf *et al.*, 2000).

Table 7.1 Typical 500 kW stack: contribution of each component in terms of impact indicators

Input	Abiotic		Water		Energy		Solar energy	
	(10^3 kg)	%	(10^3 kg)	%	(GJ)	%	(sePJ)	%
Anode (Ni/Al)	528	49.9 %	3610	44.1 %	1486	43.8 %	177	38.8 %
Cathode (Ni)	168	15.9 %	1390	17.0 %	318	9.4 %	60	13.1 %
Matrix (α-$LiAlO_2$)	46	4.3 %	246	3.0 %	224	6.6 %	23	5.0 %
Electrolyte (Li_2/Na_2CO_3)	6	0.5 %	42	0.5 %	31	4.2 %	7	1.5 %
Special stainless steel (310)	76	7.2 %	1020	12.5 %	398	11.7 %	97	21.4 %
Stainless steel (other)	234	22.2 %	1870	22.9 %	938	27.6 %	92	20.2 %
Total/stack	1058	100 %	8178	100 %	3395	100 %	456	100 %
Total/kW	2.12		16.4		6.78		0.91	

each key component of a typical 500 kW stack is given, in terms of four impact indicators: the amount of abiotic (mineral, inorganic) material used in their fabrication, the amount of water, energy and solar energy equivalent (energy, expressed in solar-energy-Joules) that was subtracted from the Earth's equilibrium state for the realization of the component and thereby not utilizable for other ends (Ulgiati *et al*., 2005).

For each component, the same analysis can be carried out regarding its constituent components, but that is outside the scope of this chapter. What can be evinced from the figures presented is the large impact that the electrodes have on the make-up of required resources, especially the anode. This is due to the large flows of abiotic material and water that are needed in the extraction and refinement processes to obtain nickel of the desired degree of purity and – in the case of the anode – the large quantity of waste material that is produced and the energy-intensive process of binding with aluminium. This also emphasizes the general profit that adequate means of recycling such a component would bring.

From the indicators of the stainless steel parts that make up the balance-of-plant (BOP), their large contribution to stack cost can be deduced, even though they require less-specialized manufacturing procedures. In contrast, the electrolyte presents the least impact on the total of required resources.

Translated into economics, there is an important factor of up-scaling that influences the total cost of a MCFC stack: the price per kW can be up to 30% lower for a 2.5 MW compared with a 250 kW plant. If we consider the stack divided into two main parts (mechanical and electrical BOP and the fuel-cell module), the BOP offers scale-up advantages similar to those seen in conventional generation technologies. The fuel-cell module can be broken down further into repeating components, i.e. the cell packages that produce power, and non-repeating components, i.e. the singular hardware that keeps the cells under compression, distributes gases and collects current from the stack. The cell package cost depends mainly on operating current density and to a smaller extent on cell size. Non-repeating components also benefit to a certain extent from the economy of scale, like the BOP. A typical distribution of the total cost is depicted in Fig. 7.4, where the decreased relative contribution of the BOP to total cost in a 3 MW stack (b) can be compared with the proportion in a smaller, 300 kW stack (a) (Farooque, 2007; Venkataraman *et al*., 2007).

At the current price level, the MCFC is still not competitive with conventional power generation systems, unless particular requirements are imposed regarding pollution, noise level or by-product utilization, where the superior performance of the MCFC gains ground in cost–benefit analysis. To really break through on the medium-to-large-scale market, however, the price per kW should be driven down from around €4000, where it stands today, to about €1500. This demands continuing efforts from materials

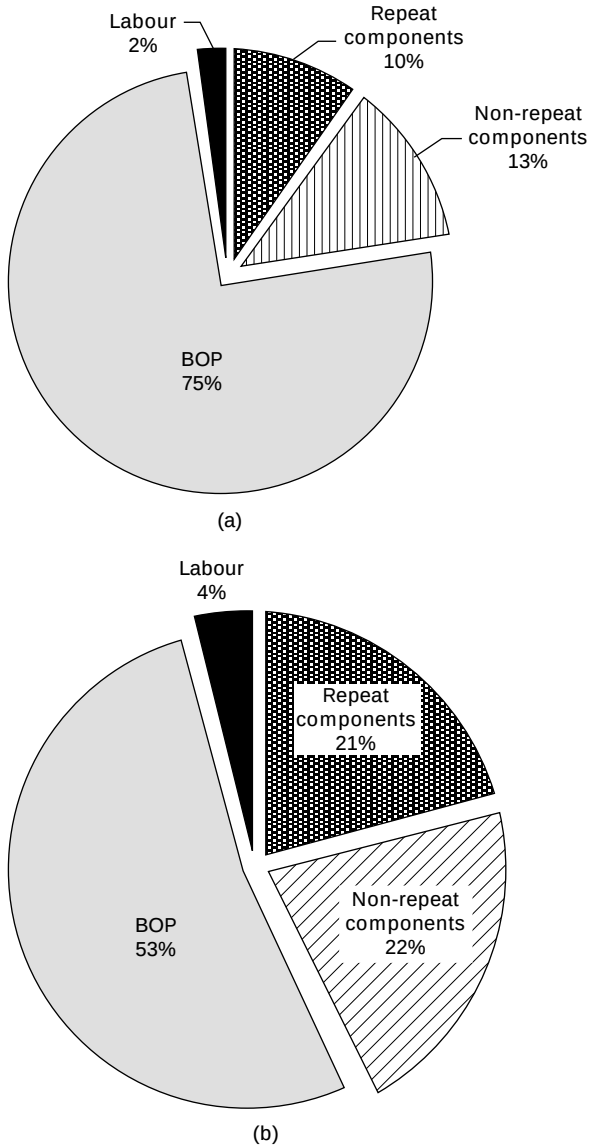

7.4 Typical cost distribution of a MCFC stack: 300 kW nominal power (a), 3 MW nominal power (b) (courtesy of FuelCell Energy).

scientists, chemists, engineers, governments and investors to supply a technology that is as reliable and cost-effective as possible and provide a base of application opportunities for the MCFC to gain a solid foothold on the world energy market.

7.4 Active components

Active components are those elements of the fuel cell that take part directly in the electrochemical conversion of the inlet reactants. In the 1950s, Dutch scientists G.H.J. Broers and J.A.A. Ketelaar, the first to develop the MCFC, used a nickel anode, a silver cathode and the ternary eutectic Li_2CO_3–Na_2CO_3–K_2CO_3 as the electrolyte, supported by MgO. Since then, a lot of progress has been made. Whereas the cell lifetime did not exceed 1000 hours in this first version, several MCFC stacks have now achieved a >20 000 h running period, with performances improving from 10 to >150 mW/cm^2. In a large part this has been thanks to improvements in the four active components mentioned, which will be dealt with in the present section.

The following issues will be addressed: what are the material requirements for ideal activity of the component? What is the present state-of-the-art material utilized and what are the main steps of the manufacturing procedure? And finally: which are the difficulties that have to be overcome before the MCFC can become a customary, fully grown technology? Which are the new developments that are taking us there?

7.4.1 Anode

The anode is the electrode where the fuel is catalytically oxidized. The MCFC, like all fuel cells, uses hydrogen as fuel, but, unlike low-temperature fuel cells, can also convert carbon monoxide, which is especially interesting from the point of view of combination with biogas, syngas or coal gas. The utilization of CO can occur through the water–gas shift reaction:

$$CO + H_2O \rightarrow H_2 + CO_2 \qquad 7.3$$

which reaches equilibrium quickly at high temperatures, but also direct oxidation of carbon monoxide is possible:

$$CO + CO_3^{2-} \rightarrow 2CO_2 + 2e^- \qquad 7.4$$

though its reaction kinetics are slower and its contribution is relatively slight to overall performance (1–3 A/m^2 of around 1000 A/m^2) (Bodén *et al.*, 2005).

Anode requirements

Thanks to the high operating temperature of the MCFC, reaction kinetics are greatly facilitated and the catalytic activity of the electrodes need not be exceptional. This avoids the necessity for noble metals, which is one of the advantages of high-temperature fuel cells. The anode, however, should be resistant to the interstitial action of hydrogen: due to its minuteness, the

hydrogen molecule tends to insert itself in gaps and vacancies, weakening the bond of the metal's crystal structure. This leads to fragility and brittleness of the material, increasing the risk of spallation or even fracture.

When considering operation on biomass-derived or coal-based fuel gas, sulphur tolerance is an important issue. The effect of introduction of sulphur compounds (in particular H_2S) is generally to poison the catalytic activity of the anode, though this may be the result of different chemical processes (Vogel and Smith, 1982). The poisoning is reversible for H_2S up to concentrations of 10 ppm by placing the anode in a perfectly sulphur-free environment for a period of time.

On the electrolyte side, the environment is more hostile still, with hot corrosion by the acidic, molten carbonate attacking the stability of the anode material. This especially places restrictions on the materials that are applicable, having to be corrosion-resistant while maintaining excellent electrochemical catalytic activity.

To promote the latter, an interfacial area with the electrolyte must be provided that is as high as possible. To this effect, the anode should be porous to the right degree: macro-porosity should provide easy access for the fuel gas; a dense micro-porosity is required to draw in the liquid carbonate through capillary force so that the oxidation reactions can take place at the catalyser surface. This area is the vital heart of electrochemical activity and the defining characteristic of the molten carbonate fuel cell, and is called the three-phase interface (see also Section 7.4.3).

Necessarily, the anode should be made of conductive material to ensure unhindered flowing of the electrons liberated by the reaction. For an allowable ohmic loss during the drawing of current in fuel cell operation, the electrical conductivity should be larger than about 100 S/m or 1 S/cm. Thus, also the anode thickness should be kept as low as possible to improve conductivity, insofar as this is compatible with adequate mechanical strength.

The anode also acts as a recipient for supplementary electrolyte, to make up for carbonates lost through evaporation or otherwise: this must be kept in mind as well when considering its final size. In stack configuration, the cells have to be able to support the comprehensive weight of the piled elements. In addition, usually a mechanical load is applied to the stack to minimize contact resistance between components and keep the stack gas-tight. Furthermore, the mechanical strength of the single fuel cells has to be such as to withstand stresses due to thermal dilation. Since the temperature distribution in a stack is never perfectly uniform, strong deformations can occur due to this phenomenon, which compromises the leak-tightness of the various components. Other mechanical thermal-degradation effects can occur, such as sintering (i.e. the decreasing of porosity due to thermal bonding of the material grains) and creep (i.e. material deformation to relieve internal stresses). A summary of requirements is given in Table 7.2.

Table 7.2 Requirements of the ideal anode

Requirement	Level
High electrocatalytic activity for H_2 oxidation	–
Resistance to H_2 interstitial interference	100% H_2 for > 40000 h
Enduring resistance to sulphur poisoning	>10 ppm S
Good wetting properties (low wetting angle)	< 45°
Porosity	45–70% 3–6 μm size
Conductivity	> 1 S/cm
Resistance to fracture, sintering, creep, thermal dilation	40000 h in full load operation
Low solubility in alkali carbonates	< 10 ppm
Low cost	–

Another important aspect concerning the anode, as mentioned, is its function as an electrolyte reservoir. As will be highlighted in the section on the electrolyte and matrix (7.4.3), one of the main problems in MCFC long-term operation is depletion of the liquid electrolyte through leakage, metal reaction and evaporation. The impregnation of the anode by an excess of electrolyte provides a remedy to this problem, but has to be weighed against the diminution of active surface-area and conductivity, and the increase of the gas phase mass transport resistance, leading to additional polarization losses. The optimal electrolyte filling degree, furthermore, depends on pore size distribution, electrode thickness, electrolyte composition and even on fuel gas composition (Bodén, 2007).

Anode: state-of-the-art in pre-commercial applications

Since the early 1970s, porous nickel has been the material used for the anode, strengthened against creep and fracture by the addition of chromium and/or aluminium. The chromium is effective against loss of surface area, pore growth and sintering, though too much addition has the negative aspect of consuming carbonate through lithiation by effect of the electrolyte. Adding alloying agents can also compromise porosity and conductivity requirements. The current level of Cr or Al addition is between 6 and 10%, which seems to have resolved most problems relating to performance and cell lifetime (Mugikura, 2003).

Anode: manufacturing procedure

For a state-of-the-art nickel anode, reinforced with 6–10% chromium, the state-of-the-art manufacturing process is tape-casting, which works synthetically as follows. (Tape-casting is the method of construction of each of the porous components of the MCFC, i.e. anode, cathode and electrolyte

matrix.) The metal powder (Nickel 255 (sole supplier Inco) with alloying additives such as chromium and other precursors to the desired degree) is mixed with a solvent, dispersant and binder to make a slurry which is then cast into a < 1 mm tape on a polyethylene carrier sheet under a moving doctor blade (see Fig. 7.5).

The obtained green tape is then dewaxed and sintered in an electric furnace at 900 °C, after which a chemical-physical analysis and uniformity measurements determine whether the electrode has obtained the right characteristics. For the proper performance of the MCFC electrodes it is important that they have a uniform thickness and microstructure, which is more difficult to achieve as the electrode area is increased, owing to longer casting and sintering times. The large area especially impedes uniform heating of the entire sheet, causing warped edges and irregular thickness.

The tape-casting process has allowed significant scale-up of the manufacturing process of the planar components and cells of 1 m^2 are now routinely manufactured. Improvements in the manufacturing process are now aimed at reducing costs. An important solution in this respect would be the possibility of utilizing water-based rather than solvent-based slurries for the nickel preparation.

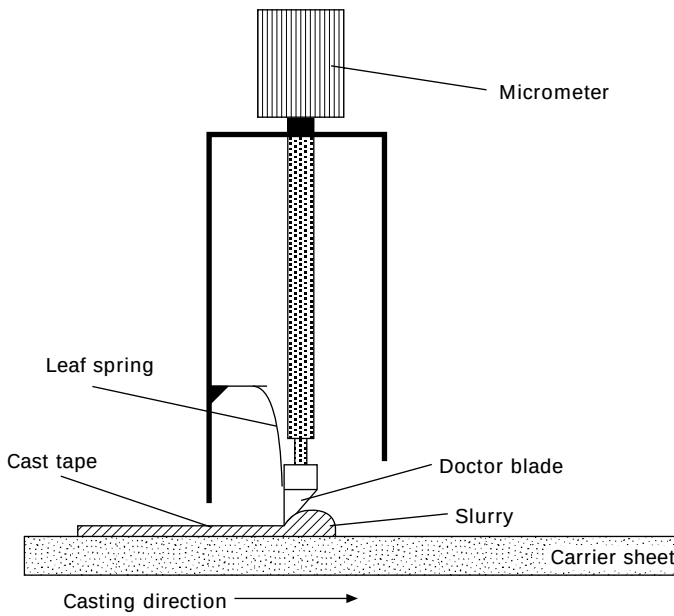

7.5 The tape-casting process with doctor blade method (adapted from Yoshikawa and Hirabayashi, 1995).

Anode: difficulties and new developments

Though the current additives to the anode base material, added to the right degree and following careful procedures for their dispersion, have in a large part solved the problem of creepage, the susceptibility to this phenomenon could still be improved. The most significant development in anode materials recently, also in this respect, is the use of ceramic oxides. In addition to providing less opportunity for carbon deposition, ceramic oxides (such as lanthanum, cerium and samarium with additives for the improvement of electronic conductivity) offer the prospects of being fuelled by dry methane, as is the case with solid oxide fuel cells (Tagawa *et al*., 2004). Moreover, ceramic-based or ceramic-coated anodes improve sulphur tolerance notably, possibly by an order of magnitude (Nam *et al*., 2005), in addition to being morphologically stable during cell operation, increasing wettability and having potentially lower material cost (Iacovangelo, 1986).

At present, no alternative metallic anodes have been identified that provide adequate resistance to sulphur poisoning: the tolerance level remains 10 ppm for unaffected momentary performance, 0.5 ppm for durable operation. Tolerance to sulphur is an essential issue where the coupling is concerned of an MCFC to a biogas, syngas or coal gas plant. The current one is a very low degree of acceptance, which pushes the cost of gas clean-up before the cell inlet to very high levels since to remove sulphur from a gas becomes exponentially more difficult as the desired outlet concentration decreases (Ekins, 2001). Research is concentrating on the solution of this problem from both sides: increase of catalyst resistance and cost reduction of efficient gas clean-up before introduction into the cell.

7.4.2 Cathode

By analogy with the anode, the electrocatalytic reduction of oxygen takes place at the cathode. Oxygen from air and carbon dioxide (recycled from the anode exit or obtained from external combustion flue gas) react with the electrons to form CO_3^{2-} ions that replenish the electrolyte and transfer current through the fuel cell (see also Fig. 7.2). Synthetically:

$$^1/_2\,O_2 + CO_2 + 2e^- \rightarrow CO_3^{2-} \qquad 7.5$$

To provide the reaction site between the oxidant stream and the charge-carrying electrolyte, the cathode must be porous at two different levels: small pores are filled with electrolyte and are responsible for transport of ions, while larger pores provide access for the gaseous species. (This dual pore size distribution is more accentuated than in the case of the anode, because of the difference in size of hydrogen and oxygen or CO_2 molecules.) The efficiency of the cathode can be improved by increasing the number of

sites where the reaction can occur, but this is not achieved by simply increasing the specific surface area: gas, electrolyte and catalyst must meet efficiently in a three-phase junction. Therefore, a network of uniformly dispersed gas, liquid and solid phase must be formed by appropriate design of the cathode material pore structure. Furthermore, a sufficiently accessible path must be maintained throughout the electrode for transport of gaseous species, electrolyte ions and electrons. The optimum cathode pore structure is thus the best possible compromise between catalytic activity, transport properties and long-term chemical and morphological stability. This optimum, however, is individual for each material, depending on crystal structure, wettability and, oxidation mechanisms, making the optimization process very difficult.

Cathode: requirements

The severe oxidizing conditions present at the cathode side limit the number of metals that can be used as electrocatalysts. Furthermore, the following requirements must be guaranteed for a material to be a good candidate for a MCFC cathode: high electronic conductivity to minimize resistance and ohmic polarization; chemical and physical stability at operative conditions of the MCFC and in a cathode environment (650 °C, O_2/CO_2 mixture, alkali carbonates) to maintain catalytic performance; low solubility in the cathode-electrolyte environment to avoid precipitation of metal in the electrolyte structure (see the following paragraph); high electrocatalytic activity for the O_2 reduction (easily oxidized); suitability for the fabrication of porous electrodes with high specific surface area; good wettability by the electrolyte in the oxidant environment; a thermal expansion coefficient that is compatible with those of the other cell components, to minimize mechanical stress during heating and in hot- or cold-spots. The requirements are summarized in Table 7.3.

Table 7.3 Requirements of the ideal cathode

Requirement	Level
High electrocatalytic activity for O_2 reduction	–
High electronic conductivity	> 1 S/cm
Low solubility	< 5 ppm
or low dissolution rate in alkali carbonates	< 1 μg/cm^{2}h
Porosity	70–80% before (*in situ*) lithiation and oxidation (60–70% after) 7–15 μm pore size
Good wettability	< 45°
Congruous thermal expansion coefficient	with other cell components
Low cost	–

The difficulty here consists of satisfying all requirements to the desired level simultaneously, as the achievement of some attributes precludes the possibility of obtaining the correct degree of certain other requirements. For example, ferrous materials manifest excellent resistance to electrolyte dissolution, but have an unacceptably low electrical conductivity. Lanthanum–perovskites, on the other hand, have suitably high electronic conductivity values, and are chemically stable in the electrolyte, but tend to manifest the same dissolution behaviour as NiO, in addition to being reactive with the state-of-the-art electrolyte matrix material, $LiAlO_2$ (Baumgartner *et al*., 1984). Reducing cell temperature would be beneficial for the durability of the cathode, as dissolution, chemical-physical degradation and thermomechanical stresses would be diminished. However, this would compromise the reactivity of the oxygen reduction as well, reducing power density. This could be improved by advanced tailoring of the electrode microstructure, to increase the number and sensitivity of the reaction sites (Selman, 2007). In general, the low-cost condition is the hardest to reconcile with the physical requirements.

Cathode: state of the art in pre-commercial applications

Before 1970 the MCFC cathode was made of silver or copper. The development approach has followed the general sequence of experimentally identifying stable materials, evaluating their properties, improving their conductivity, developing fabrication methods to attain the required complex pore structure and finally testing the cathodes in the cell. The candidate material should have the requirements described in the previous paragraph; basically, compounds that contain multivalent ions have the potential for high electronic conductivity due to intrinsic non-stoichiometry; further enhancement of conductivity can be achieved through doping.

Today, a porous nickel electrode is utilized in the cell. During the first hours of operation it is *in situ* oxidized and lithiated by the Li–K carbonates melt to lithiated-NiO (i.e. $Li_xNi^{2+}{}_{1-2x}Ni^{3+}{}_xO$). This process gives it its characteristic dual pore size distribution, required for proper functioning of the three-phase interface. The electrical conductivity of lithiated-NiO is about 10 S/cm for the dense material at 650 °C (Plomp *et al.*, 1992). This is one order of magnitude better than is required for making high-performance MCFC cathodes. By optimizing the pore structure, the potential drop at the cathode is limited to ~100 mV (@ 160 mA/cm^2) in a stack operated at 650 °C (Lundblad, 1996).

However, the problem with lithiated-NiO is that its dissolution rate in the molten carbonates is too high. The solubility *equilibrium* of Ni^{2+} in a Li–K melt is low enough, reached at an ion concentration of 30–50 ppm, but owing to the concentration gradient caused by the reducing conditions at the anode and the electric field in the cell, a driving force is put in place that

enhances the precipitation of metallic Ni particles (Freni *et al.*, 1998). This does not allow the system to reach its solubility equilibrium and the dissolution process of the cathode structure becomes continuous. As the cathode material is dispersed and transported inside the electrolyte, the dissolved Ni^{2+} precipitates as metal dendrites in the matrix and can eventually short-circuit the cell – a figurative example is given in the SEM image and corresponding nickel microanalysis output of Fig. 7.6.

The dissolution rate is pressure-dependent and by pressurizing (>4 atm) an MCFC with a NiO cathode, the lifetime has been estimated to decrease from 25 000 h to 3500 h (Baumgartner *et al.*, 1984; Plomp *et al.*, 1992). Nickel dissolution is one of the major life-limiting issues in MCFC applications today, together with electrolyte loss and matrix degradation (see Section 7.4.3).

Cathode: manufacturing procedure

Three different methods are adopted to prepare the lithiated nickel oxide cathodes for MCFCs. In the first method, Ni electrodes with the desired porosity are prepared and oxidized and lithiated inside the cell (*in situ*). The cathode is prepared with Nickel 255 powder (sole worldwide supplier Inco). A slurry for tape-casting is made using the same binders that are used in anode fabrication, a plasticizer and a dispersant agent. After removing the organic binders and solvents the tape-cast green tape is sintered in a nitrogen atmosphere at 850 °C. The nickel plaque is placed in a reducing environment at an elevated temperature to promote sintering, a step in which nickel particles bond and develop strength. This procedure produces a cathode having a thickness of 0.5 mm, a porosity in the range of 70–80% and an average pore diameter in the range of 7–15 μm. The nickel cathode is then oxidized and

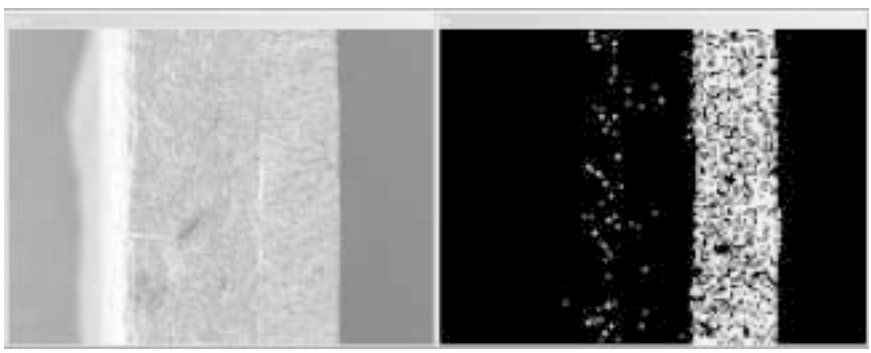

(a) (b)

7.6 Scanning electron microscope (SEM) image of single cell tile (a) with dispersed Ni precipitation in the matrix (b) for a NiO cathode after 1500 h of operation (Masci, 2007).

lithiated *in situ* at the cell operating temperature to render the completed nickel oxide cathode.

In the second method, out-of-cell oxidation and lithiation of nickel powder is carried out by mixing nickel powder with lithium carbonate followed by oxidation in air at 650 °C (ex-situ). This is then tape-cast into the finished electrode.

In the third method, the pre-lithiated nickel catalyst is formed into an electrode by the tape-casting technique after which it is subjected to in-cell or out-of-cell oxidation and sintering. For final control of the finished product, physical-chemical characterization of the catalyst and the electrode are obtained by X-ray diffraction (XRD) and mercury porosimetry respectively.

Cathode: difficulties and new developments

To solve the problem of nickel oxide dissolution it is possible to add elements (for instance rare earth species) to the melt which make it more basic (see Section 7.4.3) or to find alternative cathode materials (Baumgartner *et al.*, 1984). Many candidate materials have been investigated: ferrites, cobaltites, manganites, doped metal oxides, ilmenites, spinels and perovskites. The majority of these are either not stable in carbonate melt, or react with the $LiAlO_2$ of the matrix (Giorgi *et al.*, 1993).

The two most promising candidates are $LiFeO_2$ and $LiCoO_2$. Both these metal oxides are properly wet by the electrolyte and are more stable than NiO in the cathode environment. $LiFeO_2$ is the less expensive alternative, but its electrical conductivity is too low ($\approx$ 0.05 S/cm). Furthermore, the catalytic activity of $LiFeO_2$ seems to be less than that of lithiated-NiO or $LiCoO_2$ and its electrical conductivity is very sensitive to gas composition. Attempts to improve the conductivity characteristics of $LiFeO_2$ have been made by doping with Co, Ni, Mg and other elements, but this approach has not yet been successful.

Literature values for electrical conductivity for stoichiometric $LiCoO_2$ at 650 °C are somewhat scattered (between 0.1 and 2 S/cm), but most commonly the reported values are around 1 S/cm (Giorgi *et al.*, 1994). The catalytic activity of $LiCoO_2$ is somewhat lower, about 60% of that of lithiated-NiO. That is still five times better than that of $LiFeO_2$ (Lagergren *et al.*, 1994).

$LiCoO_2$ exhibits a dissolution behaviour similar to that of NiO, however, the dissolution rate at 1 atm is about eight to ten times smaller (Giorgi *et al.*, 1993). The pressure dependence is also smaller than that of NiO. Another advantage of $LiCoO_2$ is that Co does not precipitate so close to the cathode, thereby increasing the time before short-circuiting of the cell. Because of the high price of cobalt and the brittleness of an electrode made of solid Co, the possibility of coating nickel particles or a nickel porous electrode with lithium cobaltite has been successfully explored by various authors.

Ternary compositions of $LiFeO_2$, $LiCoO_2$ and NiO are also expected to combine in the desirable properties that are characteristic to each single material component: it is hoped that $LiFeO_2$ will reduce the solubility of the ternary material in Li–K carbonate melts, while suitable conductivity is aimed at through the adoption of NiO and $LiCoO_2$. Furthermore, the chemical potential of each of the single component materials should be lower in the $LiFeO_2$–$LiCoO_2$–NiO ternary composition, which should decrease the dissolution rate of the ternary materials in the carbonate melt.

Regarding the recent, highly interesting exploratory activities on the coupling of MCFCs with biogas and syngas, the utilization of fuel derived from alternative sources implies some difficulties regarding contaminants contained therein. Though the fuel gas is fed initially to the anode, often, to provide the CO_2 that is required at the cathode, the reacted exhaust gas from the anode is recirculated to the cathode inlet. Thus, any fuel contaminants such as sulphur, halogen compounds and nitrides will also be present at the cathode inlet, and an eventually resistant anode would shift the tolerance problem to the cathode. However, the potential to use the MCFC cathode as a CO_2 separator for sequestration implies a more immediate requirement for impurities tolerance.

7.4.3 Electrolyte and matrix

The electrolyte not only transports dissolved reactants (fuel and oxidant) to the catalysing surface, where the electrons are released and recombined, but it also conducts ionic charge between the electrodes, thereby completing the cell electric circuit. In the MCFC, the charge carriers are carbonate ions, which are formed by the oxidation reaction at the cathode – see equation (7.5). The electrolyte also has to provide a physical barrier to separate the fuel and oxidant gas streams from mixing directly. Finally, the same molten carbonates provide the gas sealing between the separator plates, that divide one elemental cell from another in stack configuration (more about this in Section 7.4.4).

Electrolyte distribution

The liquid electrolyte in the MCFC cannot be implemented without a support structure that contains it. This support is called the matrix, and has therefore a combination of requirements to satisfy: it must be porous to the right degree to be impregnated by the liquid electrolyte, while maintaining fuel and oxidant separation and providing mechanical stability; it must be resistant against the corrosive properties of the electrolyte both in the reducing conditions of the anode as in the oxidizing conditions of the cathode, being able to maintain its pore structure and stability for the projected lifetime of the fuel

cell. This pore structure must be narrowly tailored to fit the pore structures of the adjacent electrodes, so that the electrolyte distribution at the three-phase interface is optimal for the electrochemical reactions.

A stable electrolyte/gas interface in the electrodes is established exclusively due to a balance in capillary forces. Important parameters in this equilibrium are the wettability of the electrodes and matrix, and the superficial tension (γ) and contact angle (θ) of the electrolyte; the diameters D of the largest flooded pores are then related by the following equation:

$$\frac{\gamma_a \cos \theta_a}{D_a} = \frac{\gamma_c \cos \theta_c}{D_c} = \frac{\gamma_m \cos \theta_m}{D_m} \qquad 7.6$$

where the subscripts a, c and m refer to anode, cathode and matrix respectively.

To maintain the three-phase equilibrium, the pores in the matrix should be smaller than those in the electrodes. The pores in the latter are thus partially filled, while the matrix remains completely filled with liquid electrolyte. This is illustrated in Fig. 7.7. The distribution of the molten carbonate electrolyte in the three cell components (anode, cathode and matrix) is critical for the performance and endurance of MCFCs. Apart from its evident role in the electrochemical efficiency of the cell, pore distribution is also important to

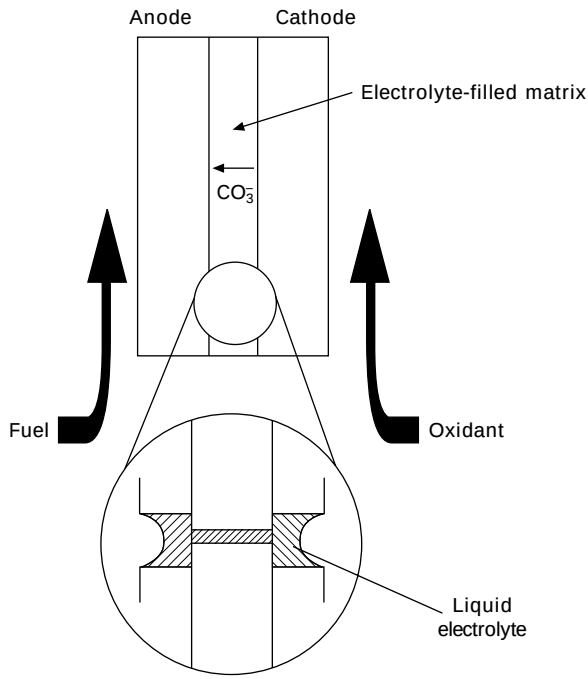

7.7 Close-up of electrolyte distribution in porous electrodes and matrix support.

compensate for electrolyte loss from the fuel cell assembly, as was observed in Section 7.4.1.

Liquid electrolyte is lost during cell operation due to reaction with electrode materials (such as *in situ* doping of the NiO cathode or reaction with the Cr in the anode), creeping effects, vaporization and corrosion, phenomena which are often interrelated: owing to the corrosive properties of molten carbonate, imperfect protection or sealing will quickly lead to material degradation and leakage passages will be created. Within these microfractures, volatilization in the flowing fuel and oxidant gases is also facilitated, causing a further dispersion of corrosive agents, and loss of the same, around the cell structure. Electrolyte loss is almost exclusively responsible for the voltage decay of a cell in long-term operation – exceeding 2–3 mV/1000 h (Frangini, 2007) – through the increase of internal resistance. The electrolyte and matrix tile account for 70% of the ohmic resistance of the cell as it is (Cassir and Belhomme, 1998).

Gas cross-over

Electrolyte and matrix have to provide a throughway for charge carriers, but have to impede migration of the gas species from one electrode to the other, or the proper functioning and the advantages of the electrochemical conversion are nullified by chaotic mixing of the reactants. This phenomenon is known as gas cross-over and has to be limited to a minimum. In general, gas cross-over is caused by two reasons: (1) changes in the characteristics of the matrix, including pore diameter and porosity and (2) depleting of the electrolyte due to volatilization and corrosion in the cell. The first phenomenon is mainly the consequence of sintering, particle growth or allotropic phase transformation, all caused by the attacking environment of the hot carbonates, and resulting in increased mean pore size and pore volume, and reduced specific area. The second results in an emptying of the matrix, leaving gas passages through the void pores for cross-over to take place. To reduce the potential for cross-over, excessive gas pressure difference between the anode and the cathode should also be avoided.

Electrolyte: requirements

Apart from the physical-electrochemical requirements mentioned above, the matrix should also have adequate mechanical resistance, to withstand stacking pressure, stresses due to thermal cycling and non-uniformity. To this effect, fibres or coarse particulates are incorporated for strengthening and crack attenuation. If possible, the matrix support should also obstruct dissolved nickel from precipitating in metallic form near the electrodes (see also Section 7.4.2). Thus, metallic supports are unsuitable (Biedenkopf *et al*., 2000). The

requirements for the electrolyte and support matrix are summarized in Tables 7.4 and 7.5.

Electrolyte state-of-the-art in pre-commercial applications

The electrolyte composition affects electrochemical activity, corrosion and electrolyte loss rate, and is the object of continuing study. For the requirement of good ionic conductivity, lithium is the best material due to its low atomic weight. In the beginning, eutectic mixtures of Li–Na carbonate (Li_2CO_3–Na_2CO_3) were used; then attention shifted to Li–K (Li_2CO_3–K_2CO_3), especially for atmospheric applications due to its increased reactivity; ternary mixtures of Li–K–Na have been investigated, but the present tendency is to go back to mixtures of Li–Na, due to their lower vapour pressure, which reduces electrolyte loss, their lower acidity and their increased activity at high operating pressure.

Essential differences between Li–K and Li–Na are as follows (Moritaa *et al.*, 2002):

- Li–Na cells have a superior output voltage to Li–K cells at 650 °C, especially under richer gas conditions. The reason for the superior performance of the Li–Na cell is the higher conductivity and lower reaction resistance of carbon dioxide at the cathode. This entails that thicker matrices can be made from Li–Na without loss of performance, with beneficial effects on mechanical strength and time to Ni shorting.
- Stabilized conditions are reached sooner with Li–Na. This is probably

Table 7.4 Requirements of the ideal carbonate electrolyte

Requirement	Level
Good ionic conductivity	> 1 S/cm
Good gas solubility	> 10^{-6} mol/cm^3
Low contact angle (good wetting properties)	< 45°
Limited corrosive activity	–

Table 7.5 Requirements of the ideal electrolyte matrix support

Requirement	Level
Crystallographic stability and resistance to dissolution in electrolyte	40 000 h in full load operation
Resistance to fracture, sintering, creep, thermal dilation	40 000 h in full load operation
Porosity	50–70% < 1 μm
Low cost	–

due to better diffusivity properties, wetting angle at the electrodes and charge carrier capability.

- The temperature dependence of Li–Na cells under atmospheric conditions is larger than that of Li–K cells, because the oxygen solubility in Li–Na carbonate is lower. Therefore, running Li–Na cells under atmospheric pressure at lower temperatures (<650 °C) quickly leads to larger voltage drops than in Li–K cells at equal conditions.
- The higher basicity of Li–Na compared with Li–K reduces cathodic dissolution.

The proportion of Li, Na and/or K in the eutectic mixture is determined by the resulting properties such as melting point, surface tension, viscosity, vapour pressure, solubility. Approximately 50 mol% Li_2CO_3 is necessary to meet the melting point and performance requirements of MCFCs, though it makes up for almost all of the electrolyte cost. Increased potassium content improves gas solubility but the conductivity is low compared to sodium and the thermal expansion mismatch with the other cell components is slightly increased (Maru *et al*., 1984).

The matrix material most commonly used until recently was high surface area submicron γ-$LiAlO_2$ powder, with Al_2O_3, ZrO_2 fibre (or derivatives) or coarse particulates incorporated for strengthening. However, long-term testing (up to 40 000 h) has evidenced a phase transition from the γ to the α allotropic phase (Tanimoto *et al*., 1998), especially in Li–Na melts, with accompanying particle growth and thus increased mean pore size and pore volume and reduced electrolyte retention capability. This deteriorates the electrochemical performance of the electrolyte, through increased carbonate loss, cross-over and ionic polarization. The adopted solution today is to start off with the denser but coarser α allotropic phase and work its pore structure to the required degree, as this phase is more stable over long periods of time, especially at lower temperatures (<650 °C). At higher temperatures, the α phase has a tendency to change to the γ phase with associated particle refining, which is much more acceptable than the contrary phenomenon. However, the cost of this material is considered high, through a combination of raw material price and the fabrication technology utilized, not lastly due to an absence of suppliers compared with γ-$LiAlO_2$ powder.

Electrolyte: manufacturing procedure

The conventional process to fabricate electrolyte structures until the 1980s involved hot pressing (at about 35 MPa) mixtures of $LiAlO_2$ and 50 vol% alkali carbonates at temperatures slightly below the melting point of the carbonate salts. The electrolyte tiles thus produced were relatively thick (1–2 mm) and difficult to produce in large sizes, because of the need for large

tooling and presses. Furthermore, hot pressing is an intermittent, batch-wise process, which can handle only one finished matrix at a time, thereby hampering mass production.

To resolve this problem, again tape-casting has been adopted (see Section 7.4.1), with due modifications of the base material powder, solvent and binders. Again, an aqueous solution for the slurry would be desirable from an environmental and commercial point of view, but $LiAlO_2$ is highly reactive with water and hydrolysis to LiOH and AlOH can take place. Korean researchers identified a possible solution to using water instead of toxic solvents, with the aid of proteins, but the matrix was not tested in cell operating conditions (Cho *et al*., 2001).

The tape-cast matrix is composed of several thin layers cross-laid on top of each other, to increase structure control and its ultimate mechanical strength, important respectively in the operation and the endurance of the electrolyte support. Multiple lamination, however, adds to manufacturing time, difficulty and cost.

Electrolyte: difficulties and new developments

In the attempt to minimize nickel dissolution rate at the cathode, apart from working on the resistance of the cathode material, research is also focused on mitigation of the dissolutive properties of the electrolyte. This effect is achieved by the use of additives that decrease electrolyte acidity. Several alkaline earth species (oxides and carbonates) have been investigated for their effectiveness in nickel dissolution mitigation: MgO, SrO, Ca/Sr/$BaCO_3$ and others (Doyon *et al*., 1987; Miyazaki *et al*., 1992, 1994, Tanimoto *et al*., 1992). Magnesium oxide has been one of the most successful so far. Though it has a rather low solubility (0.5 wt%) in the melt, addition of MgO has a large effect, reducing the solubility of nickel oxide by more than half. More recently, rare earth oxides such as lanthanum oxide are being investigated, which reduce Ni dissolution even further (Ota *et al*., 2006). At CRIEPI (Central Research Institute of Electric Power Industry) in Japan, a single laboratory cell has been functioning with this electrolyte for over 60 000 h at the time of writing, with initial shorting evidenced after 30 000 h. Tests are continuing to observe the limit of the cell's useful life (Mugikura and Morita, 2007).

Addition of alkaline earth oxides may influence the surface tension and improve the wettability of the electrodes, but also a hindrance of conductivity may result. What increases the difficulty of electrolyte management even further is segregation: in cell operation, a separation of the Li and K or Na carbonates can occur, which increases local concentration of the components. Especially in the case of potassium carbonate, it is accumulated near the cathode increasing dissolution of the latter, thereby reducing performance. Alkaline earth additives on the other hand, which should inhibit cathode

dissolution, tend to segregate towards the anode, where their effectiveness is lost (Kunz and Bregoli, 1990). However, it is important to underline the relativity of these statements, since other researchers have reported contrary, beneficial effects on segregation through addition of alkaline earth compounds (Hoffmann *et al.*, 2003). The problem of nickel dissolution and electrolyte volatilization would be successfully combatted by a reduction of cell operating temperature, but the corresponding decrease of ion solubility and wetting properties would then have to be reinforced by alternative means. Also in this case, it is clear that a compromise of effects needs to be sought.

Regarding the electrolyte support, stability of the porosity during its lifetime is of prime concern in research and development. Apart from the phase transition mentioned above, the pore structure of the matrix is affected by sintering of the particles: in the initial stage of the sintering process, rearrangement and slip of the α-$LiAlO_2$ particles promote the change with sintering time of the maximum pore diameter to a smaller size. However, recent studies have indicated that the smaller pores will change to larger ones due to rearrangement of the α-$LiAlO_2$ particles and dissolution of α-$LiAlO_2$ microparticles in the electrolyte (Zhou *et al.*, 2007). In this regard, a uniform initial particle size distribution is very important. Again, sintering is stimulated at higher temperatures.

Much cost reduction can be achieved in matrix fabrication: faster milling, casting and drying rates are needed with > 95% yield maintaining consistent matrix quality, also over large areas. Water-based slurries are also highly desired for mass fabrication efficiency, in addition to being environmentally friendly. This requires innovations to increase drying rate and the stability of $LiAlO_2$ in water.

7.5 Secondary components

The previous section dealt with the electrochemical heart of the molten carbonate fuel cell, but the exploitation of its beneficial working comes from the components that channel the flows of reactant and converted energy between the cell and the ultimate user. In this context, two classes of secondary components – if we are to term them such – can be defined: components that are not in the path of current conduction and are not in direct contact with the liquid electrolyte (Section 7.5.2), and components which are, but do not take part in the electrochemical activity that characterizes the fuel cell (essentially the bipolar plate).

7.5.1 Bipolar plate

The most critical non-active metallic component possibly suffers even harsher conditions of operation than the active components, because of its position

contemporaneously between the reducing environment of the fuel and the oxidizing environment of air in the presence of a liquid salt. In particular, the bipolar plate divides the individual cells one from the other, see Fig. 7.8. Since it is not involved in the catalytic reactions, the bipolar plate can consist of less specialized materials than the electrodes and matrix, and is usually made of stainless steel alloys, which nevertheless have to be of strongly corrosion-resistant quality. Corrosion of the metal components is, together with electrolyte loss, the main factor of long-term voltage decay of MCFCs.

Bipolate plate: requirements

A bipolar plate is commonly composed of two distinct metallic components: the separator plate and the current collector (see Fig. 7.9). (Separator plate and current collector must simultaneously satisfy various chemical, electrical and mechanical requirements and are therefore usually made of the same material, which is why we consider them as a whole under the terminology of bipolar plate.) It is based on a corrugated design that has to fulfil the following functional requirements:

- separate fuel and oxidant streams between adjacent cells, while providing electrical contact;

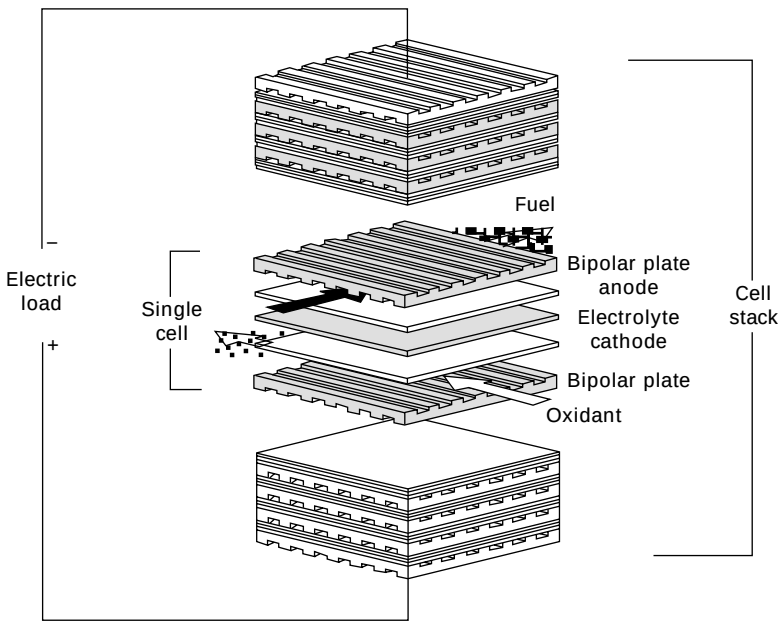

7.8 Assembly of single cells to stack configuration.

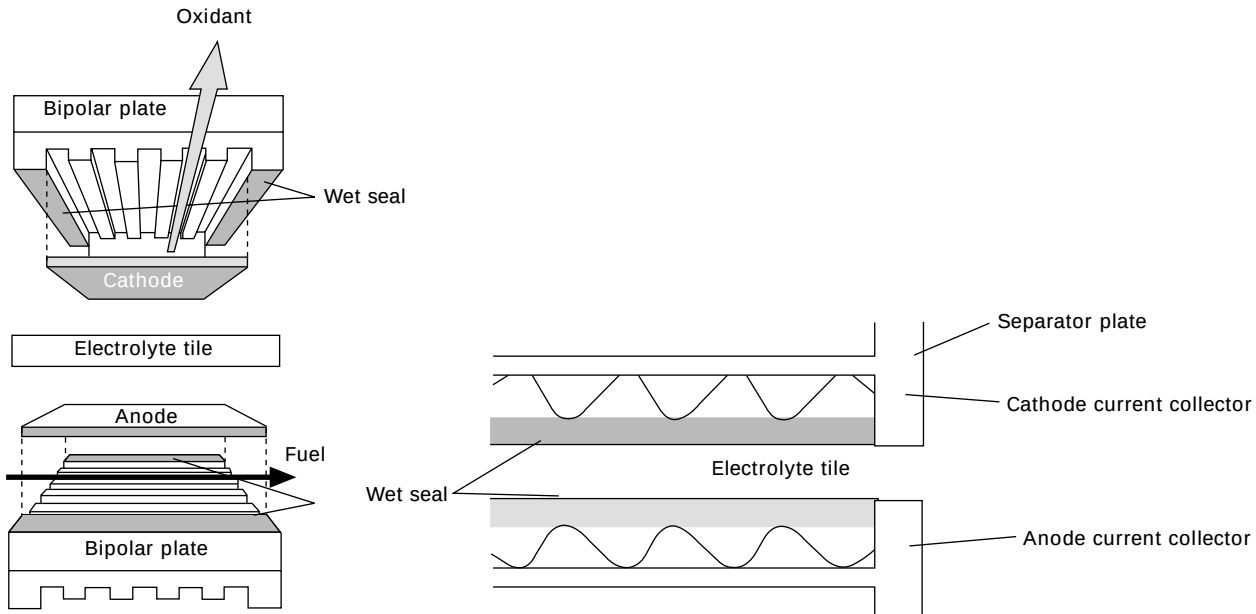

7.9 Schematic of single cell assembly and location of the wet seal (Agüero *et al.*, 2001).

- create flow channels to guide the gases from the manifolds to the electrodes;
- provide a leak-tight gas flange around the electrodes.

The last function is accomplished by extending the electrolyte tile to the plate edges where it is sandwiched between the two juxtaposing plates: this is called the wet-seal, and is indicated in Fig. 7.9. Although the width area that forms the wet seal is relatively small (usually 5–10 mm, i.e. only about five times the tile thickness), corrosion of the bipolar plate in this area is particularly critical and may lead to poor sealing with consequent gas leakage, electrolyte loss and rapid decay of cell performance. Excessive corrosion may also lead to a critical loss of electrolyte from the tile and inevitable failure of the cell. Thus, the requirement for corrosive resistance is locally much higher here than around the current collectors, which are designed so as to minimize the contact area between electrolyte and separator plate. Furthermore, the wet-seal area on the anode side is subject to about two orders of magnitude greater chemical potential gradient (between the fuel gas inside the cell and the ambient environment) than on the cathode side (where conditions are reasonably similar to ambient), promoting corrosion even further (Donado *et al*., 1984).

The most critical requirement of a bipolar plate is therefore corrosion resistance. Another important requirement is that the bipolar plate should be an excellent electric conductor. In addition, the corrosion products must also be sufficiently conductive and insoluble in the carbonate melt. Dissolution of oxide contaminants into the electrolyte can change melt chemistry, in addition to causing continuous degradation of the metal plate if the solutes precipitate away from the reaction site and 'fresh' material (especially Fe and Cr) diffuses from the substrate to the oxide surface (fluxing dissolution). Reaction of the oxide scale grown on the bipolar plate and the molten carbonate is the major source for electrolyte loss in the MCFC at the beginning of cell life, resulting in the formation of reaction products such as $LiCrO_2$, K_2CrO_4, Li_2CrO_4, $LiFeO_2$ and others (Frangini, 2003). Such loss of carbonate melt is continuous, but is attenuated as the reacting materials approach equilibrium. Then volatilization becomes the more disturbing form of electrolyte loss.

Further degradation of the bipolar plate occurs through carburization, i.e. precipitation of chromium-rich carbides inside the metal crystal structure and at grain boundaries, which leads to undue hardening of the component. This is undesirable from the point of view of its mechanical load-bearing capacity, important in large-scale stack assemblies.

Other mechanical requirements are associated with fluid flow, high temperature resistance, proper contact of the components, weldability and easy formability (see Table 7.6).

Table 7.6 Requirements of the ideal bipolar plate

Requirement	Level
Anode side: resistance to hot corrosion, carburization and H_2 interstitial effects in reducing environment	40 000 h in full load operation
Cathode side: resistance to corrosion and carburization in oxidizing environment	40 000 h in full load operation
Wet-seal: resistance to hot and galvanic corrosion in reducing and oxidizing environment	40 000 h in full load operation
Good electric conductivity (also of oxide scale)	$> 10^4$ S/cm
Stability of the corrosion products (resistance to scale fluxing and spallation)	< 1%/1000 h cell voltage decay
Low contact resistance	$< 10^{-5}\ \Omega/cm^2$ (< 10 mV drop)
Good formability	–
Low cost	–

Bipolar plate: state-of-the-art in pre-commercial applications

At present the alloy combining all the desired properties has not yet been found. The basic material of the bipolar plates currently most widely adopted is Cr–Ni ferritic stainless steel. 310S and 316L have a relatively low cost, and, in the cathode area, these alloys function well: a thick, multi-layered oxide scale is formed with good electrical conductivity and providing a reasonably efficient diffusion barrier. A mild fluxing effect of chromium across the oxide layer to soluble chromate has been reported for 316L (Yuh *et al*., 1995; Cassir and Belhomme, 1998), where higher-chrome-content steels such as 310S appear to provide enough corrosion stability for 40 000 h operation. Higher chrome contents however stimulate the driving force for reaction with the electrolyte.

The same kind of stainless steel is used at the anode side, but a pure nickel coating has to be applied, because the oxide layer formed on the stainless steel is porous and does not protect the base metal, whereas nickel is stable in reducing conditions. With the protection provided by the Ni-clad coating, the anode-side bipolar plate shows virtually no corrosion attack for up to 10 000 h of operation. Consequently, no significant loss due to contact interfacial resistance occurs (Yuh *et al*., 1995).

At the wet seal, in direct contact with the carbonate eutectic, chromia-forming alloys experience high corrosion. To create a purely passive layer, alumina-forming alloys are acceptable, but since these are difficult and expensive to manufacture into an entire bipolar plate, aluminized coatings

are adopted, which are locally applied in the area of gas sealing, since the reduced electrical conductivity of aluminium constitutes no problem there. Aluminized stainless steels provide high-temperature corrosion resistance in both oxidizing and reducing environments by forming a thin dielectric alumina film, which in the presence of the carbonate converts to $LiAlO_2$, effective in inhibiting corrosion with minimal consumption of electrolyte, thus providing the required long-term stability to the wet seal (Frangini, 2003).

Bipolar plate: manufacturing procedure

The corrugated geometry of the bipolar plates is relatively complex to mass-produce. Generally, they are formed by die-casting and deep drawing. What especially imposes difficulties in bipolar plate manufacture is the need for different coating layers to be applied. On the anode side, electroless nickel coating has excellent thickness uniformity but is not used because of the extensive cost of this method. Electrolytic nickel plating produces a very pure nickel coating but has non-uniform thickness distribution due to the corrugated shape. Therefore, to plate sufficient nickel on the recessed area of the current collector will result in some areas being excessively coated, decreasing cost-effectiveness (Yuh *et al.*, 1995).

For the preparation of the wet-seal area, various aluminizing processes have been evaluated, including painting, thermal spraying, vacuum deposition and pack cementation, but at present ion-vapour deposition (IVD) followed by diffusion heat treatment is generally considered to be the method that offers the most protective and adherent coating in the wet-seal environment (Frangini, 2003). However, IVD requires introducing the component in a vacuum chamber, making it an expensive solution for large-scale production of MCFCs. An alternative application method which is both economical and might provide even better corrosion resistance to molten carbonate, is slurry deposition. The slurry-deposited layer exhibits lower porosity of the outer scale after the diffusion treatment compared to IVD (Pérez *et al.*, 2002).

Bipolar plate difficulties and new developments

Voltage decay is mainly caused by the increase of internal resistance. In this respect, the corrosion layer on the bipolar plates (especially on the cathode current collector) is the main contributor. Efficient and cost-effective resistance to corrosion is therefore the continuing aim in the investigation of improved metal cell components. Alternative corrosion protection materials investigated recently include borosilicate glass (Keding *et al.*, 2002), a Ti/Al/N/O composite material and co-deposited chromium and aluminium (Dicks, 2004). The latter deposited on austenitic stainless steel (310S) demonstrated complete corrosion protection for the cathode side of the cell for 480 h.

Regarding aluminization of the wet-seal area, methods that do not require expensive post-deposition diffusion heat treatment would provide a major break-through in cost-effectiveness of production. In general, low-cost methods for uniform coating of the corrugated plates are desirable. But even greater is to eliminate the need for protective coating completely, and the associated increased cost and manufacturing difficulty. Thus, single-alloy bipolar current collector materials that function well at both the cathode and anode side with significant cost-benefit are strongly sought after.

In this respect, it should be commented that so far the search for corrosion-resistant materials has been primarily directed towards modifications of existing materials, whereas little investigation has been concerned with the development of novel materials, specifically designed for application in MCFCs (with the exception of NKK, a Japanese-originated nickel-based alloy), though the latter would deserve greater attention by developers.

7.5.2 Stack and balance-of-plant hardware

The components that are not in the path of current conduction and are not in direct contact with the liquid electrolyte (which largely make up the BOP) have not got the same restrictive electrochemical requirements as the active components, but still necessitate a considerable amount of resistance to material degradation, especially through oxidation and scale spallation. These components are: fuel and oxidant inlet and outlet manifolds, containment parts (pressure vessels, flanges, seals and gaskets), heaters and sensors where applicable.

Stack and balance-of-plant hardware: requirements

Having to deal with corrosive gas flows of different nature, the auxiliary components need to be protected by inert oxide coatings. Electrical conductivity of the oxide layer is not necessary, but fragmentation of the oxide scale due to stress and persisting corrosion must be inhibited as much as possible to prevent the spalled debris from blocking gas flow passages or compromising stack electrical insulation. Adequate resistance to thermal cycling in stack shut-down and start-up is required.

The life goal of these materials should be between 5 and 30 years, depending on their location and application (reactant gas manifolds vs. pressure vessels, for example). Another important consideration is cost (see Section 7.3 and Fig. 7.4).

Stack and balance-of-plant hardware: state-of-the-art in pre-commercial applications

Accelerated thermal cyclic oxidation tests in an oxidizing atmosphere at 700 °C were conducted by FuelCell Energy on many materials to assess their

suitability for these peripheral components (Yuh *et al.*, 2006). In general, oxidation in the fuel cell stack exit conditions is more severe than that in the inlet conditions, owing to the higher temperature and higher water partial pressure, as well as the presence of alkali carbonate vapour. Based on the test results, alloys with balanced Fe, Ni and Cr can be selected for various stack hardware. For example, 316L and 321 experience high oxidation rates and high spallation, which are inadequate for a life target of 40 000 operative hours. In general, 304 is better than 316 in terms of both oxidation rate and spallation. 310S, 18SR and 253MA, having either high Cr content or containing Al or Ce, have excellent oxidation resistance and adhesion due to a very fine grain structure. The oxidation rate of SS310S is about ten times lower than 316L and 321, that of 18SR about five times.

For utilization in BOP, thick-walled, lower chromium-content stainless steel components are adequate for the required endurance of the system. Reduction of component cost is the main focus of development in this field.

7.6 Conclusions

The molten carbonate fuel cell has reached a crucial stage in its development from a laboratory experiment to a mature technology that stands its own ground in the field of energy conversion. Many demonstration projects have been launched in the past ten years around the world, demonstrating the MCFC's potential in medium-to-large scale, quality power supply, thanks to its high efficiency, fuel flexibility, flexible heat-to-power ratio and low emissions. The costs per installed kW remain high, however, and the lifetime and enduring reliability of the cell stack are the main technical barriers that the MCFC has to break through to compete with the consolidated technologies of internal combustion-engine-based power generation. For full-fledged market penetration in this field, much depends on factors such as energy costs, environmental legislation, fuel availability; in certain niche applications the MCFC can already be considered economically feasible.

Apart from these external factors, there is still room for improvement of the MCFC's technological potential. In the previous sections, for each component of the system, the key points have been indicated that constitute the main challenge in this advancement. These can be summarized in a general requirement for increased power density and reduced degradation. Satisfactory, cost-effective solutions to these difficulties will launch the MCFC definitively into large-scale deployment. In order of importance, though each one needs to be addressed, the weak points that have to be overcome are:

- cathode dissolution;
- electrolyte loss;

- corrosion of metallic components;
- matrix degradation;
- anode tolerance to sulphur.

Each of these problems needs to be handled, importantly, with low-cost solutions, preferably amenable to large-scale production. In this way, the advantage in overall efficiency and low environmental impact of the MCFC compared with conventional technologies will be supported by a competitive price tag, making up the delay in one leap and leaving the road open for a challenging future where high quality is obtained with minimal waste and at acceptable cost.

7.7 Acknowledgements

The contributions of Dr Maria Carewska, Dr Stefano Frangini and Dr Silvia Bargigli to this chapter have been fundamental and are gratefully acknowledged.

7.8 References

Agüero A., García de Blas F.J., García M.C., Muelas R., Román A. (2001), 'Thermal spray coatings for molten carbonate fuel cells separator plates', *Surface Coatings Technol*. **146**, 578–85.

Baumgartner C.E., Arendt R.H., Iacovangelo C.D., Karas B.R. (1984), 'Molten carbonate fuel cell cathode materials study', *J. Electrochem. Soc.: Electrochem. Sci. Technol*., **131** (10), 2217–21.

Biedenkopf P., Bischoff M.M., Wochner T. (2000), 'Corrosion phenomena of alloys and electrode materials in molten carbonate fuel cells', *Mater. Corrosion* **51**, 287–302.

Bodén A. (2007), *The anode and the electrolyte in the MCFC*, PhD Thesis, Chemical Engineering, Royal Institute of Technology (KTH), Stockholm.

Bodén A., Lindbergh G., Sparr M. (2005), 'Investigation of the porous nickel anode in the molten carbonate fuel cell', *Proc. 7th Int. Symp. Molten Salts Chemistry & Technology*, Toulouse, 29 Aug. to 2 Sep. 2005.

Cassir M. and Belhomme C. (1998), Technological applications of molten salts: the case of the molten carbonate fuel cell, *Plasmas & Ions*, **2**, 1–13.

Cho J.Y., Hyun S.H., Hong S.A. (2001), 'Fabrication and characterization of γ-$LiAlO_2$ matrices using an aqueous tape-casting process', *J. American Ceramic Soc.*, **84** (5), 937–40.

Dicks A.L. (2004), 'Molten carbonate fuel cells', *Curr. Opin. Solid State & Mater. Sci*., **8**, 379–83.

Donado R.A., Marianowski L.G., Maru H.C., Selman J.R. (1984), 'Corrosion of the wet-seal area in molten carbonate fuel cells', *J. Electrochem. Soc*., **131**, 2535–44.

Doyon, J.D., Gilbert, T., Davies, G. (1987), 'NiO solubility in mixed alkali/alkaline earth carbonates' *J. Electrochem. Soc*., **134** (12), 3035–8.

Ekins P. (2001), 'Sustainability policy and environmental accounts', Presentation to the Statistics Sweden Workshop Sustainable Development – Models and Statistics, Keele University, Stockholm, 26–27 Apr. 2001.

Farooque M., Fuel Cell Energy (2007), personal communication.

Frangini S. (2003), 'Corrosion of structural materials in molten carbonate fuel cells: an overview', in Sequeira C.A.C., *High Temperature Corrosion in Molten Salts*, Trans Tech Publications Switzerland, 135–54.

Frangini S. (2007), 'Corrosion of metallic stack components in molten carbonates: critical issues and recent findings', presentation at the *Int. Workshop on Degradation Issues in Fuel Cells*, Crete, 19–21 Sep. 2007.

Freni S., Barone F., Puglisi M. (1998), 'The dissolution process of the NiO cathodes for molten carbonate fuel cells: state-of-the-art', *Int. J. Energy Res.*, **22**, 17–31.

Giorgi L., Carewska M., Simonetti E., Scaccia S., Croce F., Pozio A. (1993), 'Investigation on the kinetics and stability of NiO (Li) and $La_{0.8}$ $Sr_{0.2}$ CoO_3 in molten carbonates by means of electrochemical impedance spectroscopy' in Sequeira C.A.C. Picard G.S., *Electrochemical Technology of Molten Salts*, Trans Tech Publications, Switzerland, 285–302.

Giorgi L., Carewska M., Patriarca M., Scaccia S., Simonetti E., Di Bartolomeo A. (1994), 'Development and characterization of novel cathode materials for molten carbonate fuel cell', *J. Power Sources*, **49**, 227–43.

Hoffmann J., Yuh C.-Y., Godula Jopek A. (2003), 'Electrolyte and material challenges', in Vielstich W., Gasteiger H.A., Lamm A., *Handbook of Fuel Cells – Fundamentals, Technology and Applications*, Vol. 4: *Fuel Cell Technology and Applications*, John Wiley & Sons Ltd, New York, 921–40.

Iacovangelo C.D. (1986), 'Metal plated ceramic – a novel electrode material', *J. Electrochem. Soc.: Electrochem. Sci. Technol.*, **133** (7), 1359–64.

Keding R., Rüssel C., Pascual M.J., Pascual L., Durán A. (2002), 'Corrosion mechanism of borosilicate sealing glasses in molten carbonates studied by impedance spectroscopy', *J. Electroanalytical Chem.*, **528**, 184–9.

Kunz H.R. and Bregoli L.J. (1990), *Proc. 2nd Symp. Carbonate Fuel Cell Technology*, Seattle, Oct. 1990, The Electrochemical Society, **90–16**, 157

Lagergren C., Lundblad A., Bergman B. (1994), 'Synthesis and performance of $LiCoO_2$ cathodes for the molten carbonate fuel cell', *J. Electrochem. Soc.*, **141**, 2959–66.

Lundblad A. (1996), *Development and characterization of cathode materials for fuel cells*, PhD Thesis, Royal Institute of Technology (KTH), Stockholm.

Maru H.C., Paetsch L., Pigeaud A. (1984), 'Review of molten carbonate fuel cell matrix technology', in Selman J.R. and Claar T.D. *Molten Carbonate Fuel Cell Technology*, The Electrochemical Society, **84–13**, 20–53.

Masci A., ENEA (2007), personal communication.

Miyazaki Y., Yanagida M., Tanase S., Tanimoto K., Kojima T., Ohtori N., Okuyama H., Kodama T., Morimoto K., Nagashima I., Nagai C., Itoh H. (1992), *Proc. 1992 Fuel Cell Seminar*, Tucson, 29 Nov. to 2 Dec. 1992.

Miyazaki Y., Yanagida M., Tanimoto K., Kojima T., Ohtori N., Asai T. (1994), *Proc. 1994 Fuel Cell Seminar*, San Diego, 28 Nov. – 1 Dec.

Moritaa H., Komodab M., Mugikuraa Y., Izakia Y., Watanabe T., Masudac Y., Matsuyamac T. (2002), 'Performance analysis of molten carbonate fuel cell using a Li/Na electrolyte', *J. Power Sources*, **112**, 509–18.

Mugikura Y. (2003), 'Stack material and stack design', in Vielstich W., Gasteiger H.A., Lamm A., *Handbook of Fuel Cells – Fundamentals, Technology and Applications*, Vol. 4: *Fuel Cell Technology and Applications*, John Wiley & Sons Ltd., New York, 907–20.

Mugikura Y. and Morita H. (2007), 'MCFC lifetime estimation method', presentation at the *Int. Workshop on Degradation Issues in Fuel Cells*, Crete, 19–21 Sep. 2007.

Nam S.W., Yoon S.P., Devianto H., Han J., Lim T.-H. (2005), 'Fabrication and characteristics of ceramic-coated anode for molten carbonate fuel cell', *Proc. 7th Int. Symp. on Molten Salts Chemistry & Technology*, Toulouse, 29 Aug. to 2 Sep. 2005.

Ota K.I., Matsuda Y., Matsuzawa K., Mitsushima S., Kamiya N. (2006), 'Effect of rare earth oxides for improvement of MCFC', *J. Power Sources*, **160** (2), 811–15.

Pérez F.J., Duday D., Hierro M.P., Gómez C., Agüero A., García M.C., Muelab R., Sanchez Pascual A., Martinez L. (2002), 'Hot corrosion study of coated separator plates of molten carbonate fuel cells by slurry aluminides', *Surface Coatings Technol.* **161**, 293–301.

Plomp L., Veldhuis J.B.J., Sitters E.F., Van der Molen S.B. (1992), 'Improvement of molten carbonate fuel cell life time', *J. Power Sources*, **39** (3), 369–373.

Selman R. (2007), 'Fundamental research directions in high-temperature fuel cells', presentation at the *Int. Workshop on Degradation Issues in Fuel Cells*, Crete, 19–21 Sep. 2007.

Tagawa T., Yanase A., Goto S., Yamaguchi M., Kondo M. (2004), 'Ceramic anode catalyst for dry methane type molten carbonate fuel cell', *J. Power Sources*, **126**, 605–11.

Tanimoto K., Miyazaki Y., Yanagida M., Tanase S., Kojima T., Okuyama H., Kodama T. (1992), 'Cell performance of molten-carbonate fuel cell with alkali and alkaline-earth carbonate mixtures', *J. Power Sources*, **39** (3), 285–97.

Tanimoto K., Yanagida M., Kojima T., Tamiya Y., Matsumoto H., Miyazaki Y. (1998), 'Long-term operation of small-sized molten carbonate fuel cells', *J. Power Sources*, **72**, 77–82.

Tomczyk P. (2006), 'MCFC versus other fuel cells – characteristics, technologies and prospects', *J. Power Sources*, **160**, 858–62.

Ulgiati S., Bargigli S., Raugei M. (2005), Analisi di ciclo di vita della produzione di componenti innovative per celle a combustibile a carbonati fusi (Internal report), Università di Siena and ENEA.

Venkataraman R., Farooque M., Ma Z. (2007), 'Cost reduction through thermal management improvements in large scale carbonate fuel cells', *ECS Transactions*, **5** (1), 571–7.

Vogel W.M., Smith S.W. (1982), 'The effect of sulfur on the anodic H_2 (Ni) electrode in fused Li_2CO_3–K_2CO_3 at 650°C', *J. Electrochem. Soc.: Electrochem. Sci. Technol.*, **129** (7), 1441–45.

Yoshikawa K. and Hirabayashi I. (1995), 'Preparation and superconducting properties of Bi2223 thick films by the doctor-blade process', *IEEE Trans. Appl. Superconductivity* **5** (2), 1943–6.

Yuh C., Colpetzer J., Johnsen R., Farooque M., Maru H. (1995), 'Status of carbonate fuel cell materials', *J. Power Sources*, **56** (1), 1–10.

Yuh C., Kolpetzer J., Dickson K., Farooque M., Xu G. (2006), 'Carbonate fuel cell materials', *J. Materials Eng. Performance*, **15** (4), 457–62.

Zhou L., Lin H., Yi B. (2007), 'Sintering behavior of porous α-lithium aluminate matrices in molten carbonate fuel cells at high temperature', *J. Power Sources* **164** (1), 24–32.

8

Solid oxide fuel cells

K HUANG, Siemens Power Generation, Inc., USA

8.1 Introduction

The fuel cell is a device that electrochemically converts the chemical energy in fossil fuels into electrical power. The electrical efficiency of a fuel cell can be easily achieved in the range of 40–50%, depending on operating conditions, polarization loss, kind of fuel cell and type of fuel utilized. Conversely, a conventional heat engine has a typical electrical efficiency of 20–30%, particularly for less than 1 MW class, due to the limitation of the Carnot cycle. The inherent high electrical efficiency by fuel cells infers a reduced CO_2 emission per unit electricity produced if hydrocarbons are used as fuels, which has become increasingly important as we as human beings endeavor to minimize the emission of greenhouse gases in future power generation. Extremely low NO_x and SO_x emission is obviously another conceivable advantage of fuel cells over a traditional heat engine.

Of all the types of fuel cells outlined in this book, the high-temperature solid oxide fuel cell (SOFC) presents unique advantages. One of them is the fuel flexibility. Most fossil fuels, either in the gaseous or liquid state, can in principle be utilized as a fuel for a SOFC to produce electricity provided that they are properly cleaned and reformed into simple fuels such as H_2 and CO. As an example, pipeline natural gas has been successfully used by Westinghouse, later Siemens, in 100–250 kWe-class SOFC generators as fuel with integrated steam reforming technology. Co-production of heat and power, often known as combined heat and power (CHP), is another important feature of SOFC generators. The recovery of waste heat along with producing electricity enables the total energy efficiency of such a system to be as high as 85–90%. Most importantly, the high-quality, low-emission and high-efficiency electricity generated by a SOFC generator makes it ideal for off-grid distributed power generation applications.

Although the SOFC has a great potential to meet the challenges for future energy demand, development of SOFC technology into a commercial product has proved challenging. Owing to the need for high-temperature operation,

the requirements for functional materials are in general more stringent than those of low-temperature fuel cells. Two major barriers identified for commercialization of SOFC technology are reliability and product cost, both of which are closely associated with the materials used in SOFCs. Therefore, it is a rational assertion that the success of SOFC technology largely depends upon the maturity of SOFC materials.

There are five basic functional elements in a SOFC: electrolyte, cathode, anode, interconnect, cell-to-cell connector. The materials making up these components are either ceramics or metals. The functionality of an electrolyte is to transport oxygen continuously and solely in the form of O^{2-} from cathode to anode under a gradient of oxygen chemical potentials. To enable the O^{2-} migration across the electrolyte, the cathode of oxygen supply has to convert O_2 into O^{2-}, a process commonly known as oxygen reduction. Similarly, the anode of fuel supply accepts O^{2-} delivered by the electrolyte and converts it into H_2O and CO_2 by reacting with hydrocarbon fuels. The electrons required for the electrode reactions are released by the anode and arrive at the cathode via an external load, by which the production of electricity is realized. The overall driving force for a SOFC is the gradient of chemical potentials of oxygen existing between a cathode of high partial pressure of oxygen and an anode of low partial pressure of oxygen. The maximum cell voltage of a typical single SOFC with air as an oxidant typically reaches up to 1.2 volt, depending on temperature, load and fuel composition. This voltage is obviously inadequate for any type of practical application. To build up a sufficiently high voltage and power, multiple single cells have to be stacked in series and/or parallel with the aid of interconnect and cell-to-cell connectors; the latter should be pure electronic conductors and oxide-ion insulators. Like a regular battery, each SOFC component also exhibits an internal resistance to either electronic or ionic current flow, often expressed as voltage loss. The final terminal cell voltage is the open circuit voltage (or Nernst potential if no fuel loss is caused by any means) subtracted from the individual voltage loss of each cell component.

One radical requirement for an operational SOFC is to realize oxygen transport across the electrolyte in the form of O^{2-}, but not in the form of O_2. To achieve this mandate, a dense barrier between air and fuel has to be established. For the one-end closed tubular SOFC design, this barrier is easily achieved by the electrolyte and interconnect in a unique geometry, allowing air and fuel to meet only at the open end where combustion occurs after the fuel is mostly utilized over the entire cylindrical surface. No physical sealing material is needed. However, for planar SOFC design, sealing materials have to be applied along the perimeters of interconnect/electrodes and electrolyte/electrodes in order to prevent air from mixing with fuels. Sealing turns out to be one of the key elements for the success of planar SOFC technology.

In this chapter, SOFC technology is covered from the perspectives of materials that have been actively developed and are being engineered. Three major types of SOFCs, classified by the electrolyte materials used, are particularly reviewed. For each type of SOFC, the discussion primarily focuses on electrical, chemical and thermal properties of materials. At the end, the fabrication technique for each functional layer is also briefly reviewed. No review on sealing materials is attempted in this chapter mainly because of proprietary information involved. Interested readers are recommended to look into open publications.

8.2 ZrO_2-based solid oxide fuel cells

The ZrO_2-based SOFC represents the most studied and engineered system in the history of SOFC development. It is technically more mature than other types of SOFCs discussed in this chapter and therefore is likely to be in the first commercialized system. The material set to be discussed in this section includes ZrO_2-based electrolytes, $LaMnO_3$-based cathodes and the Ni–ZrO_2 cermet anode. Particular focus will be given to the properties of the electrolyte, cathode and anode. The interconnect material will be reviewed separately in Section 8.5.

8.2.1 ZrO_2-based electrolytes

The oxide-ion electrolyte must be a conductor of oxide-ions, preferentially a fast oxide-ion conductor, and an electronic insulator at the operating temperature of a SOFC. Although several oxides exhibit such a conductive behavior at elevated temperatures, the most prominent fast oxide-ion conductors are found in oxygen-deficient compounds with either the fluorite structure such as ZrO_2-, CeO_2-, Bi_2O_3-based materials or the perovskite structure such as $LaGaO_3$-based materials. In this section, ZrO_2-based electrolytes are reviewed.

Pure ZrO_2 has no practical use for a SOFC due to its low intrinsic oxide-ion conductivity and a large volume contraction (~9%) induced by a monoclinic-to-tetragonal phase transition taking place at 1170 °C. The favorable cubic structure for oxide-ion conduction is stable only at above 2370 °C. However, the cubic structure can be stabilized to room temperature by substituting Zr with alkaline-earth elements such as Ca, Mg, and Sr or rare-earth elements such as Sc and Y. More importantly, doping with 2+ and 3+ cations into Zr^{4+}-lattice introduces oxygen vacancies, a necessity for oxide-ion conduction, by the principle of charge compensation (Kröger–Vink notation) as shown in Table 8.1. Also included for comparison are those for CeO_2- and $LaGaO_3$-based electrolyte systems. In Table 8.1, O_o^x and $V_O^{\cdot\cdot}$ represent regular lattice oxygen and oxygen vacancies, respectively; M'_X or M''_X is the negatively

Table 8.1 Defect reactions illustrating creation of oxygen vacancies of ZrO_2-, CeO_2- and $LaGaO_3$-based solid electrolyte systems

	ZrO_2-based	CeO_2-based	$LaGaO_3$-based
Divalent dopant	$MO \xrightarrow{ZrO_2} M''_{Zr} + O_o^x + V_o^{\cdot\cdot}$	$MO \xrightarrow{CeO_2} M''_{Ce} + O_o^x + V_o^{\cdot\cdot}$	$SrO \xrightarrow{LaGaO_3} 2Sr'_{La} + O_o^x + V_o^{\cdot\cdot}$
Trivalent dopant	$M_2O_3 \xrightarrow{ZrO_2} 2M'_{Zr} + 3O_o^x + V_o^{\cdot\cdot}$	$M_2O_3 \xrightarrow{CeO_2} 2M'_{Ce} + 3O_o^x + V_o^{\cdot\cdot}$	$MgO \xrightarrow{LaGaO_3} 2Mg'_{Ga} + O_o^x + V_o^{\cdot\cdot}$

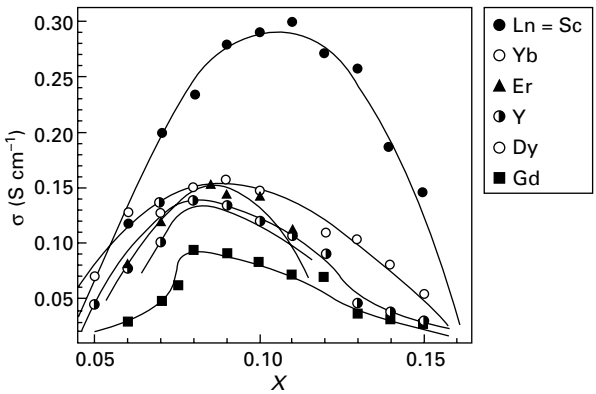

8.1 Oxide-ion conductivity of doped ZrO_2 at 1000 °C as a function of dopant level. Copyright Elsevier.

charged X lattice substituted by dopant M. To ensure the electrical neutrality in the lattice, the relationships of $2[M'_X] = [V_O^{\cdot\cdot}]$ and $[M''_X] = [V_O^{\cdot\cdot}]$ must hold for 3+ and 2+ dopants, respectively, where [ ] represents the concentration. This mass relationship appears to suggest that the higher the doping level, the higher the concentration of oxygen vacancies being created and therefore the higher the oxide-ion conductivity. In reality, the isothermal oxide-ion conductivity of a given dopant peaks at a certain doping level. This phenomenon is illustrated in Fig. 8.1, where rare-earth cations are the dopants for ZrO_2[1]. The peaks occur at 10–11 mol% for Sc and 8–9 mol % for other rare-earth dopants.

The reason behind this observation can be interpreted by the interaction between M'_{Zr} or M''_{Zr} with $V_O^{\cdot\cdot}$, forming associates of $2M'_{Zr} - V_O^{\cdot\cdot}$ or $M''_{Zr} - V_O^{\cdot\cdot}$. The formation of such clusters is stabilized at lower temperatures, typically increasing the activation energy for oxide-ion migration, ΔH_m (also known as motional enthalpy), by half of the binding energy for the associate, ΔH_t (also known as trapping enthalpy), i.e. $E_a = \Delta H_m + 1/2\Delta H_t$. Such a change in activation energy with temperature is often revealed by a kink at a characteristic

temperature or a gradual curvature over a range of temperature in Arrhenius plot of oxide-ion conductivity. Above this temperature, the clusters disassociate back into free M'_{Zr} or M''_{Zr} and $V_O^{\cdot\cdot}$, and the total activation energy returns to ΔH_m. Since the formation of larger clusters is related to cation diffusion, the aging behavior of oxide-ion conductivity observed at low temperatures is often linked to the interaction between dopants and oxygen vacancies.

For a given doping level, on the other hand, the oxide-ion conductivity was also found to vary considerably with the type of dopant[1], see Fig. 8.2. The highest conductivity observed in Sc-doped ZrO_2 is explained by the closest match in ionic radius to the host Zr^{4+} ion which minimizes the lattice elastic strain for an easy oxide-ion pass across the potential saddle point. The closest match in ionic radii between dopant and host ions can be used as a general guideline in selecting the right dopant for a host so as to achieve the highest oxide-ion conductivity.

The temperature dependence of oxide-ion conductivity $\sigma_{O^{2-}}$ of isotropic ZrO_2-based materials can be described by random walk theory[2] and has the following form

$$\sigma_{O^{2-}} T = \sigma^{o}_{O^{2-}} \exp\left(-\frac{E_a}{kT}\right) \qquad 8.1$$

$$\sigma^{o}_{O^{2-}} = \frac{Cq^2}{k} n_V (1 - n_V) l^2 \upsilon_o f\left(\frac{w}{6}\right) \exp\left(\frac{\Delta S_m}{k}\right) \qquad 8.2$$

where C is the density of equivalent sites on which the $n_V C$ mobile charge carriers move; n_V is the fraction of sites that are vacant; q = 2e is the lattice

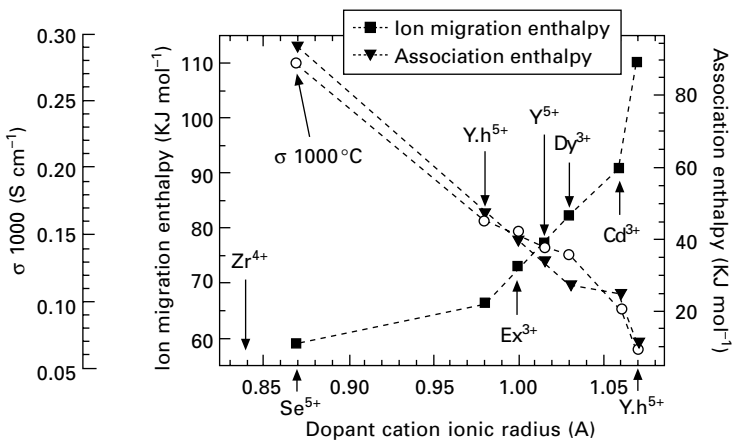

8.2 Oxide-ion conductivity of doped ZrO_2 at 1000 °C, motional enthalpy and trapping enthalpy as a function of dopant ionic radius. Copyright Elsevier.

charge of the oxygen vacancy; k is the Boltzmann's constant; υ_o is the attempt frequency of the mobile oxide-ion optical-mode vibrations (10^{12}–10^{13} Hz); l is the distance to the w nearest-neighbor equivalent sites; f is the geometrical factor of order unity that depends on the jump path; ΔS_m is the motional entropy in the motional free energy $\Delta G_m = \Delta H_m - T\Delta S_m$; E_a in eV is the activation energy, $E_a = \Delta H_m + 1/2\Delta H_t$. For a fluorite unit cell with $l = a/2$ (a is the lattice parameter), $w = 6$, $f \approx 1$, $C = 4a^{-3}$, eq. [8.2] reduces to

$$\sigma^{o}_{O^{2-}} = \frac{4e^2}{ka} n_V (1 - n_V) \upsilon_o \exp\left(\frac{\Delta S_m}{k}\right) \qquad 8.2a$$

Equation [8.1] suggests that a plot of $\ln \sigma_{O^{2-}} T$ vs $1/T$ gives a straight line, from whose slope the activation energy can be obtained. The examples of such plots are given in Fig. 8.3 for 8 mol% Y_2O_3-doped ZrO_2 (8YSZ) and 10 mol% Sc_2O_3–1 mol% CeO_2-doped ZrO_2 (10Sc1CeSZ) in the temperature range of 800–1000 °C and air[3]. The analytical expressions of the two lines are given in eqs. [8.3] and [8.4].

$$8\text{YSZ} \quad \log_{10} \sigma_{O^{2-}} T(\text{S K/cm}) = -\frac{4549}{T(\text{K})} + 5.885$$

$$R^2 = 0.9997 \; E_a = 0.91\,\text{eV} \qquad 8.3$$

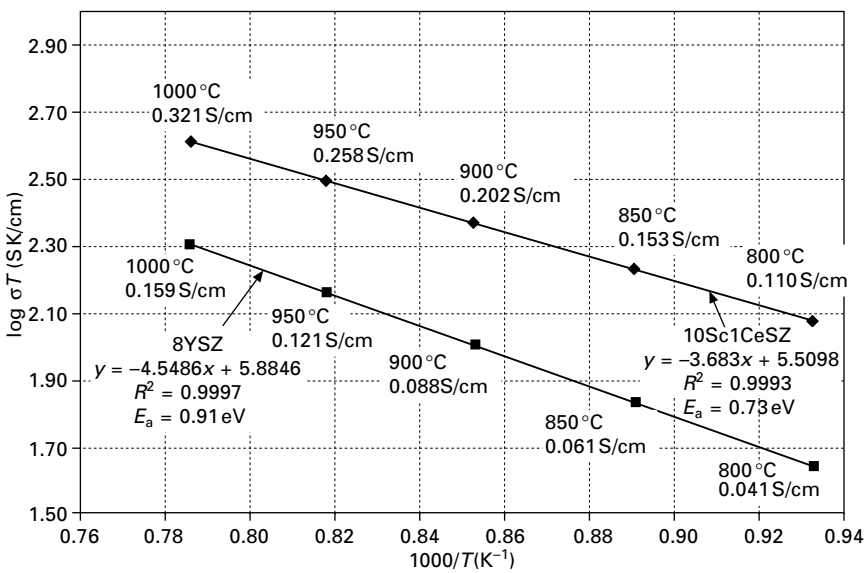

8.3 Arrhenius plots of oxide-ion conductivity of 8YSZ and 10Sc1CeSZ electrolytes.

$$10\text{SclCeSZ}\quad \log_{10}\sigma_{O^{2-}}T(\text{SK/cm}) = -\frac{3683}{T(\text{K})} + 5.510$$

$$R^2 = 0.9993\ E_a = 0.73\,\text{eV} \qquad 8.4$$

The lower E_a observed in 10Sc1CeSZ than 8YSZ is a clear indication of favorable lattice environment for oxygen-vacancy migration created by the closest ionic radius match of Sc^{3+} to Zr^{4+}.

The electrical conductivity of ZrO_2-based electrolytes is not always purely ionic. Depending upon temperature and partial pressure of oxygen, P_{O_2}, the conduction could result from contributions of oxide-ions and electrons, either in the form of electron holes or excess electrons. The production of electronic conduction can be described by the following defect equilibria between gas and solid:

$$\text{At low } P_{O_2} \qquad O_o^x = \frac{1}{2}O_2 + V_O^{\cdot\cdot} + 2e' \qquad 8.5$$

$$\text{At high } P_{O_2}, \qquad \frac{1}{2}O_2 + V_O^{\cdot\cdot} = O_o^x + 2\dot{h} \qquad 8.6$$

where e' and $\dot{h}$ represent excess electrons and electron holes, respectively. Assuming that the defect concentrations are low and the interaction between defects is negligible, application of the mass-action law to [8.5] and [8.6] yields

$$[e'] = \sqrt{\frac{K_1[O_o^x]}{[V_o^{\cdot\cdot}]}}\,P_{O_2}^{-\frac{1}{4}} = K_1' P_{O_2}^{-\frac{1}{4}} \qquad 8.7$$

$$[\dot{h}] = \sqrt{\frac{K_2[V_o^{\cdot\cdot}]}{[O_o^x]}}\,P_{O_2}^{\frac{1}{4}} = K_2' P_{O_2}^{\frac{1}{4}} \qquad 8.8$$

where K_1 and K_2 are the chemical equilibrium constants of reactions [8.5] and [8.6], respectively. $[V_O^{\cdot\cdot}]$ and $[O_o^x]$ are the concentrations of $V_O^{\cdot\cdot}$ and O_o^x, respectively, which are considered as constants. The electrical conductivity σ_j of charged particles j can be linked to its concentration $[j]$ by the Nernst–Einstein relationship

$$\sigma_j = ze[j]u_j = \frac{z^2e^2D_j}{kT}[j] \qquad 8.9$$

where ze is the charge of the defect j; e is the elementary charge; D_j is the diffusion coefficient of defect j, and has the form $D_j = D_j^o \exp(-\Delta H_j/kT)$; $[j]$ and u_j are the concentration and electrical mobility of defect j.

Substitution of [8.7], [8.8] and [8.9] into the total electrical conductivity $\sigma_t = \sigma_{O^{2-}} + \sigma_e' + \sigma_h^{\cdot}$ yields

$$\sigma_t(T, P_{O_2}) = \frac{4e^2 D_{O^{2-}}}{kT}[V_O^{\cdot\cdot}] + \frac{e^2 D_{e'}}{kT}[e'] + \frac{e^2 D_{\text{ħ}}}{kT}[\text{ħ}]$$

$$= \frac{\sigma^o_{O^{2-}}}{T}\exp\left(-\frac{\Delta H_m}{kT}\right) + \frac{\sigma^o_{e'}}{T}P_{O_2}^{-\frac{1}{4}}\exp\left(-\frac{\Delta H_{e'}}{kT}\right)$$

$$+ \frac{\sigma^o_{\text{ħ}}}{T}P_{O_2}^{\frac{1}{4}}\exp\left(-\frac{\Delta H_{\text{ħ}}}{kT}\right) \qquad 8.10$$

where $\sigma^o_{O^{2-}}$, $\sigma^o_{e'}$ and $\sigma^o_{\text{ħ}}$ are the pre-exponential terms for oxide-ion, excess electron and electron holes, respectively, as expressed in eq. [8.2]. $\Delta H_{e'}$ and $\Delta H_{\text{ħ}}$, in eV, are the motional enthalpies for excess-electron and electron-hole conductions, respectively. Equation [8.10] suggests that the excess–electron and electron–hole conductions preferentially occur at low P_{O_2} and high P_{O_2} extremes, respectively, whereas pure oxide-ion conduction dominates in the medium P_{O_2} range. The boundary of each domain is determined by the relative magnitude of electronic conductivity to oxide-ion conductivity, often expressed by the ionic transport number $t_{O^{2-}}$

$$t_{O^{2-}} = \left[1 + \left(\frac{P_{O_2}}{P_{e'}}\right)^{-\frac{1}{4}} + \left(\frac{P_{O_2}}{P_{\text{ħ}}}\right)^{\frac{1}{4}}\right]^{-1} \qquad 8.11$$

where two important parameters, $P_{e'}$ and $P_{\text{ħ}}$, are introduced. The definitions of $P_{e'}$ and $P_{\text{ħ}}$ are the partial pressures of oxygen at which $\sigma_{O^{2-}} = \sigma_{e'}$ and $\sigma_{O^{2-}} = \sigma_{\text{ħ}}$, respectively, and are therefore often known as the characteristic P_{O_2} for excess-electron and electron–hole conductions, respectively. The relationship of $P_{e'}$ and $P_{\text{ħ}}$ with temperature can be established by equating the first term in eq. [8.10] with the second and third terms, respectively

$$P_{e'} = \left(\frac{\sigma^o_{e'}}{\sigma^o_i}\right)^4 \exp\left[-\frac{4(\Delta H_{e'} - \Delta H_m)}{kT}\right] \qquad 8.12$$

$$P_{\text{ħ}} = \left(\frac{\sigma^o_i}{\sigma^o_{\text{ħ}}}\right)^4 \exp\left[-\frac{4(\Delta H_m - \Delta H_{\text{ħ}})}{kT}\right] \qquad 8.13$$

The values of $P_{e'}$ and $P_{\text{ħ}}$ can be experimentally measured using coulometric titration, EMF and electrolyte breakdown voltage techniques. Some $P_{e'}$ values are listed in Table 8.2 for ZrO_2-based electrolytes. Also listed are those for CeO_2- and $LaGaO_3$-based electrolyte systems. For ZrO_2-based as well CeO_2-based electrolytes to be discussed in the next section, the $P_{\text{ħ}}$ value is well above 1 atmosphere before hole-conduction becomes appreciable. Therefore,

Table 8.2 Characteristic partia pressures of oxygen as a function of temperature T(K) for excess ($P_{e'}$) and hole ($P_{\dot{h}}$) electronic conductions in solid electrolyte systems

Solid electrolytes	Expression	Temperature range, °C
ZrO_2-8 mol% Y_2O_3	$\log_{10} P_{e'}\,(\text{atm}) = -\dfrac{56500}{T} + 19.3$	500–1200
ZrO_2-6.4 mol% CaO	$\log_{10} P_{e'}\,(\text{atm}) = -\dfrac{51800}{T} + 17.9$	700–1600
ZrO_2-6.9 mol% MgO	$\log_{10} P_{e'}\,(\text{atm}) = -\dfrac{74370}{T} + 29.42$	1300–1600
CeO_2–10 mol% Gd_2O_3	$\log_{10} P_{e'}\,(\text{atm}) = -\dfrac{36970}{T} + 18.00$	>400
	$\sigma_{e'}T = 3.456 \times 10^9 \exp\left(-\dfrac{2.475eV}{kT}\right) P_{O_2}^{-\frac{1}{4}}$	(S/cm)
$LaGaO_3$-10 mol% SrO-20 mol% MgO	$P_{e'}\,(\text{atm}) = (1.8\pm0.5)\times10^{24} \exp\left(-\dfrac{14.0\pm0.5eV}{kT}\right)$	800–1000
	$P_{\dot{h}}\,(\text{atm}) = (6\pm2)\exp\left(-\dfrac{1.9\pm0.6eV}{kT}\right)$	

in most applications of ZrO_2- and CeO_2-based electrolytes, only excess-electron conduction is considered. Appreciable electron-hole conduction is only observed in ThO_2-based materials under atmospheric condition.

The presence of electronic conduction in a solid electrolyte of an electrochemical device, such as a solid oxide fuel cell, leads to a lowered open-circuit voltage, leaked current and therefore reduced electrical efficiency. The degree of reduction in the Nernst potential, E, by electronic conduction is given by

$$E = \frac{RT}{F}\left[\ln\frac{P_{O_2}'^{\frac{1}{4}} + P_{e'}^{\frac{1}{4}}}{P_{O_2}''^{\frac{1}{4}} + P_{e'}^{\frac{1}{4}}} + \ln\frac{P_{O_2}''^{\frac{1}{4}} + P_{\dot{h}}^{\frac{1}{4}}}{P_{O_2}'^{\frac{1}{4}} + P_{\dot{h}}^{\frac{1}{4}}}\right] \qquad 8.14$$

where P_{O_2}' and P_{O_2}'' are partial pressures of oxygen at cathode/electrolyte and anode/electrolyte interfaces, respectively. For ZrO_2-based and CeO_2-based electrolytes, hole-conduction is negligible, and eq. [8.14] can be simplified into

$$E = \frac{RT}{F}\left[\ln\frac{P_{O_2}'^{\frac{1}{4}} + P_{e'}^{\frac{1}{4}}}{P_{O_2}''^{\frac{1}{4}} + P_{e'}^{\frac{1}{4}}}\right] \qquad 8.15$$

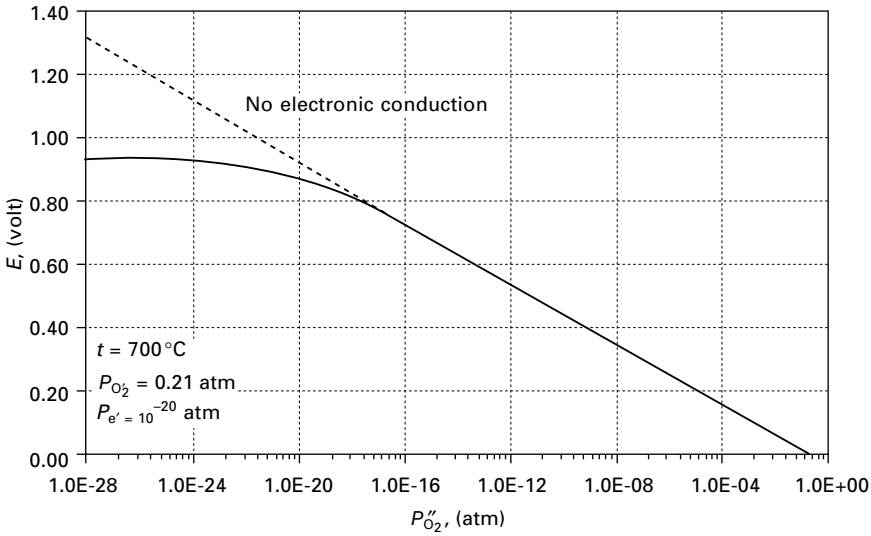

8.4 Graphical representation of eq. [8.17], showing the effect of excess electronic conduction at low P_{O_2}.

Figure 8.4 shows a graphical representation of eq. [8.15]. Evident from this figure, the appreciable deviation begins to occur as P_{O_2} approaches the characteristic $P_{e'}$. In the Section 8.3 of CeO_2-based SOFCs, the effect of electron leakage current on the electrical efficiency and power density of a fuel cell will be particularly discussed.

8.2.2 Cathode materials

$LaMnO_3$-based perovskite oxides represent the state-of-the-art cathode materials for ZrO_2-based SOFCs. The selection of this material over others such as $LaFeO_3$- and $LaCoO_3$-based perovskites is primarily based on a balanced consideration in electrical conductivity, chemical reactivity, electrocatalytic activity, and thermal expansion coefficient (TEC). $LaCoO_3$-based perovskites are known to be superior in electrical conductivity and electrocatalytic activity to $LaMnO_3$-based ones. However, the former is more reactive with ZrO_2 and has a much higher TEC than doped ZrO_2. An adequate balance in material properties is particularly important for cathode-supported SOFCs where a large thermal mismatch between the substrate and the supported layers could lead to catastrophic failure upon thermal cycling.

Pure $LaMnO_3$ perovskite is neither a good electrical conductor nor a good catalyst for oxygen reduction. Substituting alkaline-earth elements such as Ca and Sr into $LaMnO_3$ has been a common practice to enhance electrical conductivity and electrocatalytic activity while still possessing a good TEC match to ZrO_2 electrolytes. Figure 8.5 shows an example of Arrhenius plots

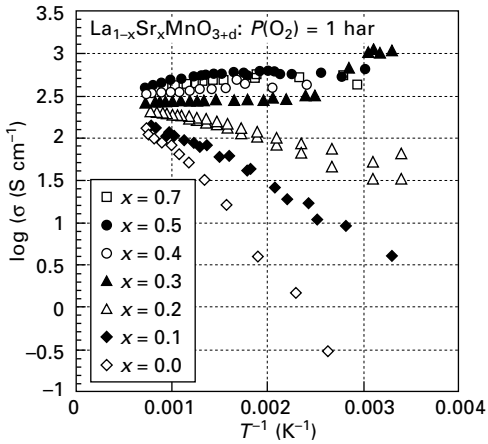

8.5 Arrhenius plot of electrical conductivity of $La_{1-x}Sr_xMnO_{3+\delta}$ at P_{O_2} = 1 atm. Copyright Elsevier.

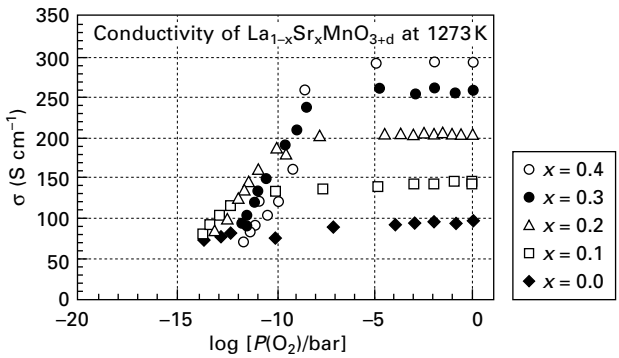

8.6 P_{O_2} dependence of electrical conductivity of $La_{1-x}Sr_xMnO_{3+\delta}$ at 1000 °C. Copyright Elsevier.

of electrical conductivity measured in O_2 of $LaMnO_3$ doped with various levels of Sr[4]. The plots agree well with eq. [8.1], from whose slope activation energies are determined to decrease with Sr-doping level. The magnitude of 0.03 to 0.25 eV suggests a predominant small-polaron hopping mechanism for electrical conduction. On the other hand, Fig. 8.6 shows the variation of isothermal conductivity with P_{O_2}, further confirming that the doped $LaMnO_3$ is a p-type conductor[3]. The generation of p-type small polarons (electron holes) is explicable from the perspective of defect chemistry, by which the presence of Ca'_{La} or Sr'_{La} requires creation of more electron holes in the form of $Mn_{Mn}^{\bullet}$ to balance the local charge. This process is best described by the following defect reactions:

$$2\,SrO \xrightarrow{LaMnO_3} 2\,Sr'_{La} + 2O_o^x + V_O^{\cdot\cdot}$$

or $$2\,CaO \xrightarrow{LaMnO_3} 2\,Ca'_{La} + 2O_o^x + V_O^{\cdot\cdot} \qquad 8.16$$

$$\frac{1}{2}O_2 + V_O^{\cdot\cdot} + 2\,Mn_{Mn}^x = O_o^x + 2\,Mn_{Mn}^{\cdot} \qquad 8.17$$

with charge neutrality relationship of $2[V_O^{\cdot\cdot}] + [p] = [Sr'_{La}]$ or $[Ca'_{La}]$. It is obvious that the concentration of electron holes $[p]$ or $[Mn_{Mn}^{\cdot}]$ increases with the dopant concentration $[Ca'_{La}]$ or $[Sr'_{La}]$.

Thermal expansion coefficients (TECs) of doped $LaMnO_3$ vary with the type of dopants, doping level, and more importantly P_{O_2}. Ca-doped $LaMnO_3$ perovskites generally have lower TECs (in the range of $10–11 \times 10^{-6}$/K) than those of Sr-doped $LaMnO_3$ ($11–12 \times 10^{-6}$/K) for a similar doping level. This difference is most likely due to the smaller ionic radius of Ca^{2+} than Sr^{2+}. As a result, Ca-doped $LaMnO_3$ is better suited for a ZrO_2-based SOFC with regard to thermal expansion match as the TEC of 8YSZ is 10.4×10^{-6}/K. For a given dopant, on the other hand, Fig. 8.7 shows a minimum of TEC occurring at roughly $x = 0.15$ and 0.20 for Sr and Ca level in $La_{1-x}AE_xMnO_3$ (AE = Ca and Sr), respectively[5]. However, one of the most important characteristics of thermal expansion behavior for the doped $LaMnO_3$ is the change with P_{O_2} under an isothermal condition, also known as 'chemical expansion'. Understanding of this behavior is critically important for cathode-supported SOFCs as the P_{O_2} at the cathode/electrolyte interface decreases with increasing cell current. If the lattice of a doped $LaMnO_3$ varies (expands or contracts) with the interfacial P_{O_2} or cell current, a chemical stress would be developed in the cathode substrate, which is often the leading cause for mechanical failure if the stress exceeds the strength of the substrate. Thermodynamically

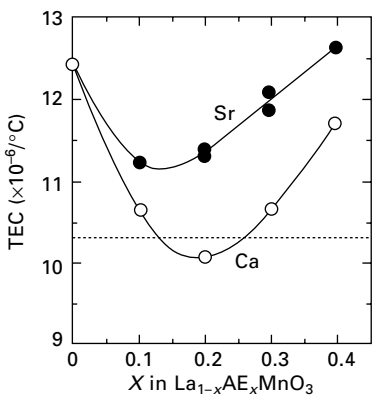

8.7 TECs as a function of doping level in $La_{1-x}AE_xMnO_3$ (AE = Ca and Sr) measured in air from 50 to 1000°C. Reproduced by permission of The Electrochemical Society.

speaking, the change of uniaxial strain ε for an isotropic solid with respect to P_{O_2} is given by[6]

$$\left(\frac{\partial \varepsilon}{\partial P_{O_2}}\right)_T = \frac{1}{3}\beta_c\left(\frac{\partial \delta}{\partial P_{O_2}}\right)_T \qquad 8.18$$

$$\beta_c = \frac{1}{V}\left(\frac{\partial V}{\partial \delta}\right)_{T,P} \qquad 8.19$$

where β_c is the chemical expansion coefficient and V is the specific volume of the solid. As suggested by eq. [8.18], how the lattice strain varies with P_{O_2} largely depends upon how the oxygen stoichiometry δ of $LaMnO_3$ changes with P_{O_2}. Figure 8.8 shows the measured variations of 3 + δ of $La_{0.8}Sr_{0.2}MnO_3$ with P_{O_2} under various temperatures[7]. As P_{O_2} decreases, 3 + δ experiences from oxygen excess (δ > 0) to oxygen stoichiometry (δ = 0) and finally to oxygen deficiency (δ < 0) before the perovskite decomposes. While it is straightforward for oxygen loss or oxygen deficiency under low P_{O_2}, the exact mechanism for oxygen excess at high P_{O_2} is still debated. One reasonable hypothesis is the formation of cation vacancies V'''_{La} and V'''_{Mn} via the following reaction[8]:

$$\frac{3}{2}O_2 + 6Mn'_{Mn} \rightarrow 3O_o^x + V'''_{La} + V'''_{Mn} + 6Mn_{Mn}^x \qquad 8.20$$

where Mn'_{Mn} represents Mn^{2+}, which is equilibrated by the charge disproportionation of Mn_{Mn}^x into Mn'_{Mn} and $Mn_{Mn}^{\cdot}$:

$$2Mn_{Mn}^x = Mn'_{Mn} + Mn_{Mn}^{\cdot} \qquad 8.21$$

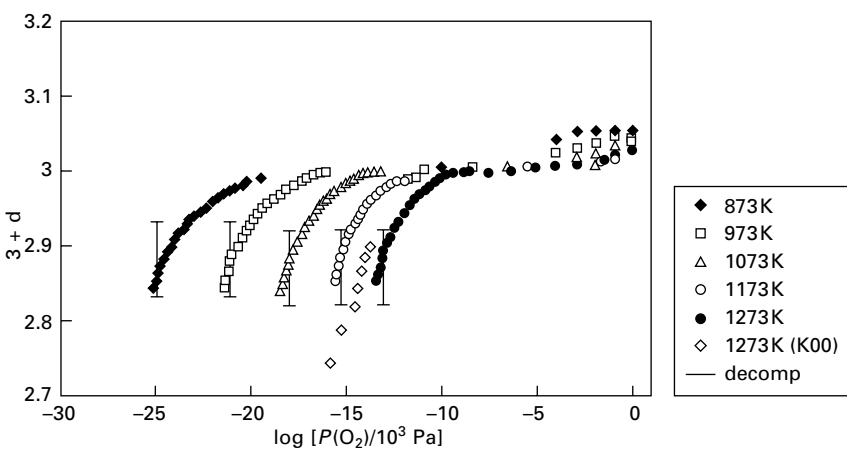

8.8 Change of oxygen stoichiometry of $La_{0.8}Sr_{0.2}MnO_{3+\delta}$ with P_{O_2} and temperature. Copyright Elsevier.

This mechanism is supported by the results of electron and neutron diffraction[9] and density measurement[10]. The creation of V'''_{La} and V'''_{Mn} implies a weakened bond-strength between cations La and Mn as well as their coordination with oxygen, leading to an increase in lattice expansion. This is analogous to the formation of oxygen vacancies at low P_{O_2}, which also results in lattice expansion. Such lattice expansion has been experimentally observed in Fig. 8.9 as the atmosphere was switched from air to pure O_2 for doped $LaMnO_3$. A schematic representation of chemical expansion of doped $LaMnO_3$ with varying P_{O_2}, based on eq. [8.18] and Fig. 8.8, is illustrated in Fig. 8.10. It is

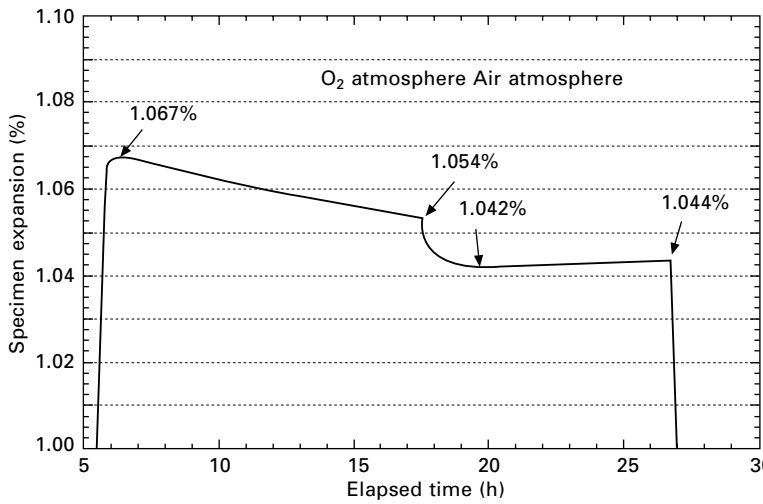

8.9 Contraction of Ca-doped $LaMnO_3$ perovskite as atmosphere is switched from pure O_2 to air at 1000 °C.

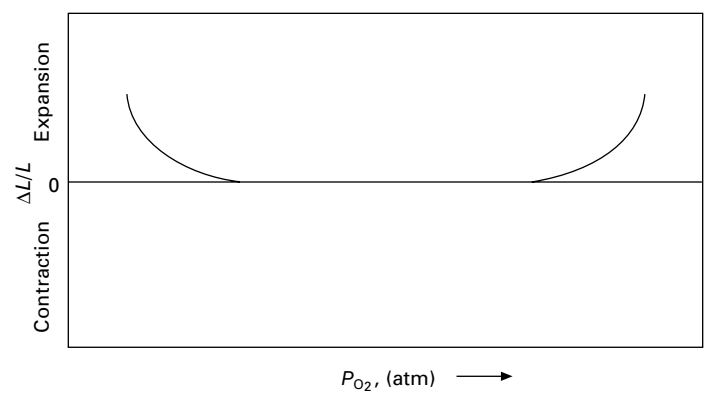

8.10 Schematic illustrations of dimensional changes in doped $LaMnO_3$ with P_{O_2}.

evident that the lattice of doped $LaMnO_3$ expands at both high and low P_{O_2}, but it remains flat at medium P_{O_2}.

Another important aspect of doped $LaMnO_3$ is the chemical reactivity with ZrO_2-based electrolytes and $LaCrO_3$-based interconnections if applicable. A general and widely accepted mechanism is the formation of the insulating phases $La_2Zr_2O_7$ and $SrZrO_3$ (for $La_{1-x}Sr_xMnO_3$ (LSM) cathode) at the contacting interface[11,12]. The presence of $La_2Zr_2O_7$ and/or $SrZrO_3$ at the interface is deleterious as it not only deactivates the catalytic activity for O_2 reduction, but also increases the ohmic resistance, therefore decreasing cell performance. A simple physical interpretation to the formation of $La_2Zr_2O_7$ involves diffusion of Mn into the ZrO_2 lattice, leaving La activity elevated in $LaMnO_3$ and therefore promoting the chemical reaction between La and Zr. The study showed that Ca-doped $LaMnO_3$ is chemically less active with ZrO_2 than Sr-doped $LaMnO_3$; Ca-doped $LaMnO_3$ begins to react readily with ZrO_2 above ~1300 °C whereas Sr-doped $LaMnO_3$ begins to react above ~1200 °C.

The polarization behavior is the most important property of a cathode. It directly determines the performance of a SOFC. Typically, the polarization process of a SOFC originates from two sources: oxygen molecular diffusion and oxide-ion transfer. The former is known as concentration polarization whereas the latter is often referred to as activation polarization. For an anode-supported SOFC, the cathode polarization is mainly dominated by the activation polarization due to the fact that the cathode layer is very thin. However, both concentration and activation polarizations become significant to the performance of a cathode-supported SOFC. By combining classical Fick's first law and Nernst equation, an analytical solution to the concentration polarization η_{conc} with current density j has been obtained for a cylindrical tubular cathode[13]

$$\eta_{conc} = \frac{RT}{4F}\left\{\ln x - \ln\left[1 - (1-x)^{1-\frac{i}{j_L}}\right]\right\} \tag{8.22}$$

$$j_L = -\frac{\ln(1-x)}{\ln(r_2/r_1)} \times \frac{4FD_{O_2}^{eff}}{RTr_2} P_t \tag{8.23}$$

where x is the molar fraction of oxygen in oxidant; j_L is the limiting current density; r_2 and r_1 are the outer and inner radii of the cathode tube, respectively; $D_{O_2}^{eff}$ is the effective oxygen diffusivity, including all the microstructural factors; P_t is the total system pressure; R, F, T have their usual meanings.

For the activation polarization process, a simple analytical solution is not always straightforward since it involves many elementary steps for a complete O_2 reduction. These elementary steps include adsorption of O_2 on the surface of doped $LaMnO_3$, dissociation of O_2 into adsorbed O_{ads} and/or O_{ads}^-, followed by surface diffusion of O_{ads} and/or O_{ads}^- to the triple-phase boundary (TPB)

where electrolyte (e. g., YSZ), cathode (e.g. LSM) and gas meet, completion of ionization of O_{ads} and/or O^{-}_{ads} to O^{2-} by electron transfer. Depending upon the rate-limiting elementary step, the actual analytical equation for describing the activation process can be very different. A common assumption for the $LaMnO_3$-based cathode, particularly for cathode-supported SOFCs, is that the last step – the ionization of O_{ads} and/or O^{-}_{ads} to O^{2-} – is rate limiting. As a result, a simplified Butler–Volmer equation, assuming single-electron (O^{-}_{ads} to O^{2-}) rate-limiting step and symmetrical ($\alpha = 0.5$) electron transfer, is often adopted to express the activation polarization η_{act} with current density j by

$$\eta_{act} = \frac{RT}{0.5F} \operatorname{arc\,sin} h\left(\frac{j}{2j_{ex}^{eff}}\right) \qquad 8.24$$

where j_{ex}^{eff} is the effective exchange current density dependent on P_{O_2}.

One of the decisive parameters for activation polarization is the linear TPB density. The greater is the linear TPB density the less is the activation polarization loss. To maximize the TPB density, the functional layer of a cathode is practically made of a composite consisting of electrolyte (e.g. YSZ) and cathode (e.g. LSM) with a relative volumetric ratio of 50:50. Tanner *et al*.[14] correlates the microstructural parameters with effective charge transfer resistance $R_{ct(eff)}$ in the low-current density limit by the following equation:

$$R_{ct(eff)} \approx \sqrt{\frac{R_{ct} d \rho_{i}}{(1 - V_v)}} \qquad 8.25$$

where R_{ct} is the intrinsic charge-transfer resistance; d and ρ_i are the grain size and ionic resistivity of the oxide-ion conducting phase (e.g. YSZ), respectively; V_v is the porosity of the functional layer (or interlayer). Equation [8.25] suggests that smaller grain size and higher conductivity of the oxide-ion conducting phase would decrease the effective charge-transfer resistance. Therefore, a mixture of doped $LaMnO_3$ with fine-grained Sc-doped ZrO_2 should give a better performance than that with YSZ[3]. Equation [8.25] also implies that lower porosity V_v would decrease the $R_{ct(eff)}$. However, lowering V_v could also increase the concentration polarization. Therefore, a balanced V_v is preferable in making the optimal composite cathode microstructure. This balanced V_v is typically found in the range of 30–35%.

8.2.3 Anode materials

To facilitate the fuel oxidation-reaction taking place at the anode and collect the current, an electrically conducting catalyst is needed. Metallic Ni is a cost-competitive and performance-effective catalyst for oxidation of H- and C-containing fuels and a good electrical conductor for carrying electrical

current. However, a direct use of Ni catalyst as an anode in the SOFC is inadequate, simply because of the large mismatch in thermal expansion coefficient between Ni and the underlying layer ZrO_2 electrolyte, and the great propensity of Ni particles to sintering, leading to loss of catalyzing surface area. If a SOFC was made of pure Ni anode, the cell performance would degrade rapidly and delamination of anode from electrolyte would occur upon thermal cycling. To circumvent these problems but still to use the Ni as a catalyst, a mixture of electrolyte powder (e.g., YSZ), Ni powder and physical pores was proposed by Spacil[15] about four decades ago. It proves to be one of the most important inventions in the SOFC history, and continues to be the dominant anode template for present development. The advantages of this composite anode are multiple. First, it mitigates the large thermal expansion mismatch existing between Ni and ZrO_2 electrolytes, which increases the sustainability to thermal cycling. Second, it provides a large number of TPB sites for fuel-oxidation reaction, facilitating the anode kinetics. Third, the porous structure ensures the gaseous reactants diffuse into the TPB sites and the gaseous products diffuse out to the bulk fuel stream with a minimal resistance. Fourth, the affinity provided by the ZrO_2-based materials in both anode and electrolyte enhances the adherence and avoids interfacial cationic interdiffusion. Fifth, the presence of ZrO_2 prevents Ni particles from sintering. This property ensures long-term stability of the anode. An ideal microstructure of anode should, therefore, consist of an interlinking Ni pathway for current conduction and a percolated pore network on which a thin layer of ZrO_2 is deposited. Figure 8.11 shows an example of such a structure of a YSZ-Ni composite anode made using an electrochemical vapor deposition (EVD) process invented by Westinghouse.

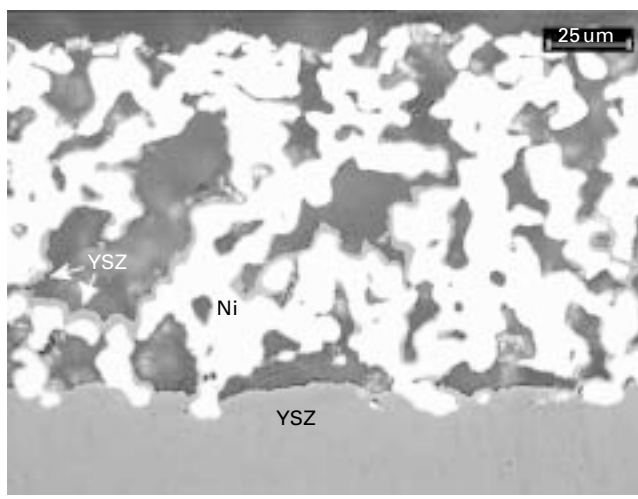

8.11 An ideal microstructure exemplified by EVD made anode.

It is the requirement for a multi-phase, porous structure that makes the performance of the anode sensitive to the volumetric ratio of the phases, porosity, thickness, relative and absolute particle size distributions of ZrO_2 and Ni particles, and sintering temperature. It is often seen that the anode performance varies greatly from one manufacturer/laboratory to another. However, a general consensus in the SOFC community in making an optimal anode can be found in that the volume ratio of ZrO_2/Ni is in the range of 50/50 to 40/60, finer ZrO_2 particles with $d_{50} \sim 0.5\,\mu m$ and coarser Ni particles with a bimodal distribution at $d_{50} \sim 0.5\,\mu m$ and $d_{50} \sim 10\,\mu m$ and a volume ratio 6:1 for each mode, respectively. The resulting porosity is in the vicinity of 30 vol%. Determined by whether a dense electrolyte film could be achieved for an anode-supported SOFC, the sintering temperature of the anode is typically in the range of 1300–1400 °C.

The activation polarization of an anode is generally described by the Butler–Volmer equation [8.24] provided that the charge-transfer process is the rate-limiting step. For instance, the ScSZ + Ni cermet anode of a Siemens cathode-supported SOFC with H_2 as a fuel exhibits a linear η–i behavior up to 0.6 A/cm^2 in a temperature range of 900–1000 °C, from whose slope the exchange current density is estimated to be in the neighborhood of 1.0–2.0 A/cm^2. However, other elementary steps involved in anode kinetics could also compete to limit the rate of H_2 oxidation, making the determination of the mechanism complicated. The elementary steps that are well accepted for anode kinetics are generally analogous to those of the cathode. Molecules of H_2 preferentially adsorb and disassociate on the surface of the catalytic Ni particles into H_{ads}, followed by diffusing along the surface of Ni towards TPB sites where oxide-ions (or vacancies) are available for oxidizing H-species, forming gaseous H_2O and releasing electrons to the external circuit via the following reaction:

$$2\,H_{ads} + O_o^x = H_2O_{(g)} + V_o^{\cdot\cdot} + 2e' \qquad 8.26$$

Figure 8.12 illustrates a schematic of such a process. If H_2 adsorption and surface diffusion steps become the rate-limiting steps, the electrode polarization

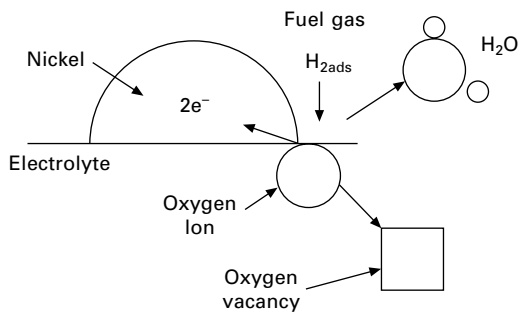

8.12 Mechanism schematic for anode reaction with H_2 fuel.

could vary with partial pressure of H_2 and H_2O[16,17], and the polarization is generally described by Langmuir-type reactions[18,19].

The concentration polarization η_{conc} of an anode can generally be formulated by a combination of Fick's diffusion equation and the Nernst equation in the following form:

$$\eta_{conc} = \frac{RT}{2F} \ln \left(\frac{1 + \frac{J}{J_L} \times \frac{1}{r}}{1 - \frac{J}{J_L}} \right) \tag{8.27}$$

$$r = \frac{P^O_{H_2O}}{P^O_{H_2}}$$

$$J_L = \frac{2F}{RT} \bullet \frac{D^{eff}_{H_2-H_2O}}{l} \bullet P^O_{H_2} \tag{8.28}$$

where $P^O_{H_2O}$ and $P^O_{H_2}$ are the partial pressures of bulk H_2O and H_2, respectively; l is the thickness of the anode; $D^{eff}_{H_2-H_2O}$ is the effective binary diffusivity of H_2–H_2O; J_L is the limiting current density. It is evident that $P^O_{H_2O}$, $P^O_{H_2}$, thickness and porosity (affecting indirectly $D^{eff}_{H_2-H_2O}$) are the variables responsible for the anode concentration polarization. However, in comparison with the cathode, the magnitude of the anode η_{conc} is not an alarming issue even for a greater thickness due to a much higher binary diffusivity of H_2–H_2O. The elegant combination of electrode substrate with faster diffusing species bestows on the anode-supported SOFC a great advantage over a cathode-supported one with regard to concentration polarization loss.

In recent years, a widely discussed and debated topic with regard to the anode is the possibility of directly oxidizing the readily available hydrocarbons by a SOFC stack without undergoing a prior reforming process. The realization of such a process is significant as it would not only simplify the SOFC system and make it cost competitive, a major issue for the commercialization of SOFC technology, but also increase the overall electrical efficiency. The primary challenge for such an SOFC system is, however, the formation of carbon on the SOFC stack by either solid-catalyzed reaction or gas-phase pyrolysis of hydrocarbons, by which the TPB sites are gradually blocked out. One of the effective approaches to avoid carbon formation is to lower the operating temperature of the Ni-based anode, by which the rate of carbon formation is constrained, while still maintaining high cell current density (or oxygen flux). This was demonstrated by Murray *et al.*[20], who operated a cell using a CeO_2-containing anode below 650 °C with dry methane as fuel. No carbon formation was reported on the cell during and after the test. In recognizing that Ni is known as a good catalyst for carbon formation as for fuel oxidation, direct feed of hydrocarbons (n-butane and toluene in this

case) into a SOFC without carbon deposition was further reported by replacing Ni with Cu[21,22], which is catalytically inactive for cracking the hydrocarbons as well as for fuel oxidation. As Cu is used only as an electronic conductor, not as a catalyst, CeO_2 was added as a known ceramic catalyst for promoting oxidation of hydrocarbons to provide the needed catalytic activity for oxidizing fuels. To alleviate the dimensional instability of CeO_2 in reducing atmospheres and to avoid high sintering temperatures, a porous ZrO_2-based skeleton was first made, into which CeO_2 and Cu were subsequently impregnated by aqueous solutions of the corresponding salts[23,24]. Since then, a direct use of heavier hydrocarbons such as iso-octane[25,26], decane and diesel[27] has been demonstrated in laboratory-scale SOFC tests. Exceptional sulfur tolerance of the Cu–CeO_2 anode has also been reported[28]. Unfortunately, no direct utilization of hydrocarbons has been shown so far on a larger-scale SOFC stack with a reasonable operating lifetime. One of the obstacles is how to deliver the dry hydrocarbons to the stack without dropping carbon on peripheral module components. As the carbon formation process is largely dictated by the kinetics not thermodynamics, careful control of residence time of hydrocarbons on module components is critical to a successful operation of SOFC generators directly fuelled by dry hydrocarbons.

8.3 CeO_2-based solid oxide fuel cells

CeO_2-based SOFCs are largely limited to low temperature (for example <600 °C) application where the electronic conduction in CeO_2 electrolytes and propensity of dimensional change due to loss of oxygen (oxygen non-stoichiometry) in reducing atmospheres can be significantly suppressed.

8.3.1 CeO_2-based electrolytes

One unique characteristic of pure $CeO_{2-\delta}$ is the appreciable variation of oxygen stoichiometry δ with temperature and P_{O_2}. This is the direct result of the Ce^{3+}/Ce^{4+} redox couple existent in $CeO_{2-\delta}$. The phases formed under a given temperature and P_{O_2} vary sensitively with actual O/Ce ratio in the form of homologues of phases Ce_nO_{2n-2}, among which some intermediate phases can also be formed[29]. Since volume change is always associated with phase change of $CeO_{2-\delta}$ and the electrical conductivity of $CeO_{2-\delta}$ is generally low, there is no practical use of $CeO_{2-\delta}$ as an electrolyte for SOFCs. However, like ZrO_2, substitution of alkaline-earth and rare earth cations into the Ce^{4+} lattice can lead to the stabilization to room temperature of the fluorite cubic phase, a crystal structure favorable for oxide-ion conduction. More importantly, the acceptor doping creates oxygen vacancies, the essential elements for oxide-ion conduction, by charge compensation of the foreign and host cations as illustrated in Table 8.1.

The conductivity of doped CeO_2 electrolytes is generally higher than that of ZrO_2-based electrolyte, particularly at low temperatures. A conductivity peak at a specific dopant level for a given type of dopant or a maximum conductivity for a specific cation at a fixed dopant concentration resembles closely the behavior of ZrO_2-based electrolytes. Figures 8.13 and 8.14 show, respectively, the two maxima mentioned above for CeO_2-based electrolytes[30].

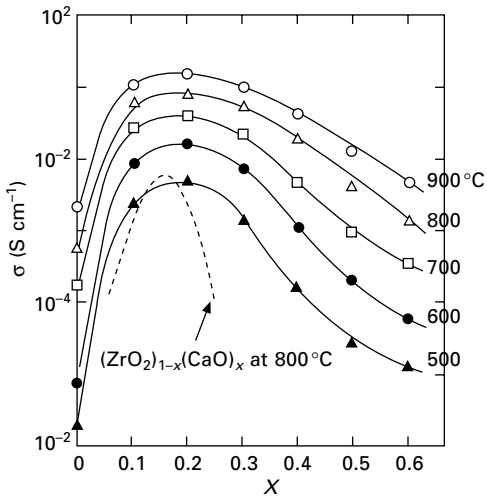

8.13 Oxide-ion conductivity of $(CeO_2)_{1-x}(Sm_2O_3)_x$ as a function of doping level x at various temperatures. Copyright Elsevier.

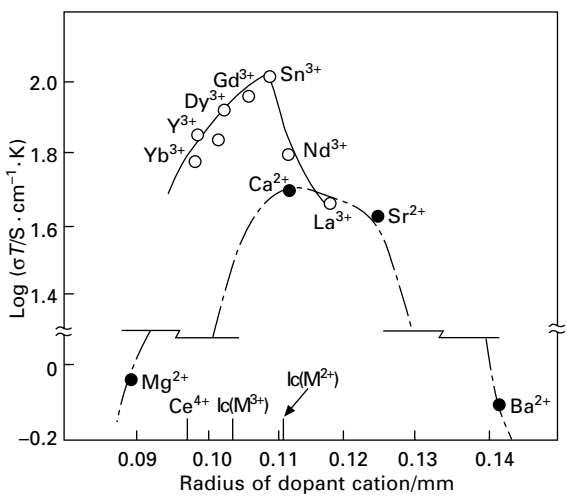

8.14 Oxide-ion conductivity of doped ceria at 800 °C against the radii of dopant cations. Copyright Elsevier.

An interpretation similar to that for ZrO_2-based electrolytes can be applied to CeO_2-based electrolytes. The conductivity maximum with concentration variation is mainly due to the interaction between dopant M'_{Ce} (or M''_{Ce}) and oxygen vacancies $V_O^{\cdot\cdot}$, leading to the formation of associates (or clusters) $2M'_{Ce} - V_o^{\cdot\cdot}$ (or $M''_{Ce} - V_o^{\cdot\cdot}$). As additional energy is needed for the association, the Arrhenius plot of conductivity often shows a kink (or a curvature) towards a low-temperature regime to reflect the increase in activation energy. On the other hand, the maximum conductivity observed for a specific dopant is the result of the closest match in ionic radius of the doping cation to that of the host Ce^{4+}, which leads to a minimization of the lattice elastic strain. For CeO_2-based electrolyte, the most favorable dopants of the rare-earth group are Gd and Sm.

The most appreciable disparity between CeO_2-based and ZrO_2-based electrolytes is the magnitude of the electronic conductivity. The presence of a variable Ce valence, namely Ce^{3+} (Ce'_{Ce}) and Ce^{4+} (Ce^x_{Ce}), considerably elevates the excess electronic conduction in reducing atmospheres by the following mechanism:

$$O_o^x + Ce_{Ce}^x = \frac{1}{2}O_2 + V_O^{\cdot\cdot} + 2Ce'_{Ce} \qquad 8.29$$

The excess electrons in the form of small polarons migrate via the Ce^{4+}–Ce^{3+} redox couple across the lattice, giving electronic conduction.

A good compilation of the oxide-ion conductivity for CeO_2-based electrolytes is given by Steele[31] for Rhodia-made low-SiO_2 (<30 ppm) $Ce_{0.9}Gd_{0.1}O_{1.95}$ (GDC10)

$$\sigma_{O^{2-}} T = 1.09 \times 10^5 \exp\left(-\frac{0.64\ \text{eV}}{kT}\right) (\text{S/cm})\ (T > 400\,^\circ\text{C}) \qquad 8.30a$$

$$\sigma_{O^{2-}} T = 1.00 \times 10^6 \exp\left(-\frac{0.77\ \text{eV}}{kT}\right) (\text{S/cm})\ (T < 400\,^\circ\text{C}) \qquad 8.30b$$

It is evident that the clusters disassociate above 400 °C. The electronic conductivity $\sigma_{e'}$ and characteristic $P_{e'}$ are given in Table 8.2. Simple calculation using equations in Table 8.2 indicates a $P_{e'}$ value of 8YSZ at 600 °C almost 20 orders of magnitude lower than that of GDC10.

The significance of electronic conduction at higher temperatures and lower P_{O_2} confines CeO_2-based electrolytes for SOFCs to low-temperature applications, e.g. below 600 °C, where the electronic conductivity can be considerably suppressed to an acceptable level. If this effect were not considered, the electrical efficiency of SOFC would be greatly compromised. In the following, a case study is given to show how electronic conduction affects the SOFC performance.

The leak oxygen flux j_{O_2} due to electronic conduction under a gradient of P_{O_2} and open-circuit condition is described by the classical Wagner equation:

$$j_{O_2} = -\frac{RT}{4^2 F^2 L}\int_{\ln P''_{O_2}}^{\ln P'_{O_2}} \frac{\sigma_{e'}\sigma_{O^{2-}}}{\sigma_{e'} + \sigma_{O^{2-}}} d\ln P_{O_2}$$

$$= -\frac{RT\sigma_{O^{2-}}}{4^2 F^2 L}\int_{\ln P''_{O_2}}^{\ln P'_{O_2}} (1 - t_{O^{2-}}) d\ln P_{O_2} \qquad 8.31$$

where L is the thickness of the electrolyte. Note that $\sigma_{O^{2-}}$ is independent of P_{O_2} for oxide-ion conductors. Substitution of eq. [8.11] into eq. [8.31] yields

$$j_{O_2} = \frac{RT\sigma_{O^{2-}}}{4F^2 L}\ln\frac{P'^{-\frac{1}{4}}_{O_2} + P^{-\frac{1}{4}}_{e'}}{P''^{-\frac{1}{4}}_{O_2} + P^{-\frac{1}{4}}_{e'}} \qquad 8.32$$

Note that $-j_{e'} = 2j_{O^{2-}} = 4j_{O_2}$ under open circuit voltage (OCV) condition. Under an external load, use of current density i_k to replace flux density j_k is more convenient. This conversion can be easily completed by the Faraday equation

$$i_k = Z_k F j_k \qquad 8.33$$

where Z_k is the charge of k-species. With a known conductivity σ_L of the external load, the ionic current density $i_{O^{2-}}$ and electron current density $i_{e'}$ across the electrolyte thickness L are given by

$$i_{O^{2-}} = \frac{RT\sigma_{O^{2-}}\sigma_L}{FL(\sigma_{O^{2-}} + \sigma_L)}\ln\frac{\sigma^o_{e'} + (\sigma_{O^{2-}} + \sigma_L)P'^{-\frac{1}{4}}_{O_2}}{\sigma^o_{e'} + (\sigma_{O^{2-}} + \sigma_L)P''^{-\frac{1}{4}}_{O_2}}$$

$$+ \frac{RT\sigma_{O^{2-}}}{FL}\ln\frac{\sigma_{O^{2-}} + \sigma^o_{e'}P'^{-\frac{1}{4}}_{O_2} + \sigma_L}{\sigma_{O^{2-}} + \sigma^o_{e'}P''^{-\frac{1}{4}}_{O_2} + \sigma_L} \qquad 8.34$$

$$i_{e'} = \frac{RT\sigma_{O^{2-}}}{FL}\ln\frac{\sigma_{O^{2-}} + \sigma^o_{e'}P'^{-\frac{1}{4}}_{O_2} + \sigma_L}{\sigma_{O^{2-}} + \sigma^o_{e'}P''^{-\frac{1}{4}}_{O_2} + \sigma_L} \qquad 8.35$$

$$i_{e'} + i_L = i_{O^{2-}} \qquad 8.36$$

where i_L is the external load current density, which is directly related to the load current density in a SOFC. Figures 8.15 and 8.16 show, respectively, the calculated electronic leak current and normalized electrical efficiency ε of a GDC10-based SOFC as a function of load current using eqs. [8.34]–[8.36] and conductivity data shown in eqs. [8.30] and Table 8.2. The electronic leakage current decreases whereas ionic current increases with load current. This finding implies that the effect of electronic conduction becomes less

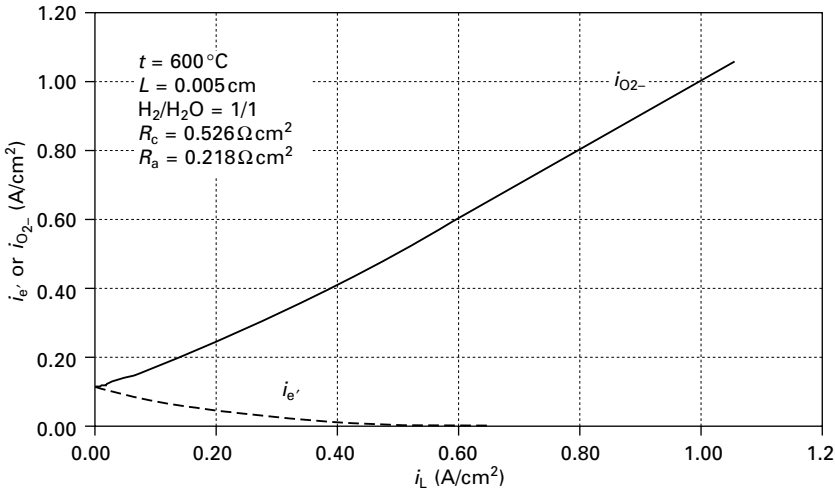

8.15 Calculated electronic leak current density of a CeO_2-based SOFC as a function of load current density under 600 °C and H_2/H_2O = 1/1.

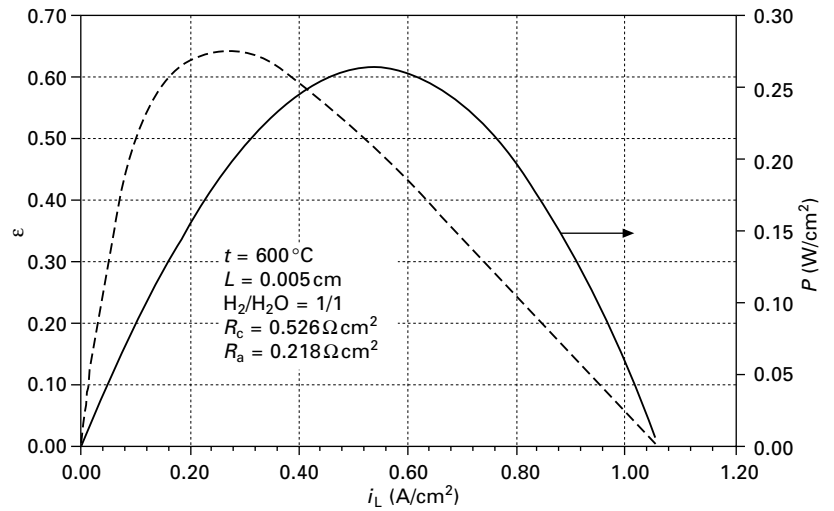

8.16 Calculated normalized electrical efficiency of a CeO_2-based SOFC as a function of load current density under 600 °C and H_2/H_2O = 1/1.

important at higher load current. The occurrence of peak efficiency at a specific current density in Fig. 8.16 is clearly the result of Fig. 8.15, which defines the achievable maximum efficiency and suggests an optimal operating current density in order to achieve the highest efficiency with reasonable power output. For a true DC efficiency, the normalized electrical efficiency should be multiplied by the thermodynamic efficiency of H_2-fuel.

8.3.2 Cathode materials

$LaCoO_3$-based and $LaFeO_3$-based perovskites are the leading cathode materials for low-temperature CeO_2-based SOFCs. In addition to a better thermal expansion match to the CeO_2-based electrolyte, these two materials as well as their mixtures in general have appreciable mixed oxide-ion and electronic conduction, by which the oxygen reduction process extends from the TPB reactive sites into the bulk of the cathode layer. As a result, the polarization losses are typically smaller than those of $LaMnO_3$-based cathode materials that rely largely on the density of the TPB. Another unique characteristic of $LaCoO_3$ and $LaFeO_3$-based materials is that they do not react with CeO_2-based electrolytes as readily as ZrO_2-based ones[32]. This advantage can be best utilized by cathode-supported SOFCs, which requires a co-sintering process for electrolyte and cathode, without compromising substantial performance loss.

The common dopants for A-sites of $LaCoO_3$ and $LaFeO_3$ are alkaline-earth elements such as Ca and Sr, whereas a mutual substitution of Co and Fe for B-sites is proven to be the best choice. Increasing the doping level generally increases the electrical conductivity in both systems. Figure 8.17 shows the effect of Sr-level on the conductivity of $LaCoO_3$ measured at

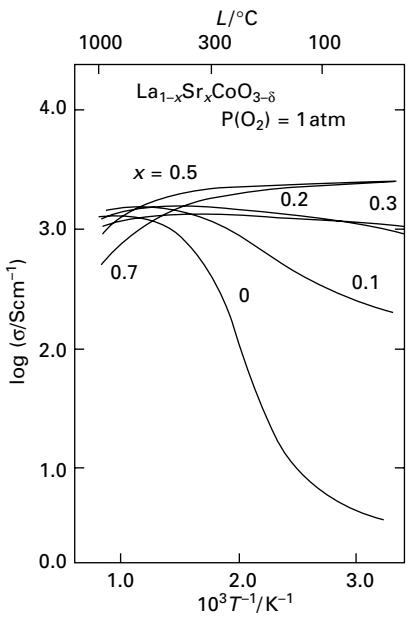

8.17 Temperature dependence of electrical conductivity of $La_{1-x}Sr_xCoO_{3-\delta}$ measured in P_{O_2} = 1 atm. Reproduced by permission of The Electrochemical Society.

various temperatures and $P_{O_2} = 1\,\text{atm}$[33]. The electronic conduction experiences a behavior change from semiconductor to metal at different dopant levels and temperatures. Such a behavior has been interpreted by the interaction of Co-3d electrons with O-2p electrons, structurally the Co–O–Co bond[34], i.e. it behaves like a metal if the rhombohedral angle is less than 60.3–60.4° whereas a semiconductor is observed at greater than 60.4°. In contrast, for $LaFeO_3$-based perovskites only semiconductor behavior was observed with much inferior electronic conductivity to $LaCoO_3$-based perovskites. On the other hand, however, TECs of $LaFeO_3$-based materials have a better match to CeO_2-based electrolytes than those of $LaCoO_3$-based ones. To best utilize the advantages exhibited by these two perovskite materials, a combination of $LaCoO_3$- and $LaFeO_3$-based materials has been systematically studied[35,36]. Figure 8.18 shows the variations of electrical conductivity with temperature and Sr-level of $La_{1-x}Sr_xCo_{0.2}Fe_{0.8}O_{3-\delta}$ system. At a Sr-level greater than 0.1, a peak conductivity was observed to occur at a certain temperature, which shifts towards lower temperature as the Sr-level increases. This behavior was further explained by Stevenson *et al.*[37] to be related to the decrease in stoichiometry of oxygen in the perovskite with temperature. Loss of oxygen creates oxygen vacancies, one of which eliminates two electron holes, therefore leading to a decrease in conductivity. With incorporation of this factor in the pre-exponential term of the Arrhenius equation, the calculated σ–t curves fit well with the measured one. The composition for the La–Sr–Co–Fe–O system was optimized to $La_{0.6}Sr_{0.4}Co_{0.2}Fe_{0.8}O_{3-\delta}$, which reflects a good balance between conductivity and TEC for CeO_2-based electrolytes.

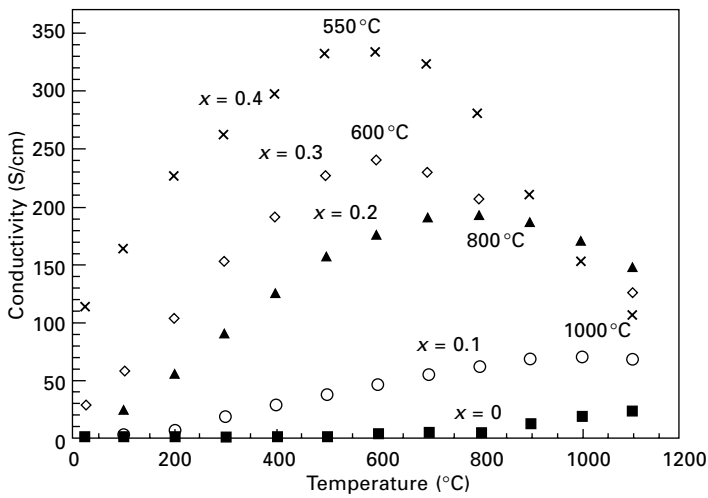

8.18 Electrical conductivity of $La_{1-x}Sr_xCo_{0.2}Fe_{0.8}O_{3-\delta}$ as a function of temperature and Sr content in air. Copyright Elsevier.

The dependence of electronic conductivity of $LaCoO_3$-based perovskites on P_{O_2} suggests a *p*-type electron hole conduction mechanism. Figure 8.19 shows that σ decreases with P_{O_2} in the range of 1–10^{-4}atm, which can be interpreted by the following defect reaction:

$$\frac{1}{2}O_2 + V_O^{\cdot\cdot} + 2Co_{Co}^{x} \rightarrow O_o^{x} + 2Co_{Co}^{\cdot} \qquad 8.37$$

As P_{O_2} decreases, the reaction shifts to the left, resulting in the creation of one oxygen vacancy for two electron holes consumed. The above p-type conduction mechanism has also been supported by Seebeck measurements where a positive Seebeck coefficient is typically observed. For $LaFeO_3$-based perovskites, a transition of p-type conductor to n-type conductor is observed as P_{O_2} decreases[38]; see Fig. 8.20. Such a transition is explicable with the aid of the following defect reaction for the p-type conduction

$$\frac{1}{2}O_2 + V_O^{\cdot\cdot} + 2Fe_{Fe}^{x} \rightarrow O_o^{x} + 2Fe_{Fe}^{\cdot} \qquad 8.38$$

and for *n*-type conduction

$$O_o^{x} + 2Fe_{Fe}^{x} \rightarrow \frac{1}{2}O_2 + V_O^{\cdot\cdot} + 2Fe_{Fe}^{\cdot} \qquad 8.39$$

with a charge disproportionation existing in the Fe species

$$2Fe_{Fe}^{x} = Fe_{Fe}^{\prime} + Fe_{Fe}^{\cdot} \qquad 8.40$$

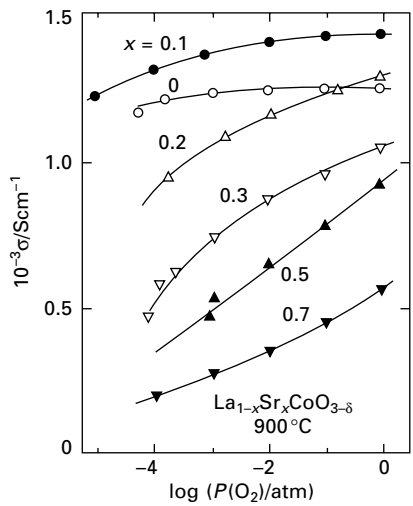

8.19 Dependence of electrical conductivity of $La_{1-x}Sr_xCoO_{3-\delta}$ on P_{O_2} measured at 900 °C. Reproduced by permission of The Electrochemical Society.

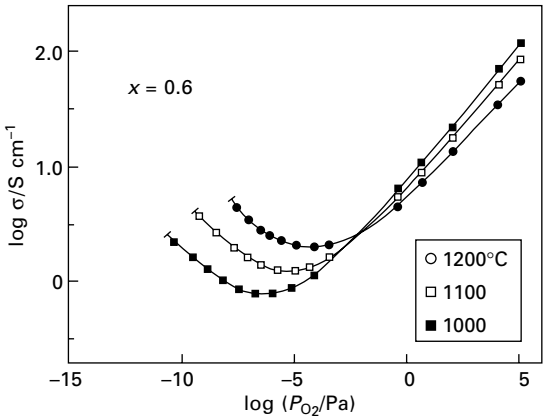

8.20 Dependence of electrical conductivity of $La_{0.40}Sr_{0.60}FeO_3$ on P_{O_2} and temperatures. Copyright Elsevier.

Unlike $LaMnO_3$-based cathode materials, $LaCoO_3$-based and $LaFeO_3$-based perovskites tend to lose the lattice oxygen more easily. Figure 8.21 shows the variations of oxygen nonstoichiometry $3-\delta$ in Sr-doped $LaCoO_{3-\delta}$ with temperature and Sr-doping level[39]. No oxygen excess was observed for all the conditions. In comparison to doped $LaCoO_3$, Fig. 8.22 shows that doped $LaFeO_3$ has smaller oxygen deficiency under a similar condition[40]. Yang and Lin[41] proposed the following semi-empirical equation to describe the nonstoichiometry δ with P_{O_2} for the La–Sr–Co–Fe–O system with reasonable agreement to the experimental data

$$\delta = \frac{3KP_{O_2}^n}{1 + KP_{O_2}^n} \qquad 8.41$$

where K and n are temperature-dependent constants. The creation of oxygen vacancies by oxygen nonstoichiometry promotes the mixed electronic and oxide-ion conduction, a favorable property for facilitating the electrode kinetics. For example, the ionic and electronic conductivities of $La_{0.6}Sr_{0.4}Co_{0.2}Fe_{0.8}O_{3-\delta}$ at 900 °C were reported to be 0.23 and 252 S/cm, respectively[37], while for $La_{0.8}Sr_{0.2}MnO_3$ the corresponding conductivities are in the order of 10^{-3} and 10^2 S/cm, respectively. However, the amount of oxygen vacancies must be controlled to avoid forming vacancy-ordering and thermal expansion mismatch to the electrolyte.

It is the presence of mixed electronic and oxide-ion conduction in $LaCoO_3$- and $LaFeO_3$-based systems that diversifies the mechanism of the rate-limiting step of oxygen reduction. As aforementioned, the activation polarization of a porous $LaMnO_3$-based cathode is generally dominated by the charge-transfer process that occurs at TPB. As the solid-state oxygen diffusion in the bulk of

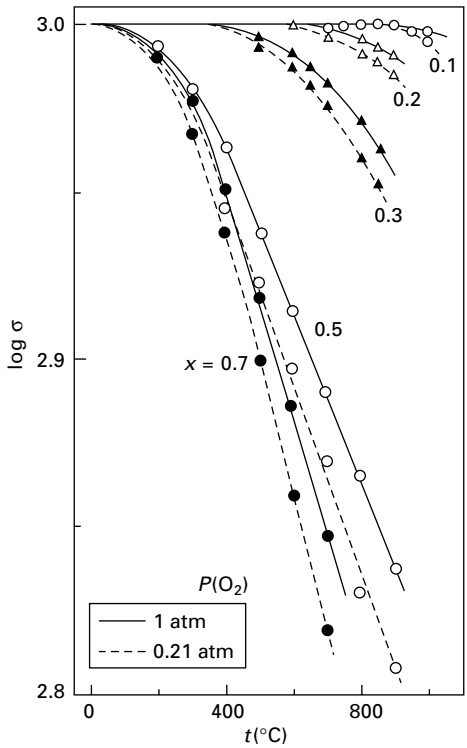

8.21 Dependence of oxygen nonstoichiometry of $La_{1-x}Sr_xCoO_{3-\delta}$ on x and temperatures. Copyright Elsevier.

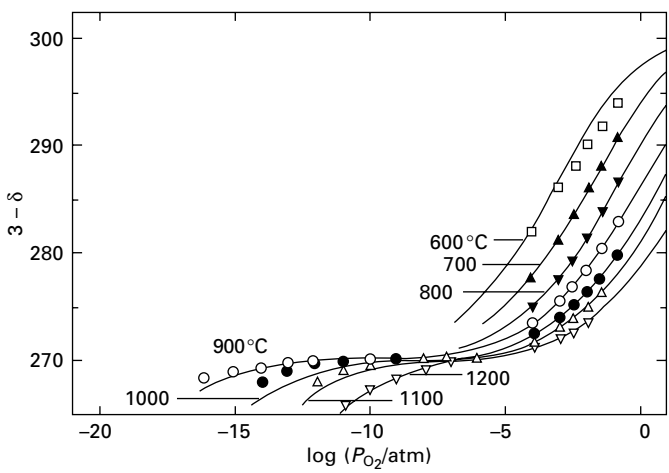

8.22 Dependence of oxygen nonstoichiometry of $La_{0.75}Sr_{0.25}FeO_3$ on P_{O_2} and temperatures. Copyright Elsevier.

a doped $LaCoO_3$ is significantly enhanced by the high oxide-ion conductivity, the rate-limiting step for the overall activation polarization changes to surface oxygen exchange (or adsorption) for a dense film[42,43], and it becomes mixed control of surface exchange and solid-state diffusion for a porous film[44,45]. The reactive zone for oxygen reduction as a result of mixed conduction is extended from the interface to the bulk of the cathode by a few microns[44].

8.3.3 Anode materials

The constituents of the anode of CeO_2-based SOFCs resemble very much those of ZrO_2-based ones, i.e. a mixture of CeO_2-electrolyte, metallic Ni and physical pores at a preferential volume ratio. Like $LaCoO_3$-based cathode materials, the introduction of mixed electronic and oxide-ion conductivity in CeO_2-based materials by the reducing atmosphere considerably enlarges the TPB reaction zone and makes it an excellent anode material. Therefore, lower electrode polarization is generally observed for a CeO_2-based anode, suitable for low-temperature SOFC applications. Figure 8.23 compares the performance of YSZ + Ni, ScSZ + Ni and Sm-CeO_2 (SDC) + Ni anodes measured by Siemens SFC. Clearly, SDC + Ni and ScSZ + Ni outperform YSZ + Ni, particularly at lower temperatures. As mentioned before and to be mentioned later, even for ZrO_2-based and $LaGaO_3$-based SOFCs, CeO_2-based anodes are often selected to boost the electrical performance. However,

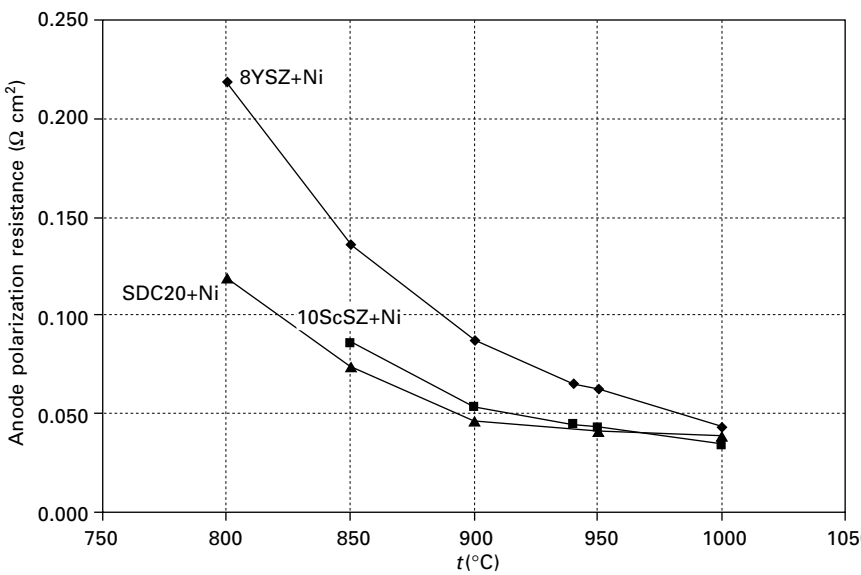

8.23 Comparison of anode polarization resistance of YSZ + Ni, ScSZ + Ni and SDC + Ni as a function of temperature.

in these two cases the thermal expansion mismatch and interfacial cationic diffusion between electrolyte and anode have to be addressed.

Another noticeable advantage for CeO_2-based anodes is the exceptional tolerance to higher sulfur in the fuel stream. This is probably the result of a stronger chemical affinity between CeO_2 and S than Ni and S. Under a typical SOFC operating condition, Ce_2O_2S is thermodynamically stable and constantly keeps S away from Ni, leaving Ni uncovered by S. In an internal study of Siemens SFC, adding CeO_2 into the anode YSZ+Ni could increase S-tolerance from 0.1 ppm to 10 ppm without causing voltage degradation.

8.4 $LaGaO_3$-based solid oxide fuel cells

A recent important development in the field of SOFC research is the discovery of $LaGaO_3$-based solid electrolytes. Based on the fact that it has higher oxide-ion conductivity at lower temperatures and shares the same crystal structure with cathode materials, it is widely anticipated that the $LaGaO_3$-based material can be an excellent choice of electrolyte for a SOFC operating below 800 °C.

8.4.1 $LaGaO_3$-based electrolytes

Oxides with perovskites and related structures have been observed in the past to exhibit moderate oxide-ion conductivity at elevated temperatures. For example, a measurement of oxide-ion conductivity of $Ba_2In_2O_5$ revealed a first-order transition at 930 °C from the brownmillerite to an oxygen-deficient perovskite structure that demonstrated fast oxide-ion conduction in the perovskite cation framework where oxygen vacancies are present and disordered[46,47]. The true perovskite system that shows superior oxide-ion conductivity was first reported by Ishihara *et al.*[48] and Feng and Goodenough[49] in the system of Sr- and Mg-doped $LaGaO_3$ (LSGM). The oxide-ion conductivity of the optimal LSGM composition reaches 0.15 S/cm at 800 °C, a value that could only be achieved for 8YSZ at 1000 °C, and is stable over time and a broad range of P_{O_2} (1–10^{-23} atm). Figure 8.24 compares oxide-ion conductivity of LSGM with all other electrolytes discussed in this chapter, 8YSZ, 10Sc1CeSZ and GDC10[50]. Clearly, LSGM exhibits its superiority over other electrolytes over the plotted temperature range 650–1000 °C.

The phase relationship of Sr- and Mg-doped $LaGaO_3$ system is not simple. Undoped $LaGaO_3$ has an orthorhombic $GdFeO_3$-type crystal structure with a space group of Pbnm and lattice parameters of a = 5.496 Å, b = 5.524 Å, c = 7.787 Å. Upon doping with Sr and Mg on La and Ga sites, respectively, the crystal structure gradually transforms to primitive cubic. Huang *et al.* systematically studied the phase relationship in La-Sr-Ga-Mg–O system[51]. The single cubic phase region identified, as shown in Fig. 8.25, is a fairly

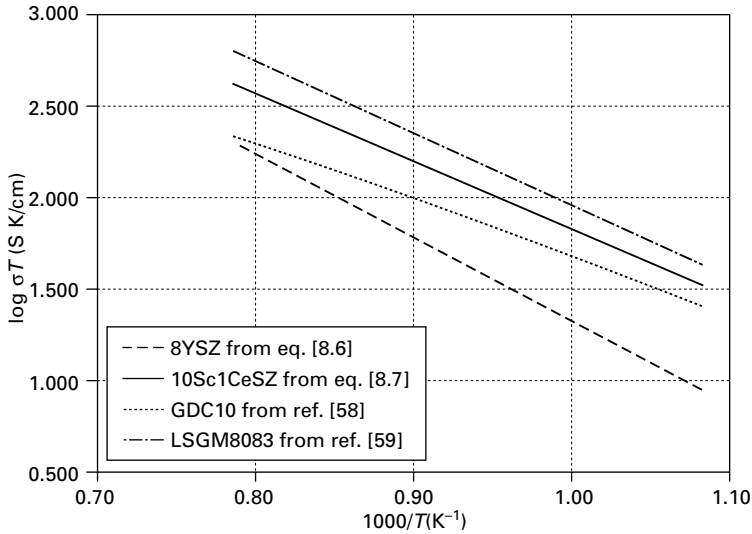

8.24 Arrhenius plot of oxide-ion conductivity measured in air of commonly used solid electrolytes.

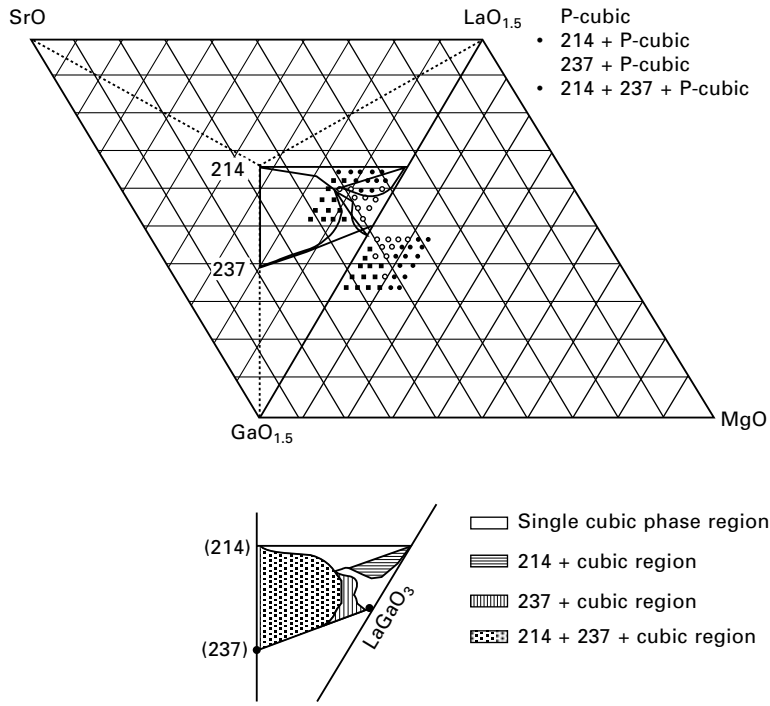

8.25 Phase diagram of La–Sr–Ga–Mg–O system.

narrow region, whose lattice parameter and space group are $a = 3.9103 \pm 0.0007$ Å and Pm3m (221), respectively. The major impurity phases are $LaSrGa_3O_7$ (JCPDS 45-0637, space group P421m (113)) and $LaSrGaO_4$ (JCPDS 24-1208, space group I4/mmm (139)).

The Arrhenius plot of oxide-ion conductivity, as shown in Fig. 8.24, revealed a progressive curvature with temperature. This behavior was explained by Huang *et al.*[51] as a result of a nucleating process for the formation of ordered vacancy clusters between $V_O^{\cdot\cdot}$ and dopant ions Sr'_{La} and Mg'_{Ga}. The proposed model simplified the observed curvature into two straight lines, separated by a characteristic temperature T^*. Below T^*, the $V_O^{\cdot\cdot} - 2Sr'_{La}$ and $V_O^{\cdot\cdot} - 2Mg'_{Ga}$ clusters form to introduce a trapping energy ΔH_t to regular motional enthalpy ΔH_m. Above T^*, all $V_O^{\cdot\cdot} - 2Sr'_{La}$ and $V_O^{\cdot\cdot} - 2Mg'_{Ga}$ clusters dissolve into the oxygen sites and the activation energy resumes to ΔH_m. Based on the proposed model, T^* was experimentally determined to be approximately 600 °C for LSGM electrolyte.

The isothermal oxide-ion conductivity of LSGM was also studied by Huang *et al.*[51] by systematically varying Sr and Mg dopant concentrations. Figure 8.26 shows the contour plot of oxide-ion conductivity at 800 °C. Based on this plot, the optimal composition of single cubic LSGM phase for

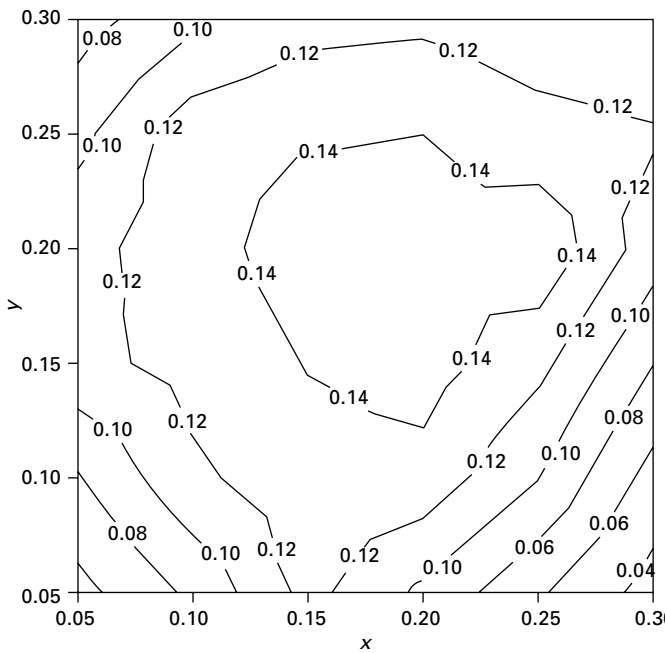

8.26 Isothermal oxide-ion conductivity contour of LSGM electrolyte at 800 °C.

the highest conductivity was found to be $La_{0.80}Sr_{0.20}Ga_{0.83}Mg_{0.17}O_{3-\delta}$, which has an Arrhenius relationship as follows:

$$\ln \sigma_{O^{2-}} T = 14.024 - \frac{0.815(\text{eV})}{kT} (\text{S/cm}) \; t > 600\,^{\circ}\text{C} \qquad 8.42$$

$$\ln \sigma_{O^{2-}} T = 17.569 - \frac{1.076(\text{eV})}{kT} (\text{S/cm}) \; t < 600\,^{\circ}\text{C} \qquad 8.43$$

Although LSGM system exhibits excellent oxide-ion conductivity, one of the concerns is the propensity of Ga being reduced, introducing n-type electronic conduction, via the following defect reaction when it is exposed to reducing atmospheres:

$$O_O^x + 2\,Ga_{Ga}^x \rightarrow \frac{1}{2}O_2 + V_O^{\cdot\cdot} + 2\,Ga'_{Ga} \qquad 8.44$$

Elevating temperature and decreasing P_{O_2} would promote the reaction. It is also possible that loss of Ga_2O_3 in $LaGaO_3$ could occur during high-temperature fabrication of LSGM materials via the following reaction:

$$(Ga_2O_3)_{LSGM} = Ga_2O_{(g)} + O_{2(g)} \qquad 8.45$$

or during operation of a SOFC via the following reaction:

$$2H_{2(g)} + (Ga_2O_3)_{LSGM} = Ga_2O_{(g)} + 2H_2O_{(g)} \qquad 8.46$$

The consequence of Ga-loss is significant, as the single-phase composition would shift into a two-phase region, causing a decrease in oxide-ion conductivity. As a prospective electrolyte, LSGM has to be stable in a reducing atmosphere. Hilpert and co-workers[52,53] systematically studied the vaporization behaviors of two compositions of LSGM, namely, $La_{0.9}Sr_{0.1}Ga_{0.8}Mg_{0.2}O_{3-\delta}$ and $La_{0.85}Sr_{0.15}Ga_{0.85}Mg_{0.15}O_{3-\delta}$, using Knudsen effusion mass spectrometry in the temperature range of 1618–1886 K and in the mixture of H_2–H_2O. They found that the thermodynamic activity of Ga_2O_3 in $La_{0.9}Sr_{0.1}Ga_{0.8}Mg_{0.2}O_{3-\delta}$ is $a(Ga_2O_3) = 2.3 \times 10^{-5}$ for 1073 K. Using available thermodynamic data for reaction [8.45] and known $a(Ga_2O_3)$, the partial pressure of formed Ga_2O(g) as a function of temperature under a typical SOFC operating condition can be calculated out and is shown in Fig. 8.27. Clearly, the vaporization process of Ga is strongly temperature-dependent. For a typical SOFC operating temperature below 1000 °C, the loss of Ga is negligible. However, the loss of Ga cannot be ignored if the processing temperature of LSGM is very high, as in the case of plasma spraying LSGM materials.

The electronic conductivity of LSGM material was also investigated by Kim and Yoo.[54] and Jang and Choi[55] using the Hebb–Wagner blocking electrode method. The levels of both p- and n-type electronic conductivities are generally higher than in ZrO_2-based electrolytes, but lower than in CeO_2-based ones.

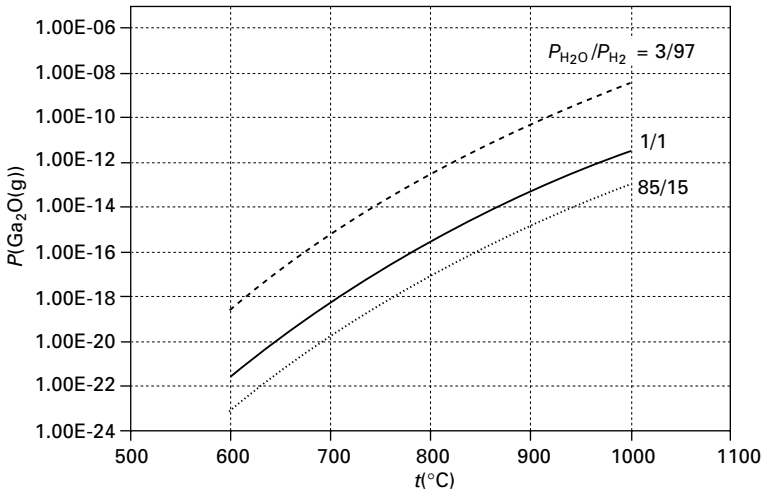

8.27 Plot of partial pressures of $Ga_2O_{(g)}$ as a function of temperature.

Increasing the Sr and Mg doping level decreases both p- and n-type electronic conductivities. The characteristic partial pressures of oxygen for hole- and excess-electron conductions[54] were given, respectively, in Table 8.2. The electrolytic domain constructed from the measured p- and n-type electronic conductivities is shown in Fig. 8.28, where it indicates a negligible electronic conduction under a typical SOFC operating condition.

8.4.2 Cathode materials

The best cathode materials for $LaGaO_3$-based SOFCs resemble those used for CeO_2-based ones, i.e. $LaCoO_3$-based perovskites despite other rare-earth cobalt-containing perovskites were also proven equally capable. The selection of this class of materials is primarily based on the facts that $LaCoO_3$-based perovskites have a good chemical compatibility[56] with $LaGaO_3$-based perovskite electrolyte in addition to their excellent electro-catalytic activity for oxygen reduction as described in the last section. Such a chemical compatibility has also been indirectly confirmed by Ishihara *et al.*[57,58], who purposely substituted a small amount of transition metals such as Fe, Co and Ni into the B-site of $LaGaO_3$ perovskites. It was reported that the oxide-ion conductivity of LSGM could be further enhanced by such a doping although the introduced electronic conduction is a major concern of using these materials for electrolytes. The thermal expansion mismatch between doped $LaCoO_3$ and LSGM is somewhat mitigated by using a thin-film $LaCoO_3$ cathode configuration on a thick LSGM electrolyte support.

Huang *et al.*[59,60] also studied other perovskite cathode materials for $LaGaO_3$-based SOFCs. It was found that $SrCo_{0.8}Fe_{0.2}O_{3-\delta}$ (SCF) exhibited the lowest

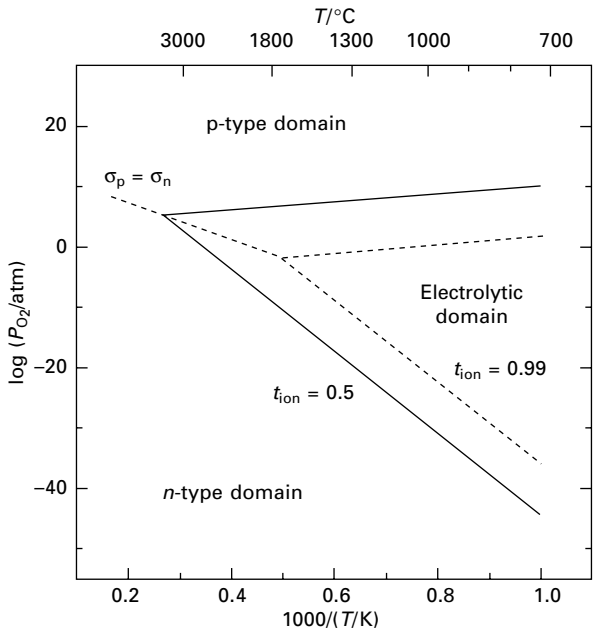

8.28 Constructed electrolytic domain of $La_{0.9}Sr_{0.1}Ga_{0.8}Sr_{0.2}O_{3-\delta}$. Copyright Elsevier.

cathode overpotential, followed by $La_{0.8}Sr_{0.2}Co_{0.8}Ni_{0.2}O_{3-\delta}$ (LSCN), $La_{0.6}Sr_{0.4}CoO_{3-\delta}$ (LSCo), $La_{0.7}Sr_{0.3}Fe_{0.8}Ni_{0.2}O_{3-\delta}$ (LSFN) and $La_{0.85}Sr_{0.15}MnO_{3-\delta}$ (LSM). Clearly, the mixed conductivity of these materials determines largely the catalytic activity of oxygen reduction and therefore the polarization loss. Independent oxygen permeation studies[61,62] also confirmed that SCF has the highest oxygen flux density, suggesting the highest oxide-ion conductivity present in this material.

8.4.3 Anode materials

A logical choice of anode for $LaGaO_3$-based SOFCs is the mixture of LSGM and Ni, an analogy to ZrO_2 + Ni and CeO_2 + Ni for ZrO_2-based and CeO_2-based SOFCs, respectively. However, a single cell test revealed an initially low anode overpotential that quickly degraded with power cycle[63]. Ni coarsening and reactivity of LSGM with Ni mechanisms were speculated to be the causes of the degradation. The post-test microstructural study[63] seemed to support the latter mechanism, considering that LSGM would react with NiO to form $LaNiO_3$ and La_2NiO_4 during the anode fabrication process. To solve this instability problem, the LSGM + Ni composite was replaced by CeO_2+Ni, which has been proven an excellent anode material owing to the

exceptional mixed conduction of CeO_2 in reducing atmospheres. Although such a change considerably improved the stability of $LaGaO_3$-based SOFCs, the fundamental reaction between LSGM and Ni at the anode/electrolyte interface remains active. To avoid the direct contact between LSGM and Ni, a buffer layer comprising only doped CeO_2 was proposed to place in between LSGM and the anode. As a result, the electrical performance was increased by a factor of two[64]. The use of a Ni-free buffer layer prevents LSGM from reacting with Ni, but the reaction between LSGM and CeO_2 still exists. This was evidently demonstrated by the work of Hrovat *et al.*[65], in which La_2O_3 in LSGM was found to diffuse easily into CeO_2, forming $Ce_{1-x}La_xO_{2-\delta}$ solid solution at 1300 °C, precipitating out the high-resistive phase $LaSrGa_3O_7$ in the LSGM matrix. Since the CeO_2-based anode of LSGM-based SOFCs is typically fabricated at 1300–1350 °C, the above reaction could well occur and form a resistive layer at the anode/electrolyte interface prior to the test. To best utilize the concept of buffer layer while preventing the reaction between LSGM and CeO_2, a modified composition of the buffer layer was proposed to counterattack the La diffusion, i.e. use of $La_{0.4}Ce_{0.6}O_{2-\delta}$ to replace commonly used $Sm_{0.2}Ce_{0.8}O_{2-\delta}$ as the buffer layer[66]. The equality in chemical activity of La in the buffer layer and in LSGM stops the La-diffusion, which therefore avoids the formation of $LaSrGa_3O_7$. As a result, both the power density and the long-term stability of the cell have been significantly improved[66].

8.5 Interconnects and cell-to-cell connectors

Interconnect in an SOFC serves as an electrical connector between two adjacent cells and a separator of cathode and anode gases. Therefore, the interconnect must be (1) a good electronic conductor and oxide-ion insulator; (2) chemically stable in both oxidizing and reducing atmospheres; (3) thermally matched to the neighboring cathode and anode and (4) physically gas tight. These combined requirements eliminate all but few metals such as Cr_2O_3 forming high-temperature alloys and ceramics such as alkaline-earth doped $LaCrO_3$. At an earlier stage of SOFC development, the high operating temperature (~1000 °C) restricts the use of metals as interconnects. The only suitable material for high-temperature SOFCs was alkaline-earth doped $LaCrO_3$ or other Cr-containing perovskites. After the emergence of high-performance anode-supported SOFCs, the operating temperature of a SOFC was significantly lowered to the range where cost-effective, commercially available high-temperature metallic alloys are suitable for use.

Metallic interconnects are generally preferable over ceramic $LaCrO_3$-based ones in many aspects. First, metallic interconnects are truly electronic conductors and oxide-ion insulators whereas ceramic ones are mixed electronic and oxide-ion conductors, particularly at lower P_{O_2} and high temperatures where oxygen vacancies are available. Second, metallic interconnects are

more cost-effective and easy to fabricate than ceramic ones. Third, metallic interconnects are mechanically strong, durable, easily machineable, and more importantly, dimensionally stable in both oxidizing and reducing atmospheres. Fourth, metallic interconnects conduct heat much more efficiently. This is particularly important for thermal management in the modern planar SOFC design where a metallic interconnect is typically used as the mechanical support of a thin assembly of cathode/electrolyte/anode and distributor of cathode and anode gases. The heat generated from fuel oxidation must be easily removed by air or endothermic internal steam reforming reaction. In contrast, ceramic interconnects are relatively weaker in mechanical strength, dimensionally unstable due to loss of oxygen at low P_{O_2} and conduct heat slowly. Nonetheless, ceramic interconnects are still in use for high-temperature cathode-supported SOFCs by Siemens SFC for the reason that they do not form high-resistance oxide-scale as do the metallic interconnects and they give a very low contact resistance to the current collector, typically Ni felt, with the aid of a plated Ni film as a contact layer. It turns out to be one of the major advantages of ceramic interconnects over metallic interconnects whose contact resistance is usually high due to insufficient contact area and formation of low-conductivity oxide scale.

In this section, we will review properties of both $LaCrO_3$-based ceramics and promising metallic interconnects. The influence of cell design on the selection of current collector in SOFC stacks will also be discussed.

8.5.1 $LaCrO_3$-based ceramic interconnects

Undoped $LaCrO_3$ has an orthorhombic $GdFeO_3$-type crystal structure with a Pbnm space group and lattice parameters a = 5.477 Å, b = 5.514 Å, c = 7.755 Å. Pure $LaCrO_3$ is a poor electronic conductor and therefore has little practical use in SOFCs. Substituting alkaline-earth metals into the La-site considerably increases the electrical conductivity as a result of increased concentration of electron holes by the doping reaction:

$$2\,MO \xrightarrow{LaCrO_3} 2\,M'_{La} + 2\,O_o^x + V_O^{\cdot\cdot} \qquad 8.47$$

$$\frac{1}{2}O_2 + V_O^{\cdot\cdot} + 2\,Cr_{Cr}^x = O_o^x + 2\,Cr_{Cr}^{\cdot} \qquad 8.48$$

Figure 8.29 shows the Arrhenius plot of electrical conductivity of the $La_{1-x}Ca_xCrO_{3-\delta}$ system measured in air[67]. As is evident, the electrical conductivity increases with Ca-doping level as predicted by eqs. [8.47] and [8.48]. The p-type small-polaron hopping conduction mechanism is further supported by Fig. 8.30, in which the electrical conductivity σ is shown to decrease with P_{O_2} at a given temperature and a given composition. Such a behavior can be empirically expressed by

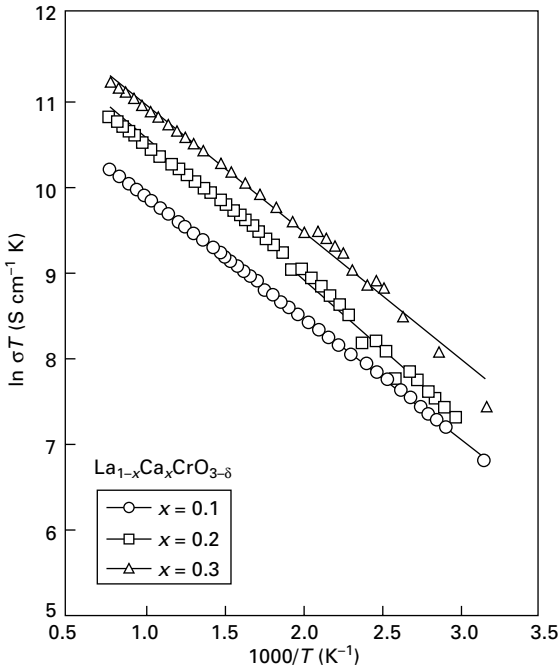

8.29 Temperature dependence of electrical conductivity of $La_{1-x}Ca_xCrO_3$ with x = 0.1, 0.2 and 0.3 measured in air. Reproduced by permission of The Electrochemical Society.

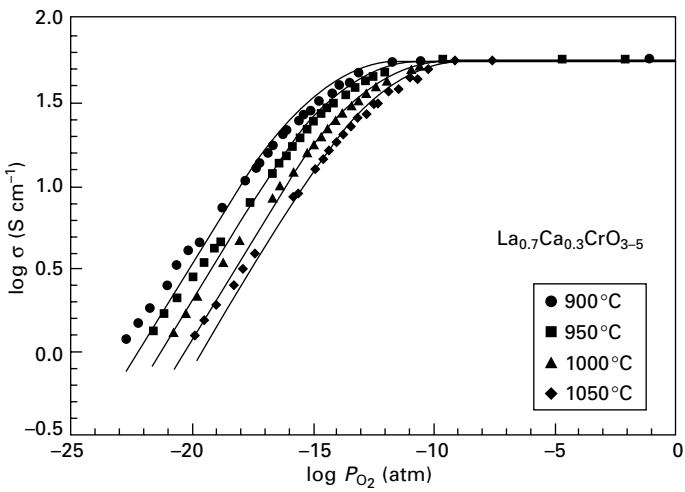

8.30 P_{O_2} dependence of electrical conductivity of $La_{0.7}Ca_{0.3}CrO_{3-\delta}$ at different temperatures. Reproduced by permission of The Electrochemical Society.

$$\sigma = \frac{1}{k_1 + k_2 P_{O_2}^{k_3}} \qquad 8.49$$

where k_1, k_2 and k_3 are composition and temperature-dependent constants, which can be determined by a non-linear least-squares fitting program of σ-P_{O_2} data points. Based on the defect model described by eq. [8.48], the oxygen nonstoichiometry $3-\delta$ as a function of P_{O_2} for a given composition $La_{0.7}Ca_{0.3}CrO_{3-\delta}$ was calculated out and is shown in Fig. 8.31. A moderate change in $3-\delta$ occurs only in the P_{O_2} range of 10^{-20}–10^{-10} atm, beyond which $3-\delta$ tends to be invariant with P_{O_2}.

One of the drawbacks resulting from oxygen nonstoichiometry in $LaCrO_3$-based materials is the emergence of mixed electronic and oxide-ion conduction. As an interconnect material, this property is highly unwanted as the mixed conductivity would lead to leaked oxygen flux, by which excessive fuels could be utilized without generating useful external electrical current. Lowered fuel efficiency is a direct consequence of mixed-conduction in interconnect and electrolyte of a SOFC. Yasuda *et al.*[68] simulated the leakage oxygen flux under various SOFC operating conditions using classical transport theory and basic parameters obtained from conductivity and diffusivity measurements. Figure 8.32 shows the calculated P_{O_2} profiles across $La_{0.7}Ca_{0.3}CrO_{3-\delta}$ under SOFC-mode ($r = -1/2$), OCV-mode ($r = 0$) and electrolyzer-mode ($r = -16$). Clearly, the overall P_{O_2}-profile is dominated by the low-P_{O_2} regime, which implies that the effective ohmic resistance of a ceramic interconnect is dictated by P_{O_2} at the fuel-side. With a P_{O_2}-profile available, the ionic leakage current density $J_{O^{2-}}$ was calculated out as a function of total load current

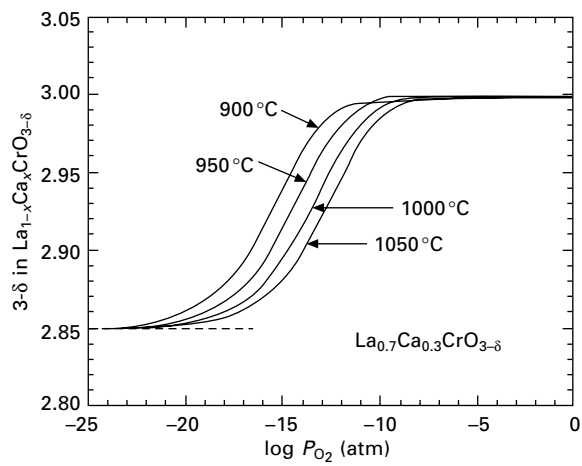

8.31 Simulated oxygen nonstoichiometry of $La_{0.7}Ca_{0.3}CrO_{3-\delta}$ as a function of P_{O_2}.

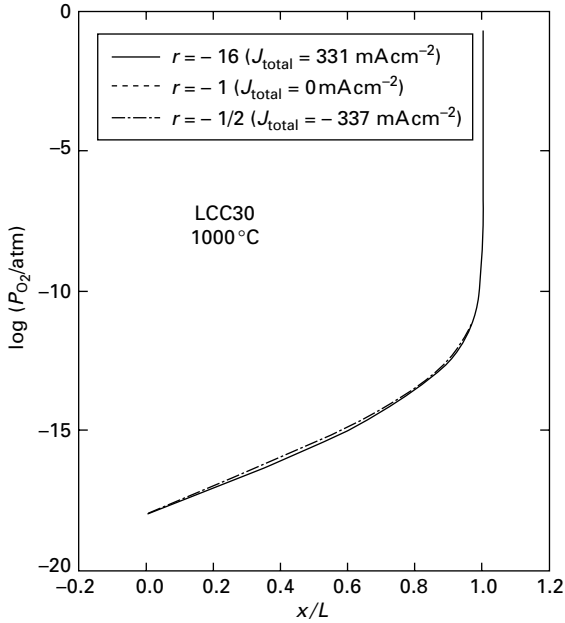

8.32 P_{O_2} -profile across $La_{0.7}Ca_{0.3}CrO_{3-\delta}$ under various operating conditions. Air P_{O_2} = 0.21 atm, fuel P_{O_2} = 10^{-18} atm. Reproduced by permission of The Electrochemical Society.

density J_{total} and is shown in Fig. 8.33. Similar to Fig. 8.15, $J_{O^{2-}}$ decreases with J_{total} in the SOFC-mode ($J_{total} < 0$). However, it is clear that the magnitude of $J_{O^{2-}}$ is unacceptable for use in a SOFC, even at 900 °C. In practice, the actual chemical composition has to be formulated to suppress the mixed conduction.

Another problem arising from P_{O_2} -dependent oxygen stoichiometry is the variations of thermal expansion coefficient with P_{O_2}. This is explicable in that loss of oxygen creates oxygen vacancies accompanied by reduction of Cr^{4+} ($Cr_{Cr}^{\cdot}$) to larger Cr^{3+} (Cr_{Cr}^{x}), allowing the lattice to expand. This behavior is clearly shown in Fig. 8.34, where the dimensional change of $La_{0.79}Sr_{0.20}CrO_{3-\delta}$ increases with decreasing P_{O_2}. The differential thermal expansion imposed on both sides of an interconnect leads to a non-uniform strain distribution within the material, resulting in warping and even cracking. The early development of ceramic interconnect-supported monolithic SOFCs was thus significantly limited. This problem is, however, avoided by depositing a thin-film of interconnect on a substantially greater cathode support in the Siemens' design.

One of the fabrication-related issues with $LaCrO_3$-based materials is the difficulty of being sintered into dense ceramics. This is due to the refractory nature of $LaCrO_3$-based materials. To overcome this problem, excess Ca or

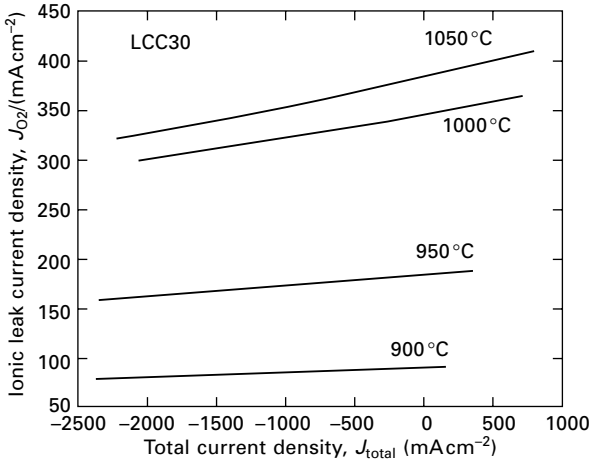

8.33 Variations of ionic leak current density with total load current of a 3 mm-thick $La_{0.7}Ca_{0.3}CrO_{3-\delta}$ Air P_{O_2} = 0.21 atm, fuel P_{O_2} = 10^{-18} atm. Reproduced by permission of The Electrochemical Society.

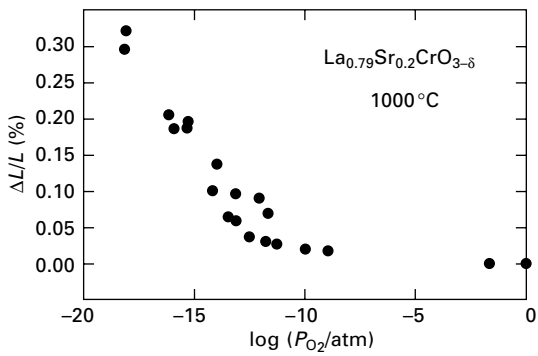

8.34 Isothermal lattice expansion of $La_{0.79}Sr_{0.20}CrO_{3-\delta}$ with P_{O_2}.

deficient Cr in Ca-doped $LaCrO_3$ perovskites was introduced[67,70]. Small excess in Ca level, for example, 0.01, considerably lowers the sintering temperature required to achieve dense ceramics[71]. The sintering mechanism for Ca-level $x > 0.25$ is explained primarily due to the formation of transient liquid phase $CaCrO_4$, which causes an initial rapid sintering shrinkage.

Unlike metallic interconnects, $LaCrO_3$-based materials are much more stable with regard to Cr vaporization under SOFC operating condition[72]. However, fabrication of $LaCrO_3$-based interconnects at elevated temperature needs to consider the loss of Cr. Plasma-sprayed $LaCrO_3$-interconnect in Siemens' cathode-supported SOFCs is a good example.

8.5.2 Metallic interconnects

The resistance to high-temperature oxidation is an essential requirement for metallic interconnects used in planar SOFCs. This requirement limits the potential candidates to high-temperature superalloys and stainless steels that form either Cr_2O_3 or Al_2O_3 scale on the surface of the base metals. The oxidation kinetics in terms of grown scale thickness x is governed by Wagner's equation of oxidation that assumes dominant bulk diffusion:

$$x^2 = k_p t = \frac{k_g}{(y_O \rho)^2} t = \frac{t}{(y_O \rho)^2} k_g^o \exp\left(-\frac{E_{ox}}{kT}\right) \qquad 8.50$$

where k_p and k_g are the parabolic rate constants expressed in thickness and mass terms, respectively; y_O is the weight fraction of oxygen in the oxide (y_O = 48/152 for Cr_2O_3); ρ is the density of the oxide scale (ρ = 5.225 g/cm^3 for Cr_2O_3); k_g^o and E_{ox} are the pre-exponential term and activation energy of the oxidation process, respectively; k is Boltzmann's constant and T is the temperature in K. In practice, k_g is often used to describe the oxidation behavior of an alloy due to the fact that k_g is the first-hand experimental data and there is no need to know the exact chemical composition of formed scale in order to convert to k_p. Table 8.3 compares the parabolic rate constants of several popular commercial Ni-based and Fe-based alloys at 800 °C and compositions of the formed scales.

To achieve an acceptable resistance to oxidation under a service temperature of 700–850 °C, a minimum of 17 wt% Cr is necessary for any metallic interconnect to be used in planar SOFCs. Higher Cr content is certainly helpful to increase oxidation resistance and lower the TEC, but it elevates the material/fabrication costs and more importantly promotes Cr volatility, which would create excessive spallation and jeopardize the long-term stability of cell performance by Cr-poisoning. The latter will be discussed in detail in

Table 8.3 Parabolic rate constants of several commercial Ni-based and Fe-based alloys at 800 °C and scale compositions

Alloys	Rate constant k_g, $\times 10^{-14}$ g^{2}cm^{-4}s^{-1}	Phase composition in the scale	TEC, $\times 10^{-6}$/K	Reference
Crofer22 APU	7.96	Cr_2O_3, $(Mn, Cr)_3O_4$	12.2 (RT–760°C)	73
E-Brite	3.53	Cr_2O_3	11.8 (RT–500 °C)	74, 75
AISI446	13.32	Cr_2O_3, $(Mn, Cr)_3O_4$	~10.9 (20–300 °C)	74
Haynes 230	3.61	Cr_2O_3, $(Mn, Cr, Ni)_3O_4$	15.2 (RT–800 °C)	74
Cr5FeY_2O_3	~0.1	Cr_2O_3	11.8 (RT–1000 °C)	76
ZMG232	k_p = 6.2 $\times 10^{-6}$ μm^2/s	Cr_2O_3, $(Mn, Cr, Fe)_3O_4$, SiO_2	12.5 (30–1000 °C)	77–79

the following paragraphs. Therefore, the upper limit of Cr for the choice of modern metallic interconnects is set to be around 22 wt%.

On the other hand, factors other than high-temperature oxidation resistance also have to be seriously considered for selecting a reliable metallic interconnect. One of them is the area specific electrical resistance, ASR, of the formed oxide-scale, which is directly related to the scale thickness and conductivity by

$$(\mathrm{ASR})^2 = \frac{k_\mathrm{p}}{\sigma^2} \times t = \left[\frac{k_\mathrm{p}^\mathrm{o}}{\sigma_\mathrm{o}^2} \exp\left(\frac{-E_\mathrm{ox} + 2E_\mathrm{el}}{kT} \right) \right] \times t \qquad 8.51$$

where σ_o and E_el are the pre-exponential term and activation energy of electrical conduction in the scale, respectively. The methodology of measuring σ of a thermally grown oxide-scale has been described in detail by Huang *et al.*[75] For a given scale thickness (a fixed oxidation kinetics), lower conductivity of the scale would obviously contribute to higher resistance and therefore higher voltage loss under load. This mandate eliminates the use of Al_2O_3-forming alloys but allows Cr_2O_3-forming alloys for interconnect application. The fact that the electrical conductivity, for example at 900 °C, of Al_2O_3 is 10^{-6} to 10^{-8} S/cm as compared to 10^{-2} to 10^{-1} S/cm for Cr_2O_3 strongly supports the selection of Cr_2O_3-forming alloys[80].

Another factor for selecting adequate metallic interconnects is the thermal expansion coefficient. A typical range of TEC in an electrode/electrolyte assembly varies from 10.5 to 12.5 $\times 10^{-6}$/K. To match this TEC, Cr-based alloys (11.0–12.5 $\times 10^{-6}$/K) and ferritic stainless steels (11.5–14.0 $\times 10^{-6}$/K) are the best candidates. A good example of Cr-based alloys is given by Ducrolloy (Cr–5wt%Fe–1wt%Y_2O_3), which was developed earlier by Plansee GmbH (Tirol Austria) in collaboration with Siemens AG for high-temperature SOFCs (900–1000 °C). It has an excellent TEC match to the electrode/electrolyte assembly. However, the biggest problem associated with high-Cr alloys is the Cr mobility at the service temperature. The volatile Cr species in the high-valence state formed under SOFC condition were identified by Hilpert *et al.*[81] to be $CrO_2(OH)_{2(g)}$ and $CrO_{3(g)}$ in air with and without moisture, respectively. Figure 8.35 shows the calculated partial pressures of Cr-species at 950 °C as a function of partial pressure of H_2O. These gaseous Cr-containing species can be entrained in the air stream and transported to the cathode/electrolyte interface where they are reduced to solid Cr_2O_3 (or further react with Mn in the LSM cathode to form $MnCr_2O_4$[82] and with Sr in the LSCF cathode to form $SrCrO_4$[83,84]) by the following cathodic reactions:

$$\mathrm{CrO_{3(g)}} + \frac{3}{2}\mathrm{V_O^{\cdot\cdot}} + 3\mathrm{e'} \rightarrow \frac{1}{2}\mathrm{Cr_2O_{3(s)}} + \frac{3}{2}\mathrm{O_o^x} \qquad 8.52$$

$$\mathrm{CrO_2(OH)_{2(g)}} + \frac{3}{2}\mathrm{V_O^{\cdot\cdot}} + 3\mathrm{e'} \rightarrow \frac{1}{2}\mathrm{Cr_2O_{3(s)}} + \mathrm{H_2O_{(g)}}\ \frac{3}{2}\mathrm{O_o^x} \qquad 8.53$$

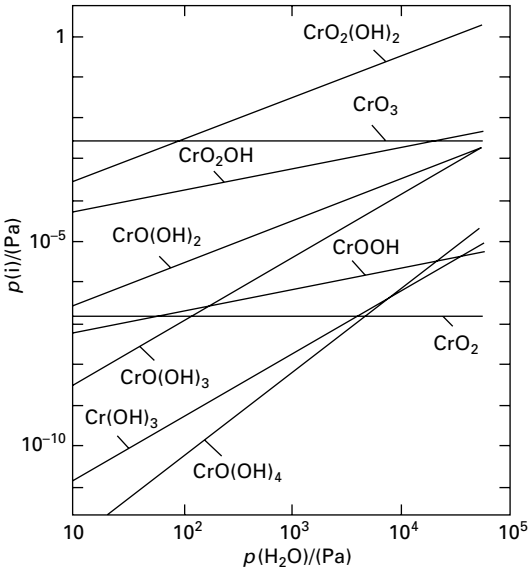

8.35 Partial pressures of Cr-species at 950 °C as a function of partial pressure of H_2O. Reproduced by permission of The Electrochemical Society.

The deposition of catalytically inactive Cr_2O_3 at the reactive TPB sites blocks the process of oxygen-reduction, leading to performance degradation. Based on the fact that Cr-based alloys are difficult and costly to fabricate and promote Cr migration, ferritic stainless steels appear to have been left as the only suitable metals to fulfill all requirements for interconnect to be used in planar SOFCs.

After this realization, development of ferritic stainless steels has accelerated in recent years to formulate sweet compositions that address various issues associated with applications in SOFCs. One of the issues with ferritic steels is the adhesion of the scale to the metal substrate. This is often observed by spallation of the scale upon oxidation cycles as growth stresses are created and released. The consequence of the spallation is serious in a sense that the growth of the scale and re-growth after spallation leads to depletion of the scale-forming element such as Cr in the metal. If the concentration of the element decreases to below a critical level, the protective scale can no longer form and rapid oxidation of the base metal such as Fe occurs, leading to a large oxygen uptake. To mitigate the spallation, surface treatment or alloying by reactive elements (RE) is often used[85–87]. To understand the scale growth mechanism, the role of the RE on metal oxidation needs to be elucidated. The common mechanism of Cr_2O_3 scale growth is assumed to be predominantly controlled by outward Cr diffusion along grain boundaries in the Cr_2O_3 scale. According to the dynamic-segregation theory[88], the presence of RE on

the surface of an alloy inhibits the normal outward short-circuit transport of cations along grain boundaries of the scale because these large RE ions diffuse more slowly than the native ion such as Cr. The inhibition of the outward transport of cations results in a reduction in the parabolic oxidation rate constants. Owing to the larger ratio of cation and anion diffusivity in Cr_2O_3, the RE has a much greater effect on parabolic rate constant in Cr_2O_3 than in Al_2O_3. The reduction can be as high as 10–100 times. Another effective way to tackle the spallation problem and reduce parabolic rate constant is to incorporate Mn into the parent steel composition[78,89]. Two examples are Crofer22 APU and ZMG232. The former was invented by Forschungzentrum Julich and manufactured by Thyssen-Krupp VDM while the latter was developed by Hitachi Metals, Inc. The presence of a limited amount of Mn (~0.50 wt%) in the Cr-containing base metal enhances oxide scale conductivity[90] and decreases Cr volatility by preferentially forming a dense and conductive spinel $MnCr_2O_4$ top layer and Cr_2O_3-rich underlayer. The confinement of Cr mobility by the dense scale would undoubtedly improve the stability of the cell performance. Table 8.4 lists the chemical compositions of several commercially available ferritic stainless steels that are widely studied for SOFC interconnects. In addition to elevated Mn-level in Crofer22 APU and ZMG232 steels, RE species such as La and Zr have also been added to improve the scale adhesion.

Although those carefully formulated Fe-Cr-Mn ferritic steels form a dense spinel scale that serves as a barrier to outward Cr and inward O diffusion and gas-phase Cr migration, the contact resistance between the scale and electrodes remain relatively high due to insufficient contact areas. In order to minimize the contact resistance, various electronically conductive oxide coatings have been tried. These oxide coatings include Sr-doped $LaMnO_3$, $LaFeO_3$, $LaCrO_3$ and $LaCoO_3$. The results are sometimes conflicting with regard to the effectiveness of the coating in improving the contact resistance and stability of cell performance[91,92]. Different application techniques of the coatings used by different researchers are probably the reason for variability. However, one fundamental requirement for the contact layer is the electronic conduction. Any involvement of oxide-ion conduction in the layer would transport oxygen in the form of O^{2-} to the surface of the underlying metal, resulting in accelerated oxidation kinetics. For this reason, doped $LaMnO_3$ may be preferable over

Table 8.4 Chemical compositions of commercially available ferritic stainless steels

Alloys	Fe	Cr	Mn	Si	C	Ti	P	S	Al	Ni	Zr	La
Crofer22 APU	Bal	22.8	0.45	–	0.005	0.08	0.016	0.002	–	–	–	0.06
ZMG232	Bal	21.97	0.50	0.40	0.02	–	–	–	0.21	0.26	0.22	0.04
E-Brite	Bal	26.0	0.01	0.025	0.001	–	0.02	0.02	–	0.09	–	–
AISI446	Bal	25.0	1.50	1.00	0.020	–	0.04	0.03	–	–	–	–

doped $LaCoO_3$ as a contact layer between cathode and interconnect. Analogous to $(Mn, Cr)_3O_4$ spinel, the spinel $(Mn, Co)_3O_4$ was also studied as a potential protective and contact layer for ferritic stainless steel interconnects. The results showed that the thermally grown, higher electronic conductivity $Mn_{1.5}Co_{1.5}O_4$ spinel effectively provided a barrier to Cr outward diffusion, leading to a reduced Cr mobility and therefore a decreased contact ASR[93].

For modern planar SOFC designs, a metallic interconnect provides a sealing platform for separating cathode and anode gas streams. As a result, the interaction between the sealing materials and metallic interconnects could have a direct impact on the stability of gas tightness over thousands of hours of operation. For example, a study showed that stainless steel AISI446 reacts readily with barium–calcium–aluminosilicate-based glass-ceramics under a typical service temperature of 750 °C[94]. When oxygen is available, the reaction product tends to be $BaCrO_4$ whereas under reducing atmosphere the reaction forms a chromium-rich solid solution by dissolving Cr_2O_3 into the glass. When designing the metallic interconnect and glass ceramics, the interaction between the two should not be ignored.

8.5.3 Cell-to-cell connectors

For a planar SOFC design, the cell-to-cell connector is the interconnect itself, which has been discussed in detail in the last section. A brief review of the cell-to-cell connectors given in this section focuses primarily on cathode-supported seal-less tubular SOFC design.

It is important to realize that the current-collection scheme for cathode-supported seal-less tubular SOFCs is advantageous over anode-supported seal-less tubular ones. This is because the cathode-supported configuration allows for current collection to take place in the fuel environment where metals like Ni and Cu are available for use. Figure 8.36 gives an example of such a current-collection scheme in a Siemens tubular SOFC bundle. In contrast, current collection in oxidizing atmospheres for an anode-supported configuration requires expensive precious metals such as Pt and Ag to survive the oxidizing atmosphere; the latter is also rather mobile during SOFC operation.

8.6 Fabrication techniques

The fabrication technique for each functional layer in a SOFC largely depends on practical SOFC designs. The selection criteria consider cost effectiveness, viability for mass production and automation, processing repeatability and precision. In this section, fabrication techniques commonly used in the SOFC industry for making thick-substrate and thin-films are reviewed.

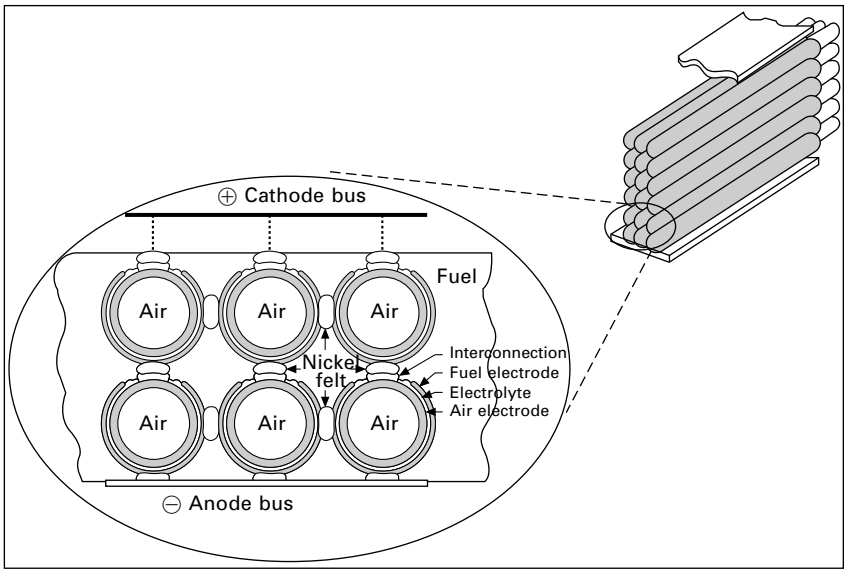

8.36 Current-collection schemes in Siemens' cathode-supported tubular SOFC bundles.

8.6.1 Substrate

A substrate in a SOFC is a mechanical support on which subsequent functional thin layers can be deposited. Therefore, it must be mechanically strong, chemically stable and thermally matched to other layers. The substrate can be electrolyte, cathode, anode or interconnect, leading to the concepts of electrolyte-, cathode-, anode- and interconnect-supported SOFC designs. Depending on the type of substrate, it can be either dense or porous.

The electrode-supported, thin-film electrolyte SOFC is the most popular design in modern SOFC technology. This is mainly because electrolyte conductivity is the lowest among SOFC functional layers, and reducing its thickness is the most effective way of minimizing the ohmic resistance. The cathode substrate was first used by Westinghouse (now Siemens) in a form of cylindrical tube to support films of electrolyte, anode and interconnect. The tubular substrate is typically fabricated by extruding a ceramic paste through a mold to a desirable diameter (inner and outer) and length. The paste is a mixture of proprietary cathode powder, organic binder and pore former. After appropriate drying, the tube is finally sintered into a porous body with a well-defined microstructure, porosity and most importantly, mechanical strength. Figure 8.37 shows a representative microstructure of such a substrate. Roughly 30–35 vol% of porosity is estimated. To ensure the quality of the substrate, chemical analysis, mechanical strength, thermal

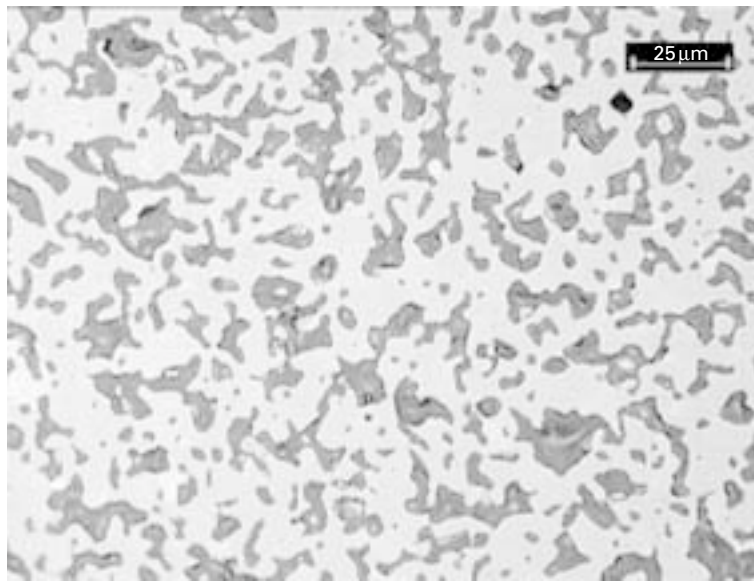

8.37 A typical microstructure of Siemens cathode substrate after sintering.

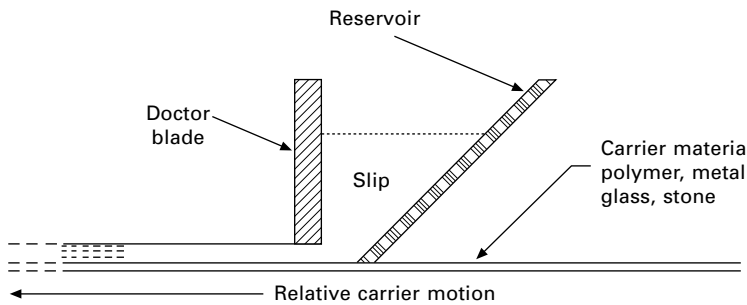

8.38 Schematic of tape-casting process.

expansion coefficient, thermal cycling shrinkage and porosity are closely monitored during batch production.

The concept of an anode-supported SOFC was first proposed by de Souza *et al*. in 1997 and demonstrated with very high electrical performance[95]. Since then, the anode-supported configuration has been widely accepted as a standard design by planar SOFC developers, particularly where low-cost ferritic stainless steel interconnects became available in the reduced temperature range (<800 °C). The commonly used technique for fabricating an anode substrate is the conventional tape-casting, as illustrated schematically in Fig. 8.38, a process well known in many other industries including electroceramics, paper, plastic and paint manufacturing. The major advantage of the tape

casting process is that it is the best way to form large-area, thin, flat ceramic or metallic parts. In a typical tape-casting process, the slip or slurry is poured into a puddle or reservoir behind the doctor blade, the carrier to be cast upon it is set in motion. The doctor blade gap between the blade and the carrier defines the wet thickness of the tape being cast. Other variables that come into play include reservoir depth, speed of carrier movement, viscosity of the slip, and shape of the doctor blade (to name just a few). The wet film of slip passes into a drying chamber of some sort, and the solvents are evaporated from the surface, leaving a dry tape on the carrier surface. The slurry or slip is typically prepared by dispersing the anode material (a mixture of YSZ and NiO) in solvents (e.g. 2-butanone/ethanol), after which binders (e.g. polyvinyl butyral), plasticizer (e.g. polyethylene glycol) and deflocculant/wetting agent (e.g. glycerol trioleate) are added. A typical thickness of substrate that can be comfortably made by tape-casting ranges from 50 to 500 μm. The *in situ* reduction of NiO to Ni ensures the wanted porosity for anode gas diffusion.

A green electrolyte substrate can also be made by the tape-casting method, followed by sintering at high temperature into a dense ceramic. Owing to the requirement to be a mechanical support, a typical thickness of electrolyte ranges from 100 to 200 μm. The assembly of cathode/electrolyte/anode is then laminated with a metallic interconnect channeled for gas distribution.

In recent years, porous metal has also been explored as a possible substrate to support SOFC functional layers[96]. The advantages include low manufacturing cost and improved durability. Moreover, the metal alloy is both thermally and electrically conductive, and it allows for simple sealing strategy. However, one of the major challenges is how to fabricate a dense electrolyte layer without compromising the integrity of the porous metal substrate. To mitigate this problem, vacuum plasma spray technique has been tried to deposit a relatively dense electrolyte layer on the porous metal substrate so that the high-temperature densification step is not needed[97].

8.6.2 Electrolyte thin film

Fabrication of quality electrolyte thin film is the most important step among all functional layers in a SOFC. The requirement for a thin and dense coating challenges the conventional ceramic fabrication techniques. These techniques can be generally classified into three categories: vapor deposition (e.g. EVD and PVD), thermal spray (e.g. atmospheric plasma spray) and slurry coating (e.g. colloidal deposition, slip casting, screen printing, electrophoresis deposition, wet powder spray, and so forth).

The EVD process was first invented in 1977 by Westinghouse Electrical Corporation (now Siemens Power Generation) to produce a thin and dense 8YSZ layer on a porous tubular Ca-doped ZrO_2 and later cathode substrates[98]. The main steps of the process are schematically illustrated in Fig. 8.39. As

the gaseous mixture of $ZrCl_4$ and YCl_3 is fed to the outer surface of the tubular substrate and steam is introduced to the inner surface at elevated temperatures, the chemical reaction first occurs at the locations where they meet, namely pores, by

$$ZrCl_4 + 2H_2O \rightarrow ZrO_2 + 4HCl$$
$$2YCl_3 + 3H_2O \rightarrow Y_2O_3 + 6HCl \qquad 8.54$$

As the gas diffusion process in the substrate is the rate-limiting step, the growth of the initial layer that closes the surface pore is linear with time. As soon as the surface pores are closed, the presence of oxide-ion and electronic conduction in the initially formed 8YSZ at elevated temperature under a gradient of oxygen chemical potential comes into play: an oxygen flux that counterbalances the electronic flux is generated. This process can be best described by the following reactions:

$$ZrCl_4 + 2O^{2-} \rightarrow ZrO_2 + 2Cl_2 + 4e'$$
$$2YCl_3 + 3O^{2-} \rightarrow Y_2O_3 + 3Cl_2 + 6e' \qquad 8.55$$

As a result, a film of 8YSZ continues to grow, whose growth rate k_p is commonly described by the classical parabolic rate Law (Wagner equation) as described in Section 8.5. The thickness L and time t relation can, therefore, be written by

$$L^2 = 2k_p t \qquad 8.56$$

At a typical EVD temperature of 1000–1200 °C, the rate constant for deposition of 8YSZ ranges from 1.1×10^{-5} to $3.8 \times 10^{-3}\,cm^2/s$. Considering both initial linear and subsequent parabolic growth rate, to achieve a 40 μm 8YSZ-film

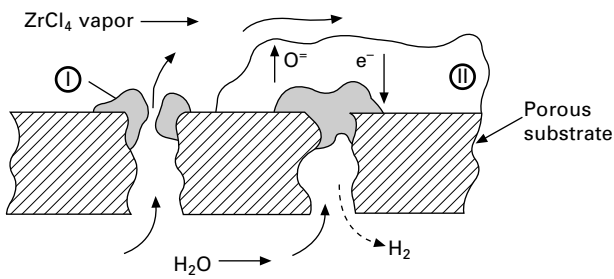

8.39 Illustration of the principle of the EVD process.

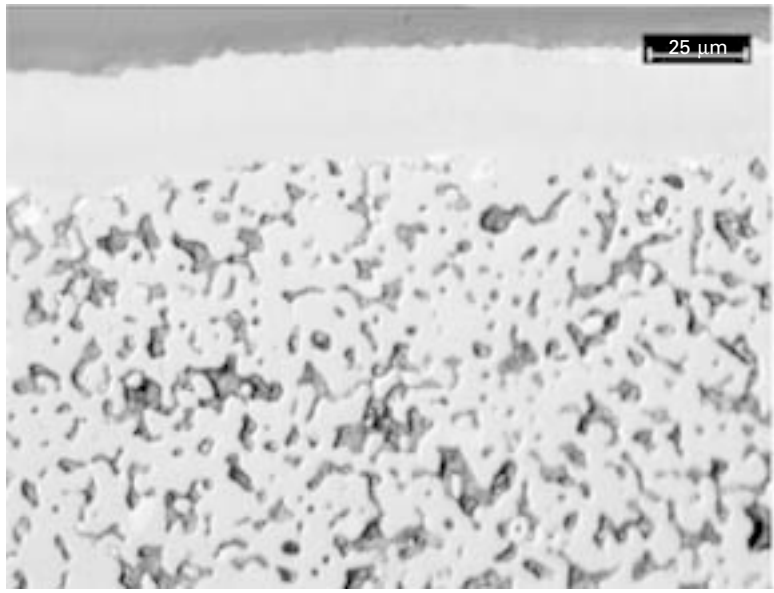

8.40 A typical microstructure of an EVD electrolyte on a porous cathode substrate.

takes approximately 40 minutes at 1000 °C and 20 minutes at 1200 °C. Figure 8.40 shows a representative microstructure of an EVD electrolyte. There is no doubt that the EVD process is capable of producing pinhole-free, thin and dense electrolyte films.

The major drawback of the EVD process in regard to mass production is, however, the high cost associated with labor, materials, waste disposal and maintenance. After successful demonstration of several SOFC generators by Westinghouse/Siemens using cathode-supported EVD electrolyte and anode, this commercially prohibitive technique was later replaced by the more productive and automation-friendly atmospheric plasma spray-coating technique.

The plasma spray process is a proven and mature surface coating technology that is widely used in aerospace and power-generation industries for thermal barrier coating application of gas turbine blades, vanes, combustor cans and turbine shrouds. The coating significantly improves the turbine blade cooling efficiency, prevents hot corrosion and, most importantly, makes the transAtlantic flight possible. The plasma spray process features injecting coating materials (metals, ceramics and polymers) into a high-velocity ionized argon gas stream (plasma). During very short residence time, the material is melted and propelled towards a substrate where it solidifies and builds up a solid coating. By controlling the motion of the plasma source or the substrate in a designated

pattern, the substrate in certain geometry can be completely or partially covered to a desired thickness. Based on the surrounding atmosphere, the plasma spray method can be categorized into conventional atmospheric (APS) and controlled atmospheric plasma spray (CAPS). Application of the APS technique to fabricate electrolyte film on a cathode substrate of a tubular SOFC was first started in the late 1990s by Westinghouse (now Siemens). After extensive parametric studies, the processing conditions were eventually qualified for plasma spraying an 8YSZ layer. Figure 8.41 shows a representative microstructure of plasma-sprayed 8YSZ on a porous cathode substrate. The shown pores are in general found closed. Low-pressure plasma spray (LPPS), one kind of CAPS, was also investigated to deposit an even denser 8YSZ layer[99]. Figure 8.42 shows the microstructure of an LPPS 8YSZ layer. It appears that LPPS is better able than APS to make a denser electrolyte.

Other conventional ceramic fabrication techniques used by worldwide SOFC developers for making electrolyte thin-film include tape-casting, screen-printing, vacuum slip casting, wet powder spraying/slurry coating and dry die-pressing. The thickness of the electrolyte varies, based on the technique, from a few to hundreds of microns. A general review of these manufacturing techniques was given by Tietz *et al.*[100]. Interested readers are recommended to look into it for more information.

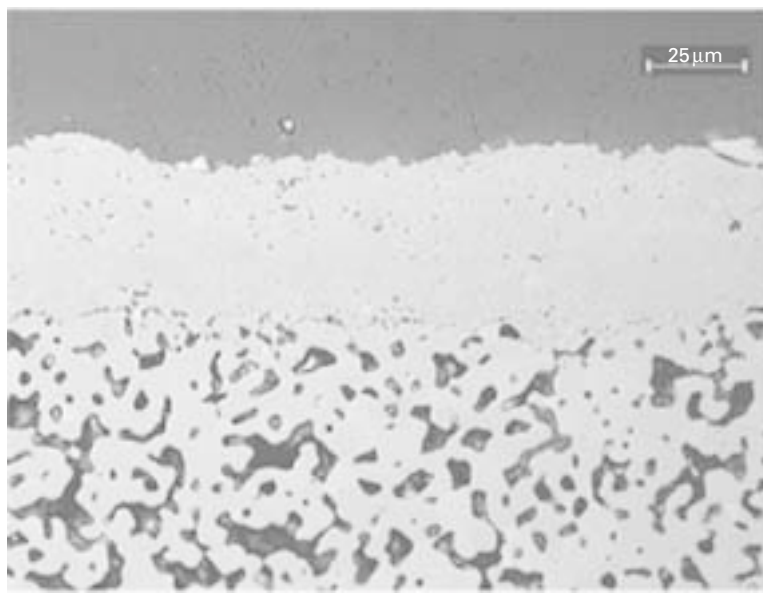

8.41 Microstructure of an APS electrolyte on a porous cathode substrate.

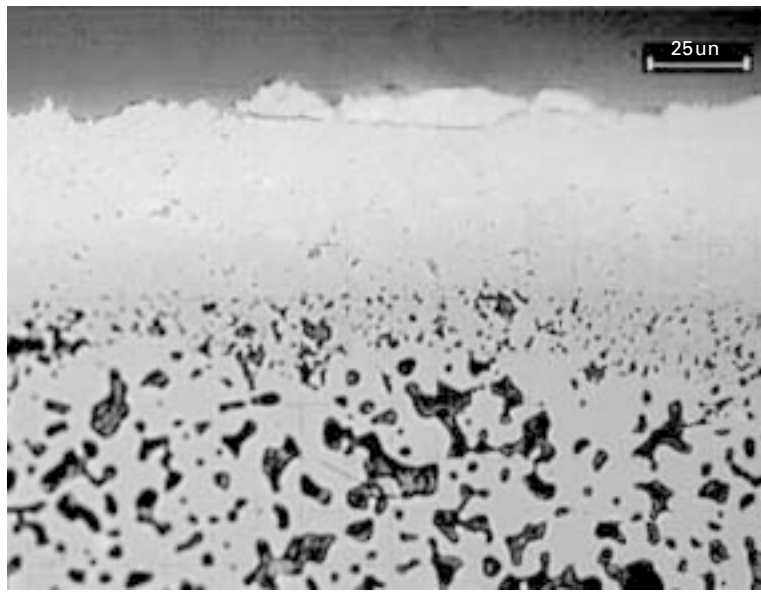

8.42 Microstructure of an LPPS electrolyte with composite cathode interlayer on a porous cathode substrate.

8.6.3 Electrode thin film

Screen-printing is the most popular method adopted by anode-supported SOFC developers for making the cathode layer. It is an attractive technique due to its maturity, automation-ability, and suitability for producing high quality, large-area coatings. It is the standard route to make ceramic capacitors in the electroceramics industry. The formulation of the ink, the printing material, is analogous to that of the tape-casting slip. The ceramic material (e.g. LSM) is first intimately dispersed in the solvent (e.g. terpineol) in the presence of a dispersant (e.g. Hypermer LP1). The binder (e.g. ethylcellolose) and plasticizer (e.g. diocthylphthalate) are then added to achieve the desired viscosity. A typical thickness of a screen-printed cathode film is approximately 20 μm. After preliminary drying, the made film undergoes burnout and calcinations and it finally bonds to the surface of the electrolyte. The solid to organic ratio and the particle size distribution of the cathode material determine mainly the resulting porosity and porosity distribution.

Siemens has demonstrated that the anode layer in a cathode-supported SOFC can be fabricated by the APS route. A powder mixture of metallic Ni, pore former and YSZ is the feedstock. One of the advantages of the APS anode is that no additional sintering step is necessary after APS processing. A representative microstructure of the APS anode is illustrated in Fig. 8.43. The slurry dip-coating method was also used by Toto as a low-cost process to make the anode coating, followed by drying and sintering steps.

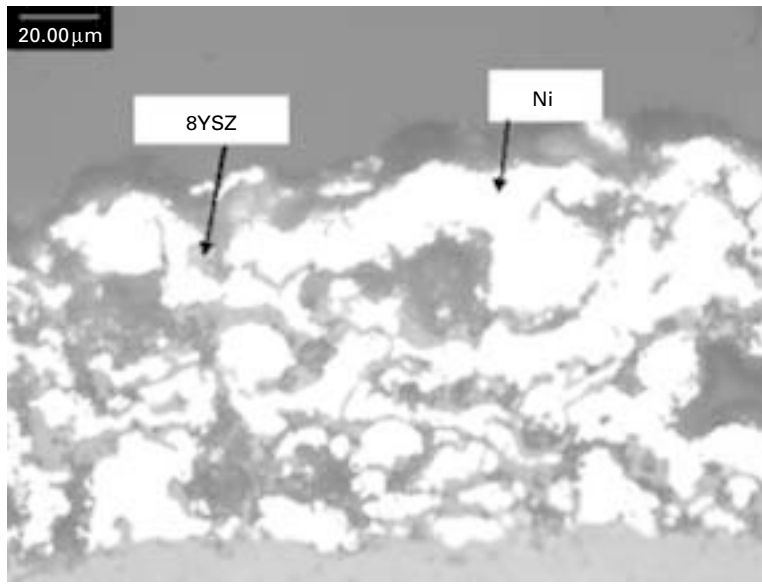

8.43 A representative microstructure of anode made from APS process.

8.6.4 Interconnection thin film and plate

Generally speaking, the ceramic $LaCrO_3$-based interconnect is difficult to sinter because of the vaporization of Cr-O species during the sintering process, which leads to enhancement of the evaporation-condensation mechanism of sintering. This process tends to suppress densification and causes coarsening of the powder[101]. To alleviate the Cr-migration problem, A-site excess or Cr deficiency in $LaCrO_3$ was formulated and found to promote sintering by forming multi-phase chromates that melt incongruently in the range of 1000–1200 °C. This strategy was also adopted by Siemens in designing the compositions of the APS interconnect feedstock. Figure 8.44 shows a representative microstructure of an APS interconnect layer on a porous cathode substrate.

In an earlier development of SOFCs, a ceramic $LaCrO_3$-based interconnect thick plate was considered to be a bipolar gas distributor. This design was quickly abandoned owing to the high manufacturing cost and emergence of anode-supported low-temperature SOFCs. A low-cost, metallic interconnect plate with functionalities of electrical/heat conduction and gas distribution was the obvious selection for anode-supported low-temperature SOFC developers. Figure 8.45 shows some examples of gas manifolding strategies of planar SOFCs with metallic interconnect in different geometries. Clearly, machine-ability of the metals favors these designs.

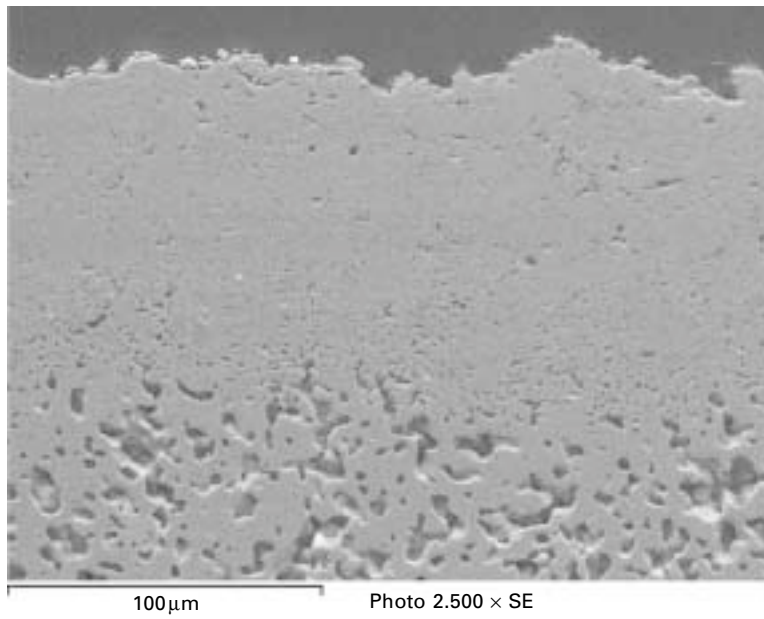

8.44 A representative SEM microstructure of ceramic interconnect on a porous cathode substrate made from APS process.

8.7 Conclusions

More than 100 years has passed since the basic concept of a SOFC was first proposed in the late 19th century. It is a mixed feeling to see today that this simple in principle and efficient in energy conversion device is still under considerable development to become a commercial product. A high product cost that is unable to compete with a conventional heat engine is the major hurdle for commercializing the SOFC technology. As a system, BOP and module contribute to a significant portion of the total cost, which have to be reduced through special design cycles. The cost for cell materials are sometimes tied to the lack of advanced materials and revolutionary fabrication techniques that could lower the cost and maintain performance at the same time.

ZrO_2-based materials are the most studied and mature electrolytes. The relevant fabrication techniques are well developed and in place to mass produce large-volume electrolyte films. Therefore, they are most likely to be the first electrolyte system in the commercial SOFC product operating in the range of 700–1000 °C. Other electrolytes such as LSGM and doped CeO_2 could potentially find application in SOFC generators operating below 800 °C and 600 °C, respectively. Viable fabrication methods are in great demand for making LSGM films on either cathode or anode substrate without compromising the performance. The operating temperature of CeO_2-based

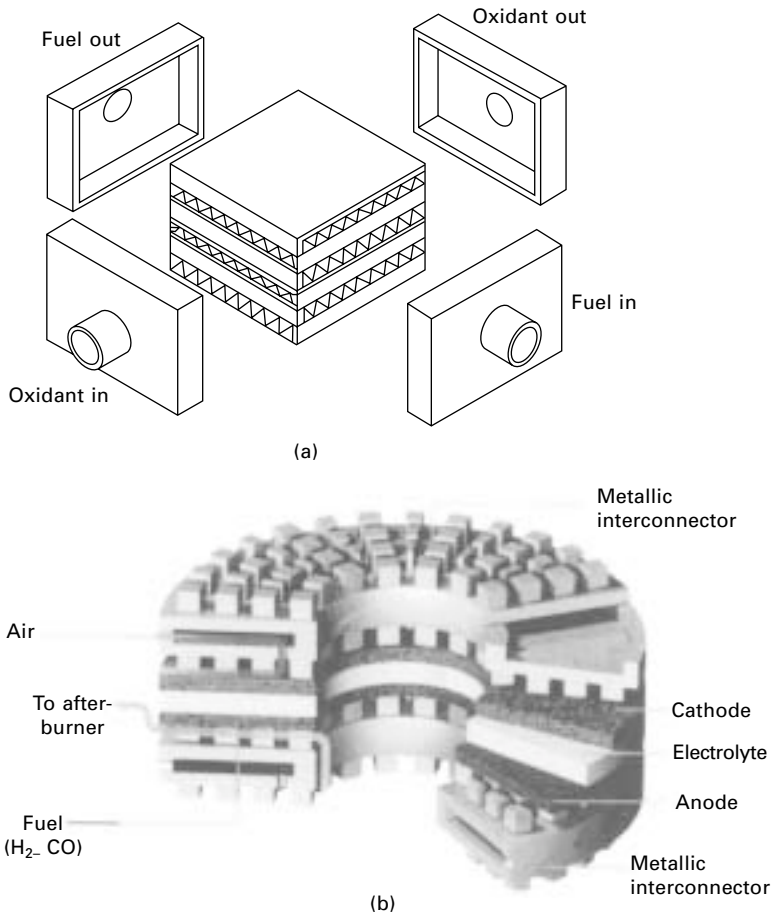

8.45 Examples of external (a) and internal (b) gas manifolds used in planar design.

SOFCs has to be limited to below 600 °C where the electronic conduction can be considerably reduced to a level that is acceptable for attaining sufficiently high electrical efficiency.

As the operating temperature is reduced, the role of cathode performance becomes even more important due to the fact that the activation energy of cathode polarization is generally greater. Therefore, for a low-temperature SOFC (<800 °C), the cathode performance dominates the overall SOFC performance. The development of a high-performing cathode composition is therefore critical. Tremendous efforts have been devoted to this area by researchers worldwide. One challenge facing the SOFC community is the fact that a high catalytic activity cathode is always associated with a high

TEC. To alleviate this contradiction, a composite form of cathode consisting of electrolyte and cathode is always chosen to meet the requirements for thermal expansion match and low polarization loss.

One of the advantages of a SOFC over other competing fuel cells is the fuel flexibility. The type of fuel with which an SOFC is able to operate is largely dependent upon the anode. Direct utilization of hydrocarbons such as natural gas, propane and other liquid fuels without pre-reforming can significantly reduce the system cost and is therefore highly desirable. The conventional Ni-based anode is prone to promoting carbon formation in handling steam-free hydrocarbons although it is an excellent catalyst for the fuel oxidation reaction. Copper has less activity in cracking hydrocarbon fuels than Ni, but it also has less activity in oxidizing fuels. Introduction of CeO_2 into a Cu-containing anode aims at balancing both requirements because CeO_2 has been proven to possess catalytic activity to oxidizing fuels. A ceramics-based anode is also a recent hot topic under active study. A suitable ceramic anode composition has been shown with excellent electronic conductivity, sufficient catalytic activity for fuel oxidation and more importantly, high resistance to carbon formation and sulfur poisoning[102]. The ceramics-based anode, if fully developed, could play a significant role in reducing system cost of the SOFC product.

Ceramic $LaCrO_3$-based interconnects find application in cathode-supported tubular SOFCs as a thin film. It is, however, expensive to use ceramic interconnects in planar design as both electrical conductor and gas distributor. The advantage of a ceramic interconnect is the low Cr volatility given by thermodynamic stability of perovskite materials. As the operating temperature of the anode-supported planar SOFCs is reduced to below 800 °C, low-cost ferritic steels, purpose designed to form dense Mn–Cr spinel scale, have been developed to replace expensive ceramic interconnects. Surface modification/coating with reactive-elements is able to reduce the growth of the scale and improve the adhesion of the scale to the metal base. Two major challenges facing planar SOFC developers using metallic interconnects are Cr mobility and high contact resistance, which are two of the reasons for performance degradation and poorer performance in the stack.

Functional layer fabrication methods depend greatly on the SOFC design and cost effectiveness. Repeatability, quality, productivity and automation-ability have to be considered seriously in selecting and designing a specific fabrication process. Bear in mind that the SOFC product cost includes cell and bundle, module and BOP. In many cases, the cost of module and BOP dominates the total cost, giving more choices for cell making. This could also be a deciding factor for which fabrication technique and materials are used.

Finally, the aim of this chapter is to review the progress in SOFC materials achieved so far. It is hoped that this concise version of review may help, to some extent, advance the development of solid oxide fuel cell technology.

8.8 Acknowledgement

The author is grateful to Professor John B. Goodenough for his invaluable comments and suggestions in the preparation of this chapter.

8.9 References

1. Y. Arachi, S. Sakai, O. Yamamoto, Y. Takeda and N. Imanishi, 'Electrical conductivity of the ZrO_2–Ln_2O_3 (Ln = lanthanides) system', *Solid State Ionics*, 1999 **121** 133–139
2. J. B. Goodenough, 'Oxide-ion electrolytes', *Ann. Rev. Mater. Res.*, 2003 **33** 91–128
3. K. Huang, 'Cell power enhancement via materials selection', *Proc. 7th Eur. SOFC forum*, Lucerne, Switzerland, 2006, P0303–037
4. J. Mizusaki, Y. Yonemura, H. Kamata, K. Ohyama, N. Mori, H. Takai, H. Tagawa, M. Dokia, K. Naraya, T. Sasamoto, H. Inaba and T. Hashimoto, 'Electrical conductivity, Seebeck coefficient, defect and electronic structure of nonstoichiometric $La_{1-x}Sr_xMnO_\delta$', *Solid State Ionics*, 2000 **132** 167–180
5. M. Mori, Y. Hiei, N. Sammes and G. A. Tompsett, 'Thermal expansion behaviors and mechanisms for Ca- and Sr-doped lanthanum manganite perovskites under oxidizing atmospheres', *J. Electrochem. Soc.*, 2000 **147** (4) 1295–1302
6. S. B. Adler, 'Chemical expansivity of electrochemical ceramics', *J. Am. Ceram. Soc.*, 2001 **84** (9) 2117–2119
7. J. Mizusaki, Y. Yonemura, H. Kamata, K. Ohyama, N. Mori, H. Takai, H. Tagawa, M. Dokia, K. Naraya, T. Sasamoto, H. Inaba and T. Hashimoto, 'Oxygen nonstoichiometry and defect equlibrium in the perovskite-type oxides $La_{1-x}Sr_xMnO_{3-\delta}$', *Solid State Ionics*, 2000 **129** 163–177
8. J. A. M. van Roosemalen and E. H. P. Cordfunke, 'The defect chemistry of $LaMnO_{3\pm\delta}$, 4 defect model for $LaMnO_{3\pm\delta}$', *J. Solid State Chem.*, 1994 **110** 109–112
9. J. A. M. van Roosemalen, E. H. P. Cordfunke and R. B. Helmholdt, 'The defect chemistry of $LaMnO_{3\pm\delta}$, 2 structural aspects of $LaMnO_{3\pm\delta}$', *J. Solid State Chem.*, 1994 **110** 100–105
10. J. A. M. van Roosemalen and E. H. P. Cordfunke, 'The defect chemistry of $LaMnO_{3\pm\delta}$, 3 the density of (La, A)$MnO_{3\pm\delta}$ (A=Ca, Sr, Ba), *J. Solid State Chem.*, 1994 **110** 106–108
11. H. Taimatsu, K. Wada and H. Kaneko, 'Mechanism of reaction between lanthanum manganite and yttria-stabilized zirconia', *J. Am. Ceram. Soc.*, 1992 **75**(2) 401–405
12. C. T. Yang and W. J. Wei, 'Reaction kinetics and mechanisms between $La_{0.65}Sr_{0.3}MnO_3$ and 8 mol% yttria-stabilized zirconia', *J. Am. Ceram. Soc.*, 2004 **87**(6) 1110–1116
13. K. Huang, 'Gas-diffusion process in a tubular cathode substrate of an SOFC: I Theoretical analysis of gas-diffusion process under cylindrical coordinate system', *J. Electrochem. Soc.*, 2004 **151** A716
14. C. W. Tanner, K. Z. Fung and A. V. Virkar, 'The effect of porous composite electrode structure on solid oxide fuel cell performance', *J. Electrochem. Soc*, 1997 **144** (1) 21–30
15. H. S. Spacil, US Patent 3,558,360, 1970
16. S. P. Jiang and S. P. S. Badwal, 'An electrode kinetics study of H_2 oxidation on Ni/Y_2O_3–ZrO_2 cermet electrode of the solid oxide fuel cell', *Solid State Ionics*, 1999 **123** 209–224
17. M. Brown, S. Primdahl and M. Mogensen, 'Structure/performance relations for Ni/

yttia-stablized zirconia anode for solid oxide fuel cells', *J. Electrochem. Soc.*, 2000 **147** (2) 475–485
18. C. Wen, R. Kato, H. Fukunaga, H. Ishitani and K. Yamada, 'The overpotential of nickel/yttia-stabilized zirconia cermet anodes used in solid oxide fuel cells', *J. Electrochem. Soc.*, 2000 **147** (6) 2076–2080
19. M. Ihara, T. Kusano and C. Yokoyama, 'Competitive adsorption reaction mechanism of Ni/yttria-stabilized zirconia cermet anodes in H_2–H_2O solid oxide fuel cells', *J. Electrochem. Soc.*, 2001 **148** (3) A209–A219
20. E. P. Murray, T. Tsai and S. A. Barnett, 'Direct-methane fuel cell with a ceria-based anode', *Nature*, 1999 **400** 649–651
21. S. Park, J. M. Vohs and R. J. Gorte, 'Direct oxidation of hydrocarbons in a solid oxide fuel cell', *Nature*, 2000 **404** 265–267
22. O. Costa-Nunes, J. M. Vohs and R. J. Gorte, 'A study of direct-conversion SOFC with n-butane at higher fuel utilization', *J. Electrochem. Soc.*, 2003 **150** (7) A858–A863
23. R. Craciun, S. Park, R. J. Gorte, J. M. Vohs, C. Wang and W. L. Worrell, 'A novel method for preparing anode cermets for solid oxide fuel cells', *J. Electrochem. Soc.*, 1999 **146** (11) 4019–4022
24. S. Park, R. J. Gorte and J. M. Vohs, 'Tape cast solid oxide fuel cells for the direct oxidation of hydrocarbons', *J. Electrochem. Soc.*, 2001 **148** (5) A443–A447
25. Z. Zhan and S. A. Barnett, 'An octane-fueled solid oxide fuel cell', *Science*, 2005 **308** 844–847
26. E. P. Murray, S. J. Harris, J. Liu and S. A. Barnett, 'Direct solid oxide fuel cell operation using isooctane', *Electrochem. Solid State Lett.* 2006 **9** (6) A292–294
27. H. Kim, S. Park, J. M. Vohs and R. J. Gorte, 'Direct oxidation of liquid fuels in a solid oxide fuel cell', *J. Electrochem. Soc.*, 2001 **148** (7) A693–A695
28. H. He, R. J. Gorte and J. M. Vohs, 'Highly sulfur tolerant Cu-ceria anodes for SOFCs', *Electrochem. Solid State Lett.*, 2005 **8** (6) A279–A280
29. M. Mogensen, N. M. Sammes and G. A. Tompsett, 'Physical, chemical and electrochemical properties of pure and doped ceria', *Solid State Ionics*, 2000 **129** 63–94
30. H. Inaba and H. Tagawa, 'Ceria-based solid electrolytes', *Solid State Ionics*, 1996 **83** 1–16
31. B. C. H. Steele, 'Appraisal of $Ce_{1-y}Gd_yO_{2-y/2}$ electrode for IT-SOFC operation at 500 °C', *Solid State Ionics*, 2000 **129** 95–110
32. J. M. Ralph, C. Rossignol and R. Kumar, 'Cathode materials for reduced-temperature SOFCs', *J. Electrochem. Soc.*, 2003 **150**(11) A1518–A1522
33. J. Mizusaki, J. Tobuchi, S. Yamauchi and K. Fueki, 'Electrical conductivity and Seebeck coefficient of nonstoichiometric $La_{1-x}Sr_xCoO_{3-\delta}$', *J. Electrochem. Soc.*, 1989 **136** 2082–2088
34. J. B. Goodenough, Bond-length fluctuation in the copper-oxide superconductors' in *Progress in Solid State Chemistry*, 1971 **5** 145–399
35. L.-W. Tai, M. M. Nasrallah, H. U. Anderson, D. M., Sparlin and S. R. Sehlin, 'Structural and electrical properties of $La_{1-x}Sr_xCo_{1-y}Fe_yO_3$, Part 2, The system $La_{1-x}Sr_xCo_{0.2}Fe_{0.8}O_{3-\delta}$ ', *Solid State Ionics*, 1995 **76** 273–283
36. L.-W. Tai, M. M. Nasrallah and H. U. Anderson, 'Thermochemical stability, electrical conductivity and Seebeck coefficient of Sr-doped $LaCo_{0.2}Fe_{0.8}O_3$', *J. Solid State Chem.*, 1995 **118** 117–124
37. J. W. Stevenson, T. R. Armstrong, R. D. Carneim, L. R. Peterson and W. J. Weber,

'Electrochemical properties of mixed conducting perovskite $La_{1-x}M_xCo_{1-y}Fe_yO_{3-\delta}$ (M = Sr, Ba, Ca)', *J. Electrochem. Soc.*, 1996 **143** (9) 2722–2729
38. M. Kim, S. Park, H. Haneda, J. Tanaka and S. Shirasaki, 'High temperature electrical conductivity of $La_{1-x}Sr_xFeO_{3-\delta}$ (x>0.5)', *Solid State Ionics*, 1990 **40/41** 239–243
39. J. Mizusaki, Y. Mima, S. Yamauchi and K. Fueki, 'Nonstoichiometry of the perovskite-type oxides $La_{1-x}Sr_xCoO_{3-\delta}$', *J. Solid State Chem.*, 1989 **80** 102–111
40. J. Mizusaki, M. Yoshihiro, S. Yamauchi and K. Fueki, 'Nonstoichiometry and defect structure of the perovskite-type oxides $La_{1-x}Sr_xFeO_{3-\delta}$', *J. Solid State Chem.*, 1985 **58** 257–266
41. Z. Yang and Y. S. Lin, 'A semi-empirical equation for oxygen nonstoichiometry of perovskite-type ceramics', *Solid State Ionics*, 2002 **150** 245–254
42. Y. L. Yang, C. L. Chen, S. Y. Chen, C. W. Chu and A. J. Jacobson, 'Impedance studies of oxygen exchange on dense thin film electrodes of $La_{0.5}Sr_{0.5}CoO_{3-\delta}$', *J. Electrochem. Soc.*, 2000 **147**(11) 4001–4007
43. H. Fukunaga, M. Koyama, N. Takahashi, C. Wen and K. Yamada, 'Reaction model of dense $Sm_{0.5}Sr_{0.5}CoO_3$ as SOFC cathode', *Solid State Ionics*, 2000 **132** 279
44. S. B. Adler, 'Mechanism and kinetics of oxygen reduction on porous $La_{1-x}Sr_xCoO_{3-\delta}$ electrodes' *Solid State Ionics*, 1998 **111** 125–134
45. S. B. Adler, J. A. Lane and B. C. H. Steele, 'Electrode kinetics of porous mixed-conducting oxygen electrodes', *J. Electrochem. Soc.*, 1996 **143**(11) 3554–3564
46. J. B. Goodenough, J. E. Ruiz-Diaz and Y. S. Zhen, 'Oxide-ion conduction in $Ba_2In_2O_5$ and $Ba_3In_2MO_8$ (M = Ce, Hf, or Zr)', *Solid State Ionics*, 1990 **44** 21–31
47. A. Manthiram, J. F. Kuo and J. B. Goodenough, 'Characterization of oxygen-deficient perovskites as oxide-ion electrolytes', *Solid State Ionics*, 1993 **62** 225–234
48. T. Ishihara, H. Matsuda and Y. Takita, 'Doped $LaGaO_3$ perovskite type oxide as a new oxide ionic conductor', *J. Am. Chem. Soc.*, 1994 **116** 3801
49. M. Feng and J. B. Goodenough, 'A superior oxide-ion electrolyte', *Eur. J. Solid State Inorg. Chem.*, 1994 **T31** 663–672
50. K. Huang, M. Feng and J. B. Goodenough, 'Synthesis and electrical properties of dense $Ce_{0.9}Gd_{0.1}O_{1.95}$ ceramics' *J. Am. Ceram. Soc.*, 1998 **81**(2) 357–362
51. K. Huang, R. Tichy and J. B. Goodenough, 'Superior perovskite oxide-ion conductor strontium- and magnesium-doped $LaGaO_3$: I, Phase relationship and electrical properties', *J. Am. Ceram. Soc.*, 1998 **81**(10) 2565–2575
52. W. K. Kupczyk, D. Kobertz, M. Miller, L. Singheiser and K. Hilpert, 'Vaporization of Sr- and Mg-doped Lanthanum gallate and implications for solid oxide fuel cells', *J. Am. Ceram. Soc.*, 2001 **148**(6) E276–E281
53. W. K. Kupczyk, D. Kobertz, M. Miller, C. Chatillon, L. Singheiser and K. Hilpert, 'Vaporization studies of the La_2O_3–Ga_2O_3 system', *J. Am. Ceram. Soc.*, 2002 **85**(9) 2299–2305
54. J. H. Kim and H. I. Yoo, 'Partial electronic conductivity and electrolytic domain of $La_{0.9}Sr_{0.1}Ga_{0.8}Mg_{0.2}O_{3-\delta}$', *Solid State Ionics*, 2001 **140** 105–113
55. J. H. Jang and G. M. Choi, 'Partial electronic conductivity of Sr and Mg doped $LaGaO_3$', *Solid State Ionics*, 2002 **154–155** 481–486
56. K. Huang, M. Feng, J. B. Goodenough and M. Schmerling, 'Characterization of Sr-doped $LaMnO_3$ and $LaCoO_3$ as cathode materials for a doped $LaGaO_3$ ceramic fuel cell', *J. Electrochem. Soc.*, 1996 **143**(11) 3630–3636
57. T. Ishihara, H. Furutani, M. Honda, T. Yamada, T. Shibayama, T. Akbay, N. Sakai, H. Yokokawa and Y. Takita, 'Improved oxide-ion conductivity in $La_{0.8}Sr_{0.2}Ga_{0.8}Mg_{0.2}O_{3-\delta}$ by doping Co', *Chem. Mater.*, 1999 **11** 2081–2088

58. T. Ishihara, T. Yamada, H. Arikawa, H. Nishiguchi and Y. Takita, 'Mixed electronic-oxide-ionic conductivity and oxygen permeating property of Fe-, Co- or Ni-doped $LaGaO_3$ perovskite oxide', *Solid State Ionics*, 2000 **135** 631–636
59. K. Huang, H. Y. Lee and J. G. Goodenough, 'Sr- and Ni-doped $LaCoO_3$ and $LaFeO_3$ perovskites – new cathode materials for solid oxide fuel cells', *J. Electrochem. Soc.*, 1998 **145**(9) 3220–3227
60. K. Huang, J. Wan and J. B. Goodenough, 'Oxide-ion conducting ceramics for solid oxide fuel cells', *J. Mater. Sci.*, 2001 **36** 1093–1098
61. T. H. Lee, Y. L. Yang, A. J. Jacobson, B. Abeles and M. Zhou, 'Oxygen permeation in dense $SrCo_{0.8}Fe_{0.2}O_{3-\delta}$ membrane: surface exchange kinetics versus bulk diffusion', *Solid State Ionics*, 1997 **100** 77–85
62. K. Huang and J. B. Goodenough, 'Oxygen permeation through cobalt-containing perovskites: surface oxygen exchange vs. lattice oxygen diffusion', *J. Electrochem. Soc.*, 2001 **148** (5) E203–E214
63. K. Huang, M. Feng and J. B. Goodenough, 'Electrode performance test on single ceramic fuel cells using as electrolyte Sr- and Mg-doped $LaGaO_3$', *J. Electrochem. Soc.*, 1997 **144** (10) 3620–3624
64. K. Huang, R. Tichy, J. B. Goodenough and C. Milliken, 'Superior perovskite oxide-ion conductor strontium- and magnesium-doped $LaGaO_3$: III, Performance tests of single ceramic fuel cells', *J. Am. Ceram. Soc.*, 1998 **81**(10) 2581–2585
65. M. Hrovat, A. Ahmad-Khanlou, Z. Samardzija and J. Holc, 'Interactions between lanthanum gallate based solid electrolyte and ceria', *Mater. Res. Bull.*, 1999 **34** (12/13) 2027–2034
66. K. Huang, J. Wan and J. B. Goodenough, 'Increasing power density of LSGM-based solid oxide fuel cells using new anode materials', *J. Electrochem. Soc.*, 2001 **148** (7) A788–A794
67. I. Yasuda and T. Hikita, 'Electrical conductivity and defect structure of calcium-doped lanthanum chromites', *J. Electrochem. Soc.*, 1993 **140** (6) 1699–1704
68. I. Yasuda and M. Hishinuma, 'Electrochemical properties of doped lanthanum chromites as interconnectors for solid oxide fuel cells', *J. Electrochem. Soc.*, 1996 **143** (5) 1583–1590
69. D. B. Meadowcroft, 'Properties of strontium-doped lanthanum chromite', *Br. J. Appl. Phys., Ser. 2*, 1969 **2** 1225–1233
70. N. Sakai, T. Kawada, H. Yokogawa and M. Dokiya, 'Sinterability and electrical conductivity of calcium doped lanthanum chromite', *J. Mater. Sci.*', 1990 **25** 4531
71. L. A. Chick, J. Liu, J. W. Stevenson, T. R. Armstrong, D. E. McCready, G. D. Maupin, G. W. Coffey and C. A. Coyle, 'Phase transitions and transient liquid-phase sintering in calcium-substituted lanthanum chromite', *J. Am. Ceram. Soc.*, 1997 **80** (8) 2109–2120
72. D. Peck, M. Miller and K. Hilper, 'Vaporization of thermodynamic activities in $La_{0.80}Sr_{0.2-x}Ca_xCrO_{3-\delta}$, x = 0.05, 0.10 and 0.15, investigated by Knudsen effusion mass spectrometry', *J. Electrochem. Soc.*, 2001 **148** (6) A657–A661
73. Z. Yang, J. S. Hardy, M. S. Walker, G. Xia, S. P. Simner and J. W. Stevenson, 'Structure and conductivity of thermally grown scales on ferritic Fe-Cr-Mn steel for SOFC interconnect applications', *J. Electrochem. Soc.*, 2004 **151** (11) A1825–A1831
74. Z. Yang, J. S. Hardy, M. S. Walker, G. Xia, S. P. Simner and J. W. Stevenson, 'Structure and conductivity of thermally grown scales on ferritic Fe-Cr-Mn steel for SOFC interconnect applications', *J. Electrochem. Soc.*, 2004 **151** (11) A1825–A1831

75. K. Huang, P. Y. Hou and J. B. Goodenough, 'Characterization of iron-based alloy interconnects for reduced temperature solid oxide fuel cells', *Solid State Ionics*, 2000 **129** 237–250
76. W. J. Qudakkers, J. Pirón-Abelián and V. Shemet, ' Metallic materials in solid oxide fuel cells', *Mater. Res.* 2004 **7** (1) 203–208
77. T. Horita, H. Kishimoto, K. Yamaji, Y. Xiong, N. Sakai, M. E. Brito and H. Yokokawa, 'Oxide scale formation and stability of Fe-Cr alloy interconnects under dual atmospheres and current flow conditions for SOFCs', *J. Electrochem. Soc.*, 2006 **153** (11) A2007–A2012
78. T. Uehara, T. Ohno and A. Toji, 'Development of ferritic Fe–Cr alloy for SOFC separator', *Proc. 5th Eur. SOFC Forum*, Lucerne, Switzerland, July 2002, p281
79. T. Horita, Y. Xiong, H. Kishimoto, K. Yamaji, N. Sakai, M. E. Brito and H. Yokokawa, 'Oxidation behavior of Fe–Cr and Ni–Cr-based alloy interconnects in CH_4–H_2O for solid oxide fuel cells', *J. Electrochem. Soc.*, 2006 **152** (11) A2193–A2198
80. P. Kofstad and R. Bredesen, 'High temperature corrosion in SOFC environments', *J. Electrochem. Soc.*, 1992 **52** 69–72
81. K. Hilpert, D. Das, M. Miller, D. H. Peck and R. Weiss, 'Chromium vapor species over solid oxide fuel cell interconnect materials and their potential for degradation processes', *J. Electrochem. Soc.*, 1996 **143** (11) 3642–3647
82. S. P. Jiang, J. P. Zhang, I. Apateanu and K. Foger, 'Deposition of chromium at Sr-doped $LaMnO_3$ electrodes in solid oxide fuel cells', *J. Electrochem. Soc.*, 2000 **147** (11) 4013–4022
83. S. P. Jiang, S. Zhang and Y. D. Zhen, 'Deposition of Cr species at (La, Sr)(Co, Fe)O_3 cathodes of solid oxide fuel cells', *J. Electrochem. Soc.*, 2006 **153** (1) A127–A134
84. E. Konysheva, H. Penkalla, E. Wessel, J. Mertens, U. Seeling, L. Singheiser and K. Hilpert, 'Chromium poisoning of perovskite cathodes by the ODS alloy Cr5Fe1Y_2O_3 and the high chromium ferritic steel Crofer22APU', *J. Electrochem. Soc.*, **153** (4) A765–A773
85. P. Y. Hou and J. Stringer, 'Effect of surface-applied reactive element oxide on the oxidation of binary alloys containing Cr', *J. Electrochem. Soc.*, 1987 **134** (7) 1836–1849
86. J. Stringer, 'The reactive element effect in high-temperature corrosion', *Mater. Sci. Eng.*, 1989 **A120** 129–137
87. K. Huang, P. Y. Hou and J. B. Goodenough, 'Reduced area specific resistance for iron-based metallic interconnects by surface oxide coatings', *Mater. Res. Bull.*, 2001 **36** 81–95
88. B. A. Pint, 'Experimental observations in support of the dynamic-segregation theory to explain the reactive-element effect', *Oxidation of Metals* 1996 **45** (1/2) 1–37
89. T. Horita, Y. Xiong, K. Yamaji, N. Sakai and H. Yokokawa, 'Evaluation of Fe-Cr alloys as interconnects for reduced operation temperature SOFCs', *J. Electrochem. Soc.*, 2003 **150** (3) A243–A248
90. Z. Lu, J. Zhu, E. A. Payzant and M. P. Paranthanman, 'Electrical conductivity of the manganese chromite spinel solid solution', *J. Am. Ceram. Soc.*, 2005 **88** (4) 1050–1053
91. Yngve Larring and T. Norby, 'Spinel and perovskite functional layers between Plansee metallic interconnect (Cr–5wt%Fe–1wt%Y_2O_3) and ceramic $(La_{0.85}Sr_{0.15})_{0.91}MnO_3$ cathode materials for solid oxide fuel cells', *J. Electrochem. Soc.*, 2000 **147** (9) 3251–3256
92. Z. Yang, G. Xia, G. D. Maupin and J. W. Stevenson, 'Evaluation of perovskite

overlay coatings on ferritic stainless steels for SOFC interconnect applications', *J. Electrochem. Soc.*, 2006 **153** (10) A1852–A1858
93. Z. Yang, G. Xia, S. P. Simner and J. W. Stevenson, 'Thermal growth and performance of manganese cobaltite spinel protection layers on ferritic stainless steel SOFC interconnects', *J. Electrochem. Soc.*, 2005 **152** (9) A1896–A1901
94. Z. Yang, K. D. Meinhardt and J. W. Stevenson, 'Chemical compatibility of barium–calcium–aluminosilicate-based sealing glasses with ferritic stainless steel interconnect in SOFCs', *J. Electrochem. Soc.*, 2003 **150** (8) A1095–A1101
95. S. de Souza, S. J. Visco and L. C. De Jonghe, 'Thin-film solid oxide fuel cell with high performance at low-temperature', *Solid State Ionics*, 1997 **98** 57–61
96. I. Villarreal, C. Jacobson, A. Leming, Y. Matus, S. Visco and L. De Jonghe, 'Metal-supported solid oxide fuel cells', *Electrochem. Solid State Lett.*, 2003 **6** (9) A178–A179
97. T. Franco, Z. Ilhan, M. Lang, G. Schiller and P. Szabo, 'Investigation of porous metallic substrates for plasma sprayed thin-film SOFCs', *Electrochem. Soc. Proc.*, 2005 **7** 344–352
98. A. O. Isenberg, *Electrochemical Society Symposium Electrode Materials, Process for Energy Conversion and Storage*, 1977, **77**(6) 572–581
99. A. Refke and G. Barbezat, 'Low pressure plasma spray (LPPS) as a tool for the deposition for functional SOFC components', *Proc. Int. Therm. Spray Conf.*, Osaka, Japan, 2004, p61
100. F. Tietz, H. P. Buchkremer and D. Stöver, 'Components manufacturing for solid oxide fuel cells', *Solid State Ionics*, 2002 **152–153** 373–381
101. H. U. Anderson and F. Tietz, 'Interconnect' in *High Temperature Solid Oxide Fuels – Fundamentals, Design and Applications*, ed. S. C. Singhal and K. Kendall, Oxford, Elsevier, 2004, p179
102. Y. Huang, R. Dass, Z. Xing and J. B. Goodenough, 'Double perovskites as anode materials for solid oxide fuel cells', *Science*, 2006 **312** 254–257

9

Regenerative fuel cells

J ANDREWS and A K DODDATHIMMAIAH,
RMIT University, Australia

9.1 Introduction: operational principles and types of regenerative fuel cell

A regenerative fuel cell (RFC) is a single device or system capable of functioning either as an electrolyser or a fuel cell (Frank, 2000). The reversible reaction most commonly used in an RFC is the splitting of water into its constituent elements, hydrogen and oxygen, and their recombination to form water once again:

$$H_2O + \text{energy} \leftrightarrow H_2 + {}^1/_2O_2 \qquad 9.1$$

Other reactions that have been investigated for RFCs are hydrogen–halogen reactions (in particular bromine) and the zinc–oxygen reaction (Mitlitsky *et al*., 1998a).

In an RFC based on the water-splitting reaction, electrical input to the cell in electrolyser mode is used to dissociate liquid water into hydrogen and oxygen gas. These gases are stored, and fed back into the RFC acting now in fuel cell mode to regenerate electricity and reform water. Alternatively, just the hydrogen is stored and the RFC draws on oxygen from the air when operating as a fuel cell. The RFC concept is thus founded upon the inherent reversibility of the water dissociation and reformation (or similar) reaction.

Coupled to a hydrogen and oxygen storage system, or just a hydrogen storage system if air is used to supply oxygen, such an RFC constitutes an integrated system for storing electrical energy for later use. RFCs therefore have potential applications in areas such as space vehicles and satellites (Mitlitsky *et al*., 1998a,b), submarines, aircraft, remote or distributed terrestrial energy supply systems, electricity storage in central grids or at a local level when there is variable energy input from solar or wind power (Andrews *et al*., 2005; Doddathimmaiah and Andrews, 2006), electricity storage at a local level (Yao *et al*., 2007), and possibly in hydrogen electric cars capable of generating some of their own hydrogen fuel when parked.

RFCs come in two basic types: discrete regenerative fuel cells and unitised regenerative fuel cells. In a discrete regenerative fuel cell (DRFC), the device used to perform the electrolysis is separate to that used as a fuel cell but these two devices are both integrated into a single system (Fig. 9.1). The overall DRFC also includes a water management system, a control system, and a gas storage system if it is to function as a standalone energy storage unit. One key advantage of a DRFC over a separate electrolyser, hydrogen storage and fuel cell, is that by integrating all functional units into a single compact system the DRFC can provide a standalone alternative technology for storing electrical energy, and hence compete directly with batteries. Additionally, a DRFC allows closing of the water cycle, whereby product water in fuel cell mode can be returned to the water storage for the electrolyser. This capability is particularly important for space, aircraft or submarine applications where water must be conserved by recycling. It may become increasingly beneficial in stationary power supply applications too in areas where supplies of fresh water are very limited. Keeping the electrolyser and fuel cell separate allows these two components to be designed to optimise their individual performance and cost effectiveness. It also allows the capacities of the cell in the two modes to be set independently, and the cell to operate in both modes simultaneously (if the overall system design permits).

A unitised regenerative fuel cell (URFC) is likewise a single device that can work in either electrolyser mode (hereafter E-mode) or fuel cell mode (FC-mode). Its essential difference compared to a DRFC is that in a URFC the same physical cell is used both as the electrolyser and fuel cell (Fig. 9.2) (Frank, 2000). Consequently this cell is truly a reversible bifunctional unit in which the basic electrochemical reaction (equation 9.1) moves in the forward direction in E-mode and in the reverse direction in FC-mode. The advantage of a URFC over a DRFC is that only one electrochemical cell is required

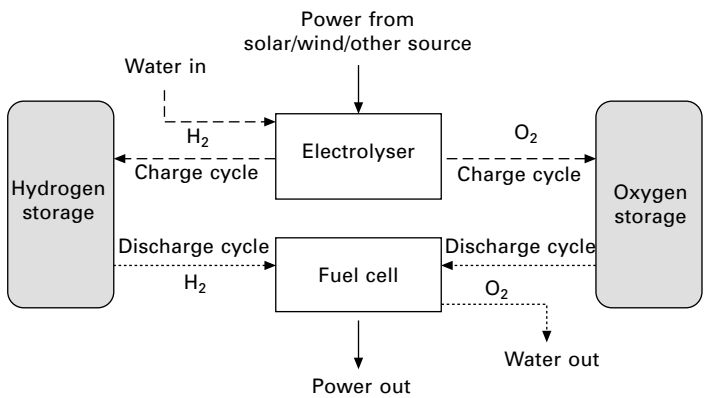

9.1 A schematic of a discrete regenerative fuel cell system (DRFC).

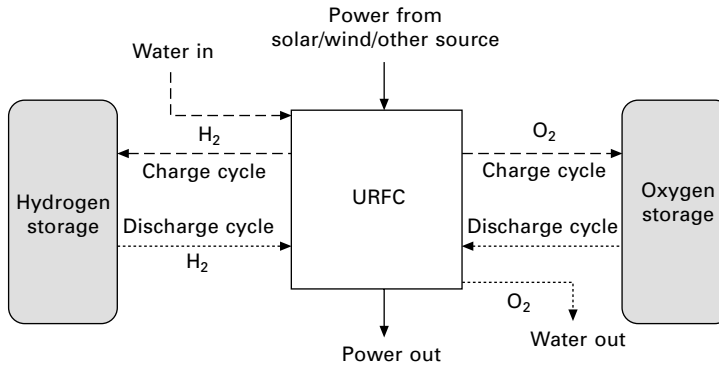

9.2 A schematic of a unitised regenerative fuel cell system (URFC).

rather than two – that is, one for the electrolyser and another for the fuel cell – offering potential cost, space and mass savings. The accompanying technical challenge is to maintain the performance of the bifunctional cell in each mode close to or equal to that of the corresponding performance of a separate electrolyser and fuel cell. Provided this challenge can be met, a URFC may be economically preferable to a DRFC since the cost of and space occupied by, as well as the mass of, one entire electrochemical cell are avoided.

The vast majority of URFCs built to date have employed a proton exchange membrane (PEM) as a solid electrolyte. PEMs are fluorinated sulphonic acid polymers or similar polymers that conduct protons (H^+ ions) but not electrons, and they have become the most popular solid electrolyte for use in dedicated fuel cells. A PEM URFC has the advantage of working at relatively low temperatures in the range 30–80 °C. However, solid oxide cells have also been used in URFCs. These cells work at high temperatures (600–1000 °C) and employ a solid non-porous metal oxide, usually Y_2O_3-stabilised ZrO_2, as electrolyte, with movement of oxygen ions providing the ionic conduction (McElroy and Gottmann, 2005; Irvine *et al.*, 2007). A URFC based on the reversible hydrogen-bromide splitting reaction ($2HBr \leftrightarrow H_2 + Br_2$) has also been developed (US Department of Energy, 1999).

Falling between the URFC and DRFC concepts is a regenerative fuel cell in which a fuel cell stack is joined directly to an electrolyser stack, so the two stacks are in line and form a single unit although separate cells are still used in E and FC-modes (Joos *et al.*, 2004). This arrangement allows efficient exchange of gases, water and sometimes also heat between the two stacks. Some have called this design a URFC too, but it does not have the defining URFC characteristic of having just one cell or stack of cells working reversibly to provide the E and FC-mode functions.

On account of their being the subject of more widespread study and use, we will concentrate on PEM URFCs in the present chapter. Moreover, URFCs

do involve development of an essentially novel unit – a reversible cell – whereas DRFC design is predominantly a process of system integration, using already available components.

9.2 The development of regenerative fuel cells

Since William Grove demonstrated the first fuel cell in 1839, the reversibility of the water splitting and recombination reaction has been well known. Interest in fuel cells grew rapidly from the 1950s onwards particularly to generate electricity for spacecraft using safe, compact and relatively lightweight technology. Early fuel cells used in the US and Soviet Union's space programs utilised hydrogen and oxygen stored on board. But it was soon recognised that a reversible cell capable of both electrolysis and power generation could be the central component of a closed-cycle regenerative energy storage and power supply system that used solar energy to split the stored water into hydrogen and oxygen. These gases could then be stored and used as required in a fuel cell to produce power, together with water once again that could be returned to the water storage tank for reuse. The only external input to the system would then be the solar energy.

An early proof of the URFC concept was provided by General Electric in 1973 when a life-cycle test of a single-cell PEM URFC showed that reversible operation was feasible without significant degradation of the cell membrane (similar to DuPont's Nafion 120) and catalyst (Mitlitsky *et al.*, 1996a).

The Lawrence Livermore National Laboratory (LLNL) worked with Hamilton Standard to design and construct the first portable URFC demonstration unit in 1993 as the ideal energy storage solution for the High Altitude Long Endurance Solar Rechargeable Aircraft (HALE SRA) program being funded by the Ballistic Missile Defence Organization (BMDO). Electricity for solar panels located on the model aircraft's elongated wings was used to drive the propellers directly during the day, with the surplus fed into a URFC in E-mode to produce hydrogen and oxygen for on-board storage in transparent polycarbonate tanks. The hydrogen and oxygen were then fed back into the URFC in FC-mode to generate power to keep the propellers turning and the plane moving during the night (Mitlitsky *et al.*, 1999a,b).

In the latter half of the 1990s, similar URFC technology began to be developed for space applications. Mitlitsky *et al.* (1996b) at LLNL developed a concept and much of the componentry for the so-called Integrated Modular Propulsion and Regenerative Electro-Energy storage system (IMPRESS) for Small Satellites. In IMPRESS a single URFC stack of cells produced hydrogen and oxygen by using solar cells to electrolyse water carried on board. These gases were then used either directly as fuel for small rocket boosters for satellite navigation, or to generate electricity for the satellite's electronic

systems using the URFC stack operating in FC mode. URFC systems with lightweight pressure vessels were also designed by LLNL for zero-emission terrestrial vehicles (Mitlitsky *et al.*, 1996b), and utility and remote power energy-storage applications, with funding support from the US Department of Energy, and Proton Energy Systems Inc. as a prime contractor for the technology development and testing of URFC stacks (Mitlitsky *et al.*, 1998a,b 1999b).

Proton Energy Systems (now called Distributed Energy Systems) has subsequently developed and commercialised its Unigen range of URFC systems (Fig. 9.3) for energy storage applications in space, defence systems, remote-area and uninterruptible power supply, zero-emission transportations systems, and possibly peak-shaving applications on utility grids, under research contracts from Electric Power Research Institute, the NASA Glenn Research Center, and the US Missile Defence Agency (Mitlitsky *et al.*, 1999b; Smith, 2000). Distributed Energy Systems offer both URFC and DRFC systems depending on the application. Unigen URFC stacks are capable of being operated to pressures of over 10 bar (Molter, 1999; Smith, 2000). In addition the company has been involved in a joint development program with Marconi to incorporate Proton's reversible fuel cells (initially with 70 kW h storage capacity) in Marconi's power systems for the telecommunications industry (Hyweb, 2001), and in developing a demonstration 1 kW solar RFC system for a completely sustainable grid-independent power supply at China Lake, USA (Power Engineering, 2003). The US companies, United Technologies Corporation and Hamilton Standard (Space and Sea Systems Division) have undertaken research and development on URFCs primarily for aerospace applications (Mitlitsky *et al.*, 1999c).

Other US companies, such as Giner Inc. and Lynntech Inc. (Fig. 9.4), have also been developing URFCs, and offer for commercial sale suitably catalysed PEM electrode assemblies for URFCs. The company, Electric Boat,

9.3 Unigen URFC systems developed for commercial sale by Proton Energy Systems (now Distributed Energy Systems): the complete unit (left) and the URFC stack (right).

9.4 A URFC stack by Lynntech Inc.

is working with the University of Connecticut on a seven-cell URFC stack coupled to a metal hydride storage system for use in submarines (University of Connecticut, 2005).

A range of other governmental, university and private sector research groups have also been working on experimental RFC systems around the world. One of the largest R&D projects on URFCs outside the United States is currently the Revcell project in the Netherlands to develop autonomous energy supply systems and uninterruptible power supplies using PV arrays and a URFC-hydrogen based system for long-term energy storage for stand-alone PV systems. This project is being conducted by Hynergreen Technologies, Spain, Fraunhofer-Gesellschaft, Germany, NedStack Fuel Cell Technology, and others (Nedstack, 2007).

9.3 Unitised regenerative fuel cells

9.3.1 Main components

The main components of a single-cell PEM URFC are shown in Fig. 9.5. At the centre of the cell is the membrane electrode assembly (MEA) comprising the solid polymer membrane (PEM) serving as the electrolyte and the electrodes. The electrodes are in contact with the membrane to allow proton flow to and from the membrane, and contain catalysts to facilitate the electrochemical reactions. The electrodes must be porous to allow flow of gases and liquid water to and from reaction sites, and also electrical conductors to carry electrons to and from the reactions taking place. Attached to the electrodes are gas diffusion backings (GDBs) that distribute incoming gases to the whole electrode surface in fuel cell mode, and allow outwards gas flow in electrolyser mode. The GDBs must also be electrical conductors to support

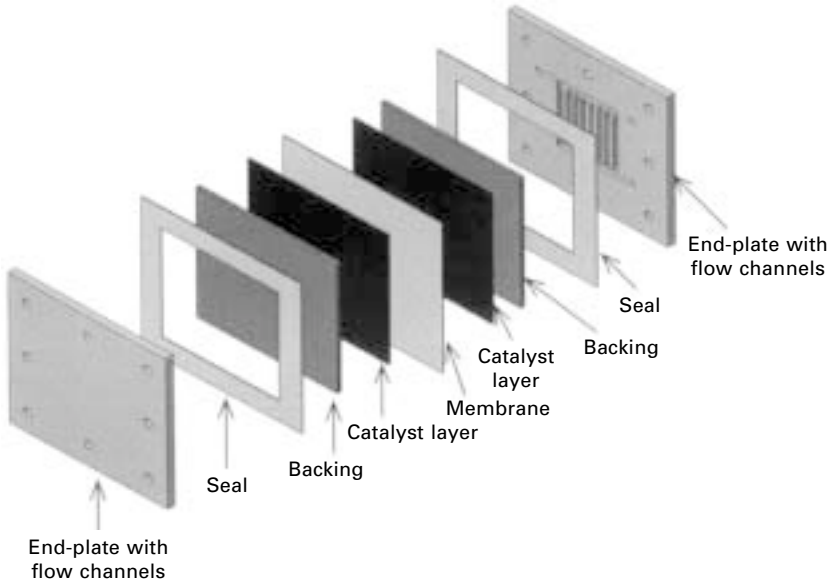

9.5 The main components of a PEM URFC. The bolts passing through the layers of the cell from endplate to endplate are not shown.

current flow from the current collector plates to and from the electrodes to the conducting end-plates, which are also the electrical terminals of the cell. Channels in the current collector layers are connected to the gas ports to allow inflow and outflow of oxygen, hydrogen and water.

9.3.2 Basic types of unitised regenerative fuel cell

Oxygen and hydrogen electrodes constant

In the most common type of URFC (Fig. 9.6) the electrode from which hydrogen is evolved in E-mode and consumed in FC-mode stays the same, so that we can call this unambiguously the 'hydrogen electrode'. Similarly oxygen is evolved and consumed at the other electrode, which can be named the 'oxygen electrode'. The electrodes serving as cathode and anode interchange between modes since the current flows in opposite directions in the two modes. We will thus use the terminology 'oxygen and hydrogen electrodes' rather than 'cathode and anode' when talking about this type of URFC to avoid confusion.

In E-mode the catalyst layer in the oxygen electrode must facilitate the water-molecule splitting reaction,

$$H_2O \rightarrow 2H^+ + 2e^- + {}^1/_2O_2$$

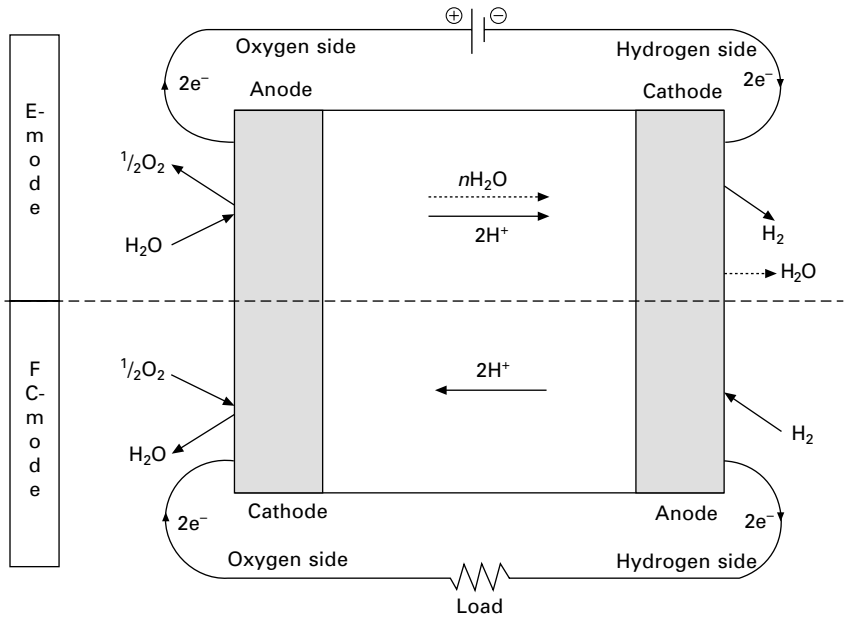

9.6 URFC design with oxygen and hydrogen electrodes remaining the same (but cathode and anode interchanging) on change between modes.

and in FC-mode the reverse water-formation reaction. So the layer must be bifunctional. The achievement of bifunctionality is a significant design challenge since most catalysts will encourage the reaction in one direction but are not so effective in encouraging the reverse reaction. For example, platinum in the oxygen electrode's catalyst layer works well in facilitating the water-formation reaction required in FC-mode, but performs poorly in encouraging the water-splitting reaction in E-mode (see, for example, Murphy *et al.*, 1995).

The catalyst layer in the hydrogen electrode must support the hydrogen formation reaction,

$$2H^+ + 2e^- \rightarrow H_2$$

in E-mode, and the reverse hydrogen-molecule splitting reaction in FC-mode. Hence once again the catalyst layer has to be bifunctional, but fortunately platinum functions well as a catalyst for both the hydrogen-molecule splitting and formation reactions. The main design and material-selection challenge therefore tends to be to achieve bifunctionality of the oxygen electrode, both in terms of catalyst efficacy and reactant kinetics, rather than on the hydrogen side. Moreover the water-splitting and formation reactions involve a number of intermediate reactions (O'Hayre *et al.*, 2005) and are far more complicated

than the hydrogen-side reactions. The oxygen-side reactions thus tend to require more catalytic assistance and higher driving electric potentials to encourage in both directions.

Advantages of this type of URFC are that gaseous hydrogen and oxygen are confined to their respective sides of the cell membrane and cannot mix. In addition, water is introduced and produced on the same side of the membrane so that the main liquid water management system can operate solely on that side. However, in E-mode water vapour mixes with the oxygen produced on the oxygen side, and water molecules are dragged across the membrane to the hydrogen electrode by H^+ ions by a process called 'osmotic drag' (Coalson, 1998) (shown as nH_2O in Fig. 9.6, where n is a small integer, since each H^+ ion drags more than one water molecule). Hence water also accumulates on the hydrogen side and water vapour mixes with the hydrogen produced. In this type of URFC both hydrogen and oxygen produced in E-mode must normally be dried before entering the storage system.

Oxygen and hydrogen electrodes interchange

An alternative type of URFC switches the electrodes in contact with oxygen and hydrogen in changing between modes, so that one electrode is the anode, and the other the cathode in both modes (Fig. 9.7). In this design type, the oxidation reactions in both modes (which consume electrons) take place at the same electrode (the cathode), and the reduction reactions (which yield electrons) take place at the other electrode (the anode). It has been argued that, because the same basic form of reaction – oxidation or reduction – is taking place at each electrode, it is easier to find suitable catalysts and produce electrodes with a long lifetime than with the first type of URFC described in the previous subsection (Murphy *et al.*, 1995). Certainly if platinum is used in the catalyst layer on both electrodes, this catalyst will perform well in facilitating the hydrogen-molecule decomposition reaction in E-mode on one electrode, and the hydrogen formation reaction on the other electrode in FC mode. But it is likely that another catalyst material would need to be added on both electrodes to support the water decomposition and formation reactions. Hence both electrodes would have a mix of catalysts, rather than just one electrode in the case of the first type of URFC.

A further disadvantage of the electrode-switching type is the potential for oxygen and hydrogen to mix on both sides of the membrane, since alternatively hydrogen and oxygen are present on each side as mode switching takes place. Such mixing would reduce cell performance and potentially lead to safety concerns if the flammability limits of hydrogen-oxygen mixtures were exceeded. To avoid these problems, flushing of the electrode compartments with an inert gas such as nitrogen is usually required when changing between modes (Jorissen, 2006).

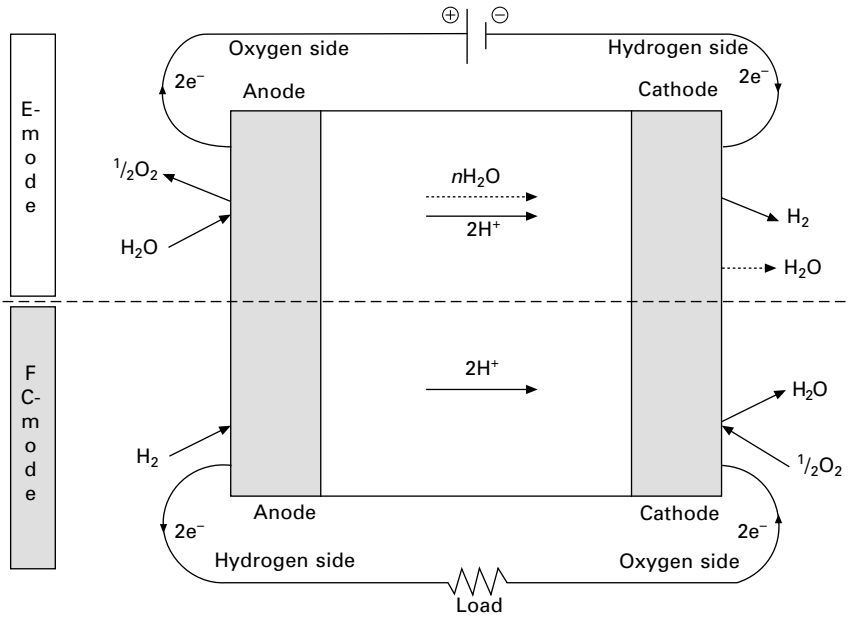

9.7 URFC design with oxygen and hydrogen electrodes switching (but cathode and anode remaining constant) on change between modes.

With water being introduced on one electrode in E-mode and formed on the other in FC- mode, the catalyst layers and associated gas diffusion backings on both electrodes must also be resistant to and not degrade in the presence of this water, and the water management system must operate equally on both electrodes.

Alternative water feed arrangements

In both the design types just described, water is fed into the URFC in E-mode to the oxygen electrode (that is, to the anode in this mode). An alternative is to feed the water in to the hydrogen electrode – that is, use cathode feed – and rely on diffusion of water molecules through the membrane to provide the water supply required for the water-splitting reaction that takes place on the oxygen electrode (Fig. 9.8). An advantage of hydrogen-side water feed is that water is present in significant quantities only on the hydrogen electrode, so that only one phase separator is required (on the hydrogen side) to separate the hydrogen gas produced from water vapour, compared with two phase separators (one on each side) in the standard type (Mitlitsky *et al.*, 1998b).

The diffusion of water from hydrogen to oxygen side in E-mode, however, is offset by the transfer of water molecules in the reverse direction by osmotic

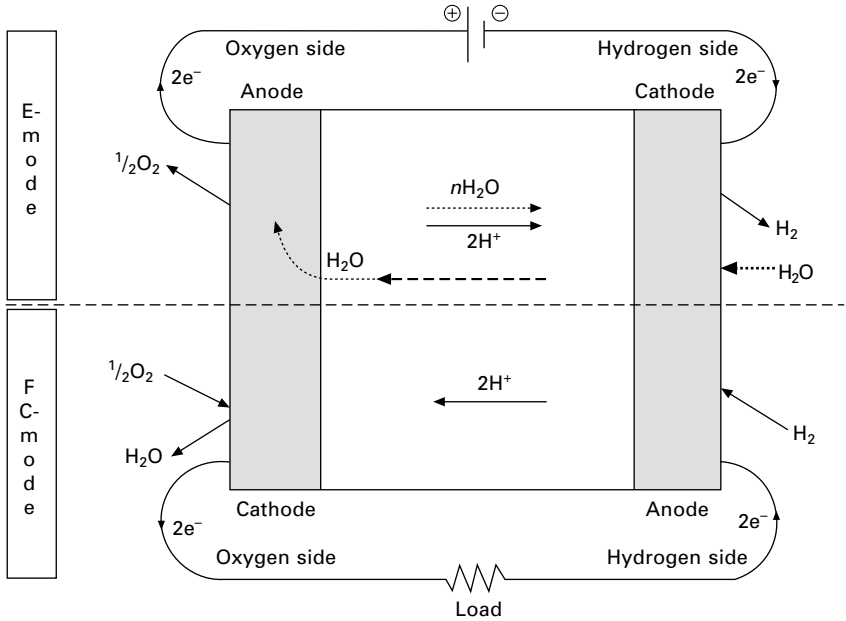

9.8 URFC design with water feed in E-mode to the hydrogen electrode (the cathode).

drag, each proton pulling with it at least four water molecules (Mitlitsky *et al*., 1998a). At high current densities, there is thus the risk of the oxygen-side drying out and the electrolysis reactions being inhibited. With oxygen-side water feed there is always excess water at this side so that drying out can never occur (Mitlitsky *et al*., 1998b).

To allow hydrophobic GDBs to be used, an alternative method of introducing liquid water into a URFC through channels within the PEM membrane structures has been developed by Lynntech (Murphy *et al*., 1995).

Functional separation of the membrane

Another type of URFC design has been proposed by Ito *et al*. (2005) that functionally separates the plane of a single membrane into one portion for water electrolysis portion and the other for FC-mode. Separate passages feed the two portions with gas and water respectively.

9.4 Membrane electrode assemblies

9.4.1 Overall structure

A schematic diagram of a typical membrane electrode assembly used in a URFC is shown in Fig. 9.9, and a scanning electron micrograph image of a

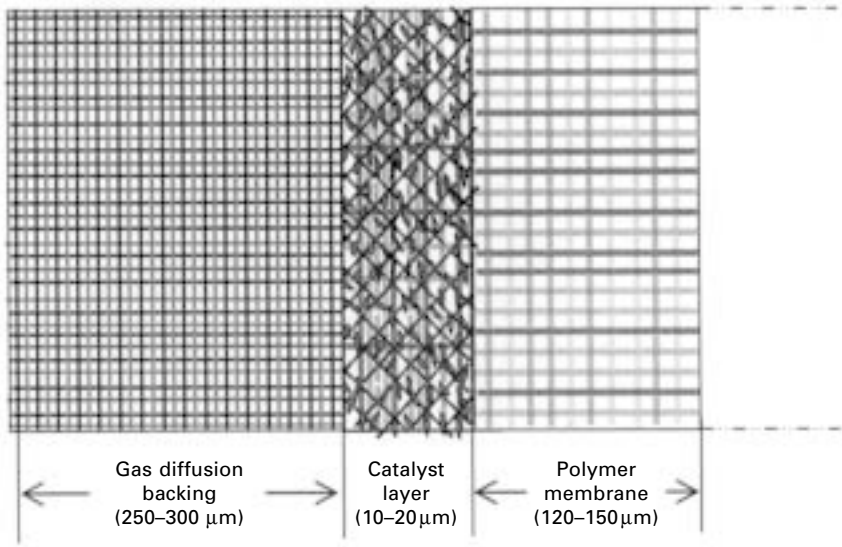

9.9 Schematic of the layers of a typical MEA, together with a GDB, as used in a URFC. The second catalyst layer and GDB to the right of the membrane are not shown.

cross-section of a MEA in Fig. 9.10. Typically the thickness of the membrane is 120–150 μm, while that of each catalyst layer is 10–20 μm. In Fig. 9.10, polymer membrane material is shown as extending into the catalyst layer to allow conduction of protons to and from the catalyst particles. This layer also contains an electrically conducting medium (diagonal net) with catalyst particles in contact with it and the membrane material. The GDB comprises two interpenetrating nets: one conducts electrons and the other is for water transport. The spaces in between the nets are for gas transport.

9.4.2 The membrane

Nafion® made by DuPont is currently the standard membrane material for PEM fuel cells (Sethuraman, 2006) and PEM URFCs. Nafion comprises a polytetrafluoroethylene (PTFE) backbone with perfluorinated-vinyl-polyether side chains containing sulphonic acid end groups. When this material is hydrated, protons (H^+ ions) become highly mobile, so that its proton conductivity can range up to 0.2 S/cm depending on the level of hydration ($S = 1/\Omega$).

Nafion comes in a number of different grades (for example, Nafion 112, 115 and 117) varying according to thickness (0.051, 0.127 and 0.178 mm respectively), and hydration and permeation properties (Sportsman *et al.*, 2002). Nafion can be purchased commercially at prices in the range $US

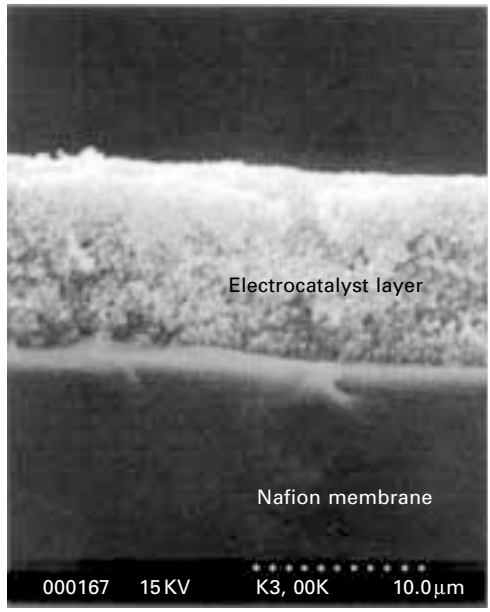

9.10 A scanning electron micrograph of an MEA in cross-section showing a catalyst layer and the membrane. Source: Ioroi *et al.* (2002).

(2007) 800–2000/m^2 (Zaidi *et al.*, 2007). The Dow Chemical Company introduced a similar perfluorinated sulphonic acid membrane for use in PEM fuel cells in 1998 with a shorter side chain than the early versions of Nafion, although the rights to manufacture this membrane were subsequently transferred to DuPont (Hoogers, 2003).

9.4.3 Catalyst layers

The catalyst layers on each face of the membrane are composite structures consisting of proton-conducting polymer as in the membrane itself, and an electron-conducting medium, usually carbon, on which a metal or metal oxide catalyst is deposited (as shown in Fig. 9.9 and Fig. 9.10). The catalyst layers must fulfil multiple functions:

- Support for the catalyst particles that act as sites at which the electrochemical reactions take place and are facilitated.
- Conduction of protons to or from these sites (via the polymer material).
- Conduction of electrons to or from these sites (via the carbon or other porous medium).
- Allowance of movement of reactants (hydrogen, oxygen and water molecules) through the porous structure of the layers to and from the sites.

Each catalyst particle should be in contact with at least one other particle in the medium that serves as the conductor of electrons so that there is a continuous path for electron flow to and from the current collector. The catalyst particle should also be linked to membrane material so that H^+ ions can access it (Cisar *et al*., 2005).

A number of methods have been developed to construct the catalyst layers of PEM fuel cells and electrolysers, and these same methods can be used to construct URFC catalyst layers. Some of the main methods specifically used for URFC catalyst layers are the following:

- The 'Decal' method: mix catalyst particles in a solution, allow the solution to diffuse into carbon cloth or other porous medium, dry, spray with Nafion, and then hot press the layer onto the membrane face, relying on the melted polymer to provide the adhesion (Wittstadt *et al*., 2005; Yim *et al*., 2005; Jorissen, 2006).
- Nafion slurries: mix prepared catalyst materials in liquid Nafion to form a slurry, paste onto the porous medium of the catalyst layer, dry and then hot press on to the membrane (Yim *et al*., 2005).
- Electrostatic deposition: deposit the metallic catalyst onto the membrane in an electrostatic plating bath, by sputtering, or by electrodeposition (Wittstadt *et al*., 2005; Sopian and Daud, 2006).
- Direct deposition of Pt catalysts on Nafion-impregnated polypyrrole (Lee *et al*., 2004).
- Chemical reduction: deposit the metal catalyst by chemical reduction of its anionic salt with hydrazine directly on to the membrane (Ahn and Holze, 1992).

In the case of the commonest type of URFC – oxygen and hydrogen electrodes remaining the same in each mode (page 348) – the catalyst used on the hydrogen side is generally platinum as Pt black. The hydrogen-side layer must, however, be able to retain its physical integrity and resist corrosion in the presence of the water molecules dragged over from the oxygen side by protons during E-mode.

The oxygen-side catalyst layer in a URFC is typically more challenging to design and construct, because of the difficulty in finding a catalyst material that functions equally well in both E and FC-modes. As mentioned earlier, platinum, for example, in the oxygen-side layer performs well in FC-mode (with a low overpotential) but poorly in E-mode (leading to a relatively high overpotential). Hence a mixture of catalyst materials is usually employed on the oxygen side. Platinum is commonly retained in the mixture for FC-mode functioning, while a range of other noble metals and their oxides have been investigated as the additive to play the lead role in E-mode. In addition, since water is usually introduced to the cell at the oxygen electrode during E-mode, the catalyst layer on this side must be able to retain its structure and

functioning in the presence of liquid water, and its constituent materials must not corrode or otherwise degrade in the presence of both this water and oxygen.

A selection from the literature of the catalyst materials and loadings that have been trialled in experimental URFCs is provided in Table 9.1. Materials mixed with Pt in the oxygen-side catalyst layer include the pure metals, iridium, ruthenium and (occasionally) rhodium and titanium, or oxides of these such as iridium oxide and ruthenium oxide. The metals may be mixed as a powder (Ioroi *et al*., 2002) or sometimes an alloy is formed, for example, between Pt and Ru. Alternatively a compound containing two or more of the active catalyst materials, such as Pt IrO_x and Pt RuO_x can be formed.

For example, in a mixed iridium–platinum catalyst, Ir will be the dominant contributor to the oxygen evolution reaction in E-mode, but will be practically inactive in FC mode when the Pt will be active. Ruthenium and ruthenium oxide play a similar role, and are sometimes also mixed with Ir and IrO_2 since the latter are less costly and also have better electrical conductivity (Cisar *et al*., 2005). Advantages of using the oxides rather than the pure metals are lower cost and greater resistance to corrosion. Further information on the performance of experimental URFCs using different catalysts and loadings is given later in Section 9.8.2, but there remains a dearth of such data collected systematically on a strictly comparable basis.

Various methods have been employed to distribute the mix of electrocatalysts across and to a lesser extent through) the catalyst layer (Fig. 9.11). One material (for example, Pt) may first be deposited by itself in the layer, and then the second material (say Ir) deposited, so that there are regions of high concentration of each material distributed randomly across the layer (Fig. 9.11a) (Ioroi *et al*., 2001). The materials may be mixed first (for example, in powder form), and the mixture subsequently distributed in the layer (Fig. 9.11b) (Ioroi *et al*., 2001). Or a compound of the two materials may first be formed and then this compound distributed (Fig. 9.11c). A complete alternative to the mixing approach is to have dual catalyst layers on the oxygen side, one layer active in E-mode and the other in FC-mode (Swette *et al*., 1992).

9.4.4 Gas diffusion and water transport layers

The GDB layer in a PEM URFC must not only provide a medium for the transport and even distribution of oxygen and hydrogen to and from the catalyst layers, but also transport water and electrons to and from these layers, and conduct heat away towards the end-plates (Fig. 9.12).

In a PEM fuel cell ‘waterproofed’ carbon paper or carbon cloth is usually adopted as the GDB, its porosity allowing passage of gases, and the carbon matrix serving as both an electrical and thermal conductor. However, as Pettersson *et al*. (2006) point out, carbon-based materials generally cannot

Table 9.1 A selection from the literature of the catalyst materials and loadings that have been trialled in experimental URFCs

Hydrogen	Oxygen side catalyst	Hydrogen side catalyst loading (mg/cm^2)	Oxygen side catalyst side catalyst loading (mg/cm^2)	Reference
Pt black	Pt black	1	1	Swette *et al*. (1994)
		4	4	Yim *et al*. (2004, 2005)
	Pt black + Ir black	2	2 (50:50 mixture)	Wittstadt *et al*. (2005)
		NA	2–4	Ioroi *et al*. (2002)
	PtIr	NA	0.5 (50:50)	Tsypkin *et al*. (2000)
		4	4 (different ratios of Pt and Ir)	Yim *et al*. (2005)
	Pt+IrO_2	0.4	0.4 (50:50 mixture)	Jorissen (2006) Liu *et al*. (2004) Zhigang *et al*. (1999)
		4	8–10	Ioroi *et al*. (2000)
	$PtIrO_x$	1	1 (40:60 mixture)	Swette *et al*. (1992)
		0.5–4	4 (different ratios of Pt and IrO_x)	Yim *et al*. (2005)
	PtRu	4	4 (different ratios of Pt and Ru)	Yim *et al*. (2005)
	PtRuIr	4	4 (different ratios of Pt Ru and Ir)	Yim *et al*. 2005)
	$PtRuO_x$	4	4 (different ratios of Pt and RuO_x)	Yim *et al*. (2005)
		1	1 (40:60)	Swette *et al*. (1994)
	RuO_2–IrO_2/Pt IrO_2 deposited Pt black	0.4	2 (Pt: IrO_2: RuO_2 = 50:25:25)	Zhang *et al*. (2007) Ioroi *et al*. (2001)
	Pt black+$Na_xPt_3O_4$	1	3 (33:67)	Swette *et al*. (1994)
	$Na_xPt_3O_4$	1	2	Swette *et al*. (1994)
	RuO–IrO_x	1	2 (50:50)	Swette *et al*. (1994)
	RhO_2	1	1	Swette *et al*. (1994)
C supported Pt	Pt black + Ir black	2	2 (50:50)	Murphy *et al*. (1995)
Pt/C	Pt black + IrO_2	0.5	3 (70:30 mixture)	Song *et al*. (2006)
Pt/Ir on C	Pt+Ir	1(Ir content 80% of Pt)	1 mg/cm^2 (Ir content 80% of Pt)	Dhar (1993)
Hamilton Standard E5	E5	1 4	1 4	Mitlisky *et al*. (1998a,b, 1999a,b,c)

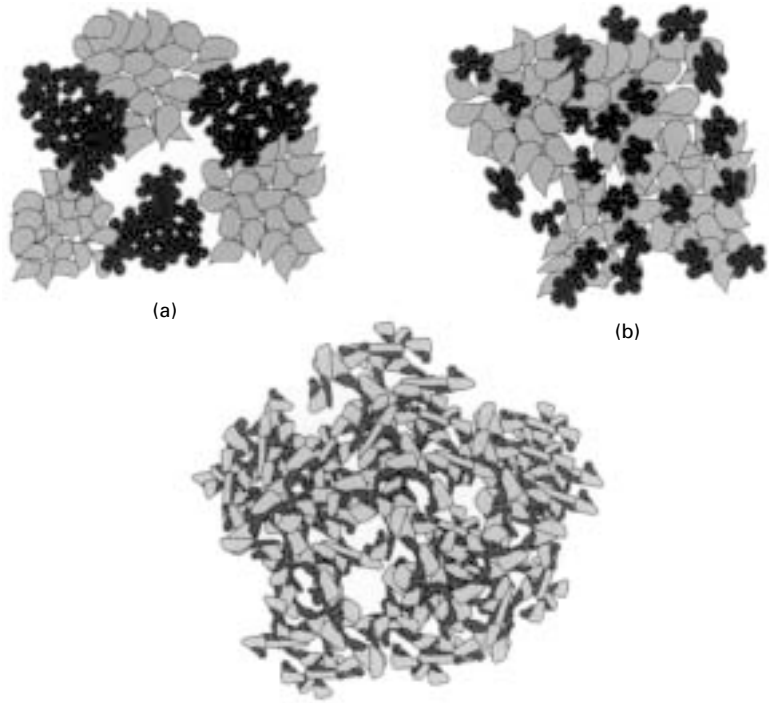

9.11 Diagrammatic representations of the various ways of achieving a mixture of two catalysts distributed throughout the oxygen-side catalyst layer: (a) sequential deposition creating concentrated regions of each material distributed randomly across the layer; (b) prior mixing of the two catalysts and then distribution of the mixture across the layer; and (c) formation of an alloy or compound between the two materials and then distribution of this compound.

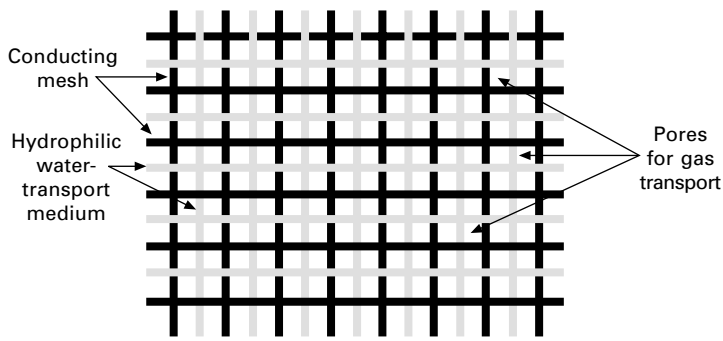

9.12 Schematic showing the basic functionality of the gas diffusion and water transport layers.

be used as the GDB of a URFC because such materials tend to corrode at high potentials on the oxygen electrode side during E-mode, and an appropriate balance between hydrophobic and hydrophilic properties must be struck to ensure proper functioning in both modes. In FC-mode the oxygen-side GDB must be sufficiently hydrophobic to prevent water flooding, and in E-mode sufficiently hydrophilic to maintain water supply for the electrolysis reaction. The hydrogen-side GDB must also be able to cope with the influx of water due to osmotic drag across the membrane by the moving protons in E-mode.

In place of carbon paper or cloth, a metal core is frequently used in the GDBs in URFCs for conduction of electrons and heat. To furnish the porosity required for gas transport, the metal core may be in the form of a woven metal cloth, mesh, perforated sheet, thin metal felts, expanded metal sheet, or metal foam. Cores in these forms made from the following metals have been investigated (Cisar *et al*., 2005):

- titanium, zirconium, hafnium, niobium and tantalum;
- aluminium, copper, nickel, protected from oxidation by appropriate coatings;
- precious metals such as platinum, gold, ruthenium, iridium and palladium;
- oxidation-resistant alloys, such as stainless steels, Inconels and Hastelloys.

Cisar *et al*. (2005) report that titanium gold-plated woven titanium cloth mesh was found to be the most effective. They further propose coating the metal core with a waterproofing agent to ensure water-free channels for gas flow, and then binding an additional electrically conducting compound to the metal core using a polymeric binder – polytetrafluoroethylene (that is, Teflon), perfluorosulphonic acids (for example, Nafion), or combinations of these. While this compound must in itself be hydrophilic to transport water to catalyst sites in E-mode, it must also be treated with small amounts of a hydrophobic material to limit water ingress sufficiently to prevent channel flooding and hence inhibition of gas flow in FC-mode. There thus need to be randomly distributed hydrophilic and hydrophobic regions throughout the GDB, which may vary in dimension between several microns and a few millimetres, or the alternating regions may be arranged in an orderly pattern. Cisar *et al*. (2005) tested the following materials for use as the additional conducting compound in the metal core:

- nitrides of tantalum, zirconium, niobium or titanium;
- titanium boride or titanium carbide;
- a mixture of ruthenium oxide and titanium–ruthenium oxide;
- a solid solution of ruthenium oxide and titanium oxide.

The latter two materials were found to be among the best performers.

An alternative approach to oxygen-side GDB design is to employ an entirely metal core and allow flooding in E-mode, but then clear the water by

blowing in air under pressure on switching to FC-mode. While this approach leads to a slightly longer time to switch between full functioning in the two modes, it permits a much simpler and cheaper GDB to be utilised.

9.5 Flow channels, seals and end-plates

Reactant and product gases, and where necessary liquid water, are carried to and from the gas diffusion layers in channels machined on the inner surfaces of plates (Fig. 9.5). The width and depth of the channels, as well as the pattern in which the machining is done, affect the evenness of the distribution of reactants and collection of products across the active area of the MEA (Das, 2002). Pressure losses in the gas manifold occur mainly on the oxygen side, since the resistance to hydrogen is very low (Mikkola, 2000). The plates must be very good electrical and thermal conductors, so are typically made from graphite or metals (Rismanchi and Akbari, 2008). Song *et al*. (2006) suggest titanium materials are the most suitable for these plates in URFCs. The plate containing the channels, or sometimes an additional metal plate, also serves as the current collector on each side of the cell, and the end-plate that holds the whole cell together (Fig. 9.5). It is in this plate (or the separate end-plate) that, if required, coolant also flows to regulate the temperature of the cell in FC-mode. Additional channels, completely separate to those for gas flow, are used for the coolant stream.

A number of different patterns for the flow channels have been tried, as in dedicated PEM fuel cells and electrolysers (Ito *et al*., 2005). Parallel channels with headers (Fig. 9.13a) is one of the simplest patterns, but may lead to pressure imbalances between adjacent channels and gas blockages (Mennola, 2000) The serpentine pattern (Fig. 9.13b) patented by Ballard Power Systems overcomes these problems because the differential pressure between inlet and outlet forces stagnant water out of the channels (Hoogers, 2003). The mirrored flow field pattern (Fig. 9.13c) has been patented by General Motors. Another option is to use a metal mesh to provide the gas flow field (Hoogers, 2003).

It is important to have good electrical contact – that is, low contact resistance – between the plate containing the gas flow channels and the GDB. Contact resistance is a function of the contact pressure between the surfaces, and hence the torque on the clamping bolts holding the layers of the overall cell together (Roshandel and Farhanieh, 2007) (Fig. 9.5).

Elastomeric gaskets and seals are required on each side of the MEA to keep the hydrogen and oxygen within their respective regions, and prevent leakage to the external environment. Materials used for such gaskets include silicone rubber, Teflon and Teflon-coated glass-fibre thread plus adhesive (Atiyeh *et al*., 2007).

An alternative design approach to having separate GDBs and gas flow channel plates is to incorporate a structure to transport gases and water

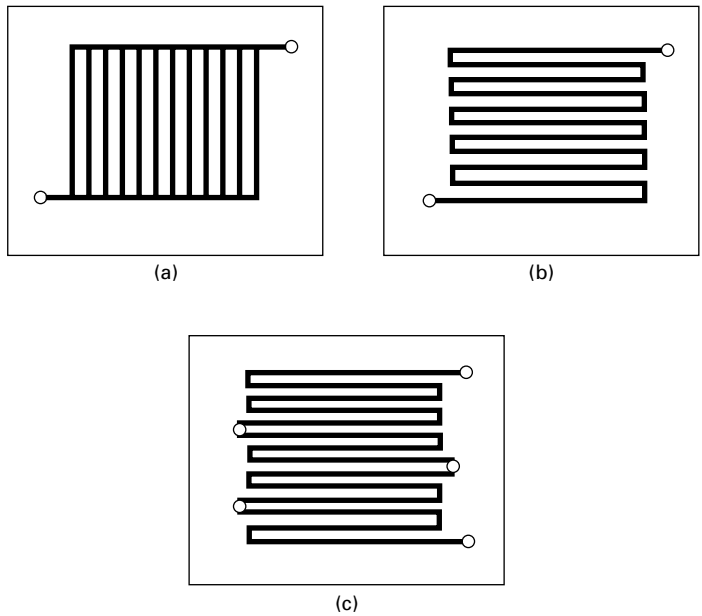

9.13 Various patterns for the gas flow channels: (a) parallel channels with headers; (b) serpentine; (c) the mirrored flow field pattern patented by General Motors (gas inlets in FC mode are shown on the right hand side and outlets on the left).

directly into the catalyst layer itself, to form so-called 'gas diffusion electrodes' (Petterson *et al*., 2006).

9.6 Unitised regenerative fuel cell stacks

The design of URFC stacks – that is, multiple URFCs laid directly one upon the other – involves similar considerations to those in designing a dedicated fuel cell stack, or a dedicated electrolyser stack, yet there are some additional challenges stemming from the required reversibility of the URFC stack. A typical arrangement for a PEM URFC stack is shown in Fig. 9.14, where the basic similarity to a PEM fuel cell stack is apparent. But key differences are the following:

- The channel configuration in the bipolar plates must provide both efficient hydrogen and oxygen gas transfer to the GDB, and water vapour from the O-side GDBs, in FC-mode; and gas flows in the reverse direction, plus water inflow to the O-side GDBs, in E-mode.
- Flooding of these channels and the passages in the GDBs must be prevented in FC-mode, otherwise incoming gas flow will be inhibited.
- The bipolar plates must be made of a good electrically and thermally

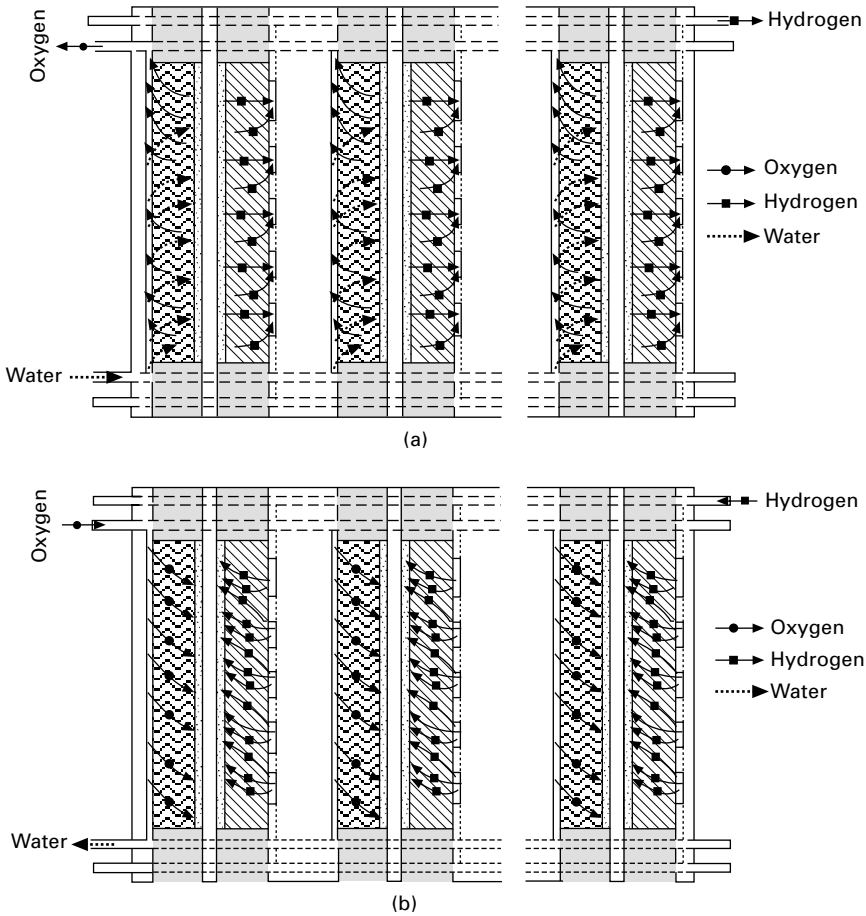

9.14 Typical arrangement of a URFC stack: (a) E-mode; (b) FC-mode.

conducting material that will not corrode in a wet oxygen-rich environment. Plates made from graphite, as often used in fuel cell stacks, have been employed, but materials such as nickel foam, titanium and stainless fibre-sintered plate are preferred in URFC stacks (Ito *et al*., 2005).

- Similar operating conditions in all cells within the stack in terms of gas flows, water flows, pressure and temperature need to be maintained in both modes, so that each cell output is around the same value.
- The water management system must in E-mode ensure sufficient water is available on the O-side electrodes of each cell in the stack, and remove water that gathers on the H-side electrodes due to osmotic drag of water molecules by H^+ ion across the membrane. On switching to FC-mode, this system must remove any excess water in O-side GDBs and flow

channels, remove water vapour produced by the overall electrochemical reaction and ensure the membrane remains hydrated.
- The flow of heat transfer fluid (usually water) through separate channels in the bipolar plates (or sometimes a separate plate) must provide cooling of the stack in FC-mode, while providing heat from the environment in E-mode.

Accordingly, water and gas flow management pose special challenges in URFC stack design. Various design and material selection features have been proposed to address these challenges (Kirk *et al*., 2003) but no standardised solution has yet evolved.

9.7 Unitised regenerative fuel cell systems

In order to function as an electrical energy storage system, a URFC or URFC stack needs to be incorporated into an overall system (Fig. 9.15). While URFC systems may vary considerably in detailed design, the principal components and their functions are generally the following:

- The URFC or URFC stack.
- Gas storages, with pressure sensors and valves actuated by the central

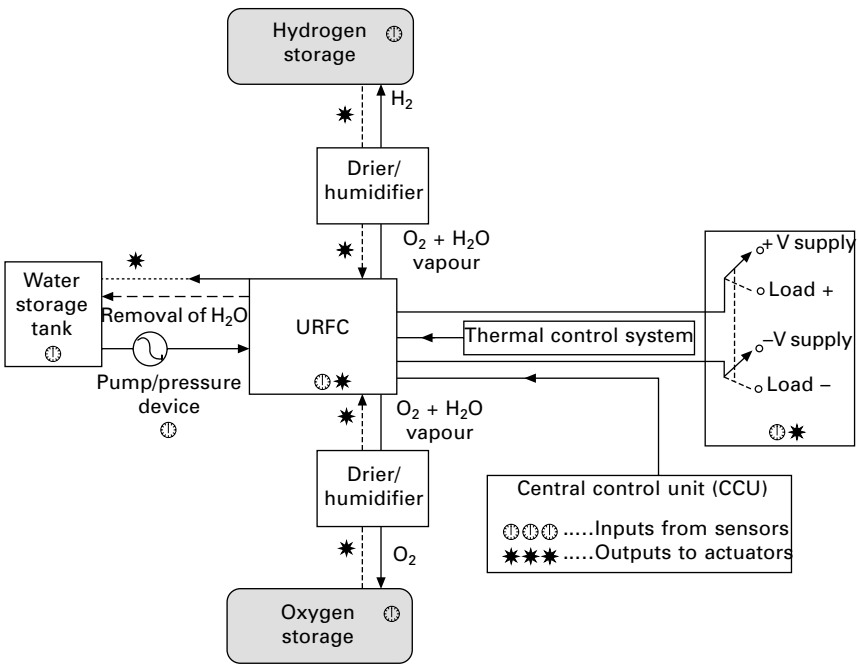

9.15 A schematic of a generalised URFC system.

control unit. To date, metal or composite cylinders have generally been used for gas storage in URFC systems, but in the future solid-state storage media such as metal hydrides may be used for hydrogen.

- Gas driers (or other phase separator), that extract water from the hydrogen–water vapour and oxygen–water vapour mixtures emanating from the stack in E-mode prior to the gases entering the storage cylinders; and gas humidifiers that add water vapour to the hydrogen and oxygen flowing from the storages before they enter the stack in FC-mode to prevent drying out of the membrane. In some systems, a 'regenerative drier' is used that performs the drying function in E-mode and the humidification function in FC mode by employing a reversible cooling/water condensation and heating/water evaporation process in the same apparatus (Burke, 2003).
- A deionised water supply and return system. A pump may be employed to introduce water into the stack during E-mode, or the pressure in the water storage tank can be maintained above that in the stack so that water is drawn in passively. Liquid water accumulates on the hydrogen-sides of each cell in E-mode due to osmotic drag, which must be removed either continuously, or before switching to FC mode. Ideally this water is returned to the water supply tank, though care must be taken to ensure the small quantity of hydrogen dissolved in it does not allow any undesirable mixtures of hydrogen and oxygen to form. Any excess water in O-side channels or GDBs must be removed on switching from E to FC mode, and is preferably returned to the water storage tank.
- A thermal regulation system that controls flow of a heat transfer fluid (usually water) through the bipolar or separate cooling plates in the URFC stack to provide cooling in FC-mode. In E-mode this flow is either stopped or maintained to supply additional heat if operation well above ambient temperature is desired.
- An overall system control unit, based on a programmable microprocessor. This unit uses real-time information about conditions in the various components from sensors (for example, pressure, temperature, gas detection, flow and level sensors) to regulate all operations automatically via actuators, log data on performance, detect any problems that arise, and if necessary set off alarms and shut down the system.

To date, relatively few URFC systems have been designed, built and operated. Some examples are Mitlitsky *et al.*'s (1996b) IMPRESS for small satellites; Burke and Jakupca's (2005) URFC design employing heat pipes for cooling in space applications; and Distributed Energy Systems' Unigen system (Fig. 9.3).

9.8 Performance and costs of unitised regenerative fuel cells

9.8.1 V–I curves in electrolyser and fuel cell modes

A number of relevant features of URFC operation can be gleaned from a consideration of typical polarisation curves for E-mode and FC-mode functioning of a PEM cell per unit effective membrane area. By normalising the curves in the two modes to unit effective membrane area we are in effect representing here the URFC situation in which a cell with a given effective area operates reversibly in the two modes. In a DRFC, on the other hand, the electrolyser cell can have a different active area to the fuel cell, and this difference must be taken into account in calculating modal current densities. Dealing with current densities rather than absolute current values, and later power densities, also facilitates comparison between cells of different areas.

Some typical V–I curves for URFCs of varying performance are shown in Fig. 9.16a – with similar characteristics to those obtained by Mitlitsky *et al*. (1998b) – and some experimentally determined curves in Fig. 9.16b. In actuality E-mode current flows in the opposite direction to FC-mode current so the current densities in the two modes have opposite sign, rather than the same sign as shown here.

In E-mode the cell current density rises steadily with increasing voltage once the cut-in voltage is exceeded, while in FC-mode the cell voltage falls with increasing current density. The E-mode and FC-mode curves thus diverge from each other on opposite sides of the reversible voltage line with increasing current density. Generally speaking good reversible cell performance is characterised by the following features on the combined polarisation curve:

- A cut-in voltage in E-mode as close to the reversible voltage (V~1.23 V, depending on cell temperature) as possible.
- An open circuit (zero current) voltage in FC-mode as close to the reversible voltage as possible.
- The slopes of the curves in E-mode and FC mode as low as possible (in absolute terms), so that the divergences from the reversible voltage line with increasing current density are minimised.
- A maximum current density in E-mode as high as possible, so that the input power density can be maximised.
- A maximum power point in FC-mode as high as possible, so that output power is maximised.

The maximum power in E-mode occurs at the maximum current density, when the cell voltage is also at a maximum. In FC-mode the maximum power occurs at a current density less than the maximum, when the magnitude of the slope of the FC-mode curve (neglecting its sign) is equal to the cell

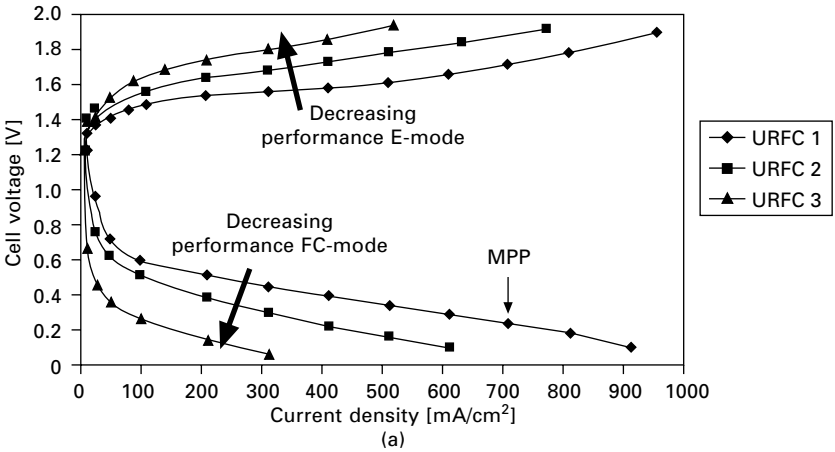

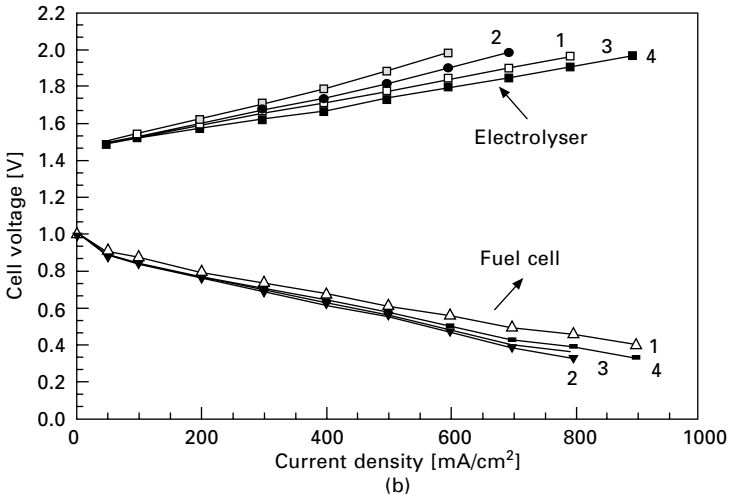

9.16 (a) Typical *V–I* curves for URFCs of varying performance. The point MPP indicates the maximum power point in FC-mode for cell 1. (b) Experimentally measured *V–I* curves for a URFC from Zhigang *et al.* (1999), where the numbers refer to successive cycles between modes.

voltage divided by the cell current density at that point, as shown by the point marked MPP for one of the FC-mode curves in Fig. 9.16a.

Inspection of the V–I curves in Fig. 9.16a thus reveals that cell number 1 performs better in both modes than cell 2, which in turn performs better than cell 3. The rank order of performance for the URFC curves shown in Fig. 9.16b, however, is different in the two modes: in E-mode, curve 4 (that is, performance in cycle 4) is best followed in turn by that in cycles 3, 1 and 2; in FC-mode, curve 1 is best, then 4, 3 and 2.

Generally the performance of a URFC in each mode will be slightly inferior to that of a separate electrolyser and fuel cell of the same effective cell areas, because of the difficulty in optimising the performance of the bifunctional electrodes in both modes. The aim of URFC design is clearly to achieve as close to the performance of comparable discrete cells as possible.

Another useful performance indicator of an RFC is the modal power ratio: the ratio of the maximum input power to the maximum output power. The modal power ratio for a URFC is necessarily greater than one, and typically in the range 2 to 10. Generally the lower the modal power ratio, the more reversibly a URFC is performing, so that minimising this ratio is also a design goal. Nevertheless, it is also necessary to take into account modal energy efficiencies in assessing overall cell performance. Of course, in a DRFC the modal power ratio can be set to whatever is desired for the particular application since the capacities of the electrolyser and fuel cell can be independently chosen.

9.8.2 Modal and roundtrip energy efficiencies

Key performance measures for an RFC are the energy efficiencies in E-mode and FC-mode, and the overall roundtrip energy efficiency.

On the basis of the high heating value (HHV) of hydrogen (142 MJ/kg), the energy efficiency in E-mode is given by:

$$\eta^{E} = \frac{\dot{m}^{E}_{H_2} \times \text{HHV}}{\text{input power density}}$$

or

$$\eta^{E} = \frac{\mu^{E} \times 1.48}{V_{\text{cell}}}$$

where $\dot{m}^{E}_{H_2}$ is the rate of production of hydrogen per unit effective area of cell (in kg/s/cm^2), the input power density is in W/cm^2, and μ^{E} is the Faraday efficiency of the cell in E-mode (the actual rate of hydrogen production expressed as a percentage of the theoretical maximum rate of hydrogen production for the given current). Hence the energy efficiency in E-mode varies with V_{cell} and thus with current density too. Maximum energy efficiency occurs when V_{cell} is at a minimum – that is, at zero current density – and energy efficiency declines with increasing current density (and hence V_{cell}) thereafter.

Similarly the energy efficiency in FC-mode is given by:

$$\eta^{FC} = \frac{\text{output power density}}{\dot{m}^{FC}_{H_2} \times \text{HHV}}$$

or

$$\eta^{FC} = \frac{\mu^{FC} \times V_{cell}}{1.48}$$

where $\dot{m}_{H_2}^{FC}$ is the rate of consumption of hydrogen per unit effective area of cell (in kg/s/cm^2), the output power density is in W/cm^2, and μ^{FC} is the fuel utilisation coefficient of the cell in FC-mode (the effective rate of hydrogen consumption by the cell for a given current, expressed as a percentage of the rate of hydrogen input) (Larminie and Dicks, 2003). Maximum energy efficiency in FC-mode occurs when V_{cell} is at a maximum – again at zero current density – as in E-mode, and energy efficiency declines with increasing current density.

If an RFC is used in a system to store electrical energy in the form of hydrogen and subsequently regenerate electricity from the hydrogen stored, the roundtrip energy efficiency of the overall energy storage system is given by:

$$\eta^{RT\ system} = \eta^{E} \times \eta^{FC} \times \eta^{storage} = \eta^{RT} \times \eta^{storage}$$

where $\eta^{storage}$ measures the net energy efficiency of the hydrogen storage system, taking into account any energy required to get the hydrogen into and out of the storage (for example, to compress the hydrogen in the case of high-pressure hydrogen gas storage, and friction losses in the form of heat on exit), and any losses of hydrogen from the storage over time. Since $\eta^{storage}$ will always be less than 100%, η^{RT} is the upper bound for the roundtrip energy efficiency of an electrical energy storage system based on an RFC.

Roundtrip energy efficiency is one of the most important performance measures of an RFC, since it indicates how much of the electrical energy input to a cell is converted to hydrogen, and in turn how much of the energy in the hydrogen generated can be converted back into electricity. It thus reflects the influence on performance of the energy efficiencies in both modes. Since η^{RT} varies with the prevailing V_{cell} values (and hence current densities) in both E- and FC-modes, a useful reference value of η^{RT} is that corresponding to the maximum input power in E-mode and the maximum output power in FC-mode. However, in a situation where the URFC operates over a range of power inputs and outputs, the average energy efficiency will be much greater than this reference value, which in effect is a lower bound or worst case value.

Measured performance data for a large number of experimental URFCs as reported in the literature are presented in Table 9.2, and their corresponding physical design characteristics given in Table 9.3. The maximum input power densities (in W/cm^2) and maximum current density (in A/cm^2) in E-mode, and maximum output power densities and current densities in FC-mode are taken directly from data or graphs given in the source papers. The values for

Table 9.2 Measured performance data for experimental URFCs reported in the literature. The corresponding physical design characteristics of these cells is given in Table 9.3. Values for the modal and roundtrip energy efficiencies are estimated (see text)

Cell	Reference	Input power density (W/cm^2)	E-mode current density (A/cm^2)	E-mode energy efficiency (%)	FC-mode output power density (W/cm^2)	FC-mode current density (A/cm^2)	FC-mode energy efficiency	Round trip energy efficiency (%)	Modal power ratio
BCS Technology	Dhar (1993)	0.75	0.15	28.1	0.12	0.39	19.2	5.4	6.4
Giner, Inc. (FC+)	Swette *et al.* (1994)	2.15	1.00	65.5	0.36	0.50	45.5	29.8	6.1
Giner, Inc. (FC and E +)	Swette *et al.* (1994)	1.75	1.00	80.4	0.50	1.00	32.1	25.8	3.5
Giner, Inc. (FC+)	Swette *et al.* (1994)	1.85	1.00	76.1	0.59	0.90	41.7	31.7	3.2
Giner, Inc.	Swette *et al.* (1994)	1.95	1.00	72.2	0.40	1.00	25.7	18.5	4.9
Fraunhofer-Institute for Solar Energy Systems	Ledjeff *et al.* (1994)	1.65	1.00	85.3	0.47	0.68	44.9	38.3	3.5
LLNL 01 (49 C)	Mitlitsky *et al.* (1998a)	0.93	0.43	65.4	0.13	0.20	42.3	27.7	7.0
LLNL 01 (82 C)	Mitlitsky *et al.* (1998a)	1.46	0.67	64.6	0.19	0.30	40.6	26.2	7.7
LLNL Cell 9734A	Mitlitsky *et al.* (1998a)	2.21	1.08	68.5	0.46	0.86	34.3	23.5	4.8
LLNL Cell 9804A	Mitlitsky *et al.* (1998a)	2.76	1.29	65.8	0.92	1.70	34.5	22.7	3.0
Dalian Institute of Technology	Zhigang *et al.* (1999)	1.80	0.90	70.4	0.36	0.90	25.7	18.1	5.0
Osaka National Research Institute	Ioroi *et al.* (2000)	1.70	1.00	82.8	0.35	0.70	32.1	26.5	4.9
National Institute of Advanced Industrial Science and Technology	Ioroi *et al.* (2001)	1.70	1.00	82.8	0.42	0.70	38.5	31.9	4.0
National Institute of Advanced	Ioroi *et al.* (2002)	0.98	0.50	72.2	0.40	0.50	51.3	37.0	2.4

Table 9.2 (Continued)

Cell	Reference	Input power density (W/cm^2)	E-mode current density (A/cm^2)	E-mode energy efficiency (%)	FC-mode output power density (W/cm^2)	FC-mode current density (A/cm^2)	FC-mode energy efficiency	Round trip energy efficiency (%)	Modal power ratio
Industrial Science and Technology-A National Institute of Advanced Industrial Science and Technology-B	Ioroi *et al.* (2002)	0.93	0.50	76.1	0.29	0.42	44.9	34.1	3.1
Zentrum fuer Sonnenenergie und Wasserstoff-Forschung Baden-Wuerttemberg	Jorissen (2006)	1.71	0.40	32.9	0.36	0.90	25.7	8.4	4.8
Dalian Institute of Technology	Yim *et al.* (2004)	2.70	1.35	70.4	0.23	0.75	19.2	13.5	12.0
Korea Institute of Energy Research	Yim *et al.* (2005)	0.80	0.50	88.0	0.70	1.40	32.1	28.2	1.1
Fraunhofer Instutute for Solar Energy Systems	Wittstadt *et al.* (2005)	1.15	0.58	70.4	0.20	0.33	38.7	27.2	5.9
Dalian Institute of Technology	Song *et al.* (2006)	3.60	2.00	78.2	0.21	1.23	10.9	8.5	17.3
LLNL IMPRESS	Mitlitsky *et al.* (1996b)	0.29			0.19				1.5

Table 9.3 The physical characteristics of the experimental URFCs for which performance data are given in Table 9.2.

Cell	Reference	Effective membrane area (cm^2)	Hydrogen side		Oxygen side		Other features
			Catalyst material	Loading (mg/cm^2)	Catalyst material	Loading (mg/cm^2)	
BCS Technology	Dhar (1993)	5	Pt/C	0.5	Pt + IrO_2	3	
Giner, Inc. (E+)	Swette *et al.* (1994)	40	Pt	1	Pt	4	Optimised for FC performance
Giner, Inc. (FC and E +)	Swette *et al.* (1994)	40	Pt		Pt/IrO_2	1–3 (40:60 mix)	Optimised for bifunctional performance
Giner, Inc. (FC+)	Swette *et al.* (1994)	40	Pt		Pt–Na_x Pt_3O_4	1–3 (67:33 mix)	2 layer catalyst structure bonded to the PEM
Giner, Inc.	Swette *et al.* (1994)	40	Pt		Pt–Na_x Pt_3O_4		Single layer of Na_x Pt_30_4 with 10% ionomer bonded to PEM
Fraunhofer-Inst for Sol. Energy Syst.	Ledjeff *et al.* (1994)	12	Pt	2–4	Ir	2-4	
LLNL IMPRESS	Mitlitsky *et al.* (1996b)	105.2	E-5		E-5		
LLNL 01 (49°C)	Mitlitsky *et al.* (1998b)	46	E-5	4	E-5	4	Performance at 49°C
LLNL 01 (82°C)	Mitlitsky *et al.* (1998b)	46	E-5	4	E-5	4	Performance at 82°C
LLNL Cell 9743A	Mitlitsky *et al.* (1998b)	46	E-5	4	E-5	4	Performance at 91°C
LLNL Cell 9804A	Mitlitsky *et al.* (1998b)	46	E-5	1	E-5	1	Performance at 91°C
Dalian Institute of Technology	Zhigang *et al.* (1999)	5	Pt black	0	Pt + Ir	0.2 (50:50 mix)	
Osaka National Research Institute	Ioroi *et al.* (2000)	10	PTFE bonded porous Pt electrode		PTFE bonded porous Pt–IrO_2	8-10 (50:50 mix)	

Table 9.3 (Continued)

Cell	Reference	Effective membrane area (cm^2)	Hydrogen side		Oxygen side		Other features
			Catalyst material	Loading (mg/cm^2)	Catalyst material	Loading (mg/cm^2)	
National Institute of Advanced Industrial Science and Technology	Ioroi *et al.* (2001)	10	Pt black		Deposited IrO_2/Pt	(20%/80%)	
National Institute of Advanced Industrial Science and Technology-A	Ioroi *et al.* (2002)	10	Pt black		Pt black + Ir black	2–4	PTFE loading 5–7% is best performer
National Institute of Advanced Industrial Science and Technology-B	Ioroi *et al.* (2002)	10	Pt black		Pt black + Ir black	2–4	Nafion loading 7–9% is best performer
Zentrum fuer Sonnenenergie und Wasserstoff-Forschung Baden-Wuerttemberg	Jorissen (2006)		Pt black	0.4	Pt black + Ir black	0.4 (50:50 mix)	
Dalian Institute of Technology	Yim *et al.* (2004)	5	Pt	0.4	Pt + IrO_2	0.2 (50:50 mix)	
Korea Institute of Energy Research	Yim *et al.* (2005)	10	Pt black	4	PtIr	4	
Fraunhofer Inst. for Solar Energy Systems	Wittstadt *et al.* (2005)	49	Pt black	2	Pt + Ir black	2	
Dalian Institute of Technology	Song *et al.* (2006)	5	Pt/C	0.5	Pt + IrO_2	3	

modal power ratios at these maximum power points are calculated directly from these experimental values.

In the absence of reported data on the hydrogen production and consumption rates, we have estimated these rates on an optimistic basis assuming a Faraday efficiency of 95% in E-mode (Ulleberg, 1998) and a fuel utilisation coefficient also of 95% in FC-mode (Larminie and Dicks, 2003). These estimated rates were then used to obtain indicative values for the energy efficiencies in the two modes and the roundtrip energy efficiency (at maximum power input and output), as shown in the shaded columns in Table 9.2. The estimates for roundtrip energy efficiency also assume zero losses of hydrogen in the storage process. These energy efficiencies should therefore be taken as indicative only (and as upper bounds), since they rely on some exogenous assumptions and are not fully based on measured experimental data. It is important in future URFC experimental studies that hydrogen production and consumption rates are measured directly so that energy efficiency data can be obtained entirely from the experimental data.

The input and output power densities of the experimental URFCs reviewed are plotted in Fig. 9.17, together with lines of constant modal power ratio between 1 and 5. As expected all cells had a modal power ratio greater than 1, with most having ratios above 3. Generally a low modal power ratio is advantageous, but in conjunction with a high value of FC-mode power density, as illustrated by the shaded region in Fig. 9.17.

The estimated roundtrip energy efficiencies at maximum power input and output are shown graphically in Fig. 9.18. As pointed out earlier, if the

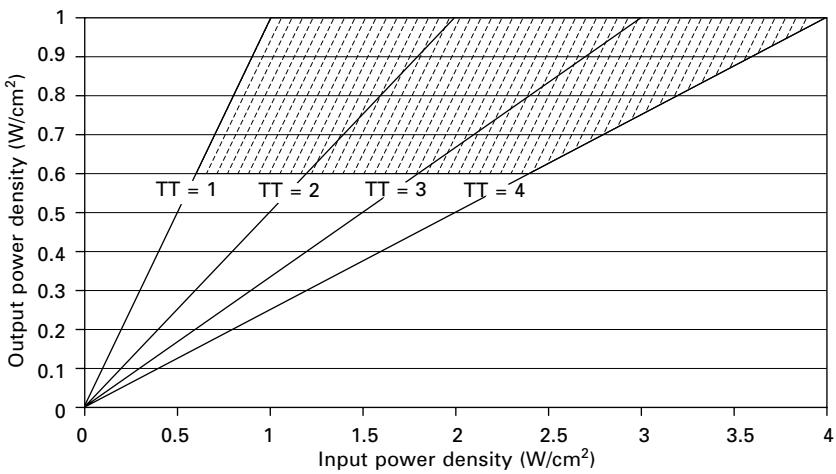

9.17 The input and output power densities of experimental URFCs (see Table 9.2), and lines of constant modal power ratio (Π). The shaded region indicates the desirable domain of operation.

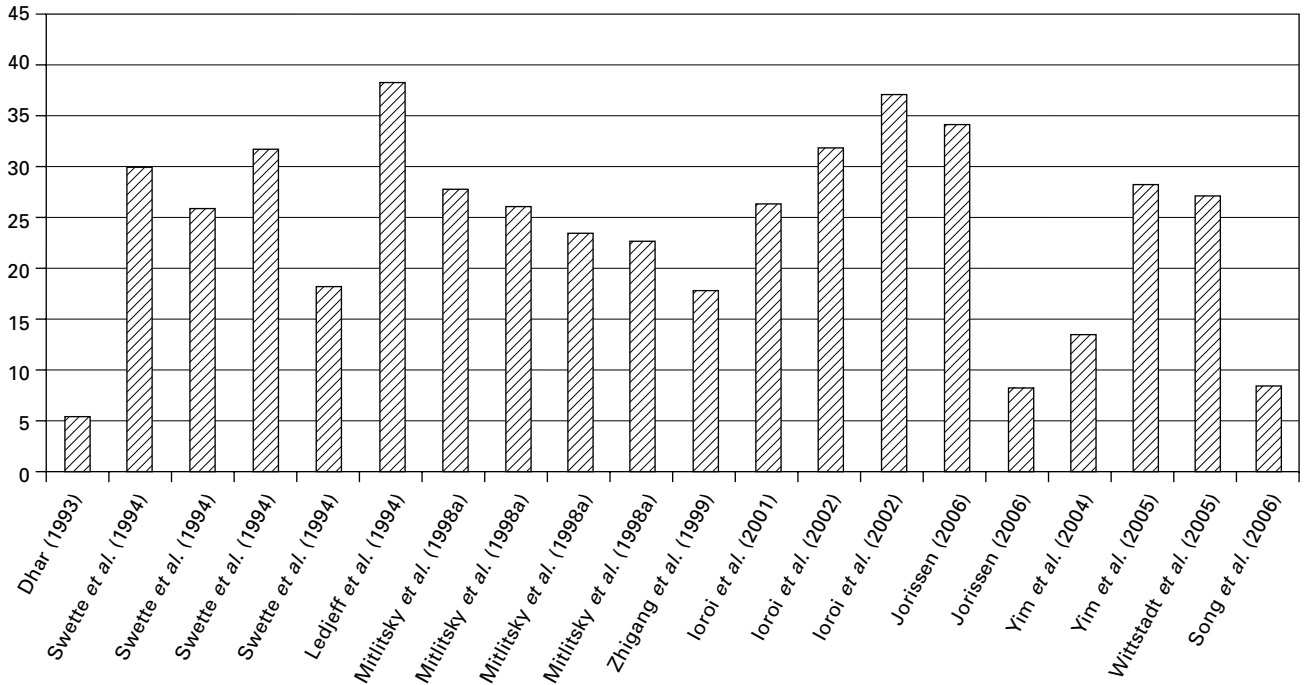

9.18 Estimated roundtrip energy efficiencies at maximum power input and output of the experimental URFCs reviewed.

URFC operates over a range of power inputs and outputs, the average roundtrip energy efficiency will be much greater than the reference value shown in this figure. Alongside roundtrip energy efficiency it is also relevant to consider the maximum power outputs of the cells in FC-mode, since together these two parameters give a good indication of a reversible cell's overall performance. The aim is to get both a high roundtrip energy efficiency and a high output power density at the same time.

Among the URFCs reviewed here, Ledjeff *et al*.'s (1994) cell, constructed at the Fraunhofer-Institute for Solar Energy Systems in Germany, has the highest estimated roundtrip energy efficiency at 38.3% (E-mode 85.3%; FC mode 44.9%). The maximum output power density was 0.4725 W/cm^2. This cell, with an active membrane area of 12 cm^2, used an Ir catalyst (loading 2 mg/cm^2) on the O-side and Pt on the H-side.

Three cells constructed at the National Institute of Advanced Industrial Science and Technology in Japan have the next highest estimated roundtrip energy efficiencies. Of these, Ioroi *et al*.'s (2002) cell came out highest at 37.0% (E-mode 72.2%; FC mode 51.3%), the latter value being the highest FC-mode energy efficiency of all the URFCs reviewed here. The maximum output power density was 0.4 W/cm^2. A mixture of Pt black and Ir black (2–4 mg/cm^2) treated with PTFE was used as the O-side catalyst and placed on Nafion 115. The PTFE content (5–7%) was found to improve the fuel cell performance.

Swette *et al*.'s (1992, 1994) cell made by Giner, Inc. also shows a relatively high estimated roundtrip energy efficiency of 31.7% (E-mode 76.1%; FC mode 41.7%), together with an output power density 0.585 W/cm^2. This cell employed a two-layer catalyst structure on the O-side (Section 9.4) consisting of very hydrophilic $Na_XPt_30_4$ (10% ionomer) and a less hydrophilic Pt transition layer bonded to the membrane.

To get an idea of the potential for improved performance of URFCs, if we combine the best E-mode performance of all the cells reviewed here (an 88% energy efficiency, by the Korea Institute of Energy Research reported by Yim *et al*., 2005), with the best FC-mode performance (51.3% by one of the National Institute of Advanced Industrial Science and Technology cells reported by Ioroi *et al*., 2001), the roundtrip energy efficiency obtained would be just over 45%. This compares with a separate electrolyser and fuel cell system maximum energy efficiency on the basis of current best-performing cells (say 95% in E-mode and 55%) of around 52%.

With respect to currently commercial systems, Proton Energy Systems claim a roundtrip energy efficiency for their Unigen 119 °F system of just under 40% at 538 mA/cm^2, just over 50% at 323 mA/cm^2, rising to a maximum of over 70% at near zero current density The energy efficiency at maximum delivered power is about 40% for this system (Molter, 1999; Smith 2000).

9.8.3 Performance degradation and lifetime

The standard way to measure the degradation in the performance of an RFC with repeated cycling between E- and FC-modes, and with duration of usage, is to measure the cell voltage for a fixed set of current densities in each mode after a given number of cycles (Mitlitsky *et al*., 1996a, 1998a,b). An increasing cell voltage in E-mode at a particular current density, and a decreasing cell voltage at a particular current density in FC-mode, indicate that cell performance is declining. Given the relationship between cell voltage and energy efficiency (Section 9.8.2), the change in cell voltage for a fixed current density with repeated cycling directly affects the modal energy efficiency.

It can be expected that the rate of performance loss with number of cycles will also depend on the form of each cycle, that is, on the respective periods of operation in E-mode and FC-mode. Mitlitsky *et al*. (1998a,b), for example, used a 5 min E-mode and 5 min FC-mode cycle. The performance loss over time, and hence the practical lifetime of the RFC, will thus depend on the number of cycles, the form of each cycle, and the time the cell is not used.

Experimental data on the degradation of URFC performance with number of cycles between modes and hence their practical lifetimes are relatively scarce. Some important pioneering work in this area was done by Mitlitsky *et al*. (1998b), who measured the change in cell voltage of a URFC with an active membrane area of 46 cm^2 at selected current densities in both E- and FC-modes at regular intervals over a total of 2000 cycles Each cycle comprised 5 min of operation at a constant current density (258 mA/cm^2) in E-mode and another 5 min operation in FC-mode (at 108 mA/cm^2). Even at the highest current density in FC-mode, this URFC showed only a small reduction in voltage, in the order of 0.5 V, after 2000 cycles.

Further experimental studies of the degradation of performance of URFCs operated according to a number of defined cycles are required to establish benchmarks for comparing URFCs of different designs, and assess their practical lifetimes.

9.8.4 Costs per unit energy stored and delivered

A first indication of the cost breakdown for a URFC can be obtained from the cost of producing a PEM fuel cell stack. For the latter, Carlson *et al*. (2005) projected a total cost of \$US360/m^2 for such a stack, comprising 78% for catalyst layers/electrodes, just over 6% for the membrane, 5% for the GDB, 5% for the end-plates/flow channels, and 6% for seals, assembly and the rest. The cost breakdown for a PEM fuel cell stack is thus heavily dominated by the cost of the catalyst layer/electrodes.

The cost of Nafion itself currently is in the range \$US 800 – 2000/m^2 (Zaidi *et al*., 2007). Typical prices on the international markets for the main metals used as catalysts in URFCs are given in Table 9.4.

Table 9.4 Typical prices on the international markets for the main metals used as catalysts in URFCs (October 2007) (sources: Los Alamos National Laboratory, 2007; Kitco, 2007; Mining Mix, 2007; Metalsplace, 2007)

Metal	Cost ($US/gram)
Pt	16–43
Ru	30
Ir	11–16

Reversible membrane electrode assemblies for use in URFCs are available commercially at a price of just over $US 100/cm^2 of active area (Lynntech, 2007). The price of these MEAs per square metre is thus very high (over $US 1 million/m^2), and the actual percentage cost of the membrane and metals used for catalysts in these early commercial products constitutes only a few percent of the total cost. Order of magnitude cost reductions can, however, be expected, when cells of much larger area are constructed.

In an URFC, the cost per unit area of the catalyst layer/electrodes would probably be higher than in a standard PEM fuel cell, owing to the additional expensive materials required for the oxygen-side catalyst layer, and the greater complexity and hence cost in forming this layer. In addition, the cost of the GDBs would be higher since more complex structures and more expensive materials than carbon cloth or paper must be used. On the other hand a URFC system will yield cost savings compared with an equivalent DRFC system that has to have two PEM cells, one as the electrolyser and the other the fuel cell, rather than just the one required by the URFC. Overall significant net cost savings through using a URFC rather than a DRFC can be expected, but at this stage the magnitude of these savings is uncertain.

The cost per unit energy stored and delivered of a URFC-based energy storage system can only be worked out with a detailed knowledge of the profile over time of the energy input and the energy supplied. Molter (1999) of Proton Energy Systems estimated that a URFC-based energy storage system with a capacity of 200 kWh would have a life-cycle cost of $US20 000 compared with $US120 000 for an equivalent lead acid battery system. The incremental life-cycle cost of adding an extra kWh of storage capacity was found to be $US30 for the URFC system, only one-fifth to one-tenth that for the battery system.

9.9 Conclusions and future trends

RFCs have a wide range of potential applications for storing electrical energy over relatively long periods and supplying it again when required. URFCs,

employing the same cell in both E and FC-modes, have economic, volumetric and mass advantages over a DRFC provided the performance of the bifunctional cell in each mode can be maintained close to that of the corresponding performance of a separate electrolyser and fuel cell.

The best-performing experimental PEM URFCs to date have roundtrip energy efficiencies in the range 30–38% at maximum power inputs and outputs, compared with a DRFC employing a very energy-efficient electrolyser and fuel cell of just over 50%. URFCs with roundtrip energy efficiencies of up to 45% should soon be technically achievable. Both URFCs and DRFCs have much higher average roundtrip energy efficiencies if operated over a range of powers. Raising the roundtrip energy efficiency above the 50% mark – arguably a necessary goal – will require advances in PEM (or other) cell design itself, and not just improvements in URFC designs. Given that the energy efficiency in FC-mode is invariably much lower than in E-mode, another approach to raising overall URFC system energy efficiency is to use heat generated by the cell when it is producing electricity for water or air heating. The URFC system would then provide combined heat and power, assuming, of course, that there is a suitable application nearby requiring low-temperature heat.

URFCs, with their lower total capital cost than DRFCs of comparable capacity, promise to enhance the economic competitiveness of hydrogen storage systems compared with alternatives such as batteries. While batteries have a higher roundtrip energy efficiency than hydrogen-based systems over the short term (up to 75%), their energy efficiency generally declines relatively fast as a result of self-discharge with the duration over which energy is stored. The URFC-based system is thus most likely to be advantageous in applications where energy has to be stored for a relatively long period (that is, several months or more), and the ratio of energy stored to power input (and output) is high. The advantages of the URFC system over a battery bank may then come in terms of both lower total volume and mass, as well as lower life-cycle costs.

Currently the main technical challenges the development of PEM URFC systems face are:

- The combined optimisation of performance in both fuel cell and electrolyser modes, so that higher roundtrip energy efficiencies can be realised. In particular, on the oxygen side, catalyst layers that have low overpotentials in both modes, and improved gas diffusion and water transport layers, are required, which can also be manufactured at low cost.
- The maintenance of the stability of the oxygen electrode, both in terms of resistance to corrosion or other degradation, and retention of structural integrity and strength after repeated cycling.
- The achievement of sustained, reliable and high-efficiency operation in both modes over a large number of modal switches and a long lifetime.

- For remote area power supply (RAPS) applications, a quick transition between full-functioning in E and FC-modes.
- Operation in E-mode at higher pressures, up to 10 or 20 bar, so that hydrogen and preferably oxygen too can be stored as compressed gas in vessels of practical size.
- Designing a balance of system that is as low cost as possible but maintains high reversible performance of the URFC.
- Mass production of URFCs and other system components to lower total costs.

There is a need for improved theoretical and computer simulation models of URFCs and URFC systems. Many more experimental studies to measure the performance of URFCs, under controlled and standardised conditions, using different catalysts and loadings, alternative gas diffusion and water transport layers, and alternative reversible cell designs, are required to find out which designs and materials are truly preferable. It is essential that these experimental studies measure hydrogen production and consumption rates as well as V-I polarisation curves so that modal and roundtrip energy efficiencies can be found directly from the experimental data.

Further experimental studies are also required into performance degradation of URFCs, operated according to a number of standard cycles over specified periods, to establish benchmarks for comparing URFCs of different designs, and assess their practical lifetimes.

Regenerative fuel cells embody the principles of reversibility that are the hallmark of sustainable energy systems of the future. Provided the technical challenges to improve energy efficiency, extend lifetimes, and lower unit costs can be surmounted, a plethora of terrestrial, aerospace and submarine applications of RFCs are present and waiting.

9.10 References

Ahn J and Holze R, 1992, 'Bifunctional electrodes for an integrated water-electrolysis and hydrogen-oxygen fuel cell with a solid polymer electrolyte', *Journal of Applied Electrochemistry*, **22**, 1167–1174.

Andrews J, Doddathimmaiah A K, Ali S M and Akbarzadeh A, 2005, 'Solar hydrogen systems for remote area power supply from a triple bottom line perspective', *Proceedings of the Solar World Congress*, Orlando, Florida, USA, August 6–12, 2005.

Atiyeh H K, Karan K, Peppley B, Phoenix A, Halliop E and Pharoah J, 2007, 'Experimental investigation of the role of a microporous layer on the water transport and performance of a PEM fuel cell', *Journal of Power Sources*, **170**, 111–121.

Burke K A, 2003, 'Unitized regenerative fuel cell system development', *First International Energy Conversion Engineering Conference* (American Institute of Aeronautics and Astronautics), Portsmouth, Virginia, 17–21 August, 2003.

Burke K A and Jakupca I, 2005, 'Unitized regenerative fuel cell system gas storage-radiator development', *Proceedings of Power Systems Conference*, Reno, Nevada, 2–4 November 2004.

Carlson E, Kopf P, Sinha J, Sriramulu S and Yang Y, 2005, 'PEM fuel cell cost status', *Fuel Cell Seminar*, Palm Springs, CA, 14–18 November 2005.

Cisar A, Murphy O J and Eric C, 2005, Lynntech, Inc., 'Bifunctional catalytic electrode', United States Patent 6,838,205, 4 January, 2005.

Coalson Jr R R, 1998, 'Unitized Regenerative Fuel Cells (URFC); Opportunities and Limitations in the Fields of Space Propulsion and Energy Storage', Master of Engineering Thesis, University of Colorado.

Das A, 2002, 'Modelling, Heat Transfer and System Integration for a 4kW Regenerative PEM Fuel Cell System', Master of Solar Energy Engineering Thesis, University of Massachusetts.

Dhar H P, 1993, 'A unitized approach to regenerative solid polymer electrolyte fuel cells', *Journal of Applied Electrochemistry*, **23**, 32–37.

Doddathimmaiah A K and Andrews J, 2006, 'The use of PEM unitised regenerative fuel cells in solar- hydrogen systems for remote area power supply', *Proceedings of the World Hydrogen Energy Conference*, Lyon, France, 12–14 June 2006.

Frank D G, 2000, 'The Effects of Cell Design and Materials of Construction on the Electrolysis Performance of a Proton Exchange Membrane Unitized Regenerative Fuel Cell', Master of Applied Science thesis, University of Toronto.

Hoogers G, 2003, *Fuel Cell Technology Handbook*, 1st edition, CRC Press, FL.

HyWeb Gazette, 2001, 'Proton Energy Systems cooperates with Marconi on reverse fuel cells for telecommunication systems', viewed 8 October 2007, http://www.hyweb.de/News/arcv201e.html#proton

Ioroi T, Kitazawa N, Yasuda K, Yamamoto Y and Takenaka H, 2000, 'Iridium oxide–platinum electrocatalysts for unitized regenerative polymer electrolyte fuel cells', *Journal of Electrochemical Society*, **147**, 2018–2022.

Ioroi T, Kitazawa N, Yasuda K, Yamamoto Y and Takenaka H, 2001, 'IrO_2 deposited Pt electrocatalysts for unitized regenerative polymer electrolyte fuel cells', *Journal of Applied Electrochemistry*, **31**, 1179–1183.

Ioroi T, Yasuda K, Siroma, Fujiwara N and Miyazaki Y, 2002, 'Thin film electrocatalyst layer for unitized regenerative polymer electrolyte fuel cells', *Journal of Power Sources*, **112**, 583–587.

Irvine J, Thomas S, Nairn J M, Connor P A, Rennie J, Feighery A, Jones F G E, Eccleston K L and Attidekou, P S, 2007, The University Court of The University of St Andrews, 'Reversible Fuel cell', International patent publication number WO 2007/091050, 16 August 2007.

Ito Y, Takai Y and Ishikawa T, 2005, Suzuki Motor Corporation, '*Fuel cell*', United States Patent 6,926,982, 9 August 2005.

Joos N I, Frank D and Cargnelli J, 2004, Hydrogenics Corporation, 'Unitized regenerative fuel cell with bifunctional fuel cell humidifier and water electrolyzer', United States Patent 6,833,207, 21 December 2004.

Jorissen L, 2006, 'Bifunctional oxygen/air electrodes', *Journal of Power Sources*, **155**, 23–32.

Kirk D W, Graydon J W and Thorpe S J, 2003, '*Electrochemical cell stacks*', United States Patent 6,527,921, 4 March, 2003.

Kitco, 2007, '24 hour spot platinum (bid)', viewed on 2 October 2007, <http://www.kitco.com/charts/liveplatinum.html>

Larminie J and Dicks A, 2003, *Fuel Cells Systems Explained*, 2nd edition, John Wiley & Sons, Chichester.

Ledjeff K, Mahlendorf F, Peinecke V and Heinzel A, 1994, 'Development of electrode/

membrane units for the reversible solid polymer fuel cell (RSPFC)', *Electrochimica Acta*, **40**(3), 315–319.

Lee H, Kim J, Park J, Joe Y and Lee T, 2004, 'Performance of polypyrrole-impregnated composite electrode for unitized regenerative fuel cell', *Journal of Power Sources*, **131**, 188–193.

Liu H, Yi B, Hou M, Wu J, Hou Z and Zhang H, 2004, 'Composite electrode for unitized regenerative proton exchange membrane fuel cell with improved cycle life', *Electrochemical and Solid-State Letters*, **7**(3), A56–A59.

Los Alamos National Laboratory viewed on 2 October 2007, 'Platinum', http://periodic.lanl.gov/elements/78.html, 'Ruthenium', http://periodic.lanl.gov/elements/44.html and 'Iridium', http://periodic.lanl.gov/elements/77.html

Lynntech Inc., 2007, M. Nelson, personal communication, Sept, 2007, College Station, Texas, USA.

McElroy J and Gottmann M 2005, '*Solid oxide regenerative fuel cell for airplane power generation and storage*, United States Patent 6,854,688, 15 February, 2005.

Mennola T, 2000, 'Design and Experimental Characterization of Polymer Electrolyte Membrane Fuel Cells', Degree of Licentiate of Technology Thesis, Helsinki University of Technology.

Metalspace, 2007, viewed on 2 October 2007, < http://metalsplace.com/news/?a=4700>

Mikkola T, 2000, 'Design and Experimental Characterization of Polymer Electrolyte Membrane Fuel Cells', Licentiate of Technology degree thesis, Helsinki University of Technology.

MiningMX, 2007, viewed on 2 October 2007, <http://www.miningmx.com/platinum/700747.htm>

Mitlitsky F, Myers B and Weisberg A H, 1996a, 'Lightweight pressure vessels and unitized regenerative fuel cells', *Fuel Cell Seminar*, Kissimmee, FL, November 17–20 1996.

Mitlitsky F, Groot W, Butler L and McElroy J, 1996b, 'Integrated Modular Propulsion and Regenerative Electro-Energy Storage System (IMPRESS) for small satellites', *10th Annual American Institute of Aeronautics and Astronautics/Utah State University Conference*, Logan, Utah, 16–20 September, 1996.

Mitlitsky F, Myers B and Weisberg A H, 1998a, 'Regenerative Fuel Systems R & D', *Proceedings of the US DOE Hydrogen Program Review*, Arlington, VA, 28–30 April 1998.

Mitlitsky F, Myers B and Weisberg A H, 1998b, 'Regenerative fuel cell systems', *Energy & Fuels*, **12**, 56–71.

Mitlitsky F, Myers B, Weisberg A H and Leonida A, 1999a, 'Applications and development of high pressure PEM systems', *Portable Fuel Cells Conference*, Lucerne, Switzerland, June 21–24 1999.

Mitlitsky F, Myers B, Weisberg A H, Molter T M and Smith W F, 1999b, 'Reversible (unitized) PEM fuel cell devices', *Portable Fuel Cells Conference*, Lucerne, Switzerland, June 21–24, 1999.

Mitlitsky F, Weisberg A H, Carter P H, Dittman M D, Myers B, Humble R W and Kare J T, 1999c, 'Water rocket – electrolysis propulsion and fuel cell power', *American Institute of Aeronautics and Astronautics Space Technology Conference and Exposition*, Albuquerque, NM, 28–30 September, 1999.

Molter T, 1999, 'Regenerative fuel cell technology and applications', Proton Energy Systems, NETL publications, *Conference Proceedings, Joint Fuel Cell Technology Review Conference*, http://www.netl.doe.gov/publications/proceedings/99/99fuelcell/fc3–9.pdf, accessed 19 Oct 2007.

Murphy O J, Cisar A J, Gonzalez-Martin A, Salinas, C E and Simpson, S F, 1995, 'A novel unitized regenerative proton exchange membrane fuel cell', *Space Electrochemical Research and Technology*, NASA Conference Publication, **3337**, 83–99.

NedStack fuel cell technology, 2007, *NedStack Projects Pending and concluded*, viewed 8 October 2007, <http://www.nedstack.com/content/NedStackProjects_100407.pdf>

O'Hayre R, Cha S W, Colella W and Prinz F B, 2005, *Fuel Cell Fundamentals*, Wiley & Sons, New York.

Petterssen J, Ramsey B and Harrison D, 2006, 'A review of the latest developments in electrodes for unitised regenerative polymer electrolyte fuel cells', *Journal of Power Sources*, **157**, 28–34.

Power Engineering, 2003, Proton Energy Systems awarded solar/PEM fuel cell power system project at China Lake, viewed 8 October 2007, http://pepei.pennnet.com/display_article/167627/6/ARCHI/none/none/Proton-Energy-Systems-awarded-solar/PEM-fuel-cell-power-system-project-at-China-Lake/

Rismanchi B and Akbari M H, 2008, 'Performance prediction of proton exchange membrane fuel cells using a three-dimensional model', *International Journal of Hydrogen Energy*, **33**, 439–448.

Roshandel R and Farhanieh B, 2007, 'The effects of non-uniform distribution of catalyst loading on polymer electrolyte membrane fuel cell performance', *International Journal of Hydrogen Energy*, **32**, 4424–4437.

Sethuraman V A, 2006, 'Durability Aspects of Polymer Electrolyte Membrane Fuel Cells', Doctor of Philosophy thesis, University of South Carolina.

Smith W, 2000, 'The role of fuel cells in energy storage', *Journal of Power Sources*, **86**, 74–83.

Song S, Zhang H, Ma X, Shao Z G, Zhang Y and Baolian Yi, 2006, Bifunctional oxygen electrode with corrosion-resistive gas diffusion layer for unitized regenerative fuel cell', *Electrochemistry Communications*, **8**(3), 399–405.

Sopian K, Daud W R W, 2006, 'Challenges and future developments in proton exchange membrane fuel cells', *Renewable Energy*, **31**, 719–727.

Sportsman S, Way D and Pez G, 2002 'Microstructural diffences among nafion perfluorosulfonate membranes', *The 13th Annual Meeting of the North American Membrane Society (NAMS)*, Long Beach, California, 11–15 May, 2002.

Swette L L, Kackley N D and LaConti A B, 1992, 'Regenerative fuel cells', *Proceedings of the 27th Intersociety Energy Conversion Engineering Conference*, Warrendale, PA, 1992.

Swette L L, Laconti A B and McCatty S A, 1994, 'Proton-exchange membrane regenerative fuel cells', *Journal of Power Sources*, **47**, 343–351.

Tsypkin M A, Lyutikova E K, Fateev V N and Rusanov, 2000, 'Catalytic layers in a reversible system comprising an electrolyzing cell and a fuel cell based on solid polymer electrolyte', *Russian Journal of Electrochemistry*, **36**(5), 545–549.

Ulleberg O, 1998, 'Stand Alone Power Systems for the Future – Optimal Design, Operation and Control of Solar Energy Hydrogen Systems', Doctor of Philosophy thesis, Norwegian Institute of Science and Technology.

University of Connecticut, 2005, 'Department of Mechanical Engineering - Senior design projects', viewed on 9 October 2007, http://www.engr.uconn.edu/me/pdf/Brochure05.pdf

US Department of Energy, 1999, *Report to Congress on the Status and Progress of the DOE Hydrogen Program*.

Wittstadt U, Wagner E and Jungmann T, 2005, 'Membrane electrode assemblies for unitised regenerative polymer electrolyte fuel cells', *Journal of Power Sources*, **145**, 555–562.

Yao W, Yang J, Wang J and Nuli Y, 2007, 'Chemical deposition of platinum nanoparticles on iridium oxide for oxygen electrode of unitized regenerative fuel cell', *Electrochemistry Communications*, **9**, 029–1034.

Yim S D, Park Lee W Y, Yoon Y G, Sohn Y J, Park G G, Yang T H and Kim C S, 2004, 'Optimization of bifunctional electrocatalyst for PEM unitized regenerative fuel cell', *Electrochimica Acta*, **50**, 713–718.

Yim S D, G G, Sohn Y J, Lee W Y, Yoon Y G, Yang T H, Um S, Yu S P and Kim C S, 2005, 'Optimization of PtIr electrocatalyst for PEM URFC', *International Journal of Hydrogen Energy*, **30**, 1345–1350.

Zaidi S M J, Rahmana S U and Zaidia H H, 2007, 'R&D activities of fuel cell research at KFUPM, *Desalination*, **209** (1–3), 319–327.

Zhang Y, Wang C, Wan N and Mao Z, 2007, 'Deposited RuO_2–IrO_2/Pt electrocatalyst for the regenerative fuel cell', *International Journal of Hydrogen Energy*, **32**, 400–404.

Zhigang S, Baolian Y and Ming H, 1999, 'Bifunctional electrodes with a thin catalyst layer for 'unitized' proton exchange membrane regenerative fuel cell', *Journal of Power Sources*, **79**, 82–85.

10

Novel fuel cells and materials

A SMIRNOVA, Connecticut Global Fuel Cell Center, USA

10.1 Introduction

Fuel cells as electrochemical power generating devices, existing nowadays in different stages of development, are of great interest due to their high efficiency, potential for low emissions and environmental protection. Depending on the amount of power produced, quality of waste heat, consumed fuel and configuration, fuel cells can be used for residential [1, 2], portable [3–6], stationary [7], and automotive [8] applications.

Among different kinds of fuel cells, low-temperature polymer electrolyte membrane fuel cells (PEMFCs) and high-temperature solid oxide fuel cells (SOFCs) based on solid ceramic materials are of major importance. In earlier stages of development PEMFCs operating on hydrogen as a fuel were considered as the most promising fuel cell type for almost all kinds of applications because of their fast start-up and tolerance to shock and vibration. However, production, storage, and distribution of hydrogen gas are considered strong limitations to PEMFCs development in addition to the fact, that expensive noble metals are used as catalysts. Thus, other PEMFCs were developed, such as those operating on liquid fuels including low molecular weight organic and inorganic compounds dissolved in water, such as methanol, ethanol, sodium borohydride, dimethylether, formic acid, and trioxane.

In comparison to PEMFCs, SOFCs were not initially considered for portable or transportation application due to high cost, slow start-up and high operating temperatures, approaching 1000 °C in earlier stages of development. With development of new ceramic nanocomposite materials followed by significant reduction in operating temperature below 600 °C and power density improvements, SOFC is considered nowadays as a major competitor to polymer-based low-temperature fuel cells.

The fuel cell technologies regarding their differences in operating temperatures possess a number of peculiarities specific for high-temperature versus low-temperature fuel cells and initiate novel approaches especially those related to nanocomposite materials. In the case of PEMFC, low

temperature of operation and CO-sensitivity of the catalysts force the cell to operate on pure hydrogen with consumption of expensive noble metals as catalysts that significantly restricts the areas of PEMFC applications. In contrast, high-temperature fuel cells can use inexpensive Ni-based anode catalyst, therefore tolerating the presence of CO_2 and consuming CO that accompanies CH_4 in biogas or reformed gas, as a fuel. However, operating temperatures above 800 °C tend to decrease the long-term endurance of the cells owing to internal sintering of the Ni particles and interdiffusion of the cell components.

Therefore, significant attempts have been made to increase operating temperature of PEMFCs in order to eliminate CO-poisoning effect [9–11] and reduce the operating temperature of SOFCs to 500–700 °C [12–18] in order to increase the fuel cell's long-term stability and allow the use of metal interconnect materials, which considerably decreases the cost.

In comparison to PEMFCs that were mostly developed as power generating devices operating on hydrogen or methanol in the case of direct methanol fuel cell (DMFC), SOFC fuel flexibility is much superior. At the same time, SOFC fuel cell requirements towards the quality of fuel are still high since low concentrations of certain impurities can damage the cell. The development of less contaminant-sensitive SOFCs is of major interest especially regarding biofuels containing a certain number of detrimental impurities, such as sulfur or H_2S, which are hazardous for both low- and high-temperature fuel cells [19–21]. In order to upgrade fuels derived from biomass fermentation, several physical, chemical and biological gas cleaning methods have been developed [22].

Since PEMFC commercialization considered as a part of future hydrogen economy is impeded by the presence of noble metal catalysts, a series of attempts have been made for the development of non-noble metal-based electrocatalysts which in comparison to noble metal catalysts are cost effective in the long term. However these catalysts still do not reach the requirements necessary for fuel cells [23, 24]. Their catalytic activity is significantly lower than the catalytic activity of noble-metal catalysts or naturally existing bio-catalysts that are known to possess twice as much catalytic activity per unit site as Pt-based catalysts. New approaches in synthesis of the nanostructured catalytic supports and catalysts based on macrocyclic compounds open new perspectives in the development of inexpensive and reliable PEMFCs for power generation.

Significant progress in fuel cell R&D for both low-temperature and high-temperature fuel cells achieved during the past few years is mostly due to the nanostructured single phase and composite materials. These materials demonstrate new multifunctional properties deriving from the synergistic combination of the characteristics of each individual component and can be considered as the most promising materials for fuel cell application.

10.2 Nanostructured elecrolyte materials

Chemical, mechanical, and electric properties of heterogeneous systems are extremely complicated since they depend on the properties of the individual phases, and the amount, shape, size, distribution, and orientation of the dispersed phase [25]. Polymer nanocomposites formed by dispersal of nanometer-sized fillers possess improved electric properties, increased tensile strength and enhanced barrier properties through the reduction in the diffusion coefficient from the increase in path length encountered by diffusing molecules and presence of an enormous number of 'passive' barrier particles [26].

Depending on operating temperature, the type of electrolyte could be different starting from polymers, such as polytetrafluoroethylenes (PTFE) or hydrocarbons and including molten salts and ceramic materials. The increasing demand for fuel cell development and commercialization makes the application of nanomaterials more significant, comparable to the interest in development of semiconductors, molecular devices, transistors, and lithography. Taxonomy of nanotechnology in the fuel-cell area includes nanoparticles, nano-wires, polymer layered nanocomposites from organoclays and montmorillonite-derived clays, and nanocrystalline ceramic materials for high-temperature applications.

10.3 Nanocomposite electrolyte materials for polymer-based fuel cells

As an example of the nanostructured polymer material for PEMFC application, the most commonly used PEMFC fluorinated electrolyte Nafion® can be considered for its relatively high stability and ionic conductivity due to the presence of sulfonic SO_3H groups that allow for proton hopping and transport of hydrated protons inside the membrane. The molecule of Nafion is a graft copolymer of tetrafluoroethylene and sulfonyl fluoride vinyl ether and possesses a copolymer molecular architecture. It is characterized by a hydrophobic PTFE backbone chain of high mechanical strength and regularly spaced shorter perfluorovinyl ether side-chains, each terminated by a hydrophilic sulfonic group. As a protonic (H^+) conductor, such a polymer contains about 20 wt% water, forming hydration shells around the fixed covalently bonded sulfonic acid groups. The conductivity is assigned to hydrated protons (H_3O^+) as protonic charge carriers that move through the transport channels of the membrane. The percolated nanostructure of Nafion® (Fig. 10.1) was confirmed by Haubold *et al*. in 2001 by means of small angle X-ray scattering (SAXS) technique [27]. The cylindrical inverted micelles up to 5 μm in size connected by channels about 1 μm in diameter explained some unusual properties of Nafion such as fast diffusion of water even below the freezing temperature, which occurs due to the lower freezing point in narrow channels [28].

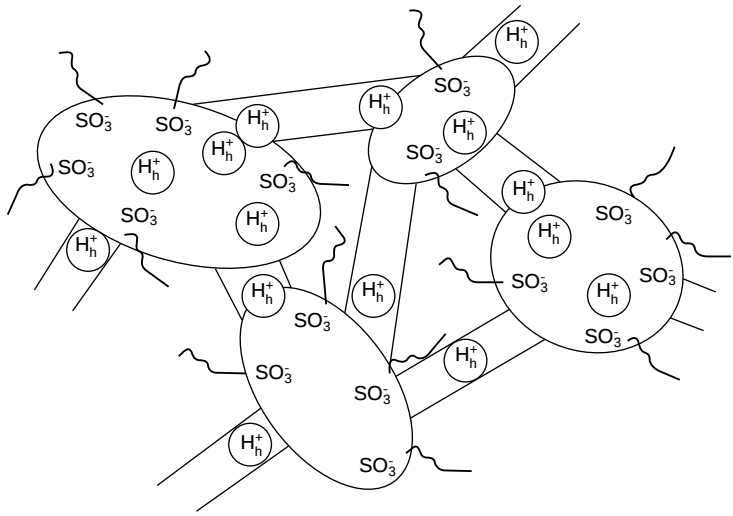

10.1 Nafion® electrolyte nanostructure or 'cluster-network model' indicating water clusters or cylindrical inverted micelles with hydrophilic sulfonic SO_3H groups attached to the side chains of hydrophobic sulfonated polytetrafluoroethylene molecule. Sulfonic groups as anionic sites possessing movable H^+ are responsible for transport of hydrated protons (H_h^+) and overall proton conductivity [29].

Unfortunately, at temperatures higher than 100 °C and low relative humidities the ability to transport protons decreases dramatically due to water cluster shrinkage; this leads to almost complete loss of conductivity.

One of the main ways to increase ionic conductivity of polymer electrolyte membranes at higher temperatures is by utilizing nanocomposite materials possessing new multifunctional properties, such as improved ionic conductivity, mechanical strength, and thermal stability as well as eliminating crossover of the fuel through the membrane. Various nanocomposite materials, specifically organic-inorganic or acidic–basic nanocomposites based on fluorinated or non-fluorinated polymers, are often used for fuel cells operating on liquid fuels [30].

A significant effect of nanoscale modification of the Nafion membrane has been demonstrated by Gribov *et al*. [31] (Fig. 10.2). Impregnation of Nafion membrane with colloidal Fe-silicate (sample 3) leads to a more than three-fold reduction of both methanol permeability and proton conductivity in comparison to unmodified Nafion 115. Interestingly, the selectivity of this composite is still close to that of pure Nafion. A membrane, activated in supercritical CO_2 (sc-CO_2) and prepared by the same method (sample 4), showed two orders of magnitude reduction in methanol permeability (8.4×10^{-9} cm^2/s) in comparison with the sample without sc-CO_2 pre-treatment

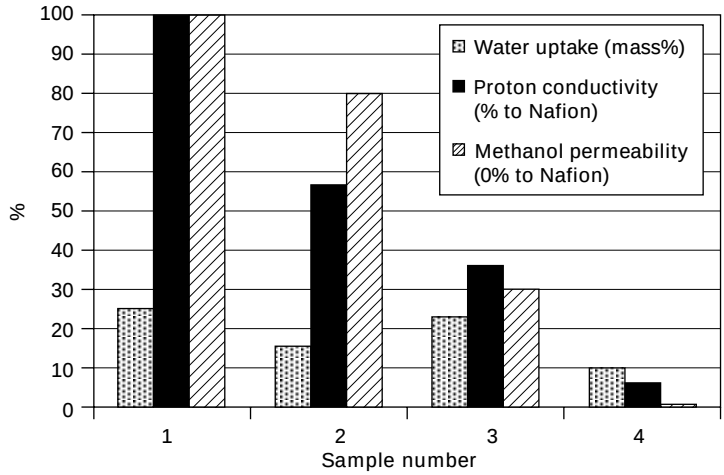

10.2 Properties of Nafion-115 compared with composite Nafion-115 membranes modified by sc-CO_2 and doped by Fe-silicate-1. Samples: 1 Nafion 115; 2 Treatment in sc-CO_2 at 45 °C and 13.1-13.8 MPa for 2 h; 3 colloid intercalation without sc-CO_2 treatment; 4 colloid intercalation and sc-CO_2 treatment. The data are taken with permission of *Journal of Materials Science* (Gribov *et al.* [31]).

(7.3×10^{-7} cm^2/s). This change is accompanied by only a six-fold reduction in proton conductivity, from 22 to 3.8 mSm/cm for the untreated and treated with sc-CO_2 material respectively. Consequently, sc-CO_2 treatment prior to modification shows a decrease in the water uptake of membrane and can be considered as an activation step. Though the detailed mechanism of such an activation step is unknown the authors assume that supercritical CO_2 treatment of the polymeric membrane results in more effective pore filling with inorganic nanoparticles.

Nafion membranes impregnated with zirconium phosphate, possessing layered structure, are shown to be stable at 150 °C in the presence of dry air or oxygen with corresponding resistance of 0.08 Ω cm^2 and conductivity comparable to that of Nafion® that equals 0.01 S/cm [32–34]. Composite membranes for DMFCs based on zeolite dispersed in a PTFE matrix show higher proton conductivities at a higher zeolite content [35].

Membranes with conductivity greater than that of Nafion® were synthesized by the addition of silicon oxide (SiO_2) to Nafion®. For such Nafion®/silica membranes at low hydrophobic silica content, the silica surrounds the hydrophilic ion-clusters and ion-channels. The tortuous Nafion® structure alters the methanol transport. High silica content increases the contribution of the polymer backbone to methanol permeability and increases proton conductivity as well as water uptake [36].

In comparison with fluorinated structures, non-fluorinated membrane nanocomposites seem to be promising alternatives that possess decreased methanol and ruthenium crossover. Poly(vinylidenedifluoride) (PVDF)-based composite membrane with nano-sized ceramic powders could exhibit high proton conductivity [37] when doped with some small molecular weight acids such as H_2SO_4, which, however, could be a reason for an acid depletion from the membrane. Because of the small pore sizes (1.5–3 nm compared with 3 nm in Nafion®), the PVDF modified with SiO_2 (16%) and 3 M sulfuric acid has two to four times lower methanol crossover and two to four times higher ionic conductivity. Impregnation of these membranes with sodium silicate solution and hydrolyzing the silicates with sulfuric acid results in gel formation that further decreases the methanol crossover by the order of magnitude in comparison with Nafion® [38]. Furthermore, these membranes are less sensitive to iron impurities.

Panero *et al*. [39] prepared nanocomposite electrolyte by swelling a silica-added PVDF membrane in H_3PO_4 aqueous solution and demonstrated the critical role of dispersed ceramic fillers in controlling the methanol permeation. The ionic conductivity increased with SiO_2 content and, at 25 wt% of SiO_2, reached $3.5 \times 10^{-2}\,S\,cm^{-1}$. The disadvantage of this approach was the tendency of H_3PO_4 to migrate [40]. A few examples of nanocomposite materials for DMFC application based on PVDF and poly(2-acrylamido-2-methyl propylene) sulfonic acid with dispersed nano-Al_2O_3 powder are presented by Shen *et al*. [41].

Aromatic poly(etheretherketones) (PEEK) modified with silanes or silica and heteropoly-acid based on $[\gamma\text{-}SiW_{10}O_{36}]^{-8}$ [42] with attached epoxy groups were developed for DMFC application. The structure is stabilized by covalent bonding between insoluble silica oxide and heteropolyacid, decreasing the solubility of the heteropolyacid in alcohol solution, methanol permeability ($0.3 \times 10^{16}\,m^2\,s^{-1}\,Pa^{-1}$), and proton conductivity ($0.01\,S\,cm^{-1}$).

Sulfonated PEEK with a carbo-group (SPEEK-WC) exhibiting a wide range of degree of sulfonation (DS) was synthesized by Regina *et al*. [43], and used to prepare polymeric and composite membranes obtained by incorporation of an amorphous zirconium phosphate sulfophenylenphosphonate ($Zr(HPO_4)(O_3PC_6H_4SO_3H)$ in a polymer matrix (Fig. 10.3). The nominal composition of the membrane was fixed at 20 wt% of Zr phosphate. The membranes were characterized by lower methanol permeability than commercial Nafion 117. Proton conductivity comparable to Nafion value ($1 \times 10^{-2}\,S\,cm^{-1}$) was achieved at 22 °C and 100% relative humidity.

Nafion and arylene-based (SPEEK) organic/inorganic hybrid nanocomposite membranes with nano-crystalline oxides were tested by Licoccia and Traversa above 120 °C [44] reaching stable conductivity values of $6.4 \times 10^{-2}\,S\,cm^{-1}$. Sulfonated poly[bis(phenoxy) phosphazene] (S-BPP) trapped in a cross-linked interpenetrating hydrophilic network of hexa(vinyloxyethoxyethoxy)

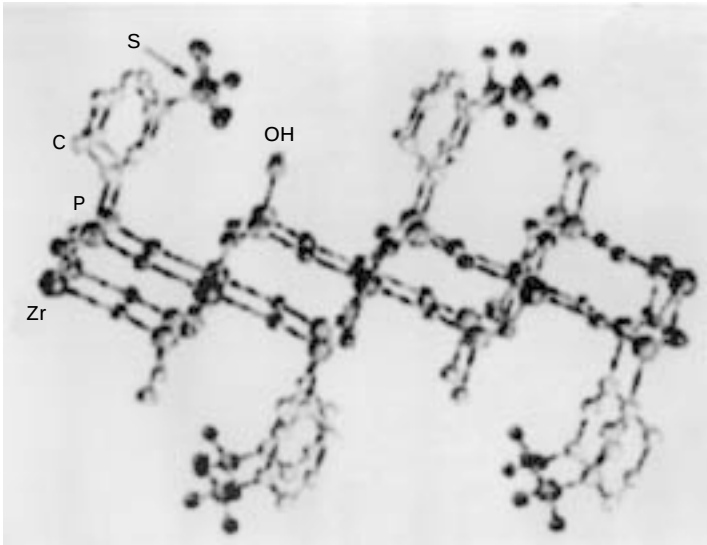

10.3 Structural model for amorphous zirconium phosphate sulfophenylen-phosphonate [Zr(HPO4) ($O_3PC_6H_4SO_3H$)]. With permission from the *Journal of Power Sources* (Regina *et al.* [43])

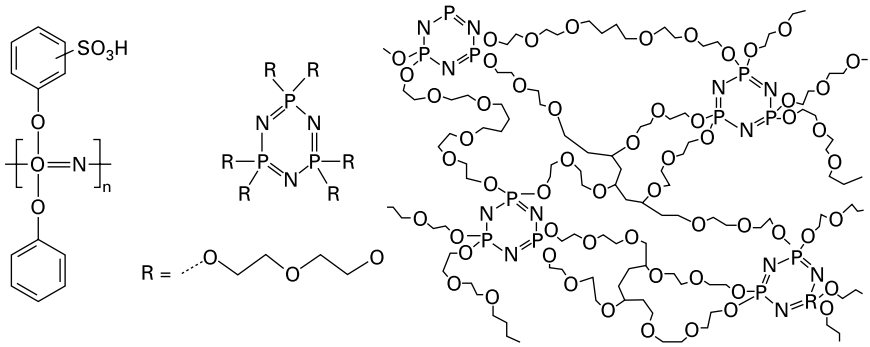

10.4 Structures of partially sulfonated poly[bis(phenoxy)phosphazene], hexa(vinyloxyethoxyethoxy) cyclotriphosphazene and idealized structure of the interpenetrating network of cross-linked hexa(vinyloxyethoxyethoxy)-cyclotriphosphazene (CVEEP). With permission from *Solid State Ionics* (Burjanadze *et al.* [45]).

cyclotriphosphazene (CVEEP) (Fig. 10.4) is another example of complicated nanocomposite proton-conducting membrane [45] demonstrating good mechanical and thermal stability combined with high ion exchange capacity in the range of 1.62–1.79 mmol g^{-1} and conductivity of 2.2×10^{-4} S cm^{-1} for s-BPP with a network made of 50 wt% CVEEP. After immersion in water, the conductivity increased up to 0.013 S cm^{-1} at 25 °C. The authors concluded

that the hydrophilic nature of the CVEEP network stabilizes the water content and enhances the proton conductivity at elevated temperatures.

Composite salt-in-polymer electrolyte membranes were prepared from poly[(bis(2-methoxyethyl)amino)$_{1-x}$(*n*-propylamino)$_x$-phosphazene] (BMEAP) with dissolved $LiCF_3SO_3$ and dispersed Al_2O_3 nanoparticles (40 nm). Membranes with good mechanical stability were obtained. However, conductivities in Al_2O_3-free membranes at 10 wt% $LiCF_3SO_3$ were very low, ranging from 3.1×10^{-7} S cm^{-1} at 30 °C to 1.8×10^{-5} S cm^{-1} at 90 °C. It is interesting to note that addition of 2 wt% Al_2O_3 nanoparticles resulted in a steep increase of the conductivity by almost two orders of magnitude compared with the homogeneous membranes [46].

Another example of hybrid networks, such as silicate sol–gel precursors of poly[bis(methoxyethoxyethoxy)phosphazene] synthesized by hydrolysis and condensation reactions was presented by Allcock *et al*. [47]. Conversion of the precursor polymers to covalently interconnected hybrid networks with controlled morphologies and physical properties was achieved. Thermal analyses showed no melting transitions for the networks and low glass transition temperatures that ranged from –38 to –67 °C. However, solid solution with lithium bis(trifluoro-methane-sulfonyl)amide in the network showed relatively low ionic conductivity value of 7.69×10^{-5} S cm^{-1}.

Fundamental understanding of polymer electrolyte fuel cells in combination with the knowledge of proton conductivity in ceramics obtained from the SOFC area (Section 10.4) resulted in development of proton-conducting ceramic- and zeolite-based [48] high-temperature PEMFC operating above 120 °C. Ionic conductivity of zeolite–polymer composites using zeolite materials and PVDF as polymer was studied by Sancho *et al*. [48] who demonstrated low activation energy for ionic conductance (5 kJ mol^{-1} in the temperature range of 20–150 °C) comparable to that of Nafion (4 kJ mol^{-1} at temperatures below 100 °C). Nanoporous anatase (TiO_2) ceramic xerogels possessing an average pore diameter of 5.8 nm and a pore volume of 0.236 cm^3 g^{-1} demonstrated proton conductivity of 0.015 S cm^{-1} at 90 °C and 81% relative humidity [49].

Based on the given examples, it is necessary to emphasize the importance of nanocomposites in the development of polymer materials with enhanced properties. They have greatly influenced the fuel cell technology and possess great potential for further improvement of fuel cell performance, reducing its cost and extending opportunities for future commercialization.

10.4 Nanocomposite electrolyte materials for ceramic fuel cells with proton conductivity

The demand for new power sources determines the need for new materials possessing high proton conductivity. A number of methods describe the

synthesis of nanocrystalline oxide powders, among them precipitation, combustion, hydrothermal and sol–gel techniques including various complexing agents such as citrates, oxalates or glycine [50, 51]. Since surfaces of the particles usually have a structure that is different from the bulk, nano-sized materials offer anomalous transport properties, chemical and catalytic activity [52].

High-temperature nanocrystalline ceramics possessing proton conductivity, such as doped cerates and zirconates, known as protonics [53], is now under investigation and can be considered a perspective material for novel sensors, gas separation membranes, electrolysers, hydrogen and steam pumps, isotope concentrators, membrane reactors, and fuel cells.

Proton-conducting ABO_3 ceramics [54] have been synthesized by a sol–gel Pechini method [55] using glycine as fuel and nitrates of the metal cations as an oxidant. The basic reaction is:

$$2C_2H_5NO_2 + A(NO_3)_3 + B(NO_3)_3 \rightarrow ABO_3 + 5H_2O\uparrow + 4N_2\uparrow + 4CO_2\uparrow$$

In this reaction glycine ($C_2H_5NO_2$) is used not only as a fuel but also as a complexing agent. The amine group ($–NH_2$) in glycine forms complexes with transition metal ions, and the carboxyl group (–COO) participates in complex formation with alkaline earth metal ions, e.g. Ca^{2+}, Ba^{2+} or Sr^{2+}. Depending on the radius of the cation the carboxyl group can form complexes with other cations used for doping, thus preventing them from precipitation before the combustion process and resulting in production of a homogeneous single phase nano-size materials.

Protonics as potential materials for fuel cells and in nuclear fusion reactors are regarded as ultimate energy generators. Iwahara *et al.* [53] reported the development of the hydrogen pumps for recovery of tritium from the mixture of hydrogen isotopes, which is produced in high-density deuterium plasma. Figure 10.5 shows the experimental apparatus of a hydrogen pump and proton-conducting ceramic tube composed of a $CaZr_{0.9}In_{0.1}O_{3-\delta}$ with an effective area of $47\,cm^2$.

The mechanism of proton conductivity in ceramics is based on the high concentration of proton defects (holes) and their mobility determined by the nature of mobile ion (H^+) and the matrix of the ceramics where this transport occurs by ion defect migration. Usually it is more difficult to improve the ion mobility than to increase the carrier concentration [56]. Thus, a few approaches were developed that enhanced the defect formation. Among them doping with ions of different valence (homogeneous doping) or heterogeneous doping, when addition of a dispersed phase to ionic crystals increases ion sorption at the interface [57] are the most well known. The first one is related to the synthesis of dispersed nanoparticles, in which the holes developed on the surface of the particle are due to the uncompensated chemical bond formation.

10.5 Experimental apparatus of hydrogen pump (left) and ceramic tube of proton conductor (right). With permission from *Solid State Ionics* (Iwahara *et al.* [53]).

The second approach implies doping with oxides, which increases defect concentration and thus decreases activation energy for conductivity. As an example, the properties of alkali metal hydrogensulfate $MeHSO_4$ (Me = Cs, Rb, K) in $(1–x)MeHSO_{4–x}A$ ($A = Al_2O_3$, TiO_2, SiO_2; $x = 0–0.9$) nanocomposite solid electrolytes were studied by Ponomareva and Lavrova [58]. The conductivity of the composites exceeded the conductivity of the individual salts by more than 3.5 orders of magnitude depending on composition and was decreasing in the order $SiO_2 > TiO_2 > Al_2O_3$.

The mechanism of mixed ionic-electronic conductivity for proton-conducting perovskites is based on proton concentration that increases with the concentration of oxygen vacancies ($V_O^{\cdot\cdot}$) [59]. The mechanism was proposed in the late 1960s by Stotz and Wagner, who suggested that water molecules dissociate at the surface according to Kröger and Wink notation:

$$H_2O_{gas} + V_O^{\cdot\cdot} + O_O^x \leftrightarrow 2(OH)_O^{+}$$

where subscripts denote the atom location in the lattice and superscripts '•' or '$^+$' and '′' indicate positive and negative charge of the species. The neutral oxygen atom (O_o) fills an oxygen vacancy ($V_O^{\cdot\cdot}$) and the two protons associate with two oxygen atoms, forming protonic defects with a positive effective charge. Thus, the introduction of protons into the perovskite structure can be interpreted as acid–base equilibrium between water molecules and oxygen vacancies. A water molecule enters an oxygen vacancy at the surface, donating

two protons to the lattice. The quasi-free protons reside near oxygen ions, hopping from one lattice site to another one by Grotthus mechanism [60].

Further, oxygen vacancies ($V_O^{\cdot\cdot}$), react with water molecules to fill lattice positions with oxide ions (O_O^x) and produce interstitial protons, H_i^+:

$$H_2O + V_O^{\cdot\cdot} \rightarrow O_o^x + 2H_i^+$$

However, owing to the small size of protons, they do not occupy a true interstitial site but attach to oxide ions, thus forming a hydroxyl ion OH_O^+:

$$O_O^x + H_i^+ \rightarrow OH_O^+$$

In this case the net reaction demonstrating the interaction of oxygen vacancies with water producing proton charge carriers can be written as:

$$H_2O + V_O^{\cdot\cdot} + O_o^x \rightarrow 2(OH_O)^+$$

Thus, in the presence of H_2, the hydrogen atoms can be directly incorporated into the perovskite structure in the form of protons and electrons (e′) through an interaction with oxide ions, leading to mixed electron-ionic conductivity.

In the case of doped cerates and zirconates proton conductivity enhancement can be achieved by homogeneous doping with trivalent cations, such as in $Ba(Zr_{1-x}Y_x)O_{3-\delta}$ where $0 \leq x \leq 0.3$ [61–63], $Ba(Y_{0.1}Zr_{0.9-x}Ce_x)O_{3-\delta}$ where $0 \leq x \leq 0.9$ [64], $Ba(Y_{0.15}Zr_{0.85-x}Ce_x)O_{3-\delta}$ where $0 \leq x \leq 0.85$ [65], or $Ba(Y_{0.15}Zr_{0.81}Y_{0.15}Zn_{0.04})O_{3-\delta}$ [66]. For every two trivalent ions, e.g. Y^{3+}, added to $BaZrO_3$, yttrium occupies some of the Zr^{4+} sites and one oxygen vacancy ($V_O^{\cdot\cdot}$) is formed to maintain electro-neutrality:

$$Y_2O_3 \rightarrow 2Y'_{Zr} + 3O_O^x + V_O^{\cdot\cdot}$$

In addition, anti-Frenkel defects or 'internal defects' are formed, resulting from thermal entropy:

$$O_O^x = V_O^{\cdot\cdot} + O_i''$$

For an intermediate temperature proton conductor, one of the possible relevant defect reactions for H_2O incorporation, followed by the corresponding equilibrium constant, may be written as

$$H_2O(g) + V_O^{\cdot\cdot} \leftrightarrow O_O^x + 2H_i^{\bullet}$$

$$K_{H_2O} = [O_O^x][H_i^{\bullet}]^2 / pH_2O[V_O^{\cdot\cdot}]$$

At high oxygen partial pressures, oxygen competes for the available oxygen vacancies. Assuming that oxygen vacancies are fully ionized [9] the reaction of oxygen incorporation can be written as:

$$\tfrac{1}{2}O_2(g) + V_O^{\cdot\cdot} \leftrightarrow O_O^x + 2h^{\bullet}$$

where $h^{\bullet}$ indicates electron holes. The corresponding constant of equilibrium can be written as:

$$K_H = [O_O^x]\, ph^2 / p_{O_2}^{1/2}\, [V_O^{\cdot\cdot}]$$

Thus, protons (H^+) from water molecules are distributed in the oxide and act as charge carriers to form a proton conductor. Proton conductivity at low oxygen partial pressures is supposed to be proportional to $p_{O_2}^{1/2}$. It is now generally accepted that protonic defects are not interstitial, but reside near or inside the electron cloud of oxygen ions and the correct notation is $[OH_O]$.

The typical proton conducting ceramics, for example $SrCe_{0.95}Yb_{0.05}O_{3-\delta}$ is a solid solution based on perovskite-type oxide $SrCeO_3$, in which 5% of Ce is replaced by Yb. The ceramics of this type exhibit p-type electronic (hole) conduction under oxidizing atmosphere free from hydrogen or water vapor at high temperature. However, when exposed to hydrogen-containing atmosphere, the electronic conductivity decreases and proton conductivity increases reaching 10^{-2} to 10^{-3} S cm^{-1} in the temperature range of 600–1000 °C.

In comparison with cerates, doped zirconates based on rare earth elements (Ca, Sr, or Ba) exhibit proton conductivity, which is about an order of magnitude lower than those of the cerates. A series of complex perovskites based on $Ba_3(CaNb_2)O_9$ or $Sr_2(ScNb)O_6$ were reported to exhibit the protonic conductivity as high as that of $BaCeO_3$-based ceramics. Though the conductivity of zirconate-based ceramics is lower than that of the cerates, they possess higher chemical and mechanical strength. In contrast to cerates, zirconates hardly react with acid solution, and they are stable against carbon dioxide gas, which reacts easily with cerate ceramics below 800 °C to form carbonates [67]. To modify their properties, additional A- and B-site doping is achieved for both cerates and zirconates.

The mobility and stability of protonic defects in acceptor-doped perovskite-type oxides ABO_3 in the system $SrTiO_3$–$SrZrO_3$–$BaZrO_3$–$BaTiO_3$ have been examined [68], demonstrating high proton conductivity and thermodynamic stability. Although changing B-site occupation leads to a significant reduction in protonic defects, alkali earth metal doping on A-site appears to be less critical. The stability of protonic defects depends on basicity of the lattice oxygen, which is influenced by both A- and B-site occupations. It was demonstrated by Kreuger *et al*. [68] that Y^{3+}, though possessing higher ionic radius than Zr^{4+}, is the optimal dopant for barium zirconate and possess significantly higher conductivity than the best oxygen ion conductors, especially at low temperatures (Fig. 10.6).

Ceria-doped $Ba_2In_2O_5$ as a proton-conducting material revealed the oxygen-deficient perovskite single phase of $Ba_2In_{2-x}(Ce^{4+})_xO_{5-\delta}$ and demonstrated relatively high proton conductivity at low temperatures that was higher in wet than in dry nitrogen (Fig. 10.7) [69]. The total electrical conductivity at 200 °C was similar in both wet and humidified nitrogen ($\log \sigma = -3.5$); however, proton conductivities at the same temperature were higher in wet than in dry N_2. The proton transference number decreased with increase in

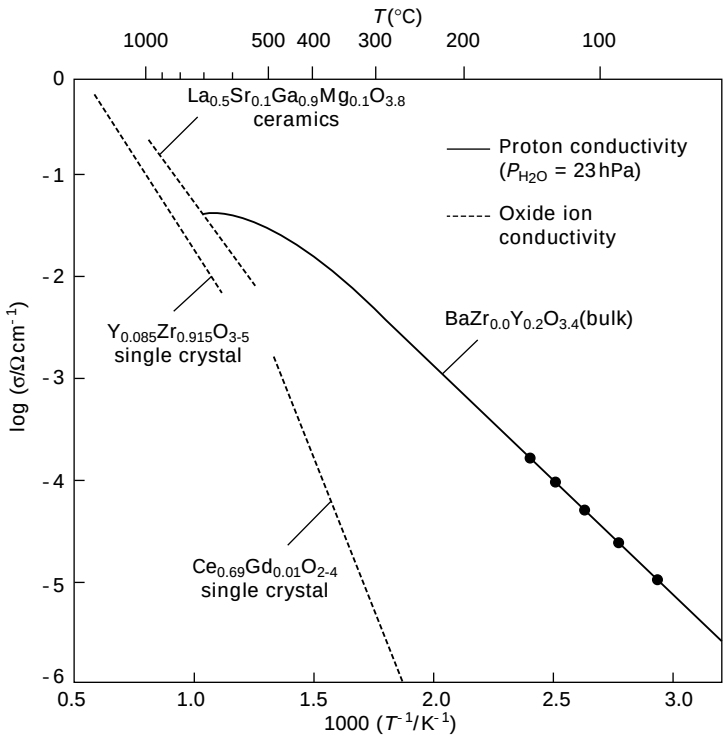

10.6 Ionic conductivity of barium zirconate in comparison to oxygen ionic conductors: yttria-stabilized zirconia, gadolinia-doped ceria, and doped lanthanum gallate. With permission of *Solid State Ionics* (Kreuger *et al.* [68]).

temperature and corresponded to 0.42 and 0.82 at 250 °C and 100 °C respectively. As a result, it was concluded that this material has mixed ionic-electronic conductivity.

Perovskite-type proton conductors $Ba(Ce,Zr)_{1-x}Sc_xO_{3-\delta}$ ($x = 0.1, 0.2$) [70] possessed increased chemical stability due to B-type Sc doping with total conductivity changing from 2.58×10^{-4} S cm^{-1} to 1.06×10^{-3} S cm^{-1} for x = 0.1 and 0.2 respectively at 600 °C. Kobayashi *et al.* [71] used A-type La doping and synthesized $Ba_{1-x}La_xSc_{1-y}Zr_yO_{3-\delta}$ possessing a single phase cubic perovskite structure in the region of $0.7 \le y \le 0.8$ for $x = 0$ and $0.5 \le y \le 0.7$ for $x = 0.1$ with total electric conductivity of 10^{-2} S cm^{-1} at 1000 °C in air, made up from oxide ions, protons, and holes.

Enormous efforts have been made to develop proton-conducting ceramic materials and composites that could be considered as an alternative to the existing low-temperature polymer electrolyte membranes and high-temperature materials with oxide ion conductivity. However, a lot still should be done

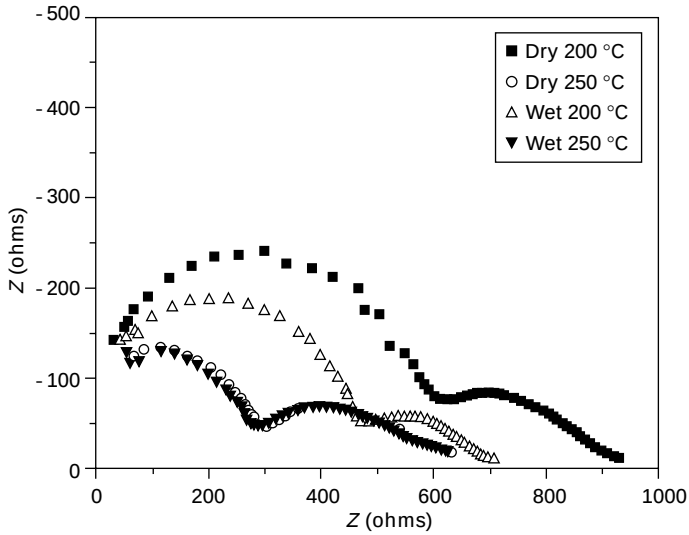

10.7 AC impedance spectra of the $Ba_2In_{2-x}(Ce^{4+})_xO_{5-\delta}$ (BIC) in wet and dry N_2 at 200 and 250 °C measuring electrical conductivity of BIC as a function of temperature in wet and dry nitrogen. With permission from *Journal of Power Sources* (Hui *et al.* [69]).

regarding chemical stability and ionic conductivity of these materials to make them viable for fuel cell applications.

10.5 Nanotechnology applied to fuel cell catalysts

It is impossible to underestimate the importance of catalysts in fuel cell R&D, since they define reactions on both anode and cathode sides of the cell and the overall cell performance. In comparison with homogeneous catalysts, where the reactants and products form a single phase, in fuel cells heterogeneous catalysts are separated from reactants and products and are usually less selective: more effort is needed to design and synthesize such catalysts. Nanotechnology presents new perspectives in achieving higher catalytic activity and stability in fuel cell environment.

10.6 Nanocomposite catalysts for polymer-based fuel cells

A nano-scale composite material is defined as a material with a structure possessing at least one of its phases in the size range usually from 1 to 100 nm. Among different catalysts for PEMFCs, nano-scale composite materials and supported metal nanoparticles have attracted a lot of attention owing to their unique properties that are directly related to the specific particle

morphology, metal dispersion, concentration, and the electronic properties of the metal within their host environment [72].

In PEMFCs, high surface area platinum [73] or Pt/Ru alloys dispersed on high surface area carbon are commonly used as electrocatalysts for the hydrogen oxidation reaction (HOR) and oxygen reduction reactions (ORR). However in the case of HOR the carbon-supported platinum catalyst possesses sufficient catalytic activity only when pure H_2 is supplied to the anode.

When H_2 is produced by steam reforming or partial oxidation of methanol, carbon monoxide as a by-product of these reactions drastically decreases the PEMFC performance by blocking the active sites for the hydrogen adsorption.

A similar effect takes place in PEMFCs operating on liquid fuels, such as in alcohol-water solution. In this case the cells are called direct alcohol fuel cells (DAFCs). The limiting factor to practical development [74] of DAFC is the poor performance of Pt catalyst on the fuel (anode) or air (cathode) electrode. Carbon monoxide molecules formed by dehydrogenation of methanol strongly adsorb on the surface of platinum or Pt/Ru alloys, blocking the active surface groups and preventing methanol molecules from adsorption.

To decrease the cost of the cell, a large number of Pt alloys with non-noble metals, such as Fe, Co, Ni, and Cu, were tested; however dissolution of metal in acidic media of PEMFC especially at high cell voltages causes fast degradation [75]. Thus, certain steps were undertaken towards non-noble metal catalysts based on transition metals, such as Fe, Co, Ni, and Cu. Among them, Ni is the most well known for its high catalytic activity and is commonly used for SOFCs operating in the range of 600–800 °C. Unfortunately, at room temperatures transition metals demonstrate negligible activity.

A number of attempts was undertaken to increase transition metal activity at room temperature by stabilizing them in cationic form similar to the one existing in biocatalysts, such as metallo-enzymes [76–78]. These naturally existing catalysts (Fig. 10.8) are well known to possess catalytic activity and selectivity that is better than all known catalysts based on noble metals. These catalysts are able to facilitate complex reactions with 100% selectivity

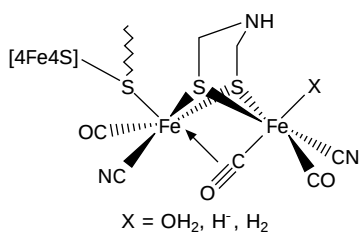

10.8 Structure of biocatalyst [Fe]-hydrogenase possessing catalytically active Fe-stabilized groups.

and possess ideal structures of internally stabilized transition metals, with catalytic activity and selectivity that is far greater than in presently known catalysts. To overcome this gap and attain high selectivity, a number of approaches have been suggested, among them non-noble metal catalysts based on intercalated compounds, electrically conducting polymers, metal-containing zeolites, or non-noble metal cations stabilized by support or macro-complexes. Though enzymatic catalysts are not stable in fuel-cell operating conditions, the displayed chemical precision inspire scientists for developing new structures of non-noble metal catalysts, most of which nowadays are based on nano-scaled architecture.

Several non-noble metal materials, such as transition metal carbides, chalcogenides [79], transition metal oxides [80], porphyrin, or phthalocyanine macrocycles [81, 82], have been extensively investigated over the years and characterized as electrocatalysts for PEMFC application.

Transition metal carbides, especially tungsten carbide, have been intensively investigated as CO-tolerant anode catalysts and showed corrosion resistance, high electrical conductivity, good resistance to CO poisoning and a platinum-like behavior for the chemisorption of hydrogen and oxygen. At low polarization the W_2C in a mixture with Pt–Ru catalyst [83] showed twice activity of the Pt–Ru catalyst when the oxidation currents were normalized to the Pt area.

A number of nitride and carbide non-noble metal catalysts were synthesized including tantalum (Ta)-added tungsten carbide (WC) [84] and were found to be active in ORR due to significant difference in electronegativities of metal and nitrogen atoms and charge transfer reaction that was proved to result in the creation of active base and/or acid sites.

Non-noble metal nanostructured electrocatalysts based on nitride of molybdenum (Mo_2N/C) [85] and tungsten nitride (W_2N/C) [86] supported on carbon black were investigated as PEMFC cathode electrocatalysts. Both catalysts showed a comparatively good catalytic activity in ORR in PEMFC and proved to be promising non-noble electrocatalyst alternatives for platinum-based catalysts.

Zhang *et al*. reported on stabilized transition metal chalcogenides, where a metal ion cluster is surrounded by several non-metal ions, heat-treated nitrogen containing macrocyclic complexes, and intercalation compounds [87]. Shioyama *et al*. indicated [88] that Cu-intercalated carbon does not show any decrease in catalytic activity due to dissolution or corrosion that usually occurs in PEMFCs. Despite the promising results, these catalysts did not possess enough catalytic activity due to low dispersion of the metal and metal agglomeration. However, using high surface area carbon modified with transition metal polymer precursor resulted in relatively high catalytic activity of nanocomposite cobalt catalyst [89] (Fig. 10.9).

Popov and co-workers [90] reported the results regarding preparation of Co-based non-noble metal catalysts from cobalt–ethylene diamine complex

on non-structured carbon supports (Ketjen Black, Vulcan XC-72, and Black Perl 2000) followed by a heat treatment at 800 °C. Some catalytic activity towards four-electron reduction of molecular oxygen has been detected and explained by better dispersion of the chelated complexes and quinone surface groups introduced by additional nitric acid treatment. The authors claim that Co becomes more reduced during the process of heat treatment; however, data on binding energy are not given and neither are the results of '*in situ*' fuel cell testing. Furthermore, non-structured carbons impede mass transport and did not allow for even distribution of ionic conductor Nafion inside the layer, thus decreasing the overall catalytic efficiency.

Carbon support as an essential part of the catalyst layer plays an extremely important role in achieving high catalytic activity and stability of the carbon-supported catalysts (Fig. 10.9). Different types of carbon supports are known, among them high surface area carbons, carbon aerogels, graphene sheets [91], and carbon nanotubes (CNT) [92]. A relatively high performance was achieved for PtRu catalysts supported on multi- and single wall nanotubes (MWNT and SWNT), reaching 100 mV at 1 A cm^{-2} in H_2 at 100 ppm CO. In DMFC operating conditions the power densities exceeded 100 mW cm^{-2} at 90 °C and 0.3 MPa. The activity of the anodes followed the sequence: PtRu/MWNT > PtRu/Vulcan XC-72 > PtRu/SWNT [93].

A high Pt loading of 32.5% on CNTs can be obtained when catalysts are prepared with ethylene glycol and Pt salt [94]. Cyclic voltammetry studies show that the Pt utilization in the fuel-cell electrodes is around 44%. However, catalysts obtained with mild nitric acid-treated CNTs give a better performance of 680 mV at 500 mA cm^{-2} and 600 mV at 800 mA c^{-2} than catalysts prepared with ethylene glycol and Pt salt.

An efficient catalytic layer configuration based on Pt nanoclusters supported on carbon black or carbon nanotubes (Fig. 10.10), allowing a significant improvement of the electrocatalytic performance in HOR at the anode and

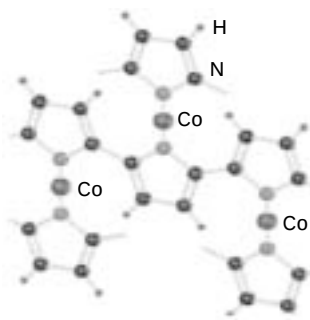

10.9 Cobalt-polypyrrole-carbon (Co-PPY-C) catalyst structure before reduction synthesized without pyrolysis at room temperature. With permission from *Nature* (Bashyam and Zelenay [89]).

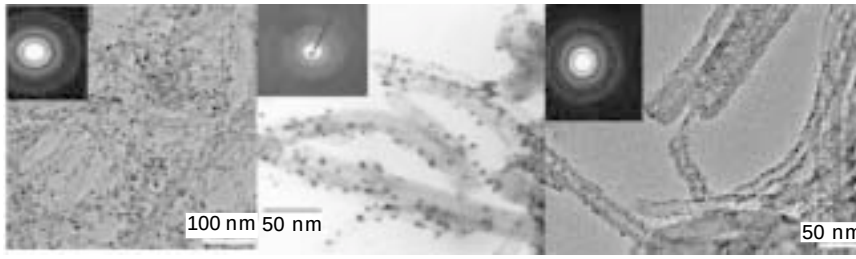

10.10 TEM images of Pt clusters supported on carbon nanotubes [95].

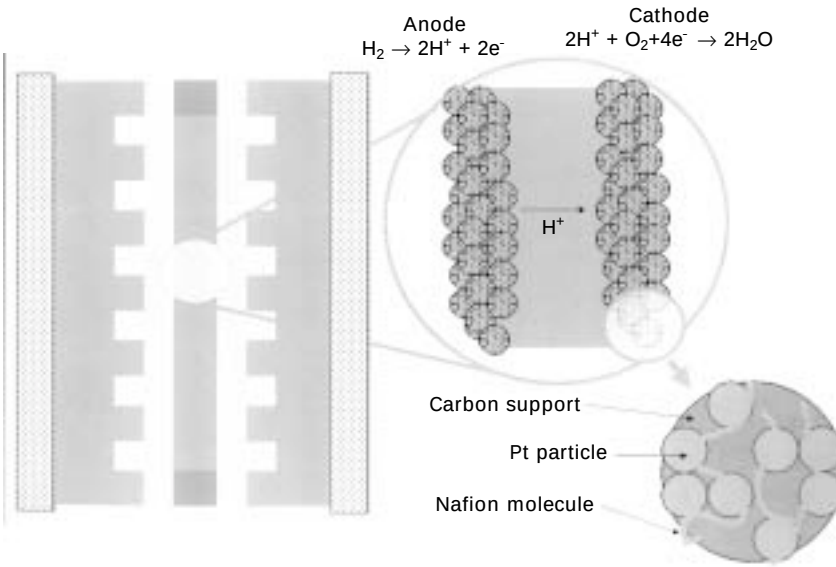

10.11 Structure of the PEMFC catalyst layer and corresponding electrochemical reactions that take place on the surface of the carbon-supported Pt catalyst.

improved CO tolerance [96], was prepared by the alcohol-reduction method in presence of surfactant as a stabilizer. The stabilization mechanism is related to the electrostatic effect with the hydrophobic part of the surfactant molecule oriented towards the particle and the charged part pointing towards solution.

In comparison with other carbon supports, nanostructured carbon supports, e.g. carbon aerogels, have certain advantages. It was demonstrated by Smirnova and co-workers [97] that carbon aerogel can be used as an excellent support for Pt catalyst (Fig. 10.11). Using carbon aerogel-supported catalysts instead of commercially available catalysts, results in exceptionally high PEMFC power densities (0.8 mW cm^{-2} at 0.5 V) at extremely low (0.1 mg cm^{-2}) catalysts

loading [98]. These results were explained by controllable porosity (Fig. 10.12), absence of inorganic impurities, and narrow pore size distribution (Fig. 10.13).

The advantage of controllable porosity allows for even distribution of polymer ionic conductor inside catalyst layer, thus providing higher catalyst utilization, narrow pore size distribution and ensures mass transport of gas molecules to the surface of the catalyst. These advantages are further reinforced by the absence of inorganic impurities which are known to decrease catalytic activity and ionic conductivity of electrolyte.

Based on publications by Smirnova and co-workers [98,99] and results confirmed by others [100, 101], it was assumed that aerogels can be used as

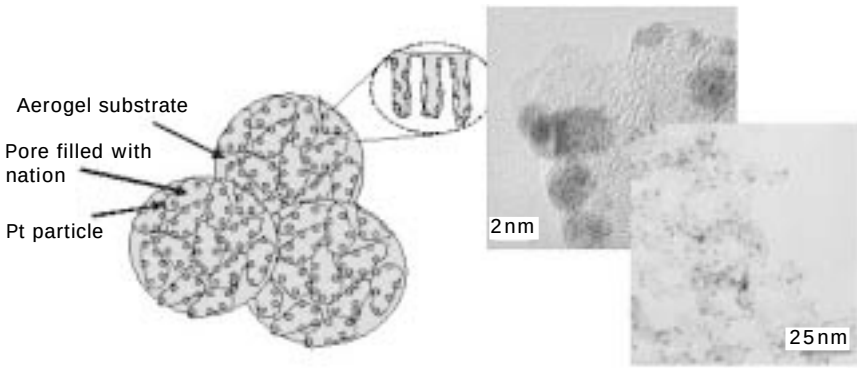

10.12 Schematics and HRTEM image of the carbon aerogel-based catalyst. Pt particles are evenly distributed on the interior of the aerogel pores filled with polymer electrolyte. HRTEM image shows Pt particles on the surface of the carbon aerogel support. With permission of Springer, '*Fuel Cell Technology*', Ed. N. Sammes.

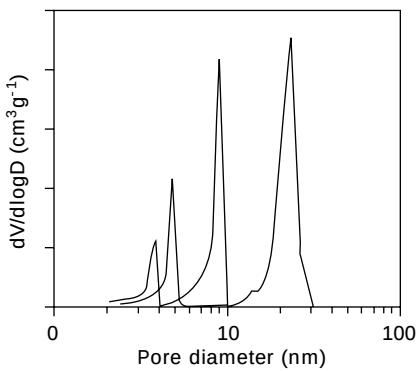

10.13 Pore size distribution in carbon aerogel Pt catalysts indicating the size of the pores for four different samples as 3, 5, 10, and 22 nm.

an exceptional nanostructured support for non-noble metal catalysts due to their controllable porosity, decreased mass transport limitations, and self-organized formation of macrocycles attached to the surface of nitrogen-modified carbon. None of this work has been done yet with non-noble metal catalysts supported on carbon aerogels.

10.7 Nanocomposite catalysts for solid oxide fuel cells

Advantages of nanocomposite materials, including lower sintering temperature and higher conductivity, move technology forwards towards development of cheap materials for SOFC manufacturing. The direct Pechini method or its variations are used in most of the latest publications for synthesis of various cathode and anode composites. The approach is based on mixing stoichiometric amounts of nitrate salts dissolved in deionized water with addition of complexing agent, for example glycine, citric or oxalic acid that after evaporation and slow heating up to 300 °C leads to combustion reaction with formation of nano-sized crystalline oxides.

Regarding the development of nanocomposite materials for SOFCs two major approaches are currently active: single-phase perovskite or perovskite-like materials used either for anode or cathode, and composite materials as a combination of metal/electrolyte ceramic phase or a few nanocomposite components. The higher operating temperature of SOFCs in comparison with PEMFC, allows the direct use of transition metals, especially as anode catalysts. Thus, Ni-based cermets as anode materials possessing mixed ionic-electronic conductivity are extensively used in most of the SOFC applications.

Complex composites comprising 50 wt%NiO and 40 wt%1Ce10ScSZ doped with 10 wt% of $La_{0.8}Sr_{0.15}Pr_{0.05}Mn_{0.2}Cr_{0.8}O_{3-\delta}$ perovskite synthesized by impregnation with aqueous solutions of polyester citric acid–ethylene glycol precursors [102] revealed pronounced chemical interaction between components in doped composite anode materials. Additional modification with Pd (0.3 wt%) or CuO (10 wt%) resulted in a high middle temperature performance in stoichiometric feed conversion of methane.

Regarding SOFC nanocomposite cathode materials [103], a few groups, including lanthanum-based Fe, Co, Ni, and Mn doped perovskites, have been developed. In the intermediate temperature range (500–600 °C) these materials possess high electronic conductivity, however, their ionic conductivity is relatively low, for instance the perovskite solid solutions of lanthanum manganite ($La_{1-x}A_xMnO_3$ where A = Sr or other alkaline-earth metal) possess almost negligible ionic conductivity. Higher ionic conductivity is known for doped lanthanum cobaltites ($La_{1-x}Sr_xCoO_{3-\delta}$) or especially lanthanum ferrite-cobaltites LSCF ($La_{0.8}Sr_{0.2}Co_{0.2}Fe_{0.8}O_3$) [104] that exhibit high electrical (340 S cm^{-1} at 550 °C) and high ionic conductivity (1×10^{-2} S cm^{-1} at 800 °C).

At 600 °C the electrical conductivities of LSCF and BSCF ($Ba_{0.5}Sr_{0.5}Co_{0.8}Fe_{0.2}O_{3-\delta}$) are 330 and 28 S cm^{-1} correspondingly. Doping with Sm in the A-site improves electrical conductivity of $(Ba_{0.5}Sr_{0.5})_{0.9}Sm_{0.1}Co_{0.8}Fe_{0.2}O_{3-\delta}$ up to 215 S cm^{-1} at 400 °C which is attributed to the increased concentration of electronic charge carriers because of the reduction of Co^{4+}, Fe^{4+} as a cathode material [105].

In general, lanthanum [106–108] and other perovskite-based oxides [109] such as $X_{0.5}Sr_{0.5}Co_{0.8}Fe_{0.2}O_{3-\delta}$ (X = Ba, La and Sm) and $La_{0.75}Sr_{0.25}Cr_{0.5}X_{0.5}O_{3-\delta}$ (X = Mn, Fe and Al) show mixed ionic–electronic conductivity when tested as SOFC electrode materials on $La_{0.9}Sr_{0.1}Ga_{0.8}Mg_{0.2}O_{2.85}$ (LSGM) electrolyte [110]. Among them [111], $Sm_{0.5}Sr_{0.5}CoO_3$ (SSC) is considered as one of the promising cathode materials for IT-SOFCs since SSC has demonstrated higher ionic conductivity than LSM, similar performance to that of LSCF, and oxygen exchange parameters higher than LSC and LSM. On the other hand, the thermal expansion coefficients (TECs) of SSC are very high (20×10^{-6} C^{-1}) which can introduce stresses during the thermocycling. The adjustment of the TEC values was achieved with Fe and Mn substitution, for example $Sm_{0.5}Sr_{0.5}Mn_{0.8}Co_{0.2}O_{3-\delta}$ which exhibits good thermal compatibility with LSGM electrolyte and electrical conductivities above 100 S cm^{-1} at 800 °C.

Besides La and Sm, other lanthanides (Ln), such as Pr, Nd, and Gd, can be used for synthesis. However, both the electrical conductivity and the oxide ion vacancy concentration decrease from La to Gd, since the pseudo-cubic lattice parameter decreases from Ln = La to Gd due to a decrease in the ionic radius of the Ln^{3+} ion. This leads to a decrease in the electrocatalytic activity for oxygen reduction. On the other hand, the TEC decreases favorably from La to Gd due to a decrease in ionic character of the Ln–O bond, thus suppressing the tendency to lose oxygen from the lattice with increasing temperature.

With regard to Gadolinia Doped Ceria (GDC) [112] as a promising electrolyte in the intermediate temperature range, Gadolinia-based cathode perovskites are considered due to the decreased influence of unfavorable reactions between cathode and electrolyte. Though a limited information regarding Gd-based catalysts is available, it is known that $Gd_xSr_{(1-x)}CoO_3$ cathode overpotential at 800 °C [113] is about one order of magnitude lower than that of lanthanum strontium manganite (LSM) at 1000 °C. It has been reported that Gadolinia and Praseodymia-based single phase cobaltites [114] achieve an area-specific resistance of approximately 0.1–0.2 Ω cm^2 at 650 °C. The structural peculiarities depending on synthesis of complex materials are reviewed in Fig. 10.14.

The results obtained by Sadykov *et al*. [115] for complex Fe, Co, Ni, Mn-containing perovskites and their nanocomposites indicate that for $La_{1-x}Sr_xMe^1_{1-y}Me^2_yO_{3+x}$ perovskites the total conductivity level at 500–800 K follows the order Ni > Co > Mn. The highest level of metallic-type conductivity

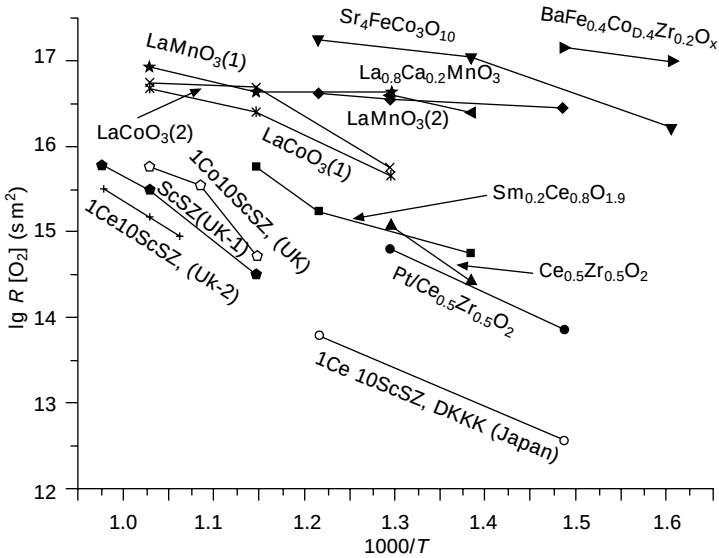

10.14 Temperature dependence of the rate of oxygen heteroexchange for a number of nanocomposite perovskites, such as $Sr_4FeCo_3O_{10}$, $Sr_4Fe_2Co_2O_{10}$, $LaMnO_3$, $Ca_{0.2}MnO_3$, $BaFe_{0.4}Co_{0.4}Zr_{0.2}O_x$, fluorite single phase or composite systems, such as $Sm_{0.2}Ce_{0.8}O_{1.9}$, $Ce_{0.5}Zr_{0.5}O_2$, $Pt/Ce_{0.5}Zr_{0.5}O_2$, and a number of materials synthesized in either Ukraine or Japan [115].

$\sim 10^3$ S cm^{-1} is revealed for $La_{0.8}Sr_{0.2}Ni_{0.4}Fe_{0.6}O_{3+x}$ and $Gd_{0.5}Sr_{0.5}CoO_{3+x}$. In the case of La_2NiO_4-type structure, e.g. $(La_{0.8}Sr_{0.2})_2Ni_{0.8}Fe_{0.32}O_{4+x}$, and doped gallates the conductivity is below 10 S cm^{-1} and 1 S cm^{-1}, respectively. For Ln–Mn composites, the total conductivity is below 10 S cm^{-1}, suggesting that Ln–Mn composites and gallates alone could be used as cathode materials. Hence, this approach can be also used for Gd-based cathode systems in order to avoid ohmic losses.

It was demonstrated that oxygen desorption starts at 150 °C for cobaltites, 250–300 °C for ferrites and nickelates, and 500 °C for manganites. In dynamic experiments, oxygen heteroexchange starts at 250 °C for cobaltites, 280 °C for nickelates, and 500 °C for manganites. At intermediate temperatures, the rate of heteroexchange is very high for pure $LaMnO_{3+x}$ due to a weak oxygen bonding with Mn^{4+} cations. For this perovskite, the lattice oxygen mobility characterized by the dynamic degree of exchange is quite low owing to the well-known absence of oxygen vacancies in the lattice. Low lattice oxygen mobility in $Sm_{0.5}Sr_{0.5}CoO_3$ possessing those vacancies is quite surprising and requires further studies. For mixed Sr-containing ferrites-cobaltites bulk/surface vacancies provide high lattice oxygen mobility along with a high rate of heteroexchange. For Ln–Mn composites the dynamic degree of exchange is higher than that of $LaMnO_{3+x}$, while the rate of heteroexchange remains

high. Similarly a high rate of heteroexchange and high lattice oxygen mobility was found for La–Sr–Fe–GDC composites.

Thus, such composites are promising for design of membranes and functionally graded cathode layers deposited on the electrolyte surface. The best La–Sr–Ni–Fe–O and La–Sr–Fe–Co–O Mixed Electronic lonic Conductor (MIECs) tested as SOFC cathodes demonstrated a stable performance in H_2/air with power density up to 800 mW/cm^2.

10.8 Other materials challenges for fuel cell materials

In the PEMFC system the amount of water produced on cathode side and brought with the gas streams on both anode and cathode sides plays a critical role in proton conduction. In order to achieve high performance, a high water content in the membrane is desirable. However, excess water can be condensed in the electrode or GDL and lead to a cell failure by impeding the gas diffusion and accessibility of the active sites on the surface of the electrocatalysts. Therefore, a number of nanomaterials approaches were applied to the PEMFC gas diffusion layers.

Gas-phase diffusion or liquid-phase transport is considered as the moving force for water transport in the flow channels of the GDL. To improve gas transport, the GDL is generally treated with PTFE to provide hydrophobic properties and reduce water saturation [116].

Carbon papers, carbon clothes, expanded and/or sintered metals and carbon nanotubes have been widely used for the gas diffusion layer (GDL) materials [117, 118]. The requirements for the GDL materials include high electric conductivity, corrosion resistance, and water and gas transport. Park *et al*. [116] investigated the GDL and micro-layer (ML) separately to determine which kind of driving forces (capillary, shear or evaporation) are dominant for controlling water transport as well as affecting cell performance (Fig. 10.15).

Effects of hydrophobic treatment and micro-porous layer (MPL) addition to a GDL in a polymer electrolyte fuel cell (PEFC) have been investigated from water balance analysis at the electrode (catalyst layer), GDL and flow channel in the cathode after a simulated start-up operation [119]. It was found that an increase in air permeability of a GDL substrate by its coarser structure increases the cumulative current, which is explained by enhancing the exhaust of the product water vapor and liquid as well as by enhancing the oxygen transport directly. Thus, the hydrophobic treatment with MPL addition and larger air permeability of a GDL substrate improve the start-up performance of a PEFC.

The effect of compression on liquid water transport and microstructure of PEMFC gas diffusion layers [120] studied using scanning electron microscopy (SEM) showed that compressing of the GDL causes the break-up of fibers

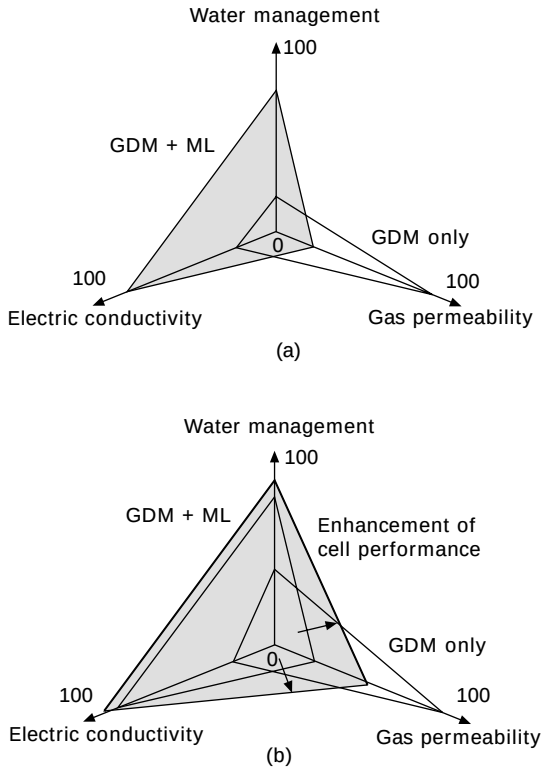

10.15 Schematic diagram on the effect of micro-layers in GDLs (a) comparison between GDM only and conventional GDL, (b) expected performance enhancement by adopting nano-materials for micro-layers. With permission of the *Journal of Power Sources* (Park *et al.* [116]).

and deterioration of the hydrophobic coating. The effect of inhomogeneous compression of GDL may lead to significant local variation of mass and PEMFC charge transport properties [121]. The removal rate of liquid water due to capillary-induced motion can be enhanced conspicuously by an increase in hydrophobicity [122] which is related to the microstructure of GDL.

10.9 Novel fuel cells based on nanocomposite materials

Fuel cell operating temperatures above 100 °C are desired to improve CO tolerance, to achieve faster reaction kinetics and easier water management, and to reduce heat exchange requirement. For this reason, novel organic/inorganic hybrid nanocomposite with incorporation of nanocrystalline ceramic oxides added to Nafion were developed that showed enhanced characteristics

at 130 °C in hydrogen and up to 145 °C in methanol solutions reaching power densities of 350 mW cm^{-2} [123]. However, a large number of nanocomposite membranes were developed for the fuel cells operating on liquid fuels, since in this case one of the factors that decrease the fuel cell performance is a crossover of the fuel through the membrane.

10.10 Polymer electrolyte fuel cells operating on liquid fuels

The PEMFC problems related to hydrogen production, storage and consumption that forced the development of liquid fuel PEMFCs have been recently overviewed by Demirci [124]. Owing to the insufficient catalytic activity of the known catalysts at low operating temperatures these fuels except methanol and formic acid cannot be considered as commercially viable. However, the significant progress that was made in the area of nanostructured catalysts and composite membranes noticeably improved their performance.

The most well-known liquid-feed fuel methanol (Table 10.1) that can be used in DMFCs is produced by steam reforming mostly from natural gas and is also used for synthesis of other liquid fuels such as dimethyl ether, dimethoxymethane, and formic acid. In respect to hydrogen, methanol has several advantages, being cheaper, easy to handle, transport and store, and having a high theoretical energy density. The second most studied liquid fuel, ethanol, is produced by hydration of acetylene or, biologically, by fermenting sugar-rich raw materials from agriculture, such as cellulose-based biomass. As the result of the reaction of fuel oxidation on the anode, all these fuels composed of carbon, hydrogen, and oxygen produce CO_2 and protons that are transported to the cathode through the polymer electrolyte membrane. The produced electrons are transported though the external circuit, producing power. Methoxy-derivatives of methane such as di-, tri-, and tetra-methoxymethane can be also considered as potential fuels in the case of new discoveries of more efficient catalysts.

Two other more rare possible fuels, specifically hydrazine and borohydride, theoretically produce N_2 and H^+ in the case of hydrazine and metaborate ion, BO_2^- and water in the case of hydrazine: $BO_4^- + 8OH^- \rightarrow 8BO_2^- + H_2O + 8e^-$.

The number of electrons involved in the reaction of fuel oxidation related to the molecular weight of fuel defines the main fuel cell parameters such as theoretical open circuit voltage (OCV) and theoretical energy conversion efficiency that in some cases could be up to 100%. However, the cleavage of the C–C bonds that are present in some of the fuels makes their oxidation into CO_2 difficult at temperatures that do not exceed 100–200 °C. These reactions are much more favorable at higher temperatures and have been successfully realized in SOFCs.

Table 10.1 Types of liquid fuels for PEMFC application and corresponding fuel cell parameters

Type of fuel	Chemical formula of the fuel	Number of electrons involved in reaction of fuel oxidation	Theoretical open circuit voltage (V)	Theoretical energy conversion efficiency (%)	References
Methanol	CH_3OH	6	1.21	97	[125-127]
Ethanol	C_2H_5OH	12	1.15	97	[128-130]
Dimethyl ether	$(CH_3)_2O$	12	1.2	95	[131-133]
Formic acid	HCOOH	2	1.4	-	[134-136]
1-Propanol	$CH_3CH_2CH_3OH$	18	1.13	97	[137-138]
2-Propanol	$CH_3CH(OH)CH_3$	18	1.12	97	[139-140]
Ethylene glycol	$C_2H_6O_2$	10	1.22	99	[141-142]
Trioxane	$C_3H_6O_3$	12	-	-	[143]
Dimethoxym ethane	$(CH_3O)_2CH_2$	16	1.23	98	[144]
Hydrazine	N_2H_4	4	1.62	100	[145-146]
Sodium borohydride	$(Na^+)BH_4^-$	8	1.64	91	[147-148]

It is necessary to note that theoretical energy conversion efficiency for PEMFCs operating on hydrogen is about 83%, which is lower than those of the higher molecular weight fuels presented in Table 10.1. From this point of view the best cell theoretically should operate on sodium borohydride.

10.11 Fuel cells operating on non-noble metal catalysts

The performance of the PEMFC cell with non-noble metal Mo_2N/C (18 wt% Mo) catalyst on the cathode [149] at 80 °C demonstrated relatively high catalytic activity (Fig. 10.16). Though the OCV was only about 0.6–0.8 V due to insufficient ORR activity, the power density of the cell was about 50–65 mW cm^{-2} during about 60 hours of operation. Increase in Mo_2N catalyst loading from 0.609 to 1.165 mg cm^{-2} demonstrated better performance that could be explained by the increase of catalyst active sites.

A nanocomposite Nafion hybrid membrane containing titanium oxide calcined at T = 400 °C as an inorganic filler was developed in order to work at medium temperature in PEFCs maintaining a suitable membrane hydration under fuel cell operative critical conditions [150]. TiO_2 ano-powder was synthesized via a sol–gel procedure by a rapid hydrolysis of $Ti(OiPr)_4$. The membrane was prepared by mixing a Nafion–dimethylacetamide (DMAc) dispersion with a 3 wt% of TiO_2 powder with the particle size of 12 nm. The results of the cell testing in the temperature range from 80 to 130 °C in

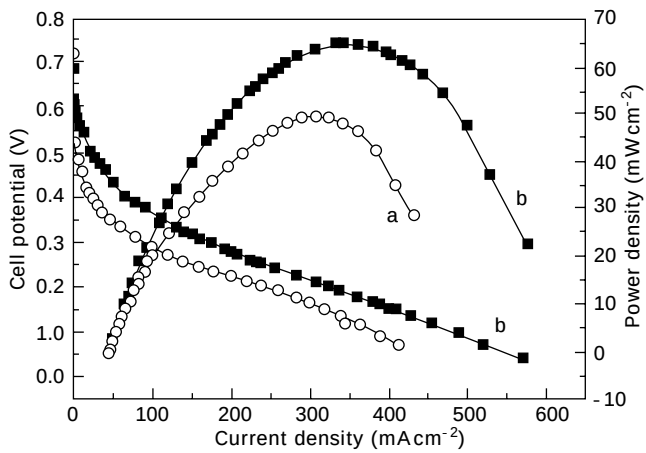

10.16 Cell performance with non-noble metal Mo_2N cathode catalyst: (a) 0.609 mg cm^{-2}; (b) 1.165 mg cm^{-2}. With permission of: H. Zhong, H. Zhang, G. Liu, Y. Liang, J. Hu, B. Yi, A novel non-noble electrocatalysts for PEMFC based on molybdenum nitride, *Electrochemistry Communications*, 8(2006) 707-712 [149].

humidified H_2/air indicated that the power density values of 0.514 and 0.256 W cm^{-2} at 0.56 V were obtained at 110 and 130 °C, respectively. Preliminary tests carried out using steam reforming (SR) synthetic fuel at about 110 °C have highlighted the benefit of the inorganic filler introduction when PEFC operates at medium temperature and with processed hydrogen. The inset in Fig. 10.17 shows a transmission electron microscopy (TEM) micrograph of TiO_2 obtained by thermal treatment of the sol–gel precursor at 500 °C.

10.12 Proton conducting solid oxide fuel cells

SOFCs using oxide proton conductors as a solid electrolyte have received more interests than traditional SOFC with oxide ion conductors because of their possible low temperature of operation between 400 and 700 °C, which is desirable for both chemical and energy conversion processes. In addition, lowering the operating temperature reduces the overall cost due to decreased material degradation and prolonged stack lifetime by utilizing metal interconnect materials.

In comparison with low- and high-temperature hydrogen energy systems, the intermediate temperature (400–600 °C) ceramic proton-conducting membranes offer significant advantages. These advantages include: easy water management and use of inexpensive catalysts in comparison with PEMFCs; no need for costly separation of water from hydrogen in electrolyzer mode; efficient separation of reformate steam without thermal management; operation as a secondary power source by using the anode gas as a fuel

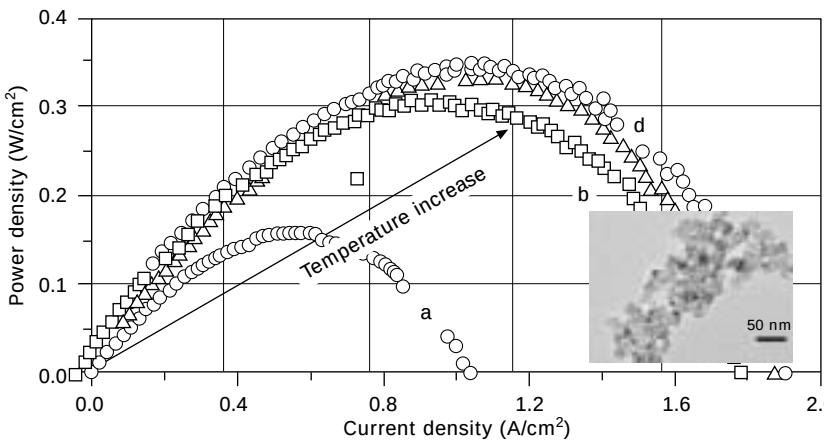

10.17 Performance of the PEMFC operating with nano-composite membranes. Power density is increasing with the operation temperature of polymer electrolyte membranes. With permission from the *Journal of Power Sources*, Licoccia and coworkers [150].

exiting from the high-temperature SOFC; low degradation effects in comparison with SOFCs, etc.

Implementation of the proton-conducting membranes is limited by either low conductivity in the case of doped zirconates or low stability in the presence of water vapour and carbon dioxide for doped cerates. One approach is to combine two perovskites and synthesize material possessing significantly higher stability and conductivity [151]. However, the conductivity of mixed cerate-zirconate membranes is still too low to reach commercialization goals [152]. Further reduction of internal resistance can be achieved by surface modification [153, 154] or doping [155].

A protonic ceramic fuel cell for high-efficiency operation with methane was proposed by Grover Coors in 2003 [156] (Fig. 10.18). Since ambipolar steam permeation from the cathode to the anode provides the steam for direct reforming of hydrocarbons, external steam injection is not required. Therefore, high thermodynamic efficiency is achieved and coking is not a problem. All of these features make it possible to construct a fuel cell of unprecedented electrical efficiency when operated on hydrocarbon fuels.

The power densities of the cell operating on hydrogen demonstrate higher maximum power density, e.g. $34\,mW\,cm^{-2}$ versus $13\,mW\,cm^{-2}$ for the cell operating on methane. However, at 80% thermodynamic efficiency, the power density on either fuel was about the same ($6\,mW\,cm^{-2}$) which was explained by the greater intrinsic efficiency of a methane cell at 1000 K than that of a hydrogen cell. Such high values of thermodynamic efficiency would not be possible with externally reformed methane, internally reformed methane

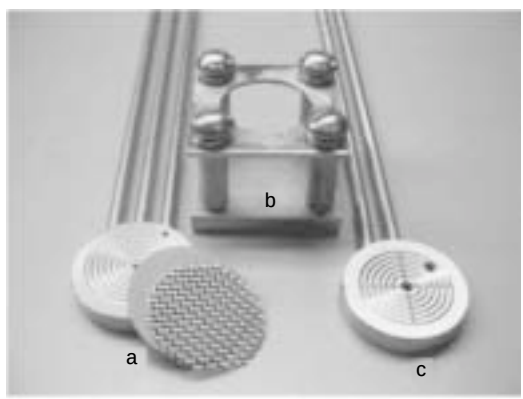

10.18 Anode bipolar disc with spiral gas distribution channel, electrolyte disk assembly (EDA) and air diffusion/current collection screen (a); cell clamping fixture (b); cathode bipolar disc inverted (c). With permission from the *Journal of Power Sources*, Grover Coors [156].

with injected steam, or methane subjected to partial oxidation, because of the decrease in fuel fugacity.

SOFC with a proton-conductive electrolyte, $BaCe_{0.9}Nd_{0.1}O_{3-\delta}$ (BCNO), was prepared by the modified Pechini method using NiO–BCNO as the anode [157] and $La_{0.5}Sr_{0.5}CoO_{3-\delta}$ (LSCO) as the cathode. At 700 °C the OCV and the peak power density of a cell with 20 μm thick BCNO electrolyte were 0.950 V and 315 mW cm^{-2}, respectively. To test possible harmful CO_2 effects on the cell performance, the cell with the BCNO electrolyte was tested in H_2 contaminated with CO_2 at 700 °C. A voltage of 0.80 V and current density about 0.220 A cm^2 were obtained that were stable during at least 17 h of operation.

10.13 Conclusion

The design and synthesis of various nanocomposite polymer and solid-state materials has emerged as a cutting edge of materials research. These materials promise significant advantages in technologies of substantial commercial interest, including power storage and generating devices, such as batteries, supercapacitors, and fuel cells that potentially could solve the problem of fossil sources of energy. However, more sytems should be investigated in order to increase catalytic activity of the catalysts, ionic conductivity for membranes, and stability in the fuel cell environment. Synergistic approaches in multidisciplinary areas of research will ensure the success of the next fuel cell generation technology.

10.14 References

1. J. E. Brown, C. N. Hendry and P. Harborne, An emerging market in fuel cells? Residential combined heat and power in four countries, *Energy Policy*, (2006).
2. M. Echigo, N. Shinke, S. Takami and T. Tabata, Performance of a natural gas fuel processor for residential PEFC system using a novel CO preferential oxidation catalyst, *Journal of Power Sources*, **132**(1–2) (2004) 29–35.
3. C. M. Miesse, W. S. Jung, K.-J. Jeong, J. K. Lee, J. Lee, J. Han, S. P. Yoon, S. W. Nam, T.-H. Lim and S.-A. Hong, Direct formic acid fuel cell portable power system for the operation of a laptop computer, *Journal of Power Sources*, **162**(1) (2006) 532–540.
4. K. Cowey, K. J. Green, G. O. Mepsted and R. Reeve, Portable and military fuel cells, *Current Opinion in Solid State and Materials Science*, **8**(5) (2004) 367–371.
5. G.-G. Park, S.-D. Yim, Y.-G. Yoon, W.-Y. Lee, C.-S. Kim, D.-J. Seo and K. Eguchi, Hydrogen production with integrated microchannel fuel processor for portable fuel cell systems, *Journal of Power Sources*, **145**(2) (2005) 702–706.
6. Y. Yamazaki, Application of MEMS technology to micro fuel cells, *Electrochimica Acta*, **50**(2–3) (2004) 663–666.

7. W. Münch, H. Frey, M. Edel and A. Kessler, Stationary fuel cells – Results of 2 years of operation at EnBW, *Journal of Power Sources*, **155**(1) (2006) 77–82.
8. H. L. MacLean and L. B. Lave, Evaluating automobile fuel/propulsion system technologies, *Progress in Energy and Combustion Science*, **29**(1) (2003) 1–69.
9. J. McBreen, M. Balasubramanian, W.-S. Yoon, K. Y. Chung, H. S. Lee, X.-Q. Yang, R. Atanasoski, A. Schmoeckel, G. D. Vermstrom and M. K. Debe, PEM fuel cells: materials issues, *ECS Transactions*, **1**(6) (2006) 149.
10. A. Smirnova, X. Dong H. Hara and N. Sammes, Aerogel based catalyst PEMFC operating at room temperature, *International Journal of Hydrogen Energy*, **3** (2006) 477–481.
11. E. Endoh, Highly durable MEA for PEMFC under high temperature and low humidity conditions, *ECS Transactions*, **3**(1) (2006) 9.
12. S. P. S. Badwal and K. Foger, Solid oxide electrolyte fuel cell review, *Ceramics International*, **22**(3) (1996) 257–265.
13. M. C. Williams, J. Strakey and W. Sudoval, U.S. DOE fossil energy fuel cells program, *Journal of Power Sources*, **159**(2) (2006) 1241–1247.
14. M.-F. Hsu, L.-J. Wu, J.-M. Wu, Y.-H. Shiu and K.-F. Lin, Solid oxide fuel cell fabricated using all-perovskite materials, *Electrochemistry Solid-State Letters*, **9** (2006) A193.
15. T. Suzuki, T. Yamaguchi, Y. Fujishiro and M. Awano, Improvement of SOFC performance using a microtubular, anode-supported SOFC, *Journal of the Electrochemical Society*, **153** (2006) A925.
16. J. Akikusa, T. Yamada and T. Kotani, Development of intermediate temperature SOFC module and system, *Meetings Abstracts – Electrochemical Society*, **501** (2006) 1034.
17. B. Feng, C. Y. Wang and B. Zhu, Catalysts and performances for direct methanol low-temperature (300°C to 600°C) solid oxide fuel cells, *Electrochemistry Solid-State Letters*, **9** (2006) A80–A81.
18. J.-H. Wan, J.-Q. Yan and J. B. Goodenough, LSGM-based solid oxide fuel cell with 1.4W/cm^2 power density and 30 day long-term stability, *Journal of the Electrochemical Society*, **152** (2005) A1511–A1515.
19. M. Duerr, S. Gair, A. Cruden and J. McDonald, Hydrogen and electrical energy from organic waste treatment, *International Journal of Hydrogen Energy*, (2006).
20. S. Gair, A. Cruden, J. McDonald, T. Hegarty and M. Chesshire, Fuel cells for power generation and waste treatment, *Journal of Power Sources*, **154**(2) (2006) 472–478.
21. M. Krumbeck, T. Klinge and B. Döding, First European fuel cell installation with anaerobic digester gas in a molten carbonate fuel cell, *Journal of Power Sources*, **157**(2) (2006) 902–905.
22. A. Demirbas, Progress and recent trends in biofuels, *Progress in Energy and Combustion Science*, **33**(1) (2007) 1–18.
23. S. Litster and G. McLean, PEM fuel cell electrodes, *Journal of Power Sources*, **130**(1–2) (2004) 61–76.
24. R. Bashyam and P. Zelenay, A class of non-precious metal composite catalysts for fuel cells, *Nature*, **443**(7) (2006) 63–66.
25. A. Lavrov, A. Smirnova, H. Gorgun and N. Sammes, Thin inclusion approach for modeling of heterogeneous conducting materials, *Journal of Power Sources*, **155**(2) (2006) 239–245.

26. L. Sridhar, R. Gupta and M. Bhardwaj, Barrier properties of polymer nanocomposites, *Indian Engineering and Chemistry Research*, **45** (2006) 8282–8289.
27. H.-G. Haubold, Th. Vad, H. Jungbluth and P. Hiller, Nano structure of NAFION: a SAXS study, *Electrochimica Act*, **46**(10–11) (2001) 1559–1563.
28. K. Schmidt-Rohr, DOE report: http://www.hydrogen.energy.gov/pdfs/ review07/ bes_5_schmidt-rohr.pdf
29. B. Smitha, S. Sridhar and A. A. Khan, Solid polymer electrolyte membranes for fuel cell applications – a review, *Journal of Membrane Science*, **259**(1–2) (2005) 10–26.
30. V. Neburchilov, J. Martin, H. Wang and J. Zhang, A review of polymer electrolyte membranes for direct methanol fuel cells, *Journal of Power Sources*, **169**(2) (2007) 221–238.
31. E. N. Gribov, E. V. Parkhomchuk, I. M. Krivobokov, J. A. Darr and A. G. Okunev, Supercritical CO_2 assisted synthesis of highly selective Nafion–zeolite nanocomposite membranes for direct methanol fuel cells, *Journal of Membrane Science*, **297**(1–2) (2007) 1–4.
32. G. Vaivars, N. M. Maxakato, T. Mokrani, L. Petric, J. Klavis, G. Gerike and V. Linkov, *Materials Science*, **10** (2004) 162–165.
33. C. Yang, S. Srinivasan, A. Arico, P. Creti and V. Baglio, Composite Nafion/zirconium phosphate membranes for direct methanol fuel cell operation at high temperature, *Electrochemical and Solid State Letters*, **4** (2001) A31–A34.
34. G. Alberti, M. Casciola, A. Donnadio, R. Narducci, M. Pica and M. Sganappa, Preparation and properties of Nafion membranes containing nanoparticles of zirconium phosphate, *Desalination*, **199**(1–3) (2006) 280–282.
35. B. Libby, W. H. Smyrl and E. L. Cussler, *Electrochemical Solid-State Letters*, **4** (2001) A197.
36. R. C. Jiang, H. R. Kunz and J. M. Fenton, *Journal of Membrane Science*, **272** (2006) 116–124.
37. E. Peled, T. Duvdevani and A. Melman, A novel proton conducting membrane, *Electrochemical Solid-State Letters*, **1** (1998) 210–211.
38. E. Peled, T. Duvdevani, A. Aharon and A. Melman, *Electrochemical Solid-State Letters*, **3** (2000) 525–528.
39. S. Panero, F. Ciuffa, A. D'Epifano and B. Scrosati, New concepts for the development of lithium and proton conducting membranes, *Electrochimical Acta*, **48** (2003) 2009–2014.
40. A. Fernicola, S. Panero and B. Scrosati, Proton-conducting membranes based an protic ionic liquids, *Journal of Power Sources*, Available online (2008).
41. J. Shen, J. Xi, W. Zhu, L. Chen and X. Qiu A nanocomposite proton exchange membrane based on PVDF, poly(2-acrylamido-2-methyl propylene sulfonic acid), and nano-Al_2O_3 for direct methanol fuel cells, *Journal of Power Sources*, **159**(2) (2006) 894–899.
42. M. L. Ponce, L. A. S. de A. Prado, V. Silva and S. P. Nunes, Membranes for direct methanol fuel cell based on modified heteropolyacids, *Desalination*, **162** (2004) 383–391.
43. A. Regina, E. Fontananova, E. Drioli, M. Casciola, M. Sganappa and F. Trotta Preparation and characterization of sulfonated PEEK-WC membranes for fuel cell applications: a comparison between polymeric and composite membranes, *Journal of Power Sources*, **160**(1) (2006) 139–147.
44. S. Licoccia and E. Traversa, Increasing the operation temperature of polymer

electrolyte membranes for fuel cells: from nanocomposites to hybrids, *Journal of Power Sources*, **159**(1) (2006) 12–20.
45. M. Burjanadze, J. Paulsdorf, N. Kaskhedikar, Y. Karatas and H.-D. Wiemhöfer, Proton conducting membranes from sulfonated poly[bis(phenoxy)phosphazenes] with an interpenetrating hydrophilic network, *Solid State Ionics*, **177**(26–32) (2006) 2425–2430.
46. N. Kaskhedikar, J. Paulsdorf, M. Burjanadze, Y. Karatas, B. Roling and H.-D. Wiemhöfer, Polyphosphazene based composite polymer electrolytes, *Solid State Ionics*, **177**(26–32) (2006) 2699–2704.
47. H. R. Allcock, Y. Chang and D. T. Welna, Ionic conductivity of covalently interconnected polyphosphazene–silicate hybrid networks, *Solid State Ionics*, **177** (5–6) (2006) 569–572.
48. T. Sancho, J. Soler and M. P. Pina, Conductivity in zeolite–polymer composite membranes for PEMFCs, *Journal of Power Sources*, **169**(1) (2007) 92–97.
49. M. T. Colomer, Nanoporous anatase ceramic membranes as fast-proton-conducting materials, *Journal of the European Ceramic Society*, **26**(7) (2006) 1231–1236.
50. I. Kaus, P. Dahl, J. Mastin, T. Grande and M.-A. Einarsrud, Synthesis and characterization of nanocrystalline YSZ powder by smoldering combustion synthesis, *Journal of Nanomaterials*, ID49283 (2006) 1–7.
51. N. Sammes, R. Phillips and A. Smirnova, Proton conductivity in stoichiometric and sub-stoichiometric yittrium doped $SrCeO_3$ ceramic electrolytes, *Journal of Power Sources*, **134** (2004) 153–159.
52. J. Maier, Defect chemistry and ion transport in nanostructured materials: Part II. aspects of nanoionics, *Solid State Ionics*, **157**(1–4) (2003) 327–334.
53. H. Iwahara, Y. Asakura, K. Katahira and M. Tanaka, Prospect of hydrogen technology using proton-conducting ceramics, *Solid State Ionics*, **168**(3–4) (2004) 299–310.
54. S. Higgins, N. Sammes, A. Smirnova, J. Kilner and G. Tompsett, Yttrium-doped Barium zirconates as ceramic conductors in the intermediate temperature range, *Journal of Fuel Science and Technology*, **4** (2008), 011003(1)–011003(4)
55. Y.-J. Yang, T.-L. Wen, H. Tu, D.-Q. Wang and J. Yang, Characteristics of lanthanum strontium chromite prepared by glycine nitrate process, *Solid State Ionics*, **135** (1–4) (2000) 475–479.
56. A. B. Yaroslavtsev, Modification of solid state proton conductors, *Solid State Ionics*, **176** (39–40) (2005) 2935–2940.
57. C. C. Liang, Conduction characteristics of the lithium iodide-aluminum oxide solid electrolytes, *Journal of the Electrochemical Society*, **120** (1973) 1289–1291.
58. V. G. Ponomareva and G. V. Lavrova, The investigation of disordered phases in nanocomposite proton electrolytes based on $MeHSO_4$ (Me = Rb, Cs, K), *Solid State Ionics*, **145** (2001) 197.
59. J. B. Goodenough, J. E. Ruiz-Diaz and Y. S. Zhen, Oxide-ion conduction in $Ba_2In_2O_5$ and $Ba_3In_2MO_8$ (M = Ce, Hf, or Zr), *Solid State Ionics*, **44** (1990) 21–31.
60. W. Grover Coors, Protonic ceramic steam-permeable membranes, *Solid State Ionics*, **178** (2007) 481–485.
61. K. D. Kreuger, Aspects of the formation and mobility of protonic charge carriers and the stability of perovskite-type oxides, *Solid State Ionics*, **125** (1999) 285–302.
62. T. Schober and H. G. Bohn, Water vapor solubility and electrochemical characterization of the high temperature proton conductor $BaZr_{0.9}Y_{0.1}O_{2.95}$, *Solid State Ionics*, **127** (2000) 351–360.

63. E. Fabbri , A. D'Epifanio, E. Di Bartolomeo, S. Licoccia and E. Traversa, Tailoring the chemical stability of $Ba(Ce_{0.8-x}Zr_x)Y_{0.2}O_{3-\delta}$ protonic conductors for Intermediate Temperature Solid Oxide Fuel Cells (IT-SOFCs), *Solid State Ionics* **179** (15-16) (2008) 558–564.
64. K. Katahira, Y Kohchi, T. Shimura and H. Iwahara, Protonic conduction in Zr-substituted $BaCeO_3$, *Solid State Ionics*, **138** (2000) 91–98.
65. K. D. Kreuger, Proton conducting oxides, *Annual Review of Materials Research*, **33** (2003) 333–359.
66. P. Babilo and S. M. Haile, Enhanced sintering of yttrium-doped barium zirconate by addition of ZnO, *Journal of the American Ceramics Society*, **88** (2005) 2362–2368.
67. A. Magrasó, F. Espiell, M. Segarra and J. T. S. Irvine, Chemical and electrical properties of $BaPr_{0.7}Gd_{0.3}O_{3-\delta}$, *Journal of Power Sources*, **169** (1) (2007) 53–58.
68. K. D. Kreuger, St. Adams, W. Münch, A. Fuchs, U. Klock and J. Maier, Proton conducting alkaline earth zirconates and titanates for high drain electrochemical applications, *Solid State Ionics*, **145** (2001) 295–306.
69. R. Hui, R. Maric, C. Decès-Petit, E. Styles, W. Qu, X. Zhang, J. Roller, S. Yick, D. Ghosh and K. Sakata, Proton conduction in ceria-doped $Ba_2In_2O_5$ nanocrystalline ceramic at low temperature, *Journal of Power Sources*, **161** (1) (2006) 40–46.
70. A. K. Azad and J. T. S. Irvine, Synthesis, chemical stability and proton conductivity of the perovskites $Ba(Ce,Zr)_{1-x}Sc_xO_{3-\delta}$, *Solid State Ionics*, **178** (7–10) (2007) 635–640.
71. T. Kobayashi, H. Watanabe, M. Hibino and T. Yao, Electrical conductivity of $Ba_{1-x}La_xSc_{1-y}Zr_yO_{3-\delta}$ with defective perovskite structure, *Solid State Ionics*, **176** (31–34) (2005) 2439–2443.
72. Y. Zhang and C. Erkey, Preparation of supported metallic nanoparticles using supercritical fluids: a review, *Journal of Supercritical Fluids*, **38** (2) (2006), 252–267.
73. A. Smirnova, X. Dong, H. Hara and N. Sammes, New generation of catalyst layers for PEMFCs based on carbon aerogel supported Pt catalyst (CASPC), in: *Fuel Cells: Reaching Towards Commercialization*, Ch.7, p. 57–72. Springer 2006.
74. E. Antolini, Platinum-based ternary catalysts for low temperature fuel cells: Part I. preparation methods and structural characteristics, *Applied Catalysis B: Environmental* **74** (3-4) (2007), 324–336.
75. H. R. Colón-Mercado and B. N. Popov, Stability of platinum based alloy cathode catalysts in PEM fuel cells, *Journal of Power Sources*, **155**(2) (2006) 253.
76. M. Königsmann, N. Donati, D. Stein, H. Schönberg, J. Harmer, A. Sreekanth and H. Grützmacherm, Metalloenzyme-inspired catalysis: selective oxidation of primary alcohols with an iridium-aminyl-radical complex, *Angewandte Chemie International Edition*, **46**(19) 3567–3570.
77. A.-M. Hays, A. R. Dunn, R. Chiu, H. B. Gray, C. D. Stout and D. B. Goodin, Conformational states of cytochrome $P450_{cam}$ revealed by trapping of synthetic molecular wires, *Journal of Molecular Biology*, **344** (2004) 455–469.
78. A. K. Udit, W. Belliston-Bittner, E. C. Glazer, Y. H. L. Nguyen, M. Gillon, M. G. Hill, M. A. Marletta, D.B. Goodin and Gray, H. B. Redox couples of inducible nitric oxide synthase. *Journal of the American Chemical Society*, **127** (2005) 11212–11213.
79. Y. Gochi-Ponce, G. Alonso-Nuñez and N. Alonso-Vante, Synthesis and electrochemical characterization of a novel platinum chalcogenide electrocatalyst

with an enhanced tolerance to methanol in the oxygen reduction reaction, *Electrochemistry Communications*, **8** (9) (2006) 1487–1491.
80. R. W. Reeve, P. A. Christensen, A. J. Dickinson, A. Hamnett and K. Scott, Methanol-tolerant oxygen reduction catalysts based on transition metal sulfides and their application to the study of methanol permeation, *Electrochimical Acta*, **45** (25-26) (2000) 4237–4250.
81. M. A. Grigoriu, D. Villers, F. Jaouen and J. P. Dodelet, Catalysts for oxygen reduction in PEM fuel cells based on Co/Fe porphyrins, Proceedings of the Electrochemical Society PV 2005-11(2005) 242–253.
82. H. A. Gasteiger, S. S. Kocha, B. Sompalli and F. T. Wagner, Activity benchmarks and requirements for Pt, Pt-alloy, and non-Pt oxygen reduction catalysts for PEMFCs, *Applied Catalysis B: Environmental*, **56**(1–2) (2005) 9–35.
83. R. Venkataraman, H. R. Kunz and J. M. Fenton, Development of new CO tolerant ternary anode catalysts for proton exchange membrane fuel cells, *Journal of the Electrochemical Society*, **150** (2003) A278–A284.
84. K. Lee, A. Ishihara, S. Mitsushima, N. Kamiya and K. Ota, Stability and electrocatalytic activity for oxygen reduction in WC + Ta catalyst, *Electrochimical Acta*, **49** (2004) 3479–3485.
85. H. Zhong, H. Zhang, G. Liu, Y. Liang, J. Hu and B. Yi, A novel non-noble electrocatalyst for PEM fuel cell based on molybdenum nitride, *Electrochemistry Communications*, **8**(5) (2006) 707–712.
86. H. Zhong, H. Zhang, Y. Liang, J. Zhang, M. Wang and X. Wang, A novel non-noble electrocatalyst for oxygen reduction in proton exchange membrane fuel cells, *Journal of Power Sources*, **164**(2) (2007) 572–577.
87. L. Zhang, J. Zhang, D. P. Wilkinson and H. Wang, Progress in preparation of non-noble electrocatalysts for PEM fuel cell reactions**,** *Journal of Power Sources*, **156**(2) (2006) 171–182.
88. H. Shioyama, Y. Yamada, A. Ueda and T. Kobayashi, Graphite intercalation compounds as PEMFC electrocatalyst supports, *Carbon*, **43** (11) (2005) 2374–2378.
89. R. Bashyam and P. Zelenay, A class of non-precious metal composite catalysts for fuel cells, *Nature*, **443**(7) (2006) 63–66.
90. N. P. Subramanian, S. P. Kumaraguru, H. Colon-Mercado, H. Kim, B. N. Popov, T. Black and D. A. Chen, Studies on Co-based catalysts supported on modified carbon substrates for PEMFC cathodes, *Journal of Power Sources*, **157**(1) (2006) 56–63.
91. N. A. Kotov, Carbon sheet solution, *Nature*, **442** (2006) 254.
92. J. Y Huang, S. Chen, Z. Q. Wang, K. Kempa, Y. M. Wang, S. H. Jo, G. Chen, M. S. Dreselhauss and Z. F. Ren, *Nature*, **439** (2006) 281.
93. M. Carmo, V. A. Paganin, J. M. Rosolen and E. R. Gonzalez, Alternative supports for the preparation of catalysts for low-temperature fuel cells: the use of carbon nanotubes, *Journal of Power Sources*, **142** (2005) 169–176.
94. N. Rajalakshmib, H. Ryub, M. M. Shaijumona and S. Ramaprabhu, Performance of polymer electrolyte membrane fuel cells with carbon nanotubes as oxygen reduction catalyst support material, *Journal of Power Sources*, **140** (2005) 250–257.
95. A. Bayrakçeken, A. Smirnova, N. Kitkamthorn, M. Arndow, L. Türker and I. Eroglu, Pt-based electrocatalysts for polymer electrolyte membrane fuels cells prepared by supercritical deposition technique, *Journal of Power Sources*, **179** (2008) 532–540.

96. M. Gangeri, S. Perathoner and G. Centi, Synthesis and performances of carbon-supported noble metal nano-clusters as electrodes for polymer electrolyte membrane fuel cells, *Inorganica Chimica Acta*, **359** (2006) 4828–4832.
97. H. Hara and A. Smirnova, Method of preparing membrane electrode assembles with aerogel supported catalyst, International Patent application: WO 2005/086914 A2.
98. A. Smirnova, X. Dong, H. Hara and N. Sammes, Aerogel based catalyst for PEMFCs operating at room temperature, *Journal of Fuel Cell Science and Technology*, **3**(1) (2006) 477–488.
99. F. Dundar, A. Smirnova, X. Dong, A. Ata and N. Sammes, Rotating disk electrode study of supported and unsupported catalysts for PEMFC application, *Journal of Fuel Cell Science and Technology*, **3** (2006) 428–433.
100. J. Wang, X. Yang, D. Wu , R. Fu, M. S. Dresselhaus and G. Dresselhaus, The porous structures of activated carbon aerogels and their effects on electrochemical performance, *Journal of Power Sources*, (2008) in press.
101. N. Joba, J. Marieb, S. Lamberta, S. Berthon-Fabryb and P. Achard, Carbon xerogels as catalyst supports for PEM fuel cell cathode, *Energy Conversion and Management*, **49** (9) (2008) 2461–2470.
102. V. Sadykov, N. Mezentzeva, R. Bunina, G. Alikina, A. Likashevich, T. Kharlamova, V. Rogov, Z. V. Zaikovskii, A. Ischenko, T. Krieger, O. Bobrenok, A. Smirnova, J. Irvine and O. Vasyliev, Effect of complex oxide promoters and Pd on activity and stability of Ni/YSZ (ScSZ) cermets as anodes for IT SOFC, *MRS Proceedings 2006 Fall Meeting*, Boston, MA.
103. V. Sadykov, N. Mezentseva, V. Muzykantov, G. Alikina, L. Batuev, A. Lukashevich, O. Bobrenok, N. Uvarov, V. Zyryanov, A. Smirnova, E. Politova, J. Kilner and C. Argirusis, Complex perovskites and their composites with doped ceria as advanced materials for solid oxide fuel cell cathodes and membranes, *Europacat VIII* 26–31 August 2007 Turku/Åbo Finland, Conference proceedings (2007).
104. G. C. Kostogloudis and C. Ftikos, Properties of A-site-deficient $La_{0.6}Sr_{0.4}Co_{0.2}Fe_{0.8}O_{3-\delta}$-based perovskite oxides, *Solid State Ionics*, **126**(1–2) (1999) 143–151.
105. S. Li, Z. Lü, N. Ai, K. Chen and W. Su, Electrochemical performance of $(Ba_{0.5}Sr_{0.5})_{0.9}Sm_{0.1}Co_{0.8}Fe_{0.2}O_{3-\delta}$ as an intermediate temperature solid oxide fuel cell cathode, *Journal of Power Sources*, **165**(1) (2007) 97–101.
106. W. Kim, H. Song, J. Moon and H. Lee, Intermediate temperature solid oxide fuel cell using $(La,Sr)(Co,Fe)O_3$-based cathodes, *Solid State Ionics*, 1**77**(35–36) (2006), 3211–3216.
107. H. Kusaba, Y. Shibata, K. Sasaki and Y. Teraoka, Surface effect on oxygen permeation through dense membrane of mixed-conductive LSCF perovskite-type oxide, *Solid State Ionics*, **177**(26–32) (2006) 2249–2253.
108. Y. Wang, S. Wang, Z. Wang, T. Wen and Z. Wen, Performance of $Ba_{0.5}Sr_{0.5}Co_{0.8}Fe_{0.2}O_{3-\delta}$-CGO-Ag cathode for IT-SOFCs, *Journal of Alloys and Compounds*, **428**(1–2) (2007) 286–289.
109. J. Peña-Martínez, D. Marrero-López, J. C. Ruiz-Morales, B. E. Buergler, P. Núñez and L. J. Gauckler, Fuel cell studies of perovskite-type materials for IT-SOFC, *Journal of Power Sources*, **159**(2) (2006) 914–921.
110. J. Peña-Martínez, D. Marrero-López, D. Pérez-Coll, J.C. Ruiz-Morales and P. Núñez Performance of XSCoF (X = Ba, La and Sm) and LSCrX' (X′ = Mn, Fe and Al) perovskite-structure materials on LSGM electrolyte for IT-SOFC, *Electrochimica Acta*, **52**(9) (2007) 2950–2958.

111. H. Lv, B. Zhao, Y. Wu, G. Sun, G. Chen and K. Hu, Effect of B-site doping on $Sm_{0.5}Sr_{0.5}M_xCo_{1-x}O_{3-\delta}$ properties for IT-SOFC cathode material (M = Fe, Mn), *Materials Research Bulletin*, **42** (12) (2007), 1999–2012.
112. K. C. Wincewicz and J. S. Cooper, Taxonomies of SOFC material and manufacturing alternatives, *Journal of Power Sources*, **140** (2005) 280–296.
113. J. M. Ralf, J. A. Kilner and B. C. H. Steele, Improving Gd-doped ceria electrolytes for solid oxide fuel cells, *Materials Research Society Sympesium Proceedings*, **575** (2001) 309.
114. C. Rossignol, J.M. Ralph, J.-M. Bae and J. T. Vaughey, $Ln_{1-x}Sr_xCoO_3$ (Ln = Gd, Pr) as a cathode for intermediate-temperature solid oxide fuel cells, *Solid State Ionics*, **175**(1–4) (2004) 59–61.
115. V. Sadykov, N. Mezenzeva, V. Musikantov, N. Sammes, J. Kilner and A. Smirnova, Cathode materials for intermediate temperature SOFCs, *Proceedings of the IMPRES International Symposium*, 2007 Kyoto, Japan.
116. G.-G. Park, Y.-J. Sohn, S.-D. Yim, T.-H. Yang, Y.-G. Yoon, W.-Y. Lee, K. Eguchi and C.-S. Kim, Adoption of nano-materials for the micro-layer in gas diffusion layers of PEMFCs, *Journal of Power Sources*, **163**(1) (2006) 113–118.
117. T. Hottinen, O. Himanen and P. Lund, Effect of cathode structure on planar free-breathing PEMFC , *Journal of Power Sources*, **138** (2004), 205–210.
118. J. Benziger, J. Nehlsen, D. Blackwell, T. Brennan and J. Itescu, Water flow in the gas diffusion layer of PEM fuel cells, *Journal of Membrane Science*, **261** (2005), 98–106.
119. H. Nakajima, T. Konomi and T. Kitahara, Direct water balance analysis on a polymer electrolyte fuel cell (PEFC): effects of hydrophobic treatment and micro-porous layer addition to the gas diffusion layer of a PEFC on its performance during a simulated start-up operation, *Journal of Power Sources*, **171**(2) (2007), 457–463.
120. A. Bazylak, D. Sinton, Z.-S. Liu and N. Djilali, Effect of compression on liquid water transport and microstructure of PEMFC gas diffusion layers, *Journal of Power Sources*, **163**(2) (2007) 784–792.
121. I. Nitta, T. Hottinen, O. Himanen and M. Mikkola, Inhomogeneous compression of PEMFC gas diffusion layer: Part I. Experimental, *Journal of Power Sources*, **171** (1) (2007), 26–36.
122. M.-H. Chang, F. Chen and H.-S. Teng, Effects of two-phase transport in the cathode gas diffusion layer on the performance of a PEMFC, *Journal of Power Sources*, **160**(1) (2006) 268–276.
124. S. Licoccia and E. Traversa, From nanocomposites to hybrids, *Journal of Power Sources*, **159**(1) (2006) 12–20.
124. U. Demirci, Direct liquid-feed fuel cells: thermodynamic and environmental concerns, *Journal of Power Sources*, **169**(2) (2007) 239–246.
125. Q. Mao, G. Sun, S. Wang, H. Sun, G. Wang, Y. Gao, A. Ye, Y. Tian and Q. Xin, Comparative studies of configurations and preparation methods for direct methanol fuel cell electrodes, *Electrochimica Acta*, **52** (2007) 6763–6770.
126. K.-Y. Song, H.-K. Lee and H.-T. Kim, MEA design for low water crossover in air breathing DMFC, *Electrochimica Acta*, **53** (2) (2007), 637–643.
127. V. Neburchilov, H. Wang and J. Zhang, Low Pt content Pt–Ru–Ir–Sn quaternary catalysts for anodic methanol oxidation in DMFC, *Electrochemistry Communications*, **9**(7) (2007) 1788–1792.
128. J. Ribeiro, D. M. dos Anjos, K. B. Kokoh, C. Coutanceau, J.-M. Léger, P. Olivi, A.

R. de Andrade and G. Tremiliosi-Filho, Carbon-supported ternary PtSnIr catalysts for direct ethanol fuel cell *Electrochimica Acta*, **52**(24) 6997–7006.
129. E. Antolini, Catalysts for direct ethanol fuel cells, *Journal of Power Sources*, **170**(1) (2007) 1–12.
130. T. Mathuraiveeran, K. Roelofs, D. Senftleben and T. Schiestel, Proton conducting composite membranes with low ethanol crossover for DEFC, *Desalination*, **200** (1–3) (2006) 662–663.
131. Y. Liu, M. Muraoka, S. Mitsushima, K.-I. Ota and N. Kamiya, Electrochemical and ATR- FTIR study of dimethyl ether and methanol electro-oxidation on sputtered Pt electrode, *Electrochimica Acta*, **52**(19) (2007) 5781–5788.
132. J.-H. Yoo, H.-G. Choi, C.-H. Chung and S. M. Cho, Fuel cells using dimethyl ether, *Journal of Power Sources*, **163**(1) (2006) 103–106.
133. S. Ueda, M. Eguchi, K. Uno, Y. Tsutsumi and N. Ogawa, Electrochemical characteristics of direct dimethyl ether fuel cells, *Solid State Ionics*, **177**(19–25) (2006) 2175–2178.
134. K.-J. Jeong, C. M. Miesse, J.-H. Choi, J. Lee, J. Han, S. P. Yoon, S. W. Nam, T.-H. Lim and T. G. Lee, Fuel crossover in direct formic acid fuel cells, *Journal of Power Sources*, **168**(1) (2007) 119–125.
135. S. Uhm, S. T. Chung and J. Lee, Activity of Pt anode catalyst modified by underpotential deposited Pb in a direct formic acid fuel cell, *Electrochemistry Communications*, **9**(8) (2007) 2027–2031.
136. X. Zhou, W. Xing, C. Liu and T. Lu, Platinum-macrocycle co-catalyst for electro-oxidation of formic acid, *Electrochemistry Communications*, **9**(7) (2007) 1469–1473.
137. M. Saito, S. Ikesaka, J. Kuwano, J. Qiao, S. Tsuzuki, K. Hayamizu and T. Okada Mechanisms of proton transport in alcohol-penetrated perfluorosulfonated ionomer membranes for fuel cells, *Solid State Ionics*, **178**(7–10) (2007) 539–545.
138. N. Fujiwara, Z. Siroma, T. Ioroi and K. Yasuda, Rapid evaluation of the electrooxidation of fuel compounds with a multiple-electrode setup for direct polymer electrolyte fuel cells, *Journal of Power Sources*, **164**(2) (2007) 457–463.
139. N. H. Jalani and R. Datta, The effect of equivalent weight, temperature, cationic forms, sorbates, and nanoinorganic additives on the sorption behavior of Nafion®, *Journal of Membrane Science*, **264**(1–2) (2005) 167–175.
140. J. Otomo, X. Li, T. Kobayashi, C. Wen, H. Nagamoto and H. Takahashi, AC-impedance spectroscopy of anodic reactions with adsorbed intermediates: electro-oxidations of 2-propanol and methanol on carbon-supported Pt catalyst, *Journal of Electroanalytical Chemistry*, **573**(1) (2004) 99–109.
141. L. Zhang, K. Lee and J. Zhang, Effect of synthetic reducing agents on morphology and ORR activity of carbon–supported nano-Pd–Co alloy electrocatalysts, *Electrochimica Acta*, **52** (28) (2007), 7964–7971.
142. A. Kundu, J. H. Jang, J. H. Gil, C. R. Jung, H. R. Lee, S.-H. Kim, B. Ku and Y. S. Oh, Micro-fuel cells – current development and applications, *Journal of Power Sources*, **170**(1) (2007) 67–78.
143. J. Platz, J. Sehested, T. Møgelberg, O. J. Nielsen and T. J. Wallington, Alternative fuel and fuel additives: atmospheric chemistry of 1,4-di- and 1,3,5-trioxane, *Journal of Aerosol Science*, **28**(6) (1997) 1104.
144. G. Kerangueven, C. Coutanceau, E. Sibert, J.-M. Léger and C. Lamy, Methoxy methane (dimethyl ether) as an alternative fuel for direct fuel cells, *Journal of Power Sources*, **157**(1) (2006) 318–324.

145. K. Yamada, K. Yasuda, N. Fujiwara, Z. Siroma, H. Tanaka, Y. Miyazaki and T. Kobayashi, Potential application of anion-exchange membrane for hydrazine fuel cell electrolyte, *Electrochemistry Communications*, **5**(10) (2003) 892–896.
146. K. Yamada, K. Asazawa, K. Yasuda, T. Ioroi, H. Tanaka, Y. Miyazaki and T. Kobayashi, Investigation of PEM type direct hydrazine fuel cell, *Journal of Power Sources*, **115**(2) (2003) 236–242.
147. J. C. Ingersoll, N. Mani, J. C. Thenmozhiyal and A. Muthaiah, Catalytic hydrolysis of sodium borohydride by a novel nickel–cobalt–boride catalyst, *Journal of Power Sources*, **173** (1) (2007), 450–457.
148. H. Cheng, K. Scott, K. V. Lovell, J. A. Horsfall and S. C. Waring, Evaluation of new ion exchange membranes for direct borohydride fuel cells, *Journal of Membrane Science*, **288**(1–2) (2007) 168–174.
149. H. Zhong, H. Zhang, G. Liu, Y. Liang, J. Hu and B. Yi, A novel non-noble electrocatalysts for PEMFC based on molybdenum nitride, *Electrochemistry Communications*, **8** (2006) 707–712.
150. A. Saccà, A. Carbone, E. Passalacqua, A. D'Epifanio, S. Licoccia**,** E. Traversa, E. Sala, F. Traini and R. Ornelas, Nafion–TiO_2 hybrid membranes for medium temperature polymer electrolyte fuel cells (PEFCs), *Journal of Power Sources*, **152**(1) (2005) 16–21.
151. T. Shimada, C. Wen, N. Taniguchi, J. Otomo and H. Takahashi, The high temperature proton conductor $BaZr_{0.4}Ce_{0.4}In_{0.2}O_{3-\alpha}$, *Journal of Power Sources*, **131**(1–2) (2004) 289–299.
152. Q. Ma, R. Peng, Y. Lin, J. Gao and G. Meng, A high-performance ammonia-fueled solid oxide fuel cell, *Journal of Power Sources*, **164** (1) (2007) 86–89.
153. D. Hirabayashi, A. Tomita, M. E. Brito, T. Hibino, U. Harada, M. Nagao and M. Sano, Solid oxide fuel cells operating without using an anode material, *Solid State Ionics*, **168**(1–2) (2004) 23–29.
154. A. Tomito, T. Hibino, M. Sano, Surface modification of doped BaCeO3 to function as an electrolyte and as an anode for SOFCs, *Electrochemical and Solid-State Letters*, **8**(7) (2005) A333–A336.
155. X Su, Q. Yan, X. Ma, W. Zhang and C. Ge, Effect of co-dopant addition on the properties of yttrium and neodymium doped barium cerate electrolyte, *Solid State Ionics*, **177**(11–12) (2006) 1041–1045.
156. W. Grover Coors, Protonic ceramic fuel cells for high-efficiency operation with methane, *Journal of Power Sources*, **118**(1–2) (2003) 150–156.
157. K. Xie, Q. Ma, B. Lin, Y. Jiang, J. Gao, X. Liu and G. Meng, An ammonia fuelled SOFC with a $BaCe_{0.9}Nd_{0.1}O_{3-\delta}$ thin electrolyte prepared with a suspension spray, *Journal of Power Sources*, **170**(1) (2007) 38–41.

11

Performance degradation and failure mechanisms of fuel cell materials

R STEINBERGER-WILCKENS, J MERGEL, A GLÜSEN, K WIPPERMANN, I VINKE, P BATFALSKY and M J SMITH,
Institute of Energy Research (IEF), Germany

11.1 Introduction

The various fields of application of fuel cells require different specifications for their service life. A minimum operation of 40 000 hours (5 years), for instance, is required from fuel cells used in stationary applications [NEP, 2007]. If fuel cell drives are to be used in mobile applications a lifetime of more than 5000 h is required for cars and 10 000 hours for buses [NEP, 2007]. For portable applications, operating times in the range of 3000–5000 h are necessary [DoE, 2006]. Today, the market breakthrough for fuel cells is still prevented by insufficient service life for most applications but especially in long-term operation, and, of course, excessive unit costs due to the lack of large-scale production.

Fuel cells, like any other electrochemical devices, experience a loss of performance during their operational life. This is termed 'degradation' and is most commonly described as a loss of cell voltage at a given operational point, which immediately translates to a loss in electrical power supplied and thus limits service life. 'Definition of end of life' (EoL) can vary, though, depending on the requirements of application. As with primary batteries, a wide range of EoL conditions can apply, mainly defined by the tolerance of the fuel cell system towards a loss of voltage. Since this is a system-specific criterion and system developers have a degree of freedom to over-size the fuel cell stack in order to incorporate a certain voltage drop, no definite limits can be stated generically. Since over-sizing again is limited by cost considerations, the EoL is conventionally thought to be defined by a total loss of 10 to 20% of voltage, i.e. power at a given current density, as compared to the 'beginning of life' (BoL) situation [Du *et al.*, 2006].

Fuel cell degradation can have a variety of causes, also depending on the type of fuel cell, i.e. the materials incorporated in these and the operational conditions. The most prominent factors influencing degradation in steady-state operation are the current density and the operational temperature. A second important set of causes for degradation are transient operation (load

and thermal cycling) and operation outside the regular window of parameters (for instance redox cycling in solid oxide fuel cells (SOFC) or dry operation of polymer electrolyte fuel cell (PEFC) membranes), often with immediate and dramatic impact on fuel cell performance. Finally, fuel and air impurities will also influence the long-term performance. We can therefore speak of three types of degradation:

1. Long-term, steady-state degradation with a continuous loss of performance.
2. Transient and cycling degradation with an incremental loss of performance 'per incident', speaking here of 'internal incidents' occurring within the fuel cell.
3. 'External influences' outside the stack (mostly from systems operation), outside the allowed operational window (which will vary among fuel cell types and even designs of the same type), that can lead to catastrophic failure or at least severe damage.

Besides this generic classification we find very specific mechanisms of degradation in the single fuel cell types which are more closely related to specific sets of materials used in these fuel cells; examples are:

- re-oxidation ('redox cycling') of SOFC anodes, referring to the conventional nickel anode materials;
- electrolyte loss in molten carbonate fuel cells (MCFC), referring to the molten salt electrolyte;
- sub-optimal water management in PEFC, referring to the specifics of charge transport in polymer electrolyte membranes; or
- carbonate formation in alkaline fuel cell (AFC) electrolytes, referring to the reaction of CO_2 from the air with the liquid electrolyte.

The overall goal of lifetime extension of fuel cells goes hand in hand with understanding the listed mechanisms and finding materials and design solutions to avoid or at least alleviate the effects. The approach of designing systems such that the stack is always kept within its ideal operational specifications ('keeping the stack happy' [Borglum *et al*., 2005]) is a valid one, nevertheless limited by economic considerations.

The term 'degradation' needs some explanation. Often, today as in the past, authors refer to the loss-of-power phenomena by the term 'ageing'. Leaving aside that this colloquial term implies a process that will take place in time anyhow, as would the ageing of human beings, it misses the clear differences in effects as listed above, of which several are less tied to a temporal development than to impinging incidents. Furthermore, it has not yet been definitely established whether degradation in fuel cells will take place during operation alone or whether some effects may also occur during idling and shut-down. This would have dramatic effects on the requirements on lifetimes as cited above, which today are considered to be operational

hours. That is, should degradation also continue during shut-down, albeit at a reduced rate, today's goals of lifetime would be far too low. This is something only practical experience in field tests can prove.

The definition of degradation needs clarification. Conventionally, degradation is given as the relative loss of voltage compared with the initial conditions at the start of the experiment or service life, i.e. $\Delta U/U$ in % (conventionally per 1000 hours of experiment (operation)) or as an absolute value (mV/1000 h). Usually tests are run galvanostatically (at fixed current) and the voltage degradation will refer to the reduction of polarisation in the *I–V* curve of the fuel cell at a given current density. Reference to Fig. 11.1, though, shows that an increase in current density will always lead to a decrease in operational voltage. Therefore the relative change in voltage will in all cases increase with increasing current density, even if the absolute change ΔU were constant. If $U_1 > U_2$ and $\Delta U_1 < \Delta U_2$, automatically $\Delta U_1/U_1$ will be less than $\Delta U_2/U_2$. Therefore the perception that current will strongly influence degradation owes its validity only partly to physical phenomena, but just as much to its own definition. The same applies to lower operating temperatures where, again, the voltage at constant current density is lower as compared with the *I–V* curve at higher temperatures and will deliver $\Delta U/U$

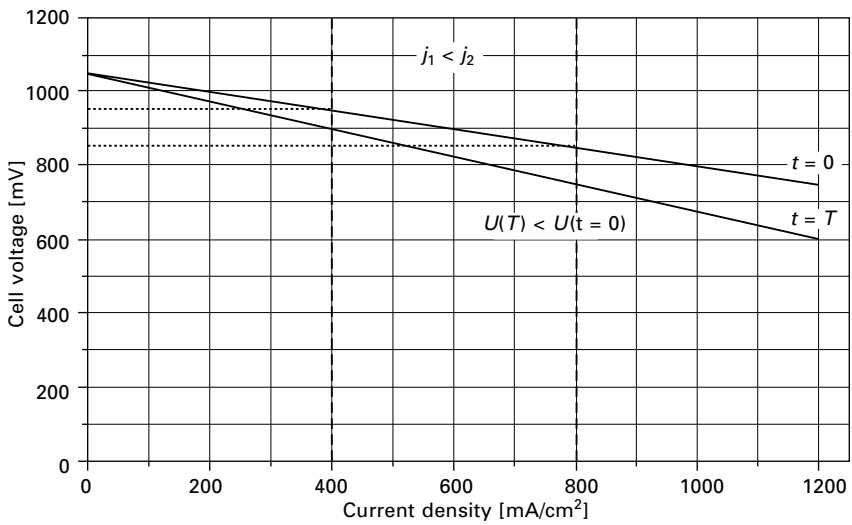

11.1 Generic *I–V* curve of a single cell or stack showing the effect of operating point on the determination of voltage degradation and the calculation of relative voltage decrease. The slope of the curves gives the area-specific resistance (ASR). Since the curves will in practice not be linear, the definition of a 'reference point' is necessary. After operation (at time *T*) the ASR has increased, resulting in lower overall voltage. Since voltage decreases with current (density), U_2 will always be lower than U_1.

values that cannot readily be interpreted without a further frame of reference (for instance total operational lifetime at given conditions).

A more tangible physical value in comparing degradation effects is the cell 'area-specific resistance' (ASR in ohm per cm^2) [Blum *et al*., 2006], which is a purely physical property depending on the temperature of the cell and the ohmic resistances of current collection and contacting, etc., but independent of current and voltage conditions. Nevertheless, the actual evolution of ASR in an experiment will of course strongly depend on the way the cell is operated. The approach of evaluating degradation in terms of ASR has not been established as a standard procedure today but is seen as a necessary one by the authors.

The following text will now further explore the degradation mechanisms for selected low-temperature (PEFC and direct methanol fuel cell, DMFC) and high-temperature fuel cells (SOFC).

11.2 Low-temperature fuel cells

The possibilities for applying low-temperature fuel cells with polymer electrolyte membranes (PEMs) range from electricity supply for portable systems and vehicles up to decentralized heat and power generation. More recently low-temperature fuel cells have been envisaged as auxiliary power units (APUs) in motor vehicles and aircraft, using carbon-containing fuels. In this case, however, it would be beneficial to use a high-temperature polymer electrolyte fuel cell (HT-PEFC), which can tolerate up to about 1 vol. % of carbon monoxide (CO). By using PBI membranes doped with phosphoric acid, for instance, operating temperatures of 160–180 °C can be achieved without any perceptible degradation in performance ensuing from the high CO content. The DMFC, which in addition to the very high energy density of methanol is also characterized by ease of handling and fuel replenishment, can be used in various power classes [Mergel *et al*., 2005]. For portable applications, commercial products are already available in the 50 W power range as battery chargers, but in the next few years it is also expected that models for light traction or material handling will come in to the market. However, in addition to high-power density and a price level comparable to existing technologies, the necessary long-term stability is also required.

Depending on the area of application and fuel cell type, the long-term stability of PEFC and DMFC is influenced by the materials used in the fuel cells and the operating conditions. Typical examples are degradation effects in the membrane electrode assembly (MEA) of hydrogen-operated PEFCs.

- Particle enlargement of the platinum catalyst and a simultaneous decrease in the active electrochemical surface due to degradation of platinum particles (dissolution/oxide formation/leaching/agglomeration/Ostwald ripening).

- Oxidation of the carbon support.
- Failure of the PEM due to pitting.
- Deterioration of mass transport due to the loss of hydrophobicity of the gas diffusion layer caused by degradation of the poly tetrafluoroethene (PTFE) used.
- Increase of electrolyte resistance due to corrosion products of the metallic bipolar plate [Cheng *et al*., 2007]
- Increase of contact resistance due to the formation of passive layers at the metallic bipolar plate.

All these degradation phenomena, and thus also the long-term stability of PEM fuel cells (PEMFC), are greatly influenced by the operating conditions. Thus, for example, particle enlargement of platinum and carbon corrosion is particularly encouraged by elevated temperatures and a high relative humidity [Borup *et al*., 2006].

In comparison to hydrogen-operated PEFCs, there is little in the literature on the ageing of DMFC. The ageing effects described for DMFC-MEAs can essentially be classified as follows:

- Degradation of ruthenium and platinum particles (dissolution/oxide formation/leaching/agglomeration/Ostwald ripening) [Knights *et al*., 2004; Piela *et al*., 2004; Cheng *et al*., 2006]
- Degradation of the polymer membrane (increase in the degree of crystallization, degradation of the sulphonic acid groups) [Cheng *et al*., 2006]
- Delamination of the electrodes (especially of the anode) from the membrane [Kim and Pivovar, 2006, Jiang *et al*., 2007].

11.3 Membrane degradation

The membrane is a central component of a PEFC. It must fulfil three tasks in order for a PEFC to work properly:

1. The membrane must separate fuel and oxidant.
2. The membrane must electrically insulate the anode from the cathode.
3. The membrane must conduct protons from anode to cathode.

Any change in the membrane that reduces the ability to fulfil one of the tasks will reduce the performance of the PEFC or even stop the fuel cell from working. The most critical task is the separation of fuel and oxidant. Most of the degradation mechanisms discussed below refer to a polymer decomposition which will lead to membrane thinning and eventually formation of holes. The electrical insulation of a membrane is generally not affected during PEFC operation. If a short-circuit occurs this is usually due to mechanical stress during cell assembly. Proton conductivity of the membranes may be

reduced by loss of proton-conducting sites as discussed below or by impurities migrating into the membrane from PEFC-stack or system components or from contaminated fuel.

11.3.1 Operating conditions

Depending on the type of fuel cell the operating conditions vary significantly. Classical PEFCs are operated at temperatures up to 80 °C and the hydrogen and/or air fed into the fuel cell are frequently humidified to ensure good proton conductivity of the membrane. High-temperature PEFCs are operated at temperatures up to 200 °C under dry conditions. DMFCs in contrast are generally operated at temperatures up to 80° C and methanol is provided as a dilute aqueous solution, so that the membrane is always fully humidified during operation.

In all cases the membrane is furthermore exposed to strongly oxidising potentials on the cathode and to potentially aggressive intermediates of the electrochemical reactions.

11.3.2 Membranes used in polymer electrolyte fuel cells

It is generally assumed that aliphatic C–H bonds are especially prone to oxidative attack and therefore membrane manufacturers generally choose polymers that do not contain aliphatic C–H bonds in the main chain. The two main groups are perfluorinated polymers and fully aromatic polymers. Proton conductivity of both groups is generally ensured by introducing sulphonic acid groups into the polymer. The polymer most commonly used for DMFC and classical PEFC is Nafion®, produced by DuPont. Nafion® is a copolymer of tetrafluoroethylene and perfluoro(4-methyl-3,6-dioxa-7-octene-1-sulphonyl fluoride). The pendant sulphonyl fluoride group is then chemically converted to sulphonic acid. The sulphonic acid groups provide good proton conductivity when the membrane is fully humidified. Therefore Nafion® is not suitable for HT-PEFC where proton conductivity must be sufficient even in the absence of water. For HT-PEFC generally nitrogen-containing aromatic polymers such as PBI are used and proton conductivity is ensured by introducing phosphoric acid into the polymer membrane.

11.3.3 Membrane degradation in classical polymer electrolyte fuel cells

Membrane degradation in classical PEFCs has been studied extensively and the results have recently been reviewed [Collier *et al*., 2006; Schiraldi, 2006]. Mechanical stress is one important reason for membrane degradation and membrane degradation can be reduced by using reinforced membranes as

shown by Liu *et al*. [2001] from Gore Fuel Cell Technologies. An important factor in membrane durability is membrane humidification. Knights *et al*. [2004] found that the time to significant gas crossover is reduced by a factor of 10 when feed gases are not humidified. Borup *et al*. [2007], however, found that fluoride emission rate, loss in open cell voltage and hydrogen crossover are highest when feed gases have intermediate humidity (20–60% relative humidity). This is a contradiction only at first glance. The important parameter is the water content in the MEA (especially in the membrane), which depends on feed gas humidification but also on a number of other operating parameters, such as flow rates, current density, flow field, gas diffusion layer and others.

It is generally assumed that H_2O_2 or peroxidic radicals play an important role in membrane degradation. Therefore an *ex situ* stability test is often performed with H_2O_2 and Fe^{2+} ions (Fenton test) [Bosnjakovic and Schlick, 2004] and fluoride ion concentration in the reagent is recorded over time. COOH groups present at the chain ends of Nafion are regarded as a point of attack for polymer degradation [Pianca *et al.*, 1999]. Therefore end-groups were removed by treating Nafion® with elemental fluorine at DuPont Fuel Cells [Curtin *et al.*, 2004]. Nafion® modified in this way exhibited a 56% decrease in fluoride emission during the Fenton test and Nafion® modified by a proprietary protection strategy not disclosed in the paper exhibited a 96% decrease in fluoride emission during the Fenton test. However, Curtin *et al*. [2004] also mention that these results do not always correspond to fuel cell accelerated degradation results. In one case, a membrane prepared from a treated polymer exhibited the same fluoride emission rate in fuel cell testing as a membrane prepared from untreated polymer. Therefore other mechanisms must play a role. Although fluoride emission is a linear function of carboxylic acid group concentration, it has a non-zero intercept, i.e. when extrapolated to zero carboxylic acid group concentration, some fluoride emission still takes place [Schwiebert *et al*., 2005] and attack at the sulphonic acid groups is regarded as one reason for that [Schiraldi, 2006]. While these papers explore the site of attack at the polymer, Mittal *et al*. [2006] explored the nature of the attacking species. They found that significant fluoride emission takes place only if H_2, O_2 and a platinum catalyst are present. This led them to conclude that the membrane degradation mechanism is most likely initiated by a species formed as a result of the H_2 and O_2 reaction on the catalyst without being able to specify its nature. Further research is needed here.

11.3.4 Membrane degradation in direct methanol fuel cells

Membrane degradation is less critical in DMFCs. Owing to the presence of aqueous methanol solution on the anode, the membrane is always fully

humidified. As methanol tends to migrate through the membrane it reduces the electrochemical potential and reactivity of the cathode. To reduce this effect, membranes used for DMFC are usually thicker and therefore mechanically more stable than membranes used for PEFC. In summary, the operating conditions identified as most critical for the PEFC are automatically avoided in the DMFC. In spite of this, Cheng *et al.* [2006] have observed an increase of crystallinity and loss of sulphonic acid groups during DMFC-operation. However, generally degradation of DMFCs is mainly caused by deterioration of the electrodes and not of the membranes.

11.3.5 Membrane degradation in high-temperature polymer electrolyte fuel cells

Membrane degradation in HT-PEFCs has not been studied systematically. Liu *et al*. [2006] found that after 510 hours of continuous operation and 90 hours of intermittent operation at 150 °C more than half the phosphoric acid had leached from the membrane. Performance did not change significantly during the first 500 hours but decreased during intermittent operation. The PBI membrane itself is regarded as chemically stable, but mechanical strength is poor when a sufficient amount of phosphoric acid is incorporated.

11.4 Electrode degradation

11.4.1 Polymer electrolyte membrane fuel cell

The durability of the catalysts is one of the important issues of PEFC research and development [Gasteiger and Mathias, 2003]. Voltage cycling in PEFCs is known to cause enhanced ageing of platinum catalysts [Woods, 1976; Darling and Meyers, 2003, 2005; Patterson 2002; Ferreira *et al*., 2005; Yasuda *et al*., 2006]. Compared with potentiostatic conditions holding the cathode potential in the region of platinum oxide formation, voltage cycling between platinum oxide formation and reduction causes an increase of platinum dissolution rate by three to four orders of magnitude, i.e. from 10^{-14} to 10^{-11}–10^{-10} g/cm^{2}s [Wang *et al*., 2006]. This source determined the equilibrium concentration of dissolved Pt under potentiostatic conditions in perchloric acid. They found, that the platinum equilibrium concentration increases monotonically from 0.65 to 1.1 V vs. standard hydrogen electrode (SHE) and decreases at potentials >1.1 V. The dissolution rates of platinum wire and supported platinum catalyst turned out to be comparable.

Ferreira *et al.* [2005] investigated the platinum coarsening mechanism in PEFCs, especially after voltage cycling between 0.6 and 1.0 V. They identified 3D-Ostwald ripening and migration of soluble platinum cations from the cathode toward the membrane as the two ageing processes responsible for

the platinum area loss. After 10 000 voltage cycles and 100 h operation time, about one-third of the original platinum surface was lost because of Ostwald ripening of platinum particles on the carbon support and another third was lost because of dissolution, chemical reduction by permeating hydrogen and precipitation within the ionomer phase. According to Ferreira *et al*. [2005], the electrochemical surface area of platinum decreased from $63\,m^2/g_{Pt}$ before cycling to $23\,m^2/g_{Pt}$ after cycling.

Depending on the local concentration of hydrogen and oxygen in the MEA and the thickness of the membrane, the platinum deposition takes place in the ionomer phase directly in the cathode/membrane interface or in the membrane [Ferreira *et al*., 2005; Yasuda *et al*., 2006]. In case of high oxygen concentration respectively low hydrogen concentration in the membrane, platinum can also be deposited in the anode [Yasuda *et al*., 2006]. As emphasized by Ferreira *et al*. [2005], the overall platinum surface loss cannot be determined by X-ray diffraction (XRD), because this technique also detects electrochemically inactive platinum particles deposited in the ionomer phase of the catalyst layer or the membrane. Suitable methods to determine the surface loss are cyclic voltammetry (*in situ*) and the analysis of transmission electron microscopy (TEM) images of pristine catalyst and aged catalyst scraped from the membrane (*ex situ*, e.g. Ferreira *et al*. [2005]). The coarsening of platinum particles is also reflected in the change of particle size distribution, obtained from the analysis of TEM images [Ferreira *et al*., 2005].

Although the ageing experiments of Ferreira were performed at 80 °C, the corrosion of platinum should be even worse at elevated temperatures, for both thermodynamic and kinetic reasons. From the temperature dependence of the standard Gibbs free energy of platinum dissolution, approximate values of platinum (Pt^{2+}) equilibrium concentrations can be calculated [Bindra *et al*., 1979; Ferreira *et al*., 2005]. For example at a cathode potential of 0.9 V, the Pt^{2+} concentration increases from $\sim 2 \times 10^{-8}$ M (80 °C) to $\sim 2 \times 10^{-7}$ M (120 °C) and $\sim 1 \times 10^{-5}$ M (200 °C). However, the measured concentrations deviate from the thermodynamic values up to one order of magnitude. This is probably because of the complex oxidation behaviour of platinum including chemisorbed oxygen, passivating layers, different soluble platinum species and to differences between polycrystalline platinum and platinum nanoparticles [Ferreira *et al*., 2005; Wang *et al*., 2006].

As already mentioned, platinum alloys with transition metals such as Co, Ni or Cr show superior catalytic activity for the oxygen reduction reaction compared with pure platinum [Mukerjee and Srinivasan 1993; Wilson, *et al*., 1993; Gasteiger *et al*., 2005; Yu *et al*., 2005]. Unfortunately, the transition metals dissolve in acidic environments during fuel cell operation. Ageing experiments under phosphoric acid fuel cell (PAFC) and PEFC operating conditions show a gradual leaching of the transition element over a period of

thousands of hours [Beard and Ross, 1990; Ralph and Hogarth, 2002; Colon-mercado and Popov, 2006]. The decrease of catalyst activity and lowering of the ionomer conductivity by the exchange of protons by dissolved transition metal ions [Ralph and Hogarth, 2002], are potential consequences.

Gasteiger *et al*. [2005] identified three possible reasons for the leaching of transition base-metal from the Pt alloy catalyst in PEFCs:

1. Excess base-metal deposited onto the carbon support during preparation.
2. Incomplete alloying due to a low alloying temperature.
3. Leaching even in case of a well-alloyed base metal.

According to Gasteiger *et al*. [2005], a pre-leaching of Pt–Me alloys is favourable to minimise the contamination of the MEA with metal cations during PEFC operation. In the case of Pt_xCo_{1-x}/C catalysts, this procedure suppresses the dissolution of Co from 37% (unleached) to 4% (multiply leached).

Antolini *et al*. [2006] reviewed the stability of Pt–M (M = first row transition metal) alloy catalysts. They pointed out that there are different, partially contradictory, findings in the literature concerning the stability of these catalysts. The discrepancies can be explained by different catalyst materials, pre-treatments, testing methods and applied operating conditions. Generally, Cr and Co alloys are found to be more stable than V, Ni and Fe alloys. However, Antolini *et al*. believe that the stability of the alloy catalysts does not depend on the kind of transition metal, but preferentially on the degree of alloying and, to a lesser extent, on the metal particle size. Thus, the higher stability of Pt–Cr and Pt–Co could be explained by the higher degree of alloying with platinum.

Ageing experiments in PEFCs revealed a positive effect of the presence of the non-precious metal on the stability of the catalyst [Mukerjee and Srinivasan, 1993; Gasteiger *et al*., 2005; Antolini *et al*., 2006]. For example, the performance of a MEA with Pt_xCo_{1-x}/C catalyst is superior to that of Pt/C over the whole operation period of 1000 hours, with comparable ageing rates and a lower surface area loss for the PtCo/C catalyst [Gasteiger *et al*., 2005]. Yu *et al*. [2005] studied the stability of PtCo/C catalysts under dynamic fuel cell operating conditions. After 2400 potential cycles, the performance loss of the PtCo/C MEA was less than that of the Pt/C MEA. At an operation temperature of 65 °C, cobalt dissolution did not influence the membrane conductance of the PtCo/C MEA. Travitsky *et al.* [2006] have investigated the stability of carbon- and silica-supported platinum-alloys such as PtCo and PtNi as cathode catalysts. According to the authors, at elevated temperatures, silica support should be more stable than carbon support (see below) and should improve wetting of the catalyst layer due to its hydrophilic properties [Travitsky *et al.*, 2006]. Of course, carbon has to be added to provide sufficient electronic conductivity. They found that after a first hot-

acid treatment, cobalt or nickel atoms dissolve from the surface of the alloy particles, leaving stable platinum rich layers, which prevent further corrosion.

As mentioned above, one of the degradation mechanisms is the corrosion of carbon support, where carbon atoms react with oxygen atoms and water by formation of gaseous products such as CO and CO_2. As a consequence, platinum particles detach from the carbon support and agglomerate. In particular, corrosion of the cathode carbon support takes place because of the high, oxidative electrode potential. This is especially a problem at elevated temperatures up to 200 °C, as applied in HT-PEFCs. Stevens and Dahn [2005] have recently investigated the thermal degradation of different carbon support materials with platinum loadings of 0–80 wt% in a temperature range of 125–195 °C at a relative humidity of 0–15% in an oven under *ex situ* conditions. Additionally, they performed accelerated ageing experiments with PEM MEAs at a cell voltage of 1.2 V and measured the electrochemical surface area by means of cyclic voltammetry [Stevens *et al.*, 2005]. It turned out that the carbon combustion increases significantly with platinum loading. Without platinum, no degradation was observed. Hence, the carbon degradation is catalysed by platinum, as already suggested in earlier works concerned with the PAFC [Connolly *et al.*, 1967; Giordano *et al.*, 1991; Passalacqua *et al.*, 1992; Knights *et al.*, 2004; Stevens *et al.*, 2005]. Especially in the temperature range of 125–150 °C, there is a significant increase of consumed carbon. In humid environments, the rate of carbon combustion increases, suggesting a parallel pathway via a heterogeneous water–gas reaction [Stevens *et al.*, 2005]:

$$C + H_2O \rightleftharpoons H_2 + CO \qquad 11.1$$

The nature of carbon support also has a great impact on the combustion rate: the reactivity is influenced by the carbon surface, surface functional groups, extent of graphitisation of the underlying carbon and size of the deposited platinum. Generally, a low surface area and a high degree of graphitisation seem to be favourable. However, the other parameters are also important: for example, Ketjen black carbon support has a lower surface area than BP 2000 (800 m^2/g vs. 1300 m^2/g) but reacts much faster than BP 2000.

Concerning corrosion of anode carbon support, fuel starvation causes a severe ageing effect, as proved by Knights *et al.* [2004] for PEFC. If fuel starvation occurs, not enough fuel is available for the anode oxidation process to maintain the electrochemical current. Thus, the anode potential will increase to a value where water can be oxidised. As a consequence, oxygen and protons are generated at the anode according to:

$$H_2O \rightarrow O_2 + 2H^+ + 2e^- \qquad 11.2$$

The protons permeate through the membrane and react with oxygen at the cathode by formation of water. Because the anode potential increases, the

cell voltage drops. In case of complete fuel starvation, if for example hydrogen is replaced by nitrogen, the cell voltage even reaches negative values [Knights *et al*., 2004].

If the anode potential reaches values higher than about 1.4 V, carbon corrodes according to the following equation:

$$C + 2H_2O \rightleftharpoons 2H_2 + CO_2 \qquad 11.3$$

The destruction of the anode catalyst support leads to a detachment of platinum and/or ruthenium particles and finally to a loss of performance. Knights *et al*. [2004] offers some strategies of anode modification to favour oxidation of water over carbon and reduce degradation:

- enhanced water retention on the anode, for instance by adding PTFE or using water blocking components like graphite;
- reduction of water oxidation potential by modifying the catalyst (e.g. enhancement of Ru amount);
- more stable catalyst support (e.g. more graphitic carbon or alternative support materials like silicon [Travitsky *et al*., 2006]);
- higher fraction of noble metal in the catalyst to reduce contact of carbon with reactants.

Another possibility to reduce corrosion is to avoid operating conditions detrimental to the catalysts, for example running the cell or the stack under load instead of open circuit conditions to prevent high potentials at the cathode catalyst.

Reiser *et al*. [2005] and Tang *et al*. [2005] report that substantial cathode catalyst corrosion does not only occur during fuel cell operation, but also during start/stop cycles. This phenomenon occurs when oxygen and hydrogen are both present in the anode compartment. Because the current is reversed in a part of the fuel cell, Reiser *et al*. [2005] label it the 'reverse-current' mechanism. An explanation for the cathode corrosion is given in Fig. 11.2. In the left side of the scheme, the normal case of a hydrogen-fed PEFC after shut-down is shown, where residues of hydrogen (region A) and oxygen (region B) establish an open cell voltage of about 1 V. If the anode outlet is not air-tight, oxygen may enter the anode compartment (region C). Furthermore, oxygen diffusion from the cathode through the membrane to the anode has to be considered. The oxygen in region C is reduced by formation of water and vice versa. The establishment of an oxygen equilibrium potential in region C brings a pronounced increase of anode potential by up to 1 V compared with region A. At the same time, the cathode potential in region D – facing region C – may reach values as high as 2 V. The high cathode potential drives water electrolysis, oxygen evolution (see equation 11.4), carbon corrosion (equations 11.5/11.6) and platinum oxidation (equations 11.7/11.8) in region D. Considering the highly acidic environment, platinum

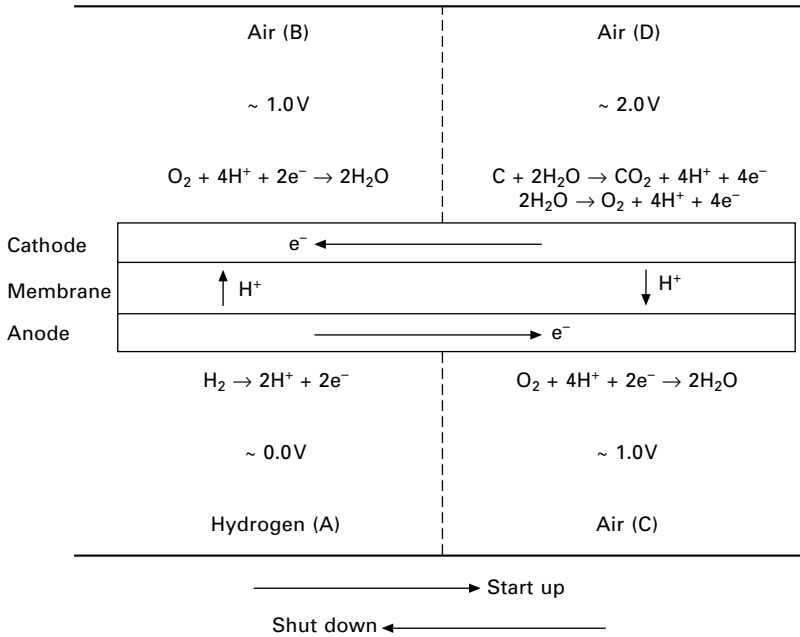

11.2 Schematic illustration of reactions in four distinct regions when an air/fuel boundary is formed at the PEFC anode, adapted from Tang *et al.* [2005].

corrosion may also take place (equation 11.9). But even if there is negligible platinum corrosion, the whole catalyst structure is destroyed by degradation of carbon support and the loose platinum particles can no longer be utilised.

The evolution of the regions A and C during start up and shut down is indicated by arrows: before start up, only air is present in the electrode compartments, no internal current is flowing and the cathode catalyst does not corrode. During start up, hydrogen is fed to the anode and gradually replaces air, thus creating region A, which extends to the right side in Fig. 11.2. This is a critical situation, where the cathode catalyst corrodes. If region A covers the whole anode, which means an anode compartment completely filled by hydrogen, the corrosion process stops. During shut down, the same process takes place, but in the reverse direction. Reiser *et al.* [2005] point out that the 'reverse-current' mechanism may also take place during operation when localised hydrogen starvation occurs.

$$2H_2O \rightarrow O_2 + 4H^+ + 4\ e^- \qquad 11.4$$

$$C + 2H_2O \rightarrow CO_2 + 4H^+ + 4\ e^- \qquad 11.5$$

$$C + O_2 \rightarrow CO_2 \qquad 11.6$$

$$Pt + xH_2O \rightarrow PtO_x + 2xH^+ + 2x\ e^- \qquad 11.7$$

$$Pt + xO_2 \rightarrow PtO_{2x} \quad 11.8$$

$$Pt \rightarrow Pt^{2+} \quad 11.9$$

Even though catalyst degradation has a major influence on PEFC performance decay, other ageing reasons have to be considered. Because the water management of PEFCs is a critical issue, the hydrophobic/hydrophilic properties of the electrodes have to be properly adjusted and should be stable under real operating conditions. As reported by Schulze *et al.* [2007], this is not the case: by means of X-ray photoelectron spectroscopy (XPS), they investigated MEA anodes and cathodes before and after fuel cell operation. The analysis of the carbon C1s peaks showed a decomposition of the hydrophobising agent PTFE as part of the electrodes. According to Schulze, the loss of hydrophobicity is more pronounced on the anode. Loss of hydrophobicity means a change of water balance, which can be recovered by drying the fuel cell. Schulze *et al*. therefore regard the loss of hydrophobicity as a reversible degradation. Additionally, they found – irreversible – agglomeration of platinum catalyst particles preferentially on the cathode. Based on these results, the cathode performance decay should mainly contribute to irreversible loss, whereas the anode performance decay should dominate the reversible part of losses. This was confirmed by an impedance analysis during 1000 h operation [Schulze *et al*., 2007], where the reversible and irreversible parts of performance losses were unravelled.

Delamination of the electrodes from the membrane is another reason for performance decay. This detrimental effect may be caused by improper preparation of catalyst coated membranes (CCM)s or even unfavourable operating conditions, such as freezing of water during cold start up below 0 °C [Wang *et al.*, 2007]. Kundu *et al.* [2006] have summarised the consequences of delamination: (i) development of flooded areas, (ii) increased contact resistance, (iii) development of pinhole areas because of higher resistive generation, (iv) loss of apparent catalytic activity (dead zones) and (v) development of areas susceptible to erosion (disintegration of mechanically weak catalyst layer).

A typical feature of ageing characteristics of PEFC and DMFC is the exponential decay in the beginning (decreasing ageing rate) followed by a more or less linear decay at the end of experiment (constant or slightly decreasing ageing rate), see 'ageing curve type 2' in Fig. 11.3. In some cases [Kuhn *et al.*, 2003; Kulikovsky *et al.*, 2004], however, the ageing rate increases during the experiment and reaches high values at the end of the ageing test, as shown in Fig. 11.3 ('ageing curve type 2'). An explanation for such behaviour was given by Kulikovsky *et al*. [2004]: usually, the local current is highest at the channel inlet. If the current at the channel inlet exceeds a critical value because of a slow ageing process, the corresponding part of MEA ages faster than before and, in extreme cases, completely fails. Under galvanostatic conditions, the smaller remaining part of MEA has to support

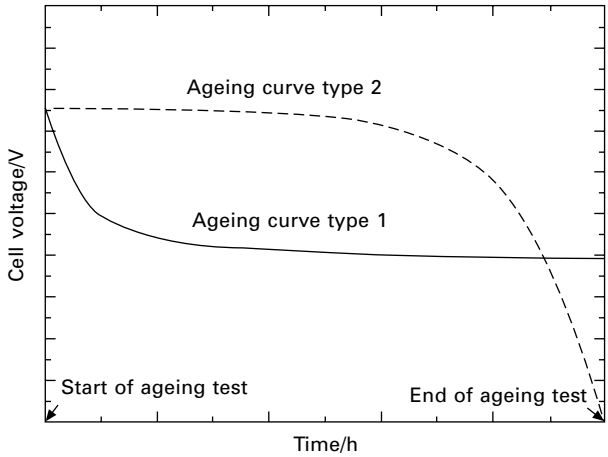

11.3 Typical ageing characteristics of PEFC and DMFC.

the current, the local currents will increase and the critical current will be exceeded faster than before. Thus, a degradation wave is formed, which propagates faster and faster in the direction of the gas flow towards the channel outlet until it stops. The 'degradation wave' model is a universal theory independent of the ageing mechanism.

11.5 Direct methanol fuel cell

Zelenay [2006] has summarised the 'unrecoverable' (irreversible) and 'recoverable' (reversible) performance losses of DMFC, analogous to the irreversible/reversible ageing effects discussed for PEFC (see above). The recoverable losses disappear after stopping and restarting the experiment, while the unrecoverable part causes a steady decrease of the starting value during the ageing experiment. The pronounced exponential decay after starting is mainly due to the reversible performance losses.

According to Zelenay, the following losses have to be considered:

- Unrecoverable performance losses:
  - loss of electrochemically active surface area of electrodes;
  - ruthenium crossover (migration) from the anode to the cathode and its re-deposition at the Pt catalyst surface;
  - irreversible loss of cathode hydrophobicity;
  - electrode delamination;
  - poor reagent distribution in individual cells of a fuel cell stack, including 'cell reversal' (negative cell voltage).
- Recoverable performance losses:
  - cathode Pt catalyst surface oxidation;

- temporary membrane dehydration;
- incipient cathode flooding.

The reasons for loss of electrochemically active surface in DMFC are similar to those described for PEFC: At first, the particle size of catalysts increases during fuel cell operation. It is the black catalysts [Cheng *et al*. 2006; Jeon *et al*., 2006] and carbon-supported platinum cathode catalysts [Havránek *et al*., 2003], in particular, which suffer particle growth. Under 'mild' galvanostatic operating conditions, carbon-supported platinum ruthenium anode catalysts seem to be more stable [Havránek *et al*., 2003]. This suggests ruthenium has a stabilising effect, preventing the agglomeration of platinum particles. Secondly, an insufficient distribution of methanol solution within the anode flow fields will lead to a local depletion of fuel, causing an increase of anode overpotential and subsequent corrosion of the catalyst, which includes platinum, ruthenium and the carbon support. If methanol supply fails completely, a cell reversal takes place (see PEFC). Finally, the access of oxygen to the methanol compartment during start/stop cycles will cause catalyst corrosion (cf. Fig. 11.2). Other than with the PEFC, the corrosion in DMFC during start/stop cycles will not be restricted to the cathode, but also concerns the ruthenium containing anode catalyst.

The corrosion of ruthenium is known to be one of the main reasons for degradation of DMFC [Connolly *et al.*, 1967; Piela *et al.*, 2004; Zelenay, 2006; Chen *et al*., 2006; Shimazaki *et al*., 2006; Sarma *et al*., 2007]. The problem is not only the loss of ruthenium, which leads to a considerable increase of anode potential, but also the migration of ruthenium through the membrane and deposition on the cathode, which lowers the mixed potential of the cathode or even increases the ohmic resistance of the ionomer. Piela *et al*. [2004] first published the effect of ruthenium crossover in DMFC. Whereas the loss of Ru in the anode is an irreversible ageing effect, the ruthenium contamination of the cathode may be partially reversed by exposing the Pt cathode to a positive potential. Ruthenium corrosion concerns both unsupported [Piela *et al*., 2004; Jeon *et al*., 2006; Zelenay, 2006; Sarma *et al*., 2007] and carbon-supported platinum ruthenium alloys [Chen *et al*., 2006; Shimazaki *et al*., 2006].

Considering the Pourbaix diagram of Ru/water [Bard, 1976], ruthenium should be thermodynamically stable under typical DMFC operating conditions (see Fig. 11.4). However, under real working conditions of fuel cell stacks, the stability of PtRu alloys will be different compared to the 'ideal' system Ru/pure water at room temperature. Piela *et al*. [2004] discussed (i) the low $Ru(OH)_3$ activity in the catalyst layer, (ii) elevated operating temperatures and (iii) the effect of alloying of ruthenium with platinum. They came to the conclusion that these effects do not change the dissolution potential of ruthenium considerably and Ru should be still stable under real operation.

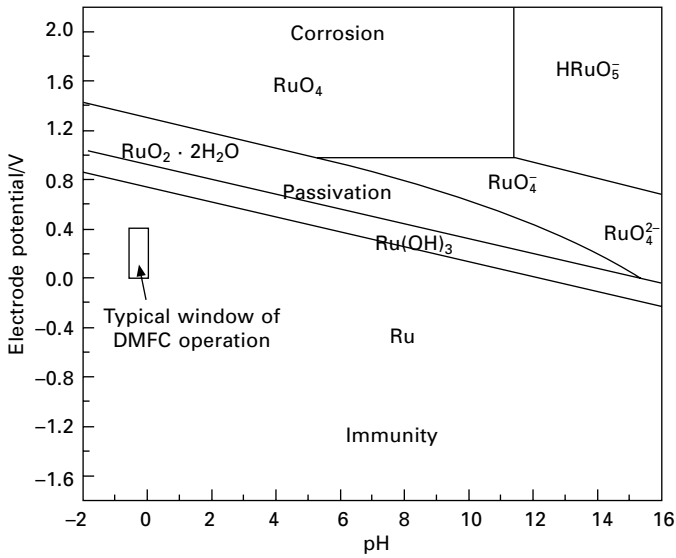

11.4 Pourbaix diagram of the Ru–H_2O system at 25 °C, adapted from Bard [1976].

Because of these considerations and their finding that Ru crossover takes place even under 'current-less' conditions, Piela *et al*. suggested an anode potential-independent mechanism via ultrafine hydrous RuO_2 particles, which can be leached out from the catalyst powder and may penetrate the Nafion membrane.

However, in real DMFC systems, it is difficult to fully exclude impurities such as metal ions or anions. In particular, halides as chloride are complexing agents, which reduce the oxidation potential of Ru and thus facilitate Ru corrosion. This is evident from Fig. 11.5 which shows the Pourbaix diagram of the Ru–H_2O system at 25 °C in the presence of 0.01 M chloride solutions [Bard, 1976], where the DMFC operating window extends into the corrosion region. Although the concentration of 0.01 M (~350 ppm) may be unrealistically high, it has been found that corrosion of ruthenium and platinum takes place even at chloride concentrations as small as 10^{-3} M (35 ppm) or 10^{-4} M (4 ppm) [IEF-3 Report, 2007]. The reversible and irreversible losses of cell voltage during temporary addition of diluted hydrochloric acid during a galvanostatic ageing test over approximately 7250 hours are shown in Fig. 11.6. This experiment was realized by changing the anode feed using either pure methanol solution or methanol solutions containing HCl. The reversible loss dominates and may be attributed to a blocking effect of chloride. This is supported by results published by Strmcnik *et al*. [2005], who found an occupation of adsorption sites of water molecules on Pt during CO oxidation. Regarding the short period of HCl addition and the relatively small chloride concentration,

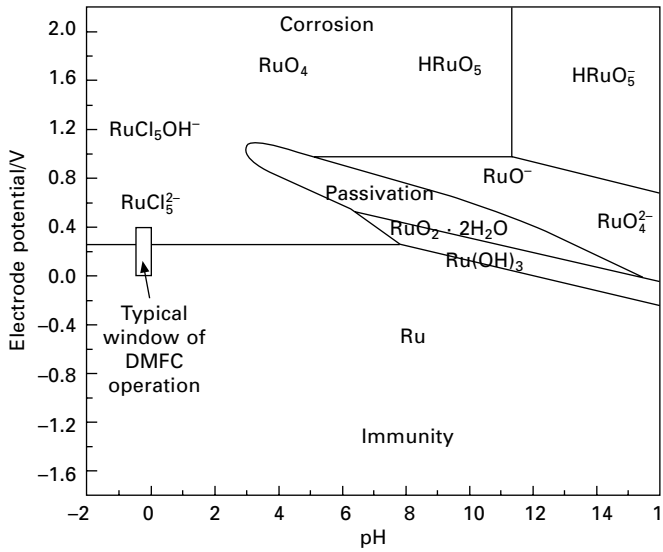

11.5 Pourbaix diagram of the Ru–H_2O system at 25 °C in 0.01 M chloride solutions, adapted from Bard [1976].

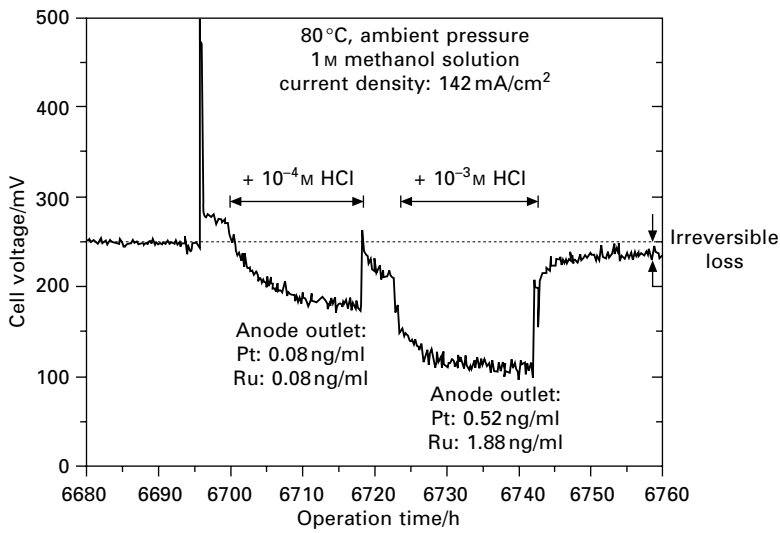

11.6 Reversible and irreversible loss of cell voltage during addition of 10^{-4} and 10^{-3} M hydrochloric acid solutions [IEF-3 Report, 2007].

the irreversible voltage loss of approximately 20 mV is remarkable. It turned out that the irreversible ageing effect was caused by catalyst corrosion. This could be verified by chemical analysis of the methanol solution leaving the anode outlet during addition of hydrochloric acid, which revealed the presence

of platinum and ruthenium (see Fig. 11.5), whereas no platinum or ruthenium was detected when pure methanol solution was used as anode feed.

Sarma *et al*. [2007] found an irreversible change of the hydrophobicity of the gas diffusion layers in both electrodes. Their energy dispersive X-ray (EDX) analysis of the aged gas diffusion layers (GDLs) yielded a significant increase of the atomic ratio of F/C in the anode GDL (F/C = 1.25) and a marked decrease in the cathode GDL (0.25) compared with a fresh GDL (0.43). They explained their result with the migration of Nafion ionomer into the anode GDL and at the same time a degradation of PTFE in the cathode GDL under electrochemical conditions, the latter effect being similar to that discussed for PEFC (see above).

Jiang *et al*. [2007] reported an anode delamination after 5000 h ageing tests with a dozen MEAs under constant voltage (0.6 V). In contrast, the cathodes of these MEAs showed no delamination. The authors explained the preferential delamination of DMFC anodes by the following reasons: (i) evolution of CO_2 bubbles at the anode side, which may loosen the binding force between anode and membrane, and, based on findings of Cheng *et al*. [2006], (ii) formation of ruthenium oxides after long-term testing. Other structural changes such as increase of crystallinity of the membrane [Cheng *et al.*, 2006] or increase of particle size may also facilitate delamination. The latter effects are, however, not restricted to the anode. A delamination of the electrodes may also occur if the membrane material and the ionomer of the catalyst layers are different and the chemical structure of both compounds is not compatible. Kim and Pivovar [2006] have, however, demonstrated that the membrane water uptake and the dimensional stability of the membrane is the key parameter for delamination. They used Nafion® ionomer as additive in the catalyst layers and polysulphone as alternative membrane material to reduce methanol crossover. They found that the interfacial resistance was smallest if membrane water uptake was well adapted to the electrode water uptake. They obtained a stable cell resistance over a period of 3000 hours of potentiostatic operation, indicating a compatible interface between polysulphone membrane and Nafion-containing electrodes.

Zelenay [2006] pointed out that among the recoverable ageing effects, the oxidation of platinum cathode catalyst has a major impact on DMFC performance. This is due to the inhibition of oxygen reduction reaction caused by formation of Pt oxide and/or hydroxide on the surface of the catalyst particles. Zelenay reported a clear correlation between the shift of oxygen reduction peak to lower cathode potentials due to Pt oxide formation and the drop of cell performance. The oxidation process takes place at higher cathode potentials and can be fully reversed by lowering the cathode potential, as reported by Eickes *et al*. [2006]. These authors proposed the so-called 'air-break' method, where they achieved a lowering of cathode potential and the following reduction of Pt oxide by periodically stopping the airflow

without changing the load. This procedure causes an instantaneous drop of cell voltage, namely in cathode potential. After restoring the airflow, a significant gain of current density is obtained. On average, a significantly higher performance of DMFC can be achieved by the 'air-break' method.

As in the case of PEFC, water management is an important issue in DMFC operation. Improper water management may cause cathode flooding and/or temporary membrane dehydration. Water management is not only determined by the operating conditions, but also by the hydrophobic properties of the GDLs, which may change during long-term operation (cf. PEFC). This is especially critical at higher current densities, when large amounts of excess water hinder the access of oxygen to the active sites.

11.6 High-temperature fuel cells

The high-temperature type fuel cell with a ceramic electrolyte, the SOFC, was initially developed mainly for stationary applications in combined heat and power (CHP) production in residential buildings and industry, and for power production. The SOFC displays a high electrical efficiency of around 50%. Target lifetimes are above 50 000 hours of operation. SOFCs can be run with hydrogen, methane, carbon monoxide, etc. in direct operation (without gas treatment) and thus offer an interesting multi-fuel capability they share with the other high-temperature type, the MCFC. More recently, the SOFC has been also considered for vehicle applications in APUs delivering electrical power on board vehicles using conventional fuels (diesel, petrol or methanol). The high efficiency and low effort of fuel processing and high operating temperature offer interesting options to on-board energy management in passenger and utility vehicles, aeroplanes, trains and ships.

SOFCs are operated at temperatures in ranges between 500 and 700 °C ('intermediate' temperature), 700–850 °C and 850–1100 °C, depending on the concept of cells used and the type of electrolyte. The highest temperature SOFC will be tubular or utilise planar electrolyte-supported cells, whereas the low and middle temperature ranges use anode-supported cells with different electrolyte types. A typical correspondence of temperature and application has not yet evolved, though the high-temperature range is reserved for SOFC with mainly ceramic components operating for stationary power generation.

Many corrosion processes are thermally activated and thus it is not surprising to find that the main degradation mechanisms in SOFC owe to the temperature of operation. An overview of the processes in an SOFC stack single repeating unit is given in Table 11.1. Various authors and projects have attempted to systematise the degradation phenomena in SOFC [Tu and Stimming, 2004; Steinberger-Wilckens *et al*., 2007], but the understanding of many effects is still underdeveloped or under dispute (cf. following sections).

The following list of possible adverse effects shows the variety involved:

Table 11.1 Overview of the main SOFC stack degradation mechanisms [Nabielek *et al.*, 2007]

Cathode side	Electrolyte	Anode side
Three phase boundary reduction Cr poisoning/ particle sintering Phase changes Interdiffusion	Phase instabilities	Ni-agglomeration Sulphur poisoning Cracking by re-oxidation Interdiffusion
Contact degradation Cracking Resistivity increase Cr transport	Interdiffusion	Contact loss by • cracking • sintering • seal swelling • temperature gradients Resistivity increase
Interconnect: • electrical resistance of scales • Cr evaporation • scale spallation • inner oxidation • mechanical deformation		Interconnect: • electrical resistance of scales • embrittlement by carburisation • scale spallation • mechanical deformation
Ceramic glass sealant • interaction with gaseous species/ contaminants • interaction between components • leakage during thermal cycling • degradation due to impurities in raw materials		

- Cathode side Cr poisoning by reduction of Cr^{6+} to Cr^{3+} at the electrolyte-cathode three-phase boundaries (TPB) combined with local stoichiometry changes by replacement of Mn through formation of CrMn spinels in lanthanum strontium manganite (LSM) cathodes.
- Changes in stoichiometry, segregation, coarsening by sintering, interaction with the electrolyte in lanthanum strontium iron cobaltite (LSCF) cathodes.
- Phase instability of the electrolyte, interdiffusion of elements from anode or cathode that reduce ionic conductivity.
- Anode side contacts: growth of insulating oxide scale, contact loss due to imperfect joining.
- Cathode side contacts: interactions/ contact loss.
- Others: leakages, steel corrosion and/ or degradation, contact loss by interconnect creep.

11.6.1 Cell degradation

SOFC cell electrodes and electrolyte are exposed to permanent high temperatures at high flows of electrical charges (currents) in an electrical

field (electrode overpotential) coupled with high gas flows and local moisture saturation. Ceramic materials and special steels appear to be the only substances capable of withstanding this demanding environment. Still, even these are not inert under these conditions and show:

- changes in morphology with consequences for gas transport, electrical conductivity, mechanical strength, and active surface area;
- changes in phase composition with consequences for electrical conductivity and mechanical strength;
- interdiffusion of substances with consequences for corrosion resistance, and electrochemical activity;
- transport of species resulting in de-mixing and de-activation.

The catalytic activity of the electrode material is determined not only by the suitability of the catalyst for the desired reactions, but especially by the active surface available to the reactants. Since the choice of materials for practical applications in SOFC is relatively limited, much effort has been spent on optimising the microstructure of electrodes in order to obtain large internal surfaces and high performance [Haanappel *et al.*, 2005a]. However, changes in microstructure will generally degrade this to a less 'complex' structure at a lower state of potential energy according to the laws of thermodynamics (maximisation of entropy). Owing to the high temperature of operation of SOFC this will include agglomeration of particles and sintering (densification) during operation.

The anode cermet of many SOFC cells is made of a YSZ structure with a percolation of electrically conducting nickel. Although the YSZ structure is stable at high temperatures as far as anode properties are concerned (see below), the nickel particles embedded in this lattice will form into increasingly larger particles, encouraged to do so by the poor adhesion to the YSZ lattice and the ensuing relative mobility of the nickel particles [Lee *et al.*, 2007]. A lower electrochemical activity of the anode will be observed due to a reduced active surface area and especially the reduction of the TPB length at the interface of anode and electrolyte [Dees *et al.*, 1987; Elangovan and Khandkár, 1991]. Since the nickel loading is often in excess of the equilibrium quantity necessary to sustain cell operation, for instance when the anode material also constitutes the support structure of the cell ('anode-supported cell', ASC), anode degradation will only be observed in the cell voltage after prolonged timespans. Once the coagulation has proceeded sufficiently, though, the current transport path will also be broken and anode electrical conductivity will cease as well. A similar effect is seen in sulphur poisoning and re-oxidation cycling (see below).

Although nickel is in a stable phase under SOFC operating conditions, $Ni(OH)_2$ is not. Rather, this compound is volatile and under high fuel utilisation conditions with high saturation of the anode with water vapour, nickel hydroxide

will form. This leads to a loss of nickel from the anode and a long-term reduction of catalytic activity and electronic conductivity [Hagen *et al*., 2006].

Cathodes are typically made of purely electrically conducting (LaSrMn) or mixed ionic and electrically conducting (LaSrCoFe) perovskites. They are tailored to transport oxygen ions efficiently by preparing off-stoichiometric structures with corresponding A-site deficiencies. As a function of current, cathode overpotential can change dramatically during few thousand hours of operation [Joergensen *et al*., 2000]. This source identifies pore formation at the cathode–electrolyte interface as the reason for decreased electrocatalytic activity due to the reduction of the TPB. Other literature suggests densification, particle sintering and a relative instability of LSCF-type cathodes as causes of cathode degradation [Mai *et al*., 2006a; Haanappel *et al*., 2006].

The 'traditional' material for the electrolyte is yttria-stabilised zirconia, either 3YSZ or 8YSZ. Both compositions are located within the field of two-phase coexistence and may undergo phase separation. This will lead to gradual changes in ionic conductivity [Müller *et al*., 2003].

Besides these processes taking place in the electrodes or electrolyte alone, various reactions between electrolyte and electrode materials are observed, although YSZ is considered as a rather stable composite. Nickel is known to dissolve in YSZ at high temperatures. Although this can be avoided during operation, the elevated temperatures necessary for sintering a gas-tight electrolyte layer may cause nickel to move into the electrolyte lattice. This will ultimately lead to electrical conductivity of the electrolyte and a reduction of ionic conductivity through contamination of the zirconia lattice [Kuzjukevics and Linderoth, 1997; Linderoth *et al*., 2001]. On the cathode side the formation of $SrZrO_3$ and $La_2Zr_2O_2$ are found, with both LSM and LSCF cathodes [Mai *et al*., 2006a]. Although it is thought that most of these compounds are formed during sintering (encouraging developers to move to cathode materials requiring lower sintering temperatures), lanthanum zirconate is also thought to form during operation of the SOFC, especially under high current densities [Heneka and Ivers-Tiffée, 2005]. In the case of LSCF cathodes it is well known that they require an interdiffusion protection layer (for instance cerium gadolinium oxide (CGO)) to prevent massive $SrZrO_3$ formation [Mai *et al*., 2006b].

Finally, at the interface of electrode and electrolyte elements are found that would not necessarily be expected from the materials used in manufacturing the SOFC cells: silicon (Si) and sodium (Na). It appears that these elements are introduced through impurities in the raw materials and during the manufacturing process accumulate at the interface of cathode and electrolyte [Liu and Jiao, 2005; Mogensen, 2005]. The deposition of these elements along the rim of the cathode material grains will block the TPB and reduce cathode activity.

11.6.2 Chromium poisoning

In the 1990s the first reports appeared on degradation phenomena related to chromium in SOFC short stacks comprising metallic interconnects. Analysis of the cathodes with EDX showed large amounts of chromium at the TPB (cf. Fig. 11.7). The source of this chromium was obviously the oxide scale of the interconnect. These consisted of 95% chromium, which was the only metal with the proper thermal expansion coefficient and an electrical conducting oxide scale able to withstand the operating temperature between 900 and 1000 °C. Experiments in inert single cell test housings with interconnect samples placed near the cathode indicated that the chromium was transported to the TPB by gas phase transport [Günther *et al.*, 1996]. Thermodynamic studies show that the vapour pressure of CrO_3 is rather high under the operating conditions in a stack [Das *et al.*, 1994]. The data also show that the humidity of the cathode gas has a large influence on the amount of chromium evaporating from the oxide. This is caused by the formation of $CrO_2(OH)_2$ which possesses a much higher vapour pressure than CrO_3. The thermodynamic data further show that the temperature has only a limited effect on the vapour pressures of these chromium species. This again means that lowering the operation temperature of the SOFC is not reducing the amount of chromium in the gas phase. One solution to this degradation problem is the use of protective coatings. Materials based on a lanthanum chromium perovskite deposited by a vacuum plasma spraying process were successfully applied [Ruckdäschel *et al.*, 1997]. The use of high-chromia alloys and protective coatings adds to the cost problem of SOFC, though.

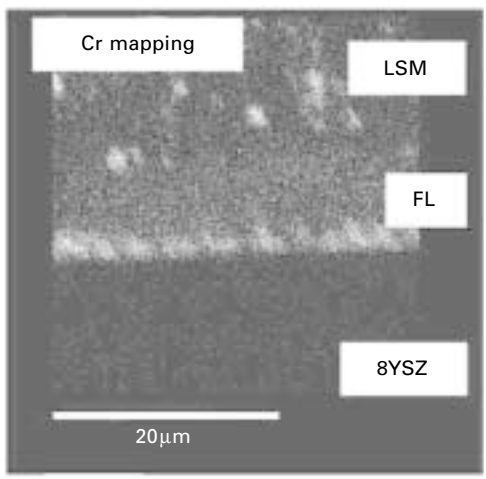

11.7 Chromium deposition at the interface of the electrolyte (8YSZ) and the electrode layer (FL) of a LSM double layer cathode.

With the lowering of the operating temperature of the SOFC to around 800 °C a different solution became feasible in the use of ferritic steels for interconnects. These steels, however, still produce chromia oxide scales and the degradation problem remains. The development of new steel compositions with tailored oxide scales that cover the chromia scale with a manganese chromia spinel scale reduced the amount of chromium being released but did not solve the problem entirely. The use of chromia blocking layers could again be an option.

Better prevention against the degradation of SOFC-cathodes by chromia should be found in understanding the underlying mechanism. Research concentrates on a number of aspects. The first question is whether the transport of chromium is a surface or a gas diffusion process. Results from ANL and PNNL [Krumpelt *et al*., 2007] seem to indicate that surface diffusion of chromia plays an important role. Early results in literature [Günther *et al*., 1996] with single layer LSM cathodes and reports on similar experiments from other groups on double layer cathodes [Vinke *et al*., 2002] seem to indicate that gas diffusion plays a predominant role.

A second point of debate is the reaction mechanism of the chromium(VI)species with the cathode material and the reaction site. Experiments performed with LSM cathodes exposed to chromium for very short times (minutes) seem to indicate that the chromium(VI) species adsorb on the electrolyte surface close to the TPB and from there react with manganese oxide species migrating outward from the cathode [Jiang *et al*., 2000].

A second mechanism proposed is a direct reaction of the chromium(VI)species with the cathode material. This may be true for LSCF cathodes. Observation of a homogeneous distribution of chromium species in the bulk of these cathodes seems to support this theory. The degradation of the SOFC cells can in this case be caused by a slow deterioration of the conductivity of the cathode material due to the reaction with chromium forming $SrCrO_4$. This would account for early reports stating that LSCF cathodes were resistant to chromium poisoning.

For LSM cathodes this homogeneous chromium distribution through the cathode is only observed when the cathode is not polarised. After prolonged polarisation the chromium is found, concentrated in a thin layer directly on the electrolyte [Konysheva *et al*., 2006]. This is a marked difference with the interaction as observed in LSCF. It strongly suggests that the interaction with LSM cathodes is not merely a homogeneous chemical reaction but is electrochemically influenced.

A possible mechanism was suggested by Hilpert *et al*. [1996] and is presented in Fig. 11.8. The overpotential caused by the electrochemical reduction of oxygen at the cathode creates sites with chemical potentials allowing the reduction of the chromium(VI) species to a lower oxidation state. This chromium species then reacts with the manganese from the cathode

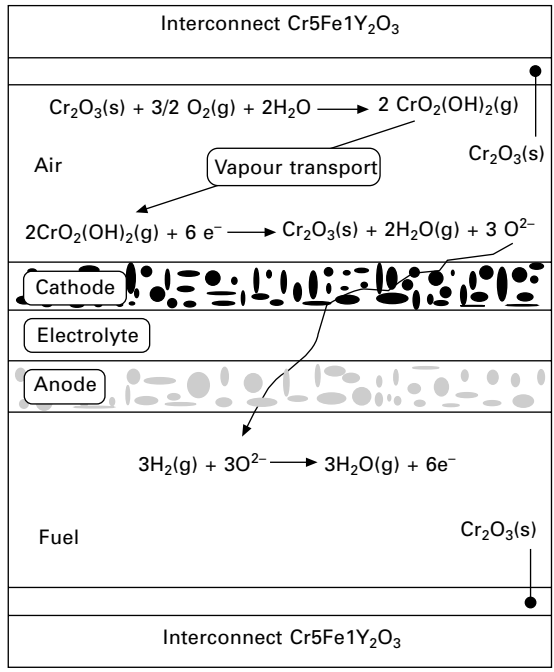

11.8 Mechanism for chromium-induced degradation of the cathode performance as proposed by Hilpert *et al.* [1996].

to form a chromium manganese spinel. This spinel phase permanently blocks the electrochemical reaction site. Impedance studies confirm that the number of reaction sites decreases when the electrode activity is degrading [Paulson and Briss, 2004]. The electrochemical reaction mechanism does not change. Recent studies show that after exposure to chromium over several thousand hours this spinell phase fills the porous structure close to the electrolyte effectively blocking the oxygen transport even further [Menzler *et al*., 2007]. The depletion of manganese from the LSM will also decrease the electronic conductivity of the cathode material adding to the loss of activity. Owing to the frequently used mixed oxide cathode (8YSZ + LSM) the blocking of the electrolyte–electrode interface does not cause an abrupt poisoning of the cathode. If the amount of electrolyte phase in the cathode layer is high enough for a percolating network the electrochemical activity of the cathode will largely be preserved. The electrode resistance will increase, though, because of the longer pathway for the oxygen vacancies to reach a reaction site.

Unfortunately the information on the reaction of chromium and the cathode is not conclusive. If this last proposed mechanism is correct then a possible solution may lie in lowering the cathode overpotential. This would prevent the reduction of the chromium(VI) species and thus prevent the blocking of the reaction sites.

11.6.3 Anode damage: sulphur and re-oxidation

High-temperature fuel cells are capable of internally reforming many carbonaceous fuels. With short chain alkane type fuels in particular this can greatly reduce the need for fuel pre-processing and yields the possibility of connecting systems directly to mains natural or town gas supplies. Equally, biogases become potentially useful fuel sources. However, all of these gases vary in specific composition and contain some level of impurities raising the question as to what influence fuel gas impurities will have on the SOFC device [Mougin *et al.*, 2007]. Removal of species harmful to the SOFC device implies gas clean-up processing and consequent costs which would preferably be avoided.

Halides, acidic cyanogens, alkali metals, silicon, heavy hydrocarbons and other possible contaminants all have the potential to cause problems; however, sulphur is without doubt the most significant problem species. Sulphur-bearing compounds are found naturally in almost all hydrocarbon fuels. They are also added to domestic gas supplies intentionally – as their strong smell acts as an alarm to potentially dangerous escapes. Irrespective of the initial S-bearing compound, under SOFC conditions the sulphur is effectively in the form of H_2S when it reaches the fuel electrode. Compared with water, H_2S is relatively acidic and thus it can reasonably be expected that the chemical basis of sulphur-anode problems is linked to acid + metal and acid + oxide type interactions.

The literature on what sulphur does and how it does it can appear relatively confused with many conflicting reports as to what p(S) levels are tolerable and what sulphur actually does in/to the anode [Feduska and Isenberg, 1983; Geyer *et al.*, 1997; Matsuzaki and Yasuda, 2000; Batawi *et al.*, 2001; Iritani *et al.*, 2001; Sasaki *et al.*, 2006; Smith and Mc Evoy, 2006]. What is agreed however is that fuel sulphur causes a deterioration in the performance of Ni–cermet anode cells. In some cases only a proportion of the damage is permanent, but in others it can be fatal, while in others still performance recovers completely when the sulphur is removed from the fuel. There is a general belief that the concentration of sulphur in the fuel is the key parameter in the degree of performance reduction/damage, but it seems more probable that there are a large number of determinant parameters, e.g., p(S), fuel flow rate, time, total nickel surface, the presence of additional functional materials and temperature. Given the large number of parameters, particularly the nickel surface area which is generally unknown and can vary hugely from one cell manufacturer to another, it is perhaps not surprising that the literature finds no absolute answers or ‘tolerance’ numbers – the probability of being able to compare like with like between different literature sources is effectively zero. The varying claims in the literature are likely to be valid enough for the specific cells and conditions investigated though and the reported results are useful qualitatively.

Generally it can be expected that sulphur 'tolerance' increases with temperature as a consequence of the decreasing stability of potential anode-sulphur compounds that could form – and also with the increasing ability of the cell to oxidise the sulphur – sulphur is after all a potential SOFC fuel. Increasing operational temperatures to offset sulphur effects, however, contradicts the current trend of attempting to reduce temperatures to allow the use of cheaper system components such as low-cost steels. There are sufficient reliable reports of bulk nickel sulphide formation identified by different experimental techniques that assure this reaction will happen despite other reports that claim the contrary. Experiments reported in literature tend to be short-term, however, and it may be that there simply has not been enough sulphur exposure time in those cases to form enough bulk material to allow its detection under the conditions employed, or that the particular operating conditions strongly disfavoured it.

As an important aside: 'long-term' exposure should imply thousands of hours under S-testing as a reasonable replication of the necessary lifespan in stationary applications and the continuous, low-level exposure to be expected from the natural gas supply. It must be noted that this sort of long-term S-testing is largely absent in the literature even for Ni–cermets. There may be very long-term effects even at very low $p(S)$ values that have not yet been observed.

Generally, it should not be assumed that a lack of thermodynamic stability suggested in calculated phase diagrams will prevent the formation of metal–sulphur compounds – at least in surface form. The interpretation of calculations seldom takes account of surface kinetics which are liable to be very important and many assume bulk phase thermodynamics which are not likely to be valid when dealing with microscopic particles with large surface to mass ratios. Other potential pitfalls in the interpretation of calculated phase diagrams can also be found – invariably relating to standard thermodynamic assumptions being invalid under the real operating conditions – one obviously suspect assumption is that of equilibrium, since no fuel cell can be in equilibrium while actually operating. It seems that phase diagrams are best viewed somewhat qualitatively and used as guidance rather than being read in any absolute sense.

On the positive side, where they do form, metal sulphides have a tendency to show fairly good (anode) catalytic and electrical properties of their own, so the effect of their slow formation need not be immediately fatal. However, eventually the formation of any bulk sulphide phase is likely to cause serious microstructural damage via particle expansion if nothing else – this has been seen and documented.

Given the gaps that remain in the, albeit improving, knowledge, of how sulphur interacts with cermet anodes, the even more limited knowledge of its effects on oxide anode materials and the lack of good quantities of long-term

testing data, it is difficult to be definitive on what failure mechanisms exist. There are some likely mechanisms that can be suggested though. The initial sulphidation of the active material surface is not likely to cause fatal damage of itself as even in the worst case the relevant sulphides/oxysulphides are likely to have good anode properties of their own – this effect will reduce performance relative to that of the original catalyst however. Fatal damage can be expected via mechanical damage due to particle expansion on any bulk sulphidation occurring. Equally the physical movement of material will cause severe integrity problems if eutectic liquid sulphide phases form – equating to a rapid hot corrosion process in general metallurgy.

A few reports have been made tentatively suggesting that the YSZ or ScSZ used in cermets and as the electrolyte can also react to some extent with H_2S to yield oxy-sulphides (for example Sasaki *et al*. [2006]). These reports rely on Raman or XPS spectroscopy showing spectral shifts that suggest there is some bonding interaction with/change to the YSZ on admission of sulphur to the system. This may be no more than surface interactions, but it indicates a high probability that even relatively stable oxides are not entirely immune to the effects of sulphur. The presence of this surface-bound sulphur suggests there is liable to be interference with oxide surface ion transport.

In conclusion, sulphur fuel contaminants are a very significant worry to the SOFC system developer/operator. There are probably no absolute 'tolerance' values that the developer can obtain from the literature (e.g. EG&G Services, [2006]) that necessarily apply to any other particular cell/system and each developer is strongly advised to carry out their own work using their cells/system and operating conditions and to carry out that work over the long term. Pending greater understanding, if the developer does not want to operate the system at higher temperatures (e.g. ca. 1000 °C), then for the time being the use of sulphur-free fuel or a desulphurisation fuel processing stage is very strongly advised.

Some hints shall be given here as to how the sulphur sensitivity of nickel anodes can be avoided. Copper-based cermets appear to show good sulphur resistance. This can be explained by much lower copper–sulphur compound stabilities [Lee *et al*., 2004]. *Prima facie*, this seems to be 'the solution'; however the general performance of these anodes is lower than the Ni–cermet and copper is problematic in other processing respects due to its low melting temperature and relatively poor catalyitc properties. Avoiding nickel as an anode constituent, though, aims in the right direction and other potential anodes are strontium titanates ($SrTiO_3$) [Blennow *et al*., 2006], chromates (e.g. LSCrM) or alternative oxides. Although these offer suitable tolerance they are difficult to integrate into SOFC cells due to problems with processing and low activity.

Besides the obvious problems of fuel contaminant sensitivity as described in depth above, using sulphur as an example, the anode can suffer major

damage through external influence in the form of oxygen. During operation the anode compartment is flooded with fuel and owns a very strong reducing atmosphere with extremely low oxygen partial pressures ($p(O) \sim 10^{-21}$). The Ni–YSZ anodes are therefore completely reduced and no nickel oxide is present. Once SOFC operation stops, though, oxygen might penetrate into the fuel compartment for various reasons:

- mechanical contraction of the fuel gas volume during cooling and ensuing negative pressure difference to the outside atmosphere;
- forced flow of air through the fuel processing unit in order to avoid coking, which will inevitably also pass the anode;
- spillages and leakages following formation of cracks in sealants and joining seams, etc.

Fundamentally, the redox problem can be traced back to the second law of thermodynamics. During repeated reduction and oxidation of the metal component of a cermet, entropy demands that the metal atoms will not remain static or return to the same positions during the atomic rearrangements that take place during re-oxidation – and thus the physical movement of material is guaranteed. This is entirely fundamental and it cannot be prevented. On reduction the forming nickel particles will tend to minimise their total energy by minimising their surface area – e.g. they will tend towards spherical particles of maximum mass. The nature of the solid-state reduction process within the ceramic skeleton severely limits the ability of the metal component to form large spherical-type particles; however, the tendency is there [Klemenso *et al*., 2006]. The result of these effects will be for the nickel to agglomerate in increasingly large particles on each cycling event.

We imagine a nickel atom moving to form a metallic particle during reduction in a void in the ceramic component of fixed volume. If that newly formed nickel particle occupies most of that void's volume then on any subsequent re-oxidation the volume expansion on conversion back to nickel oxide will be too great for the new NiO particle to be contained within the ceramic void. The effect of this is completely predictable and devastating for the ceramic cermet skeleton [Atkinson and Sarantaridis, 2007]. Colossal mechanical stresses will arise locally and the ceramic skeleton will break when local forces exceed the ceramics' yield strength. Macroscopically the cermet will be seen to disintegrate [Sarantaridis *et al*., 2007]. As few as one cycle may be sufficient to yield disintegration but this will depend on the particular cermet composition and construction and a cermet may survive a number of cycling events. Generally, though, the immediate effect on the Ni–YSZ cermet is less pronounced than that on the electrolyte layer. Figure 11.9 shows that the 'swelling' forces in the cermet of an anode supported cell exert sufficiently high forces on the thin electrolyte so that cracks can form. Figure 11.10 shows these in the electrolyte layer of a half cell. After several

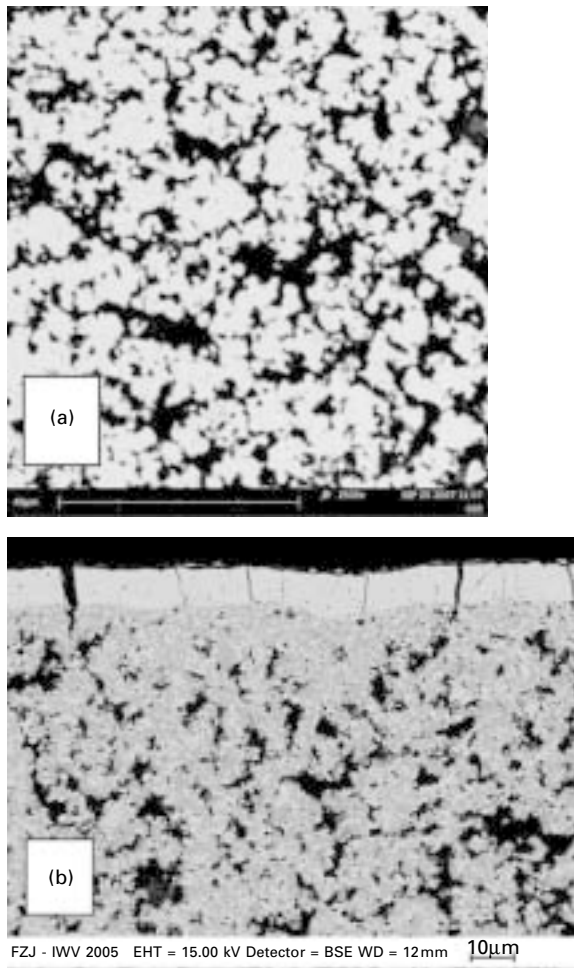

11.9 Microstructural change to a half cell subjected to re-oxidising conditions: (a) original reduced anode cermet structure, Ni and YSZ phases are practically indiscernible, (b) anode substrate (bottom), anode (middle) and electrolyte (top) half cell layered structure after complete re-oxidation; NiO (grey) and YSZ (light grey) phases can be clearly identified.

cycles the electrolyte will rupture and the cell will fail completely. The re-oxidation kinetics are strongly temperature dependent, though, and below 600 °C reaction kinetics are extremely slow.

Increasing the void volume (by reducing the metal proportion or increasing the absolute porosity) in the Ni–YSZ cermet can have a positive effect in increasing the number of redox cycles can be tolerated – by creating more space to accommodate the metal to metal oxide expansion. This approach is

11.10 Completely re-oxidised half cell sample showing crack formation in the electrolyte layer.

limited in its effect, however, by two factors. Firstly, the metal mass reduction is limited by the need to maintain adequate metal–metal particle contact through the cermet for electrical conductivity. And secondly, the movement of metal atoms during re-oxidation means that it is inevitable that eventually enough metal will have moved into enough voids of limited volume for the mechanical damage to occur. An interesting alternative approach might be to increase the elasticity/strength of the ceramic component.

Surprisingly, perhaps, oxide anode materials also have the potential to suffer from redox-type problems. With cermets the primary problem is that of extreme mechanical damage; with oxides the microstructure can remain in essence completely intact, however problems can be experienced relating to changes in the materials' electrical properties. Note that not all oxide materials have been observed to suffer from this problem. Titanate anode materials make a good example of this potential problem. To obtain the best electrical/catalytic properties from certain titanate materials a minor degree of *in situ* reduction is relied upon to yield a useful number of Ti^{3+} cations and their current-carrying electrons. These materials do not reduce to the required state readily at typical SOFC operating temperatures. The desired reduction can be achieved however under hydrogen at temperatures in excess of 1000 °C relatively quickly and the anode can be thus prepared for operation. If re-oxidation later occurs and one subsequently attempts to run the system at say 800 °C, the anode performance will be lower than desired until it eventually re-reduces itself. At 800 °C, this process could take a very long time. In the case where the particular oxide relies on a greater degree of *in situ* reduction for their best properties a broadly similar redox effect to that noted for the cermets can be expected.

Re-oxidation damage is likely to continue to be a significant issue due to its roots in fundamental physical laws. Although these laws are in themselves immutable, this does not mean there are no means to get around them. The SOFC cell and stack are not isolated components but embedded in a system environment. This receives the task of preventing any hazard to stack safety. As with sulphur, where a desulphurisation unit may be required in the balance of plant, prevention of re-oxidation might include provision of sufficient fuel gas supply under all circumstances (even during shut-down and system failure) or shut-down cycles that rapidly reduce the temperature to below 600 °C. Other options remain in the design of the cell layers: an electrolyte-supported cell will not display the large forces of the oxidised anode on the electrolyte layer as seen in the anode-supported cell (as shown in Fig. 11.10), simply because the thickness relation is fundamentally different. Therefore some evidence indicates higher tolerance of ESC to redox cycles. Caution is necessary, though, with general statements, since the exact composition of anode and electrolyte and the profile of the re-oxidation (temperature, oxygen flow, etc.) are more significant for damage done than the cell design.

11.6.4 Interaction of steels and glass sealings

Sealing materials for SOFC applications must fulfil specific requirements for stable long-term operation. In particular these are:

- hermetic sealing of both atmospheric compartments;
- providing electrical insulation between repeating units;
- coefficient of thermal expansion adapted to steel and SOFC cell materials;
- stability under oxidising and reducing conditions;
- lack of undesired reactions with the sealing partners, specifically the metallic interconnect and SOFC electrolyte;
- sufficient adhesion to the sealing partners;
- sufficient mechanical strength;
- constant mechanical, physical or chemical characteristics during operation; and
- assured contacting during stack sealing (by adapting the distance between the repeating units).

Standard joining and sealing concepts of the dissimilar and similar materials of planar SOFC stacks are often based on electrically isolating glass-ceramics. The rigid fixation of the cell in the metallic frames and the sealing of anode and cathode compartment are typically provided by glass-ceramics, for instance of the BCAS ($BaO–CaO–Al_2O_3–SiO_2$) system [Gross *et al.*, 2005]. Compositional variations and the selection of minor additives allow adjustment, within certain limits, of the thermal expansion of the sealant to the metallic interconnect and the anode substrate of the cell. Good adherence to the

metallic and ceramic joining partners can then be obtained [Malzbender *et al.*, 2003, 2005].

In order to supply a strong bond between sealing partners, a certain reactivity between sealant and materials to be joined is necessary. Glass ceramics are expected to react with the steel surfaces of the interconnect material in order to provide reliable and long-term stable bonding. This is a reaction, though, that needs to be well controlled since, considering the complexity of possible high-temperature material interactions, chemical compatibility problems may occur. As an example, rapid degradation of stack performance has been observed with special variants of the BCAS glass ceramic and ferritic steels [Batfalsky *et al.*, 2006]. Short-circuiting effects after stack operation times of only ~200 h could be attributed to the chemical interactions along the seals between interconnect and cell frame. In addition pronounced differences in reactions between the air and fuel side of the seal could be identified. Near the TPB of the oxidant atmosphere (air), glass ceramic and ferritic steel, internal and surface oxidation of the metal was observed [Menzler *et al.*, 2005]. The voluminous outward growth of highly conductive iron containing oxide 'nodules' provided conducting bridges, which short-circuited the metallic cell frame and the interconnect, otherwise separated and isolated by the sealant.

The basic effect is demonstrated in a cross-section of a glass ceramic seal between coated and uncoated ferritic steel (Fig. 11.11). Note that the specimen was prepared after short-term stack operation at 800 °C. The SEM micrograph in Fig. 11.11a shows the effect of massive outward oxidation from the unprotected ferritic steel, whereas the plasma sprayed YSZ coating completely suppresses the reaction. Under the conditions of the fuel atmosphere at the other end of the seal, the unprotected ferritic steel exhibits excessive internal oxidation accompanied by a substantial volume increase (Fig. 11.11b). Bulging of the steel is manifest in surface bending up to several hundred microns [Batfalsky *et al.*, 2006]. Again, no corrosion is visible at the YSZ coated steel surface. Figure 11.12 shows all three possibilities of cracking between interconnect and sealant, either by complete delamination (top picture) or by failure sections in which some delamination starts. These regions act as the nucleation zone for cracking.

Model experiments at laboratory scale with the unprotected ferritic steel reproduced the rapid, massive internal oxidation at the fuel side and the formation of Fe-oxide nodules on the air side [Haanappel *et al.*, 2005b]. Both effects occurred only in BCAS sealants with PbO additive on a steel containing 0.1% of both silica and aluminium. The rate of corrosion attack increased with increasing Si content in the ferritic steel.

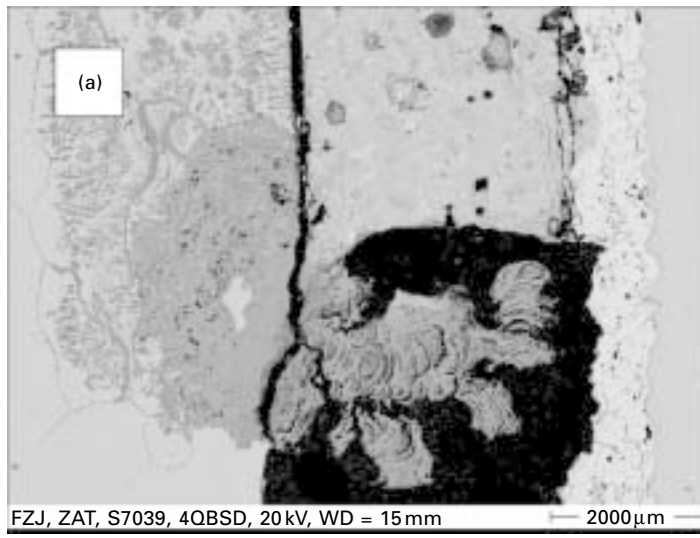

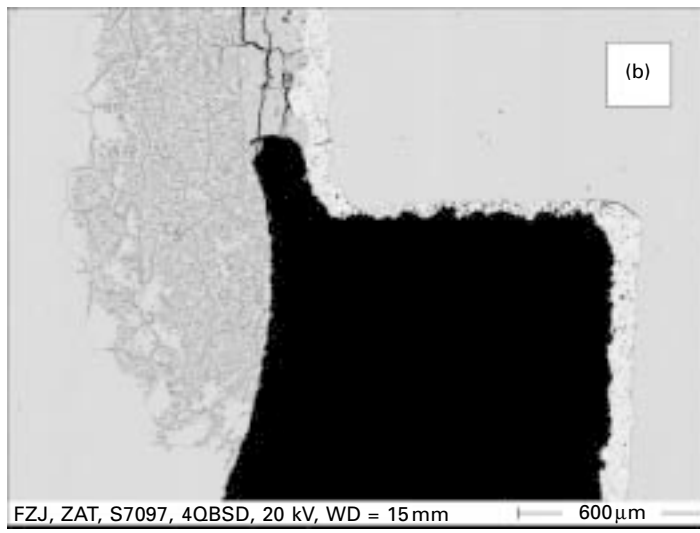

11.11 Corrosion reaction of glass ceramic with unprotected ferritic steel (left-hand side) at a stack seal. Plasma sprayed YSZ coating on steel surface (right-hand side) suppresses the corrosion. (a) Formation of
Fe-oxide nodules at air side, which can bridge the seal gap and can cause short-circuiting. (b) Internal oxidation at fuel side of seal with surface uplift of steel.

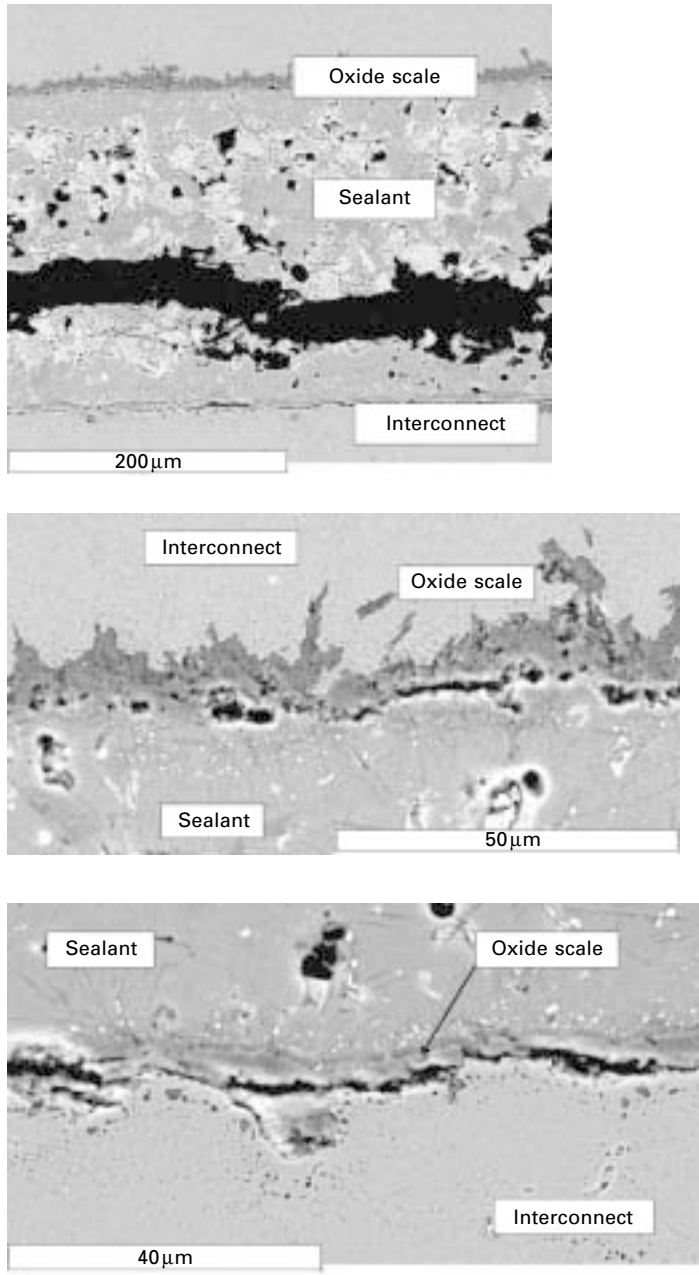

11.12 SEM cross-sections of the interaction zone sealant/interconnect after dismantling; top: crack in the sealant; middle: defect zone in the oxide scale; bottom: defect zone between oxide scale and metal (please note the varying magnifications).

11.7 References

E. Antolini, J.R.C. Salgado, E.R. Gonzalez, The stability of Pt-M(M = first row transition metal) alloy catalysts and its effect on the activity in low temperature fuel cells, *J. Power Sources*, 160, (2006), 957–968.

A. Atkinson, D. Sarantaridis, Redox Cycling of Ni-based Solid Oxide Fuel Cell Anodes, *J. Fuel Cells* 7 (2007), 246–258.

A.J. Bard (Ed.), *Encyclopedia of the Electrochemistry of the Elements*, Vol. 6, Chapter VI-8, p. 281 & 283, Marcel Dekker Inc. New York (1976).

E. Batawi, U. Weissen, A. Schuler, M. Keller, C. Voisard, in *SOFC* VII, H. Yokokawa and S.C. Singhal, eds, PV2001-16, p. 140, The Electrochemical Society Proceedings Series, Pennington, NJ (2001).

P. Batfalsky, V.A.C. Haanappel, J. Malzbender, N.H. Menzler, V. Shemet, I.C. Vinke, R.W. Steinbrech: *J. Power Sources*, **155** (2006) 128–137.

B.C. Beard, P.N. Ross Jr., *J. Electrochem. Soc*. **137** [11] (1990) 3368.

P. Bindra, S.J. Clouser, E. Yeager, *J. Electrochem. Soc*. **126** (1979) 1631.

P. Blennow, K.K. Hansen, L.R. Wallenberg, M. Mogensen, *Electrochimica Acta* **52** (2006) 1651–1661.

L. Blum, H.-P. Buchkremer, S.M. Gross, L.G.J. de Haart, J. Quadakkers, U. Reisgen, R. Steinberger-Wilckens, R.W. Steinbrech, F. Tietz, *Int. J. Appl Ceramic Technol*. **3** [6] (2006) 470–476.

B. Borglum, E. Tang, D. Prediger, M. Pastula in: *Proceedings of the 207th Meeting of the Electrochemical Society*, Symposium SOFC IX, Quebec, 15–20 May 2005, The Electrochemical Society, Pennington, NJ (2005), Vol. 2005-7.

R.L. Borup, J.R. Davey, F.H. Garzon, D.L. Wood, M.A. Inbody, *J. Power Sources* **163** (2006) 76–81.

R.L. Borup, B. Pivovar, D. Wood, J.R. Davey, F.H. Garzon, H. Xu, P.M. Welch, *Proceedings of the Conference 'Advances in Materials for Proton Exchange Fuel Cell Systems 2007'*, Asilomar, CA, (2007).

A. Bosnjakovic, S. Schlick, *J. Phys. B* **108** (2004) 4332.

W. Chen, G. Suna, Z. Liang, Q. Mao, H. Li, G. Wang, Q. Xin, H. Chang, C. Pak, D. Seung, *J. Power Sources* **160** (2006) 933–939.

C.X. Cheng, C. Peng, M. You, L. Liu, Y. Zhang, Q. Fan, *Electrochim. Acta* **51** (2006) 4620–4625.

X. Cheng, Z. Shi, N. Glass, L. Zhang, J. Zhang, D. Song, Z.-S. Liu, H. Wang, J. Shen, *J. Power Sources* **165** (2007) 739–756.

A. Collier, H. Wang, X.Z. Yuan, J. Zhang, D.P. Wilkinson, *Int. J. Hydrogen Energy* **31** (2006) 1838.

H.R. Colon-Mercado, B.N. Popov, *J. Power Sources* **155** (2006) 253–263.

J.F. Connolly, R.J. Flannery, B.L. Meyers, *J. Electrochem. Soc*. **114** (1967) 241.

D.E. Curtin, R.D. Lousenberg, T.J. Henry, P.C. Tangeman, M.E. Tisack, *J. Power Sources* **131** (2004) 41.

R.M. Darling, J.P. Meyers, *J. Electrochem. Soc*. **150** (2003) A1523.

R.M. Darling, J.P. Meyers, *J. Electrochem. Soc*. **152** (2005) A242.

D. Das, M. Miller, H. Nickel, K. Hilpert, in: *Proceedings of the First European Solid Oxide Fuel Cell Forum*, Ulf Bossel, ed., p. 703, European Fuel Cell Forum, Dübbendorf, Switzerland, (1994).

D.W. Dees, T.D. Claar, T.E. Elser, F.C. Marzek, *J. Electrochem. Soc*. **134** (1987) 2141.

DOE Hydrogen Multi-Year Research, Development and Demonstration Plan 2006, Technical

Plan – Fuel Cells, US Department of Energy, Office of Hydrogen, Fuel Cells and Infrastructure Technologies (2006).
B. Du, Q. Guo, R. Pollard, D. Rodriguez, Ch. Smith, J. Elter, *J. Minerals, Metals Mater*. **58**[8] (2006), 45–49.
EG&G Services, Parsons Inc.: *Fuel Cell Handbook*. Under contract to the US Department of Energy contract no. DE-AM26-99FT40575. 7th edition (2006).
C. Eickes, P. Piela, J. Davey, P. Zelenay, *J. Electrochem. Soc*. **153** [1] (2006) A171–A178.
S. Elangovan, A. Khandkar, in: *Proceedings of the First International Symposium on Ionic and Mixed Conducting Ceramics*, T.A. Ramanarayanan, H.L. Tuller (eds.), p. 122, 16–17 October 1991, Phoenix, AZ, The Electrochemical Society, Pennington, NJ (1991).
W. Feduska, A.O. Isenberg, *J. Power Sources* **10** (1983) 89.
P.J. Ferreira, G.J. la O', Y. Shao-Horn, D. Morgan, R. Makharia, S. Kocha, H.A. Gasteiger, *J. Electrochem. Soc*. **152** (11) (2005) A2256–A2271.
H.A. Gasteiger, M.F. Mathias, *Proceedings of the Workshop on High Temperature PEM Fuel Cells*, The Pennsylvania State University, December (2003).
H.A. Gasteiger, S.S. Kocha, B. Sompalli, F.T. Wagner, *Appl. Catal. B: Environmental* **56** [1–2] (2005), 9–35.
J. Geyer, H. Kohlmüller, H. Landes, R. Stübner, in *SOFC V*, U. Stimming, S.C. Singhal, H. Tagawa, W. Lehnert (Eds.), PV 97–40, p.585, The Electrochemical Society Proceedings Series, Pennington, N.J. (1997).
N. Giordano, P.L. Antonucci, E. Passalacqua, L. Pino, A.S. Arico, K. Kinoshita, *Electrochim. Acta*, **36** (1991) 1931.
S.M. Gross, T. Koppitz, J. Remmel, U. Reisgen, *Ceram. Eng. Sci. Proc*. **26** [4] (2005) 239.
C. Günther, H.-J. Beie, P. Greil, F. Richter, in *Proceedings of The Second European Solid Oxide Fuel Cell Forum*, Bernt Thorstensen (ed.), p. 491, European Fuel Cell Forum, Dübbendorf, Switzerland, (1996).
V.A.C. Haanappel, J. Mertens, D. Rutenbeck, C. Tropartz, W. Herzhof, D. Sebold, F. Tietz, *J. Power Sources* **141** (2005a) 216.
V.A.C. Haanappel, V. Shemet, I.C. Vinke, S.M. Gross, Th. Koppitz, N. Menzler, M. Zahid, W.J. Quadakkers, *J. Mater. Sci*. **40** (2005b), 1583–1592.
V.A.C. Haanappel, A. Mai, J. Mertens, *Solid State Ionics* **177** (2006) 2033.
A. Hagen, R. Barfod, P. Vang Hendriksen, Y.-L. Liu, S. Ramousse, *J. Electrochem. Soc*. **153** [6] (2006) A1165–A1171.
A. Havránek, K. Klafki, J. Mergel, H. Schmitz, D. Stolten, K. Wippermann, in: *Proc. 2nd European Polymer Electrolyte Fuel Cell Forum*, Luzern, D. Stolten, B. Emonts, R. Peters (eds.), p. 623, European Fuel Cell Forum, Oberrohrdorf, Switzerland (2003).
M.J. Heneka, E. Ivers-Tiffée, in: *Proc. 26th Risø International Symposium on Materials Science*, Roskilde, Denmark (2005).
K. Hilpert, D. Das, M. Miller, D.H. Peck, R. Weiss, *J. Electrochem. Soc*. **143** (1996), 3642.
IEF-3 Report 2007, p.47, Research Center Jülich, Energy Technology, Volume 63.
J. Iritani, K. Kougami, N. Komiyama, K. Nagata, K. Ikeda, K. Tomida, in *SOFC VII*, H. Yokokawa and S.C. Singhal, Editors, PV2001-16, p.63, The Electrochemical Society Proceedings Series, Pennington, NJ (2001).
M.K. Jeon, K.R. Lee, K.S. Oh, D.S. Hong, J.Y. Won, S. Li and S.I. Woo, *J. Power Sources* **158** (2006) 1344–1347.
R. Jiang, C. Rong, D. Chu, *J. Electrochem. Soc*. **154** (2007) B13–B19.

S.P. Jiang, J.P. Zhang, L. Apateanu, K. Foger, *J. Electrochem. Soc*. **147** (2000) 4013.
M.J. Jørgensen, P. Holtappels, C.C. Appel, *J. Appl. Electrochem.* **30** (2000) 411.
Y.S. Kim, B. Pivovar, *ECS Trans.* 1–8 (2006), 457.
T. Klemenso *et al.*, *Electrochem. Solid State Lett.* **9** (2006) A403.
S.D. Knights, K.M. Colbow, J. St-Pierre, D.P. Wilkinson, *J. Power Sources* **127**(2004) 127–134.
E. Konysheva, H. Penkalla, E. Wessel, Jo. Mertens, U. Seeling, L. Singheiser, K. Hilpert, *J. Electrochem. Soc*. **153** (2006) A765.
M. Krumpelt, T.A. Cruse, B. Ingram, D.-J. Liu, in: *Proc. 30th Fuel Cell Seminar*, Hawaii, Nov. (2007).
H. Kuhn, L. Gubler, T.J. Schmidt, G.G. Scherer, H.-P. Brack, K. Simbek, T. Rager, F. Geiger, in: *Proceedings of the 2nd European PEFC Forum*, D. Stolten, B. Emonts, R. Peters (eds.) pp. 69–77, vol. 1, 30 June to 4 July Lucerne, Switzerland (2003).
A.A. Kulikovsky, H. Scharmann, K. Wippermann, *Electrochem. Commun*. **6** (2004) 75–82.
S. Kundu, M.W. Fowler, L.C. Simona, S. Grot, *J. Power Sources* **157** (2006) 650–656.
A. Kuzjukevics, S. Linderoth, *Mater. Sci. Eng. A* **A232** (1997) 163–167.
K.S. Lee *et al*., *J. Solid State Electrochem.* **11** (2007) 1295.
S. Lee, J. Vohs, J. Gorte, *J. Electrochem. Soc*. **151** (2004) A1319.
S. Linderoth, N. Bonanos, K. Vels Jensen, J.B. Bilde-Sørensen, *J. Am. Ceramic Soc*. **84** (2001) 2652–2656.
G. Liu, H. Zhang, J. Hu, Y. Zhai, D. Xu, Z. Shao, *J. Power Sources* **162** (2006) 547.
W. Liu, K. Ruth, G. Rusch, *J. New Mater. Electrochem. Systems* **4** (2001) 227.
Y.L. Liu, C. Jiao, *Solid State Ionics* **176** (2005) 435.
A. Mai, M. Becker, W. Assenmacher, F. Tietz, E. Ivers-Tiffée, D. Stöver, W. Mader, *Solid State Ionics* 177 (2006a), 1965–1998.
A. Mai, V.A.C. Haanappel, S. Uhlenbruck, F. Tietz D. Stöver, *Solid State Ionics* **177** (2006b) 2103.
J. Malzbender, R.W. Steinbrech, L. Singheiser, *J. Mater. Res*. **18** (2003) 929.
J. Malzbender, R.W. Steinbrech, P. Batfalsky, *Ceram. Eng. Sci. Proc*. **26** [4] (2005) 285.
Y. Matsuzaki, I. Yasuda, *Solid State Ionics* **132** (2000) 261.
N.H. Menzler, D. Sebold, M. Zahid, S.M. Gross, Th. Koppitz, *J. Power Sources* **152** (2005) 156–167.
N.H. Menzler, L.G.J. de Haart, D. Seebold, *Solid Oxide Fuel Cells X*, K. Eguchi, S.C. Singhal and H. Yokokawa J. Mizusaki (eds)., p. 245, *ECS Transactions* **7**, Pennington, NJ (2007).
J. Mergel, P. Bogdanoff, E. Gülzow, in: *Wasserstoff und Brennstoffzellen – Energieforschung im Verbund*, p.101–107, ForschungsVerbund Sonnenergie, Berlin, (2005).
V.O. Mittal, H.R. Kunz, J.M. Fenton, *J. Electrochem. Soc*. **153** (2006) A1755.
M. Mogensen. in *Proc. 26th Risø International Symposium on Materials Science*, p.51, Roskilde, Denmark (2005).
J. Mougin, S. Ravel, E. de Vito, M. Petitjean, in: *ECS Transactions – Solid Oxide Fuel Cells*, Volume 7, June 2007, for the 10th International Symposium on Solid Oxide Fuel Cells (SOFC-X), Nara, Japan (2007).
S. Mukerjee, S. Srinivasan, *J. Electroanal. Chem*. **357** (1993) 201.
A. Müller, A. Weber, D. Herbstritt, E. Ivers-Tiffee in: Long term 8th Intl. Symposium on Solid Oxide Fuels C*ells*, Paris, 27. April to 3 May vol. 7, pp. 196–199, (2003).
H. Nabielek, L. Blum, H.-P. Buchkremer, V. Haanappel, L.G.J. de Haart, W. Quadakkers, R. Steinberger-Wilckens, R.W. Steinbrech, U. Reisgen, F. Tietz, in: *Proc. 4th Intl.*

Symposium on SOFC Materials and Technology, Annual Meeting of the American Ceramics Society (ACS), Daytona, January (2007).
NEP, Nationaler Entwicklungsplan (Version 2.1) zum 'Innovationsprogramm Wasserstoff- und Brennstoffzellentechnologie', Strategierat Wasserstoff & Brennstoffzellen, 21 March (2007) [National Development Plan (V 2.1) for the 'Innovation Programme Hydrogen and Fuel Cells' of the German government].
E. Passalacqua, P.L. Antonucci, M. Vivaldi, A. Patti, V. Antonucci, N. Giordano, K. Kinoshita, *Electrochim. Acta* **37** (1992) 2725.
T. Patterson, in *Fuel Cell Technology Topical Conference Proceedings*, G.J. Igwe, D. Mah (eds.) p.313, AIChE Spring National Meeting, New York (2002).
S.C. Paulson, V.I. Briss, in: *Solid Oxide Fuel Cells VIII*, S.C. Singhal and M. Dokiya eds., PV 03-07, p.498, The Electrochemical Society Proceedings Series, Pennington, NJ (2004).
M. Pianca, E. Barchiesi, G. Esposto, S. Radice, *J. Fluorine Chem.* **95** (1999) 71.
P. Piela, C. Eickes, E. Brosha, F. Garzon, P. Zelenay, *J. Electrochem. Soc.* **151** (2004) A2053–A2059.
T.R. Ralph, M.P. Hogarth, *Platinum Metals Rev.* **46** [1] (2002) 3–14.
C.A. Reiser, L. Bregoli, T.W. Patterson, J.S. Yi, J.D. Yang, M.L. Perry, T.D. Jarvi, *Electrochem. Solid State Lett.* **8** [6] (2005) A273–A276.
R. Ruckdäschel, R. Henne, G. Schiller, H. Greiner, in: *Solid Oxide Fuel Cells V*, U. Stimming, S.C. Singhal, H. Tagawa, W. Lehnert (eds)., PV 97-40, p. 1273, The Electrochemical Society Proceedings Series, Pennington, NJ (1997).
D. Sarantaridis, R. Rudkin, A. Atkinson, in: *ECS Transactions – Solid Oxide Fuel Cells*, Volume 7, June 2007, for the 10th International Symposium on Solid Oxide Fuel Cells (SOFC-X), Nara, Japan, (2007).
L.S. Sarma, C.-H. Chena, G.-R. Wang, K.L. Hsueh, C.-P. Huang, H.-S. Sheu, D.-G. Liu, J.-F. Lee, B.-J. Hwang, *J. Power Sources* **167** (2007) 358–365.
K. Sasaki, A. Iyoshi, M. Uchimura, N. Imamura, H. Kusaba, Y. Teraoka, H. Fuchino, K. Tsujimoto, Y. Uchida, N. Jingod, *J. Electrochemical Society* **153** [11] (2006) A2023–A2029.
D.A. Schiraldi, *Polymer Reviews* **46** (2006) 315.
M. Schulze, N. Wagner, T. Kaz, K.A. Friedrich, *Electrochim. Acta* **52** (2007) 2328–2336.
K. Schwiebert, K. Raiford, G. Nagarajan, F. Principe, G. Escobedo, *KFTCA International Symposium*, Washington, DC, December 2005, reproduced in Schiraldi (2006).
Y. Shimazaki, Y. Kobayashi, M. Sugimasa, S. Yamada, T. Itabashi, T. Miwa, M. Konno, *J. Colloid Interface Sci.* **300** (2006) 253–258.
M. Smith, A.J. McEvoy, in *Proc. 7th European SOFC Forum*, Lucerne (2006).
R. Steinberger-Wilckens, F. Tietz, B. Rietveld, O. Bucheli, R. Rosenberg, P. Stevens, P. Holtappels, in: *Proceedings of the ECS Meeting SOFC X*, Nara, Japan, June (2007).
D.A. Stevens, J.R. Dahn, *Carbon* **43** (2005) 179.
D.A. Stevens, M.T. Hicks, G.M. Haugen, J.R. Dahn, *J. Electrochem. Soc.* **152** [12] (2005) A2309–A2315.
D. Strmcnik, M. Gaberscek, S. Hocevar, J. Jamnik, *Solid State Ionics* **176** (2005) 1759–1763.
H. Tang, Z. Qi, M. Ramani, J.F. Elter, *J. Power Sources* **158** (2005) 1306–1312.
N. Travitsky, T. Ripenbein, D. Golodnitsky, Y. Rosenberg, L. Burshtein, E. Peled, *J. Power Sources* **161** (2006) 782–789.

H. Tu, U. Stimming, Advances, ageing mechanisms and lifetime in solid-oxide fuel cells, *J. Power Sources* **127** (2004) 284–293.

I.C. Vinke, L.G.J. de Haart, L. Blum, D. Stolten, in: *Proceedings of the 5th European Solid Oxide Fuel Cell Forum*, Joep Huijsmans (ed.), p.164, European Fuel Cell Forum, Dübbendorf, Switzerland (2002).

H. Wang, J. Houa, H. Yu, S. Suna, *J. Power Sources* **165** (2007) 287–292.

X. Wang, R. Kumar, D.J. Myers, *Electrochem. Solid-State Lett.* 9 [5] (2006) A225–A227.

M.S. Wilson, F.H. Garzon, K.E. Sickafus, S. Gottesfeld, *J. Electrochem. Soc*. **140** (1993) 2872.

R. Woods, in: *Electroanalytical Chemistry*, Ed. A. J. Bard, Vol. 9, p.1, Marcel Dekker, New York (1976).

K. Yasuda, A. Taniguchi, T. Akita, T. Ioroi, Z. Siroma, Phys. Chem. Chem. Phys. **8** (2006) 746–752.

P. Yu, M. Pemberton, P. Plasse, *J. Power Sources* **144** (2005) 11–20.

P. Zelenay, *ECS Trans*. **1** [8] (2006) 483.

12

Recycling and life cycle assessment of fuel cell materials

J S COOPER, University of Washington, USA

12.1 Introduction

Fuel cell technologies are expected to substantially reduce consumption of oil and emissions of pollutants such as greenhouse gases as compared with conventional combustion-based power generation technologies. Fuel cell technologies have the additional advantages of high efficiency, at times including the ability to take advantage of cogeneration or hybrid applications. While much has been done to develop fuel cell technology and emphasis has been placed on the environmental benefits of its use, less emphasis has been placed on material sources and hardware materials recovery.

As fuel cells move from laboratory and/or pilot plant settings to wide-scale deployment, an opportunity exists to consider the environmental aspects of the hardware life cycle. Here, the 'life cycle' extends from material sources (acquisition from the earth) through recovery with Section 12.2 introducing the environmental aspects of fuel cell materials. Section 12.3 continues by defining hardware recovery to include collection, separation, and subsequently system or component reuse and remanufacturing, materials recycling, or energy recovery and describing issues for hardware disassembly and recycling process availability. Section 12.4 considers the role of materials selection and recovery in the life cycle fuel cell system improvements. Finally, future trends for fuel cells centered on voluntary and mandated recovery and the movement of life cycle considerations from computational research laboratories to design complete the discussion.

12.2 Environmental aspects of fuel cells

Fuel cells promise 'clean' energy generation. Here and by in large, 'clean' refers to negligible or substantially lower operating emissions when compared with combustion-based power generation technologies. However, lower operating emissions are only part of the story for fuel cells.

First, extending the definition of 'clean' to include **hardware recovery** means component reuse, remanufacturing, materials recycling and energy recovery are considered for fuel cell maintenance and retirement processes. For example, Plug Power[1], a manufacturer of distributed proton exchange membrane fuel cell (PEMFC) systems, employs a 'zero-to-landfill' (ZTL) principle during hardware design. The ZTL principle was developed at Xerox as a part of the Lakes program [Hotchkiss *et al.*, 2000] with the goal that every product, every component, and every material should be reused, remanufactured, or recycled after it reaches the end of its service life. Essentially, Plug Power designers seek the maximum use of reusable, remanufacturable, and recyclable components and ensure that these components can be separated from the system during maintenance activities or when equipment is retired.

Plug Power designers have applied the principles of ZTL in the development of PEMFC systems that are more than 85% recyclable or reusable by weight[2]. Further, the company has found that the application of zero-to-landfill principles fosters additional benefits in system assembly and during service activities. In fact, as a result of their zero-to-landfill initiatives, Plug Power has netted over US$ 1.4 million in cost savings by the end of 2006 [Elter and Cooper, 2007]. Also, Plug reserves the right to buy their system back at the end of its life, to ensure that the minimum materials reach a landfill.

However, for Plug Power and many others involved in the development and deployment of fuel cell systems, 'clean' has more recently come to include not only the consideration of operating emissions and hardware materials recycling, but also the consideration of fuel and hardware production, system maintenance, and in fact the full fuel cell life cycle. As in Fig. 12.1, the fuel cell 'life cycle' includes the acquisition of materials and fuels (e.g. mining and agricultural activities); the processing of materials and fuels; and fuel cell manufacturing, use, maintenance, remanufacturing, and retirement including the ultimate management of materials (e.g. recycling, landfilling, and incineration). Life cycle 'environmental aspects' include for example resource use (e.g. the use of energy, natural resources, and land) and contributions to impacts such as climate change, smog formation, and damage to human health.

The assessment of life cycle environmental aspects, including hardware recycling, is described by the International Organization for Standardization's (ISO) Life Cycle Assessment (LCA) series standards in the ISO14040 series. In the ISO LCA process, material and energy use and waste are estimated for each life cycle process and for the system as a whole (e.g. how much energy

[1]See http://www.plugpower.com
[2]See http://www.plugpower.com/news/pdf/ACFJ6h2PH.pdf

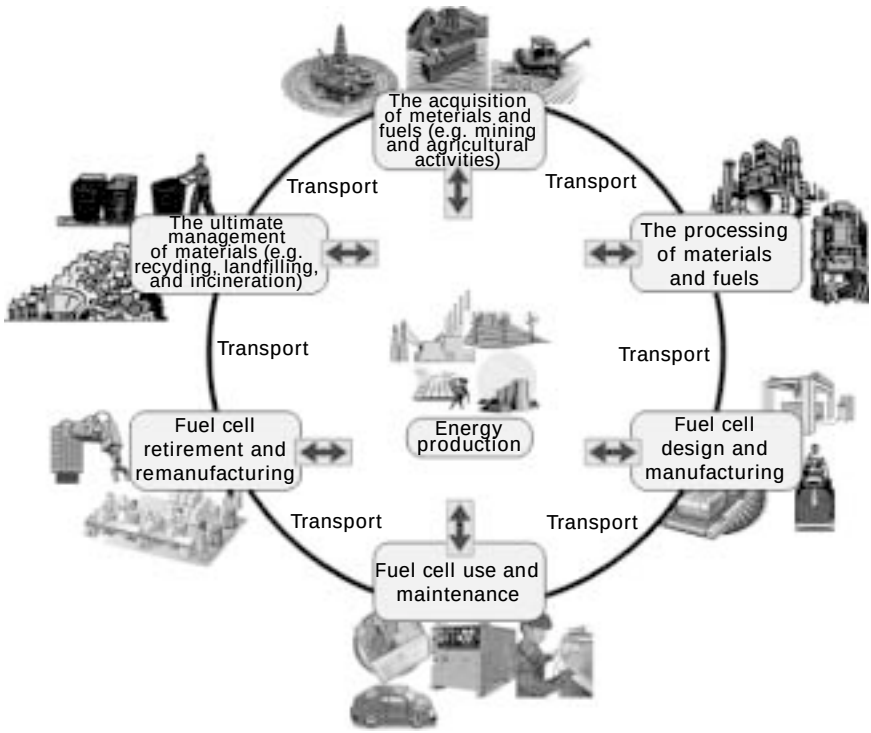

12.1 Activities combine to form the fuel cell life cycle.

is consumed and carbon dioxide is emitted by processes throughout the life cycle). From this energy and materials inventory, the contribution of the life cycle to a variety of environmental aspects is estimated (e.g. how much material is recycled or how much life cycle air emissions contribute to global climate change). As fuel cells move from the laboratory to wide-scale use, knowing the potential life cycle contribution to environmental aspects provides valuable insights into the evaluation of design variants, in the comparison to other energy generation technologies, and in meeting corporate, community, and national goals.

12.3 Fuel cell hardware recycling

Fuel cell hardware recycling promises to be an important environmental aspect of mass-produced systems. In recovery, materials are collected and separated before being reused, remanufactured, recycled, or used for energy recovery, as follows:

- *Collection* moves hardware from the point-of-use to separation sites by truck, rail, barge, ocean freighter, and/or air transport. As in the case of

Plug Power, hardware manufacturers can coordinate fuel cell hardware collection from operating sites. When technologies are prevalent throughout a region, municipal collection systems can be developed, for example as pursuant to waste electronic directives.

- *Separation systems* first purge all fluids from hardware (from fuel tanks and processors) followed by hardware separation and sometimes chemical recovery. In hardware separation, subassemblies, components, or materials are divided into groups that are compatible for subsequent processes (e.g. metals that can be recycled together). Hardware separation systems, such as those operated by a municipality or a company, can be automated or manual. In automated systems, materials can undergo shredding followed by magnetic, shape, density, or visual-based separation systems. Bras [2005] for example notes that aluminum alloys, steel, and magnesium alloys are readily separated and recycled from shredder output. When volumes offer economies of scale, automated systems can also be based on robotic disassembly for hardware separation. Manual hardware separation is essentially disassembly and can use powered hand tools and often move materials between work stations using conveyors. Although manual systems can be more suited to hardware reuse and remanufacturing systems and can more easily accept wide variations in hardware design, they require a relatively high level of skill to achieve reasonable disassembly rates. In addition, chemical recovery, including thermal, chemical, or electrochemical separation, can be used to access for example precious metals [Society of Automotive Engineers, 2003]. Following separation, materials are most often transported to recycling sites that manage specific types or classes of materials.
- *Reuse of components* tends to be preferred among hardware recycling options. Reuse refers to the direct use of components and subassemblies back into fuel cells without additional processing. The Society of Automotive Engineers [2003] notes that reuse depends on separability, the demand for reusable components in repair or replacement, component durability, the cost of new components, and the collection and distribution infrastructure. However, reuse is also hampered by design changes, as new features are incorporated into fuel cell systems old components become obsolete [Handley *et al*., 2002; Cooper, 2003].
- *Remanufacturing* is the process of restoring components, e.g. by replacing worn or damaged parts, again for use back into fuel cells. Remanufacturing issues are similar to those faced in component reuse.
- *Recycling processes* subjects materials to a variety of transformations (e.g. heat treatments to remove contaminants or combine small parts) prior to re-entering the commodity market. The level of refinement is dependent upon the requirements of the receiving products. For some materials, recycling processes seek to prepare materials with physical

and chemical properties similar to their primary/unrecycled material counterparts (e.g. in metals recycling). For other materials, recycling targets lesser quality products (known as downcycling) and are used in new products often with less stringent material requirements (e.g. in plastics recycling, lower grade plastics are often produced from higher-grade plastics).

- *Energy recovery:* Often considered the least preferable recycling option, some components and materials are used for energy generation, such as in the incineration of plastics.

Given this process flow, fuel cell hardware 'recyclability' is dependent upon two things: (1) whether or not the recyclable components and materials can be separated from incompatible materials during maintenance operations and when the fuel cell system is retired and (2) whether or not recycling processes are readily available. Whereas separability is dependent upon fuel cell stack and balance-of-plant design, availability is a function of the state of the recycling infrastructure throughout the globe.

12.3.1 Recycling process availability

'Availability' for recovery in general refers to the prevalence of facilities that reuse, remanufacture, recycle, or convert to energy components and materials of interest. Infrastructures for fuel cell reuse and remanufacture are currently managed by individual companies like Plug Power. The success of recycling depends on the cost of retrieving and processing materials from products throughout an economy and, for each type of component and material, the relation to the price of a component or material made from primary (or unrecycled) materials. By far, metals currently offer the greatest availability and other fuel cell materials (single polymers, composites, insulation, reforming media, etc.) offer the greatest opportunity for improvement.

Starting with metals, Wernick and Themelis [1998] note that metals can be recycled nearly indefinitely. Unlike polymer plastics and composites, the properties of metals can theoretically (however, often not economically) be restored fully regardless of their chemical or physical form in a given component. Thus, metals used in fuel cell stacks and the balance-of-plant are recyclable at much higher rates than other materials. In fact, according to data from both the United States Geological Survey and the British Metals Recycling Association, recycling rates in their respective study regions are quite similar with lead recycling leading at ~75% (dominated by lead acid battery recycling), followed by iron and steel, aluminum, copper, and zinc recycling [Papp, 2005; Kumar *et al.*, 2007]. By mass, these metals can dominate fuel cell systems when considering both stacks and balance-of-plant and therefore offer substantial opportunity for fuel cell hardware recycling.

Of particular interest within the context of fuel cell metals recycling are steels, catalyst metals, and metals used in batteries (for energy storage in the balance-of-plant). First, steel recycling offers perhaps the easiest path to achieving the recycling of a high percentage of the mass of any fuel cell system. This would apply, for example, to the housings of most stationary fuel cell systems (e.g. the standing enclosures around low-pressure systems and pressure vessels for high-pressure systems) as well as to interconnects, flow field plates, tie rods, piping, and heat exchangers in select designs.

Also dominant on a mass basis, metals in fuel cell system batteries may or may not offer an easy recycling option. If based on lead acid batteries (either conventional or valve regulated), wide-scale recycling can almost be guaranteed. In fact, the lead acid battery industry recycled >99% of the available lead scrap from spent lead acid batteries from 1999 to 2003, according to a report issued by the Battery Council International (BCI) in June 2005, ranking the lead recycling rate higher than that of any other recyclable material [Gabby, 2006]. However, emerging technologies such as lithium ion batteries, nickel metal hydride batteries, and ultra-capacitors offer improved energy storage performance and, should they be widely used in fuel cells systems, promise to either reduce recycling opportunities or spur the development of a new recycling infrastructure.

Unlike steel and the metals in batteries, catalyst family metals can be expected to be recycled on the basis of their value, as opposed to the dominance of their mass in fuel cell systems. For example, platinum family catalyst metals are currently quite successfully recycled from today's vehicles (including both platinum and rhodium). Bhakta [1994] notes that in today's catalytic converters, the catalyst is housed in a stainless steel canister. Therefore, to recycle the catalyst, special machines have been developed to slit the canisters and remove the catalyst. Given an estimated increase in the amount of platinum group metals in fuel cells of 15 to over 200 times that of the catalytic converter for mobile fuel cell applications, it can be expected that similar technological development would follow wide-scale deployment of fuel cells based on platinum group metals [Cooper, 2003, 2004a].

In contrast, recycling rates for nonmetallic fuel cell materials are much lower than metals throughout the world, even when considering all aspects of recycling (reuse, remanufacturing, recycling, and energy recovery). For the balance-of-plant, although fuel storage hydrides, reforming media, and insulation materials have been recycled in laboratory and/or pilot plant settings, substantial construction would be needed to support recycling for wide-scale fuel cell deployment. For the stack, flow field materials such as graphite, carbon composites, and ceramics can be expected to be chemically and physically altered during stack operation in ways that will prohibit reuse and remanufacturing. There may however be opportunities to use flow field materials in steel manufacturing or as insulation for fuel cell or other electronic

products. For the electrodes, recycling process availability for both membranes and ceramic structures is also quite low. However, again there may be an opportunity to move processes from the laboratory to wider use.

12.3.2 Material compatibility and hardware separation

Materials are incompatible for recycling when they cannot be refined together. For example, because steel and copper are incompatible in recycling processes, solid oxide fuel cells, (SOFC) interconnects must be separated from any copper components in preparation for recycling. During fuel cell design, recycling compatibility charts can be useful in guiding materials selection and the assignment of hardware configurations. Compatibility charts are typically presented for classes of materials (i.e. plastics, metals, glasses and ceramics as presented by Bras [2005]) with an excerpt for fuel cell metals presented in Table 12.1.

Unless recycling is to be dominated by reuse or remanufacturing, due to compatibility issues fuel cell hardware designers should preferably eliminate incompatible materials or, when this is not possible, they should ensure incompatible materials are easily separated. The reason elimination is preferred is that it facilitates the largest number of separation options (from heat treatment, to shredding, to manual disassembly). For example, PEMFC membrane material substitution offers one example of the benefits of incompatible materials elimination. Specifically, Handley *et al*. [2002] identify fluorine-based membranes as a contaminant in bipolar plate recycling, platinum recycling, and any instances of incineration or energy recycling. This concern

Table 12.1 Compatibility of fuel cell metals[1]

Metal	Recycling is reduced if the metal is contaminated with
All	Plating materials
Iron or steel	Copper, tin, zinc, lead, or aluminum, also steel and cast irons, should be separate from stainless
Aluminum	Iron, steel, chromium, zinc, lead, copper, magnesium, silicon, platinum group metals, also wrought and cast aluminum should be separate
Zinc	Iron, steel, lead, tin, or cadmium
Platinum group metals	Copper
Copper	Platinum group metals, mercury, beryllium, antimony, nickel, bismuth, aluminum

[1]Based in part on Bras (2005); Brezet and Van Hemel [1997]; van Schaik *et al.* [2003]

is related to the possible formation of hydrogen fluoride at elevated temperatures. Handley *et al*. suggest municipal incineration is not a favorable option for related PEMFC components in that costly hydrogen fluoride recycling plants would be needed. As an alternative, as presented by Mehta and Cooper [2003], non-fluorinated membrane materials are being investigated. However, further analysis is needed to determine if any issues can be related to the disposition of these materials.

When incompatible materials cannot be removed from fuel cell systems, designers can ensure incompatible materials are easily separable. Coulter *et al*. [1998] provide guidelines on designing for separability. For example, designers should ensure recyclable components are accessible within an assembly and avoid instances where materials are welded or attached by different or numerous fasteners. Also, Kroll *et al*. [1996] present a procedure for evaluating the ease of disassembly or separability of products for recycling which can be applied to fuel cells and facilitates all recycling aspects (reuse through energy recovery). Specifically, a rating scheme allows the translation of design properties into quantitative scores based on the number of subassemblies being disassembled, an ideal (or the minimum) number of subassemblies, and the type, direction, tools used and difficulty rating (related to availability, position, force, and time) for each disassembly task. As an example, Cooper [2004a,b] applies Kroll *et al*.'s methods to the evaluation of various PEMFC flow field plate designs for stacks used in mobile applications. She finds that disassembly efficiencies are driven by the number of subassemblies (related to the number of cells in the stack and the use of plates with integrated cooling) and the removal of manifolding and cooling fluid fixtures. Disassembly issues identified using the Kroll *et al*. method included the following:

- All fluids must be removed prior to hardware disassembly.
- The removal of all stack subassemblies up tie rods (in a single direction) required the stack be fixed (e.g. to the floor by one of the end-plates). This process was improved using a platform to raise the stack as disassembly proceeded.
- The possibility that components fuse or become brittle during stack operation may be a concern, not only for PEMFC disassembly for the purposes of recycling, but also during maintenance operations.

However, for fuel cells more than other systems designed for disassembly, separability will be trumped by the need for intimate connections between materials that are not needed for electric or heat transfer or sealing. As such, energy recovery will most likely be limited to balance of plant components (mostly polymers).

12.4 Life cycle assessment of fuel cell fuels and materials

In addition to considerations of reuse, remanufacturing, materials recycling, and energy recovery for fuel cell hardware, life cycle assessment (LCA) can be used to quantify and interpret a broader set of impacts of the fuel cell systems from extraction of the raw materials for fabrication, through the fabrication process and system operation, to ultimate disposal of the equipment. The LCA protocol has been standardized by the International Organization for Standardization [ISO 1997, 1998a,b,c, 2003] to include four research phases. The first phase, goal and scope definition, describes the reasons for carrying out the study, the intended audience, geographic and temporal considerations, the system function and boundaries, data categories, comparative (or reference) systems, impact assessment and interpretation methods, and plans for critical review. Next, in the inventory model, the life cycle is subdivided into a set of 'unit processes' such that each encompasses the activities of a single operation or a group of operations. The inventory model quantifies material and energy use and waste by each unit process such that processes are linked to one another by economic flows (flows within the economic system such as the production of biomass or the use of fuel or steel) and consume and produce environmental flows (flows out of and into the environment such as the consumption of energy, land or iron ore, or carbon dioxide emissions). Thirdly, impact assessment estimates the contribution of environmental flows to environmental benefits (such as habitat protection) and impacts (such as global warming). Finally, the interpretation step identifies sensitive parameters as well as quantifies uncertainties in results.

Because the details of hardware design are currently primarily held in the private sector and because fuel cells have yet to move from pilot or demonstration projects to wide-scale production, fuel cell LCAs have typically focused on a single prototype with one or two assumed power densities only dictating the size of the stack (i.e. the same set of materials are assumed to have two possible power densities) or a single prototype created by alternative fabrication processes (i.e. all processes are assumed to fabricate stacks of equal performance). A preferred approach builds LCA models around computational models (electrochemical and thermodynamic) of the stack and balance of plant. Such models estimate system use of fuel and generation of electricity (their efficiency) and hardware needs (as material mass and including hardware replacement) over a specified system life and can be used to compare fuel cell systems with each other (e.g. design variants of PEMFCs can be compared, PEMFC systems can be compared with phosphoric acid fuel cells, PAFCs) and to systems based on other generation technologies (e.g., fuel cells can be compared to combustion technologies).

In such LCA models, it is critical to consider (1) the origin of the fuel and,

(2) the performance of both the stack and the balance of plant over the system life for a given set of fuel cell materials. With respect to the origin of the fuel, an opportunity exists to key fuel cell materials to fuel constituents to maximize efficiency, noting at the same time that there is significant variation in the life cycle energy and emissions in fuel production (as in Table 12.2) and that materials and energy use for on-site reforming of liquid petroleum and natural gases is important to consider. When considering stack and balance of plant performance, fuel cell materials, fuel utilization by the stack, and stack durability (including materials degradation) can be very important to life cycle results.

Consider for example an LCA of SOFC modules (with each module combining many stacks within a steel pressure vessel) that are mass produced

Table 12.2 Variation in life cycle impacts from the US average hydrogen production

	Gaseous hydrogen: central generation (based on natural gas and solar, nuclear, grid electricity, coal, and biomass energy sources)	Gaseous hydrogen: on-site generation (based on natural gas, ethanol, methanol, and grid electricity)	Liquid petroleum gas	Natural gas
Total energy consumption	–60–90%	–20–530%	–80%	–90%
Fossil energy consumption	–70–30%	–20–370%	–80%	–90%
Coal consumption	0–460%	–70–1580%	–80%	–100%
Natural gas consumption	–90–0%	–10–180%	–90%	–90%
Petroleum energy consumption	10–330%	–50–1650%	260%	–70%
Contribution to climate change (from as CO_2, N_2O, & CH_4)	–80–80%	–10–180%	–90%	–90%
Contribution to photochemical smog (from CH_4, NO_x, CO, & volatite organic compounds, VOCs)	–60–30%	–20–620%	–40%	–70%
Contribution to acidification (from SO_x & NO_x)	–40–40%	–40–790%	–60%	–80%
Particulate matter emissions (as PM10)	–30–700%	–50–1010%	–80%	–100%
Particulate matter emissions (as PM2.5)	–60–290%	–30–480%	–90%	–100%

[2]Based on data for 2007 from the US Department of Energy Argonne National Laboratory's Greenhouse Gases, Regulated Emissions, and Energy Use in Transportation (GREET) Model version 2.7 available at http://greet.anl.gov/

for central power production. It can be assumed that the length of the stack flow field can be related to not only the mass of stack materials (e.g. the amount of YSZ used) but also to the stack efficiency, which subsequently dictates in part the number of modules needed to achieve the desired power. Including consideration of the balance of plant, the length of the flow field also dictates the amount of fuel available for combustion off the stacks (also related to the chemistry of balance-of-plant emissions) and therefore the energy that might also be obtained by the overall system. Finally, suppose the SOFC plant is to be compared to construction of a natural gas power plant expected to last 40 years. If the degradation of fuel cell materials or the design configuration dictates that each SOFC module be replaced every 5 years, then the full life cycle (materials production through manufacturing through collection and recovery) of the SOFC models must be computed for eight system replacements as compared with the construction of a single natural gas plant. As a result, hardware design including recovery scenarios becomes critical to life cycle improvements.

Table 12.3 presents related LCA results. In the table, life cycle energy consumption, plant steel consumption, life cycle air emissions, generation of recyclables, solid waste generation, resource consumption, and materials production water consumption are compared for a baseline SOFC system with stacks using a YSZ electrolyte and 70% externally steam reformed Natural Gas + 30% internally steam reformed NG System at 90% fuel utilization and design variants. Specifically, changes due to variation of the fuel utilization, the use of hydrogen fuel, the use of a SSZ electrolyte in place of YSZ, variations on the manufacturing sequence, and an aggressive SOFC remanufacturing scenario[3] are included. In Table 12.3, a '+' indicates the design or manufacturing alternative improves upon the baseline, a '–' indicates the design or manufacturing alternative deteriorates from the baseline, and shaded cells indicate apparent optima or combinations of design alternatives that appear to optimize a single flow.

For these same systems, the LCA revealed the following:

- SOFC stack remanufacturing will reduce the contribution to all impacts from the baseline more than any other design alternative investigated because life cycle impacts are expected to track with plant steel consumption not fuel consumption. If remanufacturing is not an option, the use of recycled steel improves the life cycle profile.
- Although both offer improvements, the use of a more conductive electrolyte is expected to result in larger reductions in life cycle impacts than a switch to hydrogen fuel.

[3]The remanufacturing scenario investigated here assumes all materials except the ceramics can be reused over the 40 year period. Further research is needed to provide better estimates of the materials and energy flows associated with SOFC remanufacturing.

Table 12.3 Summary of design alternative life cycle inventories: comparison with the baseline

	YSZ- 70% SR Natural Gas + 30% ISR NG System U_f = 0.5, baseline manufacturing scenario	YSZ- 70% SR Natural Gas + 30% ISR NG System U_f = 0.6, baseline manufacturing scenario	YSZ- 70% SR Natural Gas + 30% ISR NG System U_f = 0.7, baseline manufacturing scenario	YSZ- 70% SR Natural Gas + 30% ISR NG System U_f = 0.8, baseline manufacturing scenario	YSZ- Hydrogen Central Plants U_f = 0.9, baseline manufacturing scenario	YSZ- Hydrogen Decentralized Plants U_f = 0.9, baseline manufacturing scenario	SSZ- 70% SR Natural Gas + 30% ISR NG System, baseline manufacturing scenario	YSZ- 70% SR Natural Gas + 30% ISR NG System U_f = 0.9, Co-fired cast layers	YSZ- 70% SR Natural Gas + 30% ISR NG System U_f = 0.9, Multi-fired cast anode and deposited elect and cathode	YSZ- 70% SR Natural Gas + 30% ISR NG System Remanufacturing Scenario U_f = 0.9, baseline manufacturing scenario
LC energy consumption	+	–	+	+	–	–	+	–	+	+
Plant steel consumption	+	+	+	+	–	–	+	–	+	+
Air emissions										
CH_4	+	+	+	+	+	+	+	–	+	+
CO	+	+	+	+	+	+	+	–	+	+
CO_2	+	+	+	+	+	+	+	–	+	+
N_2O	+	+	+	+	+	+	+	–	+	+
NO_x	+	+	+	+	+	+	+	–	+	+
Particulate matter and dust	+	+	+	+	+	+	+	–	+	+
SO_x	+	+	+	+	+	+	+	–	+	+
VOC	+	+	+	+	+	+	+	–	+	+
Recyclable materials										
Recyclable copper	+	+	+	+	+	+	–	+	–	–
Recyclable carbon steel	–	–	–	+	–	–	–	+	–	–
Recyclable stainless steel	–	–	–	–	–	–	–	+	–	–

Table 12.3 (Continued)

	YSZ- 70% SR Natural Gas + 30% ISR NG System U_f = 0.5, baseline manufacturing scenario	YSZ- 70% SR Natural Gas + 30% ISR NG System U_f = 0.6, baseline manufacturing scenario	YSZ- 70% SR Natural Gas + 30% ISR NG System U_f = 0.7, baseline manufacturing scenario	YSZ- 70% SR Natural Gas + 30% ISR NG System U_f = 0.8, baseline manufacturing scenario	YSZ- Hydrogen Central Plants U_f = 0.9, baseline manufacturing scenario	YSZ- Hydrogen Decentralized Plants U_f = 0.9, baseline manufacturing scenario	SSZ- 70% SR Natural Gas + 30% ISR NG System, baseline manufacturing scenario	YSZ- 70% SR Natural Gas + 30% ISR NG System U_f = 0.9, Co-fired cast layers	YSZ- 70% SR Natural Gas + 30% ISR NG System U_f = 0.9, Multi-fired cast anode and deposited elect and cathode	YSZ- 70% SR Natural Gas + 30% ISR NG System Remanufacturing Scenario U_f = 0.9, baseline manufacturing scenario
Solid waste generation										
Materials production	+	+	+	+	+	+	+	–	+	NC
Fuel cell equipment	+	+	+	+	–	–	+	–	+	NC
BOP equipment	–	–	–	–	+	+	+	NC	NC	NC
Resource use										
Bauxite, in ground	+	+	+	–	+	+	+	–	+	+
Clay, in ground	–	–	–	–	+	+	+	–	+	+
Coal and coke (non grid)	+	+	–	–	+	+	+	–	+	+
Copper, in ground	–	–	–	–	+	+	+	–	+	+
Iron ore, in ground	+	+	+	+	+	+	+	–	+	+
Limestone, in ground	+	+	+	–	+	+	+	–	+	+
Nickel, in ground	+	+	+	+	–	–	+	–	+	+
Sand and gravel, in ground	–	–	–	–	+	+	+	–	+	+
Materials production water consump.	+	+	+	+	+	+	+	–	+	+

Cells shaded dark grey represent an apparent optima; cells shaded light grey represent improvements among NG systems only.
NC indicates ‘no change.’

- Whereas the use of the manufacturing sequence 'multi-fired cast anode and deposited elect and cathode' at an estimated stack life of six years reduces the contribution to all impacts from the system which casts two out of the three components, the use of cofired sequences at an estimated stack life of four years are expected to increase the contribution to all impacts.

Thus, by considering differences in fuel cell materials and configuration, LCA can provide very specific plant and system design guidance. Further, as in the SOFC case study, understanding opportunities for fuel cell hardware recovery, especially for component remanufacturing and materials recycling, can be important to LCA results. In this way, LCA can contribute important findings as fuel cells move from laboratory and pilot status to wide-scale production.

12.5 Future trends

Fuel cell recovery is now and may in the future be voluntary or mandated. Voluntary systems, sometimes called 'extended product responsibility,' may mean the reuse and remanufacturing of components back into a company's products as an integral part of the company's business model. It may also mean the development of a close business relationship with material recyclers. Experiences in the automotive industry provide some insights into voluntary systems. Whereas the automotive industry is subject to recovery mandates, the very developed automotive recovery infrastructure has its origins in voluntary recovery driven by large volumes and material prices. Examples include the very well-developed steel recycling industry, noting that automotive manufacturers will take credit for upwards of 90% mass recycling of automobiles on the basis of steel recycling, and the recycling of platinum from catalytic converters driven by material prices.

Recovery of fuel cells may therefore be highly influenced by the need to match current sector trends through fuel cell vehicles. However, there are substantial differences in the materials used in fuel cell and current vehicle powertrains. A related analysis is provided by Cooper [2004a] in which design variants for fuel cell stacks and vehicles are compared with internal combustion-based vehicles. Table 12.4 presents estimated changes in materials use with select materials expected to be eliminated, substantially reduced, and added to the powertrain. Given wide-scale market penetration of fuel cell vehicles, materials with critical implications for recovery include iron (with the potential to substantially reduce the supply available for recovery), platinum group metals and carbon composites (potentially adding a need for recovery process availability and highly depending on fuel cell design variants), and batteries (which for the non-lead acid options should follow an increase in recovery process availability created by hybrid electric vehicles). Finally,

Table 12.4 Analysis of materials use in fuel cell and internal combustion powertrains

	Estimated percent change in powertrain
Aluminum	–33% to 6%
Batteries	0% to 1500%
Brass	–80%
Carbon cloth or paper	Added to the powertrain
Cobalt	Added to the powertrain
Copper	100% to 140%
Corderite	Eliminated from the powertrain
Graphite	0% to 250000%
Iron	–80%
Perfluorinated sulfuric acid	Added to the powertrain
Nickel	Added to the powertrain
Other plastics	Eliminated from the powertrain to 890%
Phenolic resin	0% to 1800%
Platinum group metals	1500% to 20500%
Rubber	–11%
Steels	–10% to 150%
Titanium	Added to the powertrain

since the current practice in the automotive industry is substantial disassembly prior to recovery, fluoropolymer contamination can expected to be at least managed.

Mandated recovery systems, known as takeback systems, can be privately or publicly operated with the computer industry providing insights for fuel cells. As has been the case for information technology equipment (computers, cell phones, etc.), EU activities will soon impact fuel cells through the EU Directive on Waste Electrical and Electronic Equipment (WEEE). WEEE requires that producers of electronic equipment who sell into EU countries: (1) label their equipment to notify customers that it needs to be recycled, and (2) ensure that their products are appropriately disposed of or recycled at the end of their life. The WEEE Directive became effective on August 13, 2005, with manufacturers required to meet target objectives for recycling by December 2006. Within WEEE, fuel cells fall under the category of 'Electrical and Electronic Components' which covers all manner of devices designed to produce, conduct, direct, convert or protect the user from electrical discharge. In addition to fuel cells, this category covers batteries, connectors, passive electronic components, electrical distribution and protection equipment, fuses, other types of power supplies and conditioners, relays and timers, switches, surge suppressors, and wires and cables.

In contrast to the automotive industry where the first and second lives of vehicles can reach 20 years, the use period for computers is far less and as a result has caused a glut of equipment being retired in communities throughout the globe. At the same time, computer equipment recovery infrastructures,

particularly materials recycling, have developed throughout the globe, and at times positioning the most hazardous recovery processes where environmental regulations, related costs, and worker protection are at a minimum. As a result, WEEE has attempted to address equipment recovery. Since the continuing deployment of fuel cell systems is occurring with WEEE in place, it can be expected that increased attention will be paid to hardware recovery in the near future.

For LCA, recent years have seen advancements including protocol standardization, growth in data availability, the dissemination of advanced software tools and well-defined computational methods, and sector-focused dissemination efforts. Specifically, sector-focused dissemination efforts seek to bring the results of the very complicated computational models to a format that is useful in design processes and that are either faster than model preparation can match or simpler for the non-LCA expert to understand. The most notable example is the use of LCA in the construction of buildings, which has seen the development and wide-scale marketing of rating systems, environmental product declarations, and software tools keyed to building construction, materials, and operation. A similar future may be in store for fuel cells, with for example Plug Power's ZTL concept leading the way, and an opportunity exists to develop such systems during the continuing growth of the fuel cell industry.

12.6 Sources of further information and advice

The most comprehensive guideline for fuel cell recovery has been provided by the Society of Automotive Engineers [2003]. Coupling this document with guidelines for design for disassembly and separation [Coulter *et al*., 1998; Kroll *et al*., 1996; Regel, 2002] provides specific guidance for both mobile and stationary PEM fuel cell systems. Material differences for other fuel cell types should lie mainly in stack materials. For LCA, background on the methodology and its application can be found in Schenck's 'LCA for Mere Mortals' [Schenck, 2003].

12.7 References

Bhakta, P. (1994) 'Recent technology and trends in automotive recycling,' *Journal of Metals*, **46**, 2, 36–39

Bras, B. (2005) 'Recycling Guidelines,' Course notes for ME 4171 – Environmentally Conscious Design and Manufacture, Georgia Institute of Technology, Atlanta, Georgia, available at http://www.srl.gatech.edu/education/ME4171/DFR-Improve.ppt

Brezet, H., van Hemel C. (1997) 'Ecodesign: a promising approach to sustainable production and consumption', Publisher: Paris, France: United Nations Environment Programme, Industry and Environment, Cleaner Production; The Hague: Rathenau Institute; and Delft, Netherlands: Delft University of Technology, available at http://www.worldcatlibraries.org/wcpa/top3mset/40057803

Cooper, J.S. (2003) 'Performance analysis of the use and recycling of platinum and other catalyst metals in pem fuel cell vehicles,' *Proceedings for the Air & Waste Management Association's 96th Annual Conference and Exhibition*, June 22–25

Cooper, J.S. (2004a) 'Design analysis of PEMFC bipolar plates considering stack manufacturing and environmental impact,' *Journal of Power Sources*, **129**, 152–169

Cooper, J.S. (2004b) 'Recyclability of fuel cell power trains,' *Proceedings of the SAE 2004 World Congress*, 2004-01-1136

Coulter S., Bras B., Winslow G. and Yester S. (1998) 'Designing for materials separation: lessons from automotive recycling,' *Journal of Mechanical Design*, **120**, 501–509

Elter, J., Cooper, J.S. (2007) 'Sustainability tools: applying life cycle assessment: a fuel cell case study,' American Society of Mechanical Engineers (ASME) and American Institute of Chemical Engineers (AIChE) Sustainable Engineering Series, 5th Session

Gabby, P.N. (2006) Lead, available at http://minerals.usgs.gov/minerals/pubs/commodity/lead/lead_mcs06.pdf

Handley, C., Brandon, van der, N.P., Vorst, R. (2002) 'Impact of the European vehicle waste directive on end-of-life options for polymer electrolyte fuel cells,' *Journal of Power Sources*, **106**, 344–352

Hotchkiss, M., Kelley, C., Ott, R., Elter, J. (2000) 'The Lakes story,' *Reflections*, **1**(4) 24–31

ISO (1997) ISO14040: Environmental Management – Life Cycle Assessment – Principles and framework

ISO (1998a) ISO14041: Environmental Management – Life Cycle Assessment – Goal and scope definition and inventory analysis

ISO (1998b) ISO14042: Environmental Management – Life Cycle Assessment – Life cycle impact assessment

ISO (1998c) ISO14043: Environmental Management – Life Cycle Assessment – Life cycle interpretation

ISO (2003) ISO14047: Environmental Management – Life cycle impact assessment – Examples of ISO 14042

Kroll, E., Beardsley, B., Parulian, A. (1996) 'A methodology to evaluate the ease of disassembly for product recycling,' *IIE Transactions*, **28**, 837–845

Kumar, V., Mather, K., Chong Tan, J. (2007) 'Recycling of metals,' accessed from http://www.doitpoms.ac.uk/tlplib/recycling-metals/printall.php

Mehta, V., Cooper, J.S. (2003) 'Review and analysis of PEM fuel cell design and manufacturing,' *Journal of Power Sources*, **114** (1) 32–53

Papp, J.F. (2005) Recycling – Metals, United States Geological Survey Minerals Yearbook, available at http://minerals.usgs.gov/minerals/pubs/commodity/recycle/

Regel, T. (2002) 'Designing Technical Products for Ease oF recycling: Fundamentals and rules for design,' German Engineering Standard VDI 2243

Schenck, R. (2003) 'LCA for mere mortals,' available at http://www.iere.org/mortals.html

Society of Automotive Engineers (2003) *Recommended Practice to Design for Recycling Proton Exchange Membrane (PEM) Fuel Cell Systems*, SAE J2594

van Schaik, A., Reuter, M.A., Castro, M.B., Remmerswaal, J.A.M. (2003) 'The role of product design and liberation in the vehicle optimization of recycling passenger vehicles,' Department of Applied Earth Sciences, Delft University of Technology, tracking number 210 OP

Wernick, I., Themelis, N.J. (1998) 'Recycling metals for the environment', *Annual Reviews Energy and Environment*, **23**, 465–497

Index